FACULTY OF ENGINEERING
AND ARCHITECTURE

A Multiscale Modeling Approach to Understand Reactivity and Interactions in Complex Molecular Environments with Applications in Polymer Chemistry

Elias Van Den Broeck

Doctoral dissertation submitted to obtain the academic degree of
Doctor of Chemical Engineering

Supervisor

Prof. Veronique Van Speybroeck, PhD

Department of Applied Physics
Faculty of Engineering and Architecture, Ghent University

April 2022

GHENT
UNIVERSITY

FACULTY OF ENGINEERING AND ARCHITECTURE

A Multiscale Modeling Approach to Understand Reactivity and Interactions in Complex Molecular Environments with Applications in Polymer Chemistry

Elias Van Den Broeck

Doctoral dissertation submitted to obtain the academic degree of
Doctor of Chemical Engineering

Supervisor
Prof. Veronique Van Speybroeck, PhD

Department of Applied Physics
Faculty of Engineering and Architecture, Ghent University

April 2022

GHENT UNIVERSITY

ISBN 978-94-6355-586-9
NUR 950, 913
Wettelijk depot: D/2022/10.500/27

Members of the Examination Board

Chair

Prof. Filip De Turck, PhD, Ghent University

Other members entitled to vote

Prof. Mercedes Alonso Giner, PhD, Vrije Universiteit Brussel
Prof. Karen De Clerck, PhD, Ghent University
Prof. Ahmad Reza Mehdipour, PhD, Ghent University
Prof. Louis Vanduyfhuys, PhD, Ghent University
Prof. Johan Winne, PhD, Ghent University

Supervisor

Prof. Veronique Van Speybroeck, PhD, Ghent University

This research has been conducted at the **Center for Molecular Modeling**, in collaboration with:

- Supramolecular Chemistry Group, Ghent University (Prof. Richard Hoogenboom)
- The Organic Synthesis (ORSY) group, University of Antwerp (Prof. Bert Maes)
- The CESAM research unit from the Center for Education and research on Macromolecules at the University of Liège (Prof. Christophe Detrembleur)
- Center for Sustainable Catalysis and Engineering, KULeuven (Prof. Bert Sels)
- The department of Materials, Textiles and Chemical Engineering, Ghent University (Prof. Karen De Clerck)

Contents

Preface

Na een schamele 10 jaar op de universiteit te hebben doogebracht heb ik het summum nu wel bereikt. Het behalen van dit doctoraat is het resultaat van vier en half jaar hard werken en intensief onderzoek doen. Om te starten aan een doctoraat moet je in eerste instantie bepaalde kansen krijgen, kansen die mij werden aangeboden door verscheidene mensen in de loop der tijd en waar ik gretig gebruik van heb gemaakt. Bovendien voer je onderzoek nooit uit als individu maar als team en het spreekt dus voor zich dat er vele mensen zijn die ik expliciet dien te bedanken zowel op professioneel als persoonlijk vlak.

Ik zou graag willen beginnen met de mensen die mij de kans gegeven hebben om aan heel dit avontuur te beginnen. Mama, papa onwaarschijnlijk bedankt om mij de mogelijkheid te geven om te gaan studeren, op kot te gaan en mijzelf te ontplooien. Zonder jullie was dit zeker nooit gelukt en ik ben jullie dan ook ontzettend dankbaar.

Ook Veronique zou ik willen bedanken, in eerste instantie om mij de kans te geven om een doctoraat te starten aan jouw groep en in tweede instantie voor de begeleiding binnen het kader van mijn master- en doctoraatsthesis. Ook de zelfstandigheid die ik kreeg, is iets waar ik dankbaar voor ben. Hoewel ik het me tijdens mijn doctoraat soms beklaagd heb, heeft het me voorzien van een 'skillset' die ik ongetwijfeld kan gebruiken in de toekomst.

Ondanks het feit dat ik maar met weinig collega's van het CMM raakpunten had op het vlak van onderzoek, heb ik toch enorm veel aan hen gehad gedurende mijn doctoraat. Eerst en vooral wil ik Louis en Toon bedanken voor de wetenschappelijke input tijdens mijn onderzoek. Ook mijn kantoorgenoten Pieter en Kim wil ik bedanken voor de verlichtende *intermezzo's* tijdens de intensieve werkdagen en het wetenschappelijk advies dat ze mij gaven bij enkele moeilijke vraagstukken. Ook Leen verdient een bedankje voor de praktische en administratieve ondersteuning tijdens mijn doctoraat. Verder zou ik ook nog graag Massimo willen bedanken, met wie ik enorm goed en nauw heb samengewerkt binnen het BioFact project. De vele discussies hebben ons werk en onze chemische kennis ongetwijfeld naar een hoger niveau getild.

Naast mijn collega's zou ik ook graag mijn experimentele partners willen bedanken. Zij stelde de kritische wetenschappelijke vragen nodig om mijn onderzoek te doen en gaven de nodige experimentele input om mijn onderzoek te onder-

steunen, te valideren en mogelijk te maken. Meer specifiek bedank ik graag Jeroen, Mathias, Xian en Fabiana en bijgevolg ook Prof. Maes, Prof. Sels en Prof. Detrembleur voor de samenwerking in het kader van het BioFact project. Binnen de projecten gerelateerd aan polyoxazolines wil ik ook Jana, Prof. De Clerck, Bart en Prof. Hoogenboom bedanken. Verder is er ook heel wat onderzoek gebeurd wat niet expliciet werd opgenomen in dit doctoraat maar zeker niet minder belangrijk is. Hiervoor wil ik graag Sari, Prof. D'hooghe, Kim D. , Prof. Stevens, Kim P. en Prof. De Meester bedanken.

Tot slot, wil ik graag de 'Goldies' bedanken om mij tijdens de week en in het weekend van de nodige ontspanning, goede raad en een luisterend oor te voorzien. Natuurlijk mag ik de beste niet vergeten, Lien, jij stond me bij dag en nacht, lockdown of geen lockdown, assisteerde waar mogelijk en luisterde naar mijn gezeur als het nodig was. Expliciet wil ik je ook nog de nodige credits geven voor het professionaliseren van enkele van de figuren verwerkt in dit doctoraat en het ontwerp van de uitnodigingen.

Elias Van Den Broeck
Gent, 20 april 2022

List of Figures

List of Schemes

List of Tables

Abbreviations and Acronyms

API active pharmaceutical ingredient.

ASD amorphous solid dispersion.

BCS Biopharmaceutical Classification System.

bis-αCC bis(α-alkylidene carbonate).

BOA Born-Oppenheimer approximation.

αCC 4,4-dimethyl-5-methylene-1,3-dioxolan-2-one.

CI configurational interaction.

CROP cationic ring-opening polymerization.

CV collective variable.

DBU 1,8-diazabicyclo[5.4.0]undec-7-ene.

DFT density functional theory.

DMSO dimethylsulfoxide.

EOS Excellence of Science.

FBZ flubendazole.

FES free energy surface.

GGA generalized gradient approximation.

GIC generalized internal coordinates.

HF Hartree-Fock.

HPW hot-pressurized water.

IEF integral equation formalism.

IPM independent-particle model.

LCAO linear combination of atomic orbitals.

LCC lignin-carbohydrate complex.

LCST lower-critical-solution-temperature.

LDA local density approximation.

MD molecular dynamics.

MM molecular mechanics.

MTD metadynamics.

OFFI Open Force Field Initiative.

PAOx poly(2-alkyl/aryl-2-oxazoline).

PBC periodic boundary conditions.

PC polycarbonates.

PCM polarizable-continuum model.

PEG poly(ethylene glycol).

PES potential energy surface.

PEtOx poly(2-ethyl-2-oxazoline).

POx poly(2-oxazoline).

QM quantum mechanics.

RC reaction coordinate.

RCF reductive catalytic fractionation.

RDF radial distribution function.

SCF self-consistent field.

SCRF self-consistent reaction field.

SKIE solvent kinetic isotope effect.

step-cop step copolymerization.

STQN transit-guided quasi-Newton.

TS transition state.

TST transition-state theory.

US umbrella sampling.

$\mathcal{V}$ potential energy.

VdW Van der Waals.

WHAM weighted-histogram analysis method.

Summary

In this doctoral thesis, molecular modeling is employed to gain a fundamental understanding of reactivity and interactions in complex molecular environments. More specifically a broad range of modeling approaches is used to solve various scientific questions related to polymer chemistry, ranging from short to long timescales and from small to large scale systems. We show that molecular modeling is indeed an indispensible tool to understand polymerization features, governing molecular interactions, reaction mechanisms, reaction kinetics and material properties. Given the complexity of the studied systems, a complementary set of techniques is necessary to answer the scientific question at hand combining both static and dynamic approaches with classical and/or quantum mechanical models.

Additionally, to obtain an accurate description of the molecular system under investigation and its molecular environment, models need to account for the operating conditions such as realistic temperatures and a proper solvent environment. In this thesis we adopted, to a large extent, molecular dynamics (MD) simulations while explicitly considering the solvent environment. The work was performed in close collaboration with various experimental partners and to answer the scientific questions at hand, we had to apply a multiscale modeling approach. To this end, we have set up different protocols and workflows throughout this thesis in order to construct and equilibrate the molecular systems realistically and describe the corresponding chemistry in their complex molecular environments. Typically a trade-off is made between accuracy and computational cost when setting up the molecular model which inherently depends on the system under investigation and the scientific problem which has to be solved.

The applications studied in this thesis are situatied in two main areas, i.e. the "BioFactory" (Chapter 4) focusing on the development of next-generation (lignin-first) biorefineries and the chemistry and properties of Poly(2-alkyl-2-oxazolines) (Chapter 5). The BioFactory, refers to the BioFact Excellence of Science (EOS) project which is a collaboration between partners from the KULeuven (Prof. Bert Sels, Prof. Dirk De Vos), Université Libre de Bruxelles (Prof. Gwilherm Evano), Université de Liège (Prof. Christophe Detrembleur), University of Antwerp (Prof. Bert Maes), Leibniz-institut für Katalyse (Prof. Matthias Beller) and Ghent University (Prof. Veronique Van Speybroeck), with the mission to develop the next-generation biorefinery capable of converting wood chips to high-added value chemicals in an efficient and economically feasible way. Central within this new biorefinery concept is the *lignin-first* approach, e.g. reductive catalytic fractionation, which aims to

process lignocellulosic biomass by stabilizing and depolymerizing lignin towards a selective set of lignin monomers while the (hemi)cellulose fraction remains intact. In this dissertation we focus on the production of on the one hand platform molecules from these lignin-derived compounds which can serve as drop-in alternatives for the petrochemically based ones; and, on the other hand, on a new class of polymers, i.e. new polycarbonates, which combine CO_2-sourced bis(α-alkylidene carbonate) (bis-αCC) and thiols and (lignin-derived) alcohols. These new polycarbonates, are a more sutainable family of polymers which have interesting features for example for the production of organic glasses, packaging materials, ...

In the field of the chemistry of Poly(2-alkyl-2-oxazolines), we have investigated the reactivity of 2-oxazolines bearing unsaturated sidechains on the one hand and the application of poly(2-ethyl-2-oxazoline) for the production of new drug-delivery systems in the form of amorphous solid dispersions (ASDs), on the other hand. This work was performed in the framework of a collaboration between the Center for molecular modeling, the Supramolecular chemistry group of Prof. Richard Hoogenboom and the departement of Materials, Textiles and Chemical Engineering with the group of Prof. Karen De Clerck, both from Ghent University.

Within the framework of the BioFactory research, we have at first instance investigated the Brønsted acid catalyzed *O*- and *C*-dealkylation in hot pressurized water of lignin-derived compounds, i.e. guaiacol and dihydroconiferyl alcohol respectively, with formation of catechol which can be used as a platform molecule. This work was performed in close collaboration with Prof. Bert Maes from Organic Synthesis group from the University of Antwerp and with Prof. Bert Sels from the Center of Sustainable Catalysis and Engineering from the KULeuven. We have performed a multiscale molecular modeling approach to unravel the mechanistic features of this new conversion route for lignin-derived monomers towards the platform molecule catechol. In **Paper I**, we have used a combined static and dynamic density functional theory (DFT) approach to provide evidence that the *C*-dealkylation mechanism proceeds through a retro-vinylogical aldol condensation reaction. Within the static DFT calculations a hybrid solvation model was used to account for the solvent environment. Then, in order to investigate intermediate stability at operating conditions while accounting for the solvent more accurately, i.e. explicitly, classical MD simulations were used. This was done because different intermediates were obtained depending on the amount of solvent included in the hybrid solvation model, highlighting the need for an explicit solvent treatment. To this end, the mechanism, reactivity and kinetics of the *O*-dealkylation process was investigated in a follow-up paper applying an enhanced sampling MD approach where we account for the complex reaction environment and the operating conditions more accurately. The results of this work are reported in **Paper II** where we performed a comparative study between the reaction taking place in a heterogeneous catalyzed system with a Broønsted acidic zeolite and a homogeneous catalyzed system namely in the presence of hydrochloric acid. From first principle MD simulations we deduced kinetic and thermodynamic data, which was then used in a microkinetic model to determine the governing mechanism. The data was extracted from the simulations using in-house developed software, i.e. Ther-

moLIb. Using this approach we concluded that the *O*-dealkylation mechanism of guaiacol proceeds through a concerted S_N2 reaction with formation of catechol. Additionally it was shown that both the heterogeneous and homogeneous catalyzed systems proceed via this pathway, however, in the former system a rate acceleration is reported which was attributed to a confinement-induced activity increase of the water molecules within the zeolite. Finally, an in-depth experimental kinetic study was performed, investigating both the homo- and heterogeneous catalyzed reactions, verifying our computational results. In this work we hence revealed all mechanistic features of both the homo- and heterogeneous catalyzed systems furthermore illustrating the potential of zeolites to catalyze this conversion process as a more benign alternative. The results can be used for the future rational design of catalysts in these complex environments.

In a next step we have explored the step-copolymerization of lignin-derived monomers, i.e. diols, and dithiols with bis-αCC for the production of new polycarbonates. This work was performed in collaboration with Prof. Christophe Detrembleur from the CESAM research unit at the university of Liège. To study the organocatalyzed copolymerization, catalyzed by 7-methyl-1,5,7-triazabicyclo[4.4.0]-dec-5-ene (DBU) we have used 4,4-dimethyl-5-methylene-1,3-dioxolan-2-one (αCC) as a model cyclic carbonate, which was reacted with benzylthiol in **Paper III** and with butanol, cyclohexanol and benzylalcohol in **Paper IV**. In both papers, static DFT calculations are performed in combination with an implicit solvation model to investigate the reaction mechanism of the polymerization. In **Paper III** preliminary results were obtained, which do not account for the organocatalyst or an explicit solvent environment, whereas in **Paper IV** the model was extended and more advanced simulations were performed to explicitly account for the catalyst and to assess the intermediate stability in presence of the solvent. To this end, classical MD simulations have been used to investigate the intermediate stability and the role of the catalyst in an explicit solvent environment. Furthermore, alternative pathways for the formation of tetrasubstituted ethylene carbonates were explored in order to better accomodate the experimental results.

In **Paper III** it is shown experimentally that for the model reaction two different products can be obtained, i.e. a β-oxothiocarbonate and a tetrasubstituted ethylene carbonate, with a product distribution varying depending on the reaction time. Computationally, the preliminary DFT calculations explain this observation in terms of the difference in activation barriers for the nucleophilic attack on the different electrophilic sites of the carbonate, i.e. the carbonyl and vinylene moieties, and the stability of the resulting product. These results revealed that the β-oxothiocarbonate product is under kinetic control while the tetrasubstituted ethylene carbonate product is under thermodynamic control. In continuation of this work, alternative pathways were explored for the formation of the tetrasubstituted ethylene carbonate in **Paper IV** using more accurate models which explicitly account for the organocatalyst. In this paper, we showed, by studying the alcoholysis of αCC, that tetrasubsituted ethylene carbonates are not formed due to a nucleophilic attack on the vinylene moiety, but instead by a nucleophilic attack on the ketone functionality of the formed β-oxocarbonate. On the other hand, we show in this paper that the DBU catalyst alters the reactivity specifically for benzylalcohol

by π-type interactions affecting the stability of the intermediates. Finally, the formation of experimentally observed sideproducts is rationalized by computing electrophilicity indices for the various carbonyl moieties in the β-oxocarbonate, succesfully explaining the experimentally observed product distributions. Hence the mechanistic insights obtained in **Paper III** and **Paper IV** have helped to rationalize and steer the polymerization outcome for the step-copolymerization of bis(α-alkylidene carbonate)s with dialcohols and dithiols and may be used to further broaden the scope of this new class of polymers in the future.

The next set of applications considered in this thesis concerns another interesting class of polymers which has emerged in the past decades namely poly(2-alkyl/aryl-2-oxazoline) (PAOx). PAOx are considered as bio-inspired pseudopeptides which show similar stealth behavior to the golden standard poly(ethylene glycol) (PEG). These polymers are biocompatible and thermosensitive which make this class ideal for drug-delivery applications. PAOx are generated by the cationic ring-opening polymerization (CROP), a living chain-polymerization of 2-alkyl-2-oxazolines, for which the features can be altered through the sidechain on the 2-position (among others). In close collaboration with the Supramolecular chemistry group of Prof. Richard Hoogenboom at Ghent University, we have investigated the effect of unsaturations in the alkyl sidechain on the polymerization kinetics. This work is reported in **Paper V**. Based on previous work a rate-enhancing effect in the CROP was anticipated, by means of cation-π interactions. To this end, the effect of unsaturations sidechains on the polymerization rate was investigated for 2-(butyl)- (*n*-ButylOx), 2-(but-3-enyl)- (ButenOx), 2-(but-3-ynyl)- (ButynOx) and 2-(pent-4-enyl-)-2-oxazoline (PentynOx). A multiscale modeling approach was applied combining static and MD simulations of trimeric and pentameric systems to assess the presence of cation-π interactions and its effect on the polymerization kinetics. At first instance the solvent was not accounted for, however in a final stage the results are verified using both implicit and explicit solvent models to account for the presence of acetonitrile. We showed that a difference in polymerization kinetics exists because of a preorganization effect which stabilizes the reactant region (the pre-reactive complex) through cation-π, π-π and π-induced dipole interactions. In this way it enhances the association behavior of the attacking monomer with the growing chain end. The results indicated that *n*-ButylOx polymerizes more slowly than ButenOx which in turn is slower than ButynOx which polymerizes slighly faster or equally fast with respect to PentynOx, i.e. due to entropic constraints. This trend was then experimentally confirmed by performing kinetic experiments on the monomers of interest. Within this study, we thus showed that the apparent rate constant is increased by the presence of π-type interactions because of an increased association constant. These observations can have important implications in future polymerizations as this can either be used to explain the polymerization outcome or to devise new polymerization reactions which exploit these interactions.

Next to the polymerization kinetics of various monomers bearing unsaturated sidechains, we have also studied the application of 2-ethyl-2-oxazoline and the corresponding polymer poly(2-ethyl-2-oxazoline) (PEtOx). This is a hydrophilic polymer with lower-critical-solution-temperature behavior making it suitable for

biomedical applications. To this end, PEtOx was explored as carrier material for the construction of amorphous solid dispersions (ASDs) in order to increase the solubility and hence bioavailability of poorly water-soluble active pharmaceutical ingredient (API) (which are about 90% of all drug molecules). PEtOx can on one hand increase the dissolution rates of these APIs and on the other potentially also exert a supersaturation effect upon dissolution. This work was performed in close collarboration with Prof. Richard Hoogenboom (*vide infra*) and Prof. Karen De Clerck from the department of Materials, Textiles and Chemical Engineering (Ghent University) who have pioneered the production of these ASDs by means of electrospun nanofibers. As model active pharmaceutical ingredient (API), flubendazole (FBZ) was chosen which is a highly effective API against various tropical diseases.

At first instance it was investigated, by means of static DFT calculations, whether PEtOx can succesfully disrupt the FBZ-FBZ interactions in order to assess the potential compatability of the polymer matrix with the API. This assesment was of importance as incompatible materials will result in phase separation which is undesired for drug-delivery applications. The results showed that PEtOx and FBZ compete with one another to interact with other FBZ molecules in the ASD, which indicated the suitability of PEtOx as potential polymeric matrix.

Secondly, large scale MD simulations are performed (containing $>$ 40000 atoms) to investigate the interactions and drug mobility in its complex molecular environment. To this end, a force field was derived for PEtOx and a computational protocol was set up to generate ASD structures, containing 10 PEtOx centimers and 476 drug molecules, and to equilibrate the system towards a configuration representing the real systems more closely. We furthermore included an extensive validation procedure where we determine glass-transition temperatures, XRD-diffractograms and densities computationally. We could indeed show that our proposed computational protocol succeeds to obtain quantities in close agreement with experiment. The resulting structures thus represent the electrospun nanofibers in a realistic way.

Finally, the drug mobility was assessed by calculating the self-diffusivity of FBZ in different molecular environments. This showed that FBZ is succesfully kinetically trapped within the polymer matrix through the preparation procedure, i.e. solvent electrospinning. We furthermore showed that the strong and stable hydrogen bonding interactions between FBZ and PEtOx dominate within the ASD by analyzing the hydrogen bonding patterns and the hydrogen bonding lifetimes. Hence, overall the results showed that stable PEtOx-based ASDs with high drug-loadings can be produced by means of electrospinning because of, on the one hand, the formation of strong hydrogen bonds of the API with the polymer matrix and, on the other hand, because the API is succesfully kinetically trapped by this experimental procedure.

Within this dissertation we have successfully shown that molecular modeling is essential to understand reaction mechanisms, reaction kinetics, molecular interactions and material properties within the field of polymer science. However, given

the complexity of the systems and/or investigation, often a multiscale modeling approach is necessary. Various methods at various length and time scales yield complementary insights. In any modelling approach, an optimal balance between computational feasibility and accuracy needs to be considered. Throughout this work we furthermore provided various simulation protocols and approaches to investigate molecular systems in their complex molecular environments. On the one hand we focus on how to treat solvent explicitly and, on the other hand, how to tackle realistic polymeric systems. It was furthermore shown that accounting for the environment in an appropriate way is important to obtain accurate results. With molecular models progressing to a more accurate and more realistic level, future computational chemistry is expected to gain importance. It will be used to guide experimentalists in the rational design of experiments, materials and catalysts and to gain fundamental understanding of chemical processes. And, who knows, soon exploring chemistry becomes a hybrid study combining computations and experiments . . .

Samenvatting

In deze doctoraatsthesis wordt gebruik gemaakt van moleculaire modellering om een fundamenteel begrip te krijgen van de reactiviteit en de interacties in complexe moleculaire omgevingen. Meer specifiek wordt er een brede waaier aan modelleringsaanpakken gebruikt om verschillende wetenschappelijke vragen te beantwoorden binnen het domein van de polymeerchemie. Hierbij worden fenomenen op korte en lange tijdschalen onderzocht met zowel groot- als kleinschalige systemen. We tonen aan dat moleculair modelleren inderdaad een onmisbaar hulpmiddel is om polymerisatie eigenschappen, controllerende moleculaire interacties, reactiemechanismen, reactiekinetiek en materiaal eigenschappen te begrijpen. Gezien de complexiteit van de bestudeerde systemen, is een complementaire set aan technieken nodig om bepaalde wetenschappelijke vragen te beantwoorden waarbij statische en dynamische aanpakken gecombineerd worden met klassieke en/of kwantummechanische modellen.

Om een accurate beschrijving van het onderzochte moleculaire systeem en zijn moleculaire omgeving te kunnen bekomen, moeten modellen bovendien rekening houden met de werkingsomstandigheden, zoals een realistische temperatuur en een adequate solventomgeving. In deze thesis hebben we extensief gebruik gemaakt van moleculaire dynamica (MD) simulaties waarbij het solvent expliciet in rekening wordt gebracht. Het werk werd uitgevoerd in nauwe samenwerking met verschillende experimentele partners en er werd gebruik gemaakt van een multischaal modelleringsaanpak. Hiertoe hebben we verschillende protocollen en workflows opgesteld doorheen deze thesis om zo realistisch mogelijk moleculaire systemen te construeren en macroscopische grootheden af te leiden. Wanneer dergelijke moleculaire modellen worden opgezet, wordt er typisch een afweging gemaakt tussen accuraatheid en computationele kost waarvoor de keuze inherent samenhangt met het onderzochte systeem en het wetenschappelijk probleem dat dient opgelost te worden.

De toepassingen die bestudeerd worden in deze thesis situeren zich binnen twee belangrijke toepassingsdomeinen, namelijk de "BioFactory" (Hoofdstuk 4) gaande over de ontwikkeling van (lignin-first) bioraffinaderijen van de volgende generatie en de chemische en materiaaleigenschappen van Poly(2-alkyl-2-oxazolines) (Hoofdstuk 5). De BioFactory, refereert naar het BioFact Excellence of Science (EOS) project wat een samenwerking is tussen partners van de KULeuven (Prof. Bert Sels, Prof. Dirk De Vos), Université Libre de Bruxelles (Prof. Gwilherm Evano), Université de Liège (Prof. Christophe Detrembleur), Universiteit Antwerpen (Prof. Bert

Maes), Leibniz-institut für Katalyse (Prof. Matthias Beller) en Universiteit Gent (Prof. Veronique Van Speybroeck), met als missie de bioraffinaderijen van de volgende generatie te ontwikkelen welke instaat zijn om houtsnippers om te zetten in chemicaliën met een hoge toegevoegde waarde op een efficiënte en economisch haalbare manier. Centraal binnen dit nieuwe bioraffinaderijconcept is de *lignin-first* aanpak, zoals bijvoorbeeld reductieve katalytische fractionatie, welke doelt op het verwerken van lignocellulose biomassa door middel van stabilisatie en depolimerisatie van lignine naar een selectieve set van ligninemonomeren. Dit alles terwijl de (hemi)cellulose fractie intact blijft. In dit proefschrift focussen we enerzijds op de productie van platformmolecules, startend van deze lignine-afgeleide componenten welke gebruikt kunnen worden als drop-in alternatieven voor de petrochemisch gebaseerde componenten; en anderzijds op de productie van een nieuwe klasse van polymeren, namelijk nieuwe polycarbonaten, welke CO_2-gebaseerde bis(α-alkylidene carbonate) (bis-αCC) combineren met thiolen en (van-lignine-afgeleide) alcoholen. Deze nieuwe polycarbonaten, zijn een meer duurzame familie van polymeren en hebben interessante eigenschappen voor de productie van biologische glazen, verpakkingsmaterialen, ...

Met betrekking tot Poly(2-alkyl-2-oxazolines), hebben we aan de ene kant de reactiviteit onderzocht van 2-oxazolines met ongesatureerde zijketens en aan de andere kant een toepassing van poly(2-ethyl-2-oxazoline) waarbij het polymeer gebruikt wordt voor de productie van nieuwe medicijnafgiftesystemen in de vorm van amorfe vastestof dispersies (ASD). Dit werk werd uitgevoerd in het kader van een samenwerking tussen het Centrum voor moleculair modellering, de Supramolecular chemistry group geleid door Prof. Richard Hoogenboom en het departement of Materials, Textiles and Chemical Engineering, meer in het bijzonder de onderzoeksgroep van Prof. Karen De Clerck, beide gevestigd aan Universiteit Gent.

Binnen het kader het BioFactory onderzoek hebben we in eerste instantie de Brønsted zuur gekatalyseerde *O*- en *C*-dealkylatie in heet water onder druk van lignine-afgeleide componenten onderzocht, i.e. respectievelijk guaiacol en dihydroconiferyl alcohol, met de vorming van catechol wat gebruikt kan worden als platform molecule. Dit werk werd uitgevoerd in samenwerking met Prof. Bert Maes van de Organische Synthese groep van Universiteit Antwerpen en met Prof. Bert Sels van het Centrum voor duurzame processen en katalyse van de KULeuven. We hebben een multischaal moleculaire modelleringsaanpak uitgevoerd om de mechanistische eigenschappen van deze nieuwe conversieroute die lignine-afgeleide monomeren naar catechol omzet, te ontrafelen. In **Paper I** hebben we een gecombineerde statische en dynamische dichtheidsfunctionaal theorie (DFT) aanpak gebruikt om bewijs te leveren dat het *C*-dealkylatie mechanisme verloopt via een retro-vinylogische aldol condensatiereactie. Voor de statische DFT berekeningen werd een hybride solvatatie model gebruikt om de solvent omgeving in rekening te brengen. Vervolgens werden klassieke MD simulaties gebruikt om de stabiliteit van de intermediairen te onderzoeken bij werkingsomstandigheden waarbij expliciet rekening werd gehouden met het solvent. Dit werd gedaan omdat er verschillende intermediairen werden bekomen afhankelijk van de hoeveelheid

solvent die in rekening werd gebracht in het hybride solvatatie model, wat de nood voor een expliciete behandeling van het solvent benadrukt. In een vervolgartikel, werden hiertoe het mechanisme, de reactiviteit en de kinetiek van het *O*-dealkylatie proces onderzocht waarbij een enhanced sampling MD aanpak werd gebruikt om op een meer accurate manier rekening te houden met de complexe reactie omgeving en de werkingsomstandigheden. De resultaten van dit werk zijn gerapporteerd in **Paper II** waarin we een vergelijkende studie hebben uitgevoerd voor de reactie in een heterogeen gekatalyseerd systeem met een Brønsted zure zeoliet en een homogeen gekatalyseerd systeem, in aanwezigheid van zoutzuur. Uitgaande van MD simulaties gebasseerd op een kwantummechanische beschrijving van het potentieel energie oppervlak (PES), zogenoemde first principle MD, werden kinetische en thermodynamische data afgeleid welke vervolgens werden gebruikt in een microkinetisch model om het controllerende mechanisme te bepalen. De data werd geëxtraheerd uit de simulaties gebruikmakend van in-huis ontwikkelde software, i.e. ThermoLIB. Via deze aanpak hebben we geconcludeerd dat het *O*-dealkylatie mechanisme van guaiacol verloopt via een geconcerteerde S_N2 reactie met vorming van catechol. Daarbovenop werd er aangetoond dat deze route domineert voor zowel het heterogeen als het homogeen gekatalyseerde systeem, maar werd voor het heterogeen gekatalyseerde systeem een versnelling van de reactiesnelheid waargenomen ten opzichte van het homogene systeem. Dit werd toegeschreven aan een activiteitstoename van de water moleculen in de zeoliet geïnduceerd door de nanoporeuze omgeving. Tenslotte werd er een grondige experimentele kinetische studie uitgevoerd, zowel voor het homogene als voor het heterogene systeem, waarbij de computationele resultaten werden geverifieerd. In dit werk hebben we dus alle mechanistische eigenschappen blootgelegd voor zowel het homogeen- als het heterogeen gekatalyseerde systeem, waarbij we verder ook het potentieel van zeolieten aantonen om dergelijke conversieprocessen te katalyseren als duurzamer alternatief. De resultaten kunnen verder gebruikt worden voor het toekomstige rationele ontwerp van katalysatoren in dergelijke complexe omgevingen.

In de volgende stap hebben we de stap-copolymerisatie verkend van lignine-afgeleide monomeren, i.e. diolen, en dithiolen met bis-αCC voor de productie van nieuwe polycarbonaten. Dit werk is uitgevoerd in samenwerking met Prof. Christophe Detrembleur van de CESAM onderzoekseenheid aan de universiteit van Luik. Om de organo-gekatalyseerde copolymerisatie te bestuderen, gekatalyseerd door 1,8-diazabicyclo[5.4.0]undec-7-ene (DBU), hebben we 4,4-dimethyl-5-methylene-1,3-dioxolan-2-one (αCC) gebruikt als model component voor cyclische carbonaten, welke gereageerd werd met benzylthiol zoals beschreven in **Paper III** en met butanol, cyclohexanol en benzylalcohol opgenomen in **Paper IV**. In beide papers werden statische DFT berekeningen uitgevoerd in combinatie met een impliciet solvatatie model om zo het reactiemechanisme van de polymerisatie te onderzoeken. Waar in **Paper III** preliminaire resultaten werden bekomen, die geen rekening houden met de organokatalysator of een expliciete solventomgeving, werd in **Paper IV** het model uitgebreid en werden meer geavanceerde simulaties uitgevoerd opdat wel rekening gehouden kon worden met de katalysator en opdat de stabiliteit van de intermediairen in aanwezigheid van solvent kon worden geëvalueerd. Hiertoe

werden klassieke MD simulaties gebruikt om de stabiliteit van de intermediaire en de rol van de katalysator te onderzoeken in een expliciete solvent omgeving. Verder werden ook alternatieve routes voor de vorming van tetragesubstitueerd ethyleen carbonaten verkend om zo de experimentele resultaten beter te beschrijven.

In **Paper III** wordt experimenteel aangetoond dat voor de modelreactie twee verschillende producten kunnen worden bekomen, i.e. een β-oxothiocarbonaat en een tetragesubstitueerd ethyleen carbonaat, met een productdistributie die afhangt van de reactietijd. Computationeel werd deze observatie verklaard, via preliminaire DFT berekeningen, in termen van het verschil in activatiebarrières voor de nucleofiele aanval op de verschillende elektrofiele sites van het carbonaat, i.e. de carbonyl en de vinylene groepen, en in termen van de stabiliteit van het resulterende product. De resultaten toonden dat het β-oxothiocarbonaat product onder kinetische controle wordt gevormd terwijl het tetragesubstitueerd ethyleen carbonaat onder thermodynamische controle wordt gevormd. Als vervolg van dit werk, werden er alternatieve routes verkend in **Paper IV** voor de vorming van het tetragesubstitueerd ethyleen carbonaat gebruikmakend van meer accurate modellen die expliciet rekening houden met de organokatalysator. In dit artikel hebben we, door de alcoholyse van αCC te bestuderen, aangetoond dat tetragesubstitueerde ethyleen carbonaten niet gevormd worden door een nucleofiele aanval op de vinylene groep maar wel door de nucleofiele aanval op de keton functionaliteit van het gevormde β-oxocarbonaat. We tonen verder ook aan in dit artikel dat de DBU katalysator de reactiveit beïnvloedt, specifiek voor benzylalcohol, door middel van π-type interacties welke de stabiliteit van de intermediairen beïnvloedt. Tot slot, werd de vorming van de experimenteel waargenomen bijproducten gerationaliseerd door middel van de berekening van elektrofiliciteitsindices voor de verschillende carbonyl eenheden in het β-oxocarbonaat, waarmee de experimenteel geobserveerde productdistributies correct verklaard konden worden. Bijgevolg hebben de mechanistische inzichten, bekomen in **Paper III** en **Paper IV**, geholpen om de polymerisatie uitkomst te rationaliseren en bij te sturen voor de stap-copolymerisatie van bis-αCCs met dialcoholen en dithiolen. Verder kunnen deze resultaten gebruikt worden om het toepassingsgebied van deze nieuwe klasse van polymeren uit te breiden in de toekomst.

De volgende set toepassingen die werden onderzocht in deze thesis gaan over een andere interessante klasse van polymeren welke het laatste decennia veel interesse hebben opgewekt, namelijk poly(2-alkyl/aryl-2-oxazoline) (PAOx). PAOx worden beschouwd als bio-geïnspireerde pseudopeptiden welke een 'stealth'-gedrag vertonenen gelijkend aan de gouden standaard poly(ethylene glycol) (PEG). Deze polymeren zijn biocompatibel en temperatuursgevoelig wat hen een ideale klasse maakt voor toepassingen voor medicijnafgifte. PAOx worden gemaakt door middel van de cationic ring-opening polymerization (CROP), een levende keten-polymerisatie van 2-alkyl-2-oxazolines, waarbij de eigenschappen van het polymeer kunnen worden aangepast via (onder andere) de zijketen op de 2-positie. In nauwe samenwerking met de Supramolecular chemistry groep van Prof. Richard Hoogenboom aan Universiteit Gent hebben we het effect van ongesatureerde alkyl zijketens op de polymerisatie kinetiek onderzocht. Dit werk is gerapporteerd in **Paper V**.

Gebaseerd op eerder gepubliceerd werk, werd een vergroting van de reactiesnelheid verwacht in de CROP door de aanwezigheid van cation-π interacties. Hiertoe werd het effect van ongesatureerde zijketens op de polymerisatie snelheid onderzocht voor 2-(butyl)- (*n*-ButylOx), 2-(but-3-enyl)- (ButenOx), 2-(but-3-ynyl)- (ButynOx) en 2-(pent-4-enyl-)-2-oxazoline (PentynOx). Een multischaal modelleringsaanpak werd gebruikt waarbij statische en MD simulaties van trimerische en pentamerische systemen werden gecombineerd om zo de aanwezigheid van cation-π interacties en hun effect op de polymerisatie kinetiek te onderzoeken. Hoewel aan het begin van dit onderzoek het solvent niet in rekening werd gebracht, hebben we in een finaal stadium van het onderzoek aangetoond dat de resultaten die we bekomen ook geldig zijn in aanwezigheid van acetonitrile, gebruikmakend van zowel impliciete als expliciete solvent modellen. We hebben aangetoond dat een verschil in polymerisatie kinetiek wordt veroorzaakt door een voororganisatie effect wat de reactanten regio (meer bepaald de pre-reactieve complexen) stabiliseert via cation-π, π-π en π-geïnduceerde dipoolinteracties. Op deze manier wordt het associatie gedrag verbeterd tussen een aanvallend monomeer en een groeiende polymeer keten. De resultaten tonen aan dat *n*-ButylOx trager polymeriseert dan ButenOx, wat op zijn beurt weer trager polymeriseert dan ButynOx, wat op zijn beurt weer lichtjes sneller of even snel reageert dan Pentynox,i.e. omwille van entropische beperkingen. Deze trend werd tot slot experimenteel gevalideerd door het uitvoeren van kinetische experimenten op de onderzochte monomeren. In deze studie hebben we dus aangetoond dat de apparente snelheidsconstante wordt versneld door de aanwezigheid van π-type interacties die zorgen voor de stabilizatie van een prereactief complex. Deze observaties kunnen belangrijke implicaties hebben op toekomstige polymerisaties aangezien ze gebruikt kunnen worden voor het rationaliseren van een polymerisatie resultaat of om nieuwe polymerisatie reacties te ontwerpen die deze effecten benutten.

Naast het onderzoek van de polymerisatie kinetiek van verschillende monomeren met ongesatureerde zijketens, hebben we ook de toepassing van 2-ethyl-2-oxazoline en het corresponderende polymer poly(2-ethyl-2-oxazoline) (PEtOx) onderzocht. Dit is een hydrofiel polymeer wat 'lower-critical-solution-temperature'-gedrag vertoont, waardoor het ideaal is voor biomedische toepassingen. Hiertoe werd PEtOx bestudeerd als drager materiaal voor de constructie van ASDs om zo de oplosbaarheid en dus biobeschikbaarheid van actieve farmaceutische ingrediënten (APIs) die slecht wateroplosbaar zijn te verbeteren (wat geldt voor ongeveer 90% van alle drugs). PEtOx kan enerzijds de oplossnelheden doen toenemen en anderzijds kan het mogelijks een supersaturatie effect uitoefenen wanneer de drugs oplossen. Dit werk werd uitgevoerd in nauwe samenwerking met Prof. Richard Hoogenboom (*vide infra*) en Prof. Karen De Clerck van het departement of Materials, Textiles and Chemical Engineering aan Universiteit Gent. Deze onderzoeksgroepen waren pionier in de productie van ASDs door middel van solvent-elektrospinnen. Als model API werd flubendazole (FBZ) gekozen wat een zeer effectieve drug is tegen verschillende tropische ziekten.

In eerste instantie werd onderzocht, door middel van statische DFT berekeningen, of PEtOx in staat is om FBZ-FBZ interacties te verstoren om er achter

te komen of deze polymeer matrix mogelijks compatibel is met het API. Deze analyse was nodig omwille van het feit dat incompatibele materialen zullen leiden tot fasescheiding wat ongewenst is voor medicijnafgifte toepassingen. De resultaten toonden aan dat PEtOx en FBZ met elkaar concurreren om te interageren met andere FBZ moleculen in de ASD, wat dus wees op de geschiktheid van PEtOx als potentiële polymeer matrix.

In tweede instantie werden grootschalige MD simulaties uitgevoerd (met meer dan 40000 atomen) om zo de interacties en de drug mobiliteit te onderzoeken in deze complexe moleculaire omgeving. Hiertoe werd een krachtveld afgeleid voor PEtOx en een computationeel protocol ontwikkeld om ASD structuren te genereren, welke 10 PEtOx centimeren bevatten en 476 drug moleculen. Het protocol werd bovendien gebruikt om de structuren verder te equilibreren naar een configuratie die het echte systeem goed representeert. We hebben verder ook een grondige validatieprocedure ingevoerd waarbij we glas-transitie temperaturen, XRD-diffractogrammen en dichtheden computationeel werden bepaald. Via deze weg, konden we inderdaad aantonen dat het voorgestelde computationele protocol in staat is om grootheden te voorspellen die in goede overeenstemming zijn met het experiment. Er werd op basis hiervan geconcludeerd dat de model structuren de elektogesponnen nanovezels op een realistische manier representeren.

In een finaal stadium werd de drug mobiliteit geëvalueerd door de berekening van zelf-diffusiviteit voor FBZ in verschillende moleculaire omgevingen. Hierbij werd aangetoond dat FBZ succesvol kinetisch wordt 'gevangen' in de polymeer matrix door de bereidingswijze, i.e. solvent elektrospinnen. We hebben verder aangetoond dat de sterke en stabiele waterstofbrug interacties tussen FBZ en PEtOx domineren in de ASD door het analyseren van waterstofbrugpatronen en hun corresponderende levensduur. In het algemeen toonden de resultaten dus aan dat stabiele PEtOx-gebaseerde ASDs met een hoge drugs lading kunnen worden geproduceerd door middel van elektrospinnen, omdat er zich enerzijds sterke waterstofbruggen vormen tussen het API en de polymeer matrix en het API succesvol kinetisch wordt gevangen tijdens deze experimentele procedure anderzijds.

Samenvattend, hebben we in dit proefschrift succesvol aangetoond dat moleculair modelleren essentieel is om reactiemechanismen, reactiekinetiek, moleculaire interacties en materiaaleigenschappen binnen de polymeerwetenschappen te begrijpen. Echter, gegeven de complexiteit van een systeem en/of onderzoek, moet er vaak een multischaal modelleringsaanpak gebruikt worden. Hierbij geven verschillende methoden, die toelaten om fenomenen op verschillende tijd en lengte schalen te simuleren, complementaire inzichten. In alle geval, moet er in elke modelleringsaanpak een optimale balans worden afgewogen tussen computationele haalbaarheid en accuraatheid. Doorheen dit werk werden er bovendien verschillende simulatieprotocollen en methodologiën naar voor geschoven om moleculaire systemen te onderzoeken in hun complexe moleculaire omgevingen. Aan de ene kant hebben we gefocust op hoe men een solvent expliciet kan behandelen en langs de andere kant hoe men realistische polymerische systemen aanpakt. Er werd ook aangetoond dat het in rekening brengen van de omgeving op een correcte manier

belangrijk is voor het bekomen van accurate resultaten. Nu moleculaire modellen steeds nauwkeuriger en realistischer worden en met de toename van computationele rekenkracht, wordt er verwacht dat computationele chemie in de toekomst nog aan belang zal winnen. Het zal worden gebruikt om experimentators te begeleiden in het rationeel ontwerp van experimenten, materialen en katalysatoren en om een fundamenteel begrip te krijgen van chemische processen. En wie weet, zulen we binnenkort experimenten en berekeningen combineren in een hybride vorm om nieuwe chemie te ontdekken ...

Part I

A multiscale modeling approach to understand reactivity and interactions in complex molecular environments with applications in polymer chemistry

1

Introduction and Goals

1.1 Introduction

Computational chemistry and molecular modeling are nowadays omnipresent in many fields of chemistry ranging from organic chemistry, biochemistry, physical chemistry, polymer chemistry, polymer science and even material science. Within computational chemistry the aim is to understand and predict the structure and properties of materials and molecules by means of computer simulations and modeling. It encompasses a broad range of computer-based methods ranging from minimization and conformational analysis to the study of reaction mechanisms and material properties to gain a fundamental understanding in molecular systems. The field has evolved substantially and nowadays, depending on the level of accuracy of these applied models, we can not only better understand but also predict reaction outcomes or the behavior of materials. In a broader sense, molecular modeling combines computational chemistry with graphical visualization tools to provide a three-dimensional representation of the molecular systems and hence gain insights both quantitatively (numerically) and qualitatively (visually).[1] The enormous impact of computational chemistry within the scientific community is evident from the Figure 1.1, showing the annual growth percentage of the field measured by the number of publications, assuming an unrestricted exponential growth, inline with the work by Bornmann et al (assuming the number of publications can serve as a measure for scientific growth).[2] It indicates that the power of computational chemistry (and in extension of molecular modeling) has now found its way in

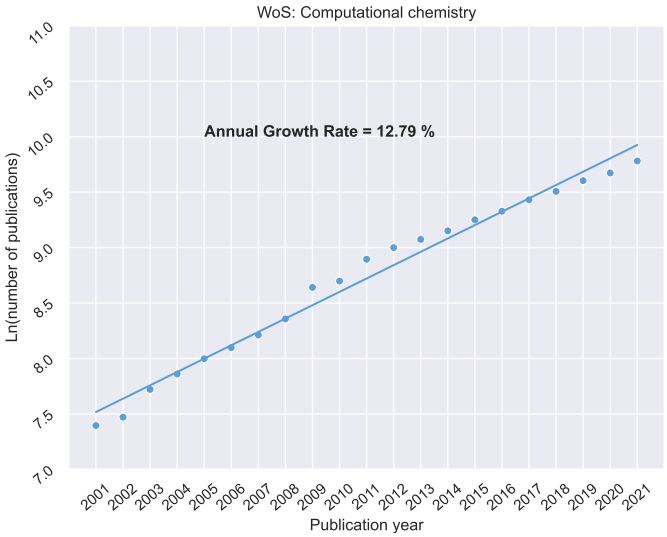

Figure 1.1. The scientific growth of Computational Chemistry within the last 20 years measured by means of the annual growth percentage (applying an unrestricted exponential growth model, inline with ref. 2) based on the Web of science search results for 'Computational chemistry'.

different branches of science. Not only has it been shown to be an invaluable tool to gain a deeper understanding of different chemical processes, it is nowadays also recognized as essential for the rational design of new molecules and materials.[3]

Computational chemistry hence enables tackling a very broad range of scientific questions, however in this thesis the topics of interest are situated mainly within various fields of polymer science.

An overview of all projects tackled within this thesis is shown in Figure 1.2 which indicates where each of the projects is situated within the field of polymer science. More specifically, the projects may be categorized in two application areas namely the reactivity and applications of poly(2-alkyl-2-oxazoline)s and conversion of lignin-derived compounds to platform molecules and subsequent production of bio-based polymers.

The former application area builds on an ongoing collaboration between the Center for molecular modeling and the Supramolecular chemistry group of Richard Hoogenboom both located at Ghent University. Herein we have investigated on one hand the reactivity of newly developed oxazolines to understand their polymerization behavior and, on the other hand, the use of poly(2-ethyl-2-oxazoline), a well established polyoxazoline, is investigated to construct new amorphous solid dispersions for drug-delivery applications. The latter application area is situated

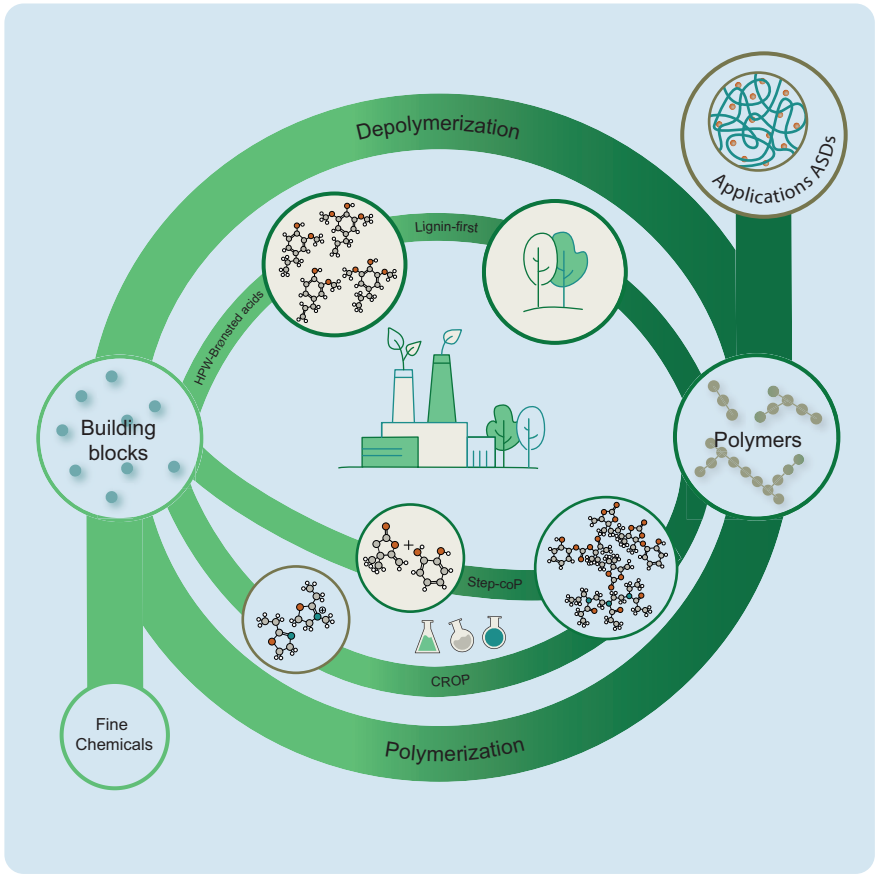

Figure 1.2. Schematic overview of the topics tackled in this doctoral thesis situating them within the field of polymer science, more in particular the polymerization and depolymerization process. Step-CoP, CROP, ASDs and HPW refer to Step co-Polymerization, Cationic Ring-Opening Polymerization, Amorphous Solid Dispersions and Hot-Pressurized Water respectively. The topics which are not tackled in this thesis, though still relevant, are depicted slightly transparant.

within an excellence of science project funded by the FWO and FNRS, i.e. Biofact [https://www.biofact.be/], with the mission to develop the next-generation biorefinery capable of converting wood chips in high-added value chemicals in an efficient and economically feasible way. It is a collaborative project with partners from KULeuven (Prof. Bert Sels, Prof. Dirk De Vos), Université Libre de Bruxelles (Prof. Gwilherm Evano), Université de Liège (Prof. Christophe Detrembleur, Prof. Antoine Debuigne), University of Antwerp (Prof. Bert Maes), Leibniz-institut für Katalyse (Prof. Matthias Beller) and Ghent University (Prof. Veronique Van

Speybroeck). In this collaboration the Center for molecular modeling is responsible for the molecular modeling tasks, with the main aim to understand reactivity of lignin derivatives in complex molecular environments. This new biorefinery concept will be capable of converting wood chips in high added-value chemicals, limiting the societal need for fossil fuels on one hand and providing more sustainable alternatives on the other. The biofact concept starts from the recently developed *lignin-first* approach which efficiently depolymerizes lignin to four main simple aromatic products in high yield. The approach fragmentates and depolymerizes lignin selectively, leaving the carbohydrate fraction unaltered and hence available for further processing.[4]

Within this thesis both small and large-scale simulations are performed ranging from 50 to $>$ 50000 atoms and length scales ranging from 5 to 75 Å depending on the project. To obtain insight into systems having this level of complexitiy, it is necessary to use a complementary set of modeling approaches.In what follows the content of the different projects tackled is briefly introduced, in view of the aforementioned application fields: namely Poly(oxazolines) and the BioFact project. More specifically, a detailed overview of the investigated systems is provided in Figure 1.3. On the left hand side the different building blocks used for the study of two types of polymerization reactions are shown, i.e. :

1. 2-alkyl-2-oxazolines **1** which are converted to their corresponding polymers, poly(2-alkyl-2-oxazolines) **4a**-**4c** via the cationic ring-opening polymerization (CROP).

2. bis(α-alkylidene carbonate) **3** and catechol **2** for the production of poly(oxo-carbonates) **5a**-**5b** and **6a**-**6b** via a step copolymerization (step-cop). Remark that catechol is chosen here as reference diol, in practice other difunctional monomers can be used.

On the right hand side the produced polymers are highlighted which can in turn be used for various applications of which one was studied i.e. the use of poly(2-alkyl-2-oxazolines) **4c** with Flubendazole **7** for the production of amorphous solid dispersions (ASDs) as drug-delivery system.

At the top side the depolymerization process of polymers is highlighted which can be used for the recovery of the corresponding building blocks. Within this thesis the conversion of lignin, a biopolymer which is a consituent of biomass next to (hemi)celllulose, towards catechol is shown on the upper side. Lignin is first depolymerized into the main lignin-derived monomers **9**-**12** via the aforementioned *lignin-first* approach of which **9** (and **10** can subsequently be converted to catechol **2** in hot-pressurized water (HPW) under Brønsted acid catalysis. The latter can then in turn be used as a building block for the production of poly(oxo-carbonates) **5a**,**6a**-**5b**,**6b** or fine chemicals (see Figure 1.2).

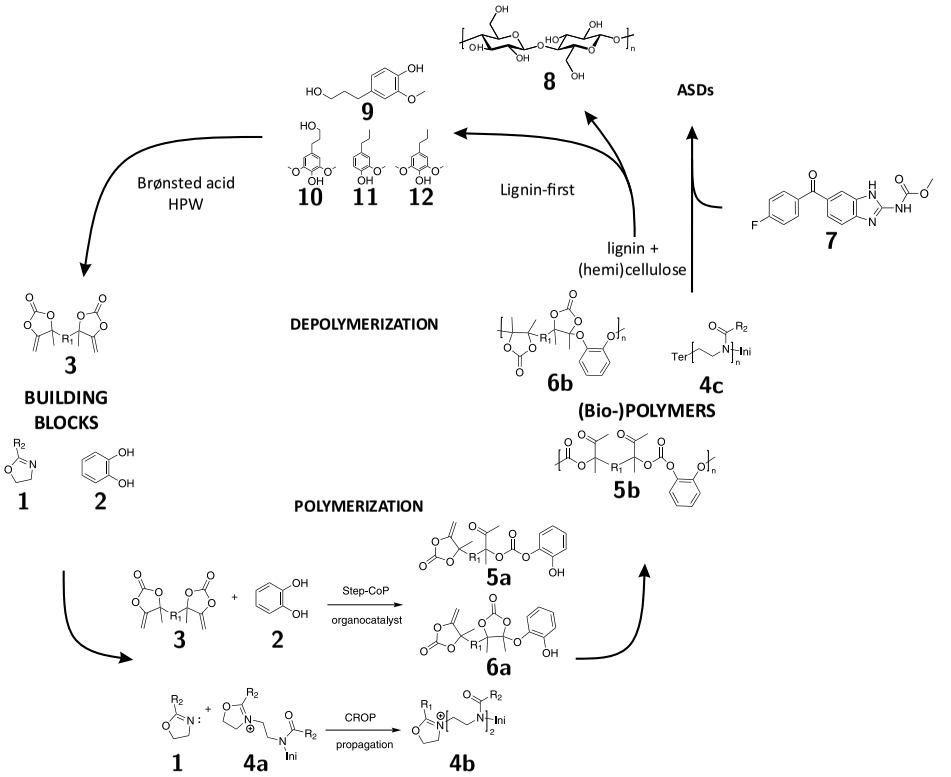

Figure 1.3. Representative overview of the reactions considered in this thesis. Starting from the building blocks on the left hand side the step copolymerization of catechol **2** with bis(α-alkylidene carbonate) **3** is shown at the bottom; and the cationic ring-opening polymerization (CROP) of 2-alkyl-2-oxazoline **1**, where R_2 represents the alkyl chain, is shown below. The resulting polymers are shown on the right hand side: poly(oxo-carbonates) **5b** and **6b**; and poly(2-alkyl-2-oxazolines) **4c**. At the top the *lignin-first* products **9**-**12** are shown where dihydroconiferyl coniferylalcohol **9** is subsequently *O*- and *C*-dealkylated towards catechol in hot-pressurized water. Ter and Ini refer to the CROP terminator unit and initiator unit respectively.

The projects discussed in this dissertation resulted in the publication of 6 peer-reviewed papers. The papers themselves are taken up in the second part of the thesis.

We distinguish papers related to the BioFact project and those related to Poly(2-alkyl-2-oxazolines):

1. Four papers related to the BioFact project:

   - On one hand the selective defunctionalization of *lignin-first* functional aromatic building blocks towards catechol is investigated. Two projects are distinguised:

     ⋆ **Paper I**: Brønsted Acid Catalyzed Tandem Defunctionalization of Biorenewable Ferulic acid and Derivates into Bio-Catechol.This paper comprises a mechanistic study covering the conversion process of dihydroconiferyl alcohol, one of the four lignin-derived monomers from the *lignin-first* biorefinery, towards catechol. The main research results are discussed in Chapter 4 Section 4.2. The research was performed in close collaboration with the Organic Synthesis (ORSY) group from the University of Antwerp (Prof. Bert Maes and Jeroen Bomon) who established this conversion in hot-pressurized water, i.e. in the condensed phase, using Brønsted acid catalysts. The process itself is a key intermediate step in the depolymerization of lignin towards platform molecules which can be used in industry as drop-in alternatives.

     ⋆ **Paper II**: The concerted *O*-demethylation of guaiacol in hot-pressurized water catalyzed by Brønsted acids. This paper covers the follow-up work of **Paper I** in which the modeling approach is extended with more advanced methods in order to describe the process more realistically and hence closer to experimental conditions. The results are discussed in Chapter 4 Section 4.2.2 shifting the focus from dihydroconiferyl discussed in Paper I to guaiacol. Guaiacol is chosen as model compound to gain more accurate mechanistic insights into the *O*-dealkylation reaction in complex molecular environments, i.e. an aqueous solvent or a porous material. Indeed we have explored the use of zeolites as more sustainable alternatives for the (often corrosive) homogeneous Brønsted acids. Mechanistic insights are hence obtained for both homo- and heterogeneously catalyzed systems enabling a thorough comparative study between two catalytic environments. The work was supported by experiments by the ORSY group (Prof. Bert Maes, Jeroen Bomon and Matthias Bal) and the Center for Sustainable Catalysis and Engineering of the KULeuven (Prof. Bert Sels and Xian Wu). Next to in-depth mechanistic insights, it was found that zeolites are a viable alternative for homogeneous Brønsted acids to catalyze the

O-demethylation highlighting that seeking for more stable catalytic systems under these conditions is worthwhile.

- On the other hand the lignin-derived building blocks, e.g. catechol, or other difunctional compounds can be used for the production of novel families of polycarbonates (e.g. poly(oxo-carbonates)) through polymerization with CO_2-sourced bis-(α-alkylidene carbonates). In this work two different functionalities were explored, i.e. thiols and alcohols, which are co-polymerized with bis-(α-alkylidene carbonates) each resulting in a dedicated paper:
  - ⋆ **Paper III**: A Switchable Domino Process for the Construction of Novel CO_2-Sourced Sulfur-Containing Building Blocks and Polymers. Here the reactivity of α-alkylidene carbonate, a CO_2-sourced building block and model compound for mechanistic studies of bis-(α-alkylidene carbonates) **3**, with respect to thiols is modelled and the proposed mechanism is investigated for the formation of β-oxothiocarbonates and tetrasubstituted ethylene carbonates. The results are covered in Chapter 4 Section 4.3.1. Understanding the reactivity is of paramount importance to explain the tunable functionality of the new polymers created by polymerizing bis(α-alkylidene carbonate) with dithiols. The research was performed in close collaboration with the CESAM research unit from the Center for Education and research on Macromolecules at the University of Liège (Prof. Christophe Detrembleur, Farid Ouhib and Fabiana Siragusa), who are pioneers within this field of research.
  - ⋆ **Paper IV**: Access to Biorenewable and CO_2 -Based Polycarbonates from Exovinylene Cyclic Carbonates. This paper is a follow-up study of **Paper III**, where the reactivity of alcohols is explored instead of thiols. Furthermore, the functioning of the catalyst and intermediate stabilities are investigated using more advanced methods. The main results are discussed in Chapter 4 Section 4.3.1, highlighting an alternative mechanism dominates the formation of these new classes of polymers and reveals more detailed information on the influence of the organocatalyst.

2. Two papers related to the Poly(2-oxazoline) work:
   - **Paper V**: Cation-π Interactions Accelerate the Living Cationic Ring-Opening Polymerization of Unsaturated 2-Alkyl-2-oxazolines. Herein the reactivity of novel 2-alkyl-2-oxazolines within the CROP is investigated in collaboration with the Supramolecular Chemistry group (Prof. Richard Hoogenboom and Bart Verbraeken). The results are discussed in Chapter 5 Section 5.1.2 revealing the influence of unsaturated sidechains on the reactivity. These unsaturations give access to easy post-functionalization and cross-linking of the produced materials.

- **Paper VI**: Stable amorphous solid dispersions of flubendazole with ultrahigh drug loading through solvent electrospinning. In this paper the use of a specific poly(2-oxazoline), i.e. poly(2-ethyl-2-oxazoline), is explored as a potential matrix material for drug-delivery applications (see Chapter 5 Section 5.2.2, Paper VI). ASDs are prepared and investigated computationally to gain insights of the governing interactions within, and the stability of, the drug-delivery system. Next to the Supramolecular Chemistry group, this project was performed in close collaboration with the department of Materials, Textiles and Chemical Engineering from Ghent University (Prof. Karen De Clerck and Jana Becelaere) who succesfully produced new poly(oxazoline)-based amorphous solid dispersions and subsequently performed experimental characterization and property determination of the formulations.

To tackle the different research questions, a broad range of methodological tools were used. Though the set of tools may vary among different projects, typically similar decisions need to be made at the beginning of a project. A schematic representation of the methodology and hence the workflow followed within the different projects is shown at the beginning of the Methodology chapter (Figure 2.1). Nonetheless, within various projects some rather specific workflows were followed and/or developed to model the problems at hand. More details on these workflows can be found in Chapter 2 (general methodology workflow), Appendix B (workflow for simulations in explicit solvent) and Appendix C (workflow for generating and simulating large-scale polymer systems). The provided workflows are intended to aid future researchers getting started with simulations in the field of polymer chemistry and/or explicit solvent simulations. Code snippets and elaborate discussions on modeling choices and approaches are provided to guide the interested reader in setting up their own simulation workflows.

This thesis, following Figure 1.2 and 1.3, is structured as follows:

- Chapter 2 provides an overview of the methods employed and approaches followed to perform molecular modeling within polymer science.
- Chapter 3, introduces some of the core concepts of polymer science needed to discuss the different projects tackled in this thesis.
- Chapter 4, introduces the BioFactory concept and discusses the projects tackled within the corresponding BioFact project (from hereon refered to as the biofactory). It covers the defunctionalization of lignin-derived monomers towards the platform molecule catechol and the production of new polycarbonates from CO_2-sourced α-alkylidene carbonates and difunctional (lignin-sourced) building blocks.
- Chapter 5, discusses the polymerization behavior of new unsaturated 2-alkyl-2-oxazolines and additionally focuses on a polymer application where

poly(2-ethyl-2-oxazoline) is used as drug-delivery system by the formulation of amorphous solid dispersions.

The thesis ends with some general conclusions and perspectives (Chapter 6). The major research results are taken up in the main part of the thesis, whereas the specific papers resulting from the PhD work are taken up in Part II of the thesis. Apart from the papers taken up in this thesis, I was also involved in some other projects which led to publications. This work is not explicitly taken up in the thesis but a full list of papers and of conference contributions can be found in Chapter VII.

1.2 Goal of this thesis

Overall the goal of this thesis is to understand the reactivity and governing molecular interactions of important chemical transformations within polymer science. The reactivity can be investigated by determining the underlying mechanisms and the corresponding reaction kinetics of a chemical transformation. In most cases it is very difficult to capture from an experimental point of view what is going on at a molecular level, although a lot of progress is made within the field of operando and in-situ spectroscopic tools.[5] Furthermore, designing experiments which can unravel the reaction mechanism can be a very tedious job as for example unstable intermediates need to be synthesized, side reactions occur, ... Nonetheless, it is recognized that knowledge at this level is vital to: (i) understand what is going on; (ii) how the chemical process can be steered in the desired direction; (iii) design new processes and materials. Hence, with this in mind, molecular modeling has become an essential tool in the quest to achieve a full molecular level understanding of the process or in the rational design of experiments and materials. In many cases molecular modeling and experimental research is performed in close synergy.

Within computational chemistry one usually needs to make a simplified version of the reality, i.e. a molecular model, to gain a fundamental understanding at the nanoscale. Regardless of the fact that the molecular model is a simplified version of reality, one still aims to describe reality as close as possible in order to determine underlying reaction mechanisms or material properties accurately. To this end, the computational chemist can rely on a plethora of tools which have been devised in the past decades where no unique approach exist to solve a scientific question. Hence, it is up to the modeler to decide which techniques/tools to use, and which operating conditions should be accounted to accurately describe the system. Next to these methodological aspects on which we will extensively elaborate on in the following chapter, also computational cost and timespan of a project should be considered. With computational cost we here refer to how long it takes to run a specific set of simulations and what computational resources are necessary.

The projects tackled within this dissertation, i.e. The biofactory and poly(2-alkyl-2-oxazolines), are generally situated within the field of polymer chemistry (shortly introduced in Chapter 3). Concerning the different subprojects tackled within this project, we distinguish the following goals:

1. We try to gain a fundamental understanding of the reaction mechanism and corresponding kinetics using molecular models which describe reality with a reasonable accuracy. Typically, depending on the available time, increasingly complex environments can be accounted for where we need to find a balance between computational cost and accuracy. One very important parameter within these models is how to appropriately describe the solvent environment and hence its influence on the reaction. In view hereof we typically apply a multiscale modeling approach to tackle different research questions at hand for a single molecular system. Hence we aim to understand the reaction and its influencing factors while accounting for the operating conditions in the most appropriate way, given a set of conditions.

2. We want to gain a fundamental understanding of the governing molecular interactions and the corresponding material properties of a poly(2-alkyl-2-oxazoline)-based drug-delivery system. As these systems are intrinsically large and relatively complex, it is the goal to gain an accurate understanding of the material by designing molecular models which represent the drug-delivery system in an accurate manner. Ultimately, we aim to achieve a molecular model and develop appropriate analysis tools to reach a predictive level of accuracy which will allow us to determine optimal drug loadings and drug-polymer compatibility.

Hence, designing molecular models capable of describing complex chemical systems in the most appropriate and realistic way is typically accompagnied by the right balance between computational cost and accuracy. This balance translates itself in finding how to describe the potential energy surface and the molecular environment (e.g. solvent or material) and which properties we aim to describe.

2

Methodology

Within this chapter some key concepts and methods used in this thesis are introduced. As will become clear, in many cases a combination of various techniques and/or methods is required to fully comprehend or make accurate predictions of the chemical reactivity or the properties of a material. Next to the theoretical background, appropriate references are given to guide the interested reader to more dedicated books and papers. A schematic representation of a typical methodology workflow is presented in Figure 2.1, each aspect of the modeling workflow is tackled in this chapter.

This chapter is organized as follows: Section 2.1 introduces the potential energy surface (PES) and Section 2.2 deals with the methods available to sample the different regions of the PES, i.e. the different sampling methods. Directly related to this is the so-called level of theory, discussed in Section 2.3 which represents the theoretical framework used to evaluate the potential energy during the sampling of the PES. Finally, because the chemistry discussed in this work is often performed in the liquid phase, we introduce various techniques to account for the solvent in Section 2.4. To allow reproducibility of the results and as a guide for future researchers entering the field, most of the workflows and scripts are documented in Appendix B. Appendix B and C furthermore include more details on how to prepare a molecular system to perform molecular simulations in complex environments.

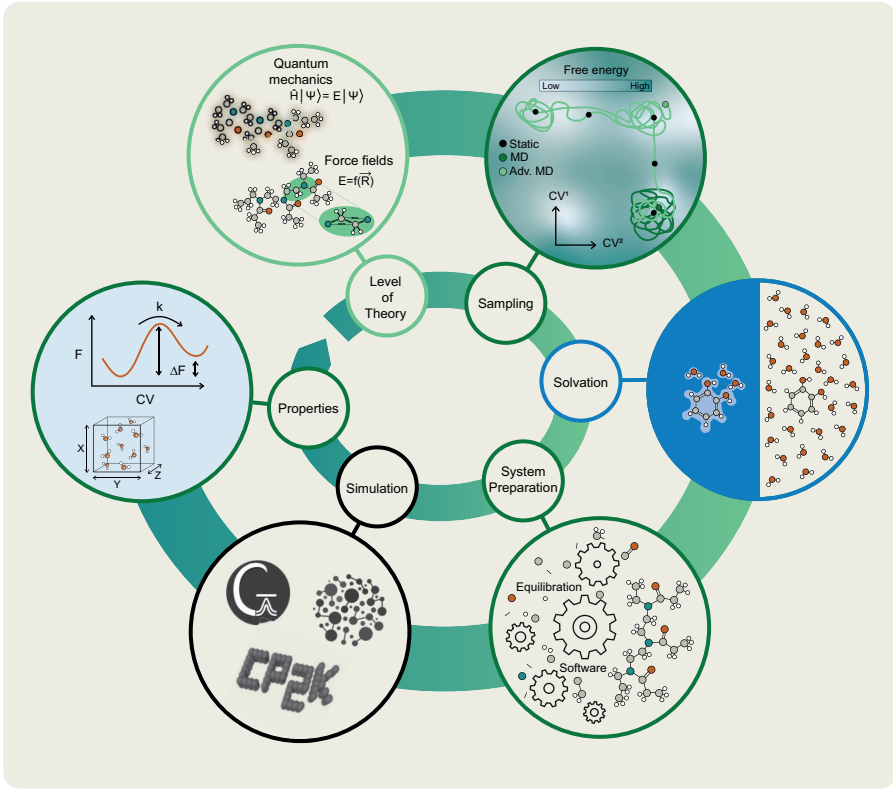

Figure 2.1. Schematic overview of a typical methodology workflow used to investigate the scientific questions tackled in this thesis.

2.1 Introduction to the Potential Energy Surface

When interested in the reactivity and stability of molecules and materials one key quantity is the energy of the system from which, by means of statistical physics, properties can be derived. Though an exact definition of the PES is discussed below, a brief introduction is appropriate. The PES essentially is a hypersurface where the energy is a function of the different degrees of freedom of the investigated system. In this section we introduce the PES in more detail. The more interested reader is referred to dedicated books by Bransden B. H. and Sakurai K. J. .[6–8]

All properties of a molecular system can be derived by solving the many-body system which is made up of nuclei and electrons which mutually interact via the Coulomb interaction. To this end one needs to solve the Schrödinger equation:

$$\hat{H}\,|\Psi\rangle = E\,|\Psi\rangle \tag{2.1}$$

with the Hamiltonian $\hat{H}$ defined as:

$$\hat{H} = \hat{T}_n + \hat{T}_e + \hat{\mathcal{V}}_{nn} + \hat{\mathcal{V}}_{ee} + \hat{\mathcal{V}}_{ne} \tag{2.2}$$

where n are the nuclei, e are the electrons and the kinetic and Coulombic potential energy parts are representad as T and $\mathcal{V}$ respectively. Remark that here the Schrödinger equation is presented in its time-independent and non-relativistic form.

To solve this equation one mostly uses the Born-Oppenheimer approximation (BOA).[9,10] This approximation relies on the large mass difference between electrons and nuclei which allows us to decouple the motion of nuclei and electrons and hence treat them subsequential instead of simultaneous (i.e. separating the nuclear and electronic contributions within the molecular wave function). This allows us to simplify equation 2.2 and define the nuclear coordinates $\overrightarrow{R}$ as a set of parameters instead of variables. One can in this case write the electronic Schrödinger equation as:

$$\hat{H}_e(\vec{r};\vec{R})\Psi_e(\vec{r};\vec{R}) = E_e\Psi_e(\vec{r};\vec{R}) \tag{2.3}$$

where $\vec{r}$ is the variable representing the electronic coordinates.

This implies that the electronic energy of the molecular system now represents a multidimensional surface in the nuclear coordinate space. In computational chemistry we will refer to these surfaces as potential energy surfaces (PES) or Born-Oppenheimer Surfaces (E_e in equation 2.3). A two-dimensional example is illustrated in Figure 2.2 where the energy is displayed w.r.t. 2 collective variables (*vide infra*).

Methodologies on how to determine this electronic energy for a given set of nuclear coordinates, i.e. solve equation 2.3, will be elaborated on in Section 2.3.

The PES itself thus describes how the electronic energy is varying with changes in the geometry of the system. When considering realistic molecular systems visualizing these multidimensional surfaces (hypersurfaces) becomes imposible. To obtain insights one can usually visualize the PES along specific nuclear coordinates or functions thereof which we will refer to as collective variables (CVs). Collective variables can hence describe a collective motion of a single or multiple atom(s) in a single variable, e.g. a distance, a coordination number, a linear combinations hereof, ... In case the CV can distinguish reactants from products and quantify the dynamical progress along the pathway from reactants to products we can refer to the CV as a reaction coordinate (RC). In what follows we will often use q to refer to a CV.[11]

In this thesis we extensively make use of reaction coordinates to describe reactive events. A proper definition of RCs can be very challenging and a few prerequisites need to be fulfilled[11]:

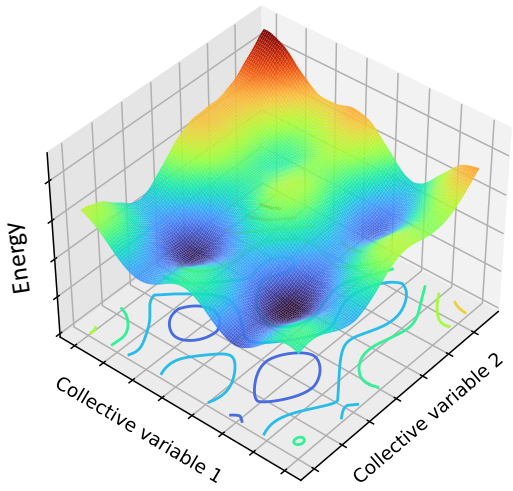

Figure 2.2. A potential energy surface or Born-Oppenheimer Surface. The variation of the energy of a molecular system with respect to two collective variables.

1. q should only depend on a instantaneous point in configurational space (thus not the full phase space).
2. q should increase monotonically moving from reactants to products.
3. Projecting the PES and the corresponding dynamics on q should result in a 1D (free) energy surface and reduced dynamics which remain consistent with trajectories in full phase space.

Apart from finding a proper description of the PES a major challenge within the field of computational chemistry is to locate the "interesting" points or regions, for example the global minimum or a transition state region on the PES. This will be discussed in the following section.

2.2 Mapping the PES

In principle two classes of sampling methods are used to locate interesting regions on the PES in this thesis, i.e. a static approach and a dynamic approach. In principle one can also use Monte Carlo based approach to sample the PES (which is in essence also a dynamic approach, i.e. ensembles of molecular states are generated *vide infra*), however such methods were not used within the framework of this

thesis. In a static approach only a few points are located on the PES, for example, for a chemical reaction one is interested in the minima corresponding to reactant and product states and the transition state corresponding to the conversion of the reactant to the product (hence three points are of interest here). Whereas in the dynamic approach one follows the system in time. To derive final macroscopic properties as measurable quantities one needs to use the principles of statistical physics. Some usefull concepts are explained in Section 2.2.1. The more interested reader in the topics tackled within this section is referred to the following references 12,13.

2.2.1 Statistical physics

Statistical physics, developed by Ludwig Boltzmann and Joshua W. Gibbs, is the scientific branch of thermodynamics linking the microscopic (atomistic) world with the macroscopic (observable) world. As the terms suggest this is done by means of a statistical framework, more specifically, using equilibrium probability distributions of microscopic states which are linked to specific macroscopic observables (depending on the boundary conditions) through statistical averages. Furthermore in the context of statistical physics and this doctoral thesis two fundamental concepts are introduced: ensembles and partition functions.

An ensemble is a concept introduced by Gibbs, and represents a collection of identical systems defined by a set of boundary conditions. The most important ensembles are the microcanonical ensemble (defined by a constant number of particles (N), a constant Volume (V) and constant energy (E), hence also called the NVE-ensemble), the canonical ensemble (constant N,V and Temperature (T), NVT-ensemble), the isothermal-isobaric ensemble (constant N, Pressure (P) and T, NPT-ensemble) and the Grand-canonical ensemble (constant chemical potential (μ), V and T, μVT-ensemble).

Partition function $\mathcal{Z}$ is a concept arising from the link between the well-known Boltzmann factor and the probability p_i of finding a molecular system in a specific state *i* (with corresponding energy, E_i) given a specific ensemble $\mathcal{Z}$ ($\mathcal{Z} = \mathcal{Z}(N,V,T)$ is used here):

$$p_i = \frac{g_i e^{-\beta E_i}}{\sum_i g_i e^{-\beta E_i}} \tag{2.4}$$

$$\mathcal{Z} = \sum_i g_i e^{-\beta E_i} \tag{2.5}$$

where $\beta = \frac{1}{k_B T}$ and g_i is the degeneracy of the state. $\mathcal{Z}$ enters the equation of the probabilities as a 'normalization factor', representing the key link between the micro- and macroscopic world. This expression in combination with the definition of

an ensemble allows us to compute the average value of finding a specific observable or quantity X within a specific ensemble, i.e. the ensemble average $\langle X \rangle$:

$$\langle X \rangle = \sum_i X_i p_i \tag{2.6}$$

which is hence linked to the partition function through the definition of p_i.

Thermodynamics

The study of different thermodynamic properties and their relationships for systems in equilibrium is typically defined as thermodynamics. One very important application of thermodynamics is the determination of optimal operating conditions (e.g. temperature and pressure) for chemical reactions by the analysis of chemical equilibria.

Thermodynamic quantities which are key for the analysis and description of chemical processes are free energy (F), entropy (S), and internal energy (U) and all their derived quantities. The link between these macroscopic quantities and the atomistic description of a molecular system can be made via the partition function $\mathcal{Z}$:

$$U = -\left(\frac{\partial \ln \mathcal{Z}}{\partial \beta}\right)_{N,V} \tag{2.7}$$

$$S = k_B \ln(\mathcal{Z}) - k_B \beta \left(\frac{\partial \ln \mathcal{Z}}{\partial \beta}\right)_{N,V} \tag{2.8}$$

$$F = -k_B T \ln(\mathcal{Z}) \tag{2.9}$$

where F is the Helmholtz free energy, i.e. the free energy defined by $\mathcal{Z}(N, V, T)$ (in contrast to the Gibbs free energy defined by $\mathcal{Z}(N, P, T)$). k_B is the Boltzmann constant, T the temperature and β is equal to $1/(k_B T)$.

Hence, by calculating $\mathcal{Z}$ one can determine all thermodynamic macroscopic properties of interest and in turn provide meaningful information about the nature of a chemical process, i.e. whether the process under consideration occurs spontaneous ($\Delta F < 0$) or not ($\Delta F > 0$). Examples of processes relevant to this work are the study of reactions, equilibria and miscibility.

Chemical kinetics

While thermodynamics covers chemical equilibria and spontanity of a reaction, chemical kinetics studies the dynamics of chemical processes. Central within this study is the determination of rate constants and rate equations for individual reactions or reaction networks. For more detailed information the reader is referred to the book by Arnaut L. and the review of De Oliveira and coworkers.[14,15]

The main approach to derive kinetic parameters is the transition-state theory (TST) developed by Eyring and Polanyi.[16,17] In essence it is a theory based on statistical mechanics which simplifies the inherent dynamical problem by assuming thermal equilibrium is maintained when progressing along the RC. This boils down to the fundamental assumption of TST which states that a quasi-equilibrium exist between a transition-state species and the reactants converting the dynamics problem into an equilibrium problem. Under this assumption the Eyring-Polanyi equation can be used to calculate the rate constant of an elementary reaction step:

$$k_{TST} = \kappa \frac{k_B T}{h} e^{\frac{-\Delta F^{\ddagger}}{RT}} \tag{2.10}$$

where κ and $\Delta F^{\ddagger}$ represent the transmission coefficient and the free activation energy, respectively, h is Planck's constant and R is the gas constant $= N_A k_B$ with N_A the constant of Avogadro. κ is used to account for quantum effects such as tunneling, typically it is considered to be equal to one.

Other than the quasi-equilibrium assumptions (which is the basis for assuming that the TS and reactants follow the Boltzmann distribution law), species are assumed not to recross the barrier once crossed; and it is assumed that a classical treatment can be used for the movement along the reaction coordinate (BOA).

2.2.2 Static approach

In a static approach one is interested in localizing relevant stationary points on the PES, i.e. the gradient of the potential energy ($\mathcal{V}$) with respect to the nuclear coordinates $\overrightarrow{R_A}$ (or the CVs) becomes zero in these stationary points:

$$\frac{\partial \mathcal{V}}{\partial \overrightarrow{R_A}} = 0 \quad \forall A \tag{2.11}$$

In the PES shown in Figure 2.3, we can now distinguish two important stationary species namely transition states (TSs) (first-order saddle points; TS_1, TS_2 and TS_3) and (local) minima (M_1, M_2, M_3 and M_4). These points are most often the points of interest to a computational chemist. Remark that often a 1D representation, i.e. a potential energy surface in function of a single RC q (here equal to CV2), will suffice to describe the relevant regions, e.g. when the change from M_1 to M_2 is investigated see Figure 2.3. Minima will represent the geometry of a molecule or material which are most likely to be found, while TSs represent the geometry attained during the transformation of one minima to another (from reactants to products).

Practical considerations

Computationally, local stationary points (minima and first-order saddle points) can be found by means of a geometry optimization (GO) and in the case of

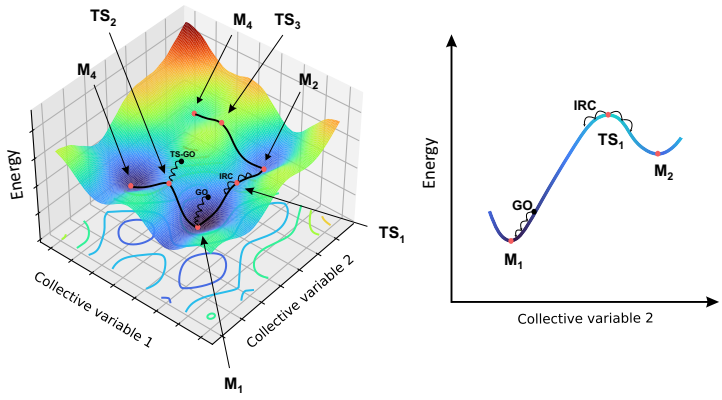

Figure 2.3. A potential energy surface with stationary points of interest and applicable computational procedures (left); A one dimensional potential energy surface describing the reaction from M_1 to M_2 with stationary points of interest. Remark that the minima on the right are not equivalent to the minima on the left hand side because they can attain any value for collective variable 1.

minima this can be achieved by using basic optimization algorithms like steepest descent.[18,19]Concerning transition state searches 'more advanced' approaches or helpfull tools exist like the transit-guided quasi-Newton method (commonly known as QST-methods), or the generalized internal coordinates (GIC) formalism in Gaussian16 (a more modern version of ModRedundant, well-known to Gaussian users).[20,21] Once the geometry corresponding to the point of interest is located it important to verify the nature of the minima and TS by performing a frequency calculation. The vibrational frequencies of a molecular system correspond to the eigenvalues of the Hessian, resulting in $3N-6$ ($3N-5$ for linear species) non-zero vibrational frequencies for an isolated molecule (-6 arises from the three rotational (or two for linear species) and three translational degrees of freedom, which will result in frequencies equal to zero).The Hessian is a $3N$ x $3N$ matrix defined by the second order derivatives of the energy with respect to the nuclear coordinates (R_N with N the number of nuclei) and hence contains valuable information on the curvature of the PES. From a quantum mechanical calculation the Hessian can be computed which is in turn used together with the so-called harmonic approximation (describing vibrational motion in terms of independent harmonic oscillators, i.e. normal modes) to derive the vibrational frequencies and the corresponding vibrational partition function (*vide infra*). For minima all frequencies should be positive while a TS should have a single imaginary vibrational frequency representing the vibrations occuring within the desired reaction. Depending on the number of degrees of freedom, locating the global minima of a PES or finding a transition state can be a tedious job.

Thermodynamic properties from static calculations

Following a static approach the total partition function $\mathcal{Z}$ can be determined, using the ideal-gas approximation, by means of the molecular partition function $Z(V,T)$ and the total number of particles N:

$$\mathcal{Z} = \frac{[Z(V,T)]^N}{N!} \tag{2.12}$$

The molecular partition function $Z(V,T)$ can in turn be partitioning as follows:

$$Z(V,T) = z_{trans} z_{rot} z_{vib} z_{elec} \tag{2.13}$$

where z_{trans} and z_{rot} are the translational and rotational contributions to the partition function depending on the masses of the nuclei and moments of inertia respectively. z_{vib} is the vibrational contribution to the partition function which can be determined via the frequencies (cfr. Hamonic approximation) and z_{elec} is the electronic contribution which can be computed from the results of the electronic structure calculation (see Section 2.3).

Kinetics from static calculations

Based on the information given above, the Eyring-Polanyi equation (Eq. 2.10) can be written in terms of total partition functions:

$$k_{TST} = \kappa(T) \frac{k_B T}{h} \frac{(\mathcal{Z}^{\ddagger}/V)}{\prod_{i=1}^{n} (\mathcal{Z}_i/V)^{\nu_i}} e^{\frac{-\Delta E_0}{RT}} \tag{2.14}$$

where $\mathcal{Z}^{\ddagger}$, $\mathcal{Z}_i$, V, ν_i are the total partition function of the transition state, the total partition function of the n reactants, the molar volume and the order with respect to reactant i, respectively. The final accuracy will depend on many factors such as the level of theory (vide infra) used to calculate the ΔE_0, TS, z_i, ... but also the approximations in the derivation of transition-state theory.

2.2.3 Dynamic approach

A more realistic representation of a PES is shown in Figure 2.4 which shows that the valleys from before are ragged rather than smooth characterized by many local minima (whether or not including the global minima). Furthermore the TS is no longer a single point but rather a transition state region covering many different configurations which belong to the activated region describing the same transformation. This highlights the need to either characterize many more points using the static approach or move on to a more advanced approach, i.e. a dynamic one, where the system is followed dynamically in time and where larger portions of the PES are taken into consideration. To this end barriers and minima will no longer be described by single point differences but instead ensembles of states will be used (see Section 2.2.1). Furthermore the resulting thermodynamic observables are now calculated by considering ensemble averages.

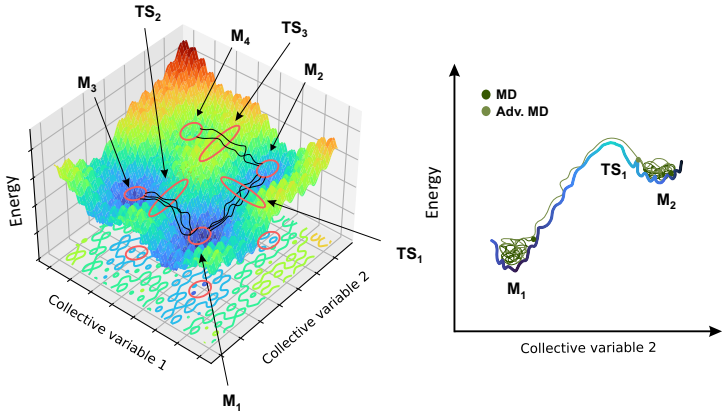

Figure 2.4. A realistic potential energy surface with regions of interest (left); A one dimensional potential energy surface describing the reaction from M_1 to M_2 highlighting different sampling techniques to investigate the respective regions of interest.

Molecular dynamics

Molecular dynamics (MD) is a central technique within the dynamic treatment of molecular systems.[22] The main assumption made in this technique is that nuclei present in the system can be treated as classical particles (as stated in the Born-Oppenheimer approximation the mass of nuclei far surpasses that of the electrons, e.g. $m_{carbon} \approx 21000 m_e$, justifying the assumption in most cases). This implies that the dynamics of the system can be described by Newton's equations of motion:

$$\overrightarrow{F_A} = m_A \frac{d^2 \overrightarrow{R_A}}{dt^2} = -\overrightarrow{\nabla}_{R_A} \mathcal{V} \tag{2.15}$$

where $\overrightarrow{F_A}$ is the force acting on nucleus A with coordinates R_A and a corresponding mass m_A. $\mathcal{V}$ represents the total potential energy of the system. Alternative to molecular dynamics one can use Monte Carlo sampling techniques, which have as a downside that dynamic properties such as diffusion coefficients can not be derived. For more detailed information on Molecular dynamics and Monte Carlo the reader is referred to the excellent book by Daan Frenkel and Berend Smith.[22]

Much like in experiments we can investigate the time evolution of a system with MD, note however that the achievable timescales are different. To this end, positions are updated every timestep (Δt) by numerical integrating the equation of motions. A typical fast and reliably algorithm to do so the Verlet algorithm. It calculates the new positions of the molecular system based on the old and current

ones, inducing an error proportionate to Δt^4.

$$\overrightarrow{R_A}(t+\Delta t) \approx 2\overrightarrow{R_A}(t) - \overrightarrow{R_A}(t-\Delta t) + \frac{\overrightarrow{F_A}(t)}{m}\Delta t^2 \tag{2.16}$$

The potential energy $\mathcal{V}$ and hence the forces in the system are calculated via for example an electronic structure method (see Section 2.3). MD can thus be used to explore the configurational space defining the PES. Depending on the property

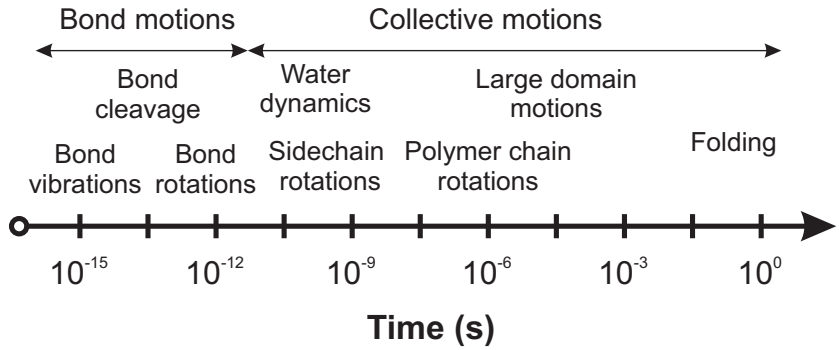

Figure 2.5. Range of time scales for the study of dynamic processes in molecular systems with classical molecular dynamics simulations. Remark that the time for a single MD step is < 5 fs.[23,24]

of interest, different time scales are required, which is illustrated in Figure 2.5. Hence, taking into account the total required simulation time to investigate a certain property, one can tune Δt and thus the total simulated time. However, Δt is a very important parameter to consider in MD as it determines, regardless of the resulting total simulated time:

1. The numerical stability of the applied algorithm, i.e. energy conservation.[25]
2. The error introduced in the integration step (thus the accuracy)
3. The simulation time, which can be reduced drastically by having larger timesteps and hence less force evaluations, which is the expensive part within each MD step.
4. The observable intramolecular vibrations, i.e. the timestep should be chosen so that it is significanly shorter than the period of the highest frequency (B) intramolecular vibration which one wants to observe within the simulations ($< 1/(2.B)$, e.g. for a wavenumber of $3000\ cm^{-1}$ (C-H bond stretch), B is $8,99.10^{13} Hz$, the period is $\approx 11 fs$ and hence a timestep of < 5 fs should be chosen to observe this frequency).[26,27]

Sampling within specific ensembles, e.g. the canonical ensemble or the isothermal-isobaric ensemble, requires algorithms to modulate a specific property. Temperature control is established by means of a thermostat such as a Nosé-hoover

thermostat or langevin integrators[28–34], while pressure control is achieved by adding a barostat like the Monte Carlo barostat used in this work which adjusts the volume of the unit cell.[35,36]

Essential within MD is the ergodicity principle which states that, when the time evolution of a molecular system is investigated for a sufficient amount of time then the time average of the observable/quantity of interest will be equal to the ensemble average. In principle this is only true for an infinite sampling time, resulting in the introduction of a small error when the sampling time is limited. In any case it is important to ensure that the phase space of interest is sufficiently sampled.

An important sidenote here is that regular MD is not a viable method to study activated processes (rare events) because the probability of reaching a TS (p_{TS}) is very low due to the increased energy with respect to the minima. Only at very unlikely fluctuations of the system will it move to these high energetic states. Classical MD would thus lack sufficient sampling to derive properties like activation barriers. In general a molecular state separated by a barrier sigificantly larger than k_BT can be deemed inaccessible during a MD simulation. This implies that for simulating rare events such as chemical reactions, more advanced methods need to be used, which are commonly referred to as enhanced sampling MD techniques.

Enhanced sampling molecular dynamics

In order to capture activated processes using MD many enhanced sampling techniques have been developed. In general three methodologies are distinguished:

1. using elevated temperatures to access highly energetic states or accelerate dynamics like simulated annealing[37] and parallel tempering[38]
2. adding an external (whether or not time-dependent) bias potential to the system as is done for example in Umbrella Sampling[39] with a time-independent bias potential and Metadynamics[40] (and the variants hereof) with a time-dependent bias potential.
3. by generating a large number of transition pathways connecting an initial and final state which is done for example in transition path sampling.[41,42]

In 2. typically collective variable(s) are used to enhance the sampling along, while for transition path sampling all degrees of freedom are used increasing its computational cost significantly. Though each of these techniques is interesting to discuss, we will limit ourselves to a short introduction to metadynamics, well-tempered metadynamics[43], multiple walker metadynamics[44] and Umbrella sampling as these were the enhanced sampling techniques used in this thesis (see Figure 2.6 for a schematic overview of the different techniques used). For more elaborate discussion on different enhanced sampling techniques the reader is referred to Refs. 45–48

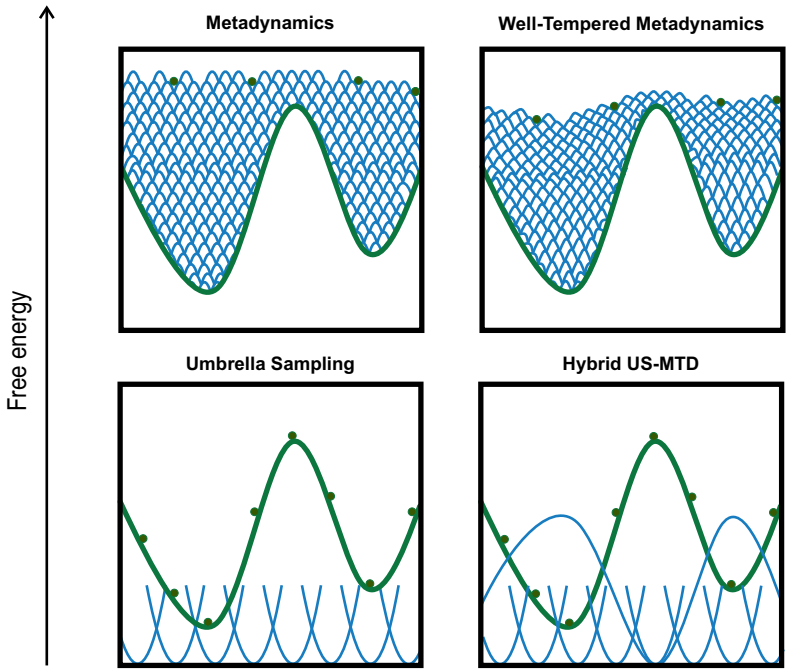

Figure 2.6. Overview of enhanced sampling techniques employed in this dissertation. The green curve represent the free energy profile, the blue curves represent the applied bias potential during the simulation and the black dots represent the separate simulations performed in parallel. In the top left the metadynamics technique is illustrated, i.e. adding a time dependent bias potential which is the sum of the depicted Gaussian Hills. In the top right well-tempered metadynamics is illustrated, where instead of fixed Gaussian hills, the hill height decreases when the simulation progresses. At the bottom left the umbrella sampling technique is shown indicating the harmonic bias potential applied in each separate simulation. At the bottom right, next to the harmonic bias potential also a polynomial bias is applied within the equilibrium simulations to account for the free energy profile obtained from a (non-converged) metadynamics simulation.

Metadynamics (MTD) In metadynamics a 'history-dependent' bias potential $\mathcal{V}_b(q,t)$ is applied during the simulation, which is constructed on-the-fly and which value depends on both the time and the value of the collective variable used to describe the process under investigation. $\mathcal{V}_b(q,t)$ itself is constructed as a sum of Gaussian hills with a predefined height (h) and width (w) each centered around a specific value of the CV $q(R)$ (q_i). Hills are deposited along the trajectory of the

$q(R)$ at a specific time interval (τ_G).

$$\mathcal{V}(q(R),t)_b = \sum_{\substack{t'=\tau_G,2\tau_G,\ldots \\ t'<t}} he^{-\frac{(q(R,t)-q(R,t'))^2}{2w^2}} \tag{2.17}$$

These hills will gradually fill up the underlying free energy surface and prevent the system from oversampling regions in space which have already been sampled. Afterwards a free energy surface can be constructed based on the additive inverse of the deposited Gaussian hills.

$$F(q,t\to\infty) = -\lim_{t\to\infty}(\mathcal{V}(q(R),t)_b) + C \tag{2.18}$$

with C a constant. These equations can easily be extended to multiple dimensions the cost is however drastically increased, i.e. typically an exponential scaling is noted[40]. A proper choice of h, w, τ_G and q is of huge importance to balance the accuracy and efficiency, though ultimately the most optimal choice for h and w depends on the variations within the underlying FES.

The advantage of metadynamics is that regions will not be 'overvisited' during the simulation, it also has the ability to provide qualitative insights on the underlying free energy of a system in a short amount of time. Though, the *a priori* knowledge of the FES required is limited, a proper choice of the CV (or a limited set of CVs) is still of great importance and knowledge of the FES can help to tune w, h and τ_G more efficiently. One last important advantage, which was already recognized in the original paper by Laio et al., is the easy parallelizability of the method. The variant of metadynamics establishing this parallelization is the multiple walker variant (*vide infra*).

The most important drawbacks of the methods are on one hand that it is hard to decide when to terminate the metadynamics run and on the other hand that in some cases systems are irreversibly pushed to regions in the configurational space which are of no interest (or even unphysical). These two drawbacks are solved by using the well-tempered variant proposed by Barducci et al. (*vide infra*).

Multiple walker MTD [44] Within this method, multiple replicas of the system are considered each associated with it own walker. Each of the walkers deposes Gaussians simultaneously to a single-history dependent potential.

Well-tempered MTD In an attempt to circumvent convergence problems and the sampling of unphysical regions in configurational space, the well-tempered approach was proposed. Here the height of the deposited Gaussian hills is changed during the simulation. In this case the bias potential is defined in the following

way:

$$\mathcal{V}(q(R),t)'_b = \sum_{\substack{t'=\tau_G,2\tau_G,\dots \\ t'<t}} h'(t) e^{-\frac{(q(R,t)-q(R,t'))^2}{2w^2}} \tag{2.19}$$

$$h'(t) = h_0\tau_G e^{-\frac{\mathcal{V}(q(R),t)_b}{k_B\Delta T}} \tag{2.20}$$

where $h_0\tau_G$ is the initial hill height and ΔT or more preciselly $\frac{T+\Delta T}{\Delta T}$, i.e. the bias factor γ, is an important design parameter which can be used to tune the convergence of the resulting FEP and the regions explored during the simulations. With $\Delta T \to \infty$ the standard metadynamics algorithm is recovered.

Within this variant, the resulting free energy profile can be derived by accounting for the bias factor:

$$F(q, t\to\infty) = -\lim_{t\to\infty}(\gamma\mathcal{V}(q(R),t)'_b) + C \tag{2.21}$$

Umbrella sampling (US) Within US, the CV-range of interest is split into a set of windows where each of the windows represents a biased MD simulation constrained to a specific part of the configurational space via a time-independent well-defined bias potential ($\mathcal{V}_b(q)$). Typically to this end harmonic potentials are applied:

$$\mathcal{V}(q)_{b,i} = \frac{1}{2}\kappa[q_i - q_{0,i}]^2 \tag{2.22}$$

with κ the force constant and q_0 the center of the umbrella placed in window i. Essential is the occurence of overlapping probability distributions with the neighboring windows. This allows one to construct the underlying FES via a post-processing algorithm such as the the weighted-histogram analysis method (WHAM).[49]

The advantages of Umbrella sampling are its high parallelizability, efficiency and accuracy, all under the assumption that the reaction coordinate can properly describe the reaction under investigation. The latter is thus also a disadvantage as *a priori* knowledge is required on the reaction coordinate.

Hybrid US-MTD Ultimately one can use umbrella sampling simulations in conjunction to metadynamics. In most cases one does not know anything about the underlying FES and it is hence recommended to use MTD in order to explore the surface and screen for proper reaction coordinates to describe the system at hand, i.e. by using large gaussian hills to scan the FES. For example using the well-tempered variant it is then possible to obtain relatively well converged FESs within a reasonable timespan. However, full convergence is only reached when the simulations are performed for a sufficient amount of time (in the time limit) and hence in many cases the results will not be converged to the level required to make accurate quantitative comparisons.[43] After this initial simulation one can

start from the obtained free energy profile F_{MTD} (i.e. obtained with MTD), which can then be used as an additional bias in the subsequent US simulation. This approach leads to a quantitative FES estimate. In practice this can be achieved by defining the inverse of the FES obtained with preliminary MTD simulations as the bias potential whether or not with an extra harmonic bias potential within the US simulations:

$$\mathcal{V}(q)_{b,i} = -F_{MTD}(q) + \frac{1}{2}\kappa[q_i - q_{0,i}]^2 \tag{2.23}$$

Hence the '*a priori*' knowledge is obtained with metadynamics within a limited amount of time, i.e. a qualitiative estimate of the FES is obtained, and subsequently umbrella sampling is used to obtain an (more) accurate estimate of the FES, i.e. a quantitative estimate.

Kinetics and thermodynamics from enhanced sampling MD simulations

Once an accurate FES is derived by means of enhanced sampling MD, it is often desired to extract kinetic data or more specifically, the rate constant, for the elementary step under investigation. However, as it is a kinetic property representing the rate at which the molecular system undergoes a change, cannot be solely derived from thermodynamic considerations. Below it is shown how the rate constant can be derived from MD simulations through the application of transition-state theory. For more detailed information on theory presented below, the reader is referred to Refs. 22,50,51 as well as Appendix A.

Combining the transition-state theory of Eyring and the Bennett-Chandler expression, the conventional way to express the rate constant, k^{TST} (the rate constant following TST) can be expressed as follows (in resemblance to the work performed by Bučko et al.):[22,50,52,53]

$$k^{TST} = A \cdot \frac{e^{-\beta F(q^{\ddagger})}}{\int_{-\infty}^{q^{\ddagger}} e^{-\beta F(q)} dq} \tag{2.24}$$

$$A = \frac{1}{2} \langle |\dot{q}| \rangle_{TS} \tag{2.25}$$

Here q represents the RC, $q^{\ddagger}$ the RC value representing the TS, $F(q)$ the free energy profile associated with the RC. A is expressed in terms of $\langle |\dot{q}| \rangle_{TS}$ which represents the ensemble average (of the absolute value) of the rate of change of q. The absolute value (and the proceeding factor 1/2) can be traced back to the fact that a system starting at the transition state is assumed to transition symmetrically towards products and reactants. However, within TST, we only count the forward transitions towards the product state and assume that once transitioning towards the product, the system nevers recrosses. It is hence a direct translation of the TST as no recrossings or movements towards the reactant region are accounted for. How one should practically calculate k^{TST} is covered

in Appendix A. The implementation of this theory is implemented in an in-house python package ThermoLIB developed by Prof. L. Vanduyfhuys allowing efficient extraction of both kinetic and thermodynamic properties (see next section) from enhanced sampling simulations.[54]

Phenomenological barriers Within the aforementioned methods, we have already highlighted how FESs are constructed from the simulation data. An important aspect which is however not tackled yet is how barrier heights are extracted. A naive interpretation would be to extract it based on the minima and maxima of the resulting free energy profile. Such approach leads to barriers which can be highly dependent on the reaction coordinate used in the simulations.[55] A more robust way is to determine phenomenological barriers ($\Delta F^{\ddagger}_{phen}$), which are independent of the reaction coordinate.[50] The concept is illustrated in a paper by Bailleul et al.[55] and is derived from the rate constant (k^{TST}, Equation 2.24) discussed in the previous section and the Eyrings-Polanyi equation (Equation 2.10):

$$\Delta F^{\ddagger}_{phen} = -k_B T \ln\left(\frac{k^{TST} h}{k_B T}\right) \tag{2.26}$$

or in terms of factor A, $\int_{-\infty}^{q^{\ddagger}} e^{-\beta \Delta F(q)} dq$ (in terms of the free energy profile relative to the reactant minimum) and the 'naive' RC-dependent free energy barrier ($\Delta F^{\ddagger}_{max-min}$):

$$\Delta F^{\ddagger}_{phen} = \Delta F^{\ddagger}_{max-min} + k_B T \ln\left(\frac{k_B T}{h} \frac{\int_{-\infty}^{q^{\ddagger}} e^{-\beta \Delta F(q)} dq}{A}\right) \tag{2.27}$$

A graphical representation is shown in Figure 2.7. Within this respect it is also worth introducing the concept of macrostates. Macrostates, or more specifically a macrostate x of a system is defined as the collection of microstates (defined by their nuclear coordinates $\vec{R}^N$) for which a collective variable takes on a value of q_x within the interval $[x, x + dx]$. This allows us to express the partition function $\mathcal{Z}$ (in the canonical ensemble) as:

$$\mathcal{Z} = \int_{-\infty}^{+\infty} \mathcal{Z}(x) dx \tag{2.28}$$

where $\mathcal{Z}(x)$ can be expressed in the canonical ensemble as:

$$\mathcal{Z}(x) = \frac{1}{\prod_i \Lambda_i^3} \int \delta[X(\vec{R}^N) - x] e^{-\beta V(\vec{R}^N)} d\vec{R}^N \tag{2.29}$$

with $\vec{R}^N$ the positions of all N particles and Λ represents the thermal wavelength resulting from analytic integration of the kinetic contributions over momentum space. This in turn allows us to express the probability of finding the system in a macrostate x, i.e. a probability density, as:

$$p(x) = \frac{\mathcal{Z}(x)}{\mathcal{Z}} \tag{2.30}$$

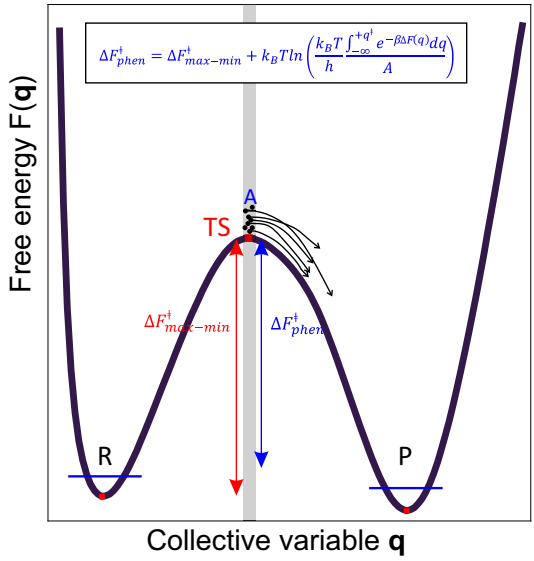

Figure 2.7. Schematic representation of a free energy profile with reactant (R) and product (P) macrostates highlighted with blue lines, red dots indicate the extrema and the gray rectangle indicates the transition state interval used for the determination of the pre-exponential factor A. Max-min - and phenomenological barriers are indicated with red and blue respectively. The former represents the difference between the maximum free energy, i.e. the free energy of the transition state, and the minimum free energy of either the reactant or product state.

Free energy transformations and projections Two important concepts in interpreting FESs obtained from enhanced sampling simulation are on one hand the transformation of the FES described in one collective variable to another CV, and on the other hand the projection or expansion of high-dimensional FESs to lower dimensional FESs or from low dimensional FESs to higher dimensional FESs, respectively. A graphical representation of these procedures is shown in Figure 2.8 (FES tranformation) and Figure 2.9 (FES projection and expansion). It is important to note, that all required information is encoded within the trajectories generated by the enhanced sampling technique, in this case an equilibrium enhanced sampling technique like Umbrella Sampling. Note that the enhanced simulations should be well equilibrated and represent an ergodic sampling.

The probability of a given system being observed with a value $q_x(R^N) = x$ (q_x representing the new collective variable which one is interested in, i.e. q_2 in Figure 2.8) given a value of $q_y(R^N) = y$ (with q_y the original collective variable used to perform the sampling, e.g. the reaction coordinate or q_1 in Figure 2.8) can be

expressed by the conditional probability $p_{x|y}(x|y)$ through Bayes theorem:

$$p_{x|y}(x|y) = \frac{p_{x,y}(x,y)}{p_y(y)} \tag{2.31}$$

Hence, in order to determine the free energy F in terms of q_x instead of q_y, i.e. $F_x(x)$ instead of $F_y(y)$, we need to calculate the probability $p(x)$ in the following way (cfr. Eqs. 2.4, 2.9):

$$p_x(x) = \int_{-\infty}^{+\infty} p_{x|y}(x|y)p_y(y)dy \tag{2.32}$$

given the relation of the partition function with the probability density (Eq. 2.30) on one hand and with the free energy on the other (Eq. 2.9), the free energy can be expressed as:

$$F_x(x) = -k_B T \ln\left(\int_{-\infty}^{+\infty} p_{x|y}(x|y)e^{-\beta F_y(y)}dy\right) \tag{2.33}$$

which is thus the free energy, determined except for a constant which is independent of x, with respect to q_x instead of q_y. The constant might however depend on N,V, T,..., which is thus irrelevant for the purposes we use it.

Now let us consider a two-dimensional FES defined by collective variables q_x and q_y (Figure 2.9, right hand side). In case one is interested in the FES defined by a third collective variable q_z (q in Figure 2.9) then we can (using a probablistic correlation) write the probability of finding a state in $q_z \in [z, z+dz]$,given the values for $q_x \in [x, x+dx]$ and $q_y \in [y, y+dy]$, as:

$$p_z(z) = \int_{-\infty}^{+\infty} p_{z|xy}(z|x,y)p_{xy}(x,y)dxdy \tag{2.34}$$

$$F_z(z) = -k_B T \ln\left(\int_{-\infty}^{+\infty} p_{z|xy}(z|x,y)e^{-\beta F_{xy}(x,y)}dxdy\right) \tag{2.35}$$

Hence establishing a projection of the original two-dimensional FES to a 'new' one-dimensional one.

When considering a one-dimensional FES defined by the collective variable q it can be valuable to extract system-dependent information, e.g. to check whether an additional CV is important in a chemical reaction, by performing appropriate deprojections and hence constructing two-dimensional free energy surfaces (Figure 2.9 with in this case $q_y = q_1$ and $q_z = q_2$). Let us consider two new collective variables q_y and q_z, then we can define a conditional probability $p_{y,z|x}$, i.e. the probability of finding the system which is in macrostate $q = q_x \in [x, x+dx]$ to have $q_y \in [y, y+dy]$ and $q_z \in [z, z+dz]$, and the resulting free energy as:

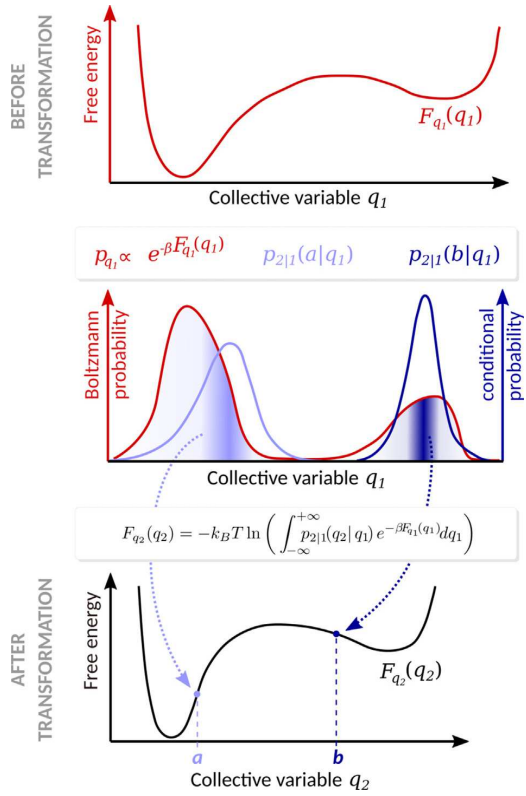

Figure 2.8. Graphical representation of a free energy profile $F_{q_1}(q_1)$, which was computed by sampling along q_1 and expressed as a function of q_1, and its transformation to the corresponding free energy profile $F_{q_2}(q_2)$ as a function of q_2. The integral can be interpreted as a weighted average of the Boltzmann probability, with weights given by the conditional probability and indicated through the shading in the middle pane. Reprinted with permission from Elsevier.[55]

$$p_{xy}(x,y) = \int_{-\infty}^{+\infty} p_{xy|q}(x,y|q) p_q(q) dq \tag{2.36}$$

$$F_{xy}(x,y) = -k_B T \ln\left(\int_{-\infty}^{+\infty} p_{xy|q}(x,y|q) e^{-\beta F_q(q)} dq\right) \tag{2.37}$$

Which is essentially an expansion of the original sampled FES to a 'new' two-dimensional FES. Remark that one of the new variables can in principle also be the original reaction coordinate, e.g. $q = q_1$ in Figure 2.9, which can for example be valuable to explore how certain collective variables change during the reaction progress.

Important is that in no way the above mentioned equations account for the bias applied within the enhanced sampling MD simulations. However, it can be shown

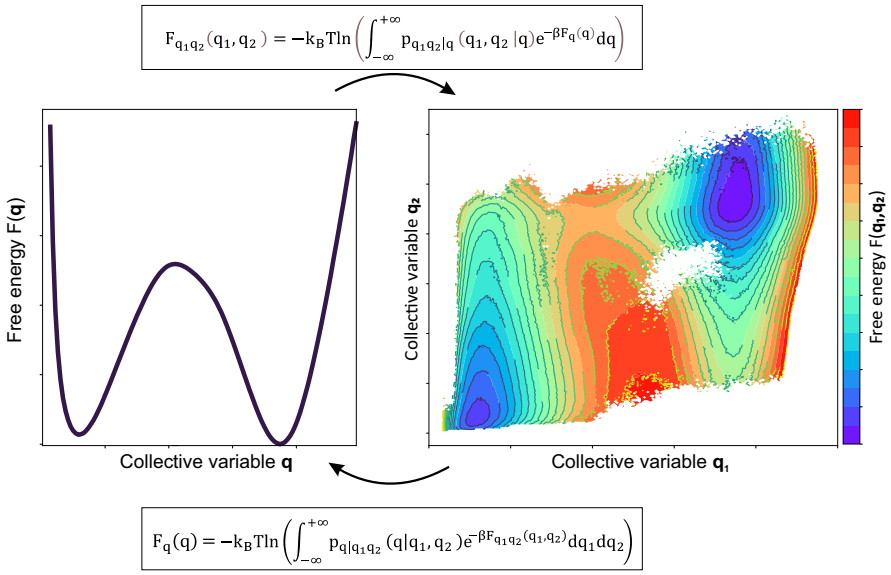

Figure 2.9. Graphical representation of the expansion (left to right) of a one dimensional free energy profile ($F(q)$) towards a two dimensional free energy profile ($F(q_1, q_2)$) and *vice versa* for the projection procedure (right to left).

that probabilities conditional in y extracted from simulations biased in y are equal to unbiased ones ($p^{(b)}_{x|y}(x|y)$ is equal to $p_{x|y}(x|y)$). Here the applied bias potential should be constant in time and only depend on the original collective variable(s), i.e. q in case of Eq. 2.37.

$$
\begin{aligned}
p_{x|y}(x|y) &= \frac{p_{xy}(x,y)}{p_y(y)} \\
&= \frac{p_{xy}(x,y)e^{-\beta V^{(b)}(y)}}{p_y(y)e^{-\beta V^{(b)}(y)}} \\
&= \frac{\int \delta[X(\vec{R}^N) - x]\delta[Y(\vec{R}^N) - y]e^{-\beta V(\vec{R}^N)}e^{-\beta V^{(b)}(y)}d\vec{R}^N}{\int \delta[X(\vec{R}^N) - x]e^{-\beta V(\vec{R}^N)}e^{-\beta V^{(b)}(y)}d\vec{R}^N} \\
&= \frac{\int \delta[X(\vec{R}^N) - x]\delta[Y(\vec{R}^N) - y]e^{-\beta V(\vec{R}^N)}e^{-\beta V^{(b)}(Y(\vec{R}^N))}d\vec{r}^N}{\int \delta[X(\vec{r}^N) - x]e^{-\beta V(\vec{R}^N)}e^{-\beta V^{(b)}(Y(\vec{R}^N))}d\vec{R}^N} \\
&= \frac{p^{(b)}_{xy}(x,y)}{p^{(b)}_y(y)} = p^{(b)}_{x|y}(x|y)
\end{aligned}
$$

Transforming, projecting and extending free energy surfaces based on conditional probabilites is also implemented within the ThermoLIB package.

2.3 Describing the PES

In Section 2.1 we introduced the PES and in Section 2.2 we have explored how to sample interesting regions of the PES. In this section we summarize some methods necessary to calculate the energy of the system for one particular molecular configuration, i.e. within the BOA. In principle to obtain the energy of a system one needs to solve the Schrödinger equation. It is interesting to recall Equation 2.2 and look into the practical implications of the BOA on the Schrödinger equation (i.e. relying on the so-called clambed nuclei assumption within this approximation) which allows us to decouple the electronic and nuclear motion and hence simplify Equation 2.2 to Equation 2.38.

$$\hat{H}_e \left|\Psi_e\right\rangle = (\hat{T}_e + \hat{\mathcal{V}}_{ee} + \hat{\mathcal{V}}_{ne}) \left|\Psi_e\right\rangle = E_e \left|\Psi_e\right\rangle \tag{2.38}$$

where the energy E, the hamiltonian H_e and the wave function $|\Psi\rangle$ are purely electronic and depend parametrically on the nuclear positions. Solving the equation exactly is however still not possible for realistic molecular systems, i.e. systems containing more than one electron, due to the presence of correlation as part of the electron-electron repulsion term ($\hat{\mathcal{V}}_{ee}$) in the Hamiltonian.

Hence appropriate approximations are imperative to computational chemistry in order to determine the energy of a molecular system. Here three important classes of methods are briefly discussed: *ab initio* methods (i.e. Hartree-Fock and Density functional theory), semi-empirical methods and force field methods. Though not discussed here, it is interesting to mention that much larger systems can be simulated using a so-called coarse-graining approach, as an extenstion to atomistic force field methods, where the atoms are not explicitly treated anymore but grouped in beads which interact with each other.[56] Additionally, the field is currently fastly evolving by development of so-called machine-learning potentials where a numerical potential is fit by a non-linear regression method to underlying QM data. It is expected that this approach will play a crucial role in the future for the discovery and rational design of new materials and molecules.[3]

2.3.1 *Ab initio* methods

Within this thesis two *ab initio* methods are discussed namely the Hartree-Fock (HF) method and density functional theory (DFT). The latter method is the preferred method of choice as it allows to obtain relatively accurate properties at a computational affordable cost. *Ab initio* (='from the beginning' in Latin) implies that these methods rely solely on fundamental laws of nature and hence not on empirical data. The interested reader is referred to an excellent review by Takao Tsuneda or more general Quantum Chemistry books.[6,8,57]

Hartree-Fock

By far the most famous *ab-initio* method is the HF method dating back to 1930 in which a single Slater determinant is proposed to approximate the many-body wavefunction. A Slater determinant is an independent particle wave function satisfying the Pauli exclusion principle (i.e. fermions, here electrons, cannot occupy the same quantum state) by introducing antisymmetry in the wave function.[58–60] In order to tackle molecular systems, another very important approximation is introduced, i.e. the linear combination of atomic orbitals-Molecular orbitals (LCAO-MO) approximation. This approximation states that molecular orbitals are written as a linear combinations of atomic orbitals (also known as basis functions).[61,62] In order to solve the Schrödinger equation using the HF method, the self-consistent field (SCF) method is employed where one starts from an initial guess for the molecular orbitals and then iteratively solves the equations untill convergence of the HF potential is reached.

One major shortcomming of the HF method is that it does not account for electron-electron correlation. More advanced methods, e.g. Post-HF methods or DFT, do incorporate correlation energy and hence provide energies closer to the 'true' electronic energy of the molecular system.[57] Examples of post-HF methods are perturbation theory (Møller-Plesset perturbation theory[63], MP2, MP3, ...) or configurational interaction (CI). However, all these methods are computationally very expensive and not feasible for the systems under investigation in this thesis. Within this thesis another many-body technique is used namely DFT which allows to include electron correlation in a computationally feasible way.

Density functional theory

As the name suggest, the electron density $\rho(\vec{r})$ (with $\vec{r}$ the electron positions) instead of the wave function plays the central role in DFT.[64,65] Below the basics of the theory are shortly introduced.

Hohenberg and Kohn were the first to show that the ground state density $\rho(\vec{r})$ is able to describe all properties of the system, and is hence equivalent to the wave function $|\Psi\rangle$ in the ground state.[66] More specifically the energy of a system may be expressed as an energy functional in terms of the density $E[\rho]$ where the ground state density can be found by applying a minimization principle such that $E_0 = \min_{\rho} E[\rho]$. In this case $E[\rho]$ can be expressed, in line with Equation 2.38, as:

$$E[\rho] = T_e[\rho] + \mathcal{V}_{ee}[\rho] + \mathcal{V}_{ne}[\rho] \tag{2.39}$$

where the kinetic and Coulombic energy parts are now explicit functions of the electron density.

In case the exact form of the functional $E[\rho]$ would be known, DFT is an exact theory. The problem however is that this functional is not exactly known.

Hence, for DFT to become a useful method, appropriate approximations need to be made to describe the functional as accurate as possible. Mathematically this boils down to finding a way to describe the electronic kinetic -, the exchange - and the correlation energy.

Finding an exact expression for the kinetic energy functional is avoided by using the so-called Kohn-Sham scheme.[67] In essence the scheme replaces the system under investigation by an equivalent independent-particle model (IPM), i.e. a single Slater determinant, which has a density equal to the original system. The Kohn-Sham non-interacting system is described by the Kohn-Sham orbitals (i.e. one particle orbitals) which are obtained by solving the Kohn-Sham equations. As these equations are dependent on the density themselves, they are solved self-consistently. Remark that the non-interacting system is only introduced to help find the exact ground state energy density but has apart from this no physical meaning. The resulting expression for the energy functional can be written as follows:

$$E[\rho] = T_S[\rho] + \int \rho(\vec{r}) v_{en}(\vec{r}) d\vec{r} + \frac{1}{2} \int \frac{\rho(\vec{r})\rho(\vec{r}')}{|\vec{r} - \vec{r}'|} d\vec{r} d\vec{r}' + E_{xc}[\rho] \tag{2.40}$$

where T_S, v_{en} and E_{xc} represent the Kohn-Sham kinetic energy functional of the IPM, the potential generated by the positive nuclei of the system and the exchange-correlation functional respectively. The exchange-correlation functional captures all parts of the kinetic energy and electron-electron interactions which are not accounted for in the three other terms. It consists of both an exchange and correlation contribution and remains the main source of errors as only (educated) guesses exist for the exchange-correlation functional. This is the reason why a pleithora of functionals have been introduced in literature, typically referred to as the functional zoo.[68]

A general expression for the exchange-correlation functional is given below:

$$E_{xc}[\rho] = \int \rho(\vec{r}) \underbrace{\epsilon_{xc}[\rho(\vec{r}), \nabla\rho(\vec{r}), \nabla\rho(\vec{r})^2, ...]}_{Functional\ zoo} d\vec{r} \tag{2.41}$$

where the energy density, ϵ_{xc}, itself is dependent on the electron density ($\rho(r)$) in the local density approximation (LDA) or on the electron density and its gradient in the generalized gradient approximation (GGA, e.g. BLYP).[69,70]

Meta-GGAs on the other hand account for the Laplacian of the density in the calculation of ϵ_{xc}. Taking it one step further (read using more costly and accurate functionals) one can use hybrid functionals, which combine both HF exchange and DFT exchange and correlation in a single formalism (e.g. B3LYP, ωB97X).[72–74] Hybrid functionals offer a very good balance between accuracy and cost and are hence the functionals to use in the study of organic molecular systems. Double hybrids on the other hand combine the strength of separate hybrids in a single

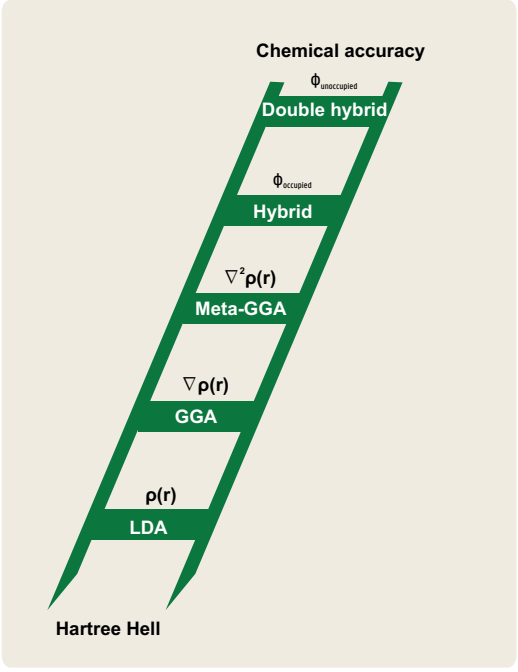

Figure 2.10. Jacobs ladder introduced by Perdew et al.[71], representing the different classes of functionals which are hierarchically ordered based on their corresponding accuracy. The different functional types progressively account for the density, its gradient, its laplacian, the occupied orbitals and the unoccupied ones for local density approximation (LDA), generalized gradient approximation (GGA), Meta-GGA, hybrid and double hybrids respectively.

function but are rather costly in terms of computational recourses and time and are hence not used in this thesis. A schematic overview is shown in Figure 2.10, which is the well known Jacobs ladder[71] representing the increased computational cost and accuracy for each approach discussed above.

Worth highlighting is the major shortcoming of DFT to describe (London) dispersion interactions, also referred to as Van der Waals (VdW) interactions, as most modern functionals only account for the (semi-)local density. They thus 'completely' ignore long-range interaction such as dispersion or other non-local correlation effects.[57] Hence to this end some functionals include dispersion corrections in their functional form, e.g. the APF functional.[75] Alternatively one can apply corrections *a posteriori* as proposed by Grimme, e.g. Grimme's D3 dispersion corrections.[76]

In general these corrections are often based on both empirical and/or accurate *ab-initio* data. Accounting for these effects is often imperative to study ther-

mochemistry and reaction kinetics using DFT. All DFT calculations performed in this thesis make use of them either by accounting for them implicitly within the functional form (ωB97X-D) or by manually adding Grimme's D3 dispersion corrections (BLYP-D3), i.e. specifying it explicitly in the input file.[77] Depending on the characteristics of the system under investigation, the desired accuracy and the available resources a different functional can be chosen. As a guideline two recent benchmark studies of Goerigk and Mardirossian can be used.[68,78]

2.3.2 Semi-empirical methods

Semi-empirical methods omit the need to calculate integrals explicitly (such as two-electron integrals) by compensation with empirical parameters. The different methods available in literature are strongly rooted within Molecular Orbital theory, but the parameters are derived from empirical reference data. In this way one can obtain approximate solutions for the Schrödinger equation in a very short amount of time. The results are unfortunately often hampered by poor accuracy. Nonetheless, it is the speed of these methods which can be highly beneficial in the search for global minima and/or transition states. Due to the empirical reference data required, the suitability of the methods is highly susceptible to the molecular system under investigation.

Within literature two models which are often used are on one hand the Austin model 1 (AM1) developed by Dewar et al. and on the other the parametric methods (PM3, PM6, PM7) developed by Stewart et al.[79–83] AM1 is used for the study of organic molecules consisting of hydrogen, carbon, oxygen and nitrogen. Concerning PM3, PM6 and PM7, the increasing number illustrated the increasing amount of data accounted for in the parameterization procedure and hence the increasing accuracy and coverage of the method. While PM3 is comparable to AM1, PM6 for instance covers 70 elements and parameter improvement for all main group elements with respect to both PM3 and AM1.[82] PM7 on the other hand is improved with respect to PM6 by including more experimental data and data from high-level *ab initio* calculations with an improved treatment of non-covalent interactions.[83]

In this work semi-empirical methods, mainly PM6 and PM7, were used to accelerate transition state searches, i.e. finding a good initial guess of a transition state before proceeding with more expensive (in terms of computational cost and time) DFT calculations.

2.3.3 Force field methods

Force fields or molecular mechanics (MM) assumes that the electronic energy of a molecular system can be expressed by an *a priori* given mathematical expression in terms of the nuclear coordinates. In this case the electronic structure problem is not solved explicitly, meaning that the PES of a system can be completely determined

based on this expression in a matter of seconds or minutes (depending on the complexity of the formula and the system size), making it feasible to describe very large systems ($\gg 100.000$ atoms) at very long timescales ($\gg ns$-scale). The postulated mathematical expression depends on the applied force field but can generally be decomposed in a covalent part describing the forces between bonded atoms and a non-covalent part describing the forces between non-bonded atoms both intra- and intermolecular, i.e. the forces acting through space (long-range interactions). Important to note is that a force field is no longer an electronic structure method, in contrast to the aforementioned methods, as electrons are no longer described explicitly.

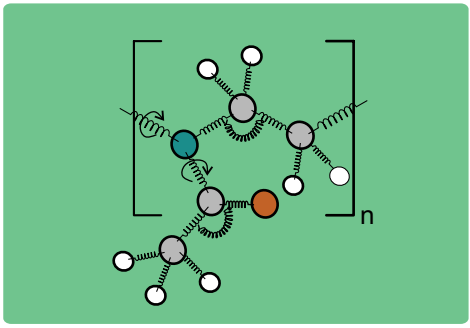

Figure 2.11. Illustration of basic polymer force field terms with some example bond-, bend and dihedral terms.

Hence the potential energy $\mathcal{V}$ can be expressed as follows:

$$\mathcal{V} = \mathcal{V}_{covalent} + \mathcal{V}_{non-covalent} \tag{2.42}$$

$$\mathcal{V}_{covalent} = \mathcal{V}_{bond} + \mathcal{V}_{bend} + \mathcal{V}_{torsion} + \mathcal{V}_{cross} + ... \tag{2.43}$$

$$\mathcal{V}_{non-covalent} = \mathcal{V}_{electrostatic} + \mathcal{V}_{VanderWaals} \tag{2.44}$$

While many different formulations exist for the covalent potential, a typical expression for the bond, bend and torsion term is given below.

$$\mathcal{V}_{bond} = \sum_i \frac{k_{bond,i}}{2}(r_i - r_{i,0})^2 \tag{2.45}$$

$$\mathcal{V}_{bend} = \sum_i \frac{k_{bend,i}}{2}(\theta_i - \theta_{i,0})^2 \tag{2.46}$$

$$\mathcal{V}_{torsion} = \sum_i \sum_m c_{torsion,i,m}[1 + cos(M_{i,m} \cdot \phi_i - \phi_{0,i,m}))] \tag{2.47}$$

where k represents the respective force constant, $c_{torsion,i,m}$ are Fourier amplitudes and $M_{i,m}$ are multiplicities of torsion term m of torsional angle (= dihedral angle) i. $r_{i,0}$, $\theta_{i,0}$, $\phi_{i,0}$ denote the equilibrium distance, angle and torsional angle respectively. Concerning the non-covalent potential energy contributions typical

expressions are shown below where we approximate the atomic electron cloud with a point charge q, i.e. a partial atomic charge, and use a Lennard-Jones potential to describe the VdW interactions:

$$\mathcal{V}_{electrostatic} = \frac{1}{2}\sum_{i\neq j}\frac{q_i q_j}{r_{ij}} \tag{2.48}$$

$$\mathcal{V}_{VanderWaals} = \sum_{i\neq j} 4\epsilon\left[\left(\frac{\sigma}{r}\right)^{12} - \left(\frac{\sigma}{r}\right)^{6}\right] \tag{2.49}$$

where ϵ displays the potential well depth, i.e. the energy at which the potential reaches its minimum, and σ the inter atomic separation where attractive and repulsive forces balance.

It is clear that a force field depends on many parameters. Those parameters can be derived from *ab-initio* training data or experimental training data to which these parameters are fit. This leads to *ab-initio*-derived force fields or empirical force fields respectively, each with its own benefits and drawbacks.

Concerning *ab-initio*-derived force fields, the in-house developed software packages QuickFF and Horton are excellent and easy to use tools to derive a system-specific force field from QM-data (e.g. from DFT calculations).[84,85] Alternative to deriving or using system-specific force fields, it is often desirable to use general force fields which are parameterized to represent a broad set of systems and related properties with reasonable accuracy, e.g. GAFF(2) or the Open Force Field Initiative small molecule force fields (OFFI).[86–88] Apart from system-specific and general-purpose force fields, also many force fields exist to describe different classes of molecules such as proteins, DNA, lipids or something as 'simple' as water (amber14, charmm36, tip4p-fp, ...).[89–91] The force fields described are non-reactive as no bond breaking or formation processes can be described. Force fields which are able to describe reactive events are referred to as reactive force fields of which ReaxFF is probably the most famous one.[92] However the accuracy is highly dependent on whether or not particular classes or systems have been accounted for in the parameterization procedure. In this thesis we do not use reactive force fields and thus they are not further discussed.

To finalize the discussion on how to calculate the energy of a molecular system,it is worthwhile mentioning that depending on the size of the molecular system one can use hybrid methodologies such as QM/MM.[57,93] With these hybrid methods one can investigate a small portion of the system, e.g. a reactive center, with high accuracy using QM methods and the rest of the system at lower accuracy using MM. Such methods were not used within the framework of this thesis and thus not further discussed here.

2.4 Solvent treatment

For most applications treated in this thesis, it is of utmost importance to account for solvent effects. Various models have been proposed in literature to treat solvent either explicitly or implicitly. The interested reader is referred to the book of Tantillo et al. or dedicated review papers.[94–97]

The method for solvent treatment is highly system dependent and is in some cases hampered by an increased computational cost when explicitly accounting for solvent molecules. Due to this increased cost different methodologies have been devised where we will distinguish three: Continuum solvation models, Explicit solvation models and hybrid models (see Figure 2.12). Some implicit and explicit approaches are applicable in both the dynamic and static approach, though a dynamic approach is normaly used to describe processes with extensive solvent effects. Each of the models is shortly introduced in the following subsections, illustrated with concrete examples.

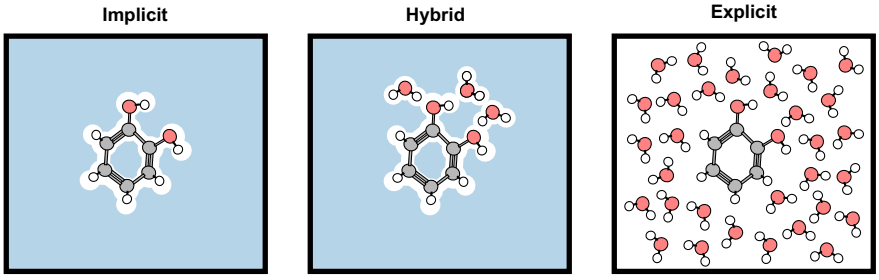

Figure 2.12. Overview of solvation approaches applied in this thesis. On the left, an implicit solvation model is used to solvate catechol; in the middle a hybrid model is used combining an implicit and a discrete number of explicit solvent molecules; on the right the solvent is treated explicitly.

The choice of the applied model highly depends on whether specific solute-solvent interaction are expected and the polarity of the molecules. When treating apolar molecules and/or no specific interactions are to be expected generally continuum models will suffice. However when polar molecules (i.e. solvents with high dielectric constants) are considered and strong non-covalent interactions (e.g. hydrogen bonds) are present in the system then one typically adopts methods beyond the continuum approach where solvent molecules are treated explicitly. The latter evidently is accompanied by an increased computational cost and should be used when considering solvent reorganization, cross-solvation shell processes (e.g. proton-shuttling) or other processes which involve substantial solvent-induced entropic effects.

2.4.1 Continuum solvation models

Within continuum models, the solvent effects are embedded within a continuum medium which is described by using macroscopic properties such as the dielectric constant ϵ, density ρ, surface tension, ... Despite the fact that specific solute-solvent interactions are lost, it has found a widespread use because a drastic decrease in computational cost is achieved with respect to an explicit treatment and long-range interactions are accounted for properly. An extensive overview of different continuum models available in literature is given by Cammi et al.[95,98] From the different continuum models available in literature, only the integral equation formalism-polarizable-continuum model (IEF-PCM) developped by Mennucci et al. is considered here (*vide infra*), however some general concepts of continuum models are highlighted below.

Generally, all continuum models are based on the following assumptions:

- a solute occupies an empty cavity
- the solvent can be treated as a continuous dielectric which can be described by macroscropic propeties
- solvent is an isotropic medium at a specified temperature and pressure which is at equilibrium
- the continuum expands to infinity in all directions
- no solute-solute interactions are present, i.e. a dilute solution is considered

To illustrate some concepts, an illustration is given for a molecule of relevance in this thesis. Let us consider the alcoholysis of exovinylene cyclic carbonate discussed in Section 4.3.1. The reaction is performed in dimethylsulfoxide (DMSO) hence when considering the reaction we would like to account for the solvent and its effect on the activation barriers. To this end the key observable of interest is the free energy of solvation ΔG_{solv} representing the work needed to bring a molecule, in this case the reactive system, from gas to the solvent phase (see Figure 2.13). In its most crude form it can be expressed as follows:

$$\Delta G_{solv} = \Delta G_{el} + \Delta G_{cav} + \Delta G_{short-range} \tag{2.50}$$

with ΔG_{el} the electrostatic contributions, ΔG_{cav}, the contribution of generating a cavity and $\Delta G_{short-range}$ the contribution of the short-range interactions, i.e. Van der Waals interactions and repulsive interactions. Within a continuum model we hence try to approximate this ΔG_{solv} which is used to correct the E_0 during the calculations. Because the charge distribution of the solute itself polarizes the environment, the calculation of ΔG_{solv} should be performed via an iterative self-consistent reaction field (SCRF) scheme.

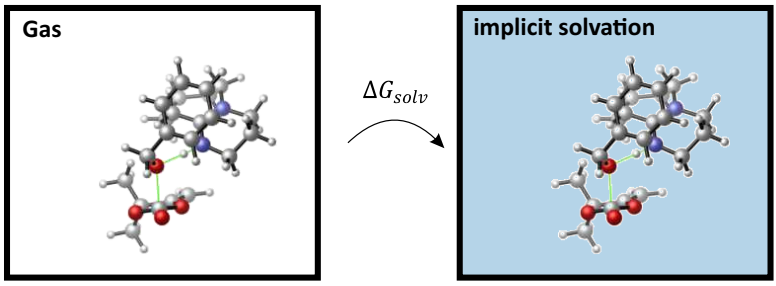

Figure 2.13. Illustration of ΔG_{solv} for a continuum model. Here illustrated for the model exovinylene cyclic carbonate used in **Paper III** and **Paper IV** which is undergoing a nucleophilic attack by benzylalcohol in the presence of an organocatalyst (DBU).

The oldest among the continuum models are the PCM models which benefit from the fact that they are independent of the solute shape and charge distribution. They treat the electostatic contribution (ΔG_{el}) by accounting for the surface charge density which is spread over the cavity surface in which the solute molecule is residing. More specifically IEF-PCM is considered to be the most general and accurate PCM-model available which in addition to the aforementioned benefits no longer depends on the cavity definition.[95]

2.4.2 Explicit and Microsolvation models

When strong specific solute-solvent interactions are present or when the solvent is of importance in the reaction mechanism then an explicit treatment becomes of paramount importance. Explicit treatments can be distinguished from one another by the amount of solvent molecules accounted for and whether or not it is used in conjunction to a continuum model, i.e. a cluster-continuum model.[99] This section encompasses both the hybrid and explicit solvation models where the core concepts are illustrated by considering the *O*-demethylation of guaiacol in hot-pressurized water which is discussed in Section 4.2.2 (see Scheme 2.1) . Within explicit solvent simulations, water poses perhaps the ideal case study as in the case of *O*-demethylation it acts both as the solvent and as one of the reactants. Furthermore it involves strong hydrogen-bonding and -presumably- also cross-shell proton hopping. Let us first consider the use of a hybrid model to describe solvation after which we increase the amount of solvent, hence omitting the need for an implicit treatment, and proceed to a full explicit description of the solvent.

Hybrid solvation models: cluster-continuum model

In case both long-range and short-range interactions (i.e. specific solute-solvent interactions) are of importance and one needs to limit the computational cost of

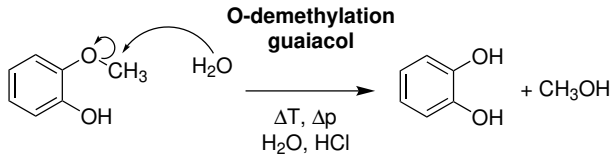

Scheme 2.1. *O*-demethylation of guaiacol with formation of catechol in hot-pressurized water.

the simulations, then a cluster-continuum approach can be of help. It includes a limited amount of solvent molecules to describe solute-solvent specific interactions and a continuum model to capture long-range solute-solvent and solvent-solvent interactions. The method has shown to give reliable results for solvation free energies when considering strong solute-solvent interactions.[99] The results are typically superior with respect to a pure continuum treatment for these systems, though inferior to a full explicit treatment. However as often computational cost needs to be considered within computational chemistry projects, the method provides a good balance between both.[100]

O-dealkylation of guaiacol involves an S_N2-mechanism with the attack of a water molecule on the methyl moiety, hence a minimum of 1 water molecule (i.e. the reacting one) should be accounted for. However as the reaction is catalyzed by a Brønsted acid one needs to account for the involvement of a hydronium ion within the reactive system. A hydronium ion is known to exist in an aqueous environment either as a Zundel - [$H_5O_2^+$] or Eigen ion [$H_9O_4^+$] and thus in order to stabilize the hydronium ion 3 extra water molecules are added to the system resulting in a total of 5 water molecules are added (see Figure 2.14 left panel). The reacting solvent and solvent-specific interactions (stabilization of the hydronium ion) are in this way accounted for.

However, this can be taken a step further by the following: 1) water molecules can hydrogen bond to the hydroxyl moiety and 2) the attacking water molecule can donate a proton to surrounding water molecules. To this end the number of water molecules can be increased to 10 which is illustrated in Figure 2.14 (right panel). Obviously the amount of solvent to add is non-trivial and non-unique, furthermore we currently do not allow for the proton to migrate beyong the first solvation shell (which is not fully accounted for anyway) and do not account for the fact that any water molecule of the water can attack the methoxy moiety (having a high entropic influence on the resulting barrier). To tackle these shortcomings it is essential to progress to a full explicit treatment of the solvent with the number of water molecules far exceeding the number used in hybrid model B of Figure 2.14.

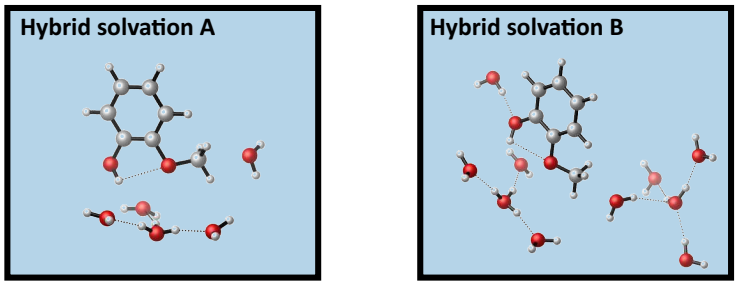

Figure 2.14. Hybrid solvation models to investigate the *O*-demethylation of guaiacol. Model A shows a structure with the minimal amount of explicit solvent molecules needed to study the investigated conversion, model B illustrates an example where we additionally account for a proton acceptor group and an extra water molecule which is hydrogen bonding with the unreacting hydroxyl moiety.

Cluster models

In order to proceed with a full explicit treatment we will introduce so-called cluster models. With cluster models we will here refer to all models accounting for multiple solvent molecules ($N_{solvent} \gg 1$) without the addition of a continuum model. The goal of the cluster models is to describe solute-solvent interactions explicitly, to account for solvent reorganization and/or to capture solvent-specific processes like proton hopping. Depending on the system, the conditions, the electronic structure method used to evaluate the electronic energy and the computational resources available, the amount of solvent molecules accounted for may vary. Ultimately the particular choice remains a trade-off between accuracy and speed which is system dependent.[101]

While true systematic approaches are absent in literature, a method which is used in some cases is the variational method.[99] In this method the number of solvent molecules is increased untill the solvation free energy reaches a minimum. This results in the addition of solvent molecules which have a significant energetic contribution. In practise, often chemical intuition and a trial-error approach are used to determine the number (and location) of solvent molecules.[100] In this thesis however, typically the system under investigation is solvated by accounting for at least one or two solvation layers surrounding the solute which is most often done by using periodic boundary conditions (*vide infra*), depending on the solvent and system under investigation. In case of the demethylation of guaiacol we want to allow proton-hopping to occur, i.e. proton transfer to and from the environment beyond the first solvation shell, and saturate all possible hydrogen bonding sites within the reactive system. To this end we want to include a minimum of two

solvation layers which we can increase depending on the computational cost. When working with various solvation layers most often periodic boundary conditions are used.

Periodic boundary conditions (PBC) enable us to treat realistic systems without the need to include all particles of the system (e.g. 6.02 x 10^{23} particles) by mimicking the presence of an infinite bulk surrounding a relatively small, representative part of the system.[22,102] The concept of PBC is illustrated in Figure 2.15 where the region which is simulated is highlighted in bold, i.e. the simulation box. The simulated box is virtually surrounded with replicate boxes (also referred to as periodic images) removing boundary effects during the actual simulation and hence circumventing the need to explicitly account for all surrounding molecules. In essence particles moving out of the simulation box, for example to the replicate box on the right, will also move in via one of its periodic images in this case the one on the left hand side.

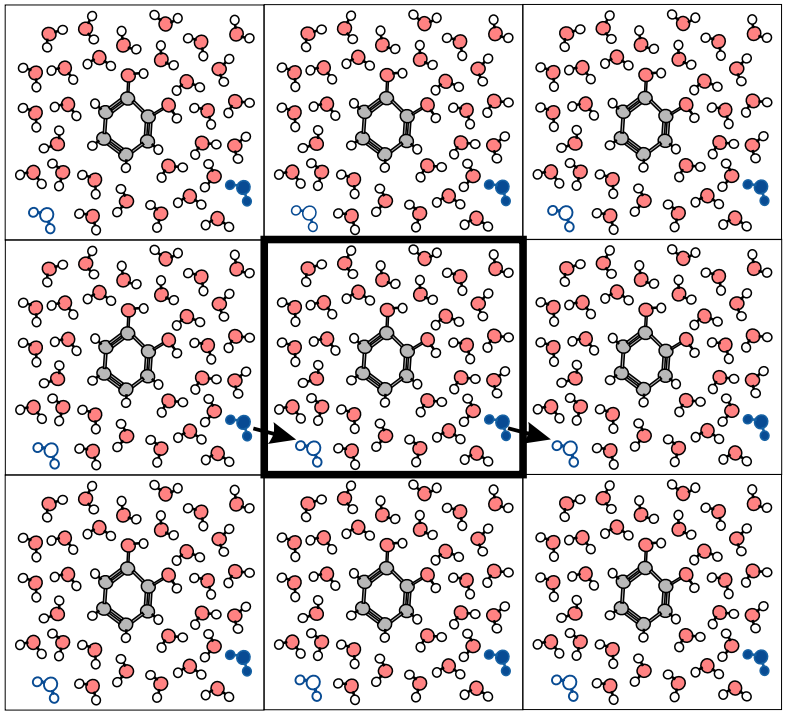

Figure 2.15. Periodic boundary conditions in 2D.

In Figure 2.16 a periodic set-up is shown illustrating the simulation box used to investigate the *O*-demethylation of guaiacol. The box includes two solvation shells, one hydronium ion and has been equilibrated at the operating conditions (see Appendix B). The periodic box contains 531 atoms.

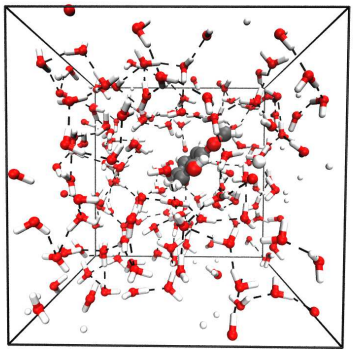

Figure 2.16. Explicit solvation model of guaiacol in hot-pressurized water at 523K and 75 bar (pre-equilibrated with the approach tackled in Appendix B).

Preparing an explicitly solvated solute, and hence setting up a so-called periodic box at the correct conditions (T,p,...), is not trivial and covers multiple aspects of this chapter. Hence a typical workflow for the construction and equilibration of solvated systems which can be used by future researches as a guideline is presented in the appendix B, tackling a case study relevant to the work presented in this thesis. The workflow can be used for the preparation of MD simulations using explicit solvation, for the prepration QM/MM simulations, to obtain initial solvated structures for static calculations, ...

2.5 System set-up and Simulation programs

Throughout the previous chapters we have already highlighted many tools to extract valuable information from both static and dynamic simulations. It is however worthwhile to highlight the key software packages used in this work and highlight how they are used for setting up systems, perfoming simulations and analyses.

System preparation is performed with Gaussview and some dedicated python packages which are illustrated in the workflows covered in Appendix B and C.[103–106]

The simulations in this doctoral thesis are performed using the following software packages, depending on the sampling method and level of theory used:

1. Gaussian16 to perform static calculations using DFT and/or semi-empirical methods.[19]

2. CP2K interfaced with PLUMED to perform classical - and enhanced sampling MD simulations.[107,108]

3. OpenMM was used to perform all force field calculations utilizing its GPU-accelerated features to speed up the simulations. In this sense systems containing up to 45000 atoms were simulated.[106]

Analysis of all results is perfomed with python or python-based packages, e.g. YAFF, ThermoLIB, MDTraj, MDAnalysis,...[109–111] For visualization purposes more dedicated programs like NCIPlot (to visualize non-covalent interactions), VMD and CylView are used.[112–114] For more detailed information on system preparation, simulations and analyses the reader is referred to the dedication papers in Part II.

3

Introduction to polymer science

Polymer science or the study of polymers, comprises polymer chemistry and polymer physics.[115] Whereas polymer chemistry focuses on the characterization, synthesis and physical properties of the macromolecules; polymer physics focuses more on the properties associated to the materials generated from polymers. Of course some overlap always exist and each branch on its own is actually a multi-disciplinary research field.[116] As it is impossible to give a comprehensive overview of the field given its broadness, only those aspects relevant for this thesis are highlighted. The more interested reader is referred to dedicated textbooks by T. P. Lodge and P. C. Hiemenz or R. J. Young and P. A. Lovell.[115,117]

At first instance we will introduce what polymers are (Section 3.1) and a brief history of how polymers and in extension polymer science evolved (Section 3.2). Then, in Section 3.3 the different polymer architectures and classes are highlighted where we subsequently focus on the different polymerization strategies used for their production (Section 3.4). In the latter we will introduce the foundations for the two polymerization reactions studied in this thesis, i.e. step copolymerization and cationic ring-opening polymerization. Finally Section 3.5 is dedicated to introduce the concept of depolymerization with the goal to recover or produce polymer building blocks or platform molecules. This section is used to set the scene for the BioFactory (Chapter 4) which is build on the concepts introduced herein.

3.1 Polymers

Polymers are a group of material which are omnipresent in the everyday society. Interchangeably referred to as macromolecules, they consist of long sequences of one or smaller building blocks. These building blocks can be referred to in many ways i.e. monomers, chemical units or repeat(ing) units (to name just a few). These monomers form the basis for a class of materials with a very broad application field finding its use in many sectors (clothing -, plastic -, automotive -, ...) or in living organisms as fundamental building block for e.g. DNA, proteins, . . . (see Figure 3.1). In general polymers originating from constituents found or derived in nature are refered to as biopolymers or biological-sourced polymers.

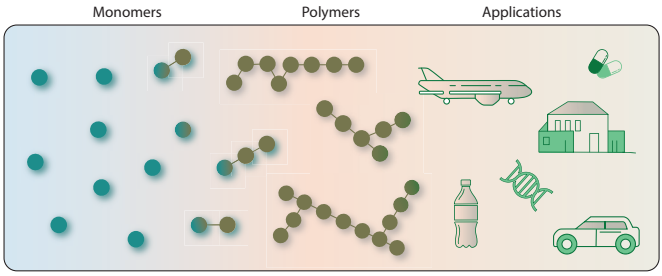

Figure 3.1. Illustration of monomers, polymers and their potential application fields.

3.2 A brief history of polymer science

Originally polymer science focused on altering the physical properties of natural occurring polymers. The most important polymers back then were cellulose and rubber, with the first application dating only from 1820.[117] Remark however that humans have used polymers, i.e. biopolymers, from the ancient times (think of wool, hemp, rubber). It took chemists nearly one hundred years (in 1910) to construct the first fully synthetic polymer: the so-called Bakelite, invented by Leo Baekeland. Bakelite is technically a phenol-formaldehyde resin. Despite Bakelite being the first synthetic (and commercial) polymer, Baekeland did not have any notion of the polymer concept and hence one instead refers to Wallace Hume Carothers as the pioneer for modern polymer science, constructing the first synthetic rubber while being employed at DuPont.[116] Later in 1953 a first Nobel Prize was awarded to Hermann Staudinger who recognized that polymers consists of covalently bound chemical units forming very large molecules which he termed macromolecules.[118] This was the first time the term 'macromolecules' got coined to describe polymers. Noteworthy is the work of Paul Flory who also received a Nobel Prize in 1974 for his theoretical and experimental contibutions to the field of physical chemistry of macromolecules.[119] Though tremendous efforts and advances have been made in the past decades, many challenges still await researchers active

in this field.

With respect to polymer science the application of molecular modeling within this field is relatively young, with the first research dating from the '70s.[120] Nonetheless with recent advances in computer hardware, software and methodology surely modeling will become an indispensible tool.[121] Depending on the research problem, the goal for a computational chemist is to:

1. Establishing reaction mechanisms and structure-reactivity trends within the polymerization process, which can in turn be used for the rational design and parameterization of kinetic models used for process optimization and polymerization control.[122]

2. Understand and predict the properties and behavior of polymeric materials.[121]

However one particular challenge in the application of modeling on polymer science is the broad spectrum of length and timescales governing the overall polymerization properties.[123] Furthermore the final polymers typically consist of many thousands of atoms making them very difficult to model with first principle models. Within this thesis a variety of complementary modeling techniques have been used to understand various aspects of the polymerization process and final properties.

3.3 Polymer architecture and classification

The application field of a polymer depends highly on its properties which in turn are mainly determined by the intrinsic properties of the building blocks and the type of connectivity between these building blocks.

Various polymer structures can be distinguished based on this connectivity:

1. Linear polymers
2. Cyclic polymers
3. Branched polymers:
   (a) comb
   (b) four-arm star
   (c) hyperbranched
4. Network polymers

which are schematically presented in Figure 3.2. In this work mainly linear polymers are studied.

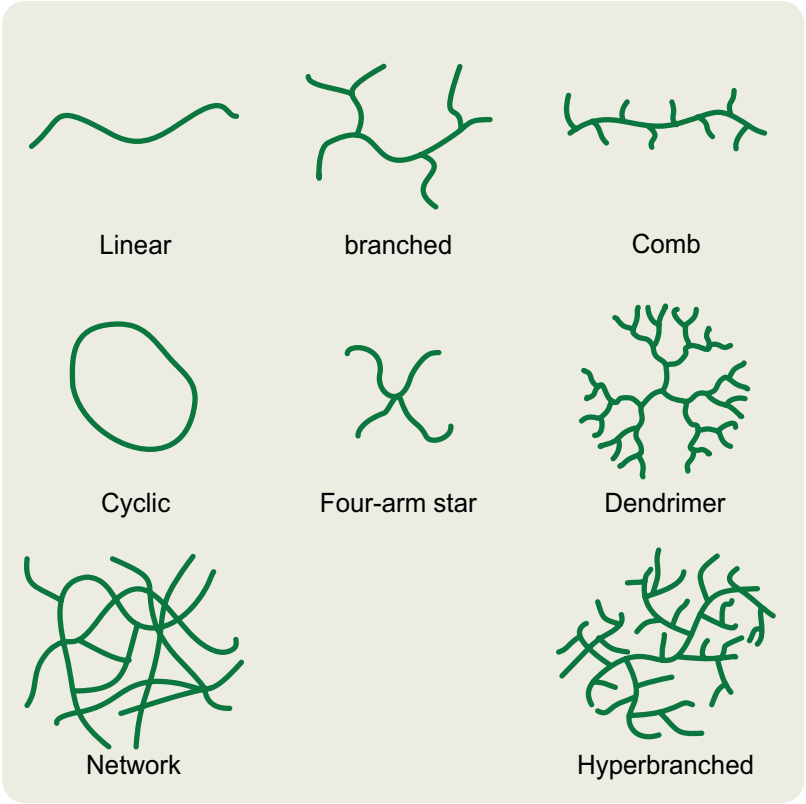

Figure 3.2. Polymer architectures.

Regarding the building blocks, a distinction is made between homopolymers and copolymers.[117] The former refers to polymers derived from a single species of monomer, or in the broader sense a structural unit (which can in theory be comprised of multiple monomers in a single building block). The latter refers to polymers which are derived from two or more monomeric species (same comment holds here, i.e. it often better to describe the copolymer in terms of its structural unit). In case three structural units are used the system is called terpolymer, and so on. In essence the properties of copolymers is determined by the nature and proportions of the different repeat units and the way these are distributed along the chain. Hence, different repeat units, or concentrations hereof, give rise to different reaction rates resulting in different architectures. A thorough understanding of the copolymerization process is hence required to control copolymer composition and the sequence distribution of the repeat units. Nonetheless, within the framework of copolymers, various combinations are distinguished that enable the description of these polymers, an overview is presented in Figure 3.3:[115]

- Random or statistical copolymers, are polymers which composition is strictly

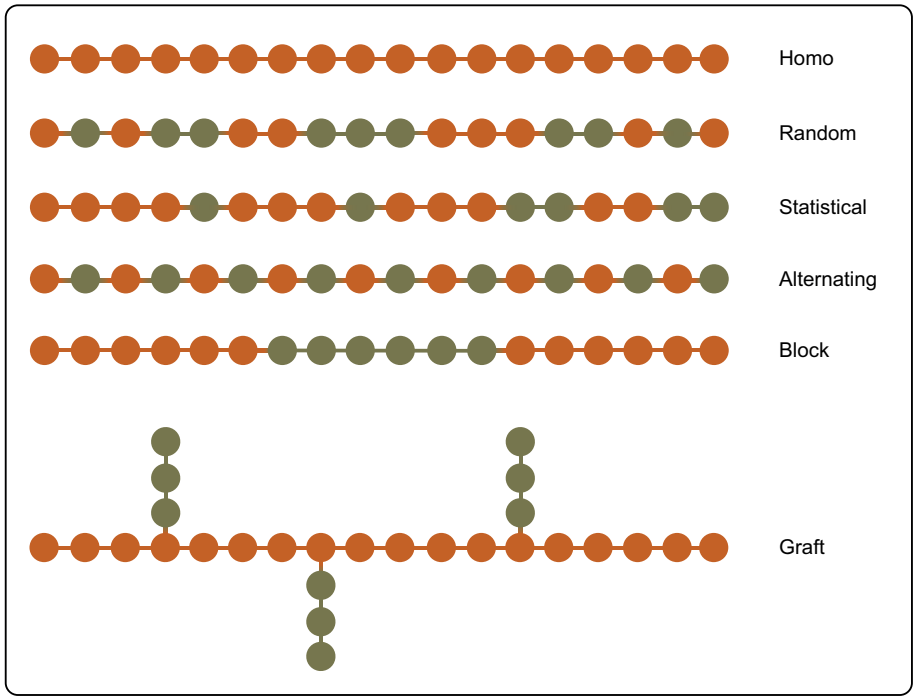

Figure 3.3. Schematic representation of copolymer categories. Circles represent a single structural unit where the different colors distinguish different repeating units. Remark that the random and statistical copolymer differ in the fact that in the former case each structural unit reacts equally fast whereas in the latter case the incorporation of the red structural unit is more probable.

determined by chance:

  - ⋆ Random copolymers: each structural unit has a 50% chance to react with the polymer chain.
  - ⋆ Statistical copolymer: one of the structural unit reacts faster (i.e. more likely) with the polymer chain and is hence depleted faster. In Figure 3.3 the red repeating unit has a higher probability of reacting.

- Alternating copolymers, polymers which have a regular pattern of alternating structural units.
- Block copolymers, polymers which have long uninterupted sequences of each monomer.
- Graft copolymers, polymers which have a single homopolymeric chain to which homopolymers of a second monomer are connected. Typically first the homopolymers are formed for each species after which polymer chain ends of monomer B are reacted with the homopolymer of monomer A.

We will see that in essence the resulting copolymer is determined based on the functional groups of the repeating units and/or the polymerization rate constants of each structural unit.

In practice, polymers are classified (regardless of its compositions) into 3 main groups: Elastomers (cross-linked rubbery polymers), Thermosets (network polymers with restricted chain motions) and Thermoplastics or simply plastics (linear and/or branched polymers). With respect to the presented work in this dissertation, the latter group is worthwhile elaborating on as the projects dealing with polymerizations or polymer applications are intrinsically all thermoplastics.

Thermoplastics are (often) amorphous materials which are difficult to crystallize upon cooling due to the highly entangled and coiled nature of the polymer chains. Those which do tend to crystallize are in many cases semi-crystalline with both amorphous and crystalline regions. Upon heating thermoplastics, two characteristic temperatures can be distinguished. On one hand if a polymer is crystalline or possesses crystalline regions, the plastic can be characterized by a melting temperature T_m. On the other hand, polymers containing amorphous regions or those which are completely amorphous can be characterized by a glass-transition temperature T_g. The T_g is the temperature at which (semi-)amorphous polymers abruptly change from a glassy, viscous state to a more mobile and less viscous rubbery state. Importantly to note is that in some cases these polymers do not melt due to the absence of an ordered phase and hence can't be characterized by a melting temperature. These characteristic temperatures can in theory be used for the validation of computational models.[124] This approach will also be followed in this thesis (see Chapter 5 and **Paper VI**).

3.4 Polymer synthesis: polymerization reactions

In view of the step copolymerization and the cationic ring-opening polymerization studied within this thesis, which are in turn used for the synthesis of polycarbonates and polyoxazolines respectively, we will briefly introduce the different classes of polymerizations and how these are distinguished from one another.[115,117] One of the best ways to distinguish different polymerization types is to consider the functionality of a repeating unit. A functionality can best be described as the chemical part of a monomer which can react to form a chain link, i.e. a link between two repeating units. Remark however that the functionality does not have to be equal to the number of functional groups. In essence polymerizations can only occur with monomers which have a functionality of 2 or more. If this condition is met a distinction can be made based on the atom balance for the polymerization. In case chemical formula stays unaltered, the type of polymerization can be referred to as *Addition polymerization* or polyadditions, whereas in case it alters we refer

to it as *condensation polymerization* or polycondensations. Nowadays a different classification is preferred based on the reaction mechanism (because condensation and addition polymerizations are not covering all types of reactions), i.e. *Step polymerizations* and *Chain polymerizations*.

3.4.1 Step polymerization

Step polymerization is also referred to as step-growth polymerization and covers all reactions in which the polymer chains grow step-wise by reactions involving any two molecular species in the system, i.e. monomer-monomer; monomer-chain or chain-chain polymerization. It is furthermore characterized by a rapid consumption of monomers in the early stages of the polymerization process. When the reaction proceeds, functionalities from different chains start to react and the degree of polymerization for each chain increases. Hence the availability of functional groups is of huge importance and impurities or other sources for side reactions should be avoided at all time to establish long polymeric chains. Regardless of the fast monomer consumption at the early stages of the process, the molecular weight of the produced polymers remains low and very long reaction times (high conversion rates) are required to obtain long 'real' polymers with high molecular weight, i.e. when chains start reacting with one another. Hence, depending on the desired properties, this can be of major importance.

The most general reaction scheme valid for the copolymerization of two monomers (possessing two functionalities) is shown below:

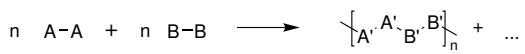

for which polyamides, polyesters and polyethers are typical examples. In case A and B are located within a single molecule the polymerization is called self-condensation, e.g. the polymerization of amino acids. In these cases linear polymers are formed, however when more than two functionalities are present in the monomers, the resulting polymer becomes far more complex with branch - and network formation as a consequence. Apart from the inherently more complex structures also the polymerization behavior itself becomes harder to predict because differences in reactivity (or molecular environment) of the functionalities will induce differences in the reaction kinetics. Understanding the reactivity and behavior of the different functionalities hence provides meaningful insights into the polymerization behavior of different building blocks.

Reaction kinetics

As highlighted by Coote et al. understanding a reaction mechanism and the corresponding reaction kinetics can be highly beneficial to optimize and steer the

polymerization process.[122] The global reaction mechanism for a step polymerization can be considered, under the assumption that functionalities A and B will always react equally independent of the chain length it is attached to i.e. the equal reactivity assumption[115]:

$$\mathrm{Y{-}P{-}A} + \mathrm{B{-}P{-}Y} \underset{\mathrm{k}_d}{\overset{\mathrm{k}_a}{\rightleftharpoons}} [\mathrm{Y{-}P{-}A{-}B{-}P{-}Y}] \xrightarrow{\mathrm{k}_r} \mathrm{Y{-}P{-}Y} \tag{3.1}$$

where $\mathrm{Y{-}P{-}A}$, $\mathrm{B{-}P{-}Y}$ and $[\mathrm{Y{-}P{-}A{-}B{-}P{-}Y}]$ represent the polymer with either functionality A or B as a chain end and the associated complex of two monomers or chains respectively. k_a and k_d are the association and dissociation rate constants and k_r the rate constant corresponding to the polymerization reaction. The 'mechanism' hence accounts for the rate at which the functionalities diffuse to and from one another.

Under steady state conditions, the rate of polymer formation can then be written as:

$$\frac{d[\mathrm{Y{-}P{-}Y}]}{dt} = \frac{k_r k_a}{k_d + k_r}[\mathrm{Y{-}P{-}A}][\mathrm{B{-}P{-}Y}] \tag{3.2}$$

Though this is a relatively simple example, it is clear that understanding k_r, and hence the governing mechanism, or the factors influencing k_r can be of huge importance to exert control of the polymerization process or to help predicting the polymerization outcome and thus polymer composition. Furthermore when the number of functionalities increases or new functionalities are created during the reaction then the situation can become much more complex where one needs to know the reactivity w.r.t. each functionality and the occuring sidereactions. In this case microkinetic models may have to be used to predict the polymerization ouctome.

3.4.2 Chain polymerization

Chain polymerization, also named chain-growth polymerization, classifies polymers which grow only by reaction of a monomer with a reactive group, i.e. monomer-reactive chain polymerization. The introduction of this reactive group is hence a key difference to the step polymerization and typically involves an initial reaction to start chain growth. Remark that chain here refers to the sequence of events triggered by this initial reaction and hence does not refer to a single polymer molecule. Within chain polymerization we distinguish 3 steps: initiation, propagation and termination. In case the termination is suppressed or eliminated the polymerization is referred to as controlled - or living polymerization respectively.[125] In contrast to step polymerization, chain polymerization is characterized by a reaction speed proportional to the initiator concentration (*vide infra*) and produces high-molecular weight polymers already at the early stages of the process. Furthermore, no real benefit is seen on the degree of polymerization when long reaction times are applied.

While for step polymerizations we can consider specific classes of polymers (like polyamides or polyesters), we can here distinguish several subclasses of chain-polymerization with typical examples as anionic polymerization, cationic polymerization, free-radical polymerization and ring-opening polymerization to name just a few. Over the years numerous techniques have been developed to perform the living counterparts for these specific reactions hence gaining ways to exert more control over the polymerization, i.e. living anionic and cationic polymerizations and controlled radical polymerizations.[126–131] Appropriate conditions are needed to maintain this type of polymerization as one needs to minimize undesired termination and/or chain transfer reactions, ideally these are avoided completely.

An important type of chain-polymerization tackled in this doctoral thesis is the living cationic ring-opening polymerization (CROP) in the framework of poly(2-alkyl-2-oxazoline) formation. This reaction was developed not long after the discovery of living polymerizations.[132–137] It is more thoroughly discussed in Chapter 5.

Reaction kinetics

Let us consider the global reaction mechanism for a chain-growth polymerization and the corresponding reaction kinetics:

1. **Initiation**: depending on the concentration and reactivity of initiator species (I), i.e. characterized by its rate constant k_i, a specific amount of reactive chains is generated hence controlling the total amount of polymer present in the end (ideally). In the case of poly(2-oxazoline)s, typically acids, alkylating agents or various types of halides are used as initiator species. Ideally this reaction is fast and complete.

$$\mathrm{I} + \mathrm{M} \xrightarrow{\mathrm{k}_i} \mathrm{P}_1{}^* \tag{3.3}$$

2. **Propagation**: monomers react with the activated species where the formed chains retain activity, i.e. in a head-to-tail fashion, with a rate constant k_p. This reaction proceeds until the termination phase occurs or is initiated.

$$\mathrm{M} + \mathrm{P}_n{}^* \xrightarrow{\mathrm{k}_p} \mathrm{P}_{n+1}{}^* \tag{3.4}$$

3. **Termination**: the intermediate reactive species are killed either by manually reacting a terminating agent with the growing polymers, or (though most often undesired) due to reactions occurring between chains i.e. combination

and disproportionation reactions.

$$\mathrm{T} + \mathrm{P}_n{}^* \xrightarrow{\mathrm{k}_t} \mathrm{P}_n\mathrm{T} \tag{3.5}$$

$$\mathrm{P}_i{}^* + \mathrm{P}_j{}^* \xrightarrow{\mathrm{k}_{t,c}} \mathrm{P}_{i+j} \tag{3.6}$$

$$\mathrm{P}_i{}^* + \mathrm{P}_j{}^* \xrightarrow{\mathrm{k}_{t,d}} P_i' + P_j' \tag{3.7}$$

$$\tag{3.8}$$

Remark that in case of a living polymerization spontaneous termination reactions do not occur. We can hence write the rate of polymerization for this specific (relatively simple) case as:

$$\frac{d[\mathrm{M}]}{dt} = -k_p[\mathrm{P}_n{}^*][\mathrm{M}] \tag{3.9}$$

with $[\mathrm{M}]$ and $[\mathrm{P}_n{}^*]$ the concentration of monomer and active species (equal to the initiator concentration) respectively, furthermore assuming that the equal reactivity assumption is valid and complete initiation has occured.

3.5 Depolymerization

In light of the broad application field of polymers, it is interesting to note that the largest proportion of global polymer production is destined for packaging purposes.[138] Despite its dominant presence in everyday society, most of these plastics have a very short first-use cycle and end up 'directly' into a waste stream.[139] These short-life plastics amount to more than 50% of the worldwide plastic waste.[140] Waste of which only a few percent is recycled or incinerated resulting in harmfull accumulation within our precious ecosystem.[141] Currently most plastics are manufactured from fossil resources which goes hand in hand with additional challenges due to the depletion of fossil-fuel resources and the accompagnied climate-change issues, both aspects can no longer be ignored.[142–144]

$$\text{monomers} \underset{\text{depolymerization}}{\overset{\text{polymerization}}{\rightleftharpoons}} \text{polymers} \xrightarrow{\text{degradation}} \text{product mixture}$$

Scheme 3.1. Schematic representation of polymerization, depolymerization en degradation processes.

To this end it is interesting to consider the process of depolymerization which in theory allows us to convert, and hence recycle, the produced polymers to their original building blocks. Depending on the produced compounds we distinguish depolymerization and degradation (see Scheme 3.1).[145] Depolymerization refers to the opposite process of polymerization in which monomers are produced.[133,146]

Degradation or more specifically polymer degradation refers to the cleavage of macromolecules into various fragments varying in size and structure (following the definition of Jellinek et al.).[147] Importantly, this definition of degradation does differ slightly from its usual definition in polymer science (which is not indicating its potential usefullness), i.e. the process by which a polymer loses its original properties due to the environment and/or workload it gets exposed to.[146]

Both methods can be used for waste management purposes though degradation is only usefull if the application does not require polymers of equal quality as the starting material or in case of thermal degradation (i.e. pyrolysis), when fuels are produced. The latter hence provides the means to mitigate part of the energy crisis using an abundant waste stream.[141,148]

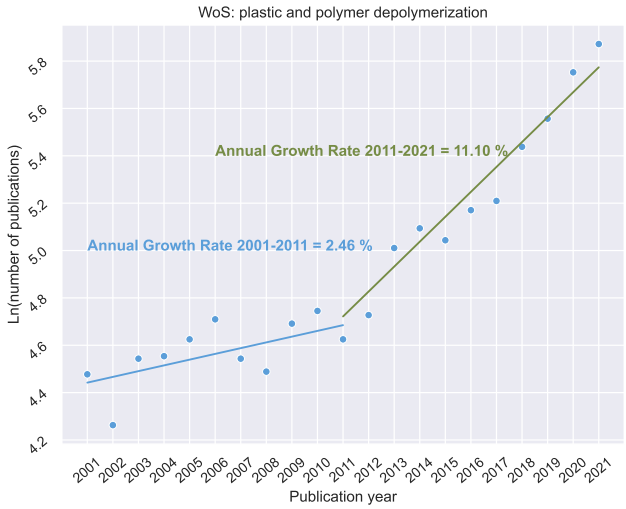

Figure 3.4. The scientific growth of Plastic depolymerization or polymer depolymerization within the last 20 years measured by means of the annual growth percentage (applying an unrestricted exponential growth model, inline with ref. 2) based on the Web of science search results for 'Plastic depolymerization or polymer depolymerization'.

Depolymerization, on the other hand, can be used for the conversion of polymers towards their original building blocks or derivatives hereof with degrees of selectivity not achievable by e.g. pyrolyis.[149] Despite the promising nature of this process it is only in the past decade that depolymerization has substantially increased in interest, as illustrated by the the increase in annual growth percentage based on a *Web of Science* search for 'Plastic depolymerization or polymer depolymerization' depicted in Figure 3.4.[2] Interesting in this respect is the recent work of

Miao et al. who provide an overview of recycling strategies for the common plastics like Poly(ethylene terephtalate); polyvinyl chloride, polypropylene, ... (based on Society of Plastics Industry).[141,150]

Taking the degradation and depolymerization processes into account in combination with the intrinsic harmfull nature of petro-based polymers, it is obvious that the scope of traditional polymer science is too narrow. Hence nowadays scientists are challenged to develop strategies to produce building block and polymers in a more sustainable way and take the full life-cycle including degradation and/or depolymerization into account (i.e. within the framework of Green chemistry and Circular economy).[144,151–153] Within this respect another strategy to develop essential chemical building blocks in a more sustainable way is to start from polymers as found in nature, e.g. biomass. An essential technology within this respect is lignocellulose biorefining where biomass is used as central starting point for the production of renewable energy, chemicals and materials.[4] With researchers recognizing the potential of biomass' main constituents, i.e. the biopolymers cellulose, hemicellulose and lignin, many different biorefinery methods have been reported.[154–156] In the scope of this thesis, we will focus on one of these biorefinery methods, namely reductive catalytic fractionation (RCF) which will be covered in the next chapter (Chapter 4).

4

The BioFactory

The Biofact Excellence of Science (EOS) project entails the development of the next-generation biorefineries, the *lignin-first* biorefinery, capable of converting wood chips in high added-value chemicals.[157–161] Here biorefinery refers to the integrated complexes in which bio-waste and/or biomass (i.e. renewable feedstocks) can be converted into useful products, e.g. fine-chemicals, materials, fuels, ...[144] This concept fits perfectly in the paradigm shift required to move from a 'take-make-consume-dispose' to a 'take-make-consume-recycle' flow of materials which is inherently accompanied by a switch from fossil resources to bio-based ones.[162] This transition to a bio-based economy is essential within climate change mitigation strategies.[163] While traditional biorefineries primarily focus on the exploitation of the carbohydrate fraction of lignocellulose feedstocks, i.e. for the production of biofuels, paper and commodity chemicals, this new biorefinery concept instead focusses on lignin which is recognized as unique feedstock for the sustainable production of aromatic building blocks.[164] A pioneer in this field is Prof. Sels from the Center for Sustainable Catalysis and Engineering of the KULeuven [https://sels-group.eu/], with whom we have closely collaborated with for **Paper I** and **II** presented in this Chapter. The traditional biorefineries first separate the lignin fraction from the carbohydrate fraction which is subsequently depolymerized into low-value materials and/or fuels via (typically) non-selective oxidative or reductive transformations.[165] The *lignin-first* biorefinery, on the other hand, aims to increase the selectivity of the depolymerization process by depolymerizing the native lignin before it is separated from the carbohydrate fraction which leads to a limited

number of aromatic compounds in the final mixtures. An additional benefit of the *lignin-first* approach is the fact that the carbohydrate fraction remains unaltered and hence its valorization is not neglected like with lignin in the traditional biorefineries. A schematic representation is given in Figure 4.1.

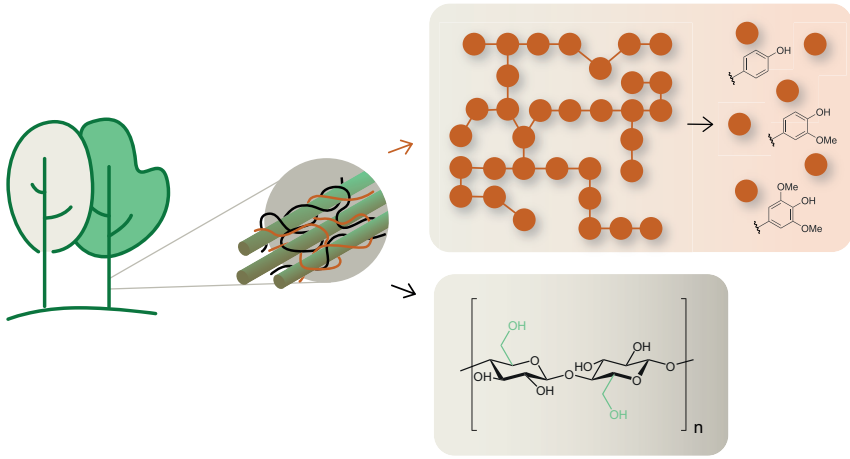

Figure 4.1. Schematic representation of the *lignin-first* concept.

Within the BioFact project the aim is to develop new synthetic procedures, i.e. downstream (catalytic) upgrading routes, for the transformation of the limited set of aromatic compounds (which we will elaborate on in the next section) into polymers, bulk - and fine chemicals (see Figure 4.2). This is where molecular modeling comes into play, as an understanding of the reactions can aid the rational design and optimization of these procedures.

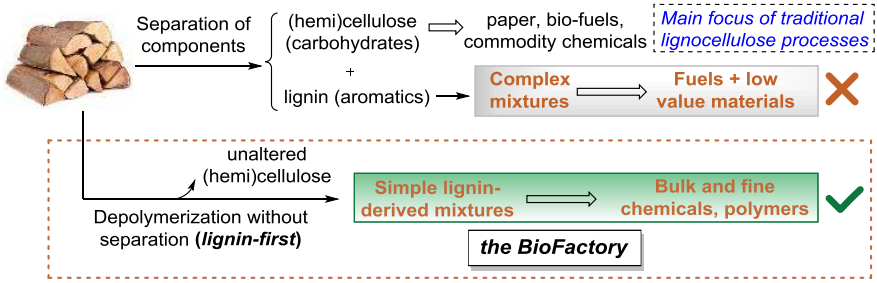

Figure 4.2. The Biofactory project proposal.

In Section 4.1 the *lignin-first* biorefinery concept is explained to further set the scene for the molecular modeling research performed within the framework of this thesis. Section 4.2 focuses on the conversion of the lignin-derived compounds towards platform molecules which can in turn be used for the production of poly-

mers, bulk - and fine chemicals. Here the results of an in-depth mechanistic study are presented for the *O*- and *C*-dealkylation of coniferylalcohol and guaiacol in hot-pressurized water where we applied a multiscale modelling approach to extract all characteristics of the reaction. This work was performed in collaboration with Prof. Bert Maes and Prof. Bert Sels. Lastly, Section 4.3 covers the investigation of the copolymerization of thiols and (lignin-derived) alcohols with CO_2-sourced alkylidene carbonates, hence tackling one of the application fields for the lignin-derived monomers. This work was perfomed with Prof. Christophe Detrembleur (UCLiège) on of the partners in the EOS project. Here the results for the mechanistic study of a model reaction are presented, elaborating on the polymerization outcome and governing features.

4.1 The *lignin-first* biorefinery

Though the philosophy of the *lignin-first* biorefinery was already introduced, it is intresting to elaborate in more detail where this idea comes from and why it took scientist so long to utilize the full potential of lignocellulosic biomass. To this end we will first introduce lignin or more specifically, this class of biopolymers. The biorefinery is based on processing lignin towards smaller chemical units.

4.1.1 Lignins

Lignins are a class of biopolymers which are build up enzymatically from monolignols (or cinnamyl alcohols), i.e. phenolic building blocks. The polymers can be found in the cell wall of every plant on the planet, where it not only strengthens the wall but also protects it from herbivors and microbial degradation.[166,167] Moreover it represents the second most abundant molecule on earth after cellulose, reaching up to 30 % of plant tissue.

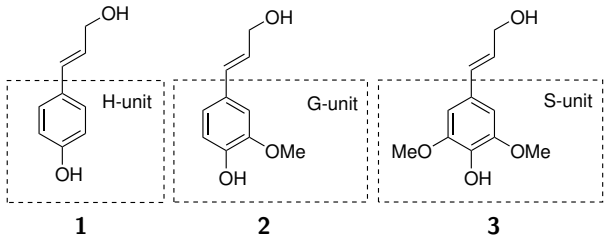

Scheme 4.1. Main monolignol building blocks of lignin, with G-unit, S-unit and H-unit refering to guaiacyl, syringyl and *p*-hydroxyphenyl, respectively.

Overall lignins are comprised of different ratios of three main monolignols i.e. *p*-coumaryl alcohol **1**, coniferyl alcohol **2** and sinapyl alcohol **3** (See Scheme 4.1).

The structural units resulting from the monolignols, once they are incorporated into the polymer, are called guaiacyl (G-unit), syringyl (S-unit) and *p*-hydroxyphenyl (H-unit). Depending on the taxa and the family of the plant different compositions of each unit are found, though even within the plant itself ratios can vary depending on e.g. the cell type.

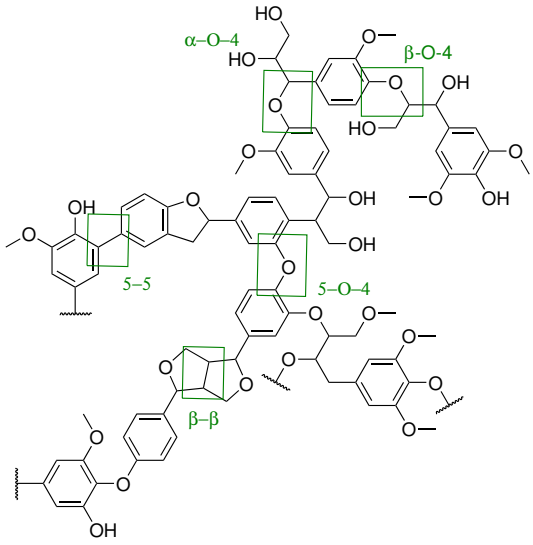

Scheme 4.2. Lignin model indicating some typical linkages.

Two dominant linkages connecting the different structural units with one another are: carbon-carbon linkages (condensed linkages) and ether linkages.[168] The most common connections are shown in Scheme 4.2 of which up to 50% typically consists of the β-O-4 linkage and is hence often targeted by depolymerization strategies. In practice two main types of lignin are distinguished: native lignin and technical lignin.

Native lignin is lignin which is both physically and chemically bound to the carbohydrate fraction (via phenyl-glycoside, benzyl-ether and benzyl-ester bonds) forming a lignin-carbohydrate complex (LCC) in plant cell walls.[169] It is hence the lignin as it is found in nature. Worthwhile noting is that because of this association with hemicellulose and cellulose, often the collective name lignocellulose is used to describe biomass derived from plants. Remark that it is this type of lignin targeted in *lignin-first* approaches.

Technical lignin or modified lignin refers to all types of lignin which are recovered from industry e.g. from pulp and paper industry, or extracted from biomass (i.e. by using methods which destroy or alter the native lignin). To name just a few: Kraft

Lignin, hydrolysis lignin, organosolv lignin, pyrolytic lignin, ... of which the name is typically derived from the extraction or recovery process.[168] However, a general problem with technical lignin originating from carbohydrate-oriented biorefineries is that the lignin is structurally altered during the fractionation (i.e. isolation) process making it a very complex feedstock for subsequent depolymerization processes.[170] As a consequence, depolymerization processes (i.e. oxidative, reductive, acid/base, solvolytic, and thermal depolymerization) lead to low monomer yields and/ or product selectivity. This causes technical lignins to typically end up as fuels or low-value materials.

Due to the complexity of this macromolecule; its variation among different sources and processing approaches; and its recalcitrance, lignin was highly underutilized for the production of valuable products.[171] Nonetheless for the economic viability of the biorefinery it is now generally accepted that valorizing the lignin part of the biomass is crucial.[172] Hence the increased interest in lignin-valorization routes and -conversion approaches.[171,173,174] In the past decades tremendous successes have been booked envisioning the use of lignin in the next-generation biorefineries.[155,156,159,171] Recent promising approaches in this view are the development of methods focussing on mild fractionation preserving the native lignin reactivity during isolation; or *lignin-first* valorization methods which we will briefly focus on in the next section.[170] One strategy which is not discussed is the use of genetic engineering to alter the biosynthetic route for lignin production and in this way produce simplified lignins (e.g. with less variety in the chemical linkages). For an extensive overview on lignin-valorization methods the reader is refered to the work of Weckhuysen et al. and Sels et al.[156,165,170]

4.1.2 The Lignin-first approach

In the *lignin-first* approach one aims to instantly depolymerize and stabilize native lignin during lignocellulose processing towards stable lignin monomers.[170] A succesfull example of this approach is reductive catalytic fractionation (RCF) (also known as catalytic upstream biorefining) in which the lignocellulosic biomass is dissolved under reductive conditions, simultaneously depolymerizing, fractionating and stabilizing the lignin while also preserving the (hemi)cellulosic fraction which thus maintains the capacity for further processing.[4,156,171] A schematic representation of this process in batch is shown in Figure 4.3.

In essence the RCF biorefinery requires, apart of lignocellulosic biomass obviously: 1) an alcohol or cyclic ether as a solvent which can be used in combination with water as a cosolvent and 2) a heterogeneous redox-active catalyst.[164,175–181] The process itself is performed in a high-pressure batch (or flow) reactor at a temperature of 180-250 °C for 2-6 hours. Afterwards a simple filtration and solvent recuperation step suffices to yield a lignin oil comprising of a limited number of monomers, dimers and small oligomers. Concerning the phenolic

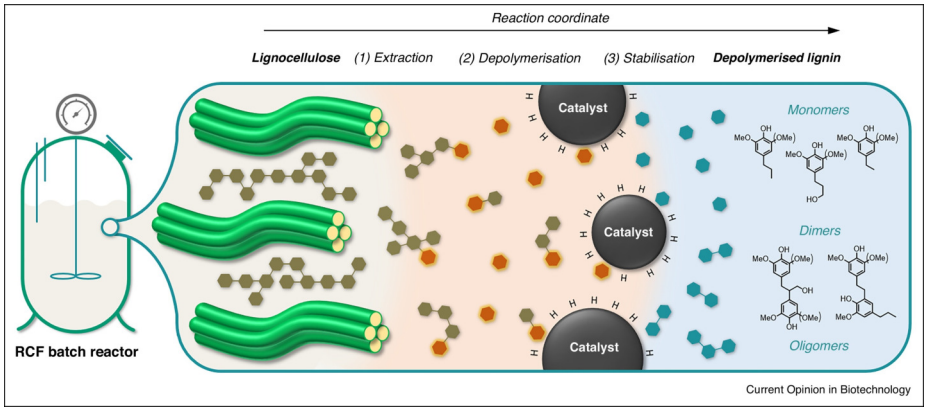

Figure 4.3. Schematic representation of RCF in batch mode displaying the three elementary steps: lignin extraction, depolymerisation and stabilisation. Depolymerisation can either occur solvolytically or catalytically (hydrogenolysis). The result is a low-molecular weight lignin oil, comprising monomers, dimers and oligomers, in addition to a carbohydrate pulp. Green hexagons represent native lignin monomer units, orange hexagons correspond to reactive units, and blue hexagons represent stabilised units. Reprinted with permission from Elsevier.[4]

monomers, mainly 4 are produced (with a yield >50% based on the carbon content of lignin): 4-*n*-propylguaiacol **4**, 4-*n*-propylsyringol **5**, 4-*n*-propanolguaiacol **6**, 4-*n*-propanolsyringol **7** shown in Scheme 4.3. The selectivity of the process can be tuned by the catalyst and the process conditions.[156,157]

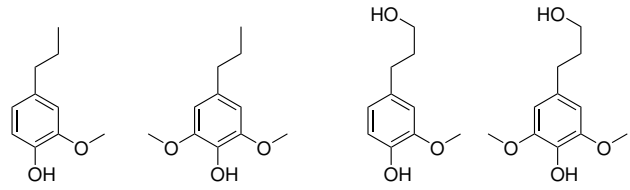

4 **5** **6** **7**

Scheme 4.3. Main arene products of the *lignin-first* biorefinery: 4-*n*-propylguaiacol **4**, 4-*n*-propylsyringol **5**, 4-*n*-propanolguaiacol **6**, 4-*n*-propanolsyringol **7**.

These products have the potential to replace fossil-fuel-based benzene, toluene and xylene (BTX) with 'drop-in' alternatives and to produce new polymer building blocks for the development of biodegradable and/or recyclable plastics.[182–187] Hence, it can circumvent a further intensification of the long-term environmental impact caused by single-use application plastics, e.g. polyethylene tetraphthalate (PET).[188–191]

The development of downstream catalytic upgrading processes (i.e. chemocatalytic or biocatalytic upgrading) which can facilitate these conversions is of major importance.[170] It is furthermore noted by Sels et al. that it is essential to develop multiple strategies for chemo- or biocatalytic upgrading to have a successful lignin valorization chain.[156]

4.2 Conversion of lignin-derived monomers to platform molecules

In view of the development of catalytic upgrading methods, a promising strategy has been proposed and investigated in **Paper I** and **Paper II**, i.e. the selective defunctionalization of lignin-derived monomers in hot-pressurized water using Brønsted acid catalysts. This strategy was explored in close collaboration with the ORSY research group of Prof. Maes from the UA and the research group of Prof. Sels from the KULeuven. Next to its attractiveness as an upgrading route, it is also a very interesting reaction from a green chemistry point of view.[192] More specifically the *O*- and *C*-dealkylation of a typical lignin monomer 4-*n*-propanolguaiacol **6**, also known as dihydroconiferylalcohol, and its *C*-defunctionalized form guaiacol **8** are reported with formation of an important drop-in platform molecule: catechol.[193] For an in-depth discussion on the results the reader is referred to the papers, however below the major computational research results are highlighted. Two approaches can be distinguished which are used to investigate the governing mechanism, on one hand a static approach is used (using a hybrid solvation model) for the computation of reaction barriers in combination with classical molecular dynamics to assess intermediate stability for which the results are presented in **Paper I**. On the other hand an enhanced sampling approach is used in **Paper II** which is applied to the *O*-dealkylation of guaiacol accounting for the operating conditions more accurately and going beyond the approach used in **Paper I**. Furthermore, **Paper I** focuses only on the homogeneously catalyzed reactions while in **Paper II** a thorough comparison is performed between the homogeneous and heterogeneously catalyzed reactions.

4.2.1 C-dealkylation of dihydroconiferylalcohol

In first instance, the *C*-dealkylation mechanism of a lignin-derived compound dihydroconiferyl alcohol **6**, or more specifically the dehydrated and isomerized intermediate isoeugenol **10** (see Scheme 4.4), is investigated by a combined experimental and computational approach. Experimentally it is reasoned that the key step for the *C*-dealkylation of dihydroconiferylalcohol is formation of a benzylic alcohol derivative, 4-(1-hydroxypropyl)guaiacol **11** which can subsequently undergo a retro-vinylogous aldol reaction after protonation of the arene unit hence allowing

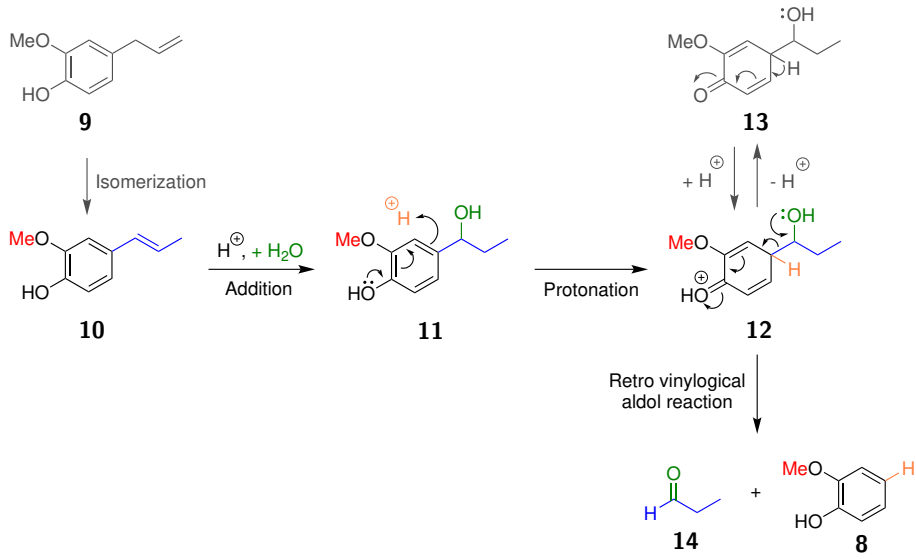

Scheme 4.4. Proposed mechanism for the *C*-dealkylation of isoeugenol **10** and eugenol **9** into guaiacol **8**.

a *C*-C bond cleavage (see Scheme 4.4). To provide evidence for this reaction step, the focus was shifted to this intermediate, as sufficient experimental evidence was available to support the formation of isoeugenol **10** and **11** starting from dihydroconiferylalcohol.

Concerning the retro-vinylogous aldol reaction, the enthalpy profile shown in Figure 4.4 provides a first insight into the mechanism. Remark that due to the large influence of the number of solvent molecules accounted for in the model the enthalpy of activation is reported instead of the free energy. The profile reveals that the protonation of the arene is rate-limiting and proceeds with an intrinsic enthalpic barrier height of 76.9 kJ.mol^{-1}. Subsequently intermediate **12** converts via a low-activated (9.4 kJ.mol^{-1}) retro-vinylogous aldol reaction to guaiacol. This hence provides evidence for the proposed reaction mechanism. However, as the solvent highly influenced the stability of **12** extra *ab initio* MD simulations were performed accounting for the operating conditions to assess its stability more accurately.

The results of these simulations are shown in Figure 4.5 which indicate that **12** is a metastable state which can deprotonate spontaneously towards intermediate **13** or eliminate the alcoholic sidechain (which in turn deprotonates spontaneously towards the corresponding aldehyde) towards the desired intermediate, guaiacol **8**, depending on the solvation environment. Note that for intermediate **13** is assumed to be in equilibrium with **12**, while elimination towards guaiacol proceeds in an irreversible way. The final proposed mechanism for *C*-dealkylation combining both the experimental and these computational results, is shown in Scheme 4.4.

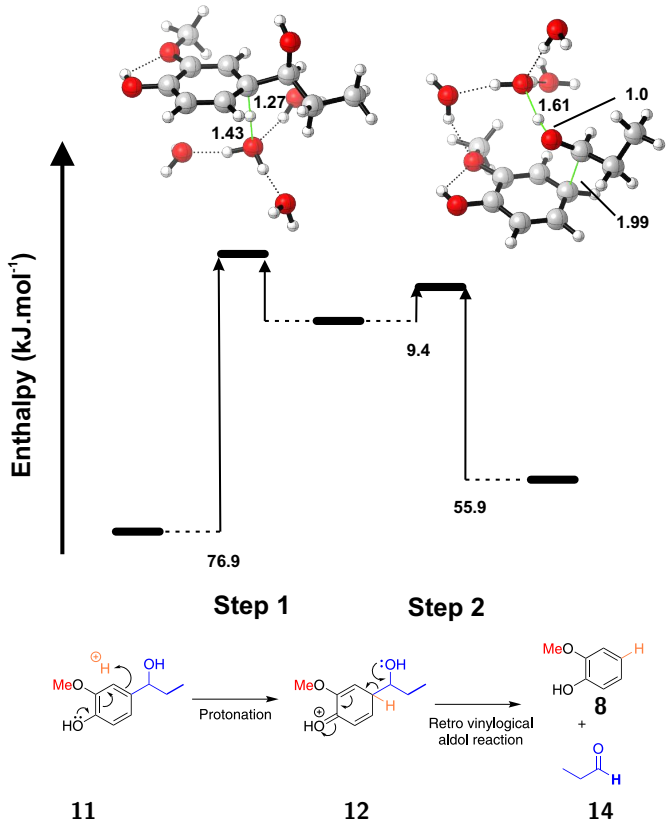

Figure 4.4. Enthalpy profile for the *C*-dealkylation. Both steps involve 4 extra water molecules. The enthalpic value for intermediate **12** corresponds to the pre-reactive complex of step 2. (ωB97X-D/6-311+G(d,p), 523.15 K, 74.02 atm, PCM($\epsilon = 78.3553$)).

The results of this study are taken up in **Paper I**.

4.2.2 O-dealkylation of guaiacol

In **Paper I**, similar to the *C*-dealkylation, both a static and classical MD approach are used to produce a set of preliminary results giving a first insight into a new proposed *O*-dealkylation pathway for guaiacol (or other lignin-derived monomers), i.e. the arene-activated routes highlighted in green in Scheme 4.5. However, recognizing the shortcomings of the static approach to describe the energetics at the operating conditions, the work was extended using an enhanced sampling MD approach in **Paper II**. Furthermore within this paper, we have not only elaborated on the homogeneous catalyzed reaction but furthermore explored the use of zeolites as heterogeneous catalyst, allowing an in-depth comparison of

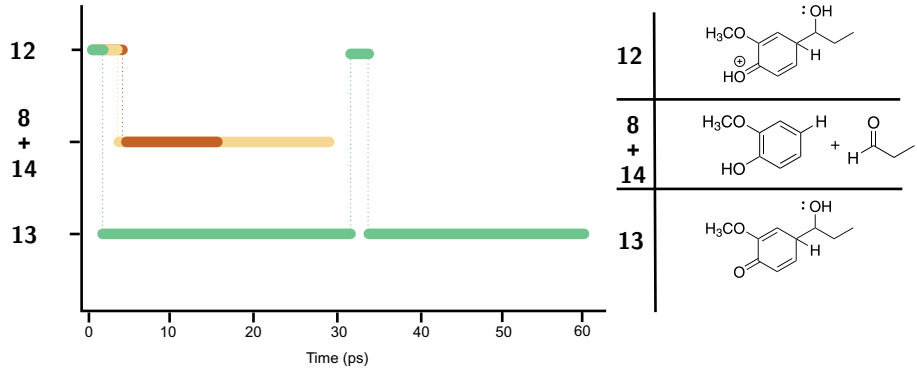

Figure 4.5. Stability of *C*-dealkylation intermediate **12** at operating conditions. Each color represents a regular MD simulation using a different input structure. Note that the length of the simulation differs because once alcohol elimination has occured the reverse reaction will not occur sponaneously. (BLYP-D3/TZVP-GTH, 523.15 K equilibrated at 74.02 atm.)

both catalytic systems on a mechanistic level. The results obtained with the heterogeneous catalyst were performed by Massimo Bocus, a PhD student at the CMM who has a solid expertise in modeling heterogeneous catalyzed systems. Remark that ultimately it is the goal to also extend the *C*-dealkylation results using the enhanced sampling MD approach.

At first instance it is anticipated that protonation of the electron-rich arene is of key importance for the *O*-demethylation where again the formation of this (protonated) activated species **15** is essential (see Scheme 4.5). Furthermore within the arene-activated routes, we distinguished two competing mechanisms. The first path, the hemiacetal path, is where we form a hemiacetal intermediate **16** with subsequent elimination of methanol, and the second path, the arene-activated S_N2 path, is where a S_N2-mechanism occurs starting from the activated species with expulsion of methanol. This mechanism was investigated in **Paper I** whereas in **Paper II** we additionally explore the *O*-activated route, in which no arene protonation takes place but instead protonation of the methoxy-oxygen activates the conversion with expulsion of methanol via a direct or *O*-activated S_N2-mechanism, i.e. with or without formation of intermediate **20** (*vide infra*). More details on this route are provided in Section 4.2.2.

Static approach

The resulting enthalpic profiles for the two arene-activated routes considered in **Paper I** are shown in Figure 4.6.

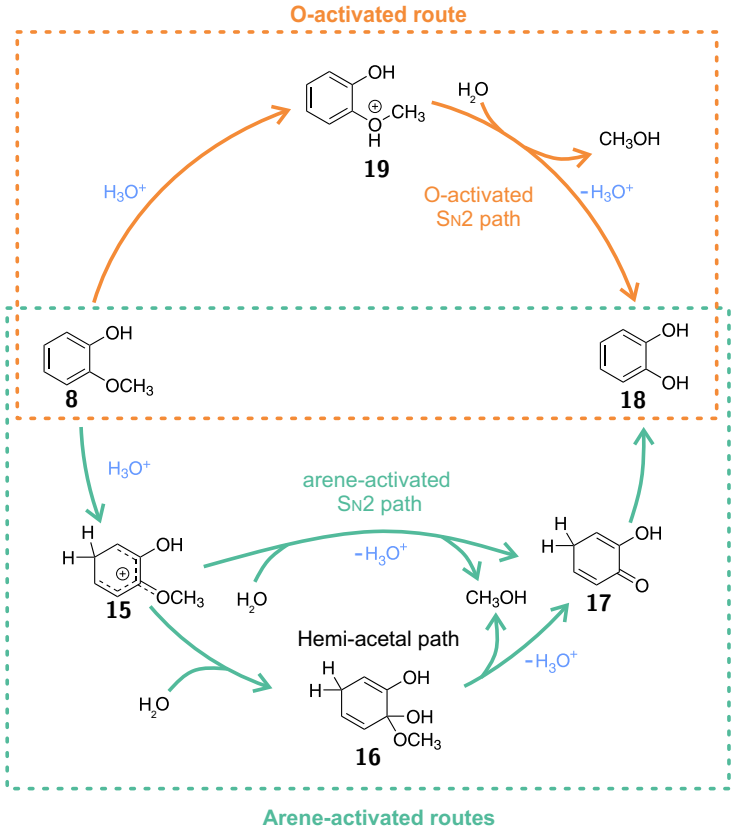

Scheme 4.5. Complete reaction scheme for the *O*-demethylation of guaiacol with formation of catechol. The *O*-activated route is colored orange. The arene-activated routes are colored green.

These indicate that the arene-activated route proceeds via a protonation of **8**. Then, based on the static approach, the formation of a hemiacetal **16** is favored with an enthalpic activation barrier of 35.1 kJ.mol^{-1} which is the rate-limiting step for the *O*-dealkylation (w.r.t. 74.7 kJ.mol^{-1} for the arene-activated S_N2 path). It is furthermore shown that -again- the solvation environment highly influences the stability of this intermediate **16** as it can eliminate methanol spontaneously towards **20** and subsequently to intermediate **17** (see Figure 4.7).Conversion towards catechol then proceeds through the (re)formation of intermediate **20** with subequent restoration of the aromaticity by deprotonating, hence forming catechol **18**.

Importantly, it is anticipated that describing entropic effects more accurately by explicitly accounting for the subcritical aqueous environment, is of major importance to determine the correct reaction mechanism at operating conditions. Hence the research was extended using an enhanced sampling approach to descriminate

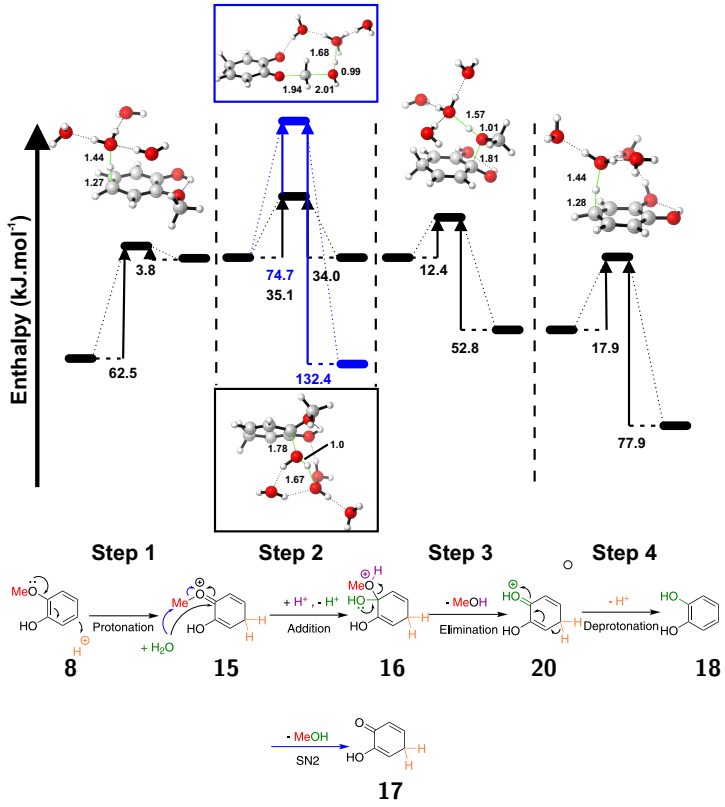

Figure 4.6. Enthalpy profile for the *O*-dealkylation. Step 1 involves 4 extra water molecules, step 2 involves 5 extra water molecules and step 3 and step 4 involve 4 extra water molecules remark that in step 4 methanol is excluded from the model. Blue arrows indicate the intrinsic enthalpy barrier for the arene-activated S_N2 path.(ωB97X-D/6-311+G(d,p), 523.15 K, 74.02 atm, PCM($\epsilon = 78.3553$)).

between the competing paths at operating conditions.

Enhanced sampling MD approach

To extend the work reported in **Paper I**, a more accurate model is used in **Paper II** (though more costly in terms of computational resources) enabling a proper description of the entropic effects at operation conditions by accounting for the solvent explicitly and using an enhanced sampling MD approach. In this paper we have furthermore explored the use of both homo- and heterogeneous Brønsted acid catalysts, e.g. hydrochloric acid and zeolites respectively. To this end, an in-depth comparison is presented of the solvated homogeneous catalytic system with the solvated β-zeolite catalytic system (see Figure 4.8). The heterogeneous

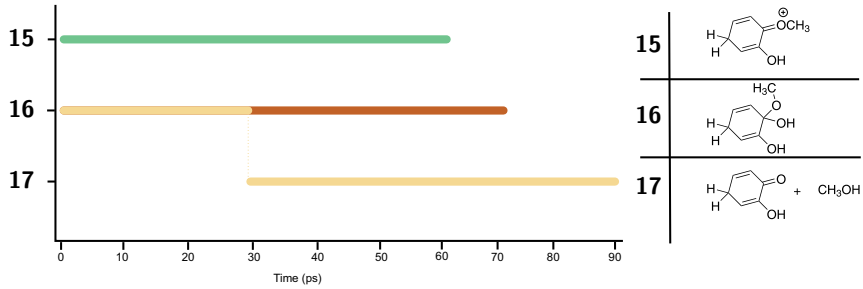

Figure 4.7. Stability of *O*-dealkylation intermediates at operating conditions. Each color represents a regular MD simulation using a different input structure. (BLYP-D3/TZVP-GTH, 523.15 K equilibrated at 74.02 atm.)

catalyst is explored as a more sustainable alternative to corrosive hydrochloric acid which is nonetheless already a relatively green *O*-dealkylating catalyst.[194] The simulation unit cells shown in Figure 4.8 account for two solvation layers (171 water molecules) for the homogeneous system whereas the amount of water in the zeolite is determined based on grand canonical Monte Carlo simulations, resulting in 22 water molecules. Each system contains one excess proton. For more details concerning the preparation of the unit cells, the reader is referred to **Paper II**.

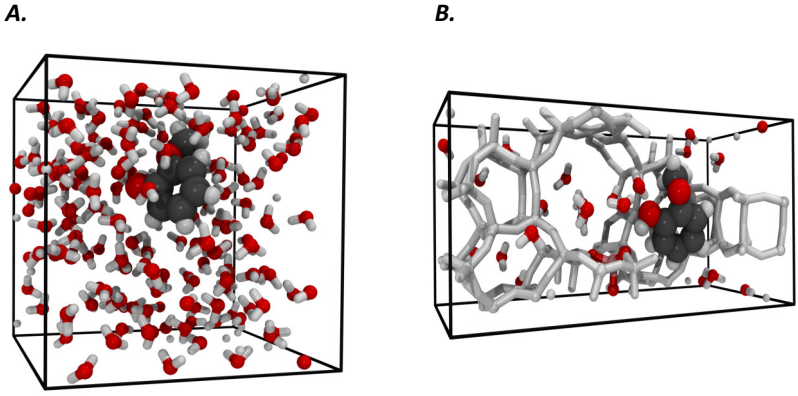

Figure 4.8. A.) The unit cell of the homogeneous system containing 170 water molecules, 1 hydronium molecule and 1 guaiacol molecule; B.) The β-zeolite unit cell of the heterogeneous system containing 22 water molecules, 1 Al substitution (Si/Al=63) and 1 guaiacol molecule.

Apart from the different pathways investigated in **Paper I**, we account for the *O*-activated mechanism reported in literature.[192,194–197] An overview of all investigated pathways in **Paper II** is shown in Figure 4.5.

At first instance, the structuring of water is investigated in both catalytic systems. By analyzing the coordination of the protonated oxygen atom in the system to the water molecules in the environment and the positioning of the water molecules within the framework, we have revealed a confinement-induced activity increase of the hydronium ion within the zeolite. Figure 4.9**B** shows the formation of ring-like clusters within the zeolite channel where all water molecules present in the pore are exposed to the hydrophobic surface of the catalyst. This structuring is the reason why hydronium, i.e. the protonated site q_P, becomes more active as it is undercoordinated in the zeolite framework w.r.t. the solvated conditions of the bulk (Figure 4.9**A**).

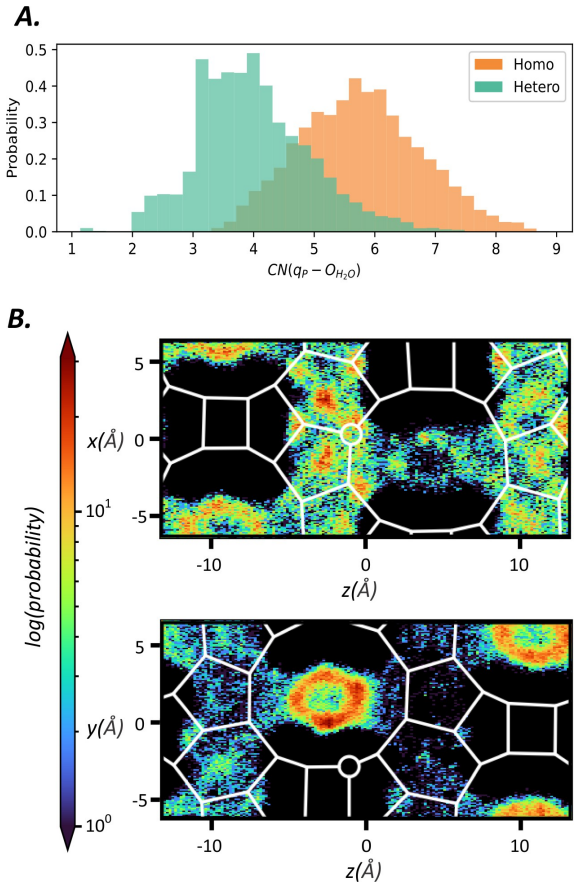

Figure 4.9. A.) Probability distribution of the coordination number (r_0=3.6,n=16,m=28) for the protonated-site q_P (based on ref.[198]) and the water molecules; B.) Probability for O_{H_2O} within the zeolite framework (white) where the circle represent the Al defect location. (Level of theory: BLYP-D3, NVT, 523K)

Secondly, in order to discriminate between the different pathways and hence

deduce the governing reaction mechanism for the *O*-dealkylation of guaiacol, both the reaction kinetics and thermodynamics of each elementary reaction step are extracted from the enhanced sampling simulations. In this work a hybrid-US-MTD approach is used to capture each elementary step of the process, for more details the reader is referred to Section 2.2.3 and to **Paper II**. A global reaction network resulting from the enhanced sampling MD simulations is shown in Figure 4.10. In fact, this scheme is an update of Scheme 4.5 where now the operating conditions and solvation effects are taken into account.

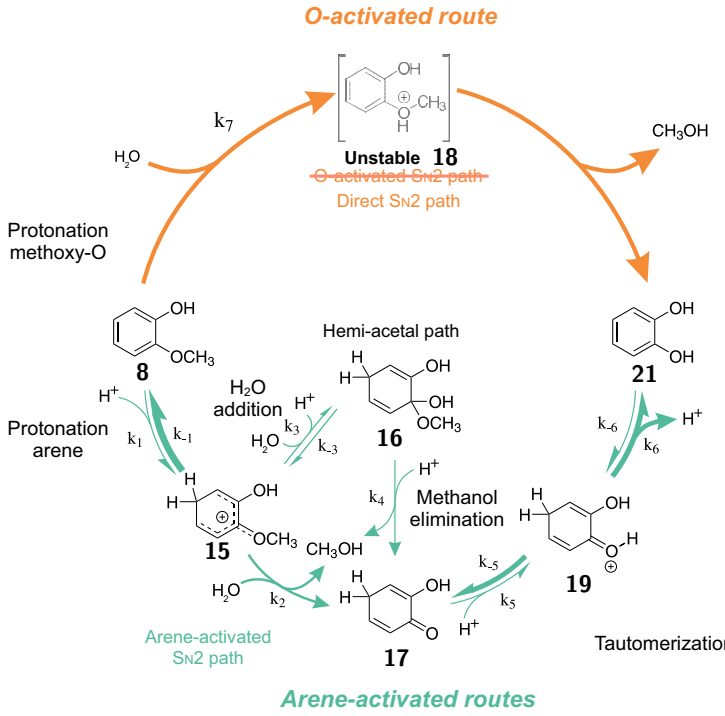

Figure 4.10. Complete mechanistic overview with intermediates and the corresponding rate constants for the *O*-demethylation of guaiacol assuming methanol evaporation, no formation of oxonium intermediate (a conclusion from the results presented in **Paper II**) and the stepwise nature of the tautomerization; Thickness of the lines indicates the relative magnitude/importance of the respective steps.

The complete solution for the resulting microkinetic model is presented in Figure 4.11, revealing that the direct S_N2 path is the preferred reaction path for the demethylation of guaiacol (and in extension of lignin-derived monomers). This observation is true for both the homo- and heterogeneous catalyzed systems, though the latter significantly speeds up the reaction ($k_{7,homo} = 9.9 \times 10^1$ and $k_{7,hetero} = 2.0 \times 10^3$). Hence, the reaction proceeds in a concerted fashion where

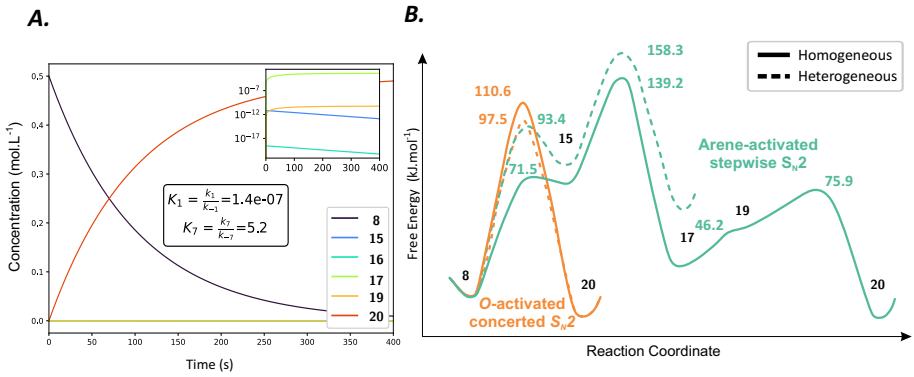

Figure 4.11. A. Solution of the rate equations of the individual steps involved in the paths considered; B. Schematic representation of the combined FES for the arene-activated route and the FEP for the *O*-activated route for both the homogeneous and the heterogeneously catalyzed system. Apparent barrier heights are shown, calculated based on phenomenological barrier heights for the arene-activated stepwise S_N2 (green) and direct S_N2 (orange). Note that the formation of the hemi-acetal (**16**) is omitted due to its irrelevance to the overall reaction and the O-activated S_N2 is omitted because formation of intermediate **18** is not observed. (Level of theory: BLYP-D3, NVT)

the methoxy moiety is protonated with subsequent attack of water on the methyl moiety eliminating methanol and forming catechol as a result. The evolution of the RC and the CV describing the methoxy protonation state is shown in Figure 4.12 which reveals the formation of an oxonium-water contact species during the reaction progress. This observation is furthermore used in the experimental verification step of this investigation. The FES furthermore highlights that the oxonium species is not a stable intermediate during the reaction.

We furthermore reveal that for the *O*-dealkylation, the arene-activation routes are not favored due to the low equilibrium constant for this first reaction step ($K_{1,homo} = 1.4 \times 10^{-7}$ and $K_{1,hetero} = 2.3 \times 10^{-8}$). The corresponding free energy profiles are shown in Figure 4.11**B**, which illustrate that the instability of intermediate **15** in combination with the subsequent apparent activation barrier of 139.2 and 158.3 kJ.mol^{-1} for the homo- and heterogeneous case respectively, are the main reason for not observing the arene-activated routes. We can furthermore see that both systems can succesfully catalyze the conversion, where the heterogeneous catalytic system performs slightly better because of an increased (hydronium) activity.

Lastly, the results are experimentally verified by measuring the solvent kinetic

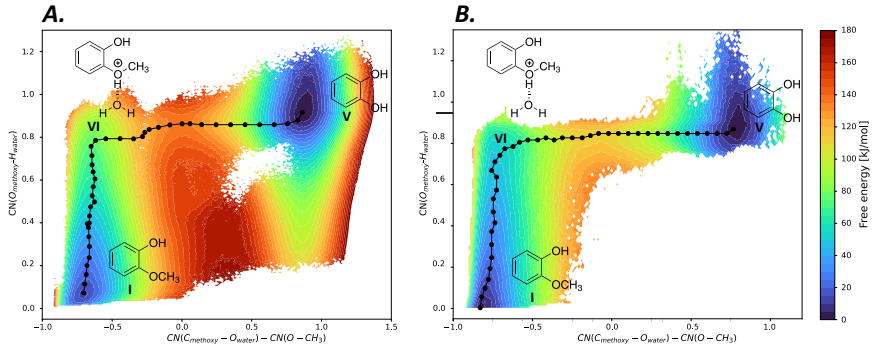

Figure 4.12. A.) Two dimensional free energy surface (i.e. 2D extension of the 1D profile) for the S_N2 mechanism of the homogeneously Brønsted acid catalyzed *O*-demethylation of guaiacol, the minimal free energy path is shown by the dotted line; B.) Two dimensional free energy surface for the S_N2 mechanism of the heterogeneously Brønsted acid catalyzed *O*-demethylation of guaiacol, the minimal free energy path is shown by the dotted line.

isotope effect (SKIE) for the reaction (see Equation 4.1). At first instance the mechanism was more thoroughly investigated computationally (using ThermoLIB, see Chapter 2), to determine both primary and secondary kinetic isotope effects.

$$\left(\frac{k_{\mathrm{H_2O}}}{k_{\mathrm{D_2O}}}\right)_{obs} = \left(\frac{k_{\mathrm{H_2O}}}{k_{\mathrm{D_2O}}}\right)_{pri} \left(\frac{k_{\mathrm{H_2O}}}{k_{\mathrm{D_2O}}}\right)_{sec} \tag{4.1}$$

Figure 4.12 reveals which primary kinetic isotope effects to expect: in both the homo- and heterogeneous case the proton transfer towards guaiacol (y-axis) has occured completely and hence no partial-bonding character of the proton is expected in the transition state. This means that a primary kinetic isotope effect of unity (or even inverse) is to be expected.[199,200] Furthermore, a neutral water molecule attacks, nucleophilically through the O atom, and only deprotonates when the TS reaches the product state (not shown, see SI **Paper II**). This indicates, based on the work by Kresge et al., that strongly inverse secondary isotope effects are to be expected because deuterium remains bonded in the transition state.[201] Hence a net inverse SKIE is to be expected based on the computational results, which is confirmed experimentally: i.e. 0.6 and 0.7 for the homogeneous and heterogeneous system respectively.

In this comparative study, we have hence revealed the potential of zeolites to catalyze *O*-demethylation of lignin-derived monomers. We furthermore provide in-depth knowledge on the governing mechanism and the role of water in these complex environments. Remarkable is the fact that at these operating conditions the *O*-dealkylation mechanism proceeds neither via *general acid catalysis*(rate-

limiting proton transfer) nor via *specific acid catalysis* (fast reversible proton transfer). Instead it proceeds through a direct S_N2-mechanism in which protonation occurs in the rate-limiting step but is already completed before reaching the TS without the formation of a stable intermediate. The results of this study can be used for the future rational design of catalysts in these complex environments. By comparing the structuring of water and hydronium in both systems a confinement-induced activity increase is revealed within zeolites resulting in an acceleration of the reaction.

4.3 Generating bio-based polymers from lignin-derived compounds

As highlighted in Chapter 3, the use of lignin shows huge potential as a bio-based feedstock for the production of biologically-sourced (and often also biodegradable) polymers.[180,202–205] Within the context of the Biofact project, focus is set on thermoplastics as the desired constructed polymeric material. These so-called bioplastics have been rediscovered in the past 30 years by both academia and industry.[206] It is expected that within the upcomming years the percentage of biobased plastics on the global market will grow significanlty due to recent advancements and surely lignin will play a crucial role herein.[180,202,207] Typically two types are distinguished, those who can serve as drop-in alternatives and those which have a chemical structure different compared to classical petrochemical-based polymers.

In the Biofact project, the use of new *lignin-first* derived building blocks is explored for the production of sustainable and low carbon footprint plastics, i.e. a novel family of functional polycarbonates (PC) is explored. To this end, bis(α-alkylidene carbonate)s (bis-αCC)s, which are new CO_2-sourced cyclic carbonates, are copolymerized with dithiols and lignin-derived diols. bis-αCCs have the advantage that mild reaction conditions can be used where high regiocontrol and product selectivity is maintained.[208] Though the application field of these new families is still in its infancy, with many features yet to be explored, their potential is being recognized by both academic and industrial stakeholders (like BASF).[209–211] Detrembleur et al. have already illustrated the relevance of **22** (see Scheme 4.6) as solid electrolytes for Li-ion batteries.[210,212]

4.3.1 Production of new lignin-based polycarbonates

PCs are a polymer class which possess interesting features for the production of organic glasses, optical fibers, packaging and other materials for automotive, electric and construction sectors.[213,214] On one hand they remain stable at high temperatures and, on the other hand, they are impact resistant with excellent

transparency. The production of a new, more sustainable, family of polycarbonates, i.e. poly(oxo-carbonates), based on CO_2-sourced bis-αCC and bio-based diols (or other difunctional building blocks: dithiols, diamines, ...) are hence very promising for the production of more sustainable materials.[155]

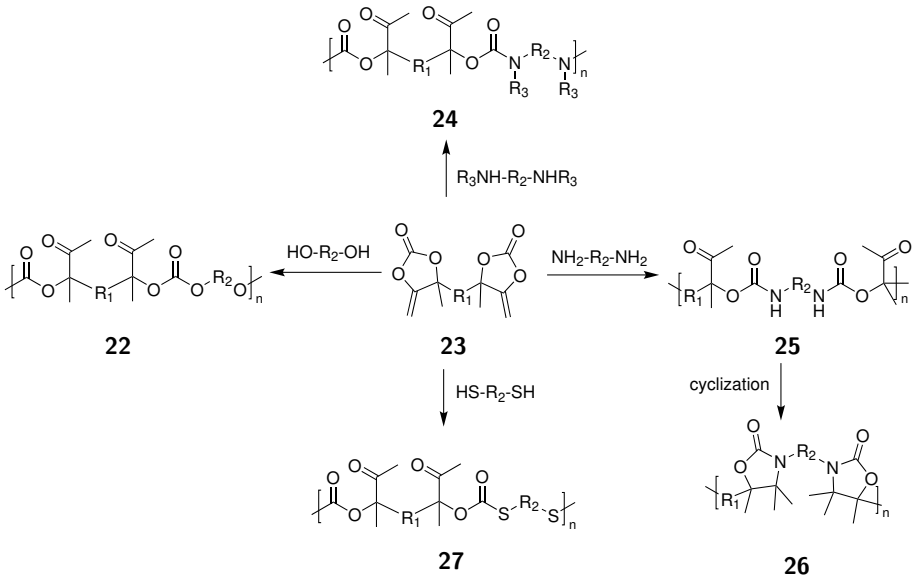

Scheme 4.6. Overview of the novel families of polycarbonates accessible through the copolymerization of difunctional building blocks with bis(α-alkylidene carbonate).

The essential building block within the new family of polycarbonates is bis(α-alkylidene carbonate) (bis-αCC) **23** (Scheme 4.6) which is a versatile, easy customizable CO_2-sourced building block which provides access to a large diversity of regioregular functional polymers, e.g. polyurethanes and polycarbonates.[215] In the past α-alkylidene carbonates were used for the preparation of β-oxocarbonates, β-oxocarbamates, β-hydroxy-1,3-oxazolidin-2-ones, α-hydroxyketones and 3-dialkylamino-oxazolidin-2-ones.[208,216–218]

Incorporation of the activating substituent i.e. the vinylene moiety, w.r.t. bis-cyclic carbonates, facilitates an increased reactivity toward nucleophiles and the means to establish regiocontrol. This for example solves problems 'hampering' the current production of poly(hydroxyurethane)s which are compounds known for their use as adhesives and coatings as greener alternative to phosgene and isocyanate-sourced polyurethanes.[215,219–221]

Remarkably only recently bis-αCCs where recognized as industrially relevant

on one hand for their use as CO_2-sourced cyclic carbonates and ,on the other hand, as monomer for the production of novel families of poly(urethane)s **24**, poly(hydroxy-oxazolidone)s **26** and poly(carbonate)s **22** by copolymerization with primary-, secondary diamines or diols respectively.[211,215] Next to amines and alcohols, also thiols can be used to establish the copolymerization for the production of thiocarbonates. The application of thiols can provide new relevant products such as poly(monothiocarbonate)s (**27**) which possess a high refractive index making them suitable for optic application and furthermore show strong binding affinity to metals making them hence excellent for e.g. water purification purposes.[212,222–224] An overview of these 'new' families is shown in Scheme 4.6.

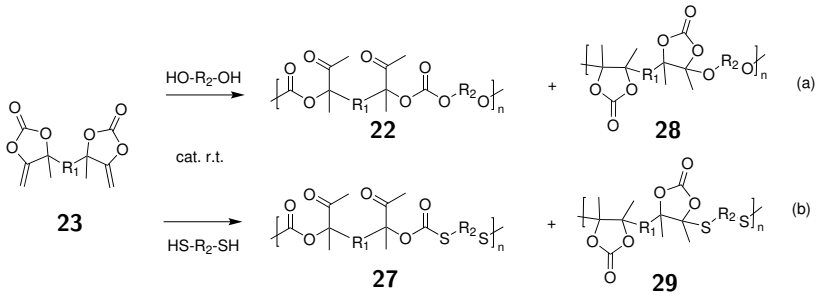

Scheme 4.7. Reaction scheme of the organocatalyzed step-growth copolymerization of bis(α-alkylidene carbonate)s with dialcohols and dithiols.

Within this dissertation, we have focused on two functional groups: thiols and alcohols, which are explored in close collaboration with Prof. Detrembleur from the CESAM research unit at the University of Liège. The overall reaction scheme of the investigated polymer synthesis routes is shown in Scheme 4.7, representing the organocatalyzed step-growth copolymerization of bis(α-alkylidene carbonate)s **23** with diols (a) and dithiols (b). Concerning the reaction kinetics of this process (see Section 3.4.1), we can remark the following: i) The structural unit is characterized by a functionality larger than two and hence the rate constants linked to the reaction between each of these functionalities will govern the resulting polymer composition. ii) the produced polymers still have functionalities present which are susceptible to further reaction (which is whether or not desired), i.e.

$$\mathrm{Y{-}P{-}A} + \mathrm{B{-}P{-}Y} \xrightarrow{\mathrm{k}_r} \mathrm{Y{-}C{-}Y} \tag{4.2}$$

where Y represents the polymeric chain and A, B and C represent functional units with C a newly formed functional unit during the polymerization process. Hence the polymerization kinetics and outcome become much more complex due to this increased functionality. An in-depth knowledge on the underlying mechanism and copolymerization features is thus required and can provide key insights to further extend the scope of bis-αCCs and the corresponding PCs. To this end we

have investigated the reactivity and selectivity of different alcohols and/or thiols towards a model α-alkylidene cyclic carbonate (*vide infra*) to gain a more thorough understanding of the polymerization reaction.

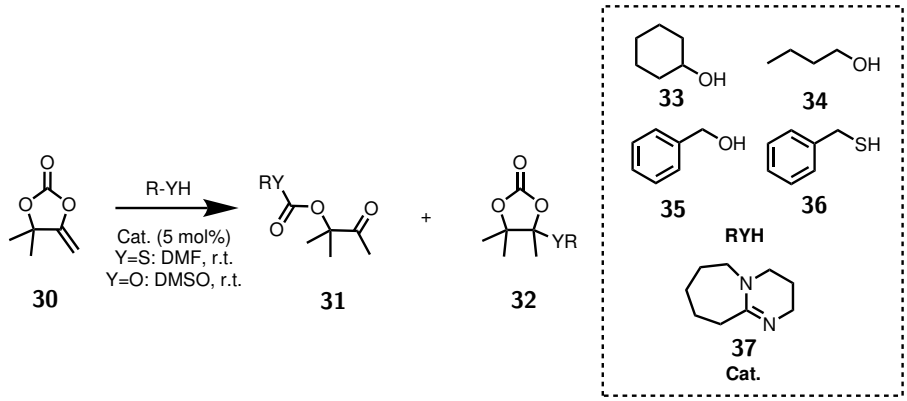

Scheme 4.8. Organocatalyzed addition of thiols and alcohols to CO_2-sourced α-alkylidene cyclic carbonates.

The model of choise to investigate the reaction mechanism and hence the intrinsic polymerization reactivity and kinetics is shown in Scheme 4.8, highlighting the model compounds used. In both papers, the mechanism is investigated using 4,4-dimethyl-5-methylene-1,3-dioxolan-2-one **30** (αCC) as model cyclic carbonate which is reacted with thiols (with the focus on benzylthiol **36**) in **Paper III**, and with alcohols **33**-**35** in **Paper IV**.[182,224] The polymerization reaction is catalyzed by the organocatalyst 1,8-diazabicyclo[5.4.0]undec-7-ene (DBU) **37**. The role of DBU was explicitly investigated in **Paper IV**. In what follows the main results of both studies are presented. Importantly, in **Paper III** preliminary results are obtained for the mechanistic study of **30**, whereas in **Paper IV** (which is actually a continuation of the work presented in **Paper III**) more advanced simulations were performed, explicitly accounting for the solvent and the organocatalyst at operating conditions.

Reactivity of αCC with benzylthiol

At first instance, the organocatalyzed thiolation of αCC **30** is investigated, resulting in the aforementioned novel families of sulfur-containing polymers.

A summary of the relevant experimental observations is shown in Table 4.1. These show that experimentally the reaction of **30** is extremely fast at room temperature with formation of the corresponding β-oxothiocarbonate **31a**. Subsequently, rearrangement towards tetrasubsituted ethylene carbonate **32a** can occur when the reaction is performed for a sufficient amount of time hence revealing the domino nature of the polymerization, something which was not observed before

Table 4.1. Scope of the organocatalyzed addition of benzylthiol to αCC.

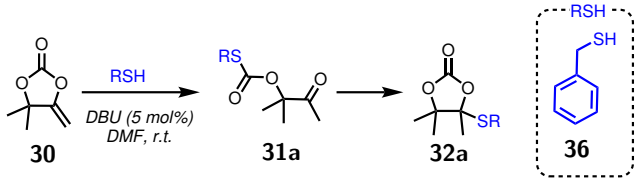

Entry	Time	Conv. αCC [%]^a	Conv. **31a** [%]^a	Yield **31a** [%]^a	Yield **32a** [%]^a
1	1 min	>99	9.1	90.9	9.1
2	2h	>99	100	0	100

^{a} conversions and yields determined by ^{1}H NMR. Conv. **30** = conversion of **30**; Conv. **31a** = conversion of **31a**. Conditions: [αCC]/[thiol] = 1/1 , αCC = 4 mmol, V_{DMF} = 1 mL, r.t.

when alcohols or amines were employed.[215] An important feature of the process is that it is recognized as being switchable because one can easily switch of the reaction by deactivating the organocatalyst, e.g. by adding acetic acid. To shed light on this reactivity and hence understand how to steer the product distribution for the production of the corresponding polymers, a first mechanism is proposed based on a DFT study using an implicit solvent model ignoring the organocatalyst, which is able to explain the observations. However, it is worth noting that in a second stage of this research a new mechanism is proposed for the formation of **32** (*vide infra*).

The results shown in Figure 4.13 indicate that the nucleophilic attack on the carbonyl species is highly favored i.e. an apparent activation barrier of 85.1 kJ.mol$^{-}1$ is obtained while the barrier heights for the two other pathways are drastically higher ($\Delta G^{\ddagger}$ = 155.6 and 185.8 kJ.mol^{-1} for pathway 2 and pathway 3 respectively). Intermediate **40a** and intermediate **41a** are noted as important intermediates before tautomerization of **41a** occurs towards the observed oxothiocarbonate. The most important feature of this pathway is its reversibility which is key to obtain full conversion towards **32a**. Though higher in activation energy, the alternative addition mode with formation of the corresponding carbonate anion **39a** favors the intermediate species which can subsequently, aided by DBUH$^+$, form the thermodynamically favored **32a**. Hence, supported by kinetic experiments, we propose that β-oxothiocarbonate formation is under kinetic control while formation of tetrasubstituted ethylene carbonate is under thermodynamic control. However, recognizing the shortcomings of the results, more advanced methods are used in

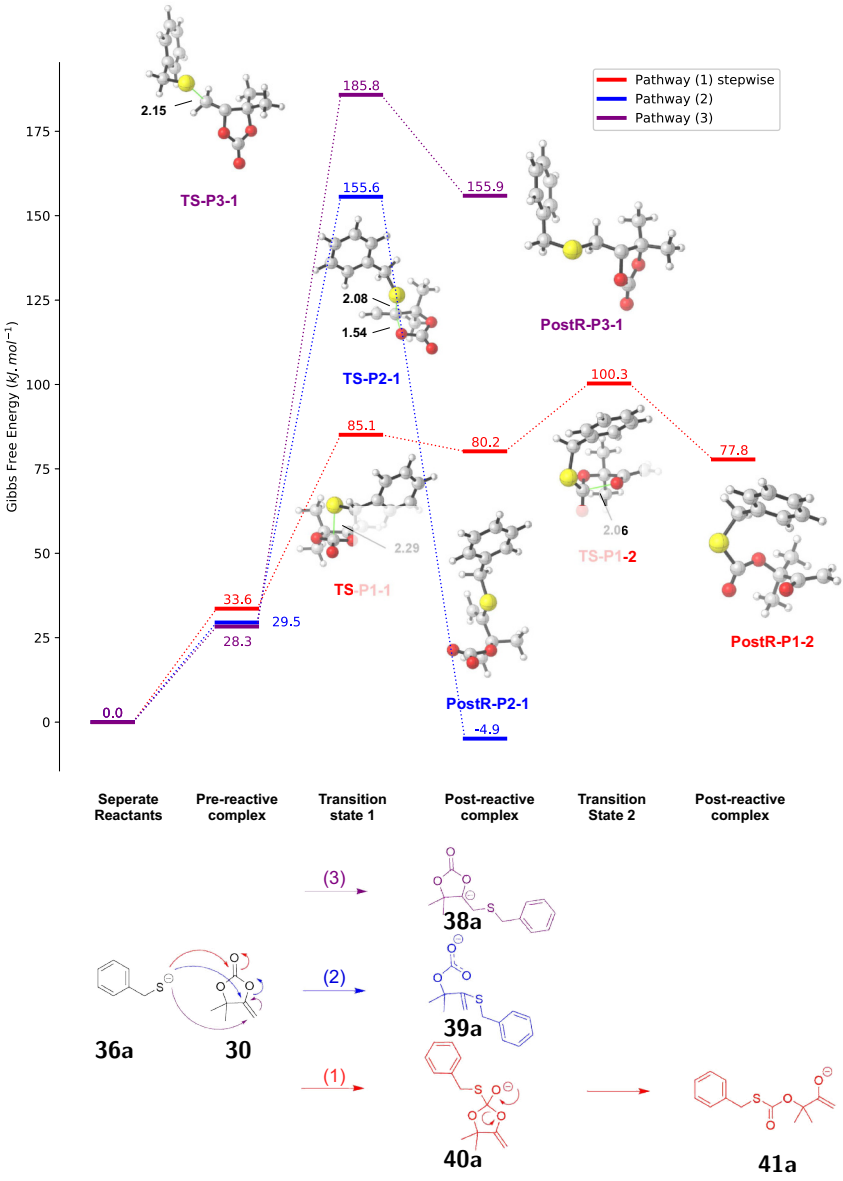

Figure 4.13. Gibbs free energy profile for pathway (1) (stepwise, TS-P1-1 and TS-P1-2), pathway (2) (concerted with formation of the ring-opening product, TS-P2-1) and pathway (3) with formation of carbanion (via TS-P3-1). Corresponding transition state and post-reactive complex geometries are shown with the critical distances displayed in Å. (ωB97X-D/6-311++G(d,p), 298K, 1 atm, PCM($\epsilon = 37.219$)).

Paper IV explicitly accounting for DBU (and the solvent) with the goal to unravel the peculiar effect of the organocatalyst. The results are discussed in the next section.

Reactivity of αCC with alcohols

In **Paper IV**, the alcoholysis of exovinylene cyclic carbonates is explored providing access to biorenewable and CO_2-based polycarbonates. The experimental results, produced by the CESAM research group, for the aforementioned model reaction (Scheme 4.8) are shown in Table 4.2, suggesting that when benzylalcohol **35** is used, side products are formed during the reaction due to a rearrangement of oxo-carbonate **31b**. Extra experiments (not shown) confirm this observation and hence illustrate the need to thoroughly understand the underlying mechanism in order to exert more control during the step-copolymerization. Understanding the mechanism can hence help to steer the polymer molar mass distribution and their corresponding microstructures.

Table 4.2. Alcoholysis of Exovinylene Cyclic Carbonate with 1-Butanol, Cyclohexanol, and Benzyl Alcohol at 80 °C.

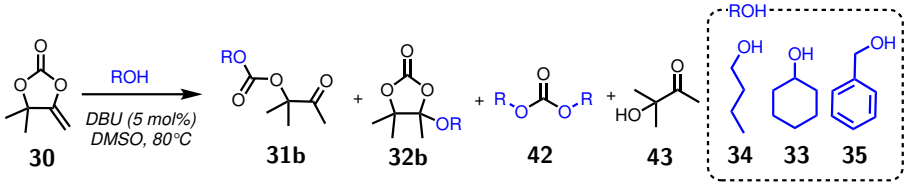

30 **31b** **32b** **42** **43** **34** **33** **35**

Entry	ROH	Time	Conv.αCC [%][a]	Yield **31b** [%][a]	Yield **32b** [%][a]	Yield **42** [%][a]	Yield **43** [%][a]
1	**34**	15 min	98	98	0	0	0
2		2h	>99	>99	0	0	0
3		24h	>99	>99	0	0	0
4		48h	>99	>99	0	0	0
5	**33**	15 min	59	59	0	0	0
6		2h	89	89	0	0	0
7		24h	>99	>99	0	0	0
8		48h	>99	>99	0	0	0
9	**35**	15 min	>99	>99	0	0	0
10		2h	>99	94	3	2	1
11		24h	>99	58	22	6	8
12		48h	>99	38	32	15	17

[a]Yield determined by ^{1}H NMR spectroscopy on the crude product. Conditions: αCC (4 mmol), alcohol (4 mmol), and DBU (0.2 mmol) in dry DMSO (1 mL) at 80 °C under a nitrogen atmosphere.

To this end, the work presented in **Paper III** is extended by exploring the influence of the organocatalyst DBU, the solvent and alternative pathways for

the formation of the tetrasubsituted ethylene carbonate. Here both static DFT calculations, to investigate the reactivity, and DFT MD calculations, to investigate intermediate stability, are performed.

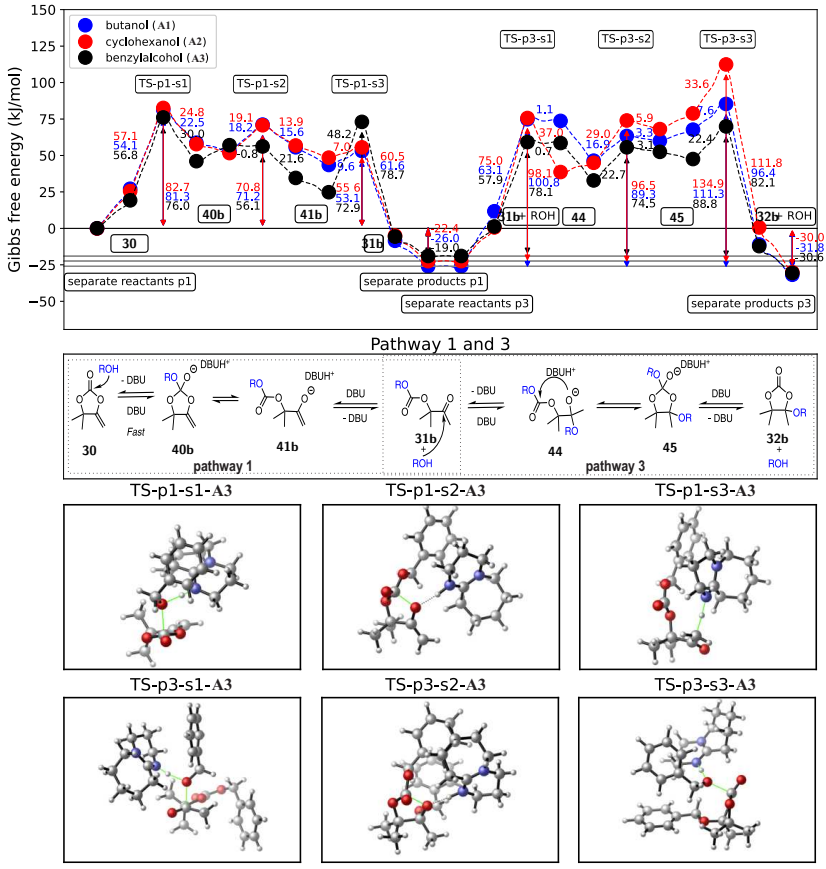

Figure 4.14. Gibbs-Free Energy Profile with the Corresponding Reaction Scheme and Transition-State Structures for Pathway 1 (p1) with the Formation of the corresponding Oxo-carbonate and for Pathway 3 (p3) with the Formation of corresponding Tetrasubstituted Ethylene Carbonate[a].

[a]The separate reactants for p3 are rescaled to the separate product of p1. Green bonds in the TS figures indicate bonds which are broken or formed. Energies in kJ.mol^{-1} (ωB97X-D/6-311++G(d,p), 298K, 1 atm, PCM($\epsilon = 46.826$)).

The Gibbs free energy profiles shown in Figure 4.14 illustrate the reactivity of **30** w.r.t. the different alcohols under investigation. The mechanism for the formation of oxo-carbonate **31b**, is similar to the one found for the thiolation (*vide supra*) though now DBU is accounted for explicitly. No significant influence

on the activation barriers for the different alcohols is found for this pathway, however intermediate stability is altered depending on the applied alcohol (*vide infra*). The formation of tetrasubsituted ethylene carbonate **32b**, on the other hand, is explained via an alternative pathway (in line with the work by Lu et al.), i.e. pathway 3, in contrast to pathway 2 presented in **Paper III**.[225] This pathway proceeds via a nucleophilic attack of a second alcohol molecule on oxo-carbonate **31b**, forming intermediate **44**. Subsequently, for **44**, a ring-closure - and elimination step occur with expulsion of an alcohol moiety to the corresponding **32b**. Furthermore, the activation barriers of the rate-limiting step of this pathway indicate that this pathways is more likely to occur for benzyl alcohol than for butanol and cyclohexanol. Indeed, computing the corresponding apparent reaction rates and their ratio w.r.t pathway 1 reveals that only in case of benzylalcohol **35** pathway 3 is competitive with pathway 1 (see Table 4.3, applying Equation 2.14, Section 2.2.2).

Table 4.3. Reaction Rates for the Rate-Determining Steps of Pathways 1 and 3 ($k_{1,p1}$ and $k_{1,p3}, M^{-2}.s^{-1}$)[a]

alcohol	$k_{1,pathway1}$	$k_{1,pathway3}$	$\frac{k_{1,pathway1}}{k_{1,pathway3}}$
benzyl alcohol (**35**)	3.05×10^{-1}	1.28×10^{-1}	2.4
butanol (**33**)	3.58×10^{-2}	1.37×10^{-5}	2607.2
cyclohexanol (**34**)	2.03×10^{-2}	3.98×10^{-5}	510.3

[a] Rate constants are calculated with respect to separate reactants or products. [ωB97-XD/6-311++G(d,p), IEFPCM($\epsilon = 46.826$), 298 K, 1 atm]

Additionally, we show that when benzylalcohol is used π-cation and π-induced dipole interactions occur with organocatalyst DBU **37** as illustrated by the non-covalent interaction plots shown in Figure 4.15. These plots are constructed with NCIPLOT which enables the visualization of non-covalent interactions based on the reduced density gradient and the electron density (and the sign of the second eigenvalue λ_2 of the electron-density Hessian).[112] Depending on the electron density and the sign of λ_2 we can distinguish between attractive ($\lambda_2 < 0$), repulsive ($\lambda_2 > 0$) and VdW ($\lambda_2 \approx 0$) interactions. On one hand these interactions increase the intermediate stabilities for benzylalcohol and they tend to lower the activation barriers. These effects are not observed neither for butanol nor for cyclohexanol.

These specific interactions between benzylalcohol and DBU were furthermore shown to prevail in an explicit solvent environment by means of DFT MD simulations. These reveal that **41b** is in equilibium with intermediate **46** whereas in case of butanol this equilibrium is shifted to **41b** (see Scheme 4.9). The

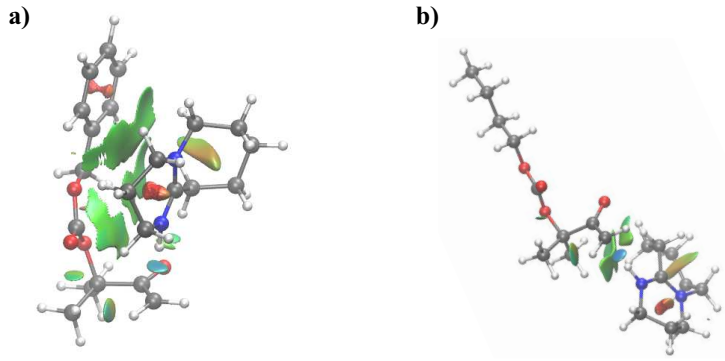

Figure 4.15. Non-covalent interaction plots for **41b** with (a) benzyl alcohol and (b) butanol as the used alcohol. Green surfaces indicate weak vdW interactions, blue surfaces indicate strong stabilizing interactions (e.g. hydrogen bonding), and red surfaces indicate repulsive/destabilizing interactions.

occurence of the equilibrium for benzylalcohol in combination with the induced π-type interactions can hence directly influence the reaction kinetics. The results of the DFT MD simulations are incorporated in the overview scheme presented in Figure 4.9, which furthermore highlights the presence of an equilibrium between **44** and **47** at operating conditions.

Finally, the experimental observation of sideproducts **42** and **43**, formed by the DBU-promoted transcarbonation of oxo-carbonate **31b**, is explained by determining the chemoselectivity of the alcohol w.r.t. the ketone and carbonate moieties. To this end, Parr functions are used as chemical descriptor for the local electrophilicity. The results of the local electrophilicity for the respective sites revealed that the nucleophilic attack on the keton moiety is prefered, explaining the favored formation of **32b** w.r.t. the transcarbonation product **42**.

Hence, in contrast to **Paper III**, these results reveal a more specific effect of the DBU catalyst on the reactivity of the monomers by π-type interactions which affect the stability of intermediates. Additionally the formation of tetrasubstituted ethylene carbonate **32** is found to proceed via a nucleophilic attack by an alcohol on the formed oxo-carbonate **31b**. The latter route is furthermore prefered with respect to the transcarbonation reaction due to a higher electrophilicity of the keton

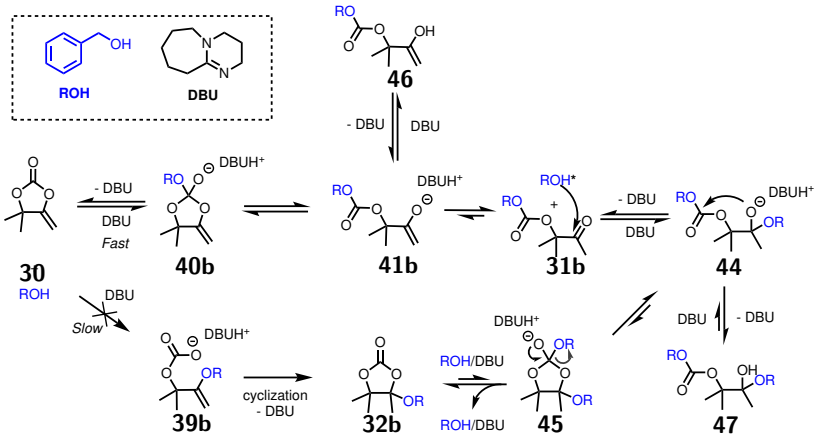

Scheme 4.9. Mechanism of Formation of Tetrasubstituted Ethylene Carbonate 2 by Addition of Benzyl Alcohol to αCC.

moiety. These insights have helped to rationalize and steer the polymerization outcome for the step-copolymerization of bis(α-alkylidene carbonate) with dialcohols and dithiols, which is further elaborated on in **Paper IV**.

To conclude, within this chapter concerning the BioFactory, we have investigated two major topics: the *O*- and *C*-dealkylation of lignin-derived compounds and the step-polymerization of bis-αCC with thiols and (lignin-derived) alcohols. Using a multiscale modeling approach, we have unraveled the mechanistic details of the different processes under investigation. Additionally, we have revealed various of the catalytic features for the homo-, hetero- and organocatalyzed reactions studied in this chapter. On the one hand we showed that both hetero- and homogeneous Brønsted acids can effectively catalyze the *O*-dealkylation of guaiacol and, on the other hand, we showed that interactions between the organocatalyst DBU and benzylalcohol enabled the formation of tetrasubstituted ethylene carbonates through π-type interactions stabilizing the reaction intermediates. The computational results presented in this chapter and in **Paper I-IV** will aid the future rational design of experiments and will help to tune polymerization conditions and outcome.

5

Poly(2-alkyl-2-oxazolines)

Poly(2-alkyl/aryl-2-oxazoline) (PAOx) **1**, often abbreviated as poly(2-oxazoline) (POx), are a group of polymers which are generated by the cationic ring-opening polymerization (CROP, *vide infra* and Chapter 3 Section 3.4.2) of 2-oxazolines **2** or following IUPAC's rules: 4,5-dihydro-oxazoles (Scheme 5.1).

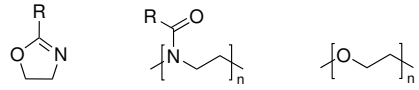

2 **1** **3**

Scheme 5.1. 2-oxazoline monomer **2**, poly(2-alkyl/aryl-2-oxazoline) (PAOx) **1**, poly(ethylene glycol) (PEG) **3**.

These cyclic imino-ethers are well known in organometallic chemistry as chemically inert ligands, and they are used by organic chemists to perform asymetric synthesis, i.e. when substituted at the C_4 and/or C_5 position.[226–229] However, it is the 2-oxazolines substituted at the C_2 position which provide access to this very interesting class of polymers poly(2-alkyl/aryl-2-oxazoline) (PAOx). POx can be considered as (bio-inspired) pseudopeptides due to their structural resemblance to polypeptides. However, they possess an increased stability w.r.t. polypeptides as the tertiary amides are not sensitive to hydrolysis conditions.[230,231] PAOx are biocompatible, thermosensitive and show stealth behavior similar to that of the 'golden standard' poly(ethylene glycol) (PEG) **3** making it hence ideal for drug-

delivery applications.[232–236]

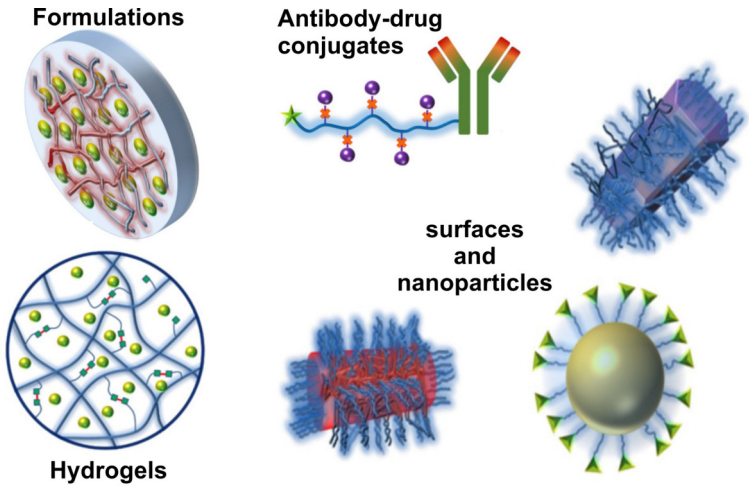

Figure 5.1. Main strategies for the use of poly(2-alkyl/aryl-2-oxazoline)s in drug-delivery applications: the preparation of drug excipients (formulations); antibody-drug conjugates; polymer therapeutics; functional surfaces and nanoparticles; and hydrogels. Reproduced from ultroxa.com/applications (ULTROXA®).

A relative broad set of strategies exist to apply PAOxs in drug-delivery apllications as illustrated in Figure 5.1 which originates from the adaptability of the C_2-substituent and the potential to tailor the resulting materials.[237] The architecture and properties of these polymers are ultimately determined by this substituent and hence by the identity of the monomeric unit. Especially when synthesizing oxazoline-based copolymers it is essential to determine the influence of this sidechain on the kinetics of the CROP in order to tune the architecture, properties and thus application field of the copolymers. Furthermore, the tunability of the sidechain enables the introduction of (protected) functionalities which can facilitate the use of the polymers in very different application fields.

In Section 5.1, we will introduce the CROP of 2-alkyl-2-oxazolines, where we differentiate between the different chain-growth polymerization steps specifically for these monomers. Then we show how molecular modeling is used to gain a thorough understanding of a specific set of sidechains on the propagation rate constants for which the results are presented in **Paper V** and discussed in Section 5.1.2. This work was a collaboration with Prof. Richard Hoogenboom of the Supramolecular chemistry group at Ghent University. In Section 5.2, the potential of poly(2-ethyl-2-oxazoline) (PEtOx) as drug-delivery system is illustrated where we subsequently focus on its use for the production of amorphous solid dispersions ASDs. The concept of an ASD is shortly introduced in Section 5.2.1. Finally in Section

5.2.2 we highlight the results of a combined experimental and computational study, presented in **Paper VI**, where ASDs are prepared by solvent-electrospinning achieving unprecedented high drug-loadings. The experimental work is performed by the group of Prof. Karen De Clerck at the department of Materials, Textiles and Chemical Engineering from Ghent University. Using large-scale molecular models we gain a fundamental understanding of the interactions present within the polymer-drug system and its impact on the resulting properties for a specific API, flubendazole (FBZ). As the systems discussed in this chapter are so complex from a modeling perspective since they may become very large, an extensive workflow, dedicated to the computational modeling of large polymeric systems, is provided in Appendix C. This workflow contains an example, some tips and tricks, and various code snippets which might be useful for new researchers starting with this advanced modeling topic.

5.1 Cationic ring-opening polymerization of 2-alkyl-2-oxazolines

The CROP of 2-alkyl-2-oxazolines, with formation of the corresponding poly(2-alkyl-2-oxazoline)s (PAOx), follows the general aspects of a chain-growth polymerization, i.e. the mechanism proceeds via initiation, propagation and termination. The living character of this polymerization can be maintained only if appropriate conditions are maintained and extreme care is taken of the reagent purity. In general no nucleophilic species or functionalities with similar characteristics are tolerated within the mixture and hence also the solvents and reagents used should be completely dry. To this end post-polymerization modifications of PAOx are an important field of interest as the aforementioned conditions restrict the potential of this reaction.[238–240] Furthermore it is believed that for the CROP of PAOx, in contrast to the general consensus for ring-opening polymerizations, not the ring strain but instead the isomerization of the cyclic imino ether to the tertiary amide is the main thermodynamic driving force for this polymerization.[241,242]

Furthermore, typically two mechanisms are distinguished for the CROP, i.e. an ionic and a covalent one (Scheme 5.2) which are not mutually exclusive, where essentially the relative nucleophilicity of the counter-ion and the oxazoline; and the electrophilicity of the active chain-end dictate the dominance of each mechanism (and in extension the equilibrium of **1a** and **1b**, *vide infra*). Apart from the counter-ion also solvent (polarity), temperature and concentrations influence the equilibrium between covalent and ionic intermediates and the dominating mechanism.[243–249] More specifically, in **Paper V** methyl tosylate is used as initiator and acetonitrile as a solvent which are known to strongly favor the ionic pathway and intermediates. We will hence only focus on this mechanism in what follows.

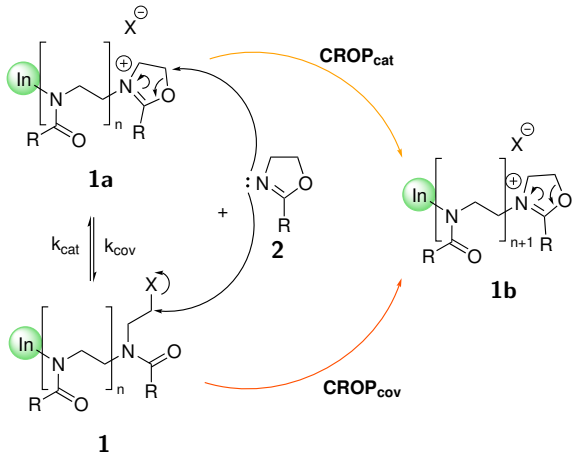

Scheme 5.2. CROP of 2-oxazolines distinguishing the ionic pathway (top) and the covalent pathway (bottom).

5.1.1 Reaction kinetics

It is generally accepted that this chain-polymerization proceeds via the following mechanism with the corresponding rate constants[250]:

1. **Initiation** with an initiation rate constant k_i forming the corresponding 2-oxazolinium cation which is in equilibrium with the covalent species. Remark that the equilibrium (k_{cat}/k_{cov}) governing the cationic and covalent species is shown for completeness and is practically controlled by the reaction conditions. Remark that the use of functional initiators can introduce important

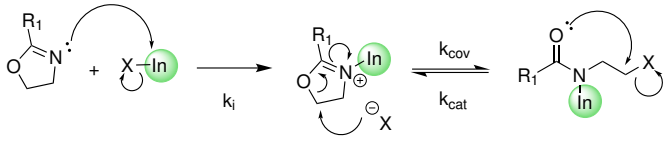

Scheme 5.3. Initiator step for the CROP of 2-alkyl-2-oxazolines.

end-group functionalities in the polymer with various application such as introduction of functional groups, production of specific polymer architectures, ...[251–256]

2. **Propagation** is generally split up into two steps, i.e. addition of the first monomer to the reactive center ($k_{p,1}$) followed by the actual propagation reaction (k_p). Again an equilibrium is present between the cationic and covalent species. The reason for this split is that after the first propagation step an intramolecular dipole-cation interaction is present stabilizing the TS and shifting the equilibrium in favor of the cationic species.[249]

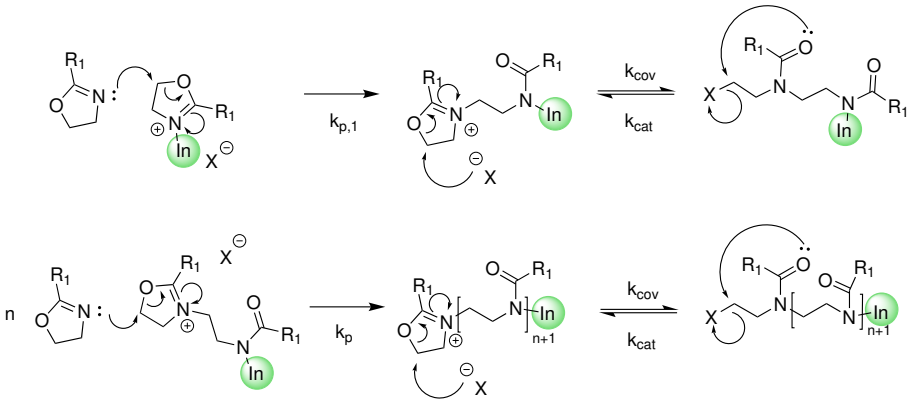

Scheme 5.4. Propagation steps for the CROP of 2-alkyl-2-oxazolines.

3. **Termination** with a termination rate constant k_t again depends on the covalent-cation equilibrium and thus the counterion and reaction conditions used. Similar to the initiation step also the termination step can be used to introduce various functionalities (with the advantage that non-compatible groups can be used as it is the end of the polymerization). Remark that termination can in theory also occur at the 2-position resulting in ester-terminated polymer chains (not shown).[257]

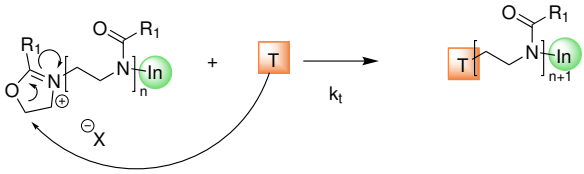

Scheme 5.5. Termination step for the CROP of 2-alkyl-2-oxazolines.

Obviously many factors can influence the reaction kinetics and hence the outcome of the CROP. However if we assume that initiation is fast (or complete) and undesired termination is absent then the polymerization rate is determined by the propagation rate with a corresponding rate constant k_p. Assuming first order kinetics, the propagation rate can be written as:

$$\frac{d[\mathrm{M}]}{dt} = -k_p[\mathrm{P}^+][\mathrm{M}] \tag{5.1}$$

with $[\mathrm{P}^+]$ the concentration of living cationic chains and $[\mathrm{M}]$ the monomer concentration.[250]

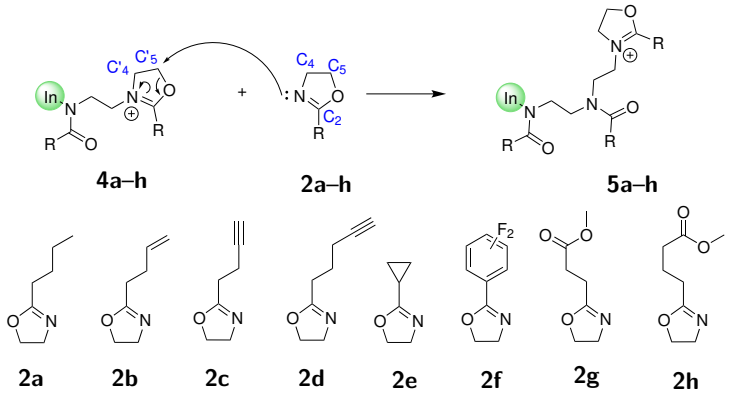

Scheme 5.6. Schematic Representation of the Second Propagation Step in the Cationic Ring-Opening Polymerization (CROP) of 2-Oxazolines, Leading to the Formation of the Corresponding Trimer 3, where In is the initiator Fragment at the Start of the Polymer Chain; (Bottom) 2-Oxazoline Structures for 2-(*n*-Butyl-2)-oxazoline (*n*-ButylOx, **2a**), 2-(But-3-enyl)-2-oxazoline (ButenOx, **2b**), 2-(But-3-ynyl)-2-oxazoline (ButynOx, **2c**), 2-(Pent-4-ynyl)-2-oxazoline (PentynOx, **2d**), 2-cyclopropyl-2-oxazoline (*c*-PrOx, **2e**),2-Difluorophenyl-2-oxazoline (*o*-DFPhOx, **2f**), 2-Methoxycarbonyl-ethyl-2-oxazoline (C_2-MestOx, **2g**) 2-Methoxycarbonyl-propyl-2-oxazoline (C_3-MestOx, **2h**).

Overall, k_p is governed by both electronic (e.g. inductive/mesomeric withdrawing or donating substituents can alter the nucleophilicity) and steric effects (e.g. bulky sidechains), with the latter effect more dominant than the former in most CROP reactions.[256,258–261] Exceptions however do exist for which electronic effects control the rate constant (see Scheme 5.6).[243,258,260,262,263] Remarkably unique effects can arise depending on the applied sidechain.

Rate acceleration ascribed to electronic effects where for example noted for *c*-propyl **2e** attributed to a (partial) π-bonding character[258]; *o*-difluorophenyl **2f** attributed to an intermolecular stabilizing fluoro-cation interaction and prevention of conjugation[262]; or for 2-methoxy-carbonylpropyl **2g** and 3-methoxy-carbonylpropyl **2h** attributed to intramolecular dipole-cation interactions.[259,260]

5.1.2 Reactivity of unsaturated 2-alkyl-2-oxazolines

In view of the aforementioned rate-enhancing effects by dipole-cation interactions, it is hypothesized in **Paper V** that a rate-enhancing effect for unsaturated sidechains occurs via cation-π interactions between the oxazolinium (the growing chain end) and the unsaturations in the sidechain. Incorporating unsaturations in the sidechains is a desirable functionality to introduce in PAOxs, as they give access to numerous applications in different branches of industry.[236,264–282] For example,

they provide an easy way for post-functionalization routes via thiol-ene and thiol-yne reactions or copper(I)-catalyzed azide cycloadditions, e.g. for the production of copolymers (where they are often combined with saturated sidechains, to for example steer the cross-linking degree). Practical uses are for example: usage as coatings for nanoparticles or stainless steel; usage as biocompatible material with anode-selective decomposition behavior; and usage as hydrogel or cross-linked nanoparticles in case network polymers are formed via a cross-linking procedure.

More specifically, the effect of unsaturations on the polymerization rate is investigated for 2-(butyl)- (*n*-ButylOx, **2a**), 2-(but-3-enyl)- (ButenOx, **2b**), 2-(but-3-ynyl)- (ButynOx, **2c**) and 2-(pent-4-enyl-)-2-oxazoline (PentynOx, **2d**) by means of an advanced modeling approach detailed in **Paper V**, for which the results are validated experimentally. This work was performed in collaboration with the the Supramolecular chemistry group of Richard Hoogenboom. Because the computational results are obtained trough the use of complementary methods, we provide an overview to guide the reader through the results in the form of a workflows (see Figure 5.2)

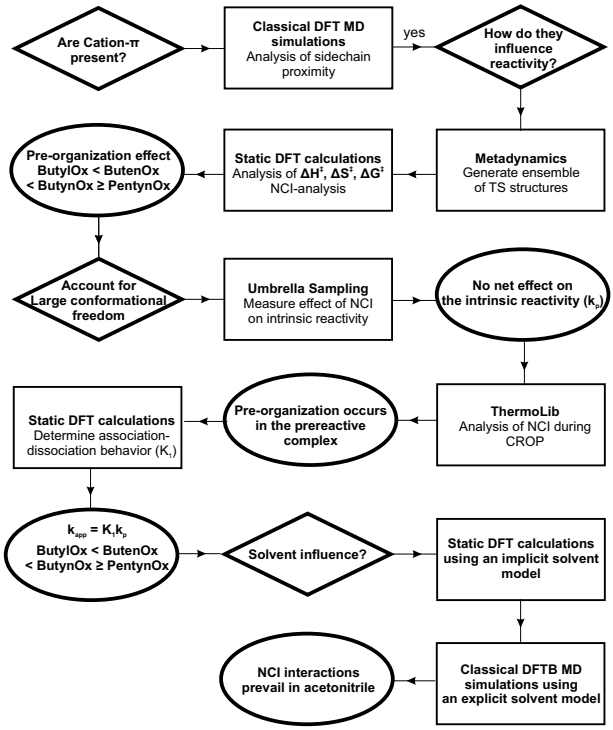

Figure 5.2. The computational workflow followed during the investigation of the effect of cation-π interactions on the CROP polymerization rate. Diamonds represent important questions, squares represent computational methods applied and elipses highlight the main conclusion(s) from a series of steps.

Cation-π Interactions: Evidence from Regular Ab Initio MD Simulations.

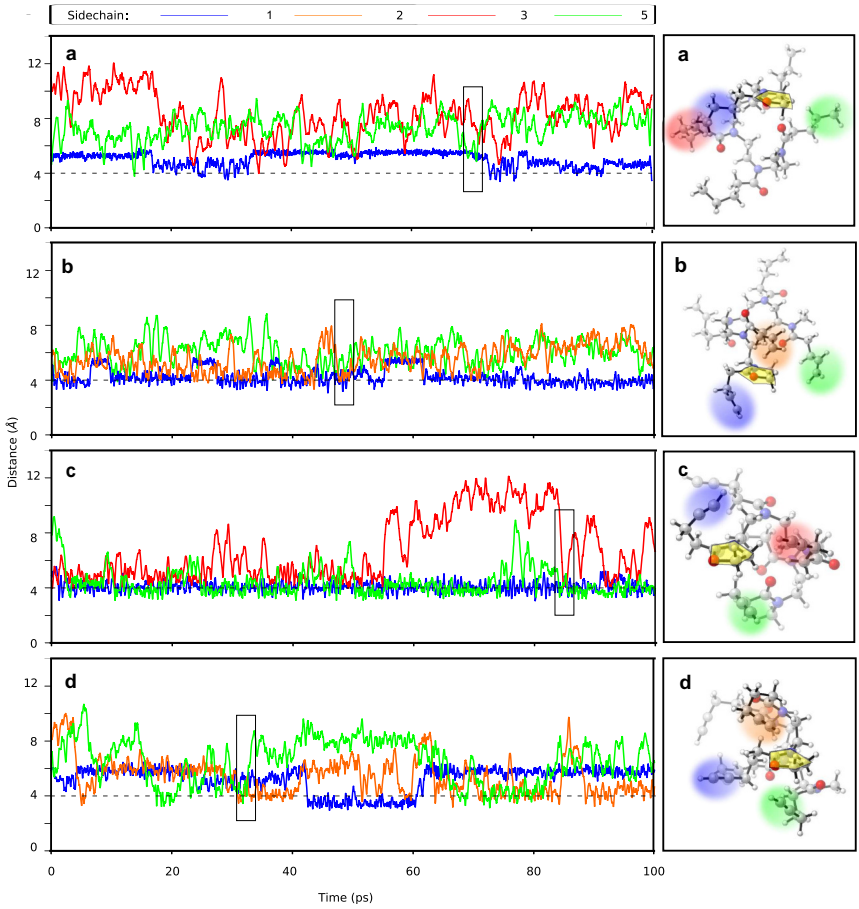

Figure 5.3. Evolution of distances for a representative MD run between the sidechain terminal bonds and the center of the 2-oxazolinium end-group (colored in yellow in the right panels) for pentaButylOx (a), pentaButenOx (b), pentaButynOx (c) and pentaPentynOx (d).
Snapshots (right-hand side) indicate the interaction pattern observed in the rectangular region time-span for each system; color codes shown at the top; see SI Section S2.1 for all the results. Reprinted with permission from Elias Van Den Broeck, Bart Verbraeken, Karen Dedecker, Pieter Cnudde, Louis Vanduyfhuys, Toon Verstraelen, Kristof Van Hecke, Valentin Victor Jerca, Saron Catak, Richard Hoogenboom, and Veronique Van Speybroeck. Cation-π interactions accelerate the living cationic ring-opening polymerization of unsaturated 2-alkyl-2-oxazolines. *Macromolecules*, 53(10):3832–3846, 2020. doi: 10.1021/acs.macromol.0c00865. Copyright 2020 American Chemical Society.

At first instance, the presence of these hypothesized cation-π interactions is investigated by *ab initio* MD. To this end, the proximity for the sidechain ends (and the carbonyl moieties, not shown) of a pentameric polymer chain to the cationic center is investigated through time, providing information on the influence of both the degree of unsaturation and the proximity of the unsaturated terminal bond on the occurence of cation-π interactions. The results for pentaButOx, pentaButenOx, pentaButynOx and pentaPentynOx are shown in Figure 5.3.

When comparing pentaButOx with the pentameric chains bearing unsaturated sidechains, the simulation results clearly show that the sidechain terminal groups for pentaButenOx, pentaButynOx and pentaPentynOx are consistently in close proximity to the oxazolinium, hence indicating the presence of cation-π interactions. Furthermore, when assessing the relative strength and hence influence of the degree of unsaturation, i.e. by means of the mean distance of the interacting state, we have shown that this distance decreases from 4.39 Å for pentaButOx to 4.11,4.07 and 3.59 Å for pentaButenOx, pentaButynOx and pentaPentynOx, respectively. This hence reflects the increased interaction strength with increasing degree of unsaturation. Remark that for the definition of an interacting state we refer to the Methodology section of **Paper V**. Furthermore, the relatively small impact of the triple-bond in ButynOx w.r.t. ButenOx is attributed to steric constraints of the 'arm-like' sidechain in ButynOx as the mean interacting distance for PentynOx is significantly lower. Nonetheless, the interacting state for the pentynyl sidechains is less prominent in comparison to the butynyl sidechains suggesting an entropic penalty in the former case.

Hence as these simulations suggest that indeed favorable cation-π interactions occur between the sidechains and the 2-oxazolinium chain-end, its effect on the propagation rate constant was investigated. Both static and enhanced sampling MD simulations are performed to elucidate the effect of cation-π interactions on the CROP propagation rate constants k_p. To this end trimeric systems are investigated, thus accounting for the cation-dipole interactions present in the growing polymeric chain (*vide supra*) while the molecular size of this system is still feasible in terms of computational cost and accuracy.[284]

Reactivity and Energetics

To assess the effect on the reactivity, a large set of transition state structures is generated, i.e. by means of metadynamics simulations, for each of the investigated systems. The transition states were statically optimized employing the hybrid B3LYP functional. It is important to note that finding transition states from scratch using a static approach can be very tedious, especially when the system contains a large number of degrees of freedom. Hence employing metadynamics (on the condition a good reaction coordinate is known) or other enhanced sampling approaches (see Section 2.2.3) can be of help to generate potential TS configurations. The results reveal a highly variable range of transition state free energies

and conformers emphasizing the complexitiy and multidimensionality of the free energy surface due to the many degrees of freedom in the trimeric systems. The obtained free energy barriers were furthermore decomposed in their enthalpic and entropic contributions, which reveal that a balance is struck between enthalpic and entropic contributions during the transition. Additionally, based on the activation barriers ($\Delta G^{\ddagger}$, see **Paper V**), the following reactivity trend is expected *n*-ButylOx $<$ ButenOx $<$ ButynOx $\geq$ PentynOx with a difference $<$ 5 kJ.mol^{-1}. It is found that in all systems a balance occurs between enthalpic and entropic contributions. Regardless of the separate contributions, the transition states lowest in free energy are still expected to dominate the minimal free energy path and are hence closer investigated. These are shown for *n*-ButylOx (**a1**), ButenOx (**b1/b2**) and ButynOx (**c2**) in Figure 5.4. Within these structures the non-covalent interactions were visualized using the NCI-plot tool (see Section 4.3.1 and the supporting information of **Paper V**).[112]

These states show that within all TS structures indeed carbonyl (dipole)-oxazolinium (cation) interactions occur regardless of the sidechain, as indicated by the blue surfaces between these moieties, in line with the regular MD results and the work by Bouten et al.[259,260] Furthermore, the analysis of the inter- and intramolecular non-covalent interactions in the governing transitions states shown in Figure 5.4 revealed the following. Firstly, for *n*-ButylOx the attacking monomer shows a so-called preorganization effect through dipole-induced dipole interactions of the carbonyl moiety in the dimeric chain with the saturated sidechain of the attacking monomer, respectively. When unsaturations are included, i.e. for ButenOx (**b1/b2**), ButynOx (**c2**) and PentynOx (**d**, (not shown)), it is observed that the number of potential interactions enabling this preorganization effect increases as now cation-π, π-π, and π-induced dipole interactions occur. Additionally, these interactions also tend to cause extra enthalpic stabilization within the TSs.

Importantly, in order to fully understand the effects of these non-covalent interactions and account for the substantial conformational freedom in the TS (confirmed by the aforementioned results), the CROP reaction is further investigated using enhanced sampling simulations, i.e. with umbrella sampling simulations. This allows us to gain a better understanding of the effect of the unsaturations in the various sidechains. Hence, the influence of the corresponding preorganization effects on the intrinsic reaction kinetics can be clarified. The results of these simulations are summarized in Table 5.1.

Suprisingly, the intrinsic reaction kinetics (k_p) are barely influenced by the unsaturations in the sidechain, with k_p varying less than one order of magnitude (Table 5.1), seemingly contradicting the results from the static - and regular MD approach. When analyzing these results in more detail, by means of appropriate free energy transformations using conditional probabilites (cfr. ThermoLIB), it is found that a clear stabilization occurs within the prereactive complex region when increasing the degree of unsaturation in the sidechain indicating that the

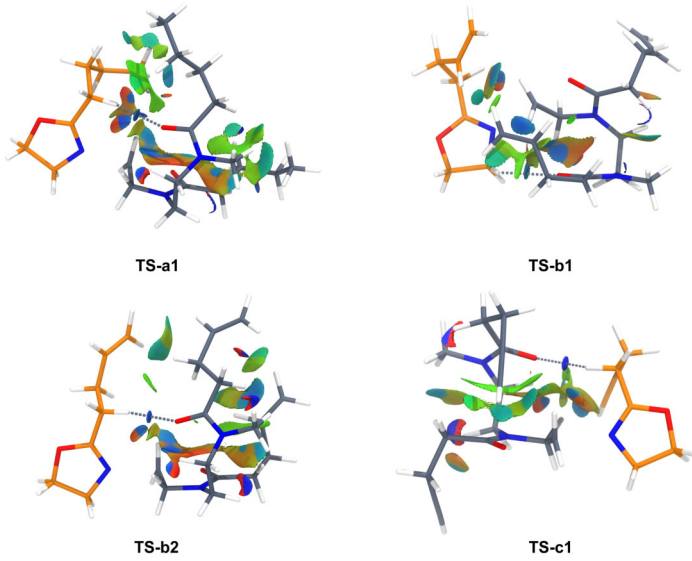

Figure 5.4. NCI-plots of the selected transition state structures for the propagation reaction of ButylOx (a), ButenOx (b) and ButynOx (c). The attacking monomer is displayed in orange and the growing polymer in gray. The 2-oxazolinium ring is opening (C–O) due to the attack of the nitrogen atom. The blue surfaces indicate stabilizing interactions, the green surface indicates van der Waals interactions, and the red surface typically indicates steric hindrance. The dotted line between the attacking monomer and growing polymer represents a stabilizing dipole-induced dipole interaction. [B3LYP-D3/6-311+G(d,p), 298 K, 1 atm)]. Reprinted with permission from Elias Van Den Broeck, Bart Verbraeken, Karen Dedecker, Pieter Cnudde, Louis Vanduyfhuys, Toon Verstraelen, Kristof Van Hecke, Valentin Victor Jerca, Saron Catak, Richard Hoogenboom, and Veronique Van Speybroeck. Cation-π interactions accelerate the living cationic ring-opening polymerization of unsaturated 2-alkyl-2-oxazolines. *Macromolecules*, 53(10):3832–3846, 2020. doi: 10.1021/acs.macromol.0c00865. Copyright 2020 American Chemical Society.

preorganization effect is manifesting itself not in the TS-region but in the reactant region.

Hence, accounting for this effect, we propose a two-step mechanism for the propagation step, similar to the approach of Değirmenci et al., where the association-dissociation process of the monomer and the growing polymeric chain are non-negligable.[285,286] Thus, the original propagation step is split in an association step

Table 5.1. Intrinsic Helmholtz free energy of activation and propagation rate constants (k_p) for the model trimeric systems under investigation obtained via US simulations. Remark that this k_p is not equal to the experimentally measured apparent rate constant. (BLYP-D3/TZVP-GTH, 413K, NVT)[a]. Reprinted with permission from Elias Van Den Broeck, Bart Verbraeken, Karen Dedecker, Pieter Cnudde, Louis Vanduyfhuys, Toon Verstraelen, Kristof Van Hecke, Valentin Victor Jerca, Saron Catak, Richard Hoogenboom, and Veronique Van Speybroeck. Cation-π interactions accelerate the living cationic ring-opening polymerization of unsaturated 2-alkyl-2-oxazolines. *Macromolecules*, 53(10):3832–3846, 2020. doi: 10.1021/acs.macromol.0c00865. Copyright 2020 American Chemical Society.

Monomer	$\Delta F^{\ddagger}_{fwd}$ [kJ.mol^{-1}]	$\Delta F^{\ddagger}_{bwd}$ [kJ.mol^{-1}]	k_p[s^{-1}][a]
n-ButylOx (a)	64	105	7.2×10^4
ButenOx (b)	63	100	1.0×10^5
ButynOx (c)	63	100	9.9×10^4
PentynOx (d)	67	116	3.0×10^4

[a] Calculated based on the method described by Bailleul et al.[55]

(with association consant k_1 and dissociation constant k_{-1}) and a propagation step with rate constant k_p:

$$\mathrm{M} + \mathrm{P}_n{}^* \underset{\mathrm{k}_{-1}}{\overset{\mathrm{k}_1}{\rightleftharpoons}} \mathrm{M{-}P}_n{}^* \tag{5.2}$$

$$\mathrm{M{-}P}_n{}^* \xrightarrow{\mathrm{k}_p} \mathrm{P}_{n+1}{}^* \tag{5.3}$$

where $\mathrm{M{-}P}_n{}^*$ is the associated complex, M is the monomer and P^* is the growing polymeric chain. This results in the following expression for the apparent rate constant (using the steady state approximation):

$$k_{app} = K_1 k_p = \frac{k_1 k_p}{k_{-1} + k_p} \tag{5.4}$$

To verify this hypothesis, the prereactive complexes of the most stable transition states (see Figure 5.4) are calculated and combined with the enhanced sampling results. Additionally, the prereactive complexes for a selection of transition states located in the static approach are also shown. The resulting free energy profiles are shown in Figure 5.5. For the equilibration step, a trend exists which reveals that an increasing degree of unsaturation favors the formation of the prereactive complex and hence increases the apparent polymerization rate. The Gibbs free energy of the prereactive complex decreases by 14 and 27 kJ.mol^{-1} for ButenOx and ButynOx with respect to *n*-ButylOx. Furthermore the length of the sidechain also affects the

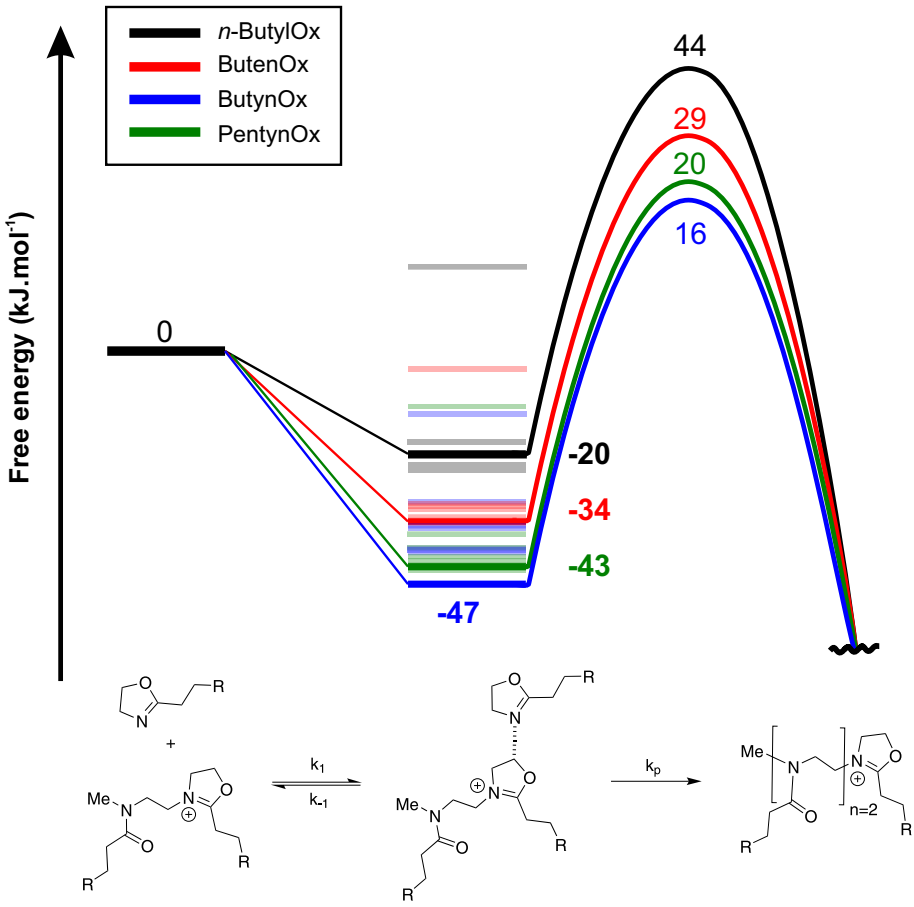

Figure 5.5. Combined free energy profile for the equilibration step and the propagation polymerization step of the CROP reaction for the different 2-oxazolines under investigation. The equilibration step is obtained by static calculations for multiple pre-reactive complexes of which an overview is found in the SI of **Paper V**, the polymerization step by enhanced MD simulations. n-ButylOx in black, ButenOx in red, ButynOx in blue and PentynOx in green. Reprinted with permission from Elias Van Den Broeck, Bart Verbraeken, Karen Dedecker, Pieter Cnudde, Louis Vanduyfhuys, Toon Verstraelen, Kristof Van Hecke, Valentin Victor Jerca, Saron Catak, Richard Hoogenboom, and Veronique Van Speybroeck. Cation-π interactions accelerate the living cationic ring-opening polymerization of unsaturated 2-alkyl-2-oxazolines. *Macromolecules*, 53(10):3832–3846, 2020. doi: 10.1021/acs.macromol.0c00865. Copyright 2020 American Chemical Society.

formation of the prereactive complex, with a Gibbs free energy of -43 kJ.mol^{-1} for PentynOx and -47 kJ.mol^{-1} for ButynOx revealing a higher entropic cost for the

PentynOx case. Thus, based on this analysis, a trend equal to the one proposed in the static approach is obtained however the underlying reason for this trend is now better understood.

Finally, we have investigated the influence of the solvent, acetonitrile, on these observations. The results are thoroughly discussed in **Paper V**. On one hand, the stability of the prereactive complexes is assessed in the solvent, by reoptimizing the gas-phase structures using an implicit solvent model. These calculations confirm that more stable complexes are obtained in the presence of unsaturated sidechains. On the other hand, regular MD simulations using an explicit solvent environment, using the DFTB level of theory, show that cation-π interactions between the monomer and the polymeric chain are not destroyed in the presence of acetonitril.[287–290]

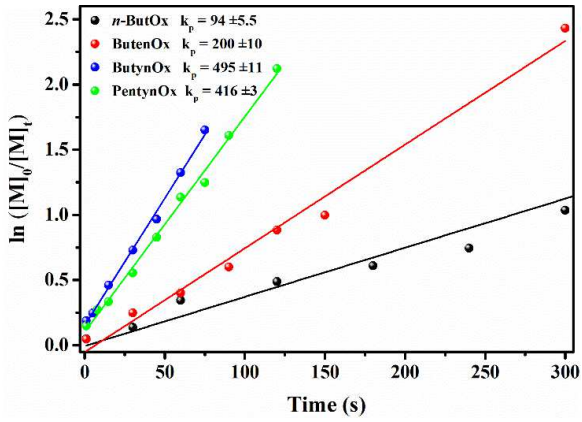

Figure 5.6. First-order kinetic plot for the cationic ring-opening polymerization of n-ButOx, ButenOx, ButynOx and PentynOx. Polymerizations performed at 140 °C in acetonitrile with 4 M monomer (M) concentration, methyl tosylate (I) as initiator, and a [M]:[I] ratio of 100. The polymerization rate constants (k_p's) are given in $10^{-3} L.mol^{-1}.s^{-1}$. Reprinted with permission from Elias Van Den Broeck, Bart Verbraeken, Karen Dedecker, Pieter Cnudde, Louis Vanduyfhuys, Toon Verstraelen, Kristof Van Hecke, Valentin Victor Jerca, Saron Catak, Richard Hoogenboom, and Veronique Van Speybroeck. Cation-π interactions accelerate the living cationic ring-opening polymerization of unsaturated 2-alkyl-2-oxazolines. *Macromolecules*, 53(10):3832–3846, 2020. doi: 10.1021/acs.macromol.0c00865. Copyright 2020 American Chemical Society.

In order to validate our results, the polymerization rate for the different monomers was determined experimentally. These results are shown in Figure 5.6, and reveal a trend equal to the one predicted by the computations hence verifying our results.

In conclusion the computational results, predict a difference in polymerization kinetics depending on the degree of unsaturation in the sidechain. The following trend is anticipated: *n*-ButylOx < ButenOx < ButynOx ≥ PentynOx. Despite that both the static and enhanced sampling approach provide the same trend, it is the more advanced analysis which revealed that the introduction of unsaturations in the sidechains enables a preorganization effect which stabilizes the prereactive complex and in this way favors association of the monomer with the growing polymer chain. Furthermore, it is shown that the differences in the preorganization effect for the different systems is based on cation-π, π-π and π-induced dipole interactions. Importantly, we find that when stabilizing interactions are present in the TS potentially no net effect occurs on the intrinsic reactivity as similar effects occur in the prereactive complex region. These findings can have important implications on other types of polymerization reactions and hence on the polymerization outcomes and should be considered in future research.

5.2 Poly(2-ethyl-2-oxazoline)-based drug-delivery systems

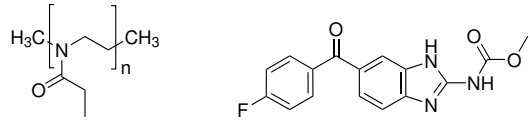

1c **6**

Scheme 5.7. Structural formulas of PEtOx (left) and flubendazole (right).

Despite the many potential applications highlighted in previous section, PAOxs have not yet found many widespread applications in industry, that is apart from PEtOx.[237] PEtOx has been marketed as high thermal stability alternative for poly(vinyl pyrrolidone) and poly(vinyl alcohol) and is sold under the tradename Aquazol®.[291] Furthermore it has got most attention among the PAOx class because it is a hydrophilic polymer that possesses so-called lower-critical-solution-temperature (LCST) behavior making it suitable for biomedical applications. This behavior translates to the fact PEtOx is soluble at low temperatures but can undergo entropy-driven demixing when heated, characterized by a transition temperature influenced by a.o. chain length.[292,293] Besides this, different studies have shown that the amide bonds present in the material are resistant to hydrolysis or decomposition under physiological conditions; and that no cytotoxicity nor mucosal irritation or tissue damage could be observed.[294–298] These factors in combination with a stealth behavior similar to PEG make poly(2-ethyl-2-oxazoline) thus suitable as potential matrix in drug formulations. One of its potential biomedical

applications which we will focus on in the next section is the use of PEtOx for the generation of amorphous solid dispersions. This work was performed in collaboration with Prof. Karen De Clerck from the department of Materials, Textiles and Chemical Engineering.

5.2.1 Amorphous solid dispersions as drug-delivery systems

Up to 90% of all drugs are characterized by a poor water solubility which is often also accompanied by slow dissolution rates (i.e. too slow in the time frame of absorption).[299–301] These factors hamper its bioavailability and prevent many drugs from being orally administered because the therapeutic effect of an orally-administered drug can only manifest itself when the active pharmaceutical ingredient (API) molecules are sufficiently dissolved in the aqueous-based gastrointestinal fluids. A very popular approach to achieve a higher apparent solubility and faster dissolution (and hence an increased bioavailability) is to convert crystalline drugs into its amorphous form.[302] This form is characterized by the lack of long-range symmetry operators i.e. translational -, orientational - and conformational order.[303] It is furthermore considered to be a glass, i.e. having the rheological properties of solids and molecular properties of liquids characterized by a T_g (see Section 3.3).[303,304] For this conversion one can distinguish two approaches: the neat API as an amorphous material (though only a limited number of examples exist for this case) or an amorphous solid dispersion (ASD). While in the former case one tries to alter the molecular packing by weakening the attractive energies between drug molecules, the latter case disrupts the packing by dispersing the drug molecules in a solid medium or carrier (i.e. the matrix referred to before).[303] One downside of the neat API approach is the decreased physical stability and hence increased molecular mobility. This is however completely solved with the ASD approach.[305–307] Remark that the molecular mobility of the API is strongly related to the shelf life of the drugs as the speed of recrystallization is altered. In this respect many Class II and IV APIs (following the Biopharmaceutical Classification System (BCS)) can hugely benefit from formulation approaches such as ASDs with an appropriate matrix, increasing solubility, dissolution rates and physical stability.[300,305,307] For its use as drug-delivery system this matrix should be hydrophilic in nature.[301,308–310] Hence these prerequisites make PEtOx an excellent candidate recipient for ASD-based drug-delivery systems.

In order to generate ASDs many preparation techniques are available where we distinguish: heat-based methods (e.g. melt/quench cooling or hot-melt extrusion[303,311]), solvent-based methods (e.g. spray drying, freeze drying, electrospraying, electrospinning, ...[307]), mechanochemical activation (e.g. cryo-milling[312]) or a combination hereof.[313] Hot-melt extrusion and spray drying are most commonly used in pharmaceutical industry because of their scalability. However, despite the plethora of manufacturing techniques, typically a low drug loading is used to avoid stability issues which can lead to phase separation and hence lower activation of

the administered drug. Pushing this boundary is hence of paramount importance for the development of next-generation ASDs.[313,314]

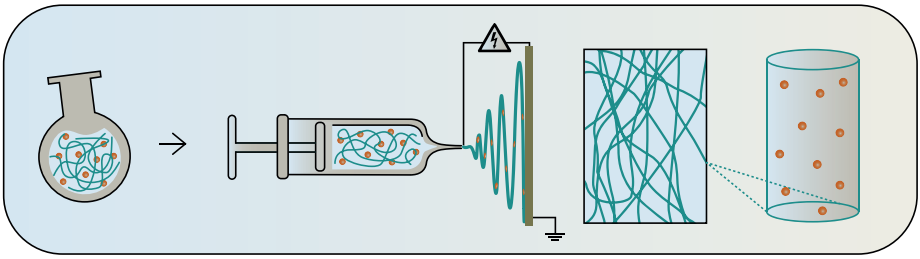

Figure 5.7. Schematic representation for the preparation of ASDs by solvent-electrospinning.

To this end, solvent electrospinning can be considered as a very promising method to generate ASDs with a high drug loading and an easy implementation and up-scalability as additional benefits.[313,315–317] The process comprises four consecutive steps:

1. Taylor cone formation at the nozzle of the spinneret
2. Ejection of a polymer jet from the cone
3. Whipping and bending the polymer jet
4. Collection of the produced nanofibers

which is schematically shown in Figure 5.7. The fibers themselves are generated by applying electrostatic forces on the working solution (i.e. dissolved polymer-API system) when it leaves the nozzle, with typical diameters below 500 nm. Interestingly the nanofibers possess a high porosity and a large specific surface area which enhance API dissolution rates. Because of the very rapid (complete) solvent evaporation API molecules are kinetically trapped inside the polymer nanofibers (decreasing diffusivity and thus molecular mobility of the drug) in a highly dispersed manner, i.e. close to its degree of dispersion in the working fluid.[307,313,317]

Ideally, to further prevent phase separation and hence recrystallization of the drugs, API-polymer miscibility should be sufficiently high. Despite the API molecules getting kinetically trapped, polymer-API interactions (i.e. non-covalent interactions such as Londen dispersion or hydrogen bonding) have a crucial role in assessing this miscibility and long-term stability of these formulations.[307,318,319] It is hence a key feature indicating the feasibility and compatibility of the desired polymer-drug ASD.

To this end PEtOx shows large potential to function as carrier material within ASDs, though only a limited number of examples exist, it has been shown to be a very promising and suitable candidate to increase dissolution rates of poorly

water-soluble APIs.[298,320,321] In addition to increased dissolution rates it also has a potential supersaturation effect upon dissolution hence allowing an even higher amount of API to be absorbed by the body.[320,321]

Investigating ASDs computationally is accompanied by many challenges, nonetheless some intriguing works have been reported.[322–328] These studies typically provide insights on the governing interactions and try to assess miscibility (and optimal drug loadings) of specific drug-polymer matrix combinations. Furthermore molecular modeling can be used to determine the mobility of the API molecules inside the material, and the properties of the ASD itself. Ideally computational research of ASD progresses to a level where one can efficiently screen drug molecules for drug-matrix compatability and determine optimal drug-loadings to use *in vivo*. In the following section we will discuss the main computational results using large-scale molecular simulations presented in **Paper VI**, which comprises the study of a PEtOx-based ASDs using flubendazole (FBZ) **6** as API-model compound.

5.2.2 PEtOx-Flubenzole ASDs

At first instance it is interesting to highlight the relevance FBZ and why it is chosen as a model compound. FBZ **6** (Scheme 5.7, *vide supra*) (a class IV compound) is a poorly water-soluble API, which thus shows low bioavailability, and is often used against gastrointestinal parasites in pigs and chickens.[305,329–331]However, it is also shown that it is a highly effective drugs against tropical diseases such as e.g. lymphatic filariasis (river blindness) and onchocerciasis (elephantiasis) which affect over 150 million people in tropical areas.[329,330,332–336] Nonetheless, due to its poor water solubility oral formulations are significanlty less effective than the parenterally administred doses. This is where PEtOx-based ASDs can provide solace, as the solubility-limited bioavailablility problems can be solved (*vide infra*) and the drug can be orally administered, which remains the preferred route.[306] Hence to this end, FBZ would hugely benefit from a bioavailability increase due to the formation of stable, biocompatible ASDs with PEtOx.

In paper **Paper VI**, the results are discussed of a combined experimental and computational study. Experimentally the solubility enhancement of FBZ is investigated following formulation of nanofibrous FBZ-PEtOx ASDs, produced by solvent electrospinning. It is hypothesized that hydrogen bonding occurs between both compounds which is crucial for the physical stability and to achieve high drug-loadings. Hence to rationalize the experimental findings, a multiscale modelling approach is used to investigate the governing interactions on one hand, and to assess the molecular mobility of the API within the polymer matrix, on the other hand. Remark that in what follows we focus on the computational results of the study, for more details on the experimental part the reader is referred to **Paper VI**.

We distinguish two approaches: Firstly, a static approach (using DFT calculations) is used to assess the competitiveness between FBZ-FBZ and FBZ-PEtOx interactions. Secondly, large scale atomistic force-field-based simulations ($>$ 40000 atoms) are performed for a realistic electrospun ASD which enable us to investigate interaction patterns within the nanofibers. These large scale simulations will furthermore allow us to extract self-diffusivity data enabling an assesment of the kinetic stability of flubendazole in the material. In order to generate these realistic ASD models, an extensive computational procedure is set up which we will further elaborate on below.

Because the methodology used to set-up simulations representing polymeric systems realistically is non-trivial, we have provided a model workflow in Appendix C giving insights on how to generate large polymeric systems and how to model them on an atomistic level. The workflow furthermore contains small code snippets in combination with some important aspects to consider when generating polymer models. These can be valuable for people starting with their own computational research concerning large polymer systems.

Generating realistic ASD models

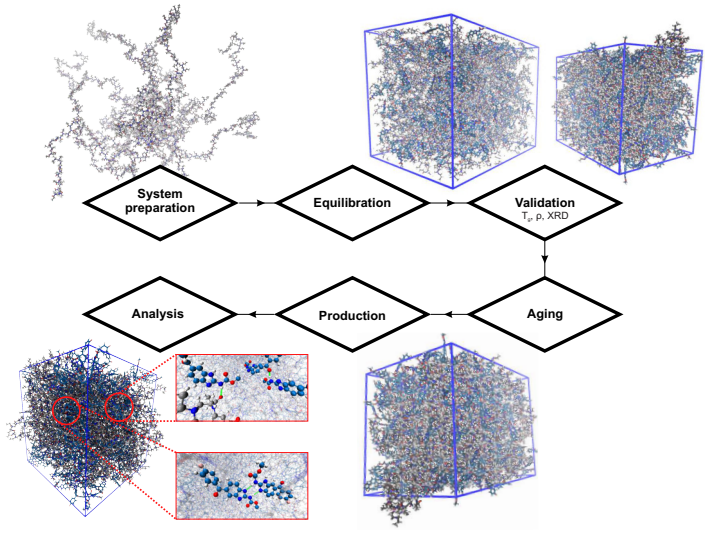

Figure 5.8. Workflow of the computational procedure to investigate amorphous solid dispersions, highlighting each step of the computational protocol. Structures illustrate the change in packing during the equilibration protocol. Upon visual inspection of the generated structure, the present interactions can be clearly observed (as highlighted under 'Analysis').

In order to construct realistic electrospun ASDs, the computational procedure which is schematically shown in Figure 5.8 is followed. The constructed model consists of 15 PEtOx chains each of 100 repeating units (centimer) which is combined with an appropriate amount of FBZ (476 molecules $\approx$ 50 w/w%). In Figure 5.8, the diamonds represent the various steps in the computational procudure which we will mainly focus on here, for more detailed explanations of the various subprotocols the reader is referred to **Paper VI**.

To perform simulations with the contructed models, a force field is derived using the in-house developed software QuickFF, more details on the derivation itself can be found in the *Supporting information* of *Paper VI*.[84,85] Afterwards, in order to equilibrate the model, an equilibration protocol is followed where the different steps are adopted from the work by Li et al.[337] However we have added one important step to this protocol, that is an aging step. We deem this necessary because the physical properties, e.g. density, are expected to gradually drift towards their equilibrium values. A process which is referred to in literature as structural relaxation or physical aging which is a direct consequence of the metastability of these ASDs.[322,338,339] In order to validate the protocol and the generated models, we have calculated density -, glass transition temperatures (T_g) - and X-ray diffractograms.

The results for this validation procedure are shown in Table 5.3 where we compare the values obtained for the FBZ-PEtOx ASD (50w/w%) with a pure polymeric amorphous material. Additionally the results for the systems used in the mobility study are shown, i.e. a pure flubendazole system (250 molecules) and a system containing 10 Flubendazole molecules dissolved in water (at a predefined concentration). The XRD-diffractograms (see **Paper VI**) reveal that the procedure is indeed capable of consistently producing amorphous dispersions. The density, on the other hand, or more specifically the uncertainty on this density and its resemblance to the experimentally observed density, reveals that the protocol is able to sufficiently relax the structure and eliminate starting configuration dependencies.[337] Furthermore, relatively good agreement is obtained compared to literature, though a clear effect of the aging step is observed, highlighting its importance and making it essential to the protocol. Concerning the glass-transition temperatures, it is shown that the impact of the drugs inside the ASDs, i.e. based on the Δ-values which represent the difference in T_g between the loaded and unloaded polymer matrix, is well described by the model and it is hence able to capture the effect of FBZ in the dispersion.

We hence show that the proposed computational procedure and the constructed force field perform well to construct realistic electrospun ASDs and describe the molecular systems under investigation, respectively. Finally, a production run (including an equilibration period in the desired ensemble) is performed to investigate the features of interest.

Table 5.3. Density ρ and glass-transition temperature T_g validation results obtained from the equilibrated and aged structures. $\rho_{equilibration}$ represents the density of the equilibrated system (before aging), ρ_{aged} represents the density of the system after the physical aging step of the protocol. T_g are the glass transition temperatures of the equilibrated structures obtained through the protocol discussed in the supporting information of **Paper VI**, Δ-values represent the difference between the T_g for the pure polymeric amorphous system and the ASD containing 50 wt% Flu. #Flu = 0 wt%, 50 wt%, 5 mg/mL and 5x5x5 crystal represent the pure polymeric system, the ASD containing 50 wt% Flu, an aqueous solution of Flu at a concentration of 5 mg/mL and a Flu 5x5x5 crystal configuration, respectively.

# Flu	$\rho_{eq.}$ (g.mL^{-1})[a]	ρ_{aged} (g.mL^{-1})[b]		T_g(K)			
		MD [b]	Exp.	MD [b]	Δ	Exp.[c]	Δ
0 (0 wt%)	1.123 $\pm$ 0.002	1.133 $\pm$ 0.006	1.14 [340]	348 $\pm$ 10	22	335 $\pm$ 0.6	25
476 (50 wt%)	1.210 $\pm$ 0.001	1.218 $\pm$ 0.005	-	370 $\pm$ 11		360 $\pm$ 0.8	
10 (5 mg/mL)	1.015 $\pm$ $4{\cdot}10^{-5}$						
250 (5x5x5 crystal)	1.462	-	1.444				

[a] 95%-Confidence intervals are constructed based on the results of ten different input structures which are subsequently bootstrapped with replacement.

[b] 95%-Confidence intervals are constructed based standard uncertainty value for the results of three different input structures for which a coverage factor of 4.30 (t-distribution) is used, assuming a gaussian-distributed observable.

[c] Standard deviation given after three measurements.

Governing interactions

To investigate the interactions present between PEtOx and FBZ we have first used a static approach for which the main results are presented in Figure 5.9. Remark that a pentameric structure is chosen for PEtOx as this accounts for all types of monomeric interactions.[283]

Figure 5.9 highlights that the pentameric structure preferably forms a so-called

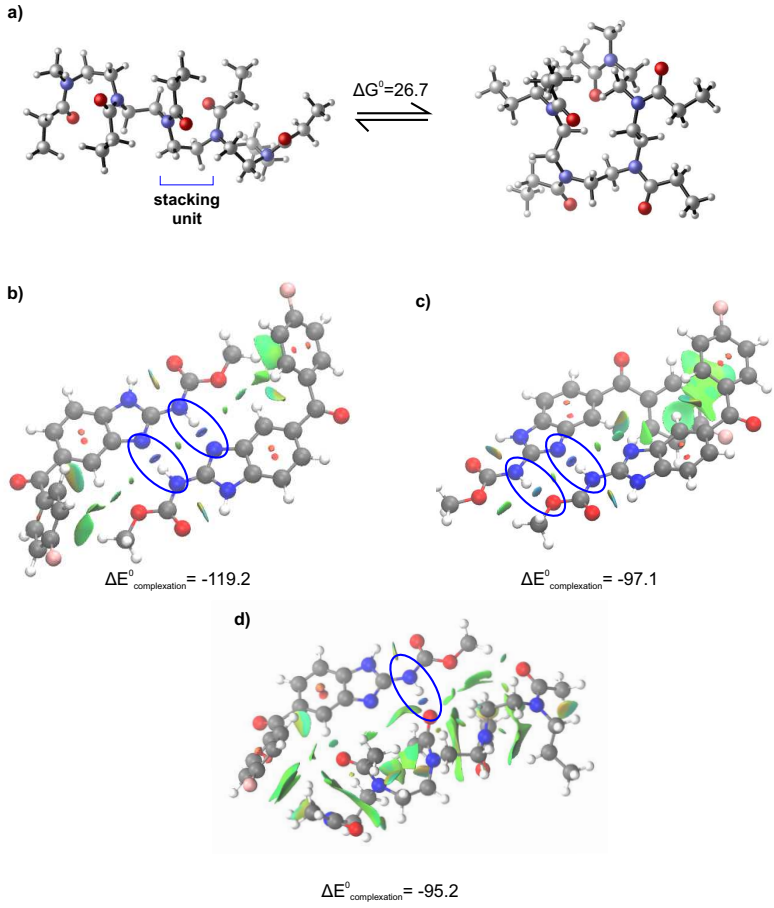

Figure 5.9. Overview of the most stable configurations based on DFT calculations. a: Different conformationally optimized pentameric structures of PEtOx. b: Most stable Flu-Flu complex with two hydrogen bonds (N-H-N); c: Flu-Flu complex with two hydrogen bonds (N-H-N and N-H-O(ether)) and π-π interactions; d: Flu-PEtOx complex with one hydrogen bond (N-H-O(carbonyl). ΔG and ΔE (Complexation energies) are given in units of kJ.mol^{-1} and calculated at the ωB97XD-6-311+G(d,p) level of theory (1 atm, 297.15K) with inclusion of include BSSE-corrections when appropriate; green surfaces represent weak van der Waals interactions, red surfaces represent repulsive interactions and blue attractive/stabilizing interactions. Hydrogen bonds are highlighted with blue ellipses.

stacking unit due to the presence of favorable interactions between subsequent repeating units (**a**), i.e. an interaction between the nitrogen lone-pair and the partial

positive charge on the carbon atom of the amide bond. Furthermore by calculating FBZ-FBZ and FBZ-PEtOx interaction energies and visualizing the corresponding non-covalent interactions, we show that the stability of both complexes is highly determined by the presence of hydrogen bonds between both structures. Based on the complexation energies, we may conclude that competition will occur for these hydrogen bonds within the material. The static approach hence reveals that the ability to form hydrogen bonds and the formation of a stacking unit are crucial features of the polymer-API formulations. Remark that the importance of the stacking unit is accounted for in the force field derivation.

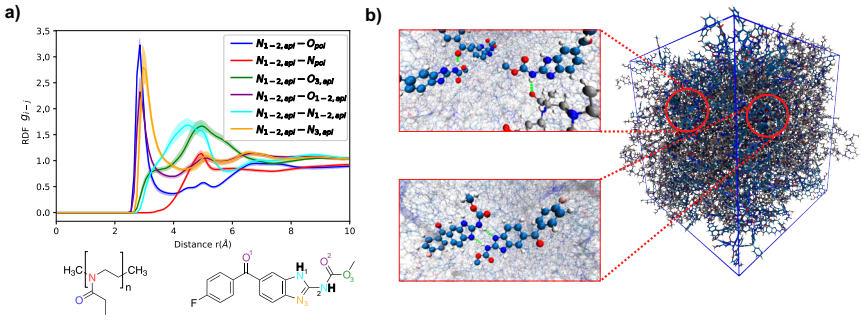

Figure 5.10. Radial distribution functions (with 95% confidence intervals) for the different highlighted atom pairs in the ASDs. b: Hydrogen bonding patterns (highlighted in green) observed within the ASD structure.

Proceeding with simulations of more realistic ASDs, we have analyzed pairwise interactions in the ASDs by means of radial distribution functions (RDFs, also denoted as g) on the one hand, and the total number of hydrogen bonds with their corresponding lifetimes, on the other hand.[341] The RDFs corresponding to the potential hydrogen bonding pairs are shown in Figure 5.10 in combination with a hydrogen bonding example found within the ASD structure. The patterns observed highlight that mainly N_3 (FBZ) and the carbonyl oxygen atoms (PEtOx and FBZ) are participating as hydrogen bond acceptors, which is confirmed by visual inspection of the simulation results (see Figure 5.10**b**). These computational results clarify and confirm the experimental observations (i.e. an experimental interaction analysis was performed using infrared spectroscopy, see **Paper VI**). Furthermore, g_{N-N}, i.e. the radial distribution function between the polymer backbone nitrogens, confirms that within the ASDs the stacking unit persists within the polymer-backbone.

To assess the dominance of each hydrogen bonding pair in the simulated ASDs and investigate what the effect is on the hydrogen bonding patterns for FBZ when dispersed inside a polymer matrix, w.r.t. the crystal structure, the total number of hydrogen bonds present during the simulation is investigated. Additionally, the

persistency and thus dynamics of the bonds is investigated by determining the continuous hydrogen-bond lifetimes (τ_c). These lifetimes measure the average time a hydrogen bonding pair remains intact and hence give an indication on the average lifetime of a hydrogen bond. Remark that once the bond is broken, it is considered broken from that moment on. The results of this analysis are displayed in Table 5.2.

Table 5.2. Fraction of occupied hydrogen-bond donors and continuous hydrogen bond lifetimes within the crystal and the ASD for the different constituents within the materials. Hydrogen bond criteria: distance $<3\mathring{A}$ and angle $> 130°$.

System	Hydrogen bond occupied by	Fraction occupied hydrogen bonds[a]	Continuous hydrogen bond lifetime τ_c (ns)[b]
50 wt% ASD	Total	0.271 ± 0.017	1.76 ± 0.420
	Flu	0.104 ± 0.018	1.25 ± 0.348
	PEtOx	0.167 ± 0.006	2.12 ± 0.464
Flu-crystal	Flu	0.145 ± 0.005	1.06 ± 0.169

[a] 95%-Confidence intervals are constructed based on the results of ten different input structures which are subsequently bootstrapped with replacement.

[b] 95%-Confidence intervals are constructed based standard uncertainty value for the results of three different input structures for which a coverage factor of 2.26 (t-distribution) is used, assuming a gaussian-distributed observable.

From these results, the expected competition based on the static approach is confirmed with PEtOx dominating as hydrogen bond acceptor for ASDs containing 50 w/w% API. Overall 17% of the hydrogen bond donors is occupied by PEtOx and 10% by FBZ. τ_c furthermore indicates that the former hydrogen bonds are much better preserved during a relatively long periods of time within the material (2.1 ns for PEtOx versus 1.2 ns for FBZ). Additionally, the effect of the ASD on FBZ-FBZ hydrogen bonds w.r.t. its crystaline form indicates (when put into perspective of literature values) that in both systems these hydrogen bonds are far from dynamic and remain very stable in the crystal and the material.[341] These results hence highlight the stability of the ASD on the one hand and the strength of the different bonds, on the other hand. The effect of these hydrogen bonds on the stability of the ASDs is also confirmed experimentally.

API mobility

Finally, the mobility of FBZ is qualitatively assessed by computing the self-diffusivity coefficient within various molecular environments, i.e. the ASD, an aqueous solution and a crystaline structure. The results are shown in Table 5.3. By comparing the

Table 5.3. Self-diffusivity constants for Flu (F-atom) in the ASD (50 w/w %, 476 Flu molecules), the crystal (5x5x5, 250 Flu molecules) and a water box (at a concentration of 5 mg/mL including 10 Flu molecules).

System	Self-diffusivity ($cm^2 \cdot s^{-1}$)[a]
ASD 50 w/w%	$5.459 \pm 1.183 \times 10^{-8}$
Flu 5x5x5 crystal	$5.456 \pm 3.2 \times 10^{-8}$
Flu-water (5mg/mL)	$2.679 \pm 1.403 \times 10^{-6}$

[a] 95%-Confidence intervals are constructed based on the results of ten different input structures which are subsequently bootstrapped with replacement.

different diffusivity constants in the various materials it is concluded that the FBZ molecules are effectively trapped within the ASD as its self-diffucivity constant is in the same order of magnitude for the crystalline form. When considering the self-diffusivity of FBZ in an aqueous environment, an increased constant is observed indicating the relatvely fast dynamics of the API in a biological environment. These results hence illustrate how the solvent electrospun polymer matrix can serve as a kinetic trap for FBZ molecules, perfectly in line with hydrogen bond lifetimes and the long-term stability experiments.

In conclusions, it is shown experimentally that solvent electrospinning is a highly promising formulation technique for the production of nanofibrous FBZ-PEtOx ASDs which enable a significant solubility increase in aqueous media. Combining both experiments with computational simulations, we find that the presence of strong, dominant and stable hydrogen bond interactions between FBZ PEtOx is responsible for an improved physical stability of the ASD with shelf life-times reaching over one year. Furthermore, experiments show that dissolution rates of FBZ in these ASDs are quadrupled compared to the crystalline form where a complete release is achieved within one hour. Additionally it is shown, based on the calculation of self-diffusivity coefficients, that FBZ is succefully kinetically trapped in the PEtOx-matrix by the preparation trough solvent electrospinning. These findings show that the electrospinning technique and the polymeric excipient PEtOx have vital features for the formulation of timestable and high-loaded ASDs increasing the drug-solubility and hence bioavailability via oral administration. It is hence clear that this technique and material show huge potential for other poorly water soluble APIs. Future work will focus on the assesment of the thermodynamics of the drug-polymer formulations by means of molecular dynamics simulations, e.g. using Flory-Huggins theory. This will enable an efficient computational screening approach for the compatibility of other BCS class II and IV APIs, i.e. poorly water-soluble drugs, with PEtOx as a polymer carrier material. Ultimately, the goal is to use computations to guide drug selection and loading optimization for the production of PEtOx-based ASDs.[342,343]

6

Conclusions and perspectives

6.1 Conclusions

In this dissertation molecular modeling was used as a tool to gain fundamental understanding of polymer-based material properties (i.e. drug-delivery application), reaction mechanisms and their corresponding reaction kinetics of reactions situated in the field of polymer science. To this end various methodologies were applied, which give insights into phenomena taking place at various length and time scales. The applications of this work are situated within two main projects, i.e. the BioFactory (Chapter 4) and Poly(2-alkyl-2-oxazolines) (Chapter 5), where we have employed a large toolbox of computational methods, ranging from small to large-scale approaches, to answer the scientific questions at hand, i.e.:

1. We have unraveled the *O*- and *C*-dealkylation for lignin-derived compounds.
2. Clarified the mechanisms of two types of polymerization reactions:
    - a step-copolymerization of CO_2-sourced carbonates with alcohols and thiols
    - The cationic ring-opening polymerization of unsaturated 2-alkyl-2-oxazolines
3. Assessed the drug-behavior and interactions in poly(2-ethyl-2-oxazoline)-based amorphous solid dispersions.

To this end, a multiscale modeling approach was used where typically a combination of DFT and force field-based methods; and a combination of static and molecular dynamics based approaches are used. Depending on the system and the scientific question a trade-off was made between accuracy and computational cost.

Concerning the conversion of lignin-derived compounds, we have investigated the Brønsted acid catalyzed *O*- and *C*-dealkylation in hot-pressurized water of guaiacol and dihydroconiferyl alcohol, respectively. Using static DFT calculations, we found proof that the *C*-dealkylation proceeds through a retro-vinylogous aldol reaction. However the employed solvent model, i.e. a hybrid or explicit solvent model, was highly deterministic for the intermediate stability which indicated that the operating conditions should be accounted for more accurately. This was done using a dynamic approach where the solvent environment was explicitly taken into account. This observation is also true for the *O*-dealkylation of guaiacol.

Therefor the work was extended using an enhanced sampling molecular dynamics approach, which allows to properly account for the complex reaction environment and to describe the energetics of the reaction at operating conditions more accurately. We have furthermore performed a comparative study to investigate the potential of heterogeneous Brønsted acids instead of the corrosive homogeneous ones. Using a microkinetic model we have shown that the *O*-dealkylation mechanism of guaiacol and in extension of lignin-derived monomers, proceeds via a direct S_N2 reaction to catechol for both the homo- and heterogeneous catalyzed system. Additionally we illustrated the potential of zeolites to catalyze this conversion process in hot pressurized water. The more advanced simulation approach provided an in-depth knowledge on the role of water in both catalytic systems revealing a confinement-induced activity increase of water within zeolites resulting in an acceleration of the reaction.

Still within the BioFact project, we moved on to the step-copolymerization of CO_2-sourced α-alkylidene cyclic carbonates with thiols or alcohols, catalyzed by an organocatalyst DBU. Here an in depth-knowledge on the governing mechanism was required to understand the copolymerization features and further enlarge the scope of this new class of polymers. At first instance we performed a preliminary set of DFT calculations, using an implicit solvation model, on a simplified model compound for bis(α-alkylidene carbonate), i.e. 4,4-dimethyl-5-methylene-1,3-dioxolan-2-one which has a reduced complexity with respect to the monomer used in the copolymerization. The preliminary results indicated that reaction with benzylthiol forms the corresponding β-oxothiocarbonate when the reaction is under kinetic control and the tetrasubstituted ethylene carbonate when performed under thermodynamic control. In essence we showed that the reactivity is dictated by the nucleophilic attack on the different electrophilic centers of the cyclic carbonate and the reversibility of the β-oxothiocarbonate formation. In a second stage of this research, when considering the copolymerization with alcohols, alternative

mechanisms were explored and a different dominant pathway for the formation of tetrasubstituted ethylene carbonates was proposed. We found that the formation of tetrasubstituted ethylene carbonates proceeds by the nucleophilic attack of a second alcohol molecule present in the environment on the ketone group of the formed β-oxocarbonate which then induces cyclization. Additionally we showed, by means of molecular dynamics simulations which accounted for the solvent explicitly, that the DBU catalyst is highly deterministic for the intermediate stability through the formation of π-type interactions for the specific case of benzylalcohol (i.e. an aromatic alcohol). It is specifically these interactions which are believed to potentially increase the reaction rates of ring-closure steps for this specific alcohol. Hence, the insights obtained from this mechanistic study on a model compound, helped to rationalize and steer the experimental polymerization outcome for the step-copolymerization of bis(α-alkylidene carbonate)s with dialcohols and dithiols.

Within the BioFact project, a multiscale modeling approach allowed us to gain a through mechanistic understanding of the *O*- and *C*-dealkylation of lignin-derived compounds on the one hand, and of the step-copolymerization of bis-αCC with thiols and (lignin-derived) alcohols, on the other hand. We furthermore provided insights on the catalytic features of the homo-, hetero and organocatalyzed reactions. These results will aid the future rational design of experiments and to steer the polymerization outcome.

With a similar goal in mind, we have also investigated the polymerization features of 2-alkyl-2-oxazolines and their use in ASDs as drug-delivery application. In the latter case we were more specifically interested in the governing interaction and resulting material properties. Regarding the production of PAOxs we have investigated the effect on the CROP kinetics of 2-alkyl-2-oxazolines bearing unsaturations in the sidechain. It was hypothesized based on previous work that these have a rate-enhancing effect because of cation-π interactions. To this end, a combined static and molecular dynamics approach was used, where both trimeric and pentameric systems are used to assess the presence of cation-π interactions and its effect on the polymerization kinetics. Furthermore, both implicit and explicit solvent models were later employed to verify that the conclusion remains valid in the presence of acetonitrile. Based hereon the following trend for the rate constants was anticipated which was later confirmed experimentally: *n*-ButylOx $<$ ButenOx $<$ ButynOx $\geq$ PentynOx, where $<$ refers to a smaller rate constant of the former with respect to the latter. We furthermore showed that this trend originates from a preoganization effect based on cation-π, π-π and π-induced dipole interactions which stabilizes the reactant region and hence influences the association behavior of the attacking monomer and the growing polymeric chain. It is important to stress that the results indicate that the use of trimeric systems suffices to investigate polymerization kinetics and that in case a stabilizing interaction occurs one can not automatically presume that this will affect the intrinsic reaction kinetics. For example here, no net effect was observed on the intrinic reactivity as the stabilizing

interactions dominate both in the reactant and transition state regions.

Concerning potential applications of PAOxs by far the most promising candidate is poly(2-ethyl-2-oxazoline) (PEtOx) which is a hydrophilic polymer that shows great potential for drug-delivery applications. To this end PEtOx-based amorphous solid dispersions are prepared both experimentally and computationally, in order to increase the bioavailability of poorly water soluble active pharmaceutical ingredient (API). In this research flubendazole (FBZ) was used which is a highly effective API against tropic diseases. It was hypothesized that hydrogen bonding between FBZ and the polymer matrix are essential for the physical stability of the ASDs and to achieve high drug loadings. At first instance static calculations are performed to assess the competitiveness between Flubendazole and PEtOx to act as hydrogen bond acceptor. These results indicated that both components of the ASD can benefit from these interactions where it was furthermore found that competition may occur between both of them.

At second instance we devised a computational protocol, using force fields and an equilibration procedure, to set up and equilibrate realistic, large scale amorphous solid dispersions models ($>$ 40000 atoms). The protocol and the generated structures were furthermore subjected to a validation step where the glass-transition temperature was predicted by the computational model. This confirmed that the computational model achieves the desired accuracy for the desired goal. Additionally it was shown, that it was necessary to include a physical aging step to describe the real system more accurately. Finally the generated structures were used to analyze the hydrogen bonding patterns and the flubendazole mobility within the dispersion. It was shown that strong, dominant and stable hydrogen bond interactions are formed between FBZ and PEtOx which are responsible for an improved physical stability of the ASD with shelf life-times reaching over one year. Mobility was furthermore assessed by means of self-diffusivity coefficients which revealed that FBZ is succefully kinetically trapped in the PEtOx-matrix by the preparation through solvent electrospinning.

Apart from the scientific questions answered throughout this thesis, we have set up different protocols and workflows to construct and equilibrate molecular models to describe the chemistry and properties in complex molecular environments. In order to guide future researches in generating these (more) realistic models, we have provided some generic workflows in the appendices. The workflows intend to systematically proceed from small-scaled molecular systems to large scale, more realistic models.

The presented work in this thesis clearly shows the importance of molecular modeling to gain fundamental understanding of reaction mechanisms, - kinetics and applications within the field of polymer science. The cases studied in this thesis show how molecular modeling is progressing to the level where it becomes

indispensible for the rational design and optimization of reactions and materials. This work also shows that a complementary set of techniques is often needed to tackle a scientific question. We have clearly shown that accounting for the solvent with an appropriate solvent model and taking into account operating conditions by performing molecular dynamics simulations are vital for an accurate description of the system. Nonetheless, as shown in this dissertation, a full understanding of the systems behavior often requires the combination of high and low accuracy methods with static and dynamic approaches. Ultimately it is up to the computational chemist to find a balance between computational cost and accuracy to tackle the scientific problem at hand.

6.2 Perspectives

6.2.1 General perspectives

In general, more accurate molecular models yield better insights in the scientific questions at hand and allow to comprehend the governing chemistry in a better way. However, the more accurate methods come with an increased computational cost, e.g. investigating reactivity using an enhanced sampling approach accounting for the solvent explicitly can quickly exceed one month of simulation time, even when sufficient computational resources are available. Within the upcoming years, it is however anticipated that due to the increasing efficiency of software, algorithms and hardware that this burden will be alleviated. However, it needs to be stressed that solely increasing computational power is not sufficient to allow a more realistic representation of the system, also new method developments will be necessary. For example current developments like machine learning potentials, quantum computing, GPU-accelerated codes, parallelization, ... will most certainly play a very important role in the future of computational chemistry.

Furthermore, investigating reactivity using a dynamic approach still has some bottlenecks as lower accuracy methods have to be used (e.g. pure functionals instead of hybrid ones) and reaction coordinates need to be known. During this work, finding optimal reaction coordinates proved to be far from trivial and we hence believe that methodological advances where proper reaction coordinates can be found in a more systematic way, will be of increasing importance in the field of computational chemistry. This might also allow to discover new mechanistic pathways and structures through computations.

Finally, to further progress in the field, collaborative efforts of scientists with various backgrounds, i.e. physicists, chemists, computer scientists, engineers will remain of utmost importance. Many subdisciplines contribute to the field of molecular modeling and hence being an expert for each of these is impossible,

this emphasizes the need to collaborate with experimentalist but also with fellow computational chemists, machine learning experts, computer scientists, ... Finally, as model systems approach real systems closer and closer, interactions with people in the industry might also be very beneficial to get track of practically inspired modeling problems. Already today such interactions are becoming more and more important, and it is foreseen that this synergy might be strenghtened even more in the near future.

6.2.2 Project-related perspectives

Within the scope of the work performed in this thesis, it is interesting to highlight some research opportunities and perspectives specifically for the applications discussed in this thesis. First of all, concerning the Biofactory-related projects, we have highlighted the potential of the combination of hot-pressurized water and Brønsted acids to catalyze the *O*-demethylation (or more general the *O*-dealkylation) of lignin-derived monomers. Hence, this process can -in time- be used to succesfully replace their fossil-fuel based counter parts. Additionally, the introduction of the hydroxyl functionality can be exploited in polymerization reactions which can hence further broaden the scope of the lignin-derived compounds, as was highlighted in **Paper IV**. Besides the *O*-dealkylation we recognize that also when investigating the *C*-dealkylation of lignin-derived monomers the operating conditions should be accounted for more appropriately as was done for the *O*-dealkylation.

For the new class of polycarbonates, on the other hand, the results presented in this thesis can be used to tune the copolymer composition, avoid sidereactions and broaden the scope of αCCs, i.e. by using different comonomers or operating conditions. Also the mechanistic insights can be exploited to engineer new (organo)catalysts which can for example catalyze the formation of tetrasubstituted ethylene carbonates for different alcohols. Furthermore, the methods used for the preparation and simulation of amorphous solid dispersions can ultimately be used to investigate material properties of the materials created with polycarbonates. In this way, computations can for example help in screening the desired copolymer compositions needed to achieve a certain material property or alternatively investigate new potential functionalities or compatible molecules.

The insights obtained for the CROP of unsaturated 2-alkyl-2-oxazolines imply that preorganization, i.e. the association between monomers and growing chainends, is a very important aspect to consider not only in step polymerization but also in specific types of chain polymerization. It can potentially be exploited in copolymerization reactions to generate new oxazoline-based copolymers or to explain the (co)polymerization behavior of unsaturated monomers. However, whether this behavior prevails in copolymerization reactions is not yet known and further research should be conducted to investigate this.

Concerning the amorphous solid dispersions, there is still much work which can be performed. Firstly, we lack automated procedures to parameterize alternative polymer compositions and secondly it would be interesting to interface the generation protocol of the molecular structures more easily with the simulation software. Furthermore, to access the predictive power of these molecular models, (new) methodologies should be implemented to determine drug-compatibility and optimal drug-loadings. These advancements would enable the easy construction of realistic models and allow to assess drug-compatibility in a predictive way. Nonetheless, we show that substantial knowledge can be obtained from regular MD simulation of large realistic polymeric models, knowledge which cannot be obtained with experiments. Hence, these simulations provide a true added-value to experimentalists.

Part II

Published papers

I

Brønsted Acid Catalyzed Tandem Defunctionalization of Biorenewable Ferulic acid and Derivates into Bio-Catechol

Elias Van Den Broeck has performed the computational research in this work.

Reprinted with permission from Jeroen Bomon, Elias Van Den Broeck, Mathias Bal, Yuhe Liao, Sergey Sergeyev, Veronique Van Speybroeck, Bert F. Sels, and Bert U. W. Maes. Brønsted acid catalyzed tandem defunctionalization of biorenewable ferulic acid and derivates into bio-catechol. *Angewandte Chemie International Edition*, 59(8):3063–3068, 2020. doi: 10.1002/anie.201913023.

Green Chemistry

International Edition: DOI: 10.1002/anie.201913023
German Edition: DOI: 10.1002/ange.201913023

Brønsted Acid Catalyzed Tandem Defunctionalization of Biorenewable Ferulic acid and Derivates into Bio-Catechol

*Jeroen Bomon, Elias Van Den Broeck, Mathias Bal, Yuhe Liao, Sergey Sergeyev, Veronique Van Speybroeck, Bert F. Sels, and Bert U. W. Maes**

Abstract: *An efficient conversion of biorenewable ferulic acid into bio-catechol has been developed. The transformation comprises two consecutive defunctionalizations of the substrate, that is, C–O (demethylation) and C–C (de-2-carboxyvinylation) bond cleavage, occurring in one step. The process only requires heating of ferulic acid with HCl (or H_2SO_4) as catalyst in pressurized hot water (250 °C, 50 bar N_2). The versatility is shown on a variety of other (biorenewable) substrates yielding up to 84 % di- (catechol, resorcinol, hydroquinone) and trihydroxybenzenes (pyrogallol, hydroxyquinol), in most cases just requiring simple extraction as work-up.*

With the decline of petroleum feedstock and the necessity to reduce CO_2 emission, society must innovate to discover new, more sustainable means to meet the needs of an ever expanding world population.[1] The manufacture of products based upon (bio)renewable resources is one of the ways to address this.[2] Particularly, (hemi)cellulose derived products have already been investigated intensively and found mature applications in industry.[3] However, these bio-polymers do not contain aromatic moieties, requiring other parts of plant tissue to produce these key entities in chemical industry. BTX, obtained in oil refinery with 60 megatons year^{-1},[4] is the current arene source of the chemical industry. Fractions thereof are transformed into building blocks of higher oxidation state and used in the production of a variety of plastics, rubbers, and other materials.[5] Biorenewables offer the potential to access intermediates toward these building blocks directly in the right oxidation state as a result of high functionality.

One particularly interesting biorenewable aromatic compound is ferulic acid (**1a**), found in plant cell walls covalently linked to (hemi)cellulose and lignin.[6] In most cases, it is obtained as a waste compound of the rice industry, by extraction from rice bran,[7] and therefore readily available on a large scale. Rice bran derived **1a** is used by Solvay to produce vanillin industrially ("Rhovanil Natural") by biocatalysis (fermentation).[8] Interestingly, **1a** contains a 4-substituted catechol moiety as core structure. Catechol (**2**) is a major commodity chemical (40 kilotons year^{-1}) petrochemically mainly produced through hydroxylation of phenol,[5a,d] synthesized from benzene by the cumene Hock process. **2** is used in a wide range of applications (anticorrosion agent, antioxidant, chelating agent, detergent) and as a raw material for pharmaceuticals, pesticides, flavors, fragrances, and polymer synthesis.[5d] "Unlocking" the catechol core from **1a** may be a great opportunity but challenging, given a sequence of two defunctionalization steps, that is, *O*- and *C*-dealkylation, is required. Metabolic pathways in fermentative processes involving such cascade have been described, but complex reaction mixtures were obtained resulting in a difficult isolation of **2**, with a yield less than 9 % and low titer (Scheme 1 a).[9] Bio-catechol manufacturing using such a biological approach may therefore not be favorable from a synthetic point of view.

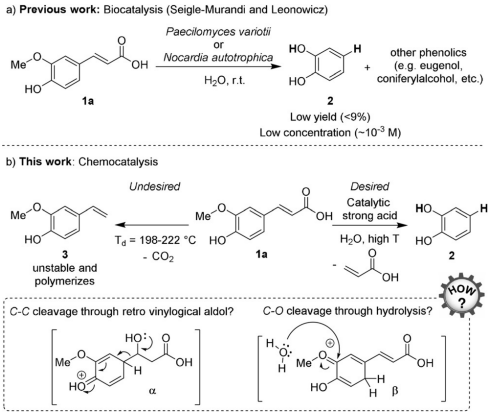

Scheme 1. Transformation of ferulic acid into bio-catechol and proposed key intermediates for *O*- and *C*-dealkylation.

Given the industrial importance of catechol and absence of a one step process utilizing a biorenewable feedstock, a high yielding chemocatalytic pathway from ferulic acid (**1a**) involving practical isolation would be appealing (Scheme 1 b). Use of ferulic acid as a substrate in chemical transformations is a serious synthetic challenge given its thermal instability—neat or in water—causing decarboxylation to 4-vinylguaiacol

[*] J. Bomon, M. Bal, Dr. S. Sergeyev, Prof. Dr. B. U. W. Maes
Organic Synthesis, Department of Chemistry, University of Antwerp
Groenenborgerlaan 171, 2020 Antwerp (Belgium)
E-mail: bert.maes@uantwerpen.be
E. Van Den Broeck, Prof. Dr. V. Van Speybroeck
Center for Molecular Modeling, Ghent University
Technologiepark 46, 9052 Zwijnaarde (Belgium)
Dr. Y. Liao, Prof. Dr. B. F. Sels
Center for Sustainable Catalysis and Engineering, KU Leuven
Celestijnenlaan 200F, 3001 Leuven (Belgium)
Supporting information and the ORCID identification number(s) for the author(s) of this article can be found under:
https://doi.org/10.1002/anie.201913023.

(**3**),[10] an unstable and easily polymerizable styrene derivative.[11] Studies on dealkylation of guaiacol derivatives are scarce since only two reports described the deallylation of eugenol into guaiacol, but unfortunately low yield (about 10%) and selectivity were obtained.[12] Application of these protocols on ferulic acid provided guaiacol below 5% yield (See Supporting Information, Section 3). Therefore, another synthetic approach to efficiently transform **1a** into catechol (**2**) has to be searched for. We reasoned that addition of water into the α,β-unsaturated acid moiety and protonation of the electron-rich arene unit of ferulic acid (**1a**) delivers an intermediate **α** (Scheme 1b), potentially allowing C–C bond cleavage through a retro vinylogical aldol reaction. To the best of our knowledge, such dealkylation reaction is unprecedented. In *O*-demethylation of guaiacols, protonation of the electron-rich arene is supposed to, again, play a key role (intermediate **β**, Scheme 1b). The published *O*-demethylations of guaiacol (**18**) with aqueous strong acids support feasibility.[13,14] Interestingly, the proposed mechanism in our hypothesis suggests *O*- rather than arene protonation as activation mode.[13] The Michael addition, *C*-dealkylation and *O*-demethylation theoretically all require only protons to act as electrophile and water as reactant and can therefore occur in a tandem fashion. These aspects make this novel route attractive from a green chemistry point of view.

Preliminary experiments revealed that heating ferulic acid (**1a**) in water at 250 °C for 3 h with an initial back pressure of 50 bar N_2 led to complete decomposition (Table 1, Entry 1), in line with its known thermal instability at atmospheric pressure.[10] This was also the case with addition of 20 mol%

Table 1: Selected optimization data of the acid catalyzed tandem *O*- and *C*-dealkylation of ferulic acid (**1a**) into catechol (**2**).

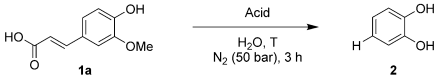

Entry	Conc. [M]	Acid (mol%)	pK_a	T [°C]	**2**[a] [%]
1	0.50	–	–	250	0
2	0.50	HOAc (20)	4.8	250	0
3	0.50	H_3PO_4 (20)	2.2	250	19
4	0.50	H_2SO_4 (20)	−3.0	250	38
5	0.50	HCl (20)	−7.0	250	42
6	0.50	HOTf (20)	−15	250	35
7	**0.13**	**HCl (50)**	**−7.0**	**250**	69 (**70**[b])
8	1.00	HCl (50)	−7.0	250	27 (27[b])
9	0.13	HCl (50)	−7.0	230	25 (36[b])
10	0.13	HCl (50)	−7.0	200	16[c]
11	0.13	HCl (50)	−7.0	175	0
12	0.13	HCl (25)	−7.0	250	43 (49[b])
13	0.13	HCl (50)	−7.0	275	58 (61[b])
14[d]	0.13	HCl (25)	−7.0	275	65 (67[b])
15	0.13	H_2SO_4 (50)	−3.0	250	41 (44[b])
16	0.13	H_2SO_4 (100)	−3.0	250	49 (55[b])

Reaction conditions: amount (0.4–3.0 mmol) **1a** in 3.0 mL H_2O to achieve the given concentration. [a] ^{1}H NMR yield determined with dimethyl sulfone as int. std. For all entries, full conversion of **1a** was observed. [b] Yield of isolated product. [c] Next to **2**, **18** was obtained in 27% yield. [d] Reaction time: 2 h.

HOAc (Entry 2). Interestingly, catechol (**2**) formation was observed (Entries 3–6) when increasing the acid strength (H_3PO_4, H_2SO_4, HCl, HOTf). Unfortunately, a low yield (19–42%) and moderate selectivity were observed in all those cases. HCl was chosen for further optimization, given its abundance and low cost. Moreover, it is recommended based on a green acid selection guide.[15] Optimization revealed the yield of **2** was increased by decreasing the concentration of **1a** (Entries 7, 8) and increasing HCl loading (Entries 7, 12), with, respectively 0.13 M and 50 mol% as optimal parameters. This way, **2** was isolated in 70% yield (Entry 7). Importantly, a high temperature is crucial for selectivity. Decreasing the temperature led to full decomposition of the substrate (Entries 7, 9–11), whereas increasing the temperature (for example to 275 °C) essentially gave the same yield after 2 h, even with half of the amount of acid (Entries 7, 13, 14). For H_2SO_4, the highest yield of **2** (55%) was observed when using a stoichiometric amount of acid (Entries 15, 16). The type of acid and amount are crucial to suppress undesired polymerizations, which could be confirmed by LC-MS. Full optimization can be found in the Supporting Information (Section 4).

The optimal reaction conditions were applied on ferulic acid derivatives (Scheme 2). Caffeic acid (**1b**), isoferulic acid (**1c**), and 3,4-dimethoxycinnamic acid (**1d**) gave catechol (**2**) in a similar yield. Dimethoxycinnamic acid isomers **1e**–**h** delivered the expected dihydroxybenzene, that is, **2**, resorcinol (**4**) or hydroquinone (**5**), in 57–84% yield. No intermediates involving only *O*- or *C*-dealkylation were observed. Remarkably, using 3,5-dimethoxycinnamic acid (**1i**) as substrate did not deliver resorcinol, which was also the case for 3,5-dihydroxycinnamic acid (**1j**). Interestingly, when a hydroxy group was introduced at the 4-position of 3,5-dimethoxycinnamic acid (**1k**), pyrogallol (**6**) was formed in 59% yield. These results show that an *ortho* or *para* relation between one of the methoxy or hydroxy groups and the propenoic acid moiety is crucial to allow *C*-dealkylation.

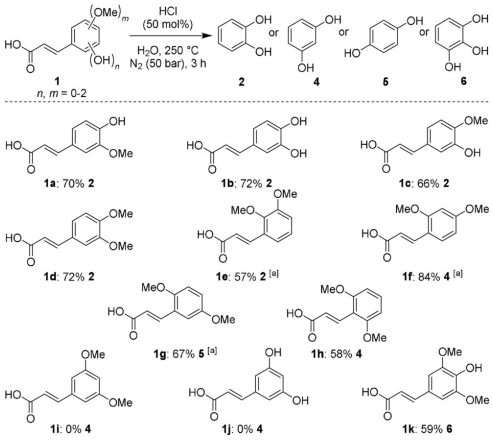

Scheme 2. *O*- and *C*-dealkylation of hydroxylated and/or methoxylated cinnamic acid regioisomers. Yields of isolated products.[a] Reaction time = 4.5 h.

Next, we examined whether other guaiacol derivatives featuring different carbon chains than a propenoic acid on the aromatic ring can be cleaved off (Scheme 3). Esters of ferulic acid reduced the yield of catechol (**2**) with increasing chain length (methyl (**8a**), ethyl (**8b**), and propyl (**8c**) ester), linked to substrate solubility. Chlorogenic acid (**9**), involved in

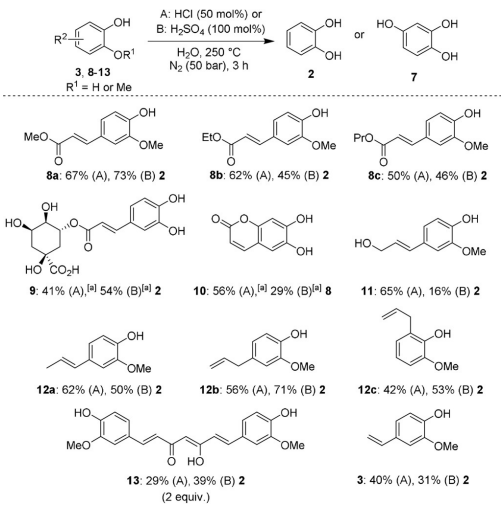

Scheme 3. *O*- and *C*-dealkylation of *C*-substituted catechol and guaiacol derived substrates. Yields of isolated products.[a] Column chromatography.

biosynthesis of lignin,[16] delivered **2** in 41% yield. Lacton esculetin (**10**), the main active ingredient of the traditional Chinese medicine Cortex Fraxini,[17] gave hydroxyquinol (**7**) with a yield of 56%. Other propenyl containing substrates, that is, coniferylalcohol (**11**), isoeugenol (**12a**), eugenol (**12b**), and *ortho*-eugenol (**12c**), also cleaved with the formation of **2** in yields ranging from 42 to 65%. Curcumin (**13**) is a registered food additive (E100) made up of two ferulic acid molecules in its biosynthesis.[18] It contains an α,β- and an α,β,γ,δ-unsaturated carbonyl chain, each connected to a guaiacol unit. Interestingly, our standard conditions also allowed C–C bond cleavage affording **2**. 4-Vinylguaiacol (**3**), the known product for thermal decomposition of **1a**,[10a] was also cleaved into **2**. Therefore, transformation of **1a** in **2** via **3** is also a possible reaction pathway. However, the significant difference in yield of **2** starting from **1a** (70%) and **3** (40%) indicate that this cannot be the only pathway. Moreover, when the reaction was performed under 50 bar of a mixture of CO_2:N_2 (60:40) rather than N_2, a similar yield of **2** (72%) was observed further supporting that decarboxylation is not an important process under our conditions. This points to addition of water into the α,β-unsaturated acid moiety forming intermediate **α** (Scheme 1b) hereby protecting it from decarboxylation into **3**. It is worth mentioning that for all these substrates in Scheme 3 the optimized reaction conditions for the defunctionalization of ferulic acid were applied (Table 1, Entry 7) without any further optimization. Fine tuning of the reaction conditions for individual compounds will further improve the yields. This is exemplified by applying alternative conditions, involving 100 mol% H_2SO_4 (Table 1, Entry 15) which sometimes gave a higher yield (**8a**, **9**, **12b**, **12c**, **13**) (Scheme 3). For all substrates, except **9** and **10**, simple work-up with extraction (no column chromatography) suffice, beneficial for the green credentials of the methodology.[19] Considering temperature was crucial in the transformation of **1a** into **2**, we have selected four other substrates (**3**, **12a**, **12b**, and **13**) to evaluate this effect. At 150 °C, under otherwise optimal reaction conditions, full decomposition of the substrate was observed in all cases, as noted for **1a** (Table 1, Entry 11). No catechol (**2**) could be detected in the crude reaction mixtures.

4-Propylguaiacol (**14**) produced 4-propylcatechol (**16**) in 97%, while unsaturated derivatives eugenol (**12b**) and isoeugenol (**12a**) exclusively gave catechol (**2**) (Scheme 4). Dihydroferulic acid (**15**), featuring a propanoic acid, transformed into dihydrocaffeic acid (**17**) in 82% yield without showing any *C*-defunctionalization, while unsaturated derivative ferulic acid (**1a**) exclusively gave **2** under the same conditions. Unsaturation in the side chain is thus primordial for the *C*-dealkylation.[20,21]

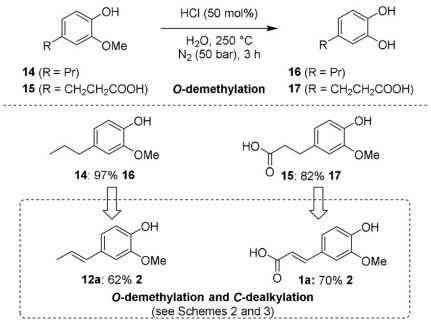

Scheme 4. *O*-demethylation of *C*-substituted guaiacol derivatives.

The proposed mechanism of the *O*- and *C*-dealkylation reaction of guaiacol derivatives is exemplified on ferulic acid (**1a**), isoeugenol (**12a**), and eugenol (**12b**) (Scheme 5). Treatment of the substrate with acid in water leads to the formation of a benzylic alcohol **A** through addition of water to the alkene. The phenolic hydroxy group directs protonation on the carbon atom *ipso* to the alkyl chain. The obtained intermediate **B** then allows C–C bond cleavage through a retro vinylogical aldol reaction, delivering guaiacol (**18**) and aldehyde **19** or **20**. First principle static and dynamic molecular simulations support the proposed *C*-dealkylation (See Supporting Information, Section 7). These calculations also revealed that this cleavage reaction is in competition with proton transfer of unstable intermediate **B** to the solvent, yielding **C**, which can reprotonate. The *O*-demethylation reaction of **18** is initiated by protonation of the arene into **D**.

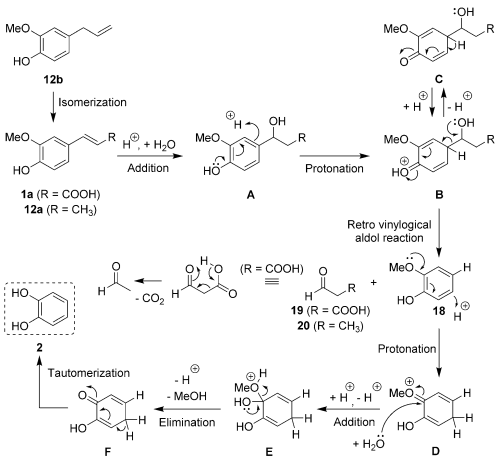

Scheme 5. Proposed mechanism for the *O*- and *C*-dealkylation of ferulic acid (**1a**), isoeugenol (**12a**), and eugenol (**12b**) into catechol (**2**).

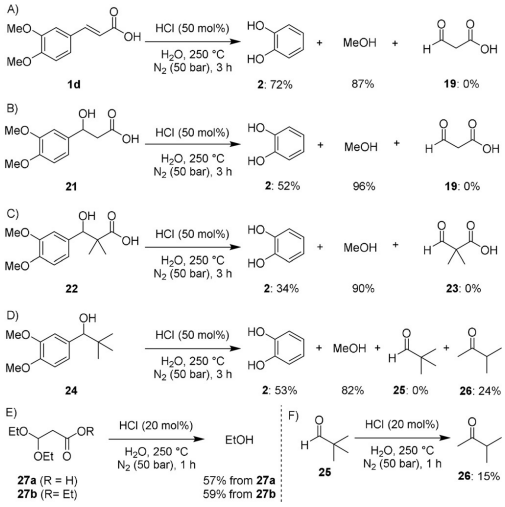

Scheme 6. Supporting experiments for the mechanism in Scheme 5. ^{1}H NMR yields of the crude reaction mixture, measured with suppression of the water signal and with dimethylsulfone as internal standard.

Subsequent addition of water gives hemiacetal **E**, which upon elimination of methanol provides 6-hydroxycylohexa-2,4-dien-1-one (**F**), in which aromaticity is restored through tautomerization to deliver **2**. Intermediates **D**, **E**, and **F** were confirmed by theoretical calculations (See Supporting Information, Section 7). These also indicated *O*-demethylation via S_N2 of water on **D** is not favored. However, accounting for the environment and operating conditions more accurately, by means of advanced molecular dynamics simulations, will further elucidate the nature of the *O*-demethylation mechanism. Demethylation initiated via *C*-arene rather than *O*-protonation is uncommon.[13] *O*- and *C*-dealkylations may also occur in the reverse order.

Model substrates were selected to further support the mechanism experimentally (Scheme 6). This study was performed with different veratrole rather than with guaiacol derivatives. 3,4-Dimethoxycinnamic acid (**1d**) transformed into catechol (**2**, 72%) (Scheme 6A). Gratifyingly, methanol (87%) was also observed in the crude reaction mixture before extraction. Benzylic alcohol **21**, also allowed cleavage into the same reaction products, supporting its potential role as intermediate formed by addition of water on the alkene moiety of **1d** (6B). However, it still remains unclear whether **21** is an intermediate in the *C*-dealkylation reaction mechanism as it can eliminate water into **1d**. Therefore **22** was selected, featuring geminal methyl groups at the β-carbon atom, blocking elimination (6C). This compound also cleaved into catechol and methanol, showing that the benzylic alcohol and not the alkene is indeed crucial in C–C cleavage. In none of the reactions 6A-C, the proposed aldehyde by-product **19** or **23** was observed in the crude reaction mixture. β-Oxopropenoic acids undergo decarboxylation at elevated temperature, leading to the formation of acetaldehyde and isobutyraldehyde which are volatile compounds, furthermore prone to polymerization.[22] This is supported with the complete decomposition of acetals **27** under the reaction conditions (6E), yielding ethanol as the only observable product. To prove the involvement of an aldehyde, another substrate was designed in which the carboxylic acid function was replaced by a methyl group (6D). Gratifyingly, **24** delivered catechol (**2**), methanol and methyl isopropyl ketone (**26**) as reaction products. **26** is a rearrangement product of pivaldehyde (**25**), which was confirmed in an independent reaction (6F).[23]

Realizing that a benzylic alcohol is primordial in the C–C bond cleavage process, we looked into the behavior of lignin model compound **28a**,[24] which contains the most abundant β-*O*-4 bond of lignin (Scheme 7).[2] Under the standard conditions, 33% catechol (**2**) could be detected which increased to 53% when halving the HCl loading. Interestingly, methanol was obtained as by-product from *O*-demethylation. Model compound **28b**, containing a guaiacol and a syringol unit cleaved into **2** (28%) and pyrogallol (**6**) (36%). Literature reports on β-*O*-4 model compound cleavage with mineral acids leads to *C*-substituted guaiacol and syringol derivatives, without removing the whole carbon chain.[25] These proceed via a benzylic cation **29** at α, inducing cleavage into C2 and C3 fragments. Use of H_2SO_4 in water at 150 °C on **28a** for example yielded 23% **18**, 12% ketone **30**, and 3% aldehyde **31**,[23b] while under our conditions at 250 °C 25% **2** and 69% methanol were formed. This remarkable difference observed is due to the protonation of the arene ring, allowing an alternative cleavage from **28**. Similarly, *O*-demethylation is induced by arene protonation, rationalizing why it is not observed in the literature procedures on lignin model compounds.[25] Hot pressurized water is known for its special

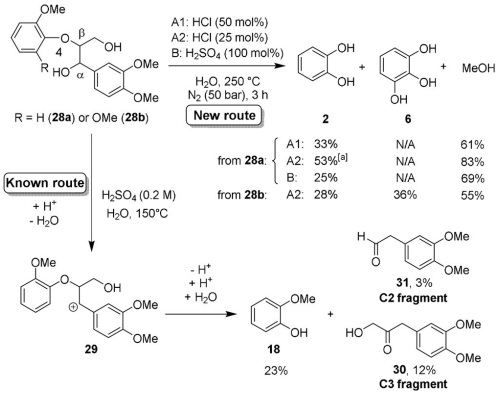

Scheme 7. *O*- and *C*-dealkylation of β-*O*-4 lignin model compounds **28** with mineral acids. ^{1}H NMR yields with dimethyl sulfone as int. std.[a] Yield of the isolated product: 42%.

features, including increased acidity, presumably responsible to access **B** and **D**.[26]

In conclusion, we have developed a novel tandem reaction for the *O*- and *C*-defunctionalization of ferulic acid into biocatechol catalyzed by Brønsted acids in hot pressurized water. The versatility of the method is demonstrated by accessing various dihydroxy- and trihydroxybenzenes from other (natural) substrates, in most cases only requiring simple extraction of the reaction mixture as work-up. A benzylic alcohol (intermediate) proved to be crucial in the *C*-dealkylation reaction. The by-product of *C*-dealkylation is the corresponding aldehyde, while for *O*-demethylation it is methanol. Considering the defunctionalization process involves several reactions, the yields obtained are good. When applying this method on lignin model compounds, featuring the most abundant β-*O*-4 bond of lignin, catechol and pyrogallol were also formed.

Acknowledgements

The authors acknowledge financial support from the Research Foundation Flanders (FWO) (WOG and BioFact Excellence of Science project Grant No. 30902231), UAntwerp (BOF), Research Board of UGent, VLAIO/Catalisti (ARBOREF), the BIO-HarT project (established by a contribution of the European Interreg V Flanders-The Netherlands program that stimulates innovation, sustainable energy, a healthy environment, and the labor market by means of cross-border projects), the Hercules and Francqui Foundation. We thank Dr. M. Smoleń, S. Adriaensen, G. Mollaert, P. Franck, and Prof. F. Lemière for their contribution and Dr. J. Snaet for the design of the cover illustration. The computational resources and services used were provided by UGent (Stevin Supercomputer Infrastructure) and the VSC (Flemish Supercomputer Center) funded by FWO.

Conflict of interest

The authors declare no conflict of interest.

Keywords: green chemistry · *O*-dealkylation · *C*-dealkylation · renewable resources · bond cleavage

How to cite: *Angew. Chem. Int. Ed.* **2020**, *59*, 3063–3068
Angew. Chem. **2020**, *132*, 3087–3092

[1] a) BP p.l.c., "BP Statistical Review of World Energy, 67th edition", **2018**; b) J. Tollefson, *Nature* **2018**, 10.1038/d41586-018-07566-07569.
[2] R. Rinaldi, R. Jastrzebski, M. T. Clough, J. Ralph, M. Kennema, P. C. Bruijnincx, B. M. Weckhuysen, *Angew. Chem. Int. Ed.* **2016**, *55*, 8164; *Angew. Chem.* **2016**, *128*, 8296.
[3] a) A. Shrotri, H. Kobayashi, A. Fukuoka, *Acc. Chem. Res.* **2018**, *51*, 761; b) J. S. Luterbacher, D. Martin Alonso, J. A. Dumesic, *Green Chem.* **2014**, *16*, 4816; c) S. Van de Vyver, J. Geboers, P. A. Jacobs, B. F. Sels, *ChemCatChem* **2011**, *3*, 82.
[4] "BTX Processing": W. A. Sweeney, P. F. Bryan, *Kirk-Othmer Encyclopedia of Chemical Technology*, Wiley, Hoboken, **2008**.
[5] a) GEP, Catechol Faces Supply Crunch While Prices Rise **2018** https://www.gep.com/mind/blog/catechol-faces-supply-crunch-while-prices-rise; b) "Phenol": M. Weber, M. Weber, M. Kleine-Boymann, *Ullmann's Encyclopedia of Industrial Chemistry*, Wiley-VCH, Weinheim, **2004**; c) "Benzene": H. O. Folkins, *Ullmann's Encyclopedia of Industrial Chemistry*, Wiley-VCH, Weinheim, **2000**; d) "Phenol Derivatives": H. Fiege, H.-W. Voges, T. Hamamoto, S. Umemura, T. Iwata, H. Miki, Y. Fujita, H.-J. Buysch, D. Garbe, W. Paulus, *Ullmann's Encyclopedia of Industrial Chemistry*, Wiley-VCH, Weinheim, **2000**.
[6] N. Gopalan, L. V. Rodriguez-Duran, G. Saucedo-Castaneda, K. M. Nampoothiri, *Bioresour. Technol.* **2015**, *193*, 534.
[7] H. T. Truong, M. D. Van, L. D. Huynh, L. T. Nguyen, A. D. Tuan, T. L. X. Thanh, H. D. Phuoc, N. Takenaka, K. Imamura, Y. Maeda, *Appl. Sci.* **2017**, *7*, 796.
[8] a) M. M. Bomgardner, *Chem. Eng. News* **2013**, *49*, 18; b) H. Priefert, J. Rabenhorst, A. Steinbuchel, *Appl. Microbiol. Biotechnol.* **2001**, *56*, 296.
[9] a) E. Malarczyk, J. Rogalski, A. Leonowicz, *Acta Biotechnol.* **1994**, *14*, 235; b) M. Rahouti, F. Seigle-Murandi, R. Steiman, K. E. Eriksson, *Appl. Environ. Microbiol.* **1989**, *55*, 2391.
[10] a) Y. Cheng, Q. Z. Xu, J. Liu, C. S. Zhao, F. M. Xue, Y. Z. Zhao, *J. Braz. Chem. Soc.* **2014**, *25*, 2102; b) W. Fiddler, W. E. Parker, A. E. Wasserman, R. C. Doerr, *J. Agric. Food Chem.* **1967**, *15*, 757.
[11] H. Takeshima, K. Satoh, M. Kamigaito, *Macromolecules* **2017**, *50*, 4206.
[12] a) T. Nimmanwudipong, R. C. Runnebaum, S. E. Ebeler, D. E. Block, B. C. Gates, *Catal. Lett.* **2012**, *142*, 151; b) J. B. Binder, M. J. Gray, J. F. White, Z. C. Zhang, J. E. Holladay, *Biomass Bioenergy* **2009**, *33*, 1122.
[13] For *O*-demethylation of guaiacol derivatives with strong acids, see: a) aq. HBr: E. Blondiaux, J. Bomon, M. Smoleń, N. Kaval, F. Lemière, S. Sergeyev, L. Diels, B. Sels, B. U. W. Maes, *ACS Sustainable Chem. Eng.* **2019**, *7*, 6906; b) aq. HBr: S. Zhao, M. M. Abu-Omar, *Biomacromolecules* **2015**, *16*, 2025; c) aq. HCl and H_2: L. Yang, W. Zhou, K. Seshan, Y. D. Li, *J. Mol. Catal. A* **2013**, *368*, 61.
[14] For other *O*-demethylations of guaiacol derivatives, see: a) Biocatalytic: E. Lanfranchi, M. Trajkovic, K. Barta, J. G. de Vries, D. B. Janssen, *ChemBioChem* **2019**, *20*, 118; b) Biocatalytic: J. E. Farnberger, N. Richter, K. Hiebler, S. Bierbaumer, M. Pickl, W. Skibar, F. Zepeck, W. Kroutil, *Commun. Chem.* **2018**, *1*, 82; c) Al and I_2: J. Tian, H. Yue, P. Yang, D. Sang, *ChemistrySelect* **2019**, *4*,

38; d) AlI_3 and DMSO: J. Tian, D. Sang, X. Tu, Z. He, M. Yao, *Synthesis* **2018**, *51*, 704; e) $AlCl_3$ and NaI: D. Sang, X. Tu, J. Tian, Z. He, M. Yao, *ChemistrySelect* **2018**, *3*, 10103; f) BBr_3: L. Li, D. Qiu, J. Shi, Y. Li, *Org. Lett.* **2016**, *18*, 3726; g) TMSI: H. D. Basavarajappa, B. Lee, H. Lee, R. S. Sulaiman, H. An, C. Magana, M. Shadmand, A. Vayl, G. Rajashekhar, E. Y. Kim, Y. G. Suh, K. Lee, S. Y. Seo, T. W. Corson, *J. Med. Chem.* **2015**, *58*, 5015; h) SIBX: A. Ozanne, L. Pouysegu, D. Depernet, B. Francois, S. Quideau, *Org. Lett.* **2003**, *5*, 2903.

[15] R. K. Henderson, A. P. Hill, A. M. Redman, H. F. Sneddon, *Green Chem.* **2015**, *17*, 945.

[16] W. Boerjan, J. Ralph, M. Baucher, *Annu. Rev. Plant. Biol.* **2003**, *54*, 519.

[17] C. Liang, W. Ju, S. Pei, Y. Tang, Y. Xiao, *Molecules* **2017**, *22*, 387.

[18] P. Oyarce, B. De Meester, F. Fonseca, L. de Vries, G. Goeminne, A. Pallidis, R. De Rycke, Y. Tsuji, Y. Li, S. Van den Bosch, B. Sels, J. Ralph, R. Vanholme, W. Boerjan, *Nat. Plants* **2019**, *5*, 225.

[19] a) E. R. Monteith, P. Mampuys, L. Summerton, J. H. Clark, B. U. W. Maes, C. R. McElroy, *Green Chem.* **2020**, *22*, 123; b) C. R. McElroy, A. Constantinou, L. C. Jones, L. Summerton, J. H. Clark, *Green Chem.* **2015**, *17*, 3111.

[20] For examples of retro Friedel–Crafts reactions of alkylphenols, see: a) Y. Liao, R. Y. Zhong, E. Makshina, M. d'Halluin, Y. van Limbergen, D. Verboekend, B. F. Sels, *ACS Catal.* **2018**, *8*, 7861; b) X. Huang, J. M. Ludenhoff, M. Dirks, X. Ouyang, M. D. Boot, E. J. M. Hensen, *ACS Catal.* **2018**, *8*, 11184; c) Y. Liao, M. d'Halluin, E. Makshina, D. Verboekend, B. F. Sels, *Appl. Catal. B* **2018**, *234*, 117; d) J. Zhang, L. Lombardo, G. Gözaydın, P. J. Dyson, N. Yan, *Chin. J. Catal.* **2018**, *39*, 1445; e) D. Verboekend, Y. Liao, W. Schutyser, B. F. Sels, *Green Chem.* **2016**, *18*, 297; f) T. Sato, T. Adschiri, K. Arai, *J. Anal. Appl. Pyrolysis* **2003**, *70*, 735; g) T. Sato, G. Sekiguchi, M. Saisu, M. Watanabe, T. Adschiri, K. Arai, *Ind. Eng. Chem. Res.* **2002**, *41*, 3124; h) G. A. Olah, G. K. S. Prakash, P. S. Iyer, M. Tashiro, T. Yamato, *J. Org. Chem.* **1987**, *52*, 1881; i) P. Schneider, M. Kraus, V. Bažant, *Collect. Czech. Chem. Commun.* **1962**, *27*, 9; j) P. Schneider, M. Kraus, V. Bažant, *Collect. Czech. Chem. Commun.* **1961**, *26*, 1636.

[21] Next to dealkylation of phenolics, also deacylation has been reported, see: a) T. Patra, S. Manna, D. Maiti, *Angew. Chem. Int. Ed.* **2011**, *50*, 12140; *Angew. Chem.* **2011**, *123*, 12344; b) A. Modak, A. Deb, T. Patra, S. Rana, S. Maity, D. Maiti, *Chem. Commun.* **2012**, *48*, 4253.

[22] "Acetaldehyde": M. Eckert, G. Fleischmann, R. Jira, H. M. Bolt, K. Golka, *Ullmann's Encyclopedia of Industrial Chemistry*, Wiley-VCH, Weinheim, **2006**.

[23] a) G. A. Olah, T. Mathew, A. Goeppert, G. Rasul, G. K. Prakash, P. M. Esteves, *J. Am. Soc. Mass Spectrom.* **2004**, *15*, 959; b) G. A. Olah, T. Mathew, E. R. Marinez, P. M. Esteves, M. Etzkorn, G. Rasul, G. K. S. Prakash, *J. Am. Chem. Soc.* **2001**, *123*, 11556.

[24] J. Buendia, J. Mottweiler, C. Bolm, *Chem. Eur. J.* **2011**, *17*, 13877.

[25] a) C. W. Lahive, P. J. Deuss, C. S. Lancefield, Z. Sun, D. B. Cordes, C. M. Young, F. Tran, A. M. Slawin, J. G. de Vries, P. C. Kamer, N. J. Westwood, K. Barta, *J. Am. Chem. Soc.* **2016**, *138*, 8900; b) M. Scott, P. J. Deuss, J. G. de Vries, M. H. G. Prechtl, K. Barta, *Catal. Sci. Technol.* **2016**, *6*, 1882; c) P. J. Deuss, M. Scott, F. Tran, N. J. Westwood, J. G. de Vries, K. Barta, *J. Am. Chem. Soc.* **2015**, *137*, 7456; d) A. Kaiho, M. Kogo, R. Sakai, K. Saito, T. Watanabe, *Green Chem.* **2015**, *17*, 2780; e) M. R. Sturgeon, S. Kim, K. Lawrence, R. S. Paton, S. C. Chmely, M. Nimlos, T. D. Foust, G. T. Beckham, *ACS Sustain. Chem. Eng.* **2014**, *2*, 472; f) S. Jia, B. J. Cox, X. Guo, Z. C. Zhang, J. G. Ekerdt, *ChemSusChem* **2010**, *3*, 1078; g) U. Westermark, B. Samuelsson, K. Lundquist, *Res. Chem. Intermed.* **1995**, *21*, 343.

[26] a) J. M. Kremsner, C. O. Kappe, *Eur. J. Org. Chem.* **2005**, 3672; b) N. Akiya, P. E. Savage, *Chem. Rev.* **2002**, *102*, 2725.

Manuscript received: October 11, 2019
Revised manuscript received: November 20, 2019
Accepted manuscript online: November 25, 2019
Version of record online: January 21, 2020

II

The concerted *O*-demethylation of guaiacol in hot-pressurized water catalyzed by Brønsted acids

Elias Van Den Broeck, Massimo Bocus, Matthias Bal, Xian Wu, Jeroen Bomon, Louis Vanduyfhuys, Bert Maes, Bert Sels, Veronique Van Speybroeck. *To Be Submitted*

Elias Van Den Broeck has performed the computational research in this work concerning the homogeneous catalyzed reaction and prepared the computational part and introduction of the manuscript.

A concerted mechanism for *O*-demethylation of guaiacol in hot pressurized water catalysed by Brønsted acids

Elias Van Den Broeck*, Massimo Bocus, Mathias Bal, Xian Wu, Jeroen Bomon, Louis Vanduyfhuys, Bert Maes, Bert Sels, Veronique Van Speybroeck*

Abstract

New biorefinery technologies, such as lignin-first approaches, are imperative to the efficiency of next-generation biomass conversion. The development and understanding of experimental benign procedures to establish the conversion of the lignin-derived monomers into drop-in molecules for the chemical industry is an active field of research contributing to the future low-carbon economy with immense market potential. Here, an in-depth mechanistic study for the Brønsted acid catalysed *O*-demethylation of guaiacol, as monomer lignin model compound, in hot pressurized water is reported. A comparative study between the homogeneous (HCl) and heterogeneous (Beta-zeolite) catalysed systems is performed based on operando molecular modelling techniques, which properly account for the molecular environment and solvent dynamics, backed with experimental kinetic data. An activity increase of the hydronium within the Beta-zeolite due to an undercoordination of the hydronium ions, accompanied by an increase in reaction rate, was identified. We furthermore reveal that a direct S_N2 mechanism, as opposed to the more generally accepted stepwise arene or *O*-activation ones, controls the conversion process both under homo- and heterogeneous catalysis in agreement with experimental solvent kinetic isotope measurements. The S_N2 reaction proceeds with formation of an oxonium-water contact pair and in case of the zeolite benefits from a higher water content due to entropic effects, aspects which can be further exploited in future catalyst design. Furthermore, the undercoordinated hydronium ion in the zeolite can interact easier with guaiacol because of a reduced energetic cost needed to bring hydronium close to guaiacol, explaining the increased activity in the heterogeneous environment. Our combined experimental and computational results shed light on the effect of a confined environment on the activity and behaviour of hydronium ions and highlight the potential to use zeolites as environmental-friendly acid catalysts for *O*-demethylation of lignin-derived guaiacols in water.

Introduction

With the sixth major climate assessment report by the IPCC published, it is crystal clear that effective mitigation strategies for climate change are of paramount importance.[1] Hence, a paradigm shift is required to move from a 'take-make-consume-dispose' to a 'take-make-consume-recycle' flow of materials, i.e. switching to circular processes, which is inherently accompanied by a change from fossil carbon resources to renewable (bio-based) ones.[2,3] Lignocellulosic biomass, consisting of a lignin and (hemi)cellulose fraction, shows the potential to fulfil the role as fundamental resource for the construction of next-generation biorefineries, where utilisation of both the lignin and carbohydrate fractions is essential for its economic viability.[4–6] To this end lignin-first methods, e.g. reductive catalytic fractionation, are an important toolbox for the valorisation of biomass by efficiently and selectively exploiting each fractions.[7–9]

Lignin mainly consists of *p*-coumaryl, coniferyl and sinapyl alcohol monomers linked through various C-O and C-C cross-linkages, giving rise to its importance as largest renewable source of aromatics.[10–14] In many model studies, the alkyl substituent of the arene is omitted due to its dependence on the depolymerization method.[6] For this reason, guaiacol is often selected as model compound for the conversion of biomass-derived aromatic substrates.[15] Additionally, guaiacol-containing compounds can be found in all bio-oils derived from grass, softwood and hardwood plants, where it has been extensively used to study general upgrading routes for biomass-derived pyrolysis oils.[16,17] In many cases, one desires to *O*-demethylate guaiacol towards catechol as this is next to phenol, BTX and cyclohexane one of the drop-in molecules with the largest market potential. After all, it is known for a variety of applications such as antioxidant, anticorrosion or chelating agent, as detergent, or as precursor for fine

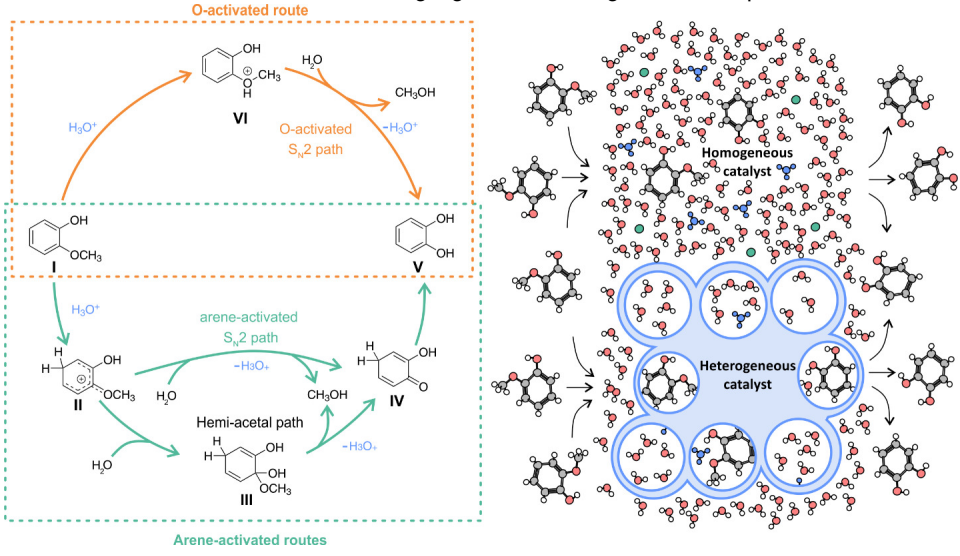

Figure 1. Literature overview and investigated molecular systems. Left) Complete reaction scheme for the *O*-demethylation of guaiacol (**I**) with formation of catechol (**V**). The *O*-activated route is coloured orange. The arene-activated paths are coloured green. Right) A schematic representation of the investigated systems: the homogeneous Brønsted acid catalysed conversion (upper side) and the heterogeneous Brønsted acid catalysed conversion (bottom side), i.e. HCl versus zeolites, both in subcritical water.

chemicals (e.g. pesticides, perfumes and pharmaceuticals) and new (biodegradable) polymeric materials.[6,14,18–24] Besides, *O*-demethylation is often the preferred first step in hydrodeoxygenation (HDO) of lignin-derived phenolics streams given the higher reactivity of catechol for oxygen removal.

For the *O*-demethylation of anisoles, like guaiacol, a variety of synthetic procedures have been reported, typically requiring the use of harsh reaction conditions and (super)stoichiometric amount(s) of hazardous, non-sustainable reagent(s) in undesired solvents producing problematic by-products.[15,25] A sustainable and scalable *O*-demethylation reaction should provide high yield and selectivity, and be performed in a non-toxic and cheap solvent applying a cost-effective and preferably recyclable catalyst.[4,25] To this end, recent studies of our groups have shown the potential and versatility of Brønsted acid catalysts (e.g. hydrochloric acid) in hot pressurized water for selective and high yielding *O*-demethylation.[25–29] Green metrics and cost analysis confirmed favourable features.[25] However, aqueous Brønsted acids at high temperature are corrosive, requiring specific Hastelloy materials increasing CapEx cost.

Heterogeneous Brønsted acids are an interesting alternative to mineral acids. Besides the general advantages of heterogeneous versus homogeneous catalysis they avoid the use of corrosive-resistant materials. Zeolites are crystalline microporous aluminosilicates that - thanks to their exceptional activity, stability and selectivity - have the potential to become the workhorse for the biorefinery of the future as they have been for decades in traditional hydrocarbons conversion.[30] Our groups recently identified Beta-zeolites as suitable catalysts for *O*-demethylation of guaiacol derivatives in hot pressurized water.[31] Interestingly, the presence of water can significantly change the catalytic properties of the zeolite. Indeed, at water concentrations exceeding 2-3 molecules per Brønsted Acid Site (BAS), the latter becomes fully solvated as hydronium ion with remarkable changes in its intrinsic reactivity and chemical interactions with organic substrates.[32–35] However, thus far it remains unclear why hydronium activity is increased for aqueous reactions performed in zeolites. Hereto molecular modelling can provide solace.[35] Reactions conducted with zeolites in subcritical water can present very different features in terms of mechanisms and kinetics with respect to the homogeneous case and, to the best of our knowledge, a thorough comparison between the two cases has been seldomly performed (**Figure 1**, right).[35]

Mechanistically two distinct routes are recognized in the literature for the Brønsted acid-catalysed *O*-demethylation of guaiacol towards catechol, i.e. an *O*- and arene-activated route (see **Figure 1**, left), with the former route being the generally accepted mechanism.[25–29] The *O*-activated route proceeds via the formation of a stable oxonium intermediate (**VI**) through oxygen protonation with subsequent S_N2 reaction. The arene-activation route involving a *C*-protonated intermediate (**II**) was recently proposed by our groups as a potential competing path.[29] However, the actual mechanism may be highly dependent on the operating conditions, necessitating the usage of advanced simulation techniques that properly account for the molecular environment and the dynamics of solvated molecules. Moreover, experimental kinetic data for both homogeneous and heterogeneous catalysis for this reaction are not available. In this paper, we report an in-depth combined computational and experimental study of the homo- and heterogeneously catalysed *O*-demethylation of guaiacol to catechol applying enhanced sampling molecular dynamic simulations and a set of kinetic and mechanistic experiments.[36] Microkinetic modelling is used to obtain insights on the

mechanistic features of the reaction, which result to be in line with the experimental observations. We elucidate the microscopic differences in the hydronium ions behaviour between the homogenous phase and the confined environment of the zeolite, providing unprecedented atomistic insights on its activity differences.

Results and discussion

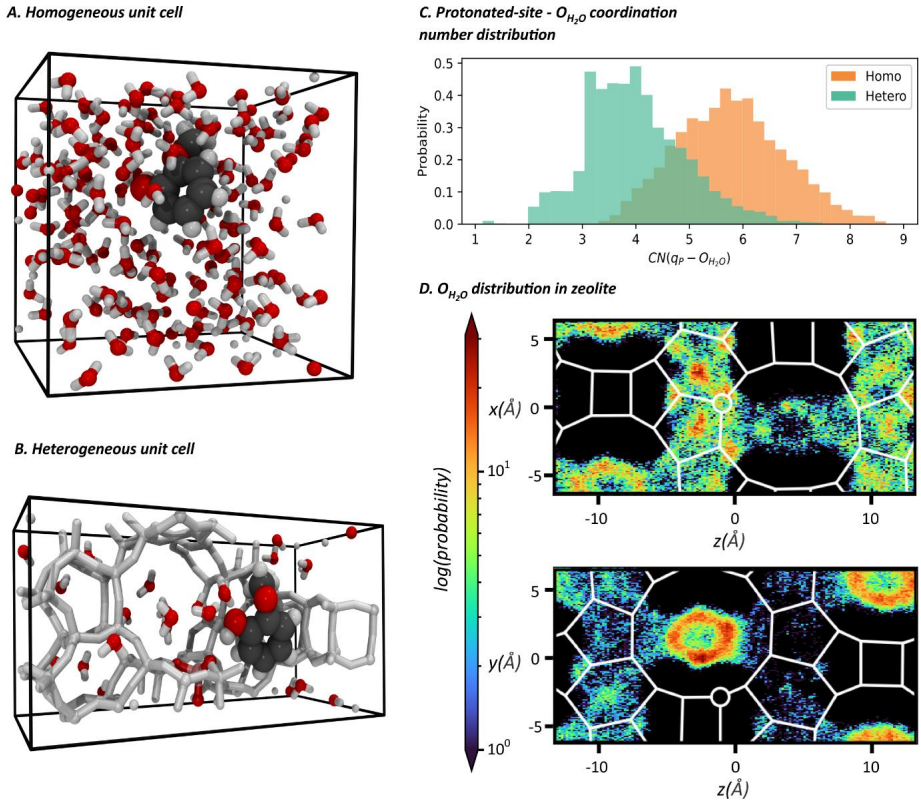

Figure 2. Structural comparison between homo- and heterogenous system. A.) The unit cell of the homogeneous system containing 170 water molecules, 1 hydronium molecule and 1 guaiacol molecule; B.) The beta zeolite unit cell of the heterogeneous system containing 22 water molecules, 1 Al substitution (Si/Al=63) and 1 guaiacol molecule; C.) Probability distribution of the coordination number (r_0=3.6, n=16, m=28) for the protonated-site q_P (based on *ref. 38*) and the water molecules, only Eigen-like structures are accounted for (see ***SI S2.1.1***); D.) Probability for O_{H_2O} within the zeolite framework (white) where the circle represent the Al defect location. (*Level of* theory: BLYP-D3, NVT, see *Methods Section*)

Both the homo- and heterogeneous catalytic systems were investigated by means of periodic *ab initio* molecular dynamics (AIMD) to realistically account for the molecular environment (**Figure 2A** and **B** respectively). More details about the system preparation, can be found in the *Methods Section* and the *Supplementary information (SI, Section **S1.1.1**).*

Structure comparison

Prior to an in-depth discussion of the governing reaction mechanism, the behavior and activity of the hydronium ion is investigated for both catalytic systems. To this end, the proton location was determined based on the definition presented in the work of Ensing *et al.*[37] The hydronium ion is shown to be in an 'Eigen-like cation' state ($[H_3O^+(H_2O)_n]$) around 93% of the time in both systems, while for the remaining ± 7% a 'Zundel cation' state ($[H_2O{\bullet\bullet}H{\bullet\bullet}OH_2]^+$) is observed (see *SI* ***S2.1.1***, **Figure S9B**). In the zeolite, the Brønsted acid sites (BAS) get readily solvated forming the hydronium ion during the simulation, as expected.[38] By tracking its location, it was found that it is relatively mobile along the channel containing the Al substitution, while diffusion in other regions of the unit cell appears to be more difficult (see **Figure S9A** in the *SI*). When examining the coordination of the protonated site (q_p) with respect to H_2O-oxygen atoms (O_{H_2O}), the hydronium ion in the zeolite is shown to be undercoordinated w.r.t. the homogeneous case and hence more active (**Figure 2C**). While in the homogeneously catalysed system the water molecules in the bulk can be fully solvated, the pore channels of molecular dimensions in the zeolite system constrain the water molecules to be in an undercoordinated surface-like state (see **Figure S8**), with the formation of tube-like water structures within the channels of the zeolite, as revealed by the probability distribution of O_{H_2O} within the framework, see **Figure 2D** (and confirmed by the difference in $O_{H_2O} - H_{H_2O}$ and $H_{H_2O} - H_{H_2O}$ radial distribution functions (rdfs), see *SI Section* ***S1.1.1***). A similar phenomenon has been reported by Bukowski *et al.* in the case of Sn-Beta.[39] We hence anticipate a confinement-induced catalytic activity enhancement. Concerning the behaviour of guaiacol in the zeolite system, it's worth highlighting that the hydrophilic portion of guaiacol, *viz*. methoxy and hydroxy moieties, faces towards the water cluster while leaving the aromatic ring occupying the hydrophobic channel, that results poorly accessible to water molecules (**Figure 2B**). This observation, in combination with the $C_{para-site} - O_{H_2O}$ rdfs (highlighting that water does not reside close to *para*-carbon site, see **Figure S7**) indicates that the earlier proposed arene-activated route could be unfavourable in the heterogeneous system. The results obtained from the AIMD simulations of the reacting systems seem then to indicate that the hydronium ions are potentially more active in the heterogeneous case, thereby speeding up proton transfer steps. To quantitatively characterize this, the whole demethylation mechanism was investigated with enhanced sampling simulations, to retrieve the respective rate constants both in the homo- and heterogenous systems.

Kinetic and thermodynamic analysis

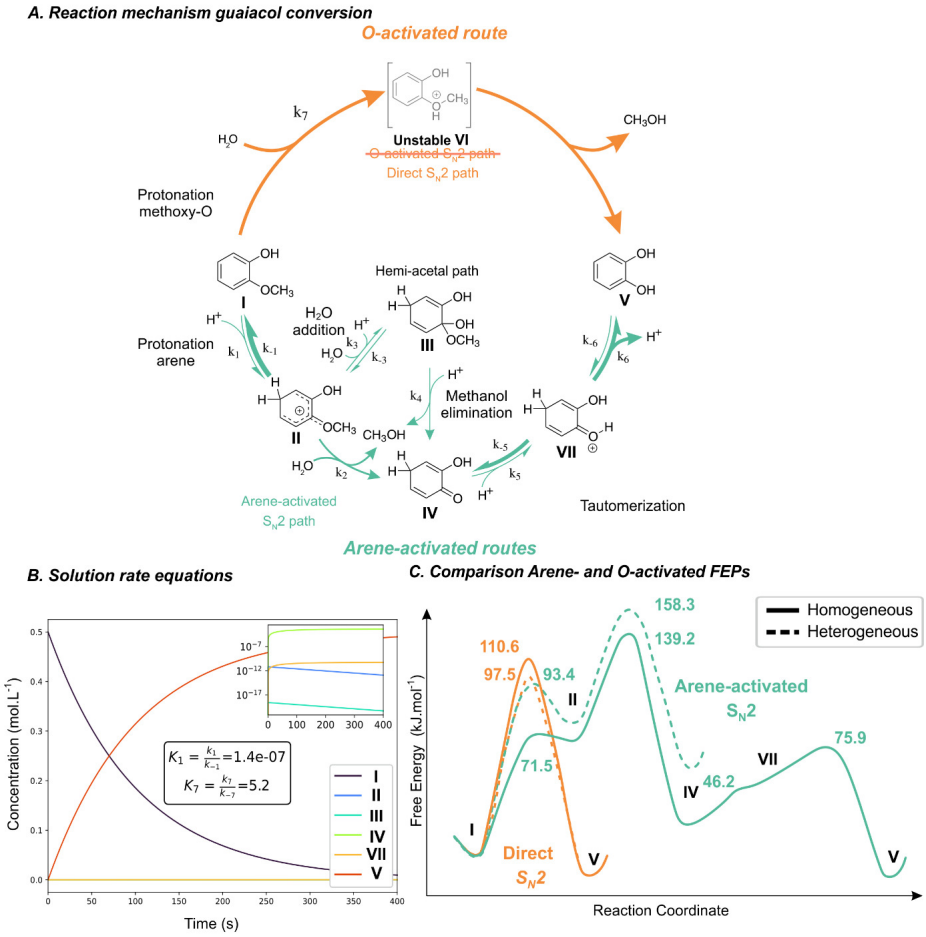

Figure 3. Reaction kinetics for the homogeneously catalysed *O*-demethylation of guaiacol. A) Complete mechanistic overview with intermediates and the corresponding rate constants assuming methanol evaporation, no formation of oxonium intermediate and the stepwise nature of the tautomerization; Thickness of the lines indicates the relative magnitude/importance of the respective steps; H^+ refers to the solvated hydronium ions $[H_3O^+(H_2O)_n]$; B) Solution of the rate equations of the individual steps involved in the paths considered (with the irreversible-step approximation, see Equations 1.1-1.6); C) Schematic representation of the combined free energy profile (FEP) for the arene-activated route and the FEP for the O-activated route for both the homogeneous and the heterogeneously catalysed system. Apparent barrier heights are shown, calculated based on phenomenological barrier heights for the arene-activated SN2 (green) and (O-activated) direct SN2 (orange). Note that the formation of the hemi-acetal (**III**) is omitted due to its irrelevance to the overall reaction and the *O*-activated SN2 is omitted because formation of **VI** is not observed. (*Level of* theory: BLYP-D3, NVT, see *Methods Section*)

To investigate the relative relevance of the routes presented in **Figure 1Error! Reference source not found.**, a series of enhanced sampling molecular dynamics (MD) simulations have been performed through a combination of well-tempered

Metadynamics and Umbrella sampling (see *Methods Section*). For a full overview of the computational results the reader is referred to the *SI Section* ***S2.1.2*** where each individual path is discussed in detail. All steps involving methanol formation are assumed to be irreversible (i.e. $k_{-2} = k_{-4} = k_{-7} = 0$) due to the much higher concentration of water (solvent) disfavouring the backward reactions and the high volatility of methanol, that makes it easier to escape the reactive solution. Due to the inability to locate stable oxonium species **VI** (as will be discussed in detail below, see **Figure 4**), the *O*-activated S_N2 path can be excluded from **Figure 1Error! Reference source not found.**. Instead, a concerted mechanism is found, i.e. a direct S_N2 path, in contrast to what was previously reported in literature.[25–29] **Figure 3** summarizes all the possible reaction paths for which kinetic and thermodynamic data were computed. A summary of the phenomenological barriers and the reaction rates for each elementary step is shown in **Table 1**, where the StepID label is introduced to identify the rate constants, the reactants and the products depicted in **Figure 3A.**

StepID	Catalyst		Rate constant *k* [s^{-1}]		K [$k_{forward}/k_{backward}$]	Phenomenological barrier ΔF [kJ·mol^{-1}]	
	Homo	Hetero	Forward	Backward		Forward	Backward
1 (**I → II**)	x		$7.9 \times 10^5 \pm 0.4 \times 10^5$	$5.8 \times 10^{11} \pm 0.2 \times 10^{11}$	**1.4×10^{-7}**	71.5 ± 0.2	2.7 ± 0.2
		x	$5.2 \times 10^3 \pm 0.4 \times 10^3$	$2.3 \times 10^{11} \pm 0.1 \times 10^{11}$	**2.3×10^{-8}**	93.4 ± 0.3	16.7 ± 0.2
2 (**II → IV**)	x		$1.01 \times 10^6 \pm 0.04 \times 10^6$	$4.9 \times 10^2 \pm 0.2 \times 10^2$	2.2×10^3	70.4 ± 0.2	103.6 ± 0.2
		x	$7.8 \times 10^4 \pm 0.5 \times 10^4$	$5.2 \times 10^3 \pm 0.3 \times 10^3$	1.5×10^1	81.6 ± 0.3	93.3 ± 0.3
3 (**II → III**)	x		$2.83 \times 10^4 \pm 0.08 \times 10^4$	$6.8 \times 10^{11} \pm 0.2 \times 10^{11}$	4.1×10^{-8}	86.0 ± 0.1	12.1 ± 0.1
		x	$8.3 \times 10^1 \pm 0.5 \times 10^1$	$6.2 \times 10^{11} \pm 0.2 \times 10^{11}$	1.3×10^{-10}	111.4 ± 0.3	12.5 ± 0.2
4 (**III → IV**)	x		$1.2 \times 10^{12} \pm 0.05 \times 10^{12}$	$7.6 \times 10^1 \pm 0.3 \times 10^1$	1.6×10^{10}	9.4 ± 0.2	111.7 ± 0.2
		-	-	-	-	-	-
5 (**IV → VII**)	x		$9.5 \times 10^{11} \pm 0.4 \times 10^{11}$	$7.4 \times 10^{14} \pm 0.3 \times 10^{14}$	1.3×10^{-3}	10.6 ± 0.2	-18.3 ± 0.2
		-	-	-	-	-	-
6 (**VII → V**)	x		$7.9 \times 10^{11} \pm 0.9 \times 10^{11}$	$8.8 \times 10^5 \pm 1.0 \times 10^5$	9.0×10^5	11.4 ± 0.5	71.0 ± 0.5
		-	-	-	-	-	-
7 (**I → V**)	x		$9.9 \times 10^1 \pm 0.3 \times 10^1$	$1.92 \times 10^1 \pm 0.06 \times 10^1$	**5.2×10^0**	110.6 ± 0.1	117.7 ± 0.1
		x	$2.0 \times 10^3 \pm 0.1 \times 10^3$	$2.3 \times 10^2 \pm 0.2 \times 10^2$	**8.7×10^0**	97.5 ± 0.3	106.8 ± 0.3

Based on the assumption that each elementary step follows first order kinetics w.r.t. each of the reactant, the set of differential equations S1.1-S1.6 (*Section* ***S2.1.2***) is extracted and solved with the concentration versus time plot presented in **Figure 3B**. The corresponding phenomenological barriers for each elementary step are shown in **Figure 3C.**

The results show that the preferred reaction path is the (*O*-activated) direct S_N2 reaction, with a phenomenological barrier of 110.6 and 97.5 kJ·mol^{-1} for the homo- and heterogeneous system respectively (**Figure 3C**), starting from guaiacol with protonation of the methoxy group and simultaneous elimination of methanol by a nucleophilic attack of water (*vide infra*). This is furthermore in line with the first-order kinetics for the Brønsted acid in both the homo- and heterogeneous case. Interestingly, in line with the work by Lercher *et al*., near zero-order kinetics for guaiacol are obtained in the heterogeneous case whereas a first-order is noticed in the homogeneous case. This can be attributed to a selective adsorption of guaiacol in the zeolite, leading to an intra-pore concentration which is almost independent of the concentration in solution.[38] For the heterogeneous system, the aforementioned increase in proton activity benefits the reaction rate significantly increasing by a factor 20 as reflected in a lower phenomenological barrier (StepID 7, **Table 1**). This observation is in qualitative agreement with experiments, where an increase in turn-over frequency (TOF) of a factor 42 is noted for the heterogeneous catalysed system with respect to the homogeneous one (*Section* ***S2.3.1.4***). For the heterogenous case, a variation of ± 5 water molecules per unit cell was also considered, to evaluate the loading impact on the computed kinetics (see ***SI* S2.1.3**). The results indicate that an increase in water loading has a strong beneficial effect on the reaction kinetics (i.e. phenomenological barriers of 111.1, 97.5 and 90.7 kJ·mol^{-1} are obtained for 17, 22 and 27 H_2O/unit cell), and *vice versa*, which is largely attributed to entropically driven effects and not because of a change in intrinsic hydronium activity.

Although it is negligible in the formation of catechol, it is worth noting that within the homogeneous arene-activated route the protonation step (StepID 1) followed by an S_N2 mechanism (StepID 2) dominates, instead of the previously reported hemiacetal mechanism (StepID 3).[29] This illustrates two essential features: (i) accounting for an explicit solvent environment is indeed of paramount importance to account for entropic effects and thus describe the reaction kinetics and the corresponding mechanism correctly; (ii) The continuous (de)protonation channel of guaiacol ($K_{1,Homo} = 1.4 \times 10^{-7}$ and $K_{1,Hetero} = 2.3 \times 10^{-8}$) is a competitive pathway though not contributing significantly to the formation of catechol in this process.

To support these mechanistic findings, a series of experiments was performed for the homogeneous catalysed system to verify the S_N character of the reaction on the one hand and the occurrence of arene protonation on the other (see *Section* **S2.2.1**). When 2-phenoxyphenol is used instead of guaiacol, no conversion towards catechol occurred and the reactant was recovered, in agreement with a S_N2 mechanism. Furthermore, when the reaction is conducted in deuterated water, ^{1}H NMR signals of the arene disappeared during the reaction (without dearylation occurring) which showed that arene protonation is indeed occurring in a reversible fashion as predicted by $K_{1,Homo}$ (see *SI Section* ***S2.2.1.2***).

Mechanistic details on the (*O*-activated) direct S_N2 path

Following the theoretical analysis mechanistic features are further extracted from the simulations by investigating the free energy landscape in terms of important collective variables. This is done using a procedure based on conditional probabilities (*SI Section* ***S2.1***) which allows to investigate how guaiacol and its reactive environment evolve during the reaction. Two of the resulting free energy profiles are shown in **Figure 4C**

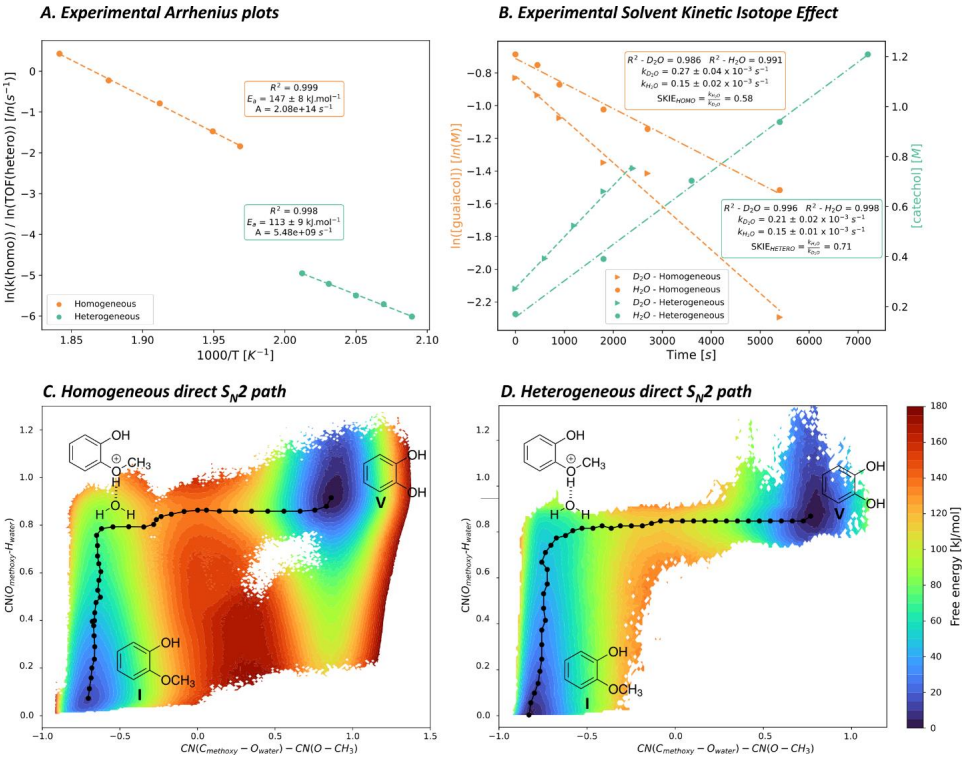

Figure 4. Results kinetic experiments and mechanistic insights. A.) Experimental Arrhenius plots for the homogeneously (orange, HCl) and heterogeneously (green, Beta-zeolite) catalysed *O*-demethylation of guaiacol in hot pressurized water.; B.) Experimental reaction progress plots in H_2O and D_2O to determine the solvent kinetic isotope effect (SKIE); C.) Two dimensional free energy surface (i.e. 2D extension of the 1D profile) for the *O*-activated concerted S_N2 path of the homogeneously catalysed *O*-demethylation of guaiacol, the minimal free energy path is shown by the dotted line; D.) Two dimensional free energy surface for the *O*-activated concerted S_N2 path of the heterogeneously catalysed *O*-demethylation of guaiacol, the minimal free energy path is shown by the dotted line. Activation energies and rate constants are reported with 95% confidence intervals ($\pm\, t_{1-\frac{\alpha}{2}n-2}.error_{std}$), the confidence intervals for the pre-exponential factor are significantly lower and hence not reported. CN = Coordination number.

and **D** (for a more extensive overview the reader is referred to the *SI)*. Furthermore, to support and validate the computational results, kinetic experiments were performed for both the homogeneous and heterogeneous case (see *SI Section **S2.2.2.4** and **S2.3.1.3***) to determine activation energies (based on Arrhenius plots) and the solvent kinetic isotope effect (SKIE). The latter is used to investigate the proton transfer mechanism in the rate-limiting step and thus verify the computational findings. The experimental results on the Arrhenius plots are presented in **Figure 4A**. Activation energies of 147 ± 8 kJ·mol^{-1} and 113 ± 9 kJ·mol^{-1} were obtained for the homo- and heterogeneous case respectively, which show in accordance to the computations that the heterogeneously catalysed reaction is energetically favoured.

The experimentally determined solvent kinetic isotope effects are presented in **Figure 4B**. A reverse SKIE of ~0.6 and ~0.7 was measured in the homo- and heterogeneous systems respectively. When considering the direct S_N2 mechanism, it is then of

paramount importance to analyse the progress of the proton transfers within the reaction in order to understand these rather unexpected experimental observations. To this end, the evolution of the $O_{methoxy}$ protonation state during the reaction is determined. The final results are shown in **Figure 4C** and **D** for the homogeneous and heterogeneous case, respectively. The minimal free energy path (MFEP) for each system is extracted by means of MEPSA.[40] Reactions in which the solvent acts both as solvent and reactant, are prone to both primary and secondary KIE and hence the observed SKIE values include the net effect of both:

$$\left(\frac{k_H}{k_D}\right)_{obs} = \left(\frac{k_H}{k_D}\right)_{sec} \left(\frac{k_H}{k_D}\right)_{pri}$$

The direct S_N2 reaction proceeds through the formation of an unstable oxonium species ($CH_3O_{methoxy} - H_{H_2O/D_2O}$) followed by the cleavage of the $CH_3 - O_{methoxy}$ bond and formation of the $CH_3 - O_{H_2O/D_2O}$ bond (see **Figure 4C** and **D**). Following the MFEP, the transition state (TS) is reached at $CN(C_{methoxy} - O_{water}) - CN(O_{methoxy} - C_{methoxy}) \approx 0.0$ (i.e. the reaction coordinate with each $CN \approx 0.45$) and $CN(O_{methoxy} - H_{water}) \approx 0.8$ (where CN stands for the coordination number, O_{water} represents all aqueous oxygen atoms, $C_{methoxy}$ and $O_{methoxy}$ the methoxy carbon and oxygen atom, respectively). This reflects that the proton transfer to $O_{methoxy}$ is already complete in the TS. Based on the work by Melander[41] and Bigeleisen[42] primary kinetic isotope effects will in this case be close to unity or even inverse $\left(\frac{k_H}{k_D}\right)_{pri} \lesssim 1$. Furthermore the work by Kresge *et al.* indicates that secondary KIE for non-reacting hydrogen atoms are strongly inverse.[43] Values of $\left(\frac{k_H}{k_D}\right) = 0.6$ for the protonation by hydronium where one of the protons is transferred and the two others remain non-reactive, have been reported.[43] For the direct S_N2 mechanism we are thus interested in the protonation state of the attacking water molecule (i.e. the water molecule attacking the *O*-methyl group). The results indicate that in both catalytic systems a neutral water molecule attacks, nucleophilically through the *O*-atom, and only deprotonates when the TS reaches the product state (**Figure S17C** and **D**). Hence, similar to Kresge's work, two non-reacting hydrogen atoms, i.e. the hydrogens of the attacking water molecule, influence the KIE and an inverse secondary SKIE is expected.[43] Combining this with the observation of a complete proton transfer in the TS, $\left(\frac{k_H}{k_D}\right)_{pri}$, the computational results align perfectly with the experimental SKIE results (**Figure 4B**), strengthening the validity of the proposed reaction mechanism.

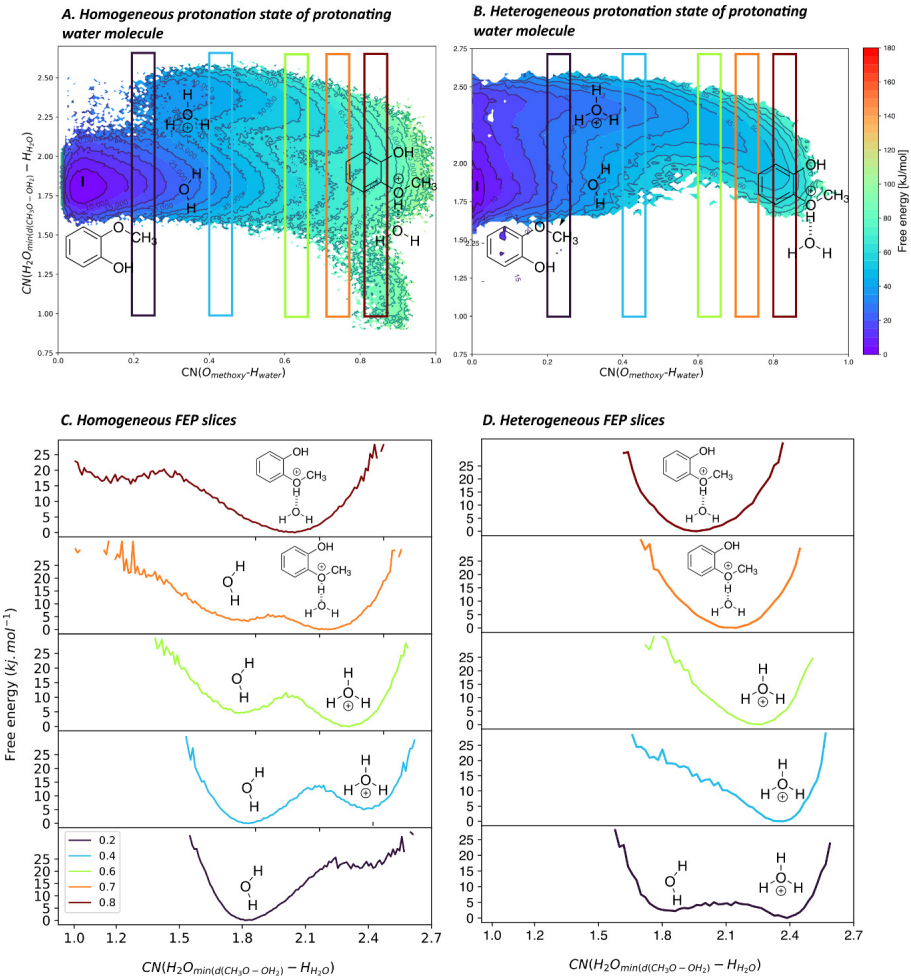

Figure 5. Protonation state of protonating water molecule. Neutral water corresponds to CN = 1.8, hydronium to CN=2.7. A.) protonation state of the water molecule closest to $O_{methoxy}$ in the homogeneously catalysed system. Slices shown in C are highlighted in the respective colors. B.) protonation state of the water molecule closest to $O_{methoxy}$ in the heterogeneous catalysed system. Slices shown in D are highlighted in the respective colors. C.) FEP of water protonation state along the collective variable describing the methoxy protonation for the homogeneously catalysed system. D.) FEP of water protonation state along the collective variable describing the methoxy protonation. Each of the profiles is constructed by cropping the respective regions from the profile shown in A and B and subsequently projecting it on the desired collective variable.

In contrast to mechanisms reported in literature, the completed proton transfer shows no stable oxonium species when correctly accounting for solvent and temperature effects.[26–28] An oxonium-water contact-pair is present instead when approaching the reaction TS, as highlighted in the structures shown in **Figure 4C** and **D**. The protonation state of the donating water molecule during the protonation of $O_{methoxy}$,

changes significantly in the homogeneous case (see **Figure *5*A** and **C,** *Section* **S2.1.2.2**). It shifts from states in which a water molecule is the dominating protonating species to states where an hydronium ion takes over ending with the (unstable) oxonium intermediate, which is in close contact to a water molecule, forming an oxonium-water contact pair. Hence, once the transfer is initiated, the proton is shuttled from within the environment towards the reactive centre. The zeolite-catalysed system rather prefers a close proximity of a hydronium ion in contrast to the observed equilibrium-shift for the homogeneous case, which is hence the main actor in the protonation process, irrespective (and similar to the homogeneous case) of the fact that an oxonium-water contact pair is formed before proceeding to catechol (see **Figure 5B** and **D**). Hence, in the zeolite the interaction between the hydronium ion and guaiacol is enhanced with respect to the homogeneous environment, because the structuring of water in the pores does not allow it to become fully solvated. The lack of a full solvation sphere, reflected in the undercoordination of the hydronium ion in the zeolite (**Figure 2C**), reduces the extra energetic penalty required to bring the hydronium ion in contact with guaiacol, explaining the increased activity. These results are furthermore strengthened by the homogeneous catalysed experiments performed using guaiacol derivatives which show an increase in reaction rate when bearing more electron rich alkyl groups, i.e. ethyl or cyclohexyl instead of methyl (*Section* ***S2.2.1.2***). Hence, based on the computational results this effect is established because of an increased electron density of the $O_{methoxy}$, due to an increased inductive effect of the sidechain, which would enable more stable oxonium-water contact-pairs and thus an overall increase in conversion rate. It is worth highlighting that the governing mechanism is hence following neither *general* nor *specific acid catalysis*, instead protonation has completed before reaching the transition state (TS) despite occurring in the rate-limiting step (at operating conditions).

Conclusion

A combined computational and experimental study investigating the mechanistic features of hetero- and homogeneously Brønsted acid catalysed *O*-demethylation of guaiacol in hot pressurized water, is presented. Enhanced sampling molecular dynamics simulations are performed at operating conditions to fully account for the essential impact of the molecular environment and the dynamics of water (molecules). The homogeneous system (i.e. aq. HCl) is thoroughly compared with the heterogeneous case (i.e. Beta-zeolite). First, a structural analysis of water reveals a confinement-induced activity increase of the hydronium ion inside the zeolite framework due to its undercoordinated surface-like occurrence, not observed in the homogeneous case. This is translated into the formation of tube-like water structures within the zeolite channels, where all water molecules are exposed to the hydrophobic surface of the zeolite and hence occur very differently from the highly solvated conditions in bulk water. Second, a complete solution of the proposed reaction network shows that *O*-demethylation proceeds via a direct S_N2 mechanism regardless of the used Brønsted acid catalyst. However, the higher proton activity in the zeolite beneficially influences its reaction rate. Additionally we show that the catalysed reaction can benefit from a high water content in the zeolite. The mechanism excludes formation of a stable oxonium-intermediate, in contrast to earlier suggestions, and an elusive oxonium-water contact pair is observed instead, which is key for further concerted conversion towards catechol.[26–28] This is furthermore in contrast to the mechanisms typically reported for *general* or *specific acid catalysis*. Formation of such oxonium-water contact pair corroborates ‘fast’ proton transfer, already complete at the

transition state. In combination with a neutral water molecule attacking the methoxy moiety, an inverse SKIE is predicted based on the mechanism and confirmed experimentally for both the homogeneous and heterogeneous case. During formation of the contact pair, the interaction between the hydronium ion and guaiacol is enhanced in the zeolite because the accompanied energetic cost to bring the undercoordinated hydronium in close proximity is reduced thus increasing its activity w.r.t. the homogeneous environment. Hence we have exposed the mechanistic characteristics for the *O*-demethylation of guaiacol in both heterogeneous and homogeneous catalytic environments, clearly emphasizing the critical differences in hydronium ion activity between the two systems. Additionally, the observation of an oxonium-water contact-pair in the rate-determining step and the role of water content in the zeolite can be used in future rational design of catalysts for other BAS-catalysed reactions in presence of water such as (de)hydrations and hydrolysis. Overall, the presented work highlights the potential of heterogeneous catalysis at subcritical aqueous conditions as these catalysts can significantly accelerate the reaction rate due to a higher intrinsic activity of the active site, while being inherently more sustainable. Seeking for more stable catalytic systems under such conditions, e.g. for biomass conversion as done recently, is thus worthwhile continuing.[44,45]

Methods

The simulation unit cells of both investigated systems are shown in **Figure 2A** and **B.** The homogeneous system accounts for two solvation layers (171 water molecules), whereas the amount of solvent molecules in the heterogeneous system was determined from grand canonical Monte Carlo (MC) simulations (22 water molecules, see **SI S1.1.1**). Each of the systems accounts for a single active site, i.e. 1 excess proton. Remark however that when exposed to hot pressurized water, zeolites are known to undergo (reversible) bond breaking in the framework, with the creation of defects such as framework-associated and extra-framework aluminium providing other challenges.[46] The development of zeolite catalysts able to withstand harsh conditions in water is an important active field of research on its own.[46] System preparation and equilibration was performed using a combination of classical molecular dynamics simulations with in-house developed force fields for the solutes and *ab initio* MD simulations at the Density Functional Theory (DFT) level in the appropriate thermodynamic ensembles.

For the homogeneous catalysed system initial system configurations are prepared by means of molecular mechanics simulations in the *isobaric-isothermal (NPT)* ensemble, whereas the heterogeneous catalysed system is prepared by means of MC/MD simulations, i.e. a combination of grand canonical Monte Carlo and molecular dynamics. The details for the system preparation can be found in the *SI.*

Subsequently, AIMD simulations are performed in the canonical ensemble by means of CP2K 5.1 with a unit cell measuring 18.7 Å x 18.7 Å x 18.7 Å and 12.7 Å x 12.7 Å x 26.7 Å (angles = 90°) for the homogeneous and heterogeneous catalysed systems respectively.[47] The BLYP-D3 functional is chosen in combination with the TZVP-GTH basis set as the level of theory.[48–51] The Nosé-hoover thermostat is used for temperature control (523 K) in combination with a timestep of 0.5 fs for the integration of the equations of motion.[52,53] The convergence criterion for the self-consistent field method is fixed at 10^{-5} Hartree. Prior to the Advanced MD simulations, systems were

equilibrated by means of regular MD.[29] Here the equilibrated structures are used to investigate the intrinsic reactivity at operating conditions. All advanced AIMD simulations are performed by means of PLUMED which is interfaced with CP2K as MD engine.[54]

In this study a 2-step AIMD approach is used to obtain a converged free energy profile (FEP), combining the speed of well-tempered multiple walker metadynamics (w-t MTD) for an efficient reaction coordinate screening and the accuracy of umbrella sampling (US) to obtain a final qualitative and quantitative estimate of the free energy surface.[54–58] The methodology is benchmarked with respect to previous work by some of the authors and a more elaborate discussion on the applied approach is given in the Appendix of the *SI*.

w-t MTD is performed using 4 to 8 walkers, a bias factor of 10-12, an initial hill height of 2 to 4 kJ·mol^{-1} and a hill width σ of 0.03. Remark that the choice of these settings is guided by our previous static DFT results.[29] The deposition rate and walkers stride was set to 100 steps, i.e. every 50 fs a hill is deposited and every 50 fs the hill deposition files are flushed. The sum_hills utility of PLUMED is used during post-processing for the construction of the FEP.

US simulations are performed to obtain an accurate estimate of the real FEP employing a harmonic bias potentials centred around the equilibrium value q_0:

$$U_b(q) = \frac{\kappa}{2}(q - q_0)^2$$

With κ the force constant typically amounting to 250 kJ·mol^{-1}. For each reaction step 'umbrellas' are positioned along the reaction coordinate with a typical increment of 0.1. For each of these umbrellas a biased MD simulation is performed, i.e. biased using an harmonic potential and a potential equal to the inverse of the 'crude' FEP. In some cases, extra umbrellas were added or force constants were increased to improve the sampling and hence the final free energy profile, e.g. a force constant of 2000 kJ·mol^{-1} is needed to sample the transition state of a (de)protonation transition state. Subsequent construction of the FEP is performed by means of the weighted histogram analysis method (WHAM) accounting for both the harmonic and additional bias (originating from the w-t MTD simulations).[59–61] For certain reaction steps the two dimensional (2D) variant is used, i.e. instead of using a single reaction coordinate two collective variables are used to describe the desired transformation. In this case 2D harmonic potentials and a 2D-wham analysis are employed. Subsequent error estimates are extracted by a bootstrapping procedure with replacement of the sampled CV-space, in total 1000 samples are generated. Mechanistic features for each elementary reaction step are extracted by means of free energy transformations using the ThermoLIB python package, for more details the reader is referred to the SI.[61]

Acknowledgements

The authors acknowledge financial support from the Research Foundation Flanders (FWO) (BioFact Excellence of Science project Grant No. 30902231). The computational resources and services used were provided by Ghent University (Stevin Supercomputer Infrastructure), the VSC (Flemish Supercomputer Center), funded by Ghent University, the Research Foundation - Flanders (FWO) and the Flemish Government. E.V.D.B, M.B., L.V. and V.V.S acknowledge funding from the fund for scientific research Flanders. V.V.S. and L.V. acknowledge the Research Board of the

Ghent University. B.U.W.M. thanks the Francqui Foundation for an appointment as Collen-Francqui professor and UAntwerp for BOF GOA support. We thank Goeminne R. for his assistance with the GCMC simulations.

References

(1) IPCC; Masson-Delmotte, V.; Zhai, P.; Pirani, A.; Connors, S. L.; Péan, C.; Berger, S.; Caud, N.; Chen, Y.; Goldfarb, L.; et al. *Climate Change 2021: The Physical Science Basis. Contribution of Working Group I to the Sixth Assessment Report of the Intergovernmental Panel on Climate Change*; 2021.

(2) Sheldon, R. A. Biocatalysis and Biomass Conversion: Enabling a Circular Economy: Biocatalysis and Biomass Conversion. In *Philosophical Transactions of the Royal Society A: Mathematical, Physical and Engineering Sciences*; Royal Society Publishing, 2020; Vol. 378. http://doi.org/10.1098/rsta.2019.0274.

(3) Mazmanian, D. A.; Jurewitz, J.; Nelson, H. T. A Governing Framework for Climate Change Adaptation in the Built Environment. *Ecol. Soc.* **2013**, *18* (4). http://doi.org/10.5751/es-05976-180456.

(4) Liao, Y.; Koelewijn, S. F.; van den Bossche, G.; van Aelst, J.; van den Bosch, S.; Renders, T.; Navare, K.; Nicolaï, T.; van Aelst, K.; Maesen, M.; et al. A Sustainable Wood Biorefinery for Low-Carbon Footprint Chemicals Production. *Science (80-.).* **2020**, *367* (6484), 1385–1390. http://doi.org/10.1126/science.aau1567.

(5) Graglia, M.; Kanna, N.; Esposito, D. Lignin Refinery: Towards the Preparation of Renewable Aromatic Building Blocks. *ChemBioEng Rev.* **2015**, *2* (6), 377–392. http://doi.org/10.1002/cben.201500019.

(6) Schutyser, W.; Renders, T.; Van Den Bosch, S.; Koelewijn, S. F.; Beckham, G. T.; Sels, B. F. Chemicals from Lignin: An Interplay of Lignocellulose Fractionation, Depolymerisation, and Upgrading. *Chemical Society Reviews*. Royal Society of Chemistry February 7, 2018, pp 852–908. http://doi.org/10.1039/c7cs00566k.

(7) Renders, T.; Van den Bossche, G.; Vangeel, T.; Van Aelst, K.; Sels, B. Reductive Catalytic Fractionation: State of the Art of the Lignin-First Biorefinery. *Current Opinion in Biotechnology*. 2019, pp 193–201. http://doi.org/10.1016/j.copbio.2018.12.005.

(8) Bartling, A. W.; Stone, M. L.; Hanes, R. J.; Bhatt, A.; Zhang, Y.; Biddy, M. J.; Davis, R.; Kruger, J. S.; Thornburg, N. E.; Luterbacher, J. S.; et al. Techno-Economic Analysis and Life Cycle Assessment of a Biorefinery Utilizing Reductive Catalytic Fractionation. *Energy Environ. Sci.* **2021**, *14* (8), 4147–4168. http://doi.org/10.1039/d1ee01642c.

(9) Abu-Omar, M. M.; Barta, K.; Beckham, G. T.; Luterbacher, J. S.; Ralph, J.; Rinaldi, R.; Román-Leshkov, Y.; Samec, J. S. M.; Sels, B. F.; Wang, F. Guidelines for Performing Lignin-First Biorefining. *Energy and Environmental Science*. The Royal Society of Chemistry January 26, 2021, pp 262–292. http://doi.org/10.1039/d0ee02870c.

(10) Zakzeski, J.; Bruijnincx, P. C. A.; Jongerius, A. L.; Weckhuysen, B. M. The Catalytic Valorization of Lignin for the Production of Renewable Chemicals. *Chem. Rev.* **2010**, *110*

(6), 3552–3599. http://doi.org/10.1021/cr900354u.

(11) Vanholme, R.; Demedts, B.; Morreel, K.; Ralph, J.; Boerjan, W. Lignin Biosynthesis and Structure. *Plant Physiol.* **2010**, *153* (3), 895–905. http://doi.org/10.1104/pp.110.155119.

(12) Liu, X.; Bouxin, F. P.; Fan, J.; Budarin, V. L.; Hu, C.; Clark, J. H. Recent Advances in the Catalytic Depolymerization of Lignin towards Phenolic Chemicals: A Review. *ChemSusChem*. Wiley-VCH Verlag September 7, 2020, pp 4296–4317. http://doi.org/10.1002/cssc.202001213.

(13) Ha, J. M.; Hwang, K. R.; Kim, Y. M.; Jae, J.; Kim, K. H.; Lee, H. W.; Kim, J. Y.; Park, Y. K. Recent Progress in the Thermal and Catalytic Conversion of Lignin. *Renew. Sustain. Energy Rev.* **2019**, *111*, 422–441. http://doi.org/10.1016/j.rser.2019.05.034.

(14) Sheldon, R. A. Green and Sustainable Manufacture of Chemicals from Biomass: State of the Art. *Green Chemistry*. Royal Society of Chemistry February 25, 2014, pp 950–963. http://doi.org/10.1039/c3gc41935e.

(15) Yang, L.; Seshan, K.; Li, Y. A Review on Thermal Chemical Reactions of Lignin Model Compounds. *Catal. Today* **2017**, *298*, 276–297. http://doi.org/10.1016/j.cattod.2016.11.030.

(16) Fan, L.; Zhang, Y.; Liu, S.; Zhou, N.; Chen, P.; Cheng, Y.; Addy, M.; Lu, Q.; Omar, M. M.; Liu, Y.; et al. Bio-Oil from Fast Pyrolysis of Lignin: Effects of Process and Upgrading Parameters. *Bioresource Technology*. Elsevier Ltd 2017, pp 1118–1126. http://doi.org/10.1016/j.biortech.2017.05.129.

(17) Sun, Z.; Fridrich, B.; de Santi, A.; Elangovan, S.; Barta, K. Bright Side of Lignin Depolymerization: Toward New Platform Chemicals. *Chem. Rev.* **2018**, *118* (2), 614–678. http://doi.org/10.1021/acs.chemrev.7b00588.

(18) Sun, Z.; Fridrich, B.; De Santi, A.; Elangovan, S.; Barta, K. Bright Side of Lignin Depolymerization: Toward New Platform Chemicals. *Chemical Reviews*. American Chemical Society January 24, 2018, pp 614–678. http://doi.org/10.1021/acs.chemrev.7b00588.

(19) Zhang, L.; Hu, G. Supply Chain Design and Operational Planning Models for Biomass to Drop-in Fuel Production. *Biomass and Bioenergy* **2013**, *58*, 238–250. http://doi.org/10.1016/j.biombioe.2013.08.016.

(20) Cheng, F.; Brewer, C. E. Producing Jet Fuel from Biomass Lignin: Potential Pathways to Alkyl-Benzenes and Cycloalkanes. *Renewable and Sustainable Energy Reviews*. Elsevier Ltd May 1, 2017, pp 673–722. http://doi.org/10.1016/j.rser.2017.01.030.

(21) Zhao, S.; Abu-Omar, M. M. Renewable Thermoplastics Based on Lignin-Derived Polyphenols. *Macromolecules* **2017**, *50* (9), 3573–3581. http://doi.org/10.1021/acs.macromol.7b00064.

(22) Bohnet, M. editor. *Ullmann's Encyclopedia of Industrial Chemistry*, 6th, compl ed.; Weinheim, 2003.

(23) Fiege, H.; Voges, H.-W.; Hamamoto, T.; Umemura, S.; Iwata, T.; Miki, H.; Fujita, Y.;

Buysch, H.-J.; Garbe, D.; Paulus, W. Phenol Derivatives. In *Ullmann's Encyclopedia of Industrial Chemistry*; Wiley-VCH Verlag GmbH & Co. KGaA: Weinheim, Germany, 2000. http://doi.org/10.1002/14356007.a19_313.

(24) Siragusa, F.; Van Den Broeck, E.; Ocando, C.; Müller, A. J.; De Smet, G.; Maes, B. U. W.; De Winter, J.; Van Speybroeck, V.; Grignard, B.; Detrembleur, C. Access to Biorenewable and CO 2 -Based Polycarbonates from Exovinylene Cyclic Carbonates. *ACS Sustain. Chem. Eng.* **2021**. http://doi.org/10.1021/acssuschemeng.0c07683.

(25) Bomon, J.; Bal, M.; Achar, T. K.; Sergeyev, S.; Wu, X.; Wambacq, B.; Lemière, F.; Sels, B. F.; Maes, B. U. W. Efficient Demethylation of Aromatic Methyl Ethers with HCl in Water. *Green Chem.* **2021**, *23* (5), 1995–2009. http://doi.org/10.1039/d0gc04268d.

(26) Wu, X.; Fu, J.; Lu, X. Kinetics and Mechanism of Hydrothermal Decomposition of Lignin Model Compounds. *Industrial and Engineering Chemistry Research*. April 10, 2013, pp 5016–5022. http://doi.org/10.1021/ie302898q.

(27) Yang, L.; Zhou, W.; Seshan, K.; Li, Y. Green and Efficient Synthesis Route of Catechol from Guaiacol. *J. Mol. Catal. A Chem.* **2013**, *368–369*, 61–65. http://doi.org/10.1016/j.molcata.2012.11.024.

(28) Li, Z.; Sutandar, E.; Goihl, T.; Zhang, X.; Pan, X. Cleavage of Ethers and Demethylation of Lignin in Acidic Concentrated Lithium Bromide (ACLB) Solution. *Green Chem.* **2020**, *22* (22), 7989–8001. http://doi.org/10.1039/d0gc02581j.

(29) Bomon, J.; Van Den Broeck, E.; Bal, M.; Liao, Y.; Sergeyev, S.; Van Speybroeck, V.; Sels, B. F.; Maes, B. U. Brønsted Acid Catalyzed Tandem Defunctionalization of Biorenewable Ferulic Acid and Derivates into Bio-Catechol. *Angew. Chemie Int. Ed.* **2019**. http://doi.org/10.1002/anie.201913023.

(30) Liao, Y.; Koelewijn, S. F.; van den Bossche, G.; van Aelst, J.; van den Bosch, S.; Renders, T.; Navare, K.; Nicolaï, T.; van Aelst, K.; Maesen, M.; et al. A Sustainable Wood Biorefinery for Low-Carbon Footprint Chemicals Production. *Science (80-.).* **2020**, *367* (6484), 1385–1390. http://doi.org/10.1126/science.aau1567.

(31) Wu, X.; Liao, Y.; Bomon, J.; Tian, G.; Bai, S.-T.; Van Aelst, K.; Zhang, Q.; Vermandel, W.; Wambacq, B.; Maes, B. U. W.; et al. Lignin-First Monomers to Catechol: Rational Cleavage of C-O and C-C Bonds over Zeolites. *ChemSusChem* **2021**. http://doi.org/10.1002/cssc.202102248.

(32) Stanciakova, K.; Weckhuysen, B. M. Water–Active Site Interactions in Zeolites and Their Relevance in Catalysis. *Trends in Chemistry*. Cell Press June 1, 2021, pp 456–468. http://doi.org/10.1016/j.trechm.2021.03.004.

(33) Bates, J. S.; Bukowski, B. C.; Greeley, J.; Gounder, R. Structure and Solvation of Confined Water and Water-Ethanol Clusters within Microporous Brønsted Acids and Their Effects on Ethanol Dehydration Catalysis. *Chem. Sci.* **2020**, *11* (27), 7102–7122. http://doi.org/10.1039/d0sc02589e.

(34) Eckstein, S.; Hintermeier, P. H.; Zhao, R.; Baráth, E.; Shi, H.; Liu, Y.; Lercher, J. A. Influence of Hydronium Ions in Zeolites on Sorption. *Angew. Chemie - Int. Ed.* **2019**, *58* (11), 3450–3455. http://doi.org/10.1002/anie.201812184.

(35) Liu, Y.; Vjunov, A.; Shi, H.; Eckstein, S.; Camaioni, D. M.; Mei, D.; Baráth, E.; Lercher, J. A. Enhancing the Catalytic Activity of Hydronium Ions through Constrained Environments. *Nat. Commun.* **2017**, *8* (1), 1–8. http://doi.org/10.1038/ncomms14113.

(36) De Wispelaere, K.; Bailleul, S.; Van Speybroeck, V. Towards Molecular Control of Elementary Reactions in Zeolite Catalysis by Advanced Molecular Simulations Mimicking Operating Conditions. *Catal. Sci. Technol.* **2016**, *6* (8), 2686–2705. http://doi.org/10.1039/c5cy02073e.

(37) Pérez de Alba Ortíz, A.; Tiwari, A.; Puthenkalathil, R. C.; Ensing, B. Advances in Enhanced Sampling along Adaptive Paths of Collective Variables. *J. Chem. Phys.* **2018**, *149* (7), 072320. http://doi.org/10.1063/1.5027392.

(38) Liu, Y.; Vjunov, A.; Shi, H.; Eckstein, S.; Camaioni, D. M.; Mei, D.; Baráth, E.; Lercher, J. A. Enhancing the Catalytic Activity of Hydronium Ions through Constrained Environments. *Nat. Commun.* **2017**, *8* (1), 1–8. http://doi.org/10.1038/ncomms14113.

(39) Bukowski, B. C.; Bates, J. S.; Gounder, R.; Greeley, J. Defect-Mediated Ordering of Condensed Water Structures in Microporous Zeolites. *Angew. Chemie - Int. Ed.* **2019**, *58* (46), 16422–16426. http://doi.org/10.1002/anie.201908151.

(40) Marcos-Alcalde, I.; Setoain, J.; Mendieta-Moreno, J. I.; Mendieta, J.; Gómez-Puertas, P. MEPSA: Minimum Energy Pathway Analysis for Energy Landscapes. *Bioinformatics* **2015**, *31* (23), 3853–3855. http://doi.org/10.1093/bioinformatics/btv453.

(41) Melander, L. Isotope Effects in Proton-Transfer Reactions. *ACTA Chem. Scand.* **1971**, *25* (10), 3821–3826.

(42) Bigeleisen, J. Correlation Of Kinetic Isotope Effects With Chemical Bonding In Three-Centre Reactions. *Pure Appl. Chem.* **1964**, *8* (3–4), 217–224. http://doi.org/10.1351/pac196408030217.

(43) Kresge, A. J.; Onwood, D. P. The Secondary Isotope Effect on Proton Transfer from the Hydronium Ion in Aqueous Solution. *J. Am. Chem. Soc.* **1964**, *86* (22), 5014–5016. http://doi.org/10.1021/ja01076a063.

(44) Zhu, J.; Liu, Z.; Xu, L.; Ohnishi, T.; Yanaba, Y.; Ogura, M.; Wakihara, T.; Okubo, T. Understanding the High Hydrothermal Stability and NH3-SCR Activity of the Fast-Synthesized ERI Zeolite. *J. Catal.* **2020**, *391*, 346–356. http://doi.org/10.1016/j.jcat.2020.08.033.

(45) Prodinger, S.; Shi, H.; Eckstein, S.; Hu, J. Z.; Olarte, M. V.; Camaioni, D. M.; Derewinski, M. A.; Lercher, J. A. Stability of Zeolites in Aqueous Phase Reactions. *Chem. Mater.* **2017**, *29* (17), 7255–7262. http://doi.org/10.1021/acs.chemmater.7b01847.

(46) Heard, C. J.; Grajciar, L.; Uhlík, F.; Shamzhy, M.; Opanasenko, M.; Čejka, J.; Nachtigall, P. Zeolite (In)Stability under Aqueous or Steaming Conditions. *Advanced Materials*. Wiley-VCH Verlag November 1, 2020, p 2003264. http://doi.org/10.1002/adma.202003264.

(47) VandeVondele, J.; Krack, M.; Mohamed, F.; Parrinello, M.; Chassaing, T.; Hutter, J. Quickstep: Fast and Accurate Density Functional Calculations Using a Mixed Gaussian and Plane Waves Approach. *Comput. Phys. Commun.* **2005**, *167* (2), 103–128.

http://doi.org/10.1016/j.cpc.2004.12.014.

(48) VandeVondele, J.; Hutter, J. Gaussian Basis Sets for Accurate Calculations on Molecular Systems in Gas and Condensed Phases. *J. Chem. Phys.* **2007**, *127* (11), 114105. http://doi.org/10.1063/1.2770708.

(49) Grimme, S.; Antony, J.; Ehrlich, S.; Krieg, H. A Consistent and Accurate Ab Initio Parametrization of Density Functional Dispersion Correction (DFT-D) for the 94 Elements H-Pu. *J. Chem. Phys.* **2010**, *132* (15), 154104. http://doi.org/10.1063/1.3382344.

(50) Becke, A. D. Density-Functional Exchange-Energy Approximation with Correct Asymptotic Behavior. *Phys. Rev. A* **1988**, *38* (6), 3098–3100. http://doi.org/10.1103/physreva.38.3098.

(51) Lee, C.; Yang, W.; Parr, R. G. Development of the Colle-Salvetti Correlation-Energy Formula into a Functional of the Electron Density. *Phys. Rev. B* **1988**, *37* (2), 785–789. http://doi.org/10.1103/physrevb.37.785.

(52) Martyna, G. J.; Klein, M. L.; Tuckerman, M. Nosé–Hoover Chains: The Canonical Ensemble via Continuous Dynamics. *J. Chem. Phys.* **1992**, *97* (4), 2635–2643. http://doi.org/10.1063/1.463940.

(53) Nosé, S. A Molecular Dynamics Method for Simulations in the Canonical Ensemble. *Mol. Phys.* **1984**, *52* (2), 255–268. http://doi.org/10.1080/00268978400101201.

(54) Tribello, G. A.; Bonomi, M.; Branduardi, D.; Camilloni, C.; Bussi, G. PLUMED 2: New Feathers for an Old Bird. *Comput. Phys. Commun.* **2014**, *185* (2), 604–613. http://doi.org/10.1016/j.cpc.2013.09.018.

(55) Laio, A.; Parrinello, M. Escaping Free-Energy Minima. *Proc. Natl. Acad. Sci. U. S. A.* **2002**, *99* (20), 12562–12566. http://doi.org/10.1073/pnas.202427399.

(56) Raiteri, P.; Laio, A.; Gervasio, F. L.; Micheletti, C.; Parrinello, M. Efficient Reconstruction of Complex Free Energy Landscapes by Multiple Walkers Metadynamics. *J. Phys. Chem. B* **2006**, *110* (8), 3533–3539. http://doi.org/10.1021/jp054359r.

(57) Barducci, A.; Bussi, G.; Parrinello, M. Well-Tempered Metadynamics: A Smoothly Converging and Tunable Free-Energy Method. *Phys. Rev. Lett.* **2008**, *100* (2). http://doi.org/10.1103/physrevlett.100.020603.

(58) Grubmüller, H.; Heymann, B.; Tavan, P. Ligand Binding: Molecular Mechanics Calculation of the Streptavidin-Biotin Rupture Force. *Science (80-.).* **1996**, *271* (5251), 997–999. http://doi.org/10.1126/science.271.5251.997.

(59) Souaille, M.; Roux, B. Extension to the Weighted Histogram Analysis Method: Combining Umbrella Sampling with Free Energy Calculations. *Comput. Phys. Commun.* **2001**, *135* (1), 40–57. http://doi.org/10.1016/s0010-4655(00)00215-0.

(60) Kumar, S.; Rosenberg, J. M.; Bouzida, D.; Swendsen, R. H.; Kollman, P. A. The Weighted Histogram Analysis Method for Free-energy Calculations on Biomolecules. I. The Method. *J. Comput. Chem.* **1992**, *13* (8), 1011–1021. http://doi.org/10.1002/jcc.540130812.

(61) Vanduyfhuys, L. ThermoLIB | Center for Molecular Modeling https://molmod.ugent.be/software/thermolib (accessed Jan 11, 2022).

Abstract Figure

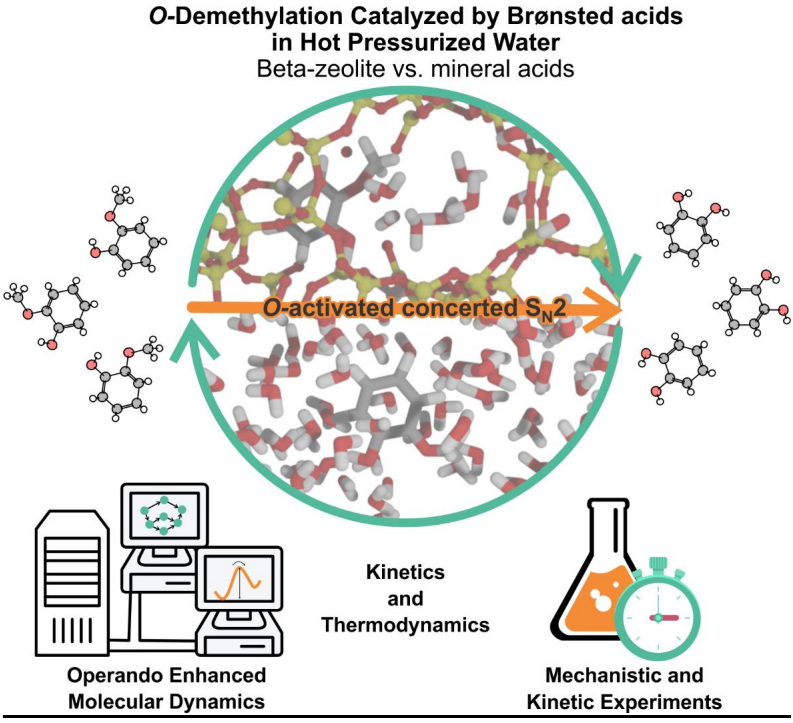

III

A Switchable Domino Process for the Construction of Novel CO_2-Sourced Sulfur-Containing Building Blocks and Polymers

Elias Van Den Broeck has performed the computational research.

Reprinted with permission from Farid Ouhib, Bruno Grignard, Elias Van Den Broeck, André Luxen, Koen Robeyns, Veronique Van Speybroeck, Christine Jerome, and Christophe Detrembleur. A switchable domino process for the construction of novel CO2 -sourced sulfur-containing building blocks and poolymers. *Angewandte Chemie International Edition*, 58(34):11768–11773, 2019. doi: 10.1002/anie.201905969.

Organocatalysis

International Edition: DOI: 10.1002/anie.201905969
German Edition: DOI: 10.1002/ange.201905969

A Switchable Domino Process for the Construction of Novel CO_2-Sourced Sulfur-Containing Building Blocks and Polymers

*Farid Ouhib[+], Bruno Grignard[+], Elias Van Den Broeck, André Luxen, Koen Robeyns, Veronique Van Speybroeck, Christine Jerome, and Christophe Detrembleur**

Abstract: *α-Alkylidene cyclic carbonates (αCCs) recently emerged as attractive CO_2-sourced synthons for the construction of complex organic molecules. Herein, we report the transformation of αCCs into novel families of sulfur-containing compounds by organocatalyzed chemoselective addition of thiols, following a domino process that is switched on/off depending on the desired product. The process is extremely fast and versatile in substrate scope, provides selectively linear thiocarbonates or elusive tetrasubstituted ethylene carbonates with high yields following a 100% atom economy reaction, and valorizes CO_2 as a renewable feedstock. It is also exploited to produce a large diversity of unprecedented functional polymers. It constitutes a robust platform for the design of new sulfur-containing organic synthons and important families of polymers.*

Carbon dioxide (CO_2) is an attractive abundant, safe, and renewable carbon source for the synthesis of organic cyclic carbonates. Today, these molecules find many and diverse applications as intermediates for fine chemical synthesis, electrolytes in Li-ion batteries, polar aprotic solvents, and monomers for the preparation of world-relevant polymers such as polycarbonates and polyurethanes.[1] The [3+2] cycloaddition of CO_2 to epoxides is the most popular and straightforward approach to five-membered cyclic carbonates[2] and, with the recent breakthroughs in their catalyzed transformations,[3] new CO_2-based organic molecules with a high degree of complexity are now accessible.[4]

α-Alkylidene cyclic carbonates (αCCs) are also rapidly emerging as another important class of industrially relevant CO_2-sourced cyclic carbonates.[5] They are produced by catalytic carboxylative coupling of propargylic alcohols with CO_2.[6] In contrast to the conventional five-membered cyclic carbonates, the presence of an exocyclic vinylic group facilitates the regioselective ring-opening of the cyclic carbonate by various nucleophiles, leading to new potentials in modern organic chemistry for the selective construction of novel molecules. The potential of αCCs for the preparation of new building blocks is enormous, but examples are still limited to β-oxocarbamates, β-oxocarbonates, β-hydroxy-1,3-oxazolidin-2-ones, α-hydroxyketones, and 3-dialkylaminooxazolidin-2-ones.[7,8] Recently, some of us demonstrated their utility for the synthesis of functional polyurethanes and polycarbonates, opening new perspectives for the design of advanced materials.[8]

The ring-opening of αCCs by thiols is potentially attractive to drastically enlarge the scope of these CO_2-based synthons but is surprisingly unexplored. It is expected to provide new relevant sulfur-containing products for both synthetic organic (e.g. thiocarbonates) and polymer chemistries (e.g. poly(monothiocarbonates)). Thiocarbonates are notably important synthetic intermediates in organic chemistry[9] and are used as protecting groups for thiols.[10] Poly(monothiocarbonate)s are attractive polymers for optic applications due to their high refractive index,[11] but also for water purification due to the strong binding ability of sulfur atom to metals.[12] Only one article reports the reaction of thiols with αCCs, and this only by UV-activated thiol–ene addition to yield the trisubstituted ethylene carbonate **1** (Scheme 1, previous work).[13]

In this work, we investigated the organocatalyzed thiolation of αCCs as an unprecedented source of a large palette of novel sulfur-containing organic scaffolds and polymers. We discovered that 1,8-diazabicyclo[5.4.0]undec-7-ene (DBU) catalyzed the quantitative ring-opening of αCCs by various thiols, yielding either the β-oxothiocarbonate **2** or the elusive tetrasubstituted ethylene carbonate **3** in high yield (Scheme 1). Product **2** was formed extremely rapidly at room temperature, whereas **3** resulted from a novel DBU-catalyzed reaction following an on/off switchable domino process. Finally, the reactions were implemented for the synthesis of novel families of sulfur-containing polymers, including unprecedented polycyclics, with functionalities that were modulated by switching on/off the domino process.

[*] Dr. F. Ouhib,[+] Dr. B. Grignard,[+] Prof. Dr. C. Jerome, Dr. C. Detrembleur
Center for Education and Research on Macromolecules (CERM)
CESAM Research Unit, University of Liège
Sart-Tilman B6a, 4000 Liege (Belgium)
E-mail: christophe.detrembleur@ulg.ac.be
E. Van Den Broeck, Prof. Dr. V. Van Speybroeck
Center for Molecular Modeling, Ghent University
Technologiepark 46, 6052 Zwijnaarde (Belgium)
Prof. Dr. A. Luxen
GIGA—CRC in vivo Imaging, University of Liege
Sart-Tilman B6A, 4000 Liège (Belgium)
Dr. K. Robeyns
Institute of Condensed Matter and Nanosciences (IMCN)
Université Catholique de Louvain
1348 Louvain-la-Neuve (Belgium)
[+] These authors contributed equally to this work.
Supporting information (including experimental details, supplementary characterizations, and computational studies) and the ORCID identification number(s) for the author(s) of this article can be found under: https://doi.org/10.1002/anie.201905969.

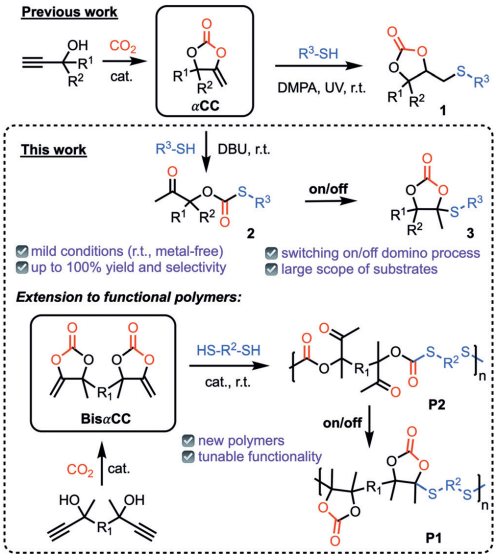

Scheme 1. Organocatalyzed addition of thiols to CO_2-sourced α-alkylidene cyclic carbonates and extension to functional polymers.

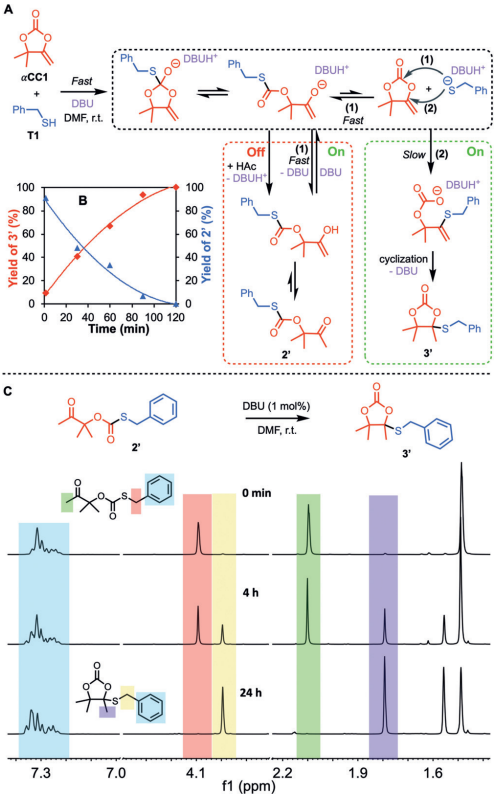

Scheme 2. A) Switchable domino process for the **αCC1**/**T1** reaction and B) plot of the yields of **2′** and **3′** vs. time; C) ^{1}H NMR study of the DBU-catalyzed rearrangement of **2′** into **3′**.

First, we tested the reaction of 4,4-dimethyl-5-methylene-1,3-dioxolan-2-one (**αCC1,** Table 1, prepared by the catalyzed carboxylative coupling of CO_2 to 2-methyl-3-butyn-2-ol) with benzylthiol **T1** under stoichiometric conditions at room temperature in DMF without any catalyst. No reaction was observed after 24 h. In order to favor the ring-opening, DBU was added, as it had been demonstrated to facilitate the ring-opening of αCCs with alcohols.[8] Surprisingly, the unexpected tetrasubstituted ethylene carbonate **3** was quantitatively formed after only 2 h at low DBU loading (1 mol%) (Table 1, entry 2). This observation is in sharp contrast to the selective DBU-catalyzed ring-opening of αCCs by alcohols or secondary diamines that yielded β-oxocarbonates or β-oxourethanes, respectively.[8] Replacing **T1** with 2-furanmethanethiol **T2** also resulted in the corresponding tetrasubstituted ethylene carbonate (Table 1, entry 10) and not the expected β-oxothiocarbonate **2**. The DBU-catalyzed addition of **T1** to **αCC1** was then followed by ^{1}H and ^{13}C NMR spectroscopy to understand the origin of this product (Supporting Information (SI), Section 2.1). After only 1 min, the cyclic carbonate was fully converted into the expected β-oxothiocarbonate **2** as the main product (91%), and the tetrasubstituted cyclic product **3** as the minor one (9%) (Table 1, entry 1). With increasing reaction time, **2** progressively disappeared in favor of **3**, suggesting that **3** resulted from a rearrangement of **2**. Product **3** was quantitatively recovered after 2 h, and its structure was confirmed by ^{1}H and ^{13}C NMR spectroscopy, HR-MS, and XRD of the recrystallized product (Scheme 2C; SI Section 4.1, Table S8).

Various CO_2-sourced αCCs (Table 1) were tested to evaluate the influence of the steric hindrance on the selectivity of the reactions after both 1 min and 2 h of reaction. All αCCs were fully converted after only 1 min of reaction, demonstrating the impressively fast ring-opening of the cyclic carbonate (see SI Sections 2.1–2.6 for kinetics of reactions). The selectivity in **2** after 1 min slightly increased with the steric hindrance, from 91% for **αCC1**, to 93.5% for **αCC2**, and to 97% for the bulkier **αCC3** (entries 1, 3, and 6, Table 1). In parallel, the selectivity in **3** after 2 h drastically decreased with the steric hindrance from 100% for **αCC1**, to 64% for **αCC2**, and 23% for **αCC3** (entries 2, 4 and 7, Table 1). Bulky groups on αCCs therefore strongly slowed down the rearrangement of **2** into **3**. When the reaction time was extended to 24 h, **2** was fully converted into **3** for **αCC2**, compared to only 47% for the bulkiest **αCC3** (entries 5 and 8, Table 1). The same trend was noted for 2-furanmethanethiol **T2** (entries 9–16). The substrate scope was further extended by screening the reaction of **αCC1** with thiols **T3** and **T4** (entries 17–22, Table 1). The corresponding products **2** were produced in high yield (98–99%) after 1 min. Product **3** was formed in 58% yield with **T3** when the reaction time was

Table 1: Scope of the organocatalyzed addition of thiols to αCCs.

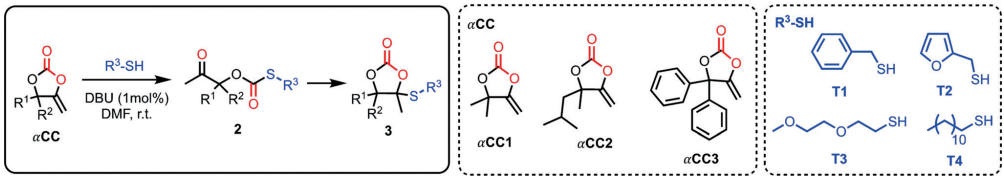

Entry	αCC	Thiol	*t*	$Conv_{αCC}$ [%][a]	$Conv_2$ [%][a]	Yield **2** [%][a]	Yield **3** [%][a]
1	**αCC1**	**T1**	1 min	>99	9.1	90.9	9.1
2			2 h	>99	100	0	100
3	**αCC2**	**T1**	1 min	>99	6.5	93.5	6.5
4			2 h	>99	64	36	64
5			24 h	>99	100	0	100
6	**αCC3**	**T1**	1 min	>99	3	97	3
7			2 h	>99	23	77	23
8			24 h	>99	47	53	47
9	**αCC1**	**T2**	1 min	>99	10.7	89.3	10.7
10			2 h	>99	100	0	100
11	**αCC2**	**T2**	1 min	>99	7.3	92.7	7.3
12			2 h	>99	66.6	33.4	66.6
13			24 h	>99	100	0	100
14	**αCC3**	**T2**	1 min	>99	5.3	94.7	5.3
15			2 h	>99	27	73	27
16			24 h	>99	56	44	56
17	**αCC1**	**T3**	1 min	>99	2	98	2
18			24 h	>99	58	42	58
19			24h[b]	>99	95	5	95
20	**αCC1**	**T4**	1 min	>99	1	99	1
21			24 h	>99	3	97	3
22			24 h[b]	>99	95	5	95

[a] Conversions and yields determined by ^{1}H NMR analysis. $Conv_{αCC}$ = conversion of αCC; $Conv_2$ = conversion of **2**. [b] Reaction at 80 °C. Conditions: [αCC]/[thiol] = 1/1, αCC = 4 mmol, V_{DMF} = 1 mL, room temperature.

extended to 24 h, whereas a trace amount of **3** was detected for **T4**. When the experiments were carried out at 80 °C for 24 h, product **3** was almost quantitatively formed in both cases. For all experiments, the products **2** were collected at high yields provided that the reactions were quenched after 1 min by the addition of acetic acid (10–20 mol %) which switched off the domino process.

The course of this domino process, illustrated in Scheme 2 A for the **αCC1/T1** reaction, is supported by computational investigations (see SI Section 3 for details). Nucleophilic attack of the thiolate on the carbonyl group provides the metastable five-membered intermediate that ring-opens into the thiocarbonate. Proton transfer from $DBUH^+$ gives the corresponding enol that tautomerizes into the thiocarbonate **2′**. This addition mode is very fast, as **2′** is formed in 91 % yield in 1 min. The process is under equilibrium, as suggested by calculations that give a free energy barrier for the back reaction of only 22.5 kJ mol^{-1} (SI Section 3, Figure S15). Importantly, the thiolate is also able to add to the carbon of the C=C bond (addition pathway (2)). Computational investigations suggest that this addition mode provides the corresponding carbonate anion adduct, which follows an irreversible intramolecular cyclization, aided by $DBUH^+$, to provide the tetrasubstituted ethylene carbonate **3′** and the release of the catalyst. A concerted mechanism might also be involved (see SI Section 3) but at this stage, it is not possible to discriminate the two mechanisms. Addition pathway (2) (stepwise or concerted) is, however, slow (complete in 2 h, Scheme 2 B) compared to pathway (1) as supported by the complete kinetic analysis of the reactions (SI Sections 2.1–2.6), and in line with higher calculated free energy barriers for pathway (2) (SI Section 3). In contrast to the formation of **2′** which is reversible, the reaction pathway to **3′** is assumed to be irreversible. Therefore **2′** is progressively fully converted into **3′** in the presence of DBU, and this irreversible reaction is the main driving force for the cyclization. The formation of **2′** is

therefore under kinetic control, whereas the formation of **3′** is under thermodynamic control. Importantly, when acetic acid was added after 1 min of reaction, the domino process was switched off. Since DBU is deactivated in this way, the reversible reaction does not occur and thus **3′** is not formed; only **2′** is collected. It is important to note that when alcohols were used instead of thiols in the presence of DBU under identical conditions, the domino process was not observed because the formation of the β-oxocarbonate is irreversible since alcoholates are poorer leaving groups than thiolates. The same conclusion prevails for the reaction with amines.

To further support this proposed mechanism, the thiocarbonate **2′** was synthesized according to conditions established in Table 1, entry 1. The purified compound was then dissolved in DMF to which 1 mol % of DBU was added (see SI Section 2.7). The transformation of **2′** into **3′** was then monitored at room temperature by ^{1}H NMR spectroscopy. Scheme 2C shows that the thiocarbonate **2′** was progressively and fully converted into **3′** (SI Section 2.7). Also, a tiny amount of **αCC1** was detected (< 1 mol %) when DBU was added to **2′** (Figure S13), supporting the reversibility of addition mode (1) (Scheme 2A). No reaction was observed in the absence of DBU. Importantly, when two different thiocarbonates were mixed in the presence of DBU, four tetrasubstituted ethylene carbonates were collected, attesting again for the reversibility of addition mode (1) (SI Section 2.8, Figure S14).

Screening experiments with other bases of different pK_a have shown that superbases such as 1,5,7-triazabicyclo-[4.4.0]dec-5-ene (TBD), 7-methyl-1,5,7-triazabicyclo-[4.4.0]dec-5-ene (MTBD), and 1,5-diazabicyclo[4.3.0]non-5-ene (DBN) also catalyzed the fast formation of the thiocarbonate **2′** (Table S9, SI Section 4.2). The rate of formation of **3′** was, however, slower than the reaction catalyzed by DBU. Weaker bases such as triethylamine (NEt3,), 1,4-diazabicyclo-[2.2.2]octane (DABCO), and 4-dimethylaminopyridine (DMAP) presented poor catalytic activity for the formation **2′** and did not catalyze the synthesis of **3′**. Mechanistic studies are ongoing in our laboratories in order to explain this difference of behavior.

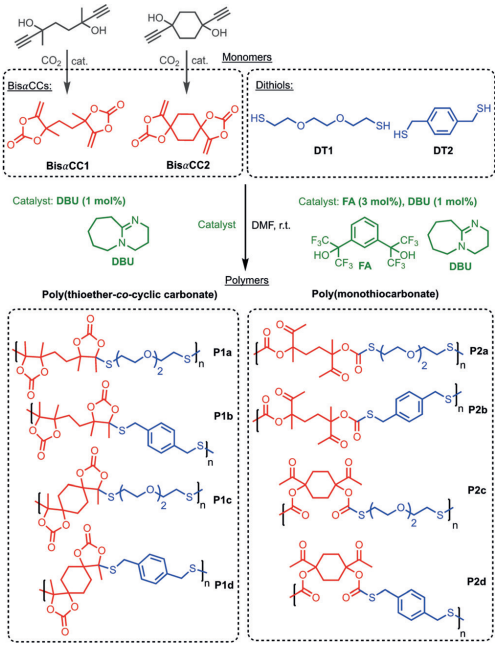

Scheme 3. Polyadditions of dithiols with bis(α-alkylidene cyclic carbonate)s.

This switchable domino process was then evaluated for the construction of novel regioregular sulfur-containing polymers, by polyaddition of CO_2-sourced bis(α-alkylidene cyclic carbonate) (**BisαCC1** and **BisαCC2**, see SI Section 4.3 for their synthesis) with dithiols (**DT1** and **DT2**) (Scheme 3). The conversions, linkage selectivity, and molecular characteristics of the polymers are collected in Table 2. The DBU-

Table 2: Scope of the step-growth polyaddition of CO_2-sourced bis(α-alkylidene cyclic carbonate)s with dithiols (see Scheme 3 for chemical structures).

Entry	BisαCC	Thiol	Catalyst	Cat. content [mol %]	Conv. [%]	M_n [g mol^{-1}][a]	M_w [g mol^{-1}][a]	$Đ$[a]	Polymer linkages[b]	T_g [°C][c]
1			DBU	1	> 99	15 900	41 000	2.58	**P1a**/**P2a**: 99/1	45
2	**BisαCC1**	**DT1**	DBU	5	> 99	54 000	105 000	1.94	**P1a**/**P2a**: 99/1	47
3			FA/DBU	3/1	95	9200	17 900	1.94	**P1a**/**P2a**: 18/82	9
4	**BisαCC1**	**DT2**	DBU	1	> 99	22 000	39 800	1.81	**P1b**/**P2b**: 99/1	126
5			FA/DBU	3/1	97	21 300	45 300	2.12	**P1b**/**P2b**: 19/81	61
6	**BisαCC2**	**DT1**	DBU	1	> 99	15 700	32 800	2.09	**P1c**/**P2c**: 99/1	76
7			FA/DBU	3/1	98	15 300	38 000	2.48	**P1c**/**P2c**: 30/70	32
8	**BisαCC2**	**DT2**	DBU	1	> 99	75 300	103 000	1.37	**P1d**/**P2d**: 99/1	–[d]
9			FA/DBU	3/1	95	20 800	42 700	2.05	**P1d**/**P2d**: 84/16	115

[a] Determined by size exclusion chromatography (SEC) in THF or DMF using PMMA for calibration. [b] Determined by ^{1}H NMR analysis in $CDCl_3$ or $[D_7]$DMF at room temperature. [c] Determined by dynamic scanning calorimetry (DSC). [d] T_g higher than the degradation temperature of the polymer; conditions: [BisαCC]/[DT] = 1/1, [BisαCC] = 2 M in DMF, room temperature, 24 h.

catalyzed polyadditions provided a novel family of polymers, poly(thioether-*co*-cyclic carbonate)s **P1a–d** (Scheme 3). All polymerizations were remarkably highly selective for the thioether-*co*-cyclic carbonate linkages (≥99%) at room temperature (Figures S41–48), and high conversions were noted after 24 h at a low organocatalyst content (1 mol%) (entries 1, 4, 6, and 8, Table 2). Moderate to high number average molar masses (M_n) were noted, ranging from 15700 to 75300 g mol^{-1}. When the catalyst loading was increased, M_n also drastically increased from 15900 to 54000 g mol^{-1} for **BisαCC1/DT1** (entry 2, Table 2). For short reaction times (5 min instead of 24 h), the polymer obtained by polymerizing the **BisαCC1/DT1** mixture was the poly(monothiocarbonate) **P2a** (90% thiocarbonate linkages) (entry 1, Table S10). These linkages were progressively fully converted into thioether-*co*-cyclic carbonate moieties, providing **P1a**, after few hours (SI Section 4.4; entries 2 and 3, Table S10; Figures S36 and S37).

Importantly, for the **BisαCC2/DT2** mixture, the polymerization was extremely fast with a conversion of 95% after only 1 min, and the selective formation of **P1d** (thioether-*co*-cyclic carbonate linkage of 95%) with a M_n of 11800 g mol^{-1} (entry 1, Table S11). The rapid formation of this linkage is assumed to be the result of the high leaving group ability of the thiolate of **DT2** (Scheme 2A), which favors the cyclization. These DBU-catalyzed polymerizations thus demonstrate that the domino process is impressively fast and efficient, also for macromolecules. Although rapidly quenching the **BisαCC1/DT1** polyaddition with acetic acid provided the expected **P2a**, only low M_n was obtained (4300 g mol^{-1}; entry 1, Table S10). In order to increase the M_n, the polymerization period was extended. However the domino process then occurred, leading to the transformation of the thiocarbonate linkages into thioether-*co*-cyclic carbonate ones (entries 2 and 3, Table S10).

With the objective to prepare polymers rich in thiocarbonate linkages and of reasonable M_n, we carried out the polymerizations in the presence of DBU (1 mol%) along with the fluorinated alcohol 1,3-bis(2-hydroxyhexafluoroisopropyl)benzene (**FA**, 3 mol%; Scheme 3, SI Section 4.6). Under these conditions, the series of poly(monothiocarbonate)s **P2a–c** with a selectivity in thiocarbonate linkages of 70–82% were prepared after 24 h (entries 3, 5, and 7, Table 2). Interestingly, by tuning the **FA** content, we have access to polymers with intermediate linkages content and functionality (Table S12, Figure S41). No polymerization was observed in the absence of DBU, even with 3 mol% **FA**. Although further mechanistic investigations are required to understand the action mode of **FA**, this novel strategy towards regioregular poly(monothiocarbonate)s with a potentially large scope of structures (aliphatic and aromatic) is an attractive alternative to the conventional epoxide/COS ring-opening copolymerization that gives access to aliphatic polymers with limited functions.[14]

The type and content of polymer linkages has a drastic influence on the glass transition temperature (T_g) of the polymer. As a general trend, T_g significantly increased with the content of thioether-*co*-cyclic carbonate linkages. The most impressive effect on T_g was noted for the polymers prepared with **DT2**, for instance a change in T_g from 61 °C to 126 °C with 19 and 99% of thioether-*co*-cyclic carbonate linkages, respectively (entries 5 and 4, Table 2). Interestingly, when **BisαCC2** was used, unusual hindered polycyclic structures were incorporated within the polymer backbone with an impressive impact on the thermal properties of the polymer. High-T_g polymers were formed when **BisαCC2** was polymerized with **DT2** (entries 8 and 9, Table 2, Figure S49).

In summary, we have developed a novel robust switchable domino process for the construction of important sulfur-containing organic molecules by the organocatalyzed chemoselective addition of thiols to CO_2-sourced α-alkylidene cyclic carbonates. Thiocarbonates but also challenging tetrasubstituted ethylene carbonates were selectively produced at high yield and at room temperature following a 100% atom economy reaction under stoichiometric conditions. This process was also exploited to prepare unprecedented regioregular sulfur-containing polymers. The "on-demand" modulation of the structure and functionality of the final product by the switching on/off of the domino process offers enormous synthetic possibilities for both organic chemistry and macromolecular engineering.

Acknowledgements

We thank the Fonds de la Recherche Scientifique (FNRS) and the Fonds Wetenschappelijk Onderzoek—Vlaanderen (FWO) for funding the EOS project n°O019618F (ID EOS: 30902231), and FNRS in the frame of the NECOPOL project (convention U.N054.17). C.D. is Research Director by F.R.S.-FNRS.

Conflict of interest

The authors declare no conflict of interest.

Keywords: carbon dioxide · domino process · organocatalysis · polymerization · synthetic methods

How to cite: *Angew. Chem. Int. Ed.* **2019**, *58*, 11768–11773
Angew. Chem. **2019**, *131*, 11894–11899

[1] a) J. Zhang, J. Yang, T. Dong, M. Zhang, J. Chai, S. Dong, T. Wu, X. Zhou, G. Cu, *Small* **2018**, *14*, 1800821; b) J. Mindemark, M. J. Lacey, T. Bowden, D. Brandell, *Prog. Polym. Sci.* **2018**, *81*, 114–143; c) M. I. Childers, J. M. Longo, N. J. Van Zee, A. M. LaPointe, G. W. Coates, *Chem. Rev.* **2014**, *114*, 8129–8152; d) S. J. Poland, D. J. Darensbourg, *Green Chem.* **2017**, *19*, 4990–5011; e) L. Maisonneuve, O. Lamarzelle, E. Rix, E. Grau, H. Cramail, *Chem. Rev.* **2015**, *115*, 12407–12439.

[2] a) M. Alves, B. Grignard, R. Mereau, C. Jerome, T. Tassaing, C. Detrembleur, *Catal. Sci. Technol.* **2017**, *7*, 2651–2684; b) G. Fiorani, W. Guo, A. W. Kleij, *Green Chem.* **2015**, *17*, 1375–1389; c) C. Martín, G. Fiorani, A. W. Kleij, *ACS Catal.* **2015**, *5*, 1353–1370; d) H. Büttner, L. Longwitz, J. Steinbauer, T. Werner, *Top. Curr. Chem.* **2017**, *375*, 1–56, e) S. Dabral, T. Schaub, *Adv. Synth. Catal.* **2019**, *361*, 223–246.

[3] J. E. Gómez, A. W. Kleij, *Curr. Opin. Green Sust. Chem.* **2017**, *3*, 55–60.

[4] W. Guo, J. E. Gómez, À. Cristòfol, J. Xie, A. W. Kleij, *Angew. Chem. Int. Ed.* **2018**, *57*, 13735 – 13747; *Angew. Chem.* **2018**, *130*, 13928 – 13941.

[5] a) S. Dabral, T. Schaub, *Adv. Synth. Catal.* **2019**, *361*, 223 – 246; b) S. Dabral, B. Bayarmagnai, M. Hermsen, J. Schießl, V. Mormul, A. S. K. Hashmi, T. Schaub, *Org. Lett.* **2019**, *21*, 1422 – 1425.

[6] a) Y.-B. Wang, Y.-M. Wang, W. Zhang, X. Lu, *J. Am. Chem. Soc.* **2013**, *135*, 11996 – 12003; b) Y. Kayaki, M. Yamamoto, T. Ikariya, *Angew. Chem. Int. Ed.* **2009**, *48*, 4194 – 4197; *Angew. Chem.* **2009**, *121*, 4258 – 4261; c) A. Boyaval, R. Mereau, B. Grignard, C. Detrembleur, C. Jerome, T. Tassaing, *ChemSusChem* **2017**, *10*, 1241 – 1248; d) R. Méreau, B. Grignard, A. Boyaval, C. Detrembleur, C. Jerome, T. Tassaing, *ChemCatChem* **2018**, *10*, 956 – 960; e) Y. Wu, Y. Zhao, R. Li, B. Yu, Y. Chen, X. Liu, C. Wu, X. Luo, Z. Liu, *ACS Catal.* **2017**, *7*, 6251 – 6255; f) Y. Yuan, Y. Xie, C. Zeng, D. Song, S. Chaemchuen, C. Chen, F. Verpoort, *Green Chem.* **2017**, *19*, 2936 – 2940; g) B. Grignard, C. Ngassamtounzoua, S. Gennen, B. Gilbert, R. Mereau, C. Jerome, T. Tassaing, C. Detrembleur, *ChemCatChem* **2018**, *10*, 2584 – 2592; h) J. Hu, J. Ma, Q. Zhu, Q. Qian, H. Han, Q. Mei, B. Han, *Green Chem.* **2016**, *18*, 382 – 385; i) S.-L. Hou, J. Dong, X.-L. Jiang, Z.-H. Jiao, B. Zhao, *Angew. Chem. Int. Ed.* **2019**, *58*, 577 – 581; *Angew. Chem.* **2019**, *131*, 587 – 591.

[7] a) C.-R. Qi, H.-F. Jiang, *Green Chem.* **2007**, *9*, 1284 – 1286; b) P. Toullec, A. Martin, M. Gio-Batta, C. Bruneau, P. Dixneuf, *Tetrahedron Lett.* **2000**, *41*, 5527 – 5531; c) Z.-H. Zhou, Q.-W. Song, L.-N. He, *ACS Omega* **2017**, *2*, 337 – 345; d) Q.-W. Song, Z.-H. Zhou, M.-Y. Wang, K. Zhang, P. Liu, J.-Y. Xun, L.-N. He, *ChemSusChem* **2016**, *9*, 2054 – 2058; e) Y. Zhao, Z. Yang, B. Yu, H. Zhang, H. Xu, L. Hao, B. Han, Z. Liu, *Chem. Sci.* **2015**, *6*, 2297 – 2301; f) N. B. Chernysheva, A. A. Bogolyubov, V. V. Semenov, *Chem. Heterocycl. Compd.* **2003**, *39*, 1057 – 1064.

[8] S. Gennen, B. Grignard, T. Tassaing, C. Jérôme, C. Detrembleur, *Angew. Chem. Int. Ed.* **2017**, *56*, 10394 – 10398; *Angew. Chem.* **2017**, *129*, 10530 – 10534.

[9] P. Chauhan, S. Mahajan, D. Enders, *Chem. Rev.* **2014**, *114*, 8807 – 8864.

[10] a) W. T. Wiesler, M. H. Caruthers, *J. Org. Chem.* **1996**, *61*, 4272 – 4281; b) K. Arai, T. Wirth, *Org. Process Res. Dev.* **2014**, *18*, 1377 – 1381.

[11] a) L.-F. Hu, Y. Li, B. Liu, Y.-Y. Zhang, X.-H. Zhang, *RSC Adv.* **2017**, *7*, 49490 – 49497; b) M. Luo, X. H. Zhang, B. Y. Du, Q. Wang, Z. Q. Fan, *Polym. Chem.* **2015**, *6*, 4978 – 4983; c) H.-B. Cao, M.-J. Shen, L.-H. Chen, *Sichuan Ligong Xueyuan Xuebao Ziran Kexueban* **2013**, *26*, 1 – 5.

[12] a) K. R. Henke, *Water Environ. Res.* **1998**, *70*, 1178 – 1185; b) M. Matlock, K. R. Henke, D. A. Atwood, *J. Hazard. Mater.* **2002**, *92*, 129 – 142.

[13] B. Liu, X. Zhang, *Gen. Chem.* **2018**, *4*, 180007.

[14] a) Y. Li, H.-Y. Duan, M. Luo, Y.-Y. Zhang, X.-H. Zhang, D. J. Darensbourg, *Macromolecules* **2017**, *50*, 8426 – 8437; b) M. Luo, X.-H. Zhang, D. J. Darensbourg, *Acc. Chem. Res.* **2016**, *49*, 2209 – 2219; c) T.-J. Yue, W.-M. Ren, L. Chen, G.-G. Gu, Y. Liu, X.-B. Lu, *Angew. Chem. Int. Ed.* **2018**, *57*, 12670 – 12674; *Angew. Chem.* **2018**, *130*, 12852 – 12856.

Manuscript received: May 14, 2019
Accepted manuscript online: June 19, 2019
Version of record online: July 18, 2019

IV

Access to Biorenewable and CO_2-Based Polycarbonates from Exovinylene Cyclic Carbonates

Elias Van Den Broeck has performed the computational research in this work and prepared the computational part of the manuscript.

Reprinted with permission from Fabiana Siragusa, Elias Van Den Broeck, Connie Ocando, Alejandro J. Müller, Gilles De Smet, Bert U W Maes, Julien De Winter, Veronique Van Speybroeck, Bruno Grignard, and Christophe Detrembleur. Access to biorenewable and CO2-based polycarbonates from exovinylene cyclic carbonates. *ACS Sustainable Chemistry & Engineering*, 9(4):1714–1728, 2021. doi: 10.1021/acssuschemeng.0c07683.

ACS Sustainable Chemistry & Engineering

pubs.acs.org/journal/ascecg

Research Article

Access to Biorenewable and CO_2-Based Polycarbonates from Exovinylene Cyclic Carbonates

Fabiana Siragusa, Elias Van Den Broeck, Connie Ocando, Alejandro J. Müller, Gilles De Smet, Bert U. W. Maes, Julien De Winter, Veronique Van Speybroeck,* Bruno Grignard,* and Christophe Detrembleur*

Cite This: *ACS Sustainable Chem. Eng.* 2021, 9, 1714–1728

Read Online

ACCESS | Metrics & More | Article Recommendations | Supporting Information

ABSTRACT: We investigate the scope of the organocatalyzed step-growth copolymerization of CO_2-sourced exovinylene bicyclic carbonates with bio-based diols into polycarbonates. A series of regioregular poly(oxo-carbonate)s were prepared from sugar- (1,4-butanediol and isosorbide) or lignin-derived (1,4-benzenedimethanol and 1,4-cyclohexanediol) diols at 25 °C with 1,8-diazabicyclo[5.4.0]undec-7-ene (DBU) as a catalyst, and their defect-free structure was confirmed by nuclear magnetic resonance spectroscopy studies. Their characterization by differential scanning calorimetry and wide-angle X-ray scattering showed that most of them were able to crystallize. When the polymerizations were carried out at 80 °C, some structural defects were introduced within the polycarbonate chains, which limited the polymer molar mass. Model reactions were carried out to understand the influence of the structure of alcohols, the temperature (25 or 80 °C), and the use of DBU on the rate of alcoholysis of the carbonate and on the product/linkage selectivity. A full mechanistic understanding was given by means of static- and dynamic-based density functional theory (DFT) calculations showing the determining role of DBU in the stability of intermediates, and its important role in the rate-determining steps is revealed. Furthermore, the origin of side reactions observed at 80 °C was discussed and rationalized by DFT modeling. As impressive diversified bio-based diols are accessible on a large scale and at low cost, this process of valorization of carbon dioxide gives new perspectives on the sustainable production of bioplastics under mild conditions.

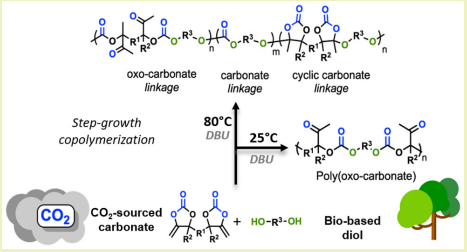

KEYWORDS: *polycarbonate, carbon dioxide valorization, alkylidene cyclic carbonate, bio-based diols, organocatalysis, thermal properties, DFT modeling, molecular dynamics*

INTRODUCTION

Polycarbonates (PCs) are widely used in the automotive industry and in the electric/electronic or construction sectors. Their unique features derived from their excellent physical properties such as high thermal stability and impact resistance combined with their excellent transparency make them suitable for organic glasses, optical fibers, resistant packaging, and so forth.[1,2] PCs are industrially manufactured by phosgenation of diols. The corrosive and highly toxic phosgene combined with the quest for polymers with reduced carbon footprint pushed the scientific community and industries to engineer novel synthetic pathways for this important polymer family.[3,4] Among the numerous processes currently investigated for producing PCs, merging carbon dioxide (CO_2) as a safe and renewable substitute to phosgene with bio-based diols appeared as a promising and appealing approach for greener PCs.[5−7] Indeed, the recent developments in biorefineries (e.g., lignin fractionation and sugar fermentation techniques) have contributed to diversify the range of bio-based alcohols and polyols that can be exploited for the production of more sustainable materials.[8,9] Although the direct copolymerization of (bio-based) diols with CO_2 is highly attractive for the preparation of PCs by an alternative phosgene-free route, this process currently remains very challenging due to the difficulty in removal of water during the polycondensation (Scheme 1a). The rare examples showed that only low molar mass PCs (M_n < 5000 g/mol) were collected using a high loading of metal oxides[10] or organocatalyst/desiccant dual systems at high temperatures, with a limited substrate scope.[6] Another attractive approach to merge CO_2 and diols for the production

Received: October 19, 2020
Revised: December 10, 2020
Published: January 14, 2021

https://dx.doi.org/10.1021/acssuschemeng.0c07683
ACS Sustainable Chem. Eng. 2021, 9, 1714−1728

Scheme 1. Synthesis of PCs by Copolymerization of Diols with CO_2 or CO_2-Sourced Building Blocks: (a) Direct Dehydrative Polycondensation of Diols with CO_2; (b) Melt Polycondensation of Acyclic Carbonates Prepared by the Dehydrative Coupling of CO_2 with Alcohols and Diols; (c) Organocatalyzed Step-Growth Copolymerization of CO_2-Sourced Exovinylene Bicyclic Carbonates with Bio-Based Diols; and (d) Step-Growth Copolymerization of bisαCCs Obtained from Epoxides, CO_2, and 1,4-Butynediol

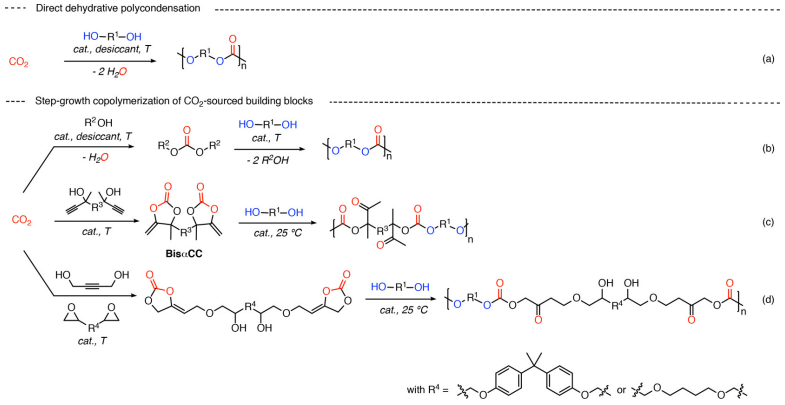

of a larger range of PCs consists of the melt polycondensation of acyclic dialkyl- (e.g., dimethyl carbonate) or diaryl-carbonates (e.g., diphenyl carbonate) with diols. The dialkyl-/diaryl-carbonates were prepared by the dehydrative coupling of CO_2 with the corresponding alcohols (Scheme 1b). Polycondensation is often carried out in a multistage process involving the fabrication of oligomers at moderate temperatures (T = 80−120 °C), followed by applying a high vacuum at higher temperatures (T > 200 °C) to remove the volatile byproducts (methanol or phenol) and pushing the reaction toward the formation of polymers of higher molar mass.[11−14] Recently, our group pioneered the exploitation of a novel family of CO_2-based monomers [bis(α-alkylidene carbonate)s, bisαCCs] for the facile construction of PCs by the organocatalyzed step-growth copolymerization with diols under mild reaction conditions (Scheme 1c).[15,16] The presence of an exovinylene group on the five-membered cyclic carbonate moiety significantly enhanced its reactivity with alcohols and controlled the regioselective ring-opening producing regioregular functional poly(oxo-carbonate)s (PCs) at room temperature up to reasonable molar masses (M_n = 17,000 g/mol). These novel monomers were produced by the zinc iodide-catalyzed carboxylative coupling of CO_2 to bis(propargylic alcohol)s. BisαCCs were also able to copolymerize with amines to produce new polyurethanes[15,17,18] or with thiols to provide novel sulfur-containing polymers, that is, polythiocarbonates and poly(cyclic carbonate-*co*-thioether)s.[19] Although this family of CO_2-sourced monomers was highlighted by BASF[20] as promising building blocks for the preparation of CO_2-based polymers, their utilization for PC synthesis is still in its infancy. In 2019, we exploited bisαCCs for chain-extending poly(ethylene glycol) (PEG) diols and producing poly(carbonate-*co*-ether)s that found promising application as solid electrolytes in Li-ion batteries.[16] The same concept adapted to a mixture of PEG diol and a dithiol enabled the production of new poly(carbonate-*co*-(thio)ether)s containing both linear and cyclic carbonate linkages within the polymer backbone that demonstrated some utility for battery applications.[21] Very recently, Schaub et al. designed new bisαCCs from 1,4-butynediol, epoxides, and CO_2 and successfully tailored low molar mass poly(β-oxo-carbonates) by polyaddition with 1,4-butanediol (Scheme 1d).[22] *In situ*-formed bisαCCs could also be polymerized by an organocatalyzed cascade reaction between a bispropargylic alcohol, CO_2, and a diol. However, only low molar mass polymers (M_n < 3000 g/mol) were collected due to the occurrence of side-reactions.[23] Hitherto, only linear aliphatic primary diols (i.e., 1,4-butanediol or PEG diol) were copolymerized with preformed bisαCCs until achieving reasonable molar masses, whereas the reactivity of bisαCCs toward biorenewable alcohols of different chemical structures remains unknown. Understanding the copolymerization features while identifying the limitations of bisαCC chemistry is key to enlarge the scope of PCs that could be produced by this appealing process.

In this work, we demonstrate that combining bisαCCs with various bio-based diols derived from sugar[24−26] or lignin[8,9] diversifies the range of regioregular PCs that can be produced (Scheme 1c). We investigate the influence of the alcohol structure [i.e., (cyclo)aliphatic or aromatic] and the temperature on the polymerization features, PC microstructure, molar mass, and their thermal properties. Kinetic studies carried out on model compounds combined with modeling also enable us to understand the formation of some unexpected linkages in the polymer chain. This study demonstrates that a large scope of functional CO_2 and bio-sourced polymers with a high biorenewable content can be easily produced by this new process, potentially enlarging the application range of PCs.

EXPERIMENTAL SECTION

Materials and Methods. Benzyl alcohol (99%), 1-butanol (98%), and cyclohexanol were purchased from Sigma-Aldrich. 1,4-Butanediol (99%), 1,4-cyclohexanediol (99%), and *trans*-1,4-cyclohexanediol were supplied by Fluorochem, while 1,8-diazabicyclo[5.4.0]undec-7-ene (DBU 99%) and 1,4-benzenedimethanol (99%) were purchased from TCI. 4,4-Dimethyl-5-methylene-1,3-dioxolan-2-one (αCC),

https://dx.doi.org/10.1021/acssuschemeng.0c07683
ACS Sustainable Chem. Eng. 2021, 9, 1714−1728

4,4′-(ethane-1,2-diyl)bis(4-methyl-5-methylene-1,3-dioxolan-2-one (C1), 1,9-dimethylene-2,4,10,12-tetraoxodispiro[4.2.4^8.2^5]-tetradecane-3,11-dione (C2) and tetrabutylammonium phenolate were synthesized, as reported elsewhere by our group.[15,19,27] All solid reagents were dried before use with azeotropic distillations in toluene. All the solvents were dried overnight on activated 3 Å molecular sieves. All the reactions were performed under an inert atmosphere of N_2.

Characterization Methods. *Nuclear Magnetic Resonance Spectroscopy.* ^{1}H nuclear magnetic resonance (NMR) analyses were performed on Bruker 400 MHz spectrometers in DMSO or $CDCl_3$ at 25 °C in the Fourier-transform mode. 16 or 64 scans for ^{1}H spectra and 512 or 2048 scans for ^{13}C spectra were recorded. Cross-polarization magic-angle spinning solid-state ^{13}C NMR spectra were collected using a Bruker AVANCE DSX-400 instrument. Samples were packed in 4 mm zirconia rotors and spun at 10 kHz.

Gas Chromatography–Mass Spectrometry. Samples were prepared by taking 100 μL of the compound mixture and diluting in acetone. The sample was filtered over a syringe filter and further diluted to a concentration of 10^{-4} to 10^{-5} M. 3 μL of the samples were injected. The apparatus used was an Agilent Technologies 7890 A GC System coupled to an Agilent Technologies 5975 C inert MSD with a triple-axis detector. As the column, an Optima 725820.30 30 m × 250 μm × 0.25 μm was selected. The carrier gas was helium. The following oven program was used: first 50 °C for 3 min, then increment of 10 °C/min up to 300 °C, followed by 300 °C for 5 min. The front inlet was heated at 200 °C. Mass was scanned from 50 to 450 amu.

Size Exclusion Chromatography. The number-average molecular weight (M_n), weight-average molecular weight (M_w), and molecular-weight dispersity (M_w/M_n) values of polymers were determined by size exclusion chromatography (SEC) in dimethylformamide (DMF) and in chloroform ($CHCl_3$). The SEC in DMF contained LiBr (0.025 M) and was performed at 55 °C (flow rate: 1 mL/min) with a Waters chromatograph equipped with three columns (Waters Styragel PSS gram 1000 Å (×2), 30 Å), a dual λ absorbance detector (Waters 2487), and a refractive index detector (Waters 2414). The SEC in chloroform was performed at 35 °C at a flow rate of 1 $cm^3 \cdot min^{-1}$, using an isocratic pump (VE 1122, Viscotek), a set of two PLgel 5 μm MIXED-C ultrahigh efficiency columns, and a Shodex SE 61 differential refractive index detector and a variable wavelength UV detector (Spectra 100, Spectra-Physics). A volume of 100 μL of sample solution in chloroform (concentration, 0.3% w/v) was injected. Polystyrene standards (Polymer Laboratories) with narrow molecular weight distributions were used to generate a calibration curve.

Positive-Ion Matrix-Assisted LASER Desorption/Ionization-Mass Spectrometry. Positive-ion matrix-assisted LASER desorption/ionization-mass spectrometry (MALDI-MS) experiments were performed using a Waters QToF Premier mass spectrometer equipped with a Nd:YAG laser operating at 355 nm (third harmonic) with a maximum output of 65 μJ delivered to the sample in 2.2 ns pulses at 50 Hz repeating rate. Time-of-flight mass analysis was performed in the reflectron mode at a resolution of about 10k (m/z 569). All samples were analyzed using *trans*-2-[3-(4-*tert*-butylphenyl)-2-methylprop-2-enylidene]malononitrile as a matrix. Polymer samples were dissolved in $CHCl_3$ to obtain 1 $mg \cdot mL^{-1}$ solution. Additionally, 40 μL of 2 $mg \cdot mL^{-1}$ NaI solution in acetonitrile was added to the polymer solution.

Thermogravimetric Analysis. Thermogravimetric analysis (TGA) was performed on a TGA2 instrument from Mettler Toledo. Approximately 5 mg of sample was heated at 20 °C/min until 600 °C under a N_2 atmosphere (20 mL/min).

Differential Scanning Calorimetry. Differential scanning calorimetry (DSC) was performed on a DSC Q2000 differential calorimeter (TA Instruments). All the experiments were performed under ultrapure nitrogen flow. Samples of 5−8 mg were used and placed in sealed aluminum pans. The samples were first heated at a rate of 10 °C min^{-1} from 25 to 150 °C. Subsequently, the samples were cooled down to −80 °C at a rate of 10 °C min^{-1} and then heated to 230 °C at 10 °C min^{-1}. The last heating cycle was used for the determination of T_g.

Flash Differential Scanning Calorimetry. Flash differential scanning calorimetry (FDSC) was performed on a Flash DSC2+ instrument from Mettler Toledo, equipped with a Huber TC-100 intracooler. The cooling rate employed was −4000 K/s, and the heating rates were 1000, 5000, and 20,000 K/s. Applying a very fast cooling rate (−4000 K/s), most samples were quenched to the amorphous state (or their crystallinity was greatly reduced), thereby facilitating the detection of their glass transition upon subsequent heating at 1000 K/s. Second, the use of fast heating rates permits avoiding cold crystallization of the samples. For the detection of the melting temperature, a cooling rate of −0.1 K/s was also employed in order to induce crystallization of the samples at −80 °C from the melted state before the subsequent heating scan at 5000 K/s. The polymers with higher values of T_m were evaluated at a heating rate of 20,000 K/s to avoid the degradation of the sample. Before each experiment, the sensor was conditioned and calibrated. A flow of nitrogen gas was applied to perform the measurements under an inert atmosphere, maintaining an 80 mL/min flow rate. For a good contact between the sample and the sensor, a fluorinated oil was casted over the sensor and then the sample was loaded. This oil does not show thermal transitions in the temperature range under study. The samples were analyzed in a range from −80 to 200 or 350 °C, depending on the thermal degradation temperature of each polymer determined by TGA. The reported values of T_g and T_m were taken from the heating runs. As the mass employed in fast chip calorimeter experiments is so small, the results are assumed to be independent of sample mass. STARe software was used to analyze the data.

Wide-Angle X-ray Scattering. Wide-angle X-ray scattering (WAXS) X-ray powder diffraction patterns were collected using a Philips X'pert PRO automatic diffractometer operating at 40 kV and 40 mA, in a $\theta-\theta$ configuration, using a secondary monochromator with Cu-Kα radiation (λ = 1.5418 Å) and a PIXcel solid state detector (active length in 2θ 3.347°). Data were collected from 5 to 70° 2θ, with a step size of 0.026° and a time per step of 150 s at RT. A 1° fixed soller slit and a divergence slit giving a constant volume of sample illumination were used.

General Procedure for the Model Reaction of αCC with Alcohols. All model reactions were conducted at 25 °C with an equimolar ratio of αCC and the nucleophile in dry DMSO (C = 4 mol/L) under a N_2 atmosphere. Kinetics were monitored by ^{1}H NMR spectroscopy following the representative procedure for the αCC−alcohol reaction: αCC (4 mmol 1 equiv) and alcohol (4 mmol 1 equiv) were added in a reaction tube with 1 mL of dry DMSO and 5 mol % DBU (0.2 mmol) compared to αCC. Samples were taken after different time intervals and analyzed by ^{1}H NMR spectroscopy to determine the αCC conversion.

General Procedure for the Synthesis of Poly(β-oxocarbonate)s. The representative procedure for the synthesis of PCs: C1 (3.93 mmol, 1 g) and 1,4-benzenedimethanol (3.93 mmol, 0.542 g) were added to a flask and then dry DMSO (5 mL) and DBU (0.196 mmol, 0.03 mL) were added under nitrogen at room temperature (25 °C). The reaction medium was then stirred at 25 °C for 24 h. At the end of the reaction, an aliquot was withdrawn to determine the conversion of monomers by ^{1}H NMR spectroscopy. The polymer was purified by precipitation in methanol/water (1:1). The polymer was then dried under vacuum at 25 °C for 48 h and analyzed by ^{1}H- and ^{13}C-NMR spectroscopy and SEC. The same procedure was carried out for the other polymers.

RESULTS AND DISCUSSION

Prior to considering the polymerizations, we first carried out a series of reactions on model compounds. The objective of these studies was to probe the reactivity of the α-alkylidene cyclic carbonate group with alcohols of various structures that mimic bio-based alcohols that will be used later in polymerization (Scheme 2). The main goal was to identify the optimal conditions for high yields and selectivity and to investigate the

https://dx.doi.org/10.1021/acssuschemeng.0c07683
ACS Sustainable Chem. Eng. 2021, 9, 1714−1728

Scheme 2. Model Compounds Mimicking the Structure of Sugar- and Lignin-Based Monomers

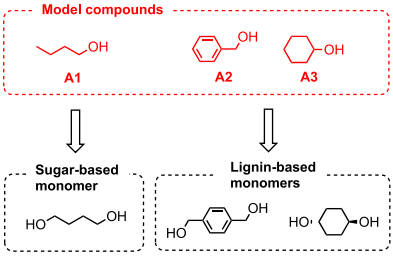

influence of the temperature on the process. Although the temperature was expected to accelerate the reactions, it might also promote some side reactions that have to be identified as they can have an impact on the polymer microstructure and molar masses. These model reactions are therefore of prime importance for understanding the polymerization processes that will be studied.

Alcoholysis of Exovinylene Cyclic Carbonate via Model Reactions. αCC (Figure 1a) was selected as the model cyclic carbonate and synthesized by the quantitative carboxylative coupling of CO_2 to 2-methyl-3-butyn-2-ol catalyzed by tetrabutyl ammonium phenolate.[27] Three alcohols, 1-butanol (**A1**), cyclohexanol (**A2**), and benzyl alcohol (**A3**), were selected based on their structural similarities with sugar- or lignin-based diols (Scheme 2) that will be involved later in the polymerizations. Butanol was also used as a benchmark for the sake of comparison with the two other alcohols.

The reactions were first realized at 25 °C under stoichiometric conditions using dry DMSO as a solvent. These stoichiometric conditions between αCC and the alcohol were selected to fit the conditions required for a step-growth polymerization that will be implemented later. As expected, no alcoholysis of αCC was observed even after 24 h for all alcohols in the absence of catalyst. The addition of 1,5-diazabicyclo(5.4.0)undec-7-ene (DBU) (5 mol % compared to αCC) was then considered as it was previously shown to catalyze the ring-opening of α-alkylidene cyclic carbonates with primary aliphatic alcohols.[15] Under these conditions, the oxo-carbonate adducts were selectively and quantitatively formed (>99% yield) after 24 h of reaction (Figure 1a). The rates of ring-opening reactions by different alcohols were determined by ^{1}H NMR analysis (Figures S1−S3) and the results are presented in Figure 1b. Primary alcohols butanol **A1** and benzyl alcohol **A3** displayed similar reactivities with αCC conversions of 78 and 69% in 2 h, respectively (Figure 1). The secondary alcohol **A2** presented a lower reactivity with a αCC conversion of 15% after 2 h. The lower reactivity of cyclohexanol was assigned to the steric hindrance around the alcohol group.

We then considered the reactions at a higher temperature (80 °C) in order to accelerate the conversion of αCC (Table 1; Figures S4−S6 in the Supporting Information). With **A1** and **A3**, αCC was selectively and almost quantitatively (>98%) converted into their corresponding oxo-carbonate **1** in a very short period of time, 15 min (Table 1, entries 1 and 9). The secondary alcohol **A2** still reacted slowly but faster compared to the same reaction carried out at 25 °C (with αCC conversion of 59% in 15 min at 80 °C; Table 1, entry 5). When the reaction time was extended further for **A2**, the corresponding oxo-carbonate **1** was selectively and quantitatively produced with no side product being identified even after 48 h at 80 °C. Importantly, despite the αCC ring-opening reaction being complete with **A3** after 15 min at 80 °C, maintaining this temperature for a longer period of time (up to 48 h) was detrimental to the selectivity of the reaction. Indeed, trace amounts of tetrasubstituted ethylene carbonate **2**, dibenzyl carbonate **3**, and hydroxyketone **4** were observed after 2 h. Moreover, the content of these side products increased substantially with the reaction time to reach 38% of **2**, 10% of **3**, and 12% of **4** after 48 h. The yield of oxo-carbonate **1** was thus decreased to 40%, while it was 99% after 15 min of reaction with **A3**. No side product was noted for the reaction of αCC with **A1**, even after 48 h at 80 °C. Note that the NMR structural identification of products **1**−**4** was confirmed by comparison of the GC−MS analysis results of the crude reaction mixture (**A3** + αCC with DBU for 48 h at 80 °C) (Figures S7−S11) with those of their commercially available or isolated reference samples (Figures S12−S16).

These observations suggested that the side products observed for the reaction of αCC with **A3** were formed by rearrangement of oxo-carbonate **1**. In order to give some clues to this hypothesis, this oxo-carbonate **1** was purified, isolated, solubilized in DMSO, and added with DBU (5 mol %) in the

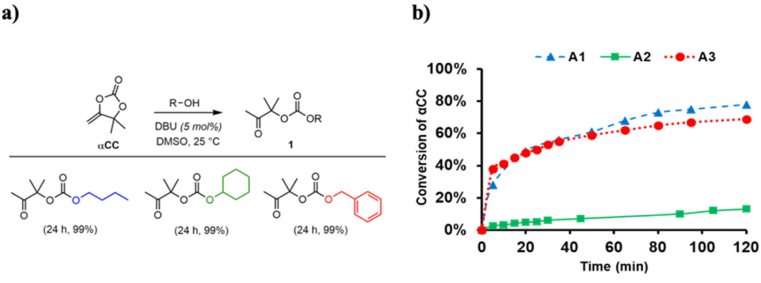

Figure 1. DBU-catalyzed alcoholysis of αCC with 1-butanol **A1**, cyclohexanol **A2**, or benzyl alcohol **A3** at 25 °C. (a) Reaction scheme and product yields after 24 h; (b) conversion of αCC vs time. Conditions: αCC (4 mmol), alcohol (4 mmol), and DBU (0.2 mmol) in dry DMSO (1 mL) at 25 °C under a nitrogen atmosphere.

https://dx.doi.org/10.1021/acssuschemeng.0c07683
ACS Sustainable Chem. Eng. 2021, 9, 1714−1728

Table 1. Alcoholysis of Exovinylene Cyclic Carbonate with 1-Butanol A1, Cyclohexanol A2, and Benzyl Alcohol A3 at 80 °C

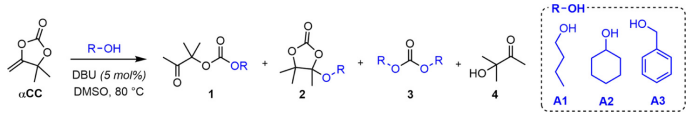

entry	R-OH	time	Conv$_{\alpha CC}$ [%]	yield 1 [%][a]	yield 2 [%][a]	yield 3 [%][a]	yield 4 [%][a]
1	A1	15 min	98	98	0	0	0
2		2 h	>99	>99	0	0	0
3		24 h	>99	>99	0	0	0
4		48 h	>99	>99	0	0	0
5	A2	15 min	59	59	0	0	0
6		2 h	89	89	0	0	0
7		24 h	>99	>99	0	0	0
8		48 h	>99	>99	0	0	0
9	A3	15 min	>99	>99	0	0	0
10		2 h	>99	94	3	2	1
11		24 h	>99	56	25	8	11
12		48 h	>99	40	38	10	12

[a]Yield determined by ^{1}H NMR spectroscopy on the crude product. Conditions: αCC (4 mmol), alcohol (4 mmol), and DBU (0.2 mmol) in dry DMSO (1 mL) at 80 °C under a nitrogen atmosphere.

Table 2. Rearrangement of Oxo-carbonate 1 (Prepared from αCC and A3) at 80 °C in the Presence or Absence of Additional A3

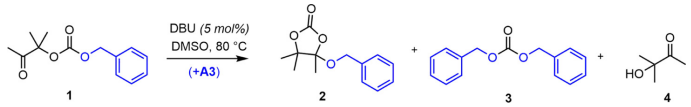

entry	R-OH	time (h)	Conv.1 [%]	yield 2 [%][a]	yield 3 [%][a]	yield 4 [%][a]
1	no	6	21	62	19	19
2		24	42	58	19	23
3[b]	A3	6	70	72	16	12
4[b]		24	88	60	23	17

[a]Yield determined by ^{1}H NMR spectroscopy of the crude product. [b]Reaction conducted in the presence of **A3** (0.5 equiv vs **1**). Conditions: oxo-carbonate **1** (4.06 mmol), DBU (0.203 mmol) in dry DMSO (1 mL) at 80 °C under a nitrogen atmosphere.

Scheme 3. Mechanism of Formation of Tetrasubstituted Ethylene Carbonate 2 by Addition of Benzyl Alcohol to αCC

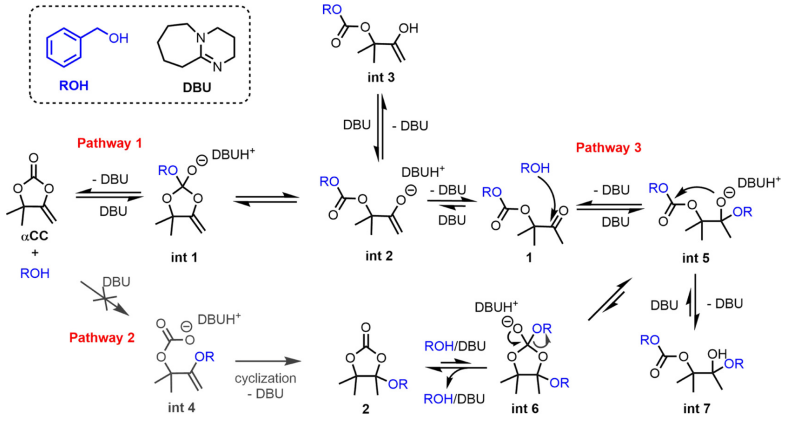

presence or absence of **A3** (0.5 equiv vs **1**). Table 2 shows the results. In both cases, the oxo-carbonate **1** was converted into tetrasubstituted ethylene carbonate **2** as the major product and into dibenzyl carbonate **3** and hydroxyketone **4** as the minor

https://dx.doi.org/10.1021/acssuschemeng.0c07683
ACS Sustainable Chem. Eng. 2021, 9, 1714−1728

Scheme 4. Gibbs-Free Energy Profile with the Corresponding Reaction Scheme and Transition-State Structures for Pathway 1 (p1) with the Formation of Oxo-carbonate 1 and for Pathway 3 (p3) with the Formation of Tetrasubstituted Ethylene Carbonate 2[a]

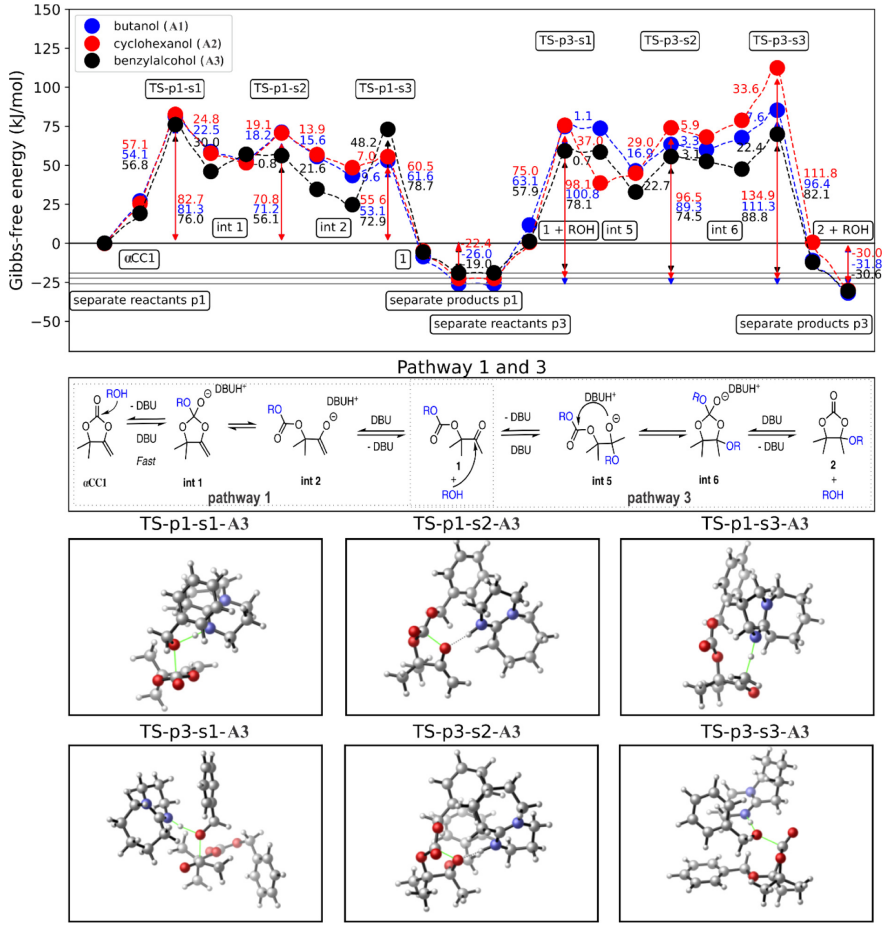

[a]The separate reactants for p3 are rescaled to the separate product of p1. Green bonds in the TS figures indicate bonds which are broken or formed. Energies in kJ·mol^{-1} (ωB97-XD/6-311++G**, IEFPCM (ϵ = 46.826), 298 K, 1 atm).

ones. The conversion of **1** increased with the reaction time, with a faster reaction noted in the presence of benzyl alcohol **A3**. Therefore, these experiments demonstrate that the formation of products **2**−**4** originated from a rearrangement of **1** and was accelerated by the addition of benzyl alcohol. The origin of these side products is of prime importance because these side reactions are expected to affect the polymer molar mass and microstructure. A thorough mechanistic investigation has therefore been performed in the next section.

Mechanistic Insight into the Alcoholysis of Exovinylene Cyclic Carbonate. Tetrasubstituted ethylene carbonates were identified by Costa et al. when αCC was generated *in situ* by the reaction of a propargylic alcohol with CO_2 in the presence of allyl alcohol or phenol catalyzed by superbases (7-methyl-1,5,7-triazabicyclo[4.4.0]dec-5-ene or 1,5,7-triazabicyclo[4.4.0]dec-5-ene) at 100 °C.[28] These side products were also observed by He et al. for similar reactions when phenol or allyl alcohol was substituted by benzyl alcohol in the presence of a silver salt (Ag_2CO_3/PPh_3) catalyst.[29] Although it was suggested that they might be formed by tautomerization of oxo-carbonate **1** and/or the addition of alcohol to the unsaturated double bond of αCC, the authors refrained from proposing any reaction mechanism.

https://dx.doi.org/10.1021/acssuschemeng.0c07683
ACS Sustainable Chem. Eng. 2021, 9, 1714−1728

Our experimental results presented in Table 1 indicate that only benzyl alcohol (**A3**) is able to form some tetrasubstituted ethylene carbonate **2**, while butanol (**A1**) and cyclohexanol (**A2**) only furnished the corresponding oxo-carbonates **1**, at least under the investigated conditions. In order to gain an insight into the origin of this reaction and to understand the importance of the structure of the alcohol on the reaction selectivity, density functional theory (DFT) calculations based on static and molecular dynamics simulations were performed (Supporting Information, Section S3).

One may suggest that the formation of tetrasubstituted ethylene carbonate **2** follows a similar reaction pathway as that used for the addition of thiols to αCC:[19] fast reversible formation of oxo-carbonate **1** by the DBU-catalyzed ring opening of αCC by benzyl alcohol (Scheme 3: pathway 1 and Supporting Information, Section S3.2.2) with the concomitant slow and irreversible addition of alcohol to the disubstituted C=C double bond forming tetrasubstituted ethylene carbonate **2** (Scheme 3: pathway 2 and Supporting Information, Section S3.2.3). However, our theoretical calculations suggest an alternative more favorable pathway for the formation of **2** starting from oxo-carbonate **1** (Scheme 3: pathways 1 and 3). Compound **1** reacts with benzyl alcohol (**A3**) that is also liberated through the reversible reaction from the carbonate. In these calculations, we accounted for the DBU catalyst and the solvent environment implicitly in the static simulations and explicitly for all intermediates in the MD simulations, respectively (Supporting Information, Section S3.1). The stability of various intermediates under operating conditions, and thus, the formation of **int 3** and **int 7** is more thoroughly discussed in the Supporting Information.

The free energy profile of the reaction (pathways 1 and 3) is shown in Scheme 4. A key feature is the acidic strength of alcohols with their pK_a values that are sufficiently high to disfavor the formation of the corresponding salt (alkoxide). Instead, alcohol and DBU form a strong hydrogen-bonded complex (Figure S18), which facilitates the subsequent reactions. Regular MD simulations of the reactant complex confirm this as they show that this hydrogen-bonded complex, and not the corresponding salt, dominates the reactant region (Supporting Information, Section S3.2.1). Furthermore, salt formation is not observed in any of the static calculations.

As shown in Scheme 4, the rate-limiting step for the formation of oxo-carbonate **1** is the nucleophilic addition of alcohol to the carbonate carbonyl of αCC (TS-p1-s1) with apparent activation energies of 76.0, 81.3, and 82.7 kJ·mol^{-1} for benzyl alcohol **A3**, butanol **A1**, and cyclohexanol **A2**, respectively (in agreement with the experiments). This mechanism is triggered by the formation of a catalyst−alcohol ion-pair complex with immediate (rate-limiting) attack of alcohol on the neighboring αCC. Based on the relative differences in the activation energies of different alcohols, which are <10 kJ·mol^{-1}, the oxo-carbonate **1** formation should occur for all alcohols used, which is confirmed experimentally (Table 1). The reverse apparent reaction barriers amount to 91.9, 79.1, and 78.0 kJ·mol^{-1} for **A1**, **A3**, and **A2**, respectively. Reverse activation energies are hence within the same order of magnitude as the forward one, which suggests the reversibility of this pathway.

Noteworthy is the presence of π−cation and π-induced dipole interactions between the catalyst DBU-H$^+$ and benzyl alcohol **A3**, which is (obviously) not present for **A1** and **A2** (Scheme 4 and Figure 2a,b). These interactions substantially

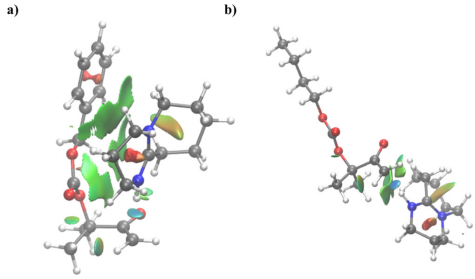

Figure 2. Non-covalent interaction plots for **int 2** with (a) benzyl alcohol and (b) butanol as the used alcohol. Green surfaces indicate weak vdW interactions, blue surfaces indicate strong stabilizing interactions (e.g., hydrogen bonding), and red surfaces indicate repulsive/destabilizing interactions.

lower the activation barrier for the formation of **int 2** (or hence for the reverse reaction) and have a strong stabilizing effect on this intermediate in contrast to the stability of **int 2** for **A1** and **A2** (Scheme 4). To illustrate this, non-covalent interaction plots are shown in Figures 2a and 2b, which indicate that **int 2** is indeed much more stable due to the presence of stabilizing interactions between the benzylic moiety and DBU-H$^+$ which are completely absent for butanol (and cyclohexanol) featuring aliphatic chains. Additionally, for benzyl alcohol, a (spontaneous) equilibrium reaction is observed between **int 2** and **int 3**; this can hence directly influence the equilibria in which **int 2** is involved (Supporting Information, Section S3.2.2, Figure S21 simulation 1 and simulation 2). An increased stability of **int 1** and **int 2**, induced by interactions between the benzylic group and DBU-H$^+$, and the extra equilibria between **int 2** and **int 3** can directly influence the reaction kinetics for both the forward and reverse pathways (and hence the subsequent formation of tetrasubstituted ethylene carbonate **2**), which is not possible for **A1** and **A2**.

Subsequently, as postulated by Lu et al.,[30] tetrasubstituted ethylene carbonate **2** can be formed through pathway 3 by a nucleophilic attack of a second alcohol molecule on the ketone of the formed oxo-carbonate **1**. This leads to the formation of **int 5** (Schemes 4 and 3, pathway 3), which is yet again the rate-determining step for this pathway. In contrast to pathway 1, we do observe significant differences for the rate-determining step of pathway 3 (>10 kJ·mol^{-1}) in line with the experimental results. Apparent activation energies for pathway 3, with respect to the separate reactants of pathway 3, are 78.1, 100.8, and 98.1 kJ·mol^{-1} for **A3**, **A1**, and **A2**, respectively. These barrier heights are in sharp contrast to the previously proposed pathway 2 (Supporting Information, Section S3.2.3, Scheme S2) as they are lowered by more than 50 kJ·mol^{-1}, showing that this new proposal is much more feasible. Furthermore, the trends for pathway 3 are in line with the experimental observations, which is not the case for pathway 2 (Supporting Information, Section S3.2.3, *vide infra*), that is, formation of tetrasubstituted ethylene carbonate is observed only for **A3**.

Intermediate stability is, similar to pathway 1, increased for benzyl alcohol, which can also be attributed to the induced π-type interactions. **Int 6** is clearly a metastable state which is prone to ring opening resulting in the formation of **int 5**. This metastability is also observed during the corresponding MD

https://dx.doi.org/10.1021/acssuschemeng.0c07683
ACS Sustainable Chem. Eng. 2021, 9, 1714−1728

simulations (Supporting Information, Section S3.2.4, Figure S23). Scheme 4 further indicates that the tetrasubstituted ethylene carbonate **2** is thermodynamically favored and that the reverse reaction barrier is drastically higher than for pathway 1 shifting the equilibrium in favor of **2**. Additionally, it is noted throughout the static and dynamic simulations that the DBU positioning is highly determining for the stability (Supporting Information, Sections S3.2.2 and S3.2.4 and Figure 2).

To elaborate on the differences for the different alcohols, rate constants are calculated for the rate-limiting steps, and the results are presented in Table 3. Both for pathways 1 and 3,

Table 3. Reaction Rates for the Rate-Determining Steps of Pathways 1 and 3 ($k_{1,p1}$ and $k_{1,p3}$, $M^{-2}\cdot s^{-1}$)[a]

alcohol	$k_{1,pathway1}$	$k_{1,pathway3}$	$k_{1,pathway1}/k_{1,pathway3}$
benzyl alcohol (**A3**)	3.05×10^{-1}	1.28×10^{-1}	2.4
butanol (**A1**)	3.58×10^{-2}	1.37×10^{-5}	2607.2
cyclohexanol (**A2**)	2.03×10^{-2}	3.98×10^{-5}	510.3

[a]Rate constants are calculated with respect to separate reactants or products. [ωB97-XD/6-311++G**, IEFPCM (ε = 46.826), 298 K, 1 atm].

benzyl alcohol **A3** has increased rate constants compared to those of butanol **A1** and cyclohexanol **A2**, especially for the latter pathway a substantial increase is observed, that is 4 orders of higher magnitude with respect to **A1** and **A2**. More interesting to compare are the ratios of the rate constants which give an indication for the preference of each system to proceed along a certain pathway in case all reactants are present, that is, oxo-carbonate **1** formation has already occurred. For benzyl alcohol, both pathways are almost equally likely, in contrast to butanol and cyclohexanol which show a large preference (up to 3 orders of magnitude) for pathway 1. This can hence explain why, assuming that the reversibility of pathway 1 is feasible for all alcohols, no tetrasubstituted ethylene carbonate is observed for either butanol and cyclohexanol.

As illustrated in Scheme 5, the side products **3** and **4** observed for the model reaction reported in Table 1 for **A3** can reasonably be obtained by the DBU-promoted transcarbonation of product **1** with benzyl alcohol as the α-hydroxyketone is a good leaving group, as also suggested by He et al.[29] In accordance with this, **3** and **4** are indeed formed in almost identical amounts. Assuming reactivity similar to pathway 1 for the different alcohols, the transcarbonation route is expected to proceed more easily for benzyl alcohol than for the aliphatic alcohols **A1** and **A2**.

Calculation of Parr functions enabled the elaboration of the difference in chemoselectivity of the alcohol attack on oxo-carbonate **1**, that is, its preferential addition to the ketone (C═O) (to form the tetrasubstituted ethylene carbonate **2**) or carbonate ((O)C═O) group (to form **3** and **4**) (Supporting Information, Sections S3.1.3 and S3.3). They showed that the formation of tetrasubstituted ethylene carbonate **2** is preferential over the transcarbonation route as C═O is more electrophilic than the carbonate site, and is therefore more prone to nucleophilic attack. This chemoselectivity is in line with the experimental results presented in Table 1.

From these modeling studies, it therefore appears that the formation of tetrasubstituted ethylene carbonate **2** proceeds through a nucleophilic attack of alcohol on the formed oxo-carbonate **1** (Scheme 3). This route explains the experimental observations and the difference in reactivity for the three different alcohols. Additionally, it is found that the DBU catalyst affects the intermediate stability. On one hand, it forms a strong hydrogen-bonded complex with the alcohol. On the other hand, for the specific combination of benzyl alcohol **A3** and DBU, it is shown that π-type interactions (e.g., cation−π, π−π, and π-induced dipole interactions) enable extra stabilization of various intermediates, which potentially increase the reaction rates. Finally, reactivity descriptors show the preference of the ketone group over carbonate toward nucleophilic attack, which explains the observed difference in yield for the tetrasubstituted ethylene carbonate **2** and the products **3** and **4** that result from the trans-carbonation route.

Synthesis of Poly(oxo-carbonate)s by Polyaddition of BisαCCs with Biosourced Diols. A series of novel poly(β-oxo-carbonate)s were prepared by the polyaddition of two different CO_2-sourced bisαCC, that is, meso-4,4′-(ethane-1,2-diyl)bis(4-methyl-5-methylene-1,3-dioxolan-2-one) (**C1**) and 1,9-dimethylene-2,4,10,12-tetraoxodispiro[4.2.4^8.2^5]-tetradecane-3,11-dione (**C2**) with equimolar amounts of sugar-(1,4-butanediol **S1** or isosorbide **S2**) or lignin-derived (1,4-benzenedimethanol **L1** or *trans*-1,4-cyclohexanediol **L2**) diols (Scheme 6, Table 4). **S1** was here used as a benchmark diol.

Polymerizations at 25 °C. First, all copolymerizations were carried out at 25 °C using DBU as an organocatalyst (5 mol % compared to **C1** or **C2**) in dry DMSO (C = 0.78 M). For all PCs synthesized, the ^{1}H NMR spectra showed a full monomer consumption after 24 h. The copolymerization of *meso*-bisαCC **C1** and 1,4-butanediol (**S1**) or isosorbide (**S2**) was homogeneous during the reaction and gave poly(oxo-carbonate)s **C1S1** and **C1S2** with weight-average molar masses (M_w) of 26,700 and 9300 g/mol, respectively (Table 4, entries 1 and 2, Figure S24). Their characterization by ^{1}H and ^{13}C NMR spectroscopy gave clear insights into the formation of regioregular oxo-carbonate linkages and the absence of polymer defects (Figure 3). The ^{1}H NMR spectra highlighted the typical resonances of methylene of **C1S1** (δ =

Scheme 5. Chemoselectivity in the DBU-Catalyzed Addition of Alcohol to Oxo-carbonate

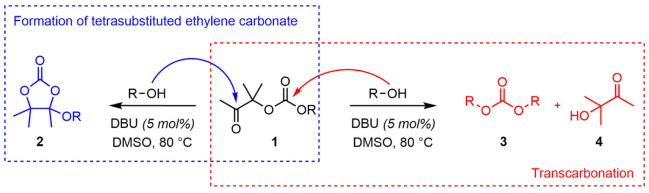

https://dx.doi.org/10.1021/acssuschemeng.0c07683
ACS Sustainable Chem. Eng. 2021, 9, 1714−1728

Scheme 6. Scope of Poly(oxo-carbonate)s Synthesized by Organocatalyzed Step-Growth Copolymerization of CO_2-Sourced bisαCCs with Bio-Based Diols

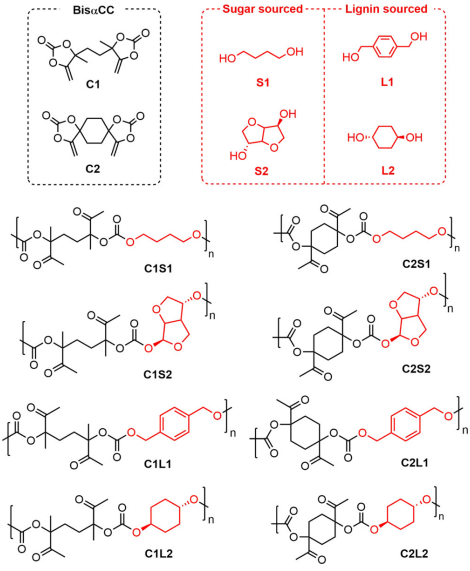

4.10 ppm) or methine of **C1S2** (δ = 5.01 ppm) adjacent to the oxo-carbonate linkages as well as signals at δ = 2.10−2.14 ppm from the methyl group of the pendant ketone moiety. The formation of oxo-carbonate linkages was further confirmed by the ^{13}C NMR resonances typical for the oxo and carbonate groups at δ = 206.0−206.5 ppm and δ = 152.9−153.6 ppm, respectively. Changing *meso*-bisαCC **C1** for *spiro*-bisαCC **C2** gave two new polymers, **C2S1** and **C2S2**, with different solubility behaviors (Table 4, entries 5 and 6). While **C2S2** displayed a M_w of 10,000 g/mol that remained soluble in DMSO during the course of the polymerization, **C2S1** precipitated during its formation and was found to be insoluble in all common organic solvents making the determination of its molar mass by SEC analysis impossible. ^{1}H and ^{13}C NMR spectra of **C2S2** gave the typical signatures of a regioregular poly(oxo-carbonate) (Figure 3). The microstructure of **C2S1** was elucidated by solid-state ^{13}C NMR spectroscopy that confirmed the formation of PC by the presence of ketone and carbonate signals at δ = 207.3 ppm and δ = 154.4 ppm, respectively (Figure S25).

The scope of poly(oxo-carbonate)s was extended to the copolymerization of **C1** or **C2** with the lignin-derived diols **L1** and **L2** (Table 4, entries 3, 4, 7, and 8). Initially, the medium was homogeneous, but the four PCs precipitated during their formation in DMSO. After 24 h, the polymers were isolated by filtration and found to be insoluble in the solvent used for SEC (DMF/LiBr or THF). However, **C1L1** and **C1L2** were found to be soluble in $CHCl_3$, and their molecular parameters were thus determined by SEC in $CHCl_3$. SEC analysis provided M_w of 13,600 g/mol for **C1L1** and 9400 g/mol for **C1L2** (Figure S26). Their ^{1}H and ^{13}C NMR spectra confirmed the formation of the corresponding regioregular poly(oxo-carbonate)s (Figure 3). As **C2L1** and **C2L2** were insoluble in many common organic solvents ($CHCl_3$, THF, DMF, DMSO, etc.), their structural characterization was only possible by solid-state ^{13}C NMR spectroscopy. Both **C2L1** and **C2L2** displayed the microstructure of a poly(oxo-carbonate) (Figure S27).

To attest for the microstructure of the polymers and get further insights into the nature of the chain-ends, the poly(oxo-carbonate) **C1S1** was selected for characterization by mass spectrometry (Figure 4). At first sight, a difference of 344 amu between each signal in the **C1S1** distributions confirms the presence of the corresponding oxo-carbonate units within the

Table 4. Poly(oxo-carbonate)s Synthesized by DBU-Catalyzed Step-Growth Copolymerization of bisαCCs with Various Diols at 25 °C: Molecular Characteristics and Thermal Properties[a]

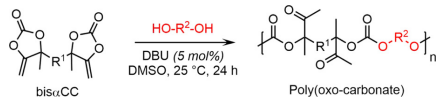

entry	polymer	M_n (g/mol)[b]	M_w (g/mol)[b]	$Đ$[b]	$T_{deg.10\%}$ (°C)[d]	T_g/T_m (°C)	X_c (%)[i] at RT
1	**C1S1**	13,400	26,700	1.99	265	41/60[e]	10
2	**C1S2**	4500	9300	2.06	256	88/--[g]	0
3	**C1L1**	6000[c]	13,600[c]	2.24[c]	216	71/84[e]	8
4	**C1L2**	6000[c]	9400[c]	1.57[c]	257	95/119[e]	8
5	**C2S1**	[h]	[h]	[h]	255	97/253[f]	46
6	**C2S2**	6800	10,000	1.47	253	153/174[e]	0
7	**C2L1**	[h]	[h]	[h]	239	104/282[f]	25
8	**C2L2**	[h]	[h]	[h]	271	--/343[f]	36

[a]Conditions: bisαCC (3.93 mmol), alcohol (3.93 mmol), DBU (0.196 mmol) in dry DMSO (5 mL) at 25 °C under a nitrogen atmosphere for 24 h. [b]Determined by SEC in DMF/LiBr. [c]Determined by SEC in $CHCl_3$. [d]Determined by TGA at 10% of weight loss. [e]Determined by FDSC analysis. The reported values of T_m were taken from the heating runs at 5000 K/s and after cooling the sample at 0.1 K/s. The reported values of T_g were taken from the heating runs at 1000 K/s and after cooling the sample at 4000 K/s. [f]Determined by FDSC analysis. The reported values of T_m and T_g were taken from the first scan at a heating rate of 20,000 K/s (to avoid degradation); The T_m values can be a mix between degradation and melting. [g]Determined by DSC analysis. [h]The polymer is insoluble in common organic solvents ($CHCl_3$, THF, DMF, or DMSO). [i]Degree of crystallinity of the powder from synthesis. The software Origin was employed to deconvolute WAXS patterns into amorphous and crystalline contributions, obtaining the degree of crystallinity by dividing the area under the crystalline peaks by the total area under the diffractogram.

https://dx.doi.org/10.1021/acssuschemeng.0c07683
ACS Sustainable Chem. Eng. 2021, 9, 1714−1728

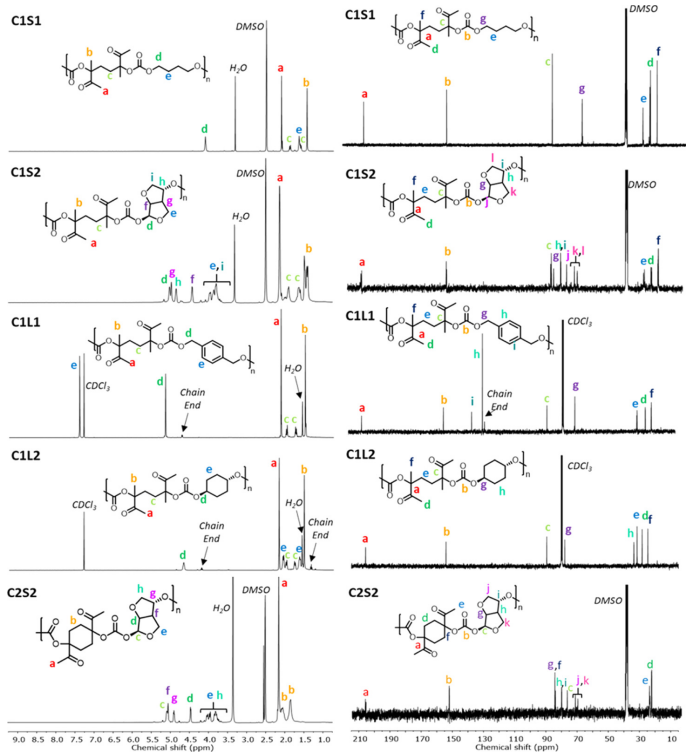

Figure 3. ^{1}H- and ^{13}C NMR characterization of poly(oxo-carbonate)s **C1S1** and **C1S2** (in DMSO-d_6), **C1L1** and **C1L2** (in $CDCl_3$), and **C2S2** (in DMSO-d_6).

polymers. Although the mass parameters (M_n or M_w) could not be determined due to the high molar-mass dispersity, the structural information also reveals that linear chains coexist with cyclic species (macrocyclic chains). The presence of macrocycles may arise from the end-to-end cyclization of the growing chains, as often observed in step-growth polymerization reactions.[31,32] **C1S1** displayed two types of chains with different end-groups. The most intense population is attributed to a linear poly(oxo-carbonate) terminated with butanediol units. The second linear distribution is associated with poly(oxo-carbonate) end-capped at one extremity by a hydroxyketone (e.g., m/z 3439.5), which may originate from the hydrolysis of the exovinylene chain-end upon MALDI characterization. It is also important to note that the cyclic species are mainly detected at low molecular weights and are probably overestimated.

Polymerizations at 80 °C. In order to accelerate the polymerizations and tentatively target PCs of higher molar masses, the polymerizations were carried out at 80 °C. For these studies, only *meso*-bisαCC **C1** was considered as it provided (at 25 °C) polymers that were soluble in common organic solvents and that could be characterized by liquid-state NMR spectroscopy and SEC analysis. For the sake of comparison, all experimental conditions were identical to the previous polymerizations, except for the temperature (80 vs 25 °C), and results are compared in Table 5. As determined by ^{1}H NMR spectroscopy for all PCs synthesized, **C1** was totally consumed after 24 h. When **C1** was copolymerized with **S1** or **L2**, polymers with oxo-carbonate linkages were obtained (Table 5, entries 1 and 3). No tetrasubstituted ethylene carbonate-type linkages were evidenced by ^{1}H NMR spectroscopy, at least within the detection limits of the technique (Figures S28 and S29, S30 and S31). These observations matched with our model reactions between αCC and **A1** or **A2** realized at 80 °C that did not reveal the formation of a 5-membered cyclic carbonate. Surprisingly, both **C1S1** and **C1L2** displayed significantly lower M_w compared to those measured for the same polymer produced at 25 °C. Indeed, **C1S1** prepared at 80 °C presented a M_w of 7000 g/mol at 80 °C (vs 26,700 g/mol at 25 °C) and **C1L2** a M_w of 7500 g/mol (vs 9400 g/mol at 25 °C) (entries 1 and 3, Table 5) (Figures S32 and S33). The transcarbonation reaction between the hydroxyl chain ends of the growing polymers and the oxo-carbonate linkages (that was favored at high temperatures, as demonstrated in the model reactions) was assumed to be responsible for the lower molar masses observed at 80 °C (Scheme 7). This side reaction left a polymer chain-end capped by an unreactive hydroxyketone and a polymer chain

https://dx.doi.org/10.1021/acssuschemeng.0c07683
ACS Sustainable Chem. Eng. 2021, 9, 1714−1728

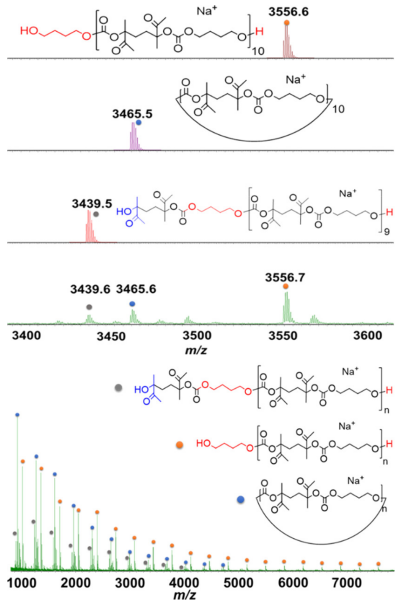

Figure 4. MALDI mass spectrum recorded for **C1S1**; the bottom part of the figure corresponds to the experimental mass spectrum, while the upper part is a magnification of the m/z area between 3400 and 3600 g/mol, showing a comparison between the experimental mass spectrum and the theoretical isotopic model.

bearing a new carbonate linkage. The presence of the hydroxyketone chain end was suggested by the presence of new singlets in the ^{1}H NMR spectra of **C1S1** or **C1L2** at 2.22 ppm (characteristic of a methyl group attached to an oxo group) and 1.30 ppm. The presence of a shoulder at 4.07 ppm (for **C1S1**) or 4.46 ppm (for **C1L2**) in the signals typical for the methylene or methine adjacent to the oxo-carbonate moieties attested the new carbonate linkage resulting from this transcarbonation reaction. By comparison of the relative intensities of peaks at 2.22 and 2.10 ppm, one quantified the level of the carbonate defect to 4% for **C1S1** and 6% for **C1L2**.

The occurrence of the transcarbonation side reaction on the polymer molar mass was further illustrated by carrying out three identical polymerizations of **C1** with **S1** at 80 °C and by stopping them at different periods of time (1, 6, and 24 h). The results are presented in Table S4 (Supporting Information). It comes out that the comonomers were rapidly consumed at the early stage of the reaction, giving the formation of a polymer of moderate molar mass (M_w = 10,000 g/mol after 1 h). However, with the reaction time, the polymer molar mass was decreased to 5800 g/mol after 24 h due to the occurrence of the transcarbonation reaction. This polymer molar mass is also illustrated in Figure S34 with the SEC chromatograms that shifted toward lower molar mass values with the reaction time. The transcarbonation was, however, slow and long reaction times were needed to observe the structural defects on the polymer.

When **C1** was copolymerized with **L1**, a polymer with a low M_w of 3500 g/mol (vs 13,600 g/mol at 25 °C) was synthesized after 24 h (Table 5, entry 2, Figure S35). Here also, PCs terminated by the hydroxyketone moiety and bearing some carbonate defects originating from the transcarbonation reaction were observed at a content of 8%. In contrast to the two previous examples, one also noticed the formation of additional five-membered cyclic carbonate linkages within the polymer microstructure with a content of 12%, as determined by ^{1}H NMR spectroscopy (Figure S36), in accordance with the model reactions with benzyl alcohol. Indeed, new methylene and methyl resonances of a tetrasubstituted ethylene carbonate unit were detected at 4.50, 1.63, and 1.45 ppm. The formation of these cyclic carbonate moieties was further corroborated by ^{13}C NMR spectroscopy by a new carbonyl signal at 145.0 ppm, two quaternary carbons at 82.3 and 108.2 ppm, and two methyl peaks attached to the carbonate cycle at 23.1 and 26.0 ppm (Figure S37).

Conclusively, structural defects were generated within the PC backbone when polymerizations were carried out at 80 °C, at least for long reaction times. They resulted from a slow transcarbonation reaction that furnished carbonate defect linkages and end-capped hydroxyketone PCs. In some cases (with 1,4-benzenedimethanol), an additional side reaction occurred by the slow addition of alcohol to the ketone group of the oxo-carbonate followed by cyclisation, forming a cyclic carbonate linkage in line with the observations made on the model reactions.

Thermal Properties of Poly(oxo-carbonate)s. The thermal properties of all defect-free poly(oxo-carbonate)s prepared at 25 °C were evaluated by TGA, standard DSC, and differential fast scanning calorimetry (FDSC), whose results are summarized in Table 4. The thermal degradation profiles of PCs are illustrated in Figure S38. The four polymers **C1S1**, **C1S2**, **C2S1**, and **C2S2** displayed moderate thermal stabilities with decomposition temperatures at 10% weight loss, $T_{d10\%}$, between 255 and 265 °C. Copolymers made from **L2** showed thermal stability in the same range of temperature with a $T_{d10\%}$ of 257 and 271 °C, respectively, for **C1L2** and **C2L2**. Changing the aliphatic diols by the aromatic diol **L1** led to polymers **C1L1** and **C2L1** with lower thermal stability, as attested by $T_{d10\%}$ of 216 and 239 °C. PCs containing the aromatic group also left some char at 600 °C (6 wt % for **C1L1** and 14 wt % for **C2L1**), whereas all other aliphatic PCs were almost completely decomposed at this temperature.

Remarkably, all poly(oxo-carbonate)s reported in Table 4 were able to crystallize (except for the sample **C1S2** that remained amorphous), as indicated by the reported melting point values. The glass-transition temperature (T_g) and the melting temperature (T_m) of the semicrystalline PCs were determined by standard DSC and FDSC. FDSC was employed to quench semi-crystalline samples employing cooling rates of 4000 °C/s. In this way, the fastest crystallizing samples were either quenched to the amorphous state or their crystallinities were substantially reduced. The T_g could therefore be easily determined during a subsequent heating scan. When the melting point of the sample was higher than 200 °C, the FDSC was used to heat the sample at 20,000 °C/s to avoid degradation as much as possible and still detect the melting endotherm.

From the copolymer series illustrated in Table 4, **C1S2** made from *meso*-bisαCC and isosorbide was amorphous with only a T_g at 88 °C (Figure S39). All the other samples were

https://dx.doi.org/10.1021/acssuschemeng.0c07683
ACS Sustainable Chem. Eng. 2021, 9, 1714−1728

Table 5. Comparison of the Structure of the Carbonate Linkages and Macromolecular Characteristics of the PCs Prepared by DBU-Catalyzed Copolymerization of bisαCCs with Diols at 25 and 80 °C in dry DMSO[a]

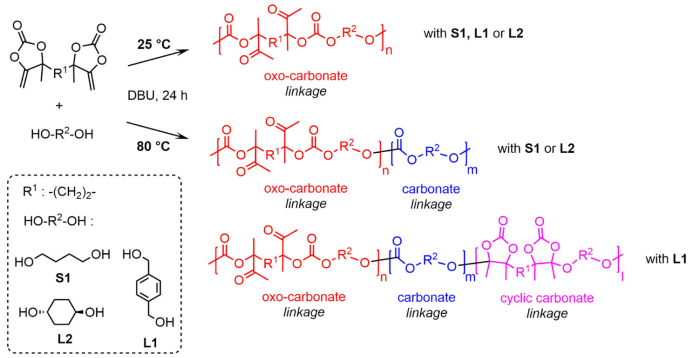

entry	polymer	T (°C)	Conv. C1 (%)	oxo-carbonate linkage (%)	cyclic carbonate linkage (%)	carbonate linkage (%)	M_n (g/mol)[b]	M_w (g/mol)[b]	$Đ$[b]
1	**C1S1**	25	>99	100	0	0	13,400	26,700	1.99
		80	>99	96	0	4	3800	7000	1.84
2	**C1L1**	25	>99	100	0	0	6000[c]	13,600[c]	2.24[c]
		80	>99	80	12	8	1900[c]	3500[c]	1.83[c]
3	**C1L2**	25	>99	100	0	0	6000[c]	9400[c]	1.57[c]
		80	>99	94	0	6	3300[c]	7500[c]	2.25[c]

[a]Conditions: bisαCC (3.93 mmol), alcohol (3.93 mmol), DBU (0.196 mmol) in dry DMSO (5 mL) at 25 or 80 °C, under a nitrogen atmosphere. [b]Determined by SEC in DMF/LiBr. [c]Determined by SEC in $CHCl_3$.

Scheme 7. Transcarbonation Reaction between the Hydroxyl Chain Ends of the Growing Polymers and the Oxo-carbonate Linkages

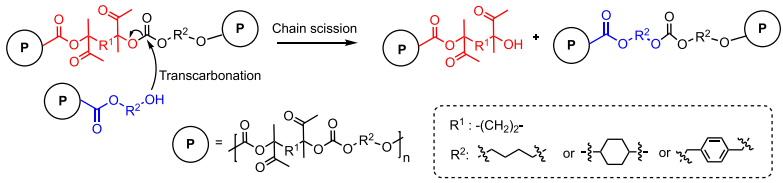

semi-crystalline, and their T_g and T_m values are reported in Table 4 (Figures S40–S46). Based on their chemical structures illustrated in Scheme 6, a close correlation was found between the high values of T_g/T_m transitions and the chain rigidity in most cases, as expected.

Figure 5 shows the WAXS diffractograms of selected samples. The presence of well-defined diffraction peaks confirmed the semi-crystalline character of the samples. Their crystallinities were estimated by deconvoluting the areas of the WAXS patterns into amorphous and crystalline contributions. Then, the degree of crystallinity was obtained by dividing the area under the crystalline peaks by the total area under the diffractogram. Crystallinity values varied from 8% for the less crystalline **C1L2** sample to 46% for the most crystalline **C2S1** sample (entries 4 and 5, Table 4). The crystalline structure of the novel poly(oxo-carbonate)s prepared here is unknown, so we cannot assign the reflections to the crystallographic planes that originate them. Establishing the crystalline structure of polymers is, however, beyond the scope of the present paper. Nevertheless, judging by the

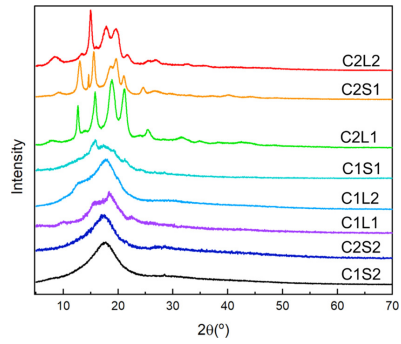

Figure 5. WAXS patterns taken at room temperature of poly(oxo-carbonate)s.

https://dx.doi.org/10.1021/acssuschemeng.0c07683
ACS Sustainable Chem. Eng. 2021, 9, 1714−1728

changes in diffraction angles and their corresponding distances (Supporting Information, Table S5), the polymers all crystallized in different types of unit cells, as their chemical structure varies significantly from one another, and hence, in molecular chain packing within their respective crystalline structures.

CONCLUSIONS

The emergence of CO_2-sourced exovinylene bicyclic carbonates (bisαCCs) in polymer science prompted us to investigate the scope and limitations of their organocatalyzed step-growth copolymerization with biorenewable diols to PCs. Model reactions were first carried out on small molecules in order to understand the structural influence of alcohols, the temperature (25 or 80 °C), and the use of an organocatalyst (DBU) on the rate of cyclic carbonate ring-opening and product selectivity. Based on these studies, a series of regioregular and defect-free poly(oxo-carbonate)s of different structures and reasonable molar masses (M_w up to 26,700 g/mol) were prepared at 25 °C using sugar- (1,4-butanediol and isosorbide) or lignin-derived (1,4-benzenedimethanol and 1,4-cyclohexanediol) diols and two different CO_2-sourced bis-αCCs. By performing the polymerizations at 80 °C, structural defects were, however, introduced within the poly(oxo-carbonate) chains, that is, a second type of carbonate linkage originated from transcarbonation reactions in all cases. When 1,4-benzenedimethanol was used, an additional side reaction was noted and provided tetrasubstituted ethylene carbonate linkages. These side reactions observed at 80 °C limited the polymer molar mass for long reaction times. The mechanism of formation of these side reactions was considered by DFT modeling on model compounds. It was found that the tetrasubstituted ethylene carbonate linkage proceeded through a nucleophilic attack of the alcohol on the ketone group of the formed oxo-carbonate, inducing cyclization. Importantly, the DBU catalyst influenced the intermediate stability. It formed a strong hydrogen-bonded complex with the alcohol and, for the specific combination of benzyl alcohol (a model compound of 1,4-benzenedimethanol) and DBU, π-type interactions (e.g., cation$-\pi$, $\pi-\pi$, and π-induced dipole interactions) were noted and enabled extra stabilization of various intermediates, which potentially increased the reaction rates. Finally, reactivity descriptors enabled explaining the observed difference in yield for the tetrasubstituted ethylene carbonate linkage and the linear carbonate (originating from transcarbonation).

Finally, the thermal properties of poly(oxo-carbonate)s designed at 25 °C were evaluated by thermogravimetry (TGA), standard DSC, and FDSC. Depending on their microstructures, poly(oxo-carbonate)s presented a degradation temperature between 216 and 271 °C. With the exception of one poly(oxo-carbonate) made from isosorbide that was amorphous with a glass-transition temperature (T_g) of 88 °C, all the other PCs were semi-crystalline with a melting temperature (T_m) ranging from 60 to 343 °C. Preliminary WAXS studies confirmed the ability of these PCs to crystallize.

This work highlights the potential of this process for the facile preparation of PCs using diols and carbon dioxide as bioresources under mild reaction conditions and shows how the polymer linkages can be modified by the experimental conditions. The fraction of biorenewables (CO_2 + diol) incorporated in the polymers is high (50−60 wt %), attesting for the importance of the process for the more sustainable production of plastics. The level of sustainability of these materials might be further increased by proposing greener routes to producing bisαCCs. Indeed, their current synthesis uses petro-based diones (1,4-cyclohexanone or 2,5-hexanedione in this work) and Grignard's reagent (ethynyl magnesium bromide) to prepare the propargylic alcohols needed for coupling to CO_2. Bio-based approaches might consist of starting from 1,4-cyclohexanone prepared from succinic acid[33] or 2,5-hexanedione obtained by the hydrolysis of sugar-derived 2,5-dimethylfuran.[34,35] Grignard reagents will still have to be used; however, bispropargylic alcohols might be easily obtained from calcium carbide as the acetylene source.[36,37]

ASSOCIATED CONTENT

Supporting Information

The Supporting Information is available free of charge at https://pubs.acs.org/doi/10.1021/acssuschemeng.0c07683.

^{1}H and ^{13}C NMR spectra of model compounds and polymers; GC-FID and MS spectra of model reactions; DFT calculations of the side reaction and DFT protocols; and SEC chromatograms, TGA curves, and DSC and FDSC curves of polymers (PDF)

AUTHOR INFORMATION

Corresponding Authors

Veronique Van Speybroeck − *Center for Molecular Modeling, University of Ghent, 9052 Zwijnaarde, Belgium;* orcid.org/0000-0003-2206-178X; Email: veronique.vanspeybroeck@ugent.be

Bruno Grignard − *Center for Education and Research on Macromolecules (CERM), CESAM Research Unit, University of Liège, 4000 Liege, Belgium;* orcid.org/0000-0002-6016-3317; Email: bruno.grignard@uliege.be

Christophe Detrembleur − *Center for Education and Research on Macromolecules (CERM), CESAM Research Unit, University of Liège, 4000 Liege, Belgium;* orcid.org/0000-0001-7849-6796; Email: christophe.detrembleur@uliege.be

Authors

Fabiana Siragusa − *Center for Education and Research on Macromolecules (CERM), CESAM Research Unit, University of Liège, 4000 Liege, Belgium*

Elias Van Den Broeck − *Center for Molecular Modeling, University of Ghent, 9052 Zwijnaarde, Belgium;* orcid.org/0000-0002-9609-4333

Connie Ocando − *POLYMAT and Faculty of Chemistry, University of the Basque Country UPV/EHU, 20018 Donostia-San Sebastián, Spain;* orcid.org/0000-0003-4123-1879

Alejandro J. Müller − *POLYMAT and Faculty of Chemistry, University of the Basque Country UPV/EHU, 20018 Donostia-San Sebastián, Spain; IKERBASQUE, Basque Foundation for Science, Bilbao 48013, Spain;* orcid.org/0000-0001-7009-7715

Gilles De Smet − *Organic Synthesis Division, Department of Chemistry, University of Antwerp, 2020 Antwerp, Belgium*

Bert U. W. Maes − *Organic Synthesis Division, Department of Chemistry, University of Antwerp, 2020 Antwerp, Belgium;* orcid.org/0000-0003-0431-7606

Julien De Winter − *Mass Spectrometry Research Group, Interdisciplinary Center of Mass Spectrometry (CISMa),*

University of Mons, 7000 Mons, Belgium; orcid.org/0000-0003-3429-5911

Complete contact information is available at: https://pubs.acs.org/10.1021/acssuschemeng.0c07683

Notes

The authors declare no competing financial interest.

■ ACKNOWLEDGMENTS

The authors from Liege, Ghent, and Antwerp thank the "Fonds National pour la Recherche Scientifique" (F.R.S.-FNRS) and the Fonds Wetenschappelijk Onderzoek—Vlaanderen (FWO) for financial support in the frame of the EOS project no. O019618F (ID EOS: 30902231). The authors from Liege thank the CESAM Research Unit for financial support and Dr. Olivier Coulembier (University of Mons, Belgium) for SEC analyses of $CHCl_3$. C.O. acknowledges "Diputación Foral de Gipuzkoa" in the framework program "Fellows Gipuzkoa de Atracción y Retención de Talento". The authors thank for the technical and human support provided by SGIker (UPV/EHU/ERDF, EU), in particular, to the general X-ray service of the UPV/EHU: Molecules and Material unit. C.D. is the F.R.S.-FNRS Research Director. B.U.W.M. thanks the Francqui Foundation for appointment as the Collen-Francqui professor. The computational resources and services used were provided by Ghent University (Stevin Supercomputer Infrastructure), the VSC (Flemish Supercomputer Center), funded by the Research Foundation—Flanders (FWO). This work was supported by the Research Board of the Ghent University (BOF). The UMONS MS laboratory acknowledges F.R.S.-F.N.R.S. for its contribution to the acquisition of the Waters QToF Premier mass spectrometer and for continuing support.

■ REFERENCES

(1) Kyriacos, D. *Polycarbonates*; Elsevier Ltd, 2017.

(2) Fukuoka, S.; Tojo, M.; Hachiya, H.; Aminaka, M.; Hasegawa, K. Green and Sustainable Chemistry in Practice: Development and Industrialization of a Novel Process for Polycarbonate Production from CO_2 without Using Phosgene. *Polym. J.* **2007**, *39*, 91−114.

(3) Kim, W. B.; Joshi, U. A.; Lee, J. S. Making Polycarbonates without Employing Phosgene: An Overview on Catalytic Chemistry of Intermediate and Precursor Syntheses for Polycarbonate. *Ind. Eng. Chem. Res.* **2004**, *43*, 1897−1914.

(4) Fukuoka, S.; Fukawa, I.; Adachi, T.; Fujita, H.; Sugiyama, N.; Sawa, T. Industrialization and Expansion of Green Sustainable Chemical Process: A Review of Non-Phosgene Polycarbonate from CO_2. *Org. Process Res. Dev.* **2019**, *23*, 145−169.

(5) Grignard, B.; Gennen, S.; Jérôme, C.; Kleij, A. W.; Detrembleur, C. Advances in the Use of CO_2 as a Renewable Feedstock for the Synthesis of Polymers. *Chem. Soc. Rev.* **2019**, *48*, 4466−4514.

(6) Tamura, M.; Ito, K.; Honda, M.; Nakagawa, Y.; Sugimoto, H.; Tomishige, K. Direct Copolymerization of CO_2 and Diols. *Sci. Rep.* **2016**, *6*, 24038.

(7) Huang, J.; Worch, J. C.; Dove, A. P.; Coulembier, O. Update and Challenges in Carbon Dioxide-Based Polycarbonate Synthesis. *ChemSusChem* **2020**, *13*, 469−487.

(8) Schutyser, W.; Renders, T.; Van Den Bosch, S.; Koelewijn, S.-F.; Beckham, G. T.; Sels, B. F. Chemicals from Lignin: An Interplay of Lignocellulose Fractionation, Depolymerisation, and Upgrading. *Chem. Soc. Rev.* **2018**, *47*, 852−908.

(9) Sun, Z.; Fridrich, B.; De Santi, A.; Elangovan, S.; Barta, K. Bright Side of Lignin Depolymerization: Toward New Platform Chemicals. *Chem. Rev.* **2018**, *118*, 614−678.

(10) Gong, Z.-J.; Li, Y.-R.; Wu, H.-L.; Lin, S. D.; Yu, W.-Y. Direct Copolymerization of Carbon Dioxide and 1,4-Butanediol Enhanced by Ceria Nanorod Catalyst. *Appl. Catal., B* **2020**, *265*, 118524−118536.

(11) Jiang, Z.; Chen, L.; Wenchun, X.; Gross, R. A. Controlled Lipase-Catalyzed Synthesis of Poly(Hexamethylene Carbonate). *Macromolecules* **2007**, *40*, 7934−7943.

(12) Meabe, L.; Lago, N.; Rubatat, L.; Li, C.; Müller, A. J.; Sardon, H.; Armand, M.; Mecerreyes, D. Polycondensation as a Versatile Synthetic Route to Aliphatic Polycarbonates for Solid Polymer Electrolytes. *Electrochim. Acta* **2017**, *237*, 259−266.

(13) Sun, J.; Kuckling, D. Synthesis of High-Molecular-Weight Aliphatic Polycarbonates by Organo-Catalysis. *Polym. Chem.* **2016**, *7*, 1642−1649.

(14) Naik, P. U.; Refes, K.; Sadaka, F.; Brachais, C.-H.; Boni, G.; Couvercelle, J.-P.; Picquet, M.; Plasseraud, L. Organo-Catalyzed Synthesis of Aliphatic Polycarbonates in Solvent-Free Conditions. *Polym. Chem.* **2012**, *3*, 1475−1480.

(15) Gennen, S.; Grignard, B.; Tassaing, T.; Jérôme, C.; Detrembleur, C. CO_2 -Sourced α-Alkylidene Cyclic Carbonates: A Step Forward in the Quest for Functional Regioregular Poly(Urethane)s and Poly(Carbonate)S. *Angew. Chem., Int. Ed.* **2017**, *56*, 10394−10398.

(16) Ouhib, F.; Meabe, L.; Mahmoud, A.; Eshraghi, N.; Grignard, B.; Thomassin, J.-M.; Aqil, A.; Boschini, F.; Jérôme, C.; Mecerreyes, D.; Detrembleur, C. CO_2 -Sourced Polycarbonates as Solid Electrolytes for Room Temperature Operating Lithium Batteries. *J. Mater. Chem. A* **2019**, *7*, 9844−9853.

(17) Gennen, S.; Grignard, B.; Jérôme, C.; Detrembleur, C. CO_2-Sourced Non-Isocyanate Poly(Urethane)s with PH-Sensitive Imine Linkages. *Adv. Synth. Catal.* **2019**, *361*, 355−365.

(18) Habets, T.; Siragusa, F.; Grignard, B.; Detrembleur, C. Advancing the Synthesis of Isocyanate-Free Poly(Oxazolidones)s: Scope and Limitations. *Macromolecules* **2020**, *53*, 6396−6408.

(19) Ouhib, F.; Grignard, B.; Van Den Broeck, E.; Luxen, A.; Robeyns, K.; Van Speybroeck, V.; Jerome, C.; Detrembleur, C. A Switchable Domino Process for the Construction of Novel CO_2 -Sourced Sulfur-Containing Building Blocks and Polymers. *Angew. Chem., Int. Ed.* **2019**, *58*, 11768−11773.

(20) Dabral, S.; Schaub, T. The Use of Carbon Dioxide (CO_2) as a Building Block in Organic Synthesis from an Industrial Perspective. *Adv. Synth. Catal.* **2019**, *361*, 223−246.

(21) Ouhib, F.; Meabe, L.; Mahmoud, A.; Grignard, B.; Thomassin, J.-M.; Boschini, F.; Zhu, H.; Forsyth, M.; Mecerreyes, D.; Detrembleur, C. Influence of the Cyclic versus Linear Carbonate Segments in the Properties and Performance of CO_2 -Sourced Polymer Electrolytes for Lithium Batteries. *ACS Appl. Polym. Mater.* **2020**, *2*, 922−931.

(22) Dabral, S.; Licht, U.; Rudolf, P.; Bollmann, G.; Hashmi, A. S. K.; Schaub, T. Synthesis and Polymerisation of α-Alkylidene Cyclic Carbonates from Carbon Dioxide, Epoxides and the Primary Propargylic Alcohol 1,4-Butynediol. *Green Chem.* **2020**, *22*, 1553−1558.

(23) Tounzoua, C. N.; Grignard, B.; Brege, A.; Jerome, C.; Tassaing, T.; Mereau, R.; Detrembleur, C. A Catalytic Domino Approach toward Oxo-Alkyl Carbonates and Polycarbonates from CO_2 , Propargylic Alcohols, and (Mono- and Di-)Alcohols. *ACS Sustain. Chem. Eng.* **2020**, *8*, 9698−9710.

(24) Kricheldorf, H. R. "Sugar Diols" as Building Blocks of Polycondensates. *J. Macromol. Sci., Chem.* **1997**, *37*, 599−631.

(25) Yu, Y.; Pang, C.; Jiang, X.; Yang, Z.; Ma, J.; Gao, H. Copolycarbonates Based on a Bicyclic Diol Derived from Citric Acid and Flexible 1,4-Cyclohexanedimethanol: From Synthesis to Properties. *ACS Macro Lett.* **2019**, *8*, 454−459.

(26) Burgard, A.; Burk, M. J.; Osterhout, R.; Van Dien, S.; Yim, H. ScienceDirect Development of a Commercial Scale Process for Production of 1 , 4-Butanediol from Sugar. *Curr. Opin. Biotechnol.* **2016**, *42*, 118−125.

(27) Grignard, B.; Ngassamtounzoua, C.; Gennen, S.; Gilbert, B.; Méreau, R.; Jerome, C.; Tassaing, T.; Detrembleur, C. Boosting the Catalytic Performance of Organic Salts for the Fast and Selective

Synthesis of α-Alkylidene Cyclic Carbonates from Carbon Dioxide and Propargylic Alcohols. *ChemCatChem* **2018**, *10*, 2584−2592.
(28) Ca', N. D.; Gabriele, B.; Ruffolo, G.; Veltri, L.; Zanetta, T.; Costa, M. Effective Guanidine-Catalyzed Synthesis of Carbonate and Carbamate Derivatives from Propargyl Alcohols in Supercritical Carbon Dioxide. *Adv. Synth. Catal.* **2011**, *353*, 133−146.
(29) Zhou, Z.-H.; Song, Q.-W.; Xie, J.-N.; Ma, R.; He, L.-N. Silver(I)-Catalyzed Three-Component Reaction of Propargylic Alcohols, Carbon Dioxide and Monohydric Alcohols: Thermodynamically Feasible Access to β-Oxopropyl Carbonates. *Chem.—Asian J.* **2016**, *11*, 2065−2071.
(30) Zhou, H.; Zhang, H.; Mu, S.; Zhang, W.-Z.; Ren, W.-M.; Lu, X.-B. Highly Regio- And Stereoselective Synthesis of Cyclic Carbonates from Biomass-Derived Polyols: Via Organocatalytic Cascade Reaction. *Green Chem.* **2019**, *21*, 6335−6341.
(31) Kricheldorf, H. R. Cyclic Polymers: Synthetic Strategies and Physical Properties. *J. Polym. Sci., Part A: Polym. Chem.* **2010**, *48*, 251−284.
(32) Josse, T.; De Winter, J.; Gerbaux, P.; Coulembier, O. Cyclic Polymers by Ring-Closure Strategies Angewandte. *Angew. Chem., Int. Ed.* **2016**, *55*, 13944−13958.
(33) Nielsen, A. T.; Carpenter, W. R. 1,4-Cyclohexanedione. *Org. Synth.* **1965**, *45*, 25.
(34) Nikbin, N.; Caratzoulas, S.; Vlachos, D. G. On the Brønsted Acid-Catalyzed Homogeneous Hydrolysis of Furans. *ChemSusChem* **2013**, *6*, 2066−2068.
(35) Li, Y.; Lv, G.; Wang, Y.; Deng, T.; Wang, Y.; Hou, X.; Yang, Y. Synthesis of 2,5-Hexanedione from Biomass Resources Using a Highly Efficient Biphasic System. *ChemistrySelect* **2016**, *1*, 1252−1255.
(36) Hosseini, A.; Seidel, D.; Miska, A.; Schreiner, P. R. Fluoride-Assisted Activation of Calcium Carbide: A Simple Method for the Ethynylation of Aldehydes and Ketones. *Org. Lett.* **2015**, *17*, 2808−2811.
(37) Sum, Y. N.; Yu, D.; Zhang, Y. Synthesis of Acetylenic Alcohols with Calcium Carbide as the Acetylene Source. *Green Chem.* **2013**, *15*, 2718−2721.

https://dx.doi.org/10.1021/acssuschemeng.0c07683
ACS Sustainable Chem. Eng. 2021, 9, 1714−1728

V

Cation-π Interactions Accelerate the Living Cationic Ring-Opening Polymerization of Unsaturated 2-Alkyl-2-oxazolines

Elias Van Den Broeck has performed the computational research in this work and prepared the computational part and introduction of the manuscript.

Reprinted with permission from Elias Van Den Broeck, Bart Verbraeken, Karen Dedecker, Pieter Cnudde, Louis Vanduyfhuys, Toon Verstraelen, Kristof Van Hecke, Valentin Victor Jerca, Saron Catak, Richard Hoogenboom, and Veronique Van Speybroeck. Cation-π interactions accelerate the living cationic ring-opening polymerization of unsaturated 2-alkyl-2-oxazolines. *Macromolecules*, 53(10):3832–3846, 2020. doi: 10.1021/acs.macromol.0c00865.

Macromolecules

pubs.acs.org/Macromolecules

Article

Cation–π Interactions Accelerate the Living Cationic Ring-Opening Polymerization of Unsaturated 2-Alkyl-2-oxazolines

Elias Van Den Broeck, Bart Verbraeken, Karen Dedecker, Pieter Cnudde, Louis Vanduyfhuys, Toon Verstraelen, Kristof Van Hecke, Valentin Victor Jerca, Saron Catak, Richard Hoogenboom,* and Veronique Van Speybroeck*

Cite This: *Macromolecules* 2020, 53, 3832–3846

Read Online

ACCESS | Metrics & More | Article Recommendations | Supporting Information

ABSTRACT: Cation–dipole interactions were previously shown to have a rate-enhancing effect on the cationic ring-opening polymerization (CROP) of 2-oxazolines bearing a side-chain ester functionality. In line with this, a similar rate enhancement—via intermolecular cation–π interactions—was anticipated to occur when π-bonds are introduced into the 2-oxazoline side-chains. Moreover, the incorporation of π-bonds allows for facile postfunctionalization of the resulting poly(2-oxazoline)s with double and triple bonds in the side-chains via various click reactions. Herein, a combined molecular modeling and experimental approach was used to study the CROP reaction rates of 2-oxazolines with side-chains having varying degrees of unsaturation and side-chain length. The presence of cation–π interactions and the influence of the degree of unsaturation were initially confirmed by means of regular molecular dynamics simulations on pentameric systems. Furthermore, a combination of enhanced molecular dynamics simulations, static calculations, and a thorough analysis of the noncovalent interactions was performed to unravel to what extent cation–π interactions alter the reaction kinetics. Additionally, the observed trends were confirmed also in the presence of acetonitrile as solvent, in which experimentally the polymerization is performed. Most intriguingly, we found only a limited effect on the intrinsic reaction kinetics of the CROP and a preorganization effect in the reactive complex region. The latter effect was established by the unsaturated side-chains and the cationic center through a complex interplay between cation–π, π–π, π–induced dipole, and cation–dipole interactions. These findings led us to propose a two-step mechanism comprised of an equilibration step and a CROP reaction step. The influence of the degree of unsaturation, through a preorganization effect, on the equilibration step was determined with the following trend for the polymerization rates: *n*-ButylOx < ButenOx < ButynOx ≥ PentynOx. The trend was experimentally confirmed by determining the polymerization rate constants.

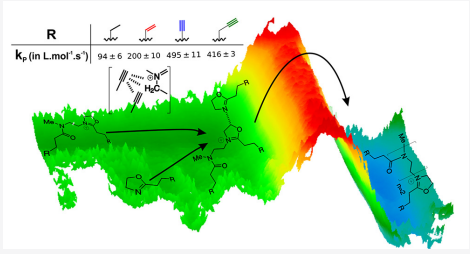

INTRODUCTION

The living cationic ring-opening polymerization (CROP) has long been known to provide wide access to poly(2-oxazoline)s with controlled end-group functionality.[1−9] Substituents on the 2-, 4-, and 5-positions can influence the propagation rates (k_p) significantly by electronic and/or steric effects, which govern the reaction (Scheme 1).[10−15] Despite their slow polymerization rates, 2-oxazolines substituted at the sp^3-hybridized carbons C_4 and C_5 can still be of interest as chemically inert ligands in organometallic chemistry or in asymmetric synthesis.[16−20] In contrast to the 4- and 5-substituted-2-oxazolines, 2-oxazolines substituted at the C_2 position provide access to a very interesting class of polymers: poly(2-alkyl/aryl-2-oxazoline)s (PAOx), which are biocompatible as well as thermosensitive and showed stealth behavior similar to poly(ethylene glycol) (PEG) and thus can be used in drug-delivery systems.[5,7,8,21,22]

Furthermore, the properties of PAOx are highly tunable by altering the C_2 substituent (see Scheme 1) of the monomer, which also enables introduction of (protected) side-chain functionalities.[7,11,23−26] Of particular interest in this study are 2-oxazoline monomers with alkene and alkyne functionalities, more specifically, 2-(but-3-enyl)-2-oxazoline (ButenOx, Scheme 1, **1b**), 2-(but-3-ynyl)-2-oxazoline (ButynOx, Scheme 1, **1c**), and 2-(pent-4-ynyl)-2-oxazoline (PentynOx, Scheme 1, **1d**). These functionalities are of interest for various click reactions, such as copper(I)-catalyzed azide cycloaddition as

Received: April 14, 2020
Published: May 4, 2020

https://dx.doi.org/10.1021/acs.macromol.0c00865
Macromolecules 2020, 53, 3832–3846

Scheme 1. (Top) Schematic Representation of the Second Propagation Step in the Cationic Ring-Opening Polymerization (CROP) of 2-Oxazolines, Leading to the Formation of the Corresponding Trimer 3, Where *In* Is the Initiator Fragment at the Start of the Polymer Chain; (Bottom) 2-Oxazoline Structures for 2-(*n*-Butyl-2)-oxazoline (*n*-ButylOx, 1a), 2-(But-3-enyl)-2-oxazoline (ButenOx, 1b), 2-(But-3-ynyl)-2-oxazoline (ButynOx, 1c), 2-(Pent-4-ynyl)-2-oxazoline (PentynOx, 1d), 2-Difluorophenyl-2-oxazoline (*o*-DFPhOx, 1e), 2-Methoxycarbonylethyl-2-oxazoline (C_2-MestOx, 1f) 2-Methoxycarbonyl-propyl-2-oxazoline (C_3-MestOx, 1g)

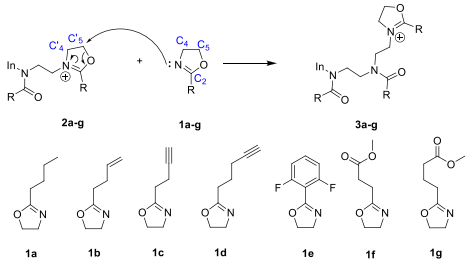

well as thiol−ene and thiol−yne reactions, which enable facile postfunctionalization of the resulting polymers. Click reactions on PAOx are typically performed by using copolymers and have found many practical applications, such as the introduction of targeting molecules on polymeric chains,[27] coatings of nanoparticles[28−31] or stainless steel,[31−33] creation of biocompatible materials with anode-selective deposition behavior,[33,34] and many others.[23,35−39] In addition, post-polymerization modification readily enables the introduction of side-chains that are not compatible with the CROP of 2-oxazolines.[40] Moreover, cross-linking of alkene- and/or alkyne-functionalized PAOx has been applied for the development of hydrogels or core−shell cross-linked nanoparticles.[22,25,41−43]

In general, the propagation rate constants for the CROP of 2-alkyl-2-oxazolines (Scheme 1) are governed by both electronic and steric effects, though the latter tends to have a more significant impact in most CROP reactions.[10,14] This effect explains the slower polymerization rates when increasing the alkyl chain from methyl up to propyl, with only marginal effects for longer side-chains.[14] Nonetheless, a few remarkable cases have been noted in the literature, some by the presenting authors, where electronic effects become prominent, particularly when functional groups or cyclic structures are introduced in the side-chain.[10−12,15,44,45] The use of a cyclic side-chain, such as *c*-propyl, was accompanied by an unexpected increase in propagation rate constant when compared to 2-oxazolines bearing its skeletal isomers, *i*-propyl and *n*-propyl.[10] This remarkable observation was theoretically rationalized by Goossens et al. using density functional theory (DFT) calculations, where the electronic effect of the cyclic side-chain in 2-*c*-propyl-2-oxazoline (*c*PrOx) was shown to become more significant during the CROP than the steric effect, which dominates in 2-*i*-propyl-2-oxazoline which was found to have a lower propagation rate constant than 2-*n*-propyl-2-oxazoline and *c*PrOx. This acceleration for the CROP of *c*PrOx was ascribed to the well-known (partial) π-bonding character of *c*-propyl carbons next to an imine.[10] The zwitterionic resonance structure shown in Scheme 2 is favored in the presence of this cyclic side-chain (through π-type

Scheme 2. Resonance Forms for *c*PrOx

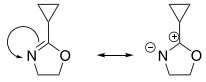

conjugation);[10] hence, the monomer's ability to perform a nucleophilic attack is significantly enhanced, positively influencing the reactivity of this S_N2-type reaction.

Another case in which electronic effects significantly influence the propagation rate constant was reported by Lobert et al. for the CROP of fluorinated and nonfluorinated analogues of 2-phenyl-2-oxazoline (PhOx).[15] When the phenyl side-chain and the 2-oxazoline ring are coplanar, the phenyl side-chain can withdraw electron density from the 2-oxazoline ring through conjugation; this effect is further enhanced when the phenyl ring is fluorinated. Hence, *meta-fluorinated* (*m*-FPhOx) and *para*-fluorinated PhOx (*p*-FPhOx) monomers have lower CROP rates than PhOx due to the decreased nucleophilicity of the monomer. However, *ortho*-substitution disrupts the conjugation by sterically preventing planarity (out-of-plane angle of 3°−4°). As a result, the electron-withdrawing effect of the fluoro-substituted phenyl side-chain is reduced to an inductive effect, which is much less effective than the electron-withdrawing effect through conjugation. Therefore, the propagation rate constant for *ortho*-monofluorinated PhOx (*o*-FPhOx) is significantly higher in comparison to the parent PhOx. In the 2-*o*-difluorophenyl-2-oxazoline system (Scheme 1, *o*-DFPhOx, **1e**), nonplanarity was further increased (out-of-plane angle of 39°), leading to a 2-fold increase of the propagation rate constant when compared to *o*-FPhOx. This latter effect was then confirmed by using MMFF94 calculations, which showed that in the case of *o*-DFPhOx there were two contributing factors. First, the steric clash caused by the *ortho*-fluorine substituent on the phenyl ring resulted in a nonplanar geometry with respect to the 2-oxazoline ring, effectively preventing conjugation, and as a result, the nucleophilicity of the 2-oxazoline was not significantly reduced. Second, a clear intermolecular interaction was shown to occur between the *ortho*-fluorine substituent and the cationic reaction center, which was hypothesized to increase the electrophilicity of the 2-oxazolinium cation, enhancing the CROP rates. Hence, this latter point indicates that dipole−cation interactions could also have a significant impact on the polymerization kinetics.

In view of prior studies that showed the varying effect of different side-chains on 2-oxazoline CROP propagation rate constants, Bouten et al. investigated the propagation rate constants of 2-oxazoline monomers with methyl ester substituents, namely, 2-methoxycarbonylethyl-2-oxazoline (Scheme 1, C_2-MestOx, **1f**) and 2-methoxycarbonylpropyl-2-oxazoline (Scheme 1, C_3-MestOx, **1g**).[11,12] Even though the propagation rate constants of the methyl ester-substituted 2-oxazolines were expected to be lower than their counterparts bearing aliphatic side-chains due to the electron-withdrawing ester functionality, faster propagation rate constants were experimentally observed. The authors rationalized these findings using DFT calculations, where they showed that the observed rate enhancement was mainly caused by the numerous inter- and intramolecular interactions between the

https://dx.doi.org/10.1021/acs.macromol.0c00865
Macromolecules 2020, 53, 3832−3846

carbonyl group of the side-chains and the active oxazolinium chain-end. The dipole−cation interaction between the carbonyl and the 2-oxazolinium moieties was shown to further increase the electrophilic nature of the chain-end, in particular, on the C'_S carbon atom, favoring nucleophilic attack (Scheme 1) and leading to the observed increase in CROP rate constants.

In the aforementioned studies, the CROP propagation rate constants of both *o*-DFPhOx[15] (Scheme 1, **1e**) and $C_{2/3}$-MestOx[11,12] (Scheme 1, **1f,g**) were increased by 2-oxazoline side-chains bearing electron-withdrawing groups (fluorine and carbonyl, respectively). The resulting intermolecular interaction between the electron-withdrawing species and the 2-oxazolinium chain-end further enhances both the electrophilic nature of the ring and the rate of the polymerization reaction. Both studies demonstrated that fine-tuning the side-chain of 2-oxazolines could induce rate-enhancing effects in CROP.

Based on this knowledge, a similar rate enhancement may be hypothesized when π-bonds are incorporated into 2-oxazoline side-chains, resulting in intermolecular cation−π interactions between the side-chain and the cationic chain-end, thereby potentially increasing their CROP rate constants. This hypothesis is proposed here for the first time and will be validated based on a combined experimental and molecular modeling study to investigate the CROP reaction rate constants of 2-oxazolines with side-chains of varying degrees of unsaturation (Scheme 1, monomers **1a−d**). The factors that affect the propagation rate constants were thoroughly examined by means of static DFT calculations and *ab initio* molecular dynamics simulations. We also tested the effect of the solvent on the specific interactions in the polymerization system. These computational predictions were further verified by an experimental kinetic study for monomers **1a−d** (Scheme 1) revealing that the computational evidence for cation−π interactions are translated into acceleration of the CROP of 2-oxazoline monomers with unsaturated side-chains. Despite the numerous previous reports on the CROP (co)polymerization of such monomers, this is the first in-depth study revealing faster polymerization resulting from cation−π interactions.

COMPUTATIONAL METHODOLOGY

In contrast to earlier modeling efforts, a multilevel modeling approach is applied in this study, where information about transition states is obtained from static DFT calculations while the conformational flexibility of the growing polymer chain is assessed from molecular dynamics studies. DFT-based simulations were performed on two types of model systems for each monomer **1a−d** (Scheme 1): a pentameric system, to monitor the presence and persistence of cation−π interactions, and a trimeric system, to compare the intrinsic reactivity of the monomers toward CROP monomer addition reactions.

Static Calculations. To compare the relative activation barriers for the prototypical CROP propagation step depicted in Scheme 1, a series of static calculations were performed on 2-oxazoline monomers **1a−d**. Methyl is taken as initiator fragment for the CROP in the systems under investigation, which is in accordance with the frequent use of methyl tosylate and methyl triflate as initiator in experimental studies. The B3LYP/6-311+G(d,p) level of theory was used for geometry optimizations to which Grimme's D3 dispersion corrections were added to take into account noncovalent and long-range interactions.[46] This functional has been proven to give reliable results for similar systems.[47−50] Normal-mode analysis was used to characterize the nature of the energetic minima and first-order saddle points (transition states (TSs)). To generate a representative set of reactant complexes, intrinsic reaction coordinate calculations are performed for a limited number of TSs.[51−53] Additionally, the solvent effects on the obtained complexes are assessed by using the integral equation formalism variant of the polarized continuum model (IEF-PCM).[54] All static calculations were performed using the Gaussian 16 package.[55] TS guesses were generated by using enhanced sampling simulations, namely metadynamics, which provided a critical distance for the TS region and sufficient sampling to explore the conformational flexibility of the TSs (see Supporting Information section S1.1).[56]

Molecular Dynamics Simulations. The CP2K software package[57] was utilized to carry out nonperiodic molecular dynamics (MD) simulations. The BLYP functional along with additional Grimme D3 dispersion corrections and the TZVP-GTH basis set were used to perform *ab initio* MD.[46,57−60] Given the extensive number of first-principles molecular dynamics simulations that were performed, it was impossible to use the hybrid B3LYP functional in view of computational time. However, the BLYP functional has shown to give a reasonable description of noncovalent interactions when D3 corrections are included with comparable performance to dispersion corrected hybrid functionals such as B3LYP-D3.[61] This basis set is a combination of Gaussian basis functions and plane waves (GPW) with a cutoff energy of 320 Ry.[62,63] The equations of motion were integrated with a time step of 0.5 fs. All systems were simulated by using the canonical ensemble at 413 K, which is controlled by a Nosé−Hoover thermostat chain of length five.[64,65] The pentameric ButylOx, ButenOx, and ButynOx were simulated by using a cubic box of 29 Å × 29 Å × 29 Å. For the pentameric PentynOx a box size of 33 Å was used. The solvent environment (acetonitrile) and the counter-ion (tosylate or triflate) were not considered in these first-principles MD-based simulations as this would require the simulations of a complete explicit solvent shell and would become computationally unfeasible. Emenike and co-workers have shown, by the use of molecular balances, that free energy differences for similar noncovalent interactions in the gas phase may be overestimated but in general are within the context of the values in solution, i.a., for acetonitrile.[66,67] Furthermore, cation−π interactions among other interactions were shown to prevail in acetonitrile by other experimental groups, which is in line with the theoretical work reported by Dougherty et al.[68−71] To verify our findings and this assumption, the density-functional tight binding (DFTB) method implemented in CP2K (enabling dispersion corrections; an Ewald-type method for Coulomb interactions and the self-consistent field method) is used to perform semiempirical MD simulations (see Supporting Information section S2.2.3) which allow us to investigate the influence of an explicit solvent environment in a computational efficient manner (*vide infra*).[72−76]

To achieve a sufficient sampling of the phase space for the *ab initio MD*, the system was first equilibrated for 10 ps followed by a production run of 100 ps. For each system, three separate simulations were run in parallel with three different initial geometries. More specifically, a folded, an extended, and a random coil conformation were used for each pentameric system to consider the flexibility of the chain. Initially, the presence of cation−π interactions was determined by analyzing the evolution of the distances of the penultimate side-chain bonds toward the cationic center with a cutoff distance of 4 Å,

https://dx.doi.org/10.1021/acs.macromol.0c00865
Macromolecules 2020, 53, 3832−3846

well-known as the optimal distance for these types of interactions.[77,78]

To further analyze and compare the MD results of the different systems, and thus elaborate on the strength of the interaction with the cationic center, the sampled phase space for the side-chains attached to the oxazolinium moiety was divided into two distinct regions depending on the proximity of the terminal side-chain bond to the cationic center (see Supporting Information section S2.1.2 and Figure S7). The distribution of the interaction distances allows the selection of two interfaces for each system, which enables a division into two different states: one "interacting" and one "noninteracting".[79,80] If a conformation is located in between these interfaces, the state will be classified as "interacting" if its previous conformation was classified as "interacting", and vice versa. This methodology was adopted from Van Erp and coworkers.[81] The relative strength of the cation−π interaction (or cation-induced dipole in the case of ButylOx) is evaluated through the mean distance between the side-chain terminal bond and the cationic ring attained in the interacting state. To explicitly test the effect of the acetonitrile solvent, this procedure was also conducted at the DFTB level of theory (see Supporting Information section S2.2.3.1).

Umbrella Sampling Simulations. Because the CROP propagation step is an activated process, it would not be observed within a regular MD simulation within a reasonable simulation time. Hence, we performed enhanced sampling molecular dynamics as well. More specifically, a series of gas-phase umbrella samplings were performed to determine the free energy profile for the second propagation step of the CROP.[82]

In the umbrella sampling (US) method the reaction coordinate is subdivided into a number of windows along the proposed reaction coordinate q. For the CROP reaction, the collective variable (CV) of choice was defined as the difference between distances of the breaking and the forming bonds: d(C−N) − d(C−O) (as schematically shown in Scheme 3).[83,84] By the selection of a proper CV, which uniquely describes the reaction coordinate q, US simulations could be used to sample specific regions of the free energy surface. The reactant and product regions are described by CV values higher than 0.1 and lower than −0.1, respectively.

Scheme 3. Collective Variable for the CROP Reaction

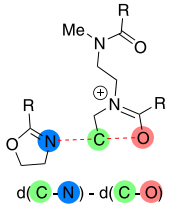

The CP2K software was used as the MD engine and interfaced with the PLUMED module to perform the US simulations.[85,86] For each system, umbrellas were placed along the CV from −2.8 to 3.2 Å with an increment of 0.1 Å, hence 59 windows. For each of these windows a biased MD simulation is performed. Initial configurations for each window were randomly selected from a moving bias potential simulation, which encapsulates the entire reaction coordinate region of interest. Sufficient sampling was ensured by employing harmonic bias potentials centered around the equilibrium value q_0 and with bias spring constant κ.

$$U_b(q) = \frac{\kappa}{2}(q - q_0)^2$$

The κ value was chosen at 250 kJ mol^{-1} Å^{-2}. Furthermore, in a second phase, the CV range was extended to 5.4 Å by placing an extra 10 windows with an increment of 0.2 Å and a κ value of 100 kJ mol^{-1} Å^{-2} to explore the reactant region more extensively. Subsequently, the free energy profiles were reconstructed by combining the sampled collective variable distribution in each window by using the weighted histogram analysis method (WHAM).[87−89] To extract Helmholtz free energies of activation from these profiles and kinetic data (using additional trajectory information about the US simulations), a method based on transition state theory is used which was applied by our research group before.[90] Assessment of convergence for the obtained profiles has been performed using the bootstrap method (see the Supporting Information).

Furthermore, the constructed 1D free energy profiles are transformed into 2D free energy surfaces (see Supporting Information section S1.3) with newly proposed collective variables based on the noncovalent interaction analysis (*vide infra*), e.g., the distance between the side-chain terminal bonds and the oxazolinium ion or the distance between the attacking monomer side-chain terminal bond and those of the growing polymer. This was done to analyze both the broadness of the various regions and the effect of noncovalent interactions hereon.

To assess the effect of the solvent environment on the prereactive complex region, umbrella sampling simulations are performed to constrain the system within the prereactive complex region. Hence, umbrellas were placed along the CV range of this prereactive region (from 0.0 to 10.5 Å) with an increment of 0.5 Å and a κ value of 100 kJ mol^{-1} Å^{-2} resulting in 20 windows. The results are discussed in the Overall Reactivity Pattern section (*vide infra*) and section S.2.2.3.2 of the Supporting Information.

Noncovalent Interactions Analysis. Analysis of intermolecular interactions was performed using the Non-Covalent Interaction (NCI) index plot tool, NCIPLOT (see Supporting Information section S1.2).[91,92] A cutoff for both the reduced gradient and the electron density is required to visualize specific interactions and discriminate between them. These were selected based on the graph of the reduced gradient in function of the electron density ($\rho(\mathbf{r})$, multiplied with the sign of λ_2) produced by NCIPLOT. This allowed for a more specific determination of the optimal plotting cutoff to capture and distinguish the different important interactions for each transition state. A typical cutoff for the systems under investigation is 0.025 for the electron density and 0.3 for the reduced gradient.

RESULTS AND DISCUSSION

Theoretical Results. To investigate the effect of introducing unsaturated side-chains to 2-oxazolines on the CROP, four different monomers with side-chains of varying degrees of unsaturation were chosen (Scheme 1, monomers **1a**−**d**), covering a saturated side-chain (**1a**), double (**1b**) and triple bonds (**1c** and **1d**), and a change in the distance between the triple bond and the 2-oxazoline ring. The presence/

https://dx.doi.org/10.1021/acs.macromol.0c00865
Macromolecules 2020, 53, 3832−3846

absence of cation−π interactions between the unsaturated side-chains and the cationic chain-end were investigated via regular MD simulations that were performed on pentameric systems of each monomer. Subsequently, the influence of the cation−π interaction on the propagation rate constant was explored by modeling the second propagation step (the formation of a trimeric chain) of the CROP reaction for **1a−d** by using both static DFT calculations to map the reaction free energy profile as well as enhanced sampling *ab initio* techniques to sample the broadness of the conformational space in both the reactant and transition state region. In the first instance, the simulation results were thoroughly and comparatively analyzed for all four systems to elucidate differences in their reactivity, indeed revealing evidence for cation−π interactions. In the second instance, the computational hypothesis was confirmed experimentally. To this end, the monomers **1a−d** were synthesized, and their CROP propagation rate constants were experimentally determined in an effort to validate the computational predictions for the relative CROP reaction rates.

Cation−π Interactions: Evidence from Regular Ab Initio MD Simulations. In the aforementioned study by Bouten et al., a semiempirical MD simulation on a decameric C_2-MestOx system (Scheme 1, **1f**) demonstrated the consistent presence of cation−dipole interactions between the side-chain carbonyl moieties and the 2-oxazolinium chain-end.[11] To investigate the proximity of the side-chain-ends of the pentameric chains from monomers **1a−d** shown in Scheme 4, the distance of the first side-chain up to the fifth side-chain, marked as s1 to s5, respectively, to the cationic center marked in yellow was followed. Additionally, the proximity of the carbonyl moieties was also investigated (marked in green in Scheme 4). If a distinct difference between the simulations for the systems with the unsaturated side-chains, namely pentaButenOx, pentaButynOx, and pentaPentynOx, and the reference system bearing a saturated butyl side-chain, pentaButylOx, is observed, this will serve as an indicator of the presence of cation−π interactions. Furthermore, these simulations will help shed light on the influence of both the degree of unsaturation and the proximity of the unsaturated terminal bond on the occurrence of cation−π interactions.

Scheme 4. Pentameric Chains with Side-Chains of Differing Degrees of Unsaturation: PentaButylOx (a), PentaButenOx (b), PentaButynOx (c), and PentaPentynOx (d)[a]

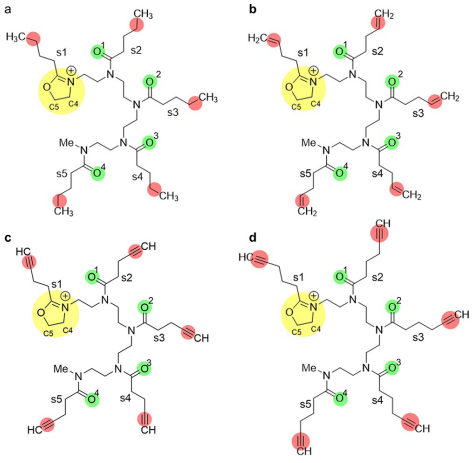

[a]Cationic chain-ends, backbone carbonyl groups, and side-chain terminal groups are shown in yellow, green, and red, respectively. s1−s5 and O^1−O^4 refer to side-chains 1−5 and carbonyl groups 1−4, respectively.

Figure 1 shows the time evolution of the distance between the side-chain terminal bonds and the cationic chain-end for each system (a complete overview of all regular MD results is found in the Supporting Information, Figures S2−S5). The MD results show a clear correlation between the degree of unsaturation and the extent of interactions occurring between the side-chain terminal bonds and the center of the 2-oxazolinium moiety. For the pentaButylOx system (Figure 1a), as anticipated, no specific interaction was observed between the side-chains and the cationic center. However, for pentaButenOx, pentaButynOx, and pentaPentynOx, simulations clearly show consistent proximity (∼4 Å) between the side-chain terminal groups and the 2-oxazolinium chain-end throughout the simulation (Figure 1b−d). In most instances, multiple side-chains were shown to interact with the 2-oxazolinium cation, which was further verified through the orientation and proximity of the side-chains in the snapshots shown for each system (Figure 1, snapshots represent the interactions in the time span of the rectangular region). It should also be noted that regardless of the substituent's nature, the side-chains occasionally come relatively close to the cationic center due to cation−dipole (carbonyl) interactions, which are present in all systems. These interactions cause a prominent folded conformation in all pentameric structures (see section S2.1.1 and Figures S2−S5 in the Supporting Information).

To evaluate the relative strength of the cation−π interaction for the different systems, distinct "interacting" and "non-interacting" states are defined for the side-chain terminal bond attached to the oxazolinium ion for which the mean distance within the former state will act as an indicator for the corresponding interaction strength, as previously explained in the Methodology section, allowing to distinguish each interaction between the side-chain and the cationic chain-end. Note that this side-chain (Scheme 4, s1) is always in close proximity to the cationic center due to its connectivity, and in the case of pentaButylOx, a cation-induced dipole interaction with the chain-end is always possible, albeit significantly weaker and less persistent than a cation−π interaction. In contrast to pentaButylOx, the systems bearing unsaturated side-chains exhibited distinct "interacting" states between their side-chain terminal bond and their 2-oxazolinium centers (see section S2.1.2 and Figure S7 of the Supporting Information), giving further evidence for the occurrence of "cation−π" interactions. Furthermore, the influence of the degree of unsaturation is clear from the mean interaction distance, which decreases from 4.39 Å for ButylOx to 4.11, 4.07, and 3.59 Å for ButenOx, ButynOx, and PentynOx, respectively. This decrease in mean interaction distance reflects the increase in interaction strength between the side-chain terminal bonds and the cationic center (from cation-induced dipole to cation−π interactions). Although the interaction distance for ButynOx only slightly decreases with respect to ButenOx, we anticipate this interaction to be significantly stronger as it is hampered by

https://dx.doi.org/10.1021/acs.macromol.0c00865
Macromolecules 2020, 53, 3832−3846

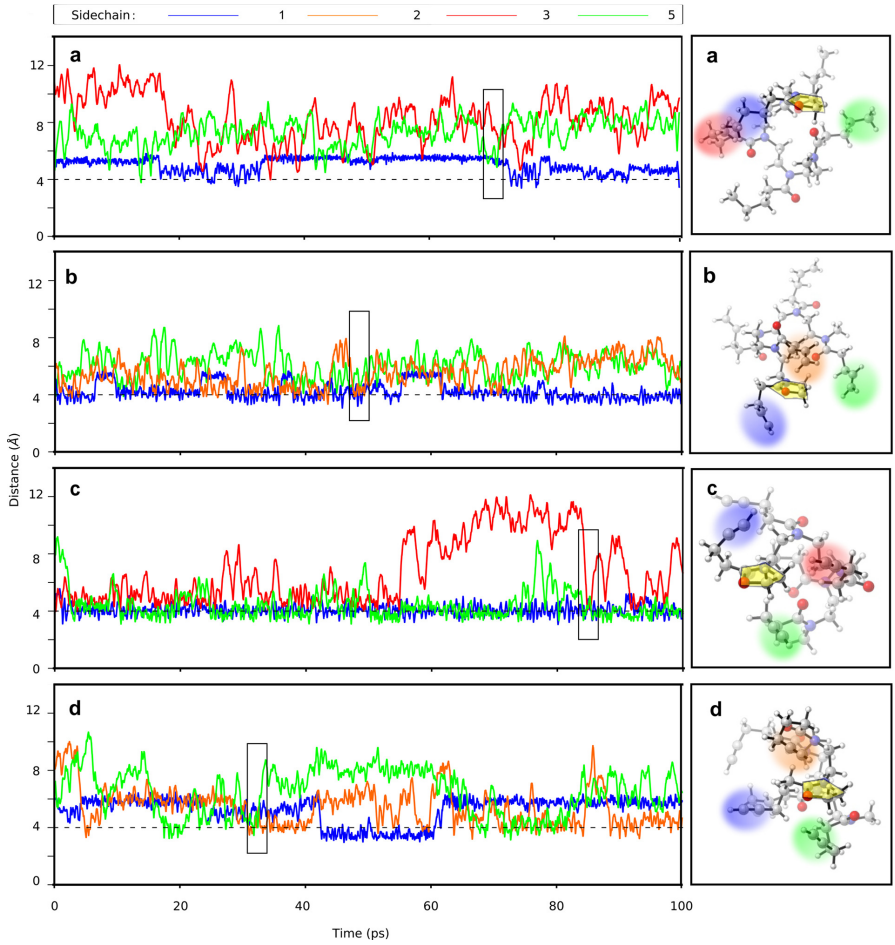

Figure 1. Evolution of distances for a representative MD run between the side-chain terminal bonds and the center of the 2-oxazolinium end-group (colored in yellow in the right panels) for pentaButylOx (a), pentaButenOx (b), pentaButynOx (c), and pentaPentynOx (d). Snapshots (right-hand side) indicate the interaction pattern observed in the rectangular region time span for each system; color codes shown at the top (see Supporting Information section S2.1 for all the results).

steric constraints for its shorter "arm-like" side-chain with respect to PentynOx, which does show this increase in strength. Additionally, comparison of the ButynOx and PentynOx simulations (see section S2.1 as well as Figures S4, S5, and S7 of the Supporting Information) suggests an entropic penalty for the pentyn side-chains, as the interacting state is less prominent in comparison to ButynOx.

In conclusion, the regular first-principles MD simulations provide evidence for the occurrence of favorable cation−π interactions between unsaturated side-chains and the cationic 2-oxazolinium chain-end. In the next section, the intrinsic reaction kinetics will be studied for a trimeric model system to investigate whether these cation−π interactions will also affect the reaction kinetics. We also evaluated whether these interactions are preserved in the presence of acetonitrile, which was indeed the case (section S.2.2.3 of the Supporting Information).

Reactivity and Energetics: Static DFT vs Enhanced Sampling Ab Initio Dynamics Calculations. The present study aims to elucidate the effect that cation−π interactions may have on the CROP propagation rate constants. However, it is important to first distinguish whether these monomers may have different intrinsic reactivity resulting from the different electronic nature of their side-chains. For this purpose, smaller dimeric model systems (Scheme 5) were

https://dx.doi.org/10.1021/acs.macromol.0c00865
Macromolecules 2020, 53, 3832−3846

chosen to determine the activation barrier for the second propagation step of the CROP propagation reaction.

Scheme 5. Schematic Representation of Trimeric Model System Used in the Second Propagation Step of CROP

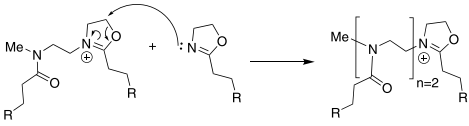

As the systems under study are extremely flexible, we opted to initially explore the transition state region by metadynamics simulations. From these simulations a representative set of transition states were extracted that were further optimized by using static DFT calculations. Relevant states were selected based on a critical distance; more information is provided in Supporting Information section S1.1. For each of the systems **1a−d** in Scheme 1, about 70−90 transition states were identified by using this procedure. A summary of all reaction barriers for each of these states is given in Supporting Information section S2.2 and Tables S1−S4. All conformers are shown with respect to their corresponding separate reactant in which the unfolded conformer of the dimer is taken for comparability. The highly variable range of transition state free energies and conformers emphasizes both the complexity and the multidimensionality of the free energy surface due to the many degrees of freedom (DoF). A summary of the obtained free energy barriers and separate enthalpic and entropic contributions are visually shown in Figure 2. Some transition states that are expected to control the minimal free energy path connecting the separate reactants and the trimer are indicated by **a1**, **b1**/**b2**, **c1**, and **d1** in Figure 2 for *n*-ButylOx, ButenOx, ButynOx, and Pentynox, respectively. The corresponding free energy barriers reveal the following trend *n*-ButylOx > ButenOx > ButynOx ≤ PentynOx with a difference of <5 kJ mol^{-1} between ButynOx and PentynOx. It is important to note that the values here correspond to separate reactants and that the observed effect of the side-chain could be originating from the preorganization effect in which the side-chain has preferable interactions with the reacting center or from the intrinsic reaction kinetics. For ButenOx, including an unsaturation in the side-chain mainly enables extra enthalpic stabilization with respect to the saturated side-chains for *n*-ButylOx. This yields an extra stabilization of the ButenOx transition states lowering the activation barrier by 12.6 kJ mol^{-1} with respect to *n*-ButylOx. Increasing the degree of unsaturation from a double to a triple bond, i.e., from ButenOx to ButynOx, a further enthalpic stabilization effect is observed with a change in Gibbs free energy of 12.3 kJ mol^{-1} with respect to ButenOx. However, the most stable transition states for ButynOx, on average, show higher entropic barriers with respect to ButenOx which can be explained by the more rigid-arm-like (sp-hybridized) structure of the butynyl side-chain showing less flexibility than the butenyl side-chain (*vide infra*). For the PentynOx system, a higher entropic penalty is also observed, and thus, the overall reaction kinetics may be expected to be lower compared to the Butynox system. This balance between enthalpic and entropic effects causes the free energies of the controlling TSs of PentynOx to be slightly higher than for ButynOx with a difference in ΔG of 3.8 kJ mol^{-1}. The higher entropic dependence for PentynOx thus confirms the suggestion for the entropic penalty for the pentyn side-chains (*vide supra*). Hence, the influence of both the degree of unsaturation and

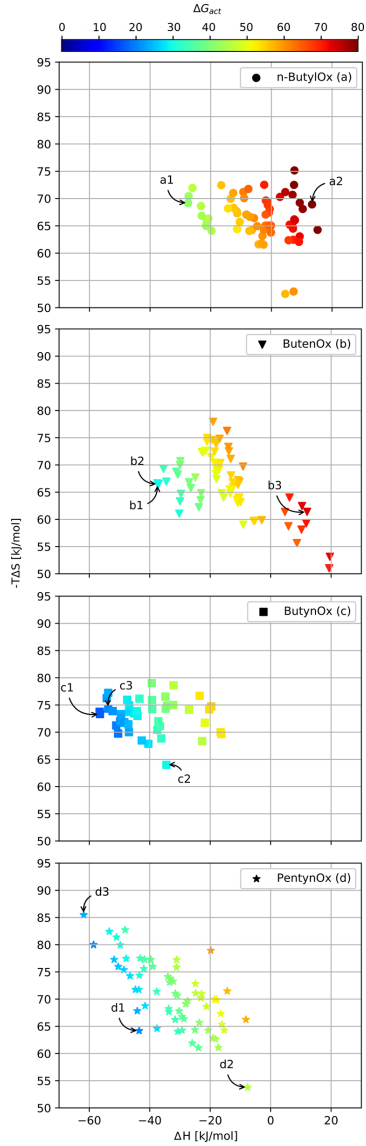

Figure 2. Optimized transition states for the systems under investigation (B3LYP-D3/6-311+G(d,p), 298 K, in vacuum). Entropy and enthalpy with respect to the separate reactants with the unfolded dimer as a reference.

https://dx.doi.org/10.1021/acs.macromol.0c00865
Macromolecules 2020, 53, 3832−3846

the side-chain length is shown to exist, indicating the possible positive effect of the cation−π interaction on the Gibbs free activation barriers. To obtain more insight into the inter- and intramolecular interactions at play in the various TSs, an extensive analysis was performed using the NCI-plot tool.[91]

Intra- and Intermolecular Interactions. Because the most important differences between *n*-ButylOx, ButenOx, and ButynOx systems are the enthalpic contributions (based on Figure 2), we explored which interactions are causing this extra stabilization and, hence, find the controlling inter- and intramolecular interactions for the CROP reaction of the respective systems. In Figure 3, the NCI plots for the most

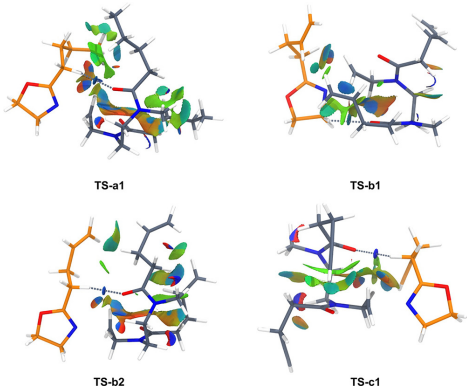

Figure 3. NCI plots of the selected transition state structures for the propagation reaction of ButylOx (**a**), ButenOx (**b**), and ButynOx (**c**) (see Figures S16−S19 for multiple viewpoints of **a**, **b**, **c**, and PentynOx (**d**)). The attacking monomer is displayed in orange and the growing polymer in gray. The 2-oxazolinium ring is opening (C- -O) due to the attack of the nitrogen atom. The blue surfaces indicate stabilizing interactions, the green surface indicates van der Waals interactions, and the red surface typically indicates steric hindrance. The dotted line between the attacking monomer and growing polymer represents a stabilizing dipole−induced dipole interaction.

stable (lowest Gibbs free energy) TS conformations are shown for the formation of triButylOx, triButenOx, and triButynOx, which were discussed in the previous section (*vide supra*). The PentynOx system is discussed in Supporting Information section S2.1.1 as well as the other transition states indicated in Figure 2.

For the propagation reaction resulting in triButylOx, **TS-a1** shows interactions between the carbonyl moiety of the amide ($CH_3NH\mathbf{C{=}O}$) and the 2-oxazolinium carbon atoms ($O\mathbf{C}H_2CH_2N$) as indicated by the blue surfaces in between these moieties. This is in line with the finding for the pentameric systems (see section S2.1.1 and Figures S2−S5) and previous work by Bouten et al. for methyl ester-functionalized 2-oxazoline monomers.[11,12] This interaction is also observed for the other systems and will hence not be responsible for the extra stabilization effect present in the unsaturated systems (see Figure 3, section S2.2.1, and Figures S9−S12). Structure **TS-a1** (Figure 3) shows that for triButylOx no significant stabilizing interactions (which would be indicated in blue) are present between the polymer side-chains and the reactive center of the 2-oxazolinium. However, stabilizing interactions are observed between the attacking monomer side-chain and both the carbonyl moiety (a dipole−induced dipole interaction indicated by the dotted line and blue surface perpendicular to it between $NCC\mathbf{H}_2$ and $C{=}\mathbf{O}$) and the terminal side-chain of the dimer (indicated by blue/green surfaces between the orange and gray side-chains) which is ascribed to a preorganization effect. It is anticipated that this effect will be stronger or more pronounced in the case of unsaturated side-chains.

For triButenOx both **TS-b1** and **TS-b2** are shown in Figure 3 because the interactions present will dominate the transition state landscape and can be compared to triButylOx to investigate the effect of the unsaturation in the side-chain. However, their conformations are very different with respect to each other and, connected with this, so are the dominating NCI. In contrast to **TS-a1**, a clear stabilizing interaction occurs between the unsaturated moiety of the growing polymer and the 2-oxazolinium moiety for **TS-b1** (indicated by a blue surface between $\mathbf{CH_2{=}CH}$ and $CH_2\mathbf{CH_2}N$), which is the anticipated cation−π interaction. Additional stabilizing cation−π interactions are present between the attacking monomer side-chain and the 2-oxazolinium ($\mathbf{CH_2{=}CH}$ and $CH_2\mathbf{CH_2}O$). This latter interaction indicates again the presence of a preorganization effect between the attacking monomer and the growing polymer. Remarkably, this TS dominated by cation−π interactions is equally favorable than **TS-b2**, which is not showing any cation−π interactions. **TS-b2** is dominated by both π−π and π-induced dipole ($\mathbf{CH_2{=}CH}$ and $CH\mathbf{CH_2}CH_2$) interactions between the side-chains, causing enthalpic stabilization equal to the cation−π interactions observed for **TS-b1** (see Figure 2). These latter interactions can again be ascribed to a preorganization effect that is present between the monomer and the growing polymer, which, hence, is stronger than the effect present in **TS-a1** (based on the enthalpic stability see Figure 2). For the CROP of ButynOx, similar conclusions can be made for **TS-c1** and **TS-c3** (see Figure 3, section 2.2.1, and Figure S10) as was done for **TS-b1** and **TS-b2**. Hence, the most important results from the NCI analysis are that, on one hand, the governing inter- and intramolecular interactions show different patterns and indicate that unsaturations in the side-chains give access to a range of interactions providing extra enthalpic stabilization and, on the other hand, that cation−π, π−π, dipole−induced dipole, and π-induced dipole interactions are present between the attacking monomer and the growing polymer, indicating an important preorganization effect in all investigated systems.

In summary, these results indicate that the difference in the Gibbs free energy of the investigated systems can be ascribed to the degree of unsaturation and their corresponding interaction patterns. Furthermore, it is found that cation−π interactions are not solely responsible for stabilizing the TS structures but that it is rather a combination of cation−π, π−π, dipole−induced dipole, and π−induced dipole interactions. These interactions are also causing a preorganization effect between the attacking monomer and the dimer.

These static simulations already provide insights into the governing interactions, but as there is a substantial conformational freedom in the TS region and to obtain further in-depth insights into both the preorganization effect and the intrinsic reaction kinetics, the CROP reaction was further investigated by using enhanced sampling MD simulations.

Overall Reactivity Pattern Using Enhanced Sampling MD Simulations. An accurate description of the free energy

https://dx.doi.org/10.1021/acs.macromol.0c00865
Macromolecules 2020, 53, 3832−3846

profiles is imperative to understand the influence of the degree of unsaturation on the intrinsic reactivity of the 2-oxazoline monomers. To this end, enhanced sampling simulations, namely umbrella sampling simulations, were performed for each system to investigate the effect of the side-chain on the activation barriers and to account for the conformational flexibility of the TS region (*vide supra*). The results are shown in Table 1, and the corresponding energy profiles can be found in section S2.2.2.1 and Figures S12−S15.

Table 1. Intrinsic Helmholtz Free Energies of Activation and Propagation Rate Constants (k_p) for the Model Trimeric Systems under Investigation Obtained via US Simulations[a]

monomer	$\Delta F^{\ddagger}_{fwd}$ (kJ/mol)	$\Delta F^{\ddagger}_{bwd}$ (kJ/mol)	k_p[a] (s^{-1})
n-ButylOx (**a**)	64	105	7.2×10^4
ButenOx (**b**)	63	100	1.0×10^5
ButynOx (**c**)	63	100	9.9×10^4
PentynOx (**d**)	67	116	3.0×10^4

[a]Note that this k_p is not equal to the experimentally measured apparent rate constant (BLYP/TZVP-GTH, 413 K, NVT). Calculated based on the method described by Bailleul et al.[90]

Interestingly, the intrinsic reaction kinetics seem to be barely affected by the degree of unsaturation in the side-chain. Moreover, the impact of the degree of unsaturation as estimated from the propagation rate constants does not agree with the conclusions drawn from the regular MD simulation nor from the static calculations. The effect of unsaturation in the side-chain on the reactant, product, or TS regions is in first instance assessed by calculating the RMSD between different snapshots corresponding to a specific value of the collective variable (see section S2.2.2.1.1). However, no preferred states were observed, and further exploration was needed. Hence, at second instance the one-dimensional free energy profiles were transformed to two-dimensional free energy surfaces in terms of a new set of collective variables that is chosen based on the conclusions from the NCI analysis. Moreover, these variables are expected to show preferred conformations (and hence preferred CV values) within the reactant, product, and/or TS region. To construct two-dimensional free energy profiles, extra information was extracted from the US trajectories in the form of conditional probabilities. More details on this transformation can be found in section S1.3. These profiles not only reveal the broadness of the product, TS, and reactant region (in line with the RMSD results) but also give further insights into preferred reactant and TS regions with respect to this new set of collective variables shown in the 2D free energy profiles (Figure 4, section S2.2.2.1.1, and Figures S18−S22). Herein, as is the case for all shown profiles, the *x*-axis represents the CV defined in Scheme 3 with the reactant region situated from 1 to 5.4 Å (hence on the right side of the profiles), and the product region is from −2.6 to −1 Å (on the left side).

Overall the proposed collective variables do not provide new insights into possible stabilizing effects within the TS region apart from the previously discussed cation−dipole interaction (see section S2.2.2.1.1 and Figure S21). Nonetheless, for the prereactive complex region a clear stabilization occurs when increasing the degree of unsaturation. This indicates that the preorganization effect will not manifest itself by stabilizing the TS but it will by stabilizing the reactant region. Figure 4 nicely illustrated this effect by the occurrence of a more stable prereactive complex region appearing around D3 equal to 4.5 Å for monomers **1a** to **1c** (also section 2.2.2.1, Figure S19 D2, and Figure S21 D5 show this trend). This observation holds for PentynOx (**1d**) as well and is entirely in agreement with the preorganization effect extracted from the NCI-analysis.

From these computational results we conclude that the reaction kinetics will not only be controlled by the intrinsic reactivity of the monomer and propagating cationic chain-end but should be described by a two-step mechanism, similar to the approach of Değirmenci et al., where the apparent rate constant can be split into two contributions: on the one hand, the equilibration constant (K_1) which accounts for the association (k_1) and dissociation (k_{-1}) of the growing polymer chain and the attacking monomer and, on the other hand, the CROP propagation rate constant (k_p) (see Scheme 6).[93,94]

Based on the steady-state approximation, the apparent rate constant for the first-order reaction kinetics is in this case defined as

$$k_{app} = K_1 k_p = \frac{k_1 k_p}{k_{-1} + k_p}$$

To this end the prereactive complexes of the previously discussed most stable TSs (see Figures 2 and 3 **a1**, **b1**, **b2**, **c1**, and **d2**) are calculated statically (see section S2.2.2.2). By combination of the enhanced MD simulations with these static DFT calculations, the role of the observed preorganization effect is clarified. In Figure 5, the free energy profiles for both the equilibration step and the CROP reaction step are displayed schematically. The prereactive complexes of the most stable TSs are highlighted in bold. Note that the free energy differences obtained for the equilibration step of the separate reactants and thus the formation of the prereactive complex are obtained from static calculations while the CROP reaction barriers are obtained from enhanced MD simulations.

On the left, a clear difference exists in the equilibration step with formation of the prereactive complex depending on the degree of unsaturation. The trend reveals that an increasing degree of unsaturation favors the formation of the prereactive complex and thus also favors the reaction kinetics (by its effect on k_{app}), with a decrease in Gibbs free energy of 14 and 27 kJ mol^{-1} for the prereactive complex of the most stable TSs of ButenOx and ButynOx with respect to *n*-ButylOx. This trend is also valid for the other computed prereactive complexes (see Table S6). Furthermore, the side-chain length also affects the formation of the prereactive complex as it is slightly less stable for PentynOx than for ButynOx (−43 and −47 kJ mol^{-1}, respectively). This side-chain length dependence is, however, not seen for all selected TSs which is attributed to the entropy effects which are poorly accounted for in this static approach. Additionally the prereactive complexes were reoptimized by using an implicit solvent model to get a first indication of the influence of the solvent (see section S2.2.2.2 and Table S6, values between brackets), which indeed reveal more stable complexes in the presence of an unsaturated side chain.

As the polymerization experimentally takes place in the presence of acetonitrile, it needs to be verified whether the preorganization effect through cation−π interactions still occurs in the presence of acetonitrile, where also a competitive stabilization with the cationic center could occur through the π bonds of the acetonitrile environment. To assess its effect on the cation−π interactions in the prereactive complex region,

https://dx.doi.org/10.1021/acs.macromol.0c00865
Macromolecules 2020, 53, 3832−3846

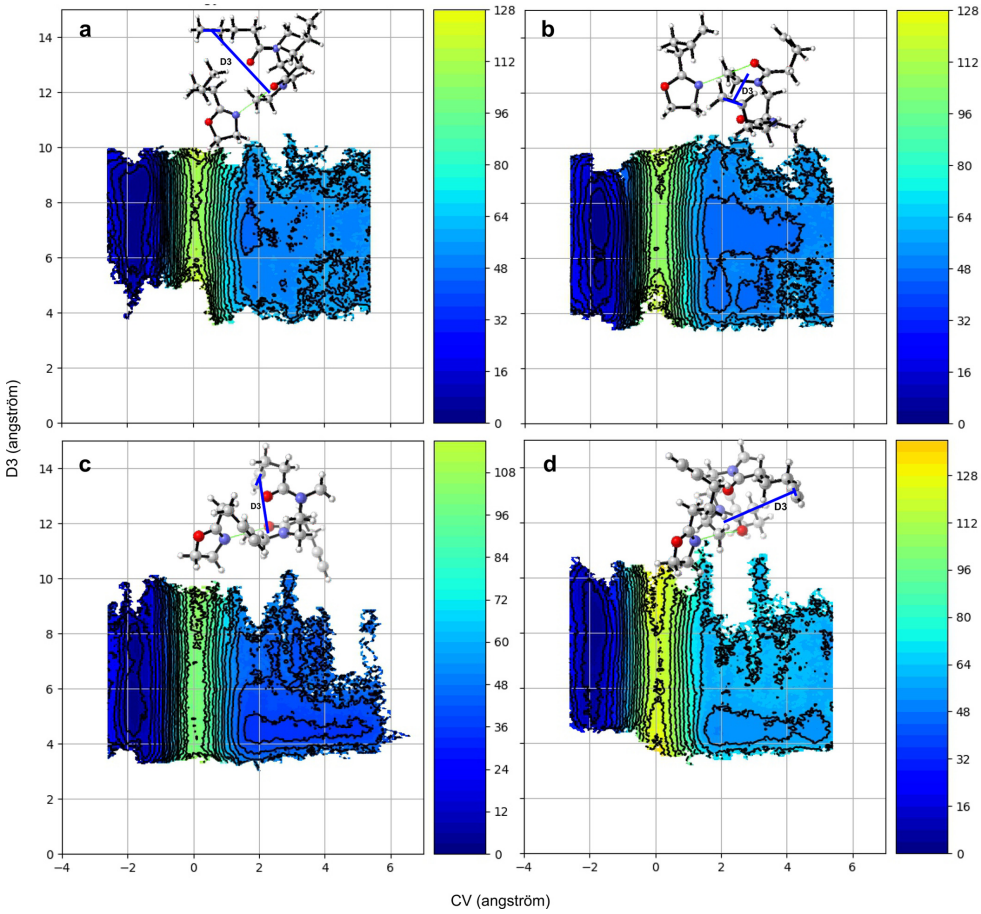

Figure 4. Two-dimensional free energy profiles for ButylOx (**a**), ButenOx (**b**), ButynOx (**c**), and PentynOx (**d**) constructed based on the method described in section S1.3. Color scale is in kJ mol^{-1}. The proposed new collective variable is the distance of the penultimate bond of the terminal side-chain and the cationic center shown in blue in the structures (D3) and represented by the *y*-axis. The *x*-axis is the collective variable describing the reaction, which is sampled in the US simulations. The reactant region is on the right and the product region on the left.

Scheme 6. Reaction Steps Controlling the Kinetics for the CROP of the Investigated 2-Alkyl-2-oxazolines; Monomer M, Polymer P$^+$, and Prereactive Complex M−P$^+$

$$M + P^+ \underset{k_{-1}}{\overset{k_1}{\rightleftharpoons}} M\cdots P^+ \qquad M\cdots P^+ \xrightarrow{k_P} P^+$$

US simulations are performed by using the DFTB method in this specific part of the reaction profile. The ability of DFTB to capture cation−π interactions was first benchmarked by using the pentameric *n*-ButylOx and ButynOx systems (see section S2.2.3.1). The cation−π interactions in the prereactive complex region are again analyzed by constructing two-dimensional free energy profiles based on conditional probabilities. The results are shown in Figure 6 and section S2.2.3.2 and indicate that even in the presence of acetonitrile the cation−π interactions are present in a wide range of the prereactive complex region (see [1] and [2] in Figure 6). This can be seen from the short distances attained by D1, which represents the distance between the attacking monomer π-bond and the cationic center, even at CV values of 6−7.5 Å. In case acetonitrile would destroy the cation−π interactions, these interacting distances would have not been observed. Remarkably, there is no significant barrier observed between the prereactive complex region and the region in which no interactions occur between the monomer and the dimer (7.5−11 Å); this potentially indicates that the CV of our choice is not a proper variable to account for this preorganization effect

https://dx.doi.org/10.1021/acs.macromol.0c00865
Macromolecules 2020, 53, 3832−3846

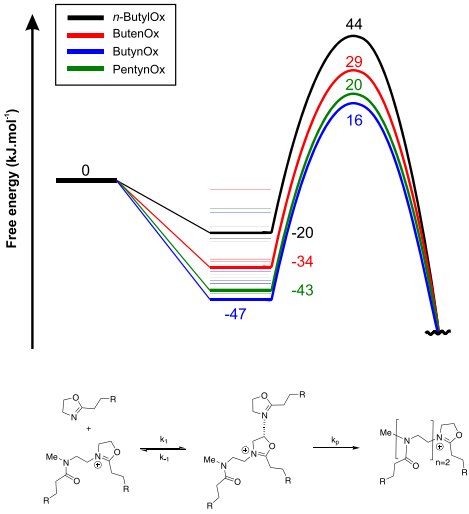

Figure 5. Combined free energy profile for the equilibration step and the actual polymerization step of the CROP reaction for the different 2-oxazolines under investigation. The equilibration step is obtained by static calculations for multiple prereactive complexes, of which an overview is found in section S2.2.2.2, the polymerization step by enhanced MD simulations. *n*-ButylOx is shown in black, ButenOx in red, ButynOx in blue, and PentynOx in green.

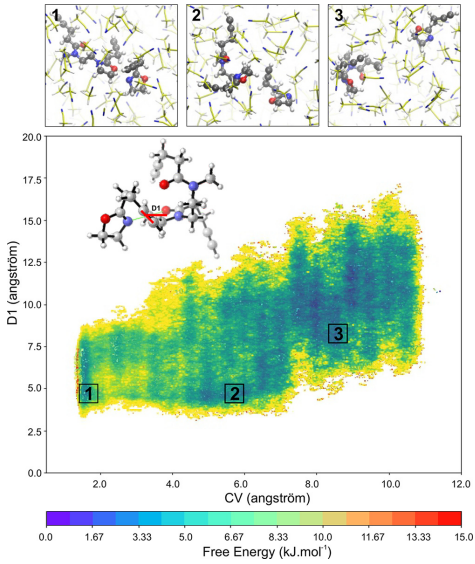

Figure 6. Two-dimensional free energy profile for ButynOx in the presence of acetonitrile constructed based on the method described in section S1.3. Color scale is in kJ mol^{-1}. The proposed new collective variable is the distance of the penultimate bond of the attacking monomer side-chain toward the cationic center shown in red in the structure (D1) and represented by the *y*-axis. The *x*-axis is the collective variable describing the reaction, which is used to sample the prereactive complex region through US simulations. The reactant region is shown spanning from 1.0 to 10.5 Å. Snapshots on the top of the figure indicate the presence of cation−π interaction in an explicit solvent environment.

as it is unable to distinguish between an interacting state and a noninteracting state within an explicit solvent environment. More work is necessary to study how proper collective variables may be chosen in the presence of solvents. This is however beyond the scope of this study.

Hence, overall these results predict a difference in rate constants between the different systems based on the association behavior of the monomer and the growing polymer involved in the CROP reaction of 2-alkyl-2-oxazolines. It is thus anticipated that the apparent propagation rate constants for the polymerization kinetics for the different systems will show the following trend: *n*-ButylOx < ButenOx < ButynOx ≥ PentynOx. This trend is equal to the one predicted during the thorough static analysis of the transition state region of the different 2-oxazolines. Importantly, this more advanced analysis revealed that the difference in reactivity due to the cation−π interactions affects the association behavior of the monomer with the growing polymer chain rather than the intrinsic barrier heights of the CROP propagation reaction. Furthermore, it was shown that the preorganization effect based on cation−π, π−π, and π−induced dipole interactions is responsible for this difference in association behavior even in the presence of acetonitrile.

Experimental Results. To assess how the computationally established cation−π interactions (*vide supra*) translate in an acceleration of the CROP of 2-oxazoline monomers with unsaturated side-chains, the monomers **1a−d** were synthesized and their polymerization kinetics determined, as will be discussed in the following. Full experimental details, including the single crystal X-ray structure of monomer **1c**, are included in section S3.

Polymerization Kinetics. The polymerization kinetics of the monomers were investigated under the same, previously optimized, conditions, namely in acetonitrile with 4 M monomer concentration and methyl tosylate as initiator (monomer to initiator ratio of 100) at 140 °C under microwave irradiation. For all the monomers, the first-order kinetic plots of monomer consumption with respect to the reaction time revealed a linear relationship (Figure 7), thus demonstrating a constant amount of propagating species indicative of the absence of termination as well as fast initiation. Furthermore, the number-average molecular weight (M_n) increased linearly with conversion, while the dispersity ($Đ$) remained below 1.30 (see section S3.3 as well as Figures S27 and S28), demonstrating that the polymerizations proceeded in a living/controlled manner. The first-order kinetic plot (Figure 7) clearly revealed that the polymerization rate constant changes upon variation of the substituent in the 2-position. The unsaturated monomers polymerize significantly faster than *n*-ButylOx (k_p = (94 ± 6) × 10^{-3} L mol^{-1} s^{-1}), ranging from a factor of 2 for ButenOx (k_p = (200 ± 10) × 10^{-3} L mol^{-1} s^{-1}) to an increase in rate by a factor of 4−5 for PentynOx (k_p = (416 ± 3) × 10^{-3} L mol^{-1} s^{-1}) and ButynOx (k_p = (496 ± 11) × 10^{-3} L mol^{-1} s^{-1}). Within the field of polymerization reactions, such 4-fold rate enhancements are regarded as significant.[12,93,95−101] Nonetheless, such rate accelerations correspond to relatively minor differences in reaction barriers of only a few kJ/mol, which is a challenge for theoretical methods to achieve. Nonetheless, as we systematically found differences in the intermolecular interactions with a broad range of methods and in the presence of solvent, there is solid evidence for the theoretically established acceleration of the CROP by cation−π interactions of unsaturated bonds in the 2-oxazoline monomer side-chains.

https://dx.doi.org/10.1021/acs.macromol.0c00865
Macromolecules 2020, 53, 3832−3846

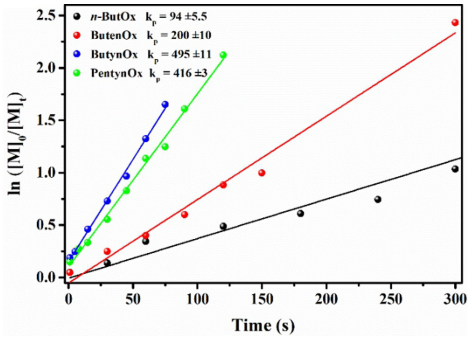

Figure 7. First-order kinetic plot for the cationic ring-opening polymerization of *n*-ButOx, ButenOx, ButynOx, and PentynOx. Polymerizations were performed at 140 °C in acetonitrile with 4 M monomer (M) concentration, methyl tosylate (I) as initiator, and a [M]:[I] ratio of 100. The polymerization rate constants (k_p's) are given in 10^{-3} L mol^{-1} s^{-1}.

CONCLUSIONS

In this work, we have established proof for the presence of cation−π interactions in ButenOx, ButynOx, and PentynOx by first-principles MD simulations, as these were not present in the reference system (*n*-ButylOx). Additionally, an effect of the degree of unsaturation is theoretically confirmed, and an entropic penalty for the longer side-chain is observed. To explore to what extent the intrinsic kinetics are affected by the side-chain, complementary calculations have been performed on the second propagation step of the CROP in combination with a thorough analysis of the governing noncovalent interactions. First a static approach revealed that complex interaction patterns are governing a very broad transition state region, and it was concluded that an interplay occurs between cation−π, π−π, π−induced dipole, and cation−dipole interactions. These interactions were also shown to enable a preorganization effect between the attacking monomer and the growing polymer chain-end. Furthermore, a larger entropic dependence of the PentynOx system, suggested by the regular MD simulations, was confirmed. Second, because of the substantial conformational freedom, enhanced sampling MD simulations were performed to accurately describe the effect of the side-chain on the intrinsic barrier heights. Limited effects were observed, and hereto the width of reactant, product, and transition state regions was assessed by the construction of two-dimensional free energy surfaces through conditional probabilities, extracted from the enhanced sampling simulations. These revealed that the previously observed preorganization effect enables stabilization of preferentially the prereactive complex region through the presence of cation−π interactions among others. Combining the conclusion of the static and enhanced sampling approach led to the proposal of a two-step mechanism involving the equilibration process with formation of the prereactive complex next to the actual CROP step. By use of a static approach, the equilibration step of the reactants toward the prereactive complex is shown to be the rate-determining step, as a clear difference is observed depending on the degree of unsaturation of the side-chain. Based on the computational conclusions, the following trend in reaction kinetics was anticipated, which was then confirmed by experiments that revealed the following order in the apparent propagation rate constants: *n*-ButylOx < ButenOx < ButynOx ≥ PentynOx. The insights obtained in this study are potentially of great importance to different monomers which polymerize through a cationic, or even anionic, polymerization mechanism. Our study clearly shows how the polymerization kinetics can be altered through preorganization effects induced by interactions between the active center of the growing polymer and neighboring group effects. Irrespective of the specific results for this polymerization system, the modeling strategy yields valuable information about how to investigate polymerization kinetics and the way it is affected by noncovalent, stabilizing interactions and by the presence of solvent interactions. With regard to the modeling of polymerization reactions, we have shown that investigating trimeric systems suffices to investigate both intrinsic reactivity and side-chain flexibility, in line with previous study by Izgorodina et al.[102] Furthermore, in case a stabilizing interaction occurs within the transition states, e.g., cation−π or π−π interactions, these potentially have no net effect on the intrinsic reactivity because similar stabilization effects occur in the prereactive complex region. To finalize, preorganization effects established through the aforementioned interactions can induce significant rate-enhancing effects by guiding the growth of the polymer more efficiently. Such effects might be of great importance in copolymerization reactions to control monomer distributions within the resulting polymers.

ASSOCIATED CONTENT

Supporting Information

The Supporting Information is available free of charge at https://pubs.acs.org/doi/10.1021/acs.macromol.0c00865.

Figures S1−S28, Schemes S1−S3, and Tables S1−S6 (PDF)

Crystallographic data (CIF)

AUTHOR INFORMATION

Corresponding Authors

Veronique Van Speybroeck − *Center for Molecular Modeling, Ghent University, 9052 Zwijnaarde, Belgium;* orcid.org/0000-0003-2206-178X; Email: veronique.vanspeybroeck@ugent.be

Richard Hoogenboom − *Supramolecular Chemistry Group, Centre of Macromolecular Chemistry (CMaC), Department of Organic and Macromolecular Chemistry, Ghent University, 9000 Gent, Belgium;* orcid.org/0000-0001-7398-2058; Email: Richard.hoogenboom@ugent.be

Authors

Elias Van Den Broeck − *Center for Molecular Modeling, Ghent University, 9052 Zwijnaarde, Belgium;* orcid.org/0000-0002-9609-4333

Bart Verbraeken − *Supramolecular Chemistry Group, Centre of Macromolecular Chemistry (CMaC), Department of Organic and Macromolecular Chemistry, Ghent University, 9000 Gent, Belgium*

Karen Dedecker − *Center for Molecular Modeling, Ghent University, 9052 Zwijnaarde, Belgium*

Pieter Cnudde − *Center for Molecular Modeling, Ghent University, 9052 Zwijnaarde, Belgium;* orcid.org/0000-0002-6735-0078

https://dx.doi.org/10.1021/acs.macromol.0c00865
Macromolecules 2020, 53, 3832−3846

Louis Vanduyfhuys − *Center for Molecular Modeling, Ghent University, 9052 Zwijnaarde, Belgium*

Toon Verstraelen − *Center for Molecular Modeling, Ghent University, 9052 Zwijnaarde, Belgium;* orcid.org/0000-0001-9288-5608

Kristof Van Hecke − *XStruct, Department of Chemistry, Ghent University, B-9000 Ghent, Belgium;* orcid.org/0000-0002-2455-8856

Valentin Victor Jerca − *Supramolecular Chemistry Group, Centre of Macromolecular Chemistry (CMaC), Department of Organic and Macromolecular Chemistry, Ghent University, 9000 Gent, Belgium; Centre for Organic Chemistry "Costin D. Nenitzescu", Romanian Academy, Bucharest 060023, Romania;* orcid.org/0000-0001-6997-4979

Saron Catak − *Center for Molecular Modeling, Ghent University, 9052 Zwijnaarde, Belgium; Department of Chemistry, Bogazici University, 34342 Istanbul, Turkey;* orcid.org/0000-0002-4396-8375

Complete contact information is available at: https://pubs.acs.org/10.1021/acs.macromol.0c00865

Author Contributions

E.V.D.B. and B.V. contributed equally to this work.

Notes

The authors declare no competing financial interest.

■ ACKNOWLEDGMENTS

The computational resources and services used were provided by Ghent University (Stevin Supercomputer Infrastructure), the VSC (Flemish Supercomputer Center), funded by the Research Foundation - Flanders (FWO). Further this work is supported by the Research Board of the Ghent University (BOF). K.V.H. thanks the Special Research Fund (BOF) − UGent (project 01N03217) for funding. V.V.S., P.C., and K.D. acknowledge funding from the European Union's Horizon 2020 research and innovation program (consolidator ERC grant agreement no. 647755 - DYNPOR (2015-2020)). The Fund for Scientific Research Flanders and the Research Board of the Ghent University (BOF) is acknowledged for funding.

■ REFERENCES

(1) Bassiri, T. G.; Levy, A.; Litt, M. Polymerization of Cyclic Imino Ethers. I. Oxazolines. *J. Polym. Sci., Part B: Polym. Lett.* **1967**, *5* (9), 871−879.

(2) Seeliger, W.; Aufderhaar, E.; Diepers, W.; Feinauer, R.; Nehring, R.; Thier, W.; Hellmann, H. Recent Syntheses and Reactions of Cyclic Imidic Esters. *Angew. Chem., Int. Ed. Engl.* **1966**, *5* (10), 875−888.

(3) Tomalia, D. A.; Sheetz, D. P. Homopolymerization of 2-Alkyl- and 2-Aryl-2-Oxazolines. *J. Polym. Sci., Part A-1: Polym. Chem.* **1966**, *4* (9), 2253−2265.

(4) Kagiya, T.; Narisawa, S.; Maeda, T.; Fukui, K. Ring-Opening Polymerization of 2-Substituted 2-Oxazolines. *J. Polym. Sci., Part B: Polym. Lett.* **1966**, *4* (7), 441−445.

(5) Zalipsky, S.; Hansen, C. B.; Oaks, J. M.; Allen, T. M. Evaluation of Blood Clearance Rates and Biodistribution of Poly(2-Oxazoline)-Grafted Liposomes§. *J. Pharm. Sci.* **1996**, *85* (2), 133−137.

(6) Mero, A.; Pasut, G.; Via, L. D.; Fijten, M. W. M.; Schubert, U. S.; Hoogenboom, R.; Veronese, F. M. Synthesis and Characterization of Poly(2-Ethyl 2-Oxazoline)-Conjugates with Proteins and Drugs: Suitable Alternatives to PEG-Conjugates? *J. Controlled Release* **2008**, *125* (2), 87−95.

(7) Luxenhofer, R.; Han, Y.; Schulz, A.; Tong, J.; He, Z.; Kabanov, A. V.; Jordan, R. Poly(2-Oxazoline)s as Polymer Therapeutics. *Macromol. Rapid Commun.* **2012**, *33* (19), 1613−1631.

(8) Hoogenboom, R. Poly(2-Oxazoline)s: A Polymer Class with Numerous Potential Applications. *Angew. Chem., Int. Ed.* **2009**, *48* (43), 7978−7994.

(9) Monnery, B. D.; Jerca, V. V.; Sedlacek, O.; Verbraeken, B.; Cavill, R.; Hoogenboom, R. Defined High Molar Mass Poly(2-Oxazoline)S. *Angew. Chem., Int. Ed.* **2018**, *57* (47), 15400−15404.

(10) Goossens, H.; Catak, S.; Glassner, M.; de la Rosa, V. R.; Monnery, B. D.; De Proft, F.; Van Speybroeck, V.; Hoogenboom, R. Cationic Ring-Opening Polymerization of 2-Propyl-2-Oxazolines: Understanding Structural Effects on Polymerization Behavior Based on Molecular Modeling. *ACS Macro Lett.* **2013**, *2* (8), 651−654.

(11) Bouten, P. J. M.; Hertsen, D.; Vergaelen, M.; Monnery, B. D.; Catak, S.; van Hest, J. C. M.; Van Speybroeck, V.; Hoogenboom, R. Synthesis of Poly(2-Oxazoline)s with Side Chain Methyl Ester Functionalities: Detailed Understanding of Living Copolymerization Behavior of Methyl Ester Containing Monomers with 2-Alkyl-2-Oxazolines. *J. Polym. Sci., Part A: Polym. Chem.* **2015**, *53* (22), 2649−2661.

(12) Bouten, P. J. M.; Hertsen, D.; Vergaelen, M.; Monnery, B. D.; Boerman, M. A.; Goossens, H.; Catak, S.; van Hest, J. C. M.; Van Speybroeck, V.; Hoogenboom, R. Accelerated Living Cationic Ring-Opening Polymerization of a Methyl Ester Functionalized 2-Oxazoline Monomer. *Polym. Chem.* **2015**, *6*, 514−518.

(13) Luef, K. P.; Hoogenboom, R.; Schubert, U. S.; Wiesbrock, F. Microwave-Assisted Cationic Ring-Opening Polymerization of 2-Oxazolines. *Adv. Polym. Sci.* **2015**, *274*, 183−208.

(14) Hoogenboom, R.; Fijten, M. W. M.; Thijs, H. M. L.; van Lankvelt, B. M.; Schubert, U. S. Microwave-Assisted Synthesis and Properties of a Series of Poly(2-Alkyl-2-Oxazoline)S. *Des. Monomers Polym.* **2005**, *8* (6), 659−671.

(15) Lobert, M.; Köhn, U.; Hoogenboom, R.; Schubert, U. S. Synthesis and Microwave Assisted Polymerization of Fluorinated 2-Phenyl-2-Oxazolines: The Fastest 2-Oxazoline Monomer to Date. *Chem. Commun.* **2008**, *0* (12), 1458.

(16) Bloksma, M. M.; Schubert, U. S.; Hoogenboom, R. Poly(Cyclic Imino Ether)s Beyond 2-Substituted-2-Oxazolines. *Macromol. Rapid Commun.* **2011**, *32* (18), 1419−1441.

(17) Hallett, A. J.; O'Brien, T. M.; Carter, E.; Kariuki, B. M.; Murphy, D. M.; Ward, B. D. Copper(II) Complexes of Pyridine-Oxazoline (Pyox) Ligands: Coordination Chemistry, Ligand Stability, and Catalysis. *Inorg. Chim. Acta* **2016**, *441*, 86−94.

(18) Kim, S.-G.; Kim, K.-H.; Jung, J.; Shin, S. K.; Ahn, K. H. Unprecedented Chiral Molecular Recognition in a C3-Symmetric Environment. *J. Am. Chem. Soc.* **2002**, *124* (4), 591−596.

(19) Fritschi, H.; Leutenegger, U.; Pfaltz, A. Chiral Copper-Semicorrin Complexes as Enantioselective Catalysts for the Cyclopropanation of Olefins by Diazo Compounds. *Angew. Chem., Int. Ed. Engl.* **1986**, *25* (11), 1005−1006.

(20) Bellemin-Laponnaz, S.; Gade, L. H. A Modular Approach to C1 and C3 Chiral N-Tripodal Ligands for Asymmetric Catalysis. *Angew. Chem., Int. Ed.* **2002**, *41* (18), 3473−3475.

(21) Knop, K.; Hoogenboom, R.; Fischer, D.; Schubert, U. S. Poly(Ethylene Glycol) in Drug Delivery: Pros and Cons as Well as Potential Alternatives. *Angew. Chem., Int. Ed.* **2010**, *49* (36), 6288−6308.

(22) Luef, K. P.; Petit, C.; Ottersböck, B.; Oreski, G.; Ehrenfeld, F.; Grassl, B.; Reynaud, S.; Wiesbrock, F. UV-Mediated Thiol-Ene Click Reactions for the Synthesis of Drug-Loadable and Degradable Gels Based on Copoly(2-Oxazoline)S. *Eur. Polym. J.* **2017**, *88*, 701−712.

(23) Gress, A.; Völkel, A.; Schlaad, H. Thio-Click Modification of Poly[2-(3-Butenyl)-2-Oxazoline]. *Macromolecules* **2007**, *40* (22), 7928−7933.

(24) Hoogenboom, R.; Schlaad, H. Bioinspired Poly(2-Oxazoline)S. *Polymers (Basel, Switz.)* **2011**, *3* (4), 467−488.

(25) Kelly, A. M.; Hecke, A.; Wirnsberger, B.; Wiesbrock, F. Synthesis of Poly(2-Oxazoline)-Based Hydrogels with Tailor-Made

Swelling Degrees Capable of Stimuli-Triggered Compound Release. *Macromol. Rapid Commun.* **2011**, *32* (22), 1815−1819.
(26) Bouten, P.; Lava, K.; van Hest, J.; Hoogenboom, R. Thermal Properties of Methyl Ester-Containing Poly(2-Oxazoline)S. *Polymers (Basel, Switz.)* **2015**, *7* (12), 1998−2008.
(27) Katagiri, K.; Takasu, A.; Higuchi, M. Synthesis of Glycopolymer Containing Cell-Penetrating Peptides as Inducers of Recombinant Protein Expression under the Control of Lactose Operator/Repressor Systems. *Biomacromolecules* **2016**, *17* (5), 1902−1908.
(28) Manzenrieder, F.; Luxenhofer, R.; Retzlaff, M.; Jordan, R.; Finn, M. G. Stabilization of Virus-like Particles with Poly(2-Oxazoline)S. *Angew. Chem., Int. Ed.* **2011**, *50* (11), 2601−2605.
(29) Bissadi, G.; Weberskirch, R. Efficient Synthesis of Polyoxazoline-Silica Hybrid Nanoparticles by Using the "Grafting-onto" Approach. *Polym. Chem.* **2016**, *7* (6), 1271−1280.
(30) Tauhardt, L.; Kempe, K.; Gottschaldt, M.; Schubert, U. S. Poly(2-Oxazoline) Functionalized Surfaces: From Modification to Application. *Chem. Soc. Rev.* **2013**, *42* (42), 7998−8011.
(31) Engelhardt, N.; Ernst, A.; Kampmann, A.-L.; Weberskirch, R. Synthesis and Characterization of Surface Functional Polymer Nanoparticles by a Bottom-Up Approach from Tailor-Made Amphiphilic Block Copolymers. *Macromol. Chem. Phys.* **2013**, *214* (24), 2783−2791.
(32) Trumbo, D. L. Epoxidized Poly(Decenyloxazoline) in Thermoset Coatings. *J. Coatings Technol. Res.* **2006**, *3* (1), 87−88.
(33) Hayashi, T.; Takasu, A. Design of Electrophoretic and Biocompatible Poly(2-Oxazoline)s Initiated by Perfluoroalkanesulfoneimides and Electrophoretic Deposition with Bioactive Glass. *Biomacromolecules* **2015**, *16* (4), 1259−1266.
(34) Rother, M.; Nussbaumer, M. G.; Renggli, K.; Bruns, N. Protein Cages and Synthetic Polymers: A Fruitful Symbiosis for Drug Delivery Applications, Bionanotechnology and Materials Science. *Chem. Soc. Rev.* **2016**, *45* (22), 6213−6249.
(35) Ying, W. B.; Kim, S.; Lee, M. W.; Go, N. Y.; Jung, H.; Ryu, S. G.; Lee, B.; Lee, K. J. Toward a Detoxification Fabric against Nerve Gas Agents: Guanidine-Functionalized Poly[2-(3-Butenyl)-2-Oxazoline]/Nylon-6,6 Nanofibers. *RSC Adv.* **2017**, *7* (25), 15246−15254.
(36) ten Brummelhuis, N.; Schlaad, H. Stimuli-Responsive Star Polymers through Thiol-Yne Core Functionalization/Crosslinking of Block Copolymer Micelles. *Polym. Chem.* **2011**, *2* (5), 1180.
(37) Diehl, C.; Schlaad, H. Thermo-Responsive Polyoxazolines with Widely Tuneable LCST. *Macromol. Biosci.* **2009**, *9* (2), 157−161.
(38) Hartlieb, M.; Kempe, K.; Schubert, U. S. Covalently Cross-Linked Poly(2-Oxazoline) Materials for Biomedical Applications - from Hydrogels to Self-Assembled and Templated Structures. *J. Mater. Chem. B* **2015**, *3* (4), 526−538.
(39) Fimberger, M.; Behrendt, A.; Jakopic, G.; Stelzer, F.; Kumbaraci, V.; Wiesbrock, F. Modification Pathways for Copoly(2-Oxazoline)s Enabling Their Application as Antireflective Coatings in Photolithography. *Macromol. Rapid Commun.* **2016**, *37* (3), 233−238.
(40) Schmitz, M.; Kuhlmann, M.; Reimann, O.; Hackenberger, C. P. R.; Groll, J. Side-Chain Cysteine-Functionalized Poly(2-Oxazoline)s for Multiple Peptide Conjugation by Native Chemical Ligation. *Biomacromolecules* **2015**, *16* (4), 1088−1094.
(41) Dargaville, T. R.; Lava, K.; Verbraeken, B.; Hoogenboom, R. Unexpected Switching of the Photogelation Chemistry When Cross-Linking Poly(2-Oxazoline) Copolymers. *Macromolecules* **2016**, *49* (13), 4774−4783.
(42) Lee, L.-C.; Lu, J.; Weck, M.; Jones, C. W. Acid-Base Bifunctional Shell Cross-Linked Micelle Nanoreactor for One-Pot Tandem Reaction. *ACS Catal.* **2016**, *6* (2), 784−787.
(43) Dargaville, T. R.; Park, J. R.; Hoogenboom, R. Poly(2-Oxazoline) Hydrogels: State-of-the-Art and Emerging Applications. *Macromol. Biosci.* **2018**, *18* (6), 1800070.
(44) Park, J.-S.; Kataoka, K. Comprehensive and Accurate Control of Thermosensitivity of Poly(2-Alkyl-2-Oxazoline)s via Well-Defined Gradient or Random Copolymerization. *Macromolecules* **2007**, *40* (10), 3599−3609.
(45) Kobayashi, S.; Tokuzawa, T.; Saegusa, T. Cationic Ring-Opening Isomerization Polymerization of 2-[p-(Substituted)Phenyl]-2-Oxazolines. Effects of the Substituent on the Reactivities. *Macromolecules* **1982**, *15* (3), 707−710.
(46) Grimme, S.; Antony, J.; Ehrlich, S.; Krieg, H. A Consistent and Accurate *Ab Initio* Parametrization of Density Functional Dispersion Correction (DFT-D) for the 94 Elements H-Pu. *J. Chem. Phys.* **2010**, *132* (15), 154104.
(47) Piens, N.; Goossens, H.; Hertsen, D.; Deketelaere, S.; Crul, L.; Demeurisse, L.; De Moor, J.; Van den Broeck, E.; Mollet, K.; Van Hecke, K.; et al. Reactivity of 3-Oxo-β-Lactams with Respect to Primary Amines-An Experimental and Computational Approach. *Chem. - Eur. J.* **2017**, *23* (71), 18002−18009.
(48) Burns, L. A.; Mayagoitia, Á. V.; Sumpter, B. G.; Sherrill, C. D. Density-Functional Approaches to Noncovalent Interactions: A Comparison of Dispersion Corrections (DFT-D), Exchange-Hole Dipole Moment (XDM) Theory, and Specialized Functionals. *J. Chem. Phys.* **2011**, *134* (8), 084107.
(49) Peng, Q.; Duarte, F.; Paton, R. S. Computing Organic Stereoselectivity - from Concepts to Quantitative Calculations and Predictions. *Chem. Soc. Rev.* **2016**, *47* (51), 6081−6408.
(50) Goerigk, L.; Grimme, S. A Thorough Benchmark of Density Functional Methods for General Main Group Thermochemistry, Kinetics, and Noncovalent Interactions. *Phys. Chem. Chem. Phys.* **2011**, *13* (14), 6670−6688.
(51) Dykstra, C. E. *Theory and Applications of Computational Chemistry: The First Forty Years*; Elsevier: 2005.
(52) Fukui, K. The Path of Chemical Reactions - the IRC Approach. *Acc. Chem. Res.* **1981**, *14* (12), 363−368.
(53) Hratchian, H. P.; Schlegel, H. B. Accurate Reaction Paths Using a Hessian Based Predictor-Corrector Integrator. *J. Chem. Phys.* **2004**, *120* (21), 9918−9924.
(54) Tomasi, J.; Mennucci, B.; Cammi, R. Quantum Mechanical Continuum Solvation Models. *Chem. Rev.* **2005**, *105*, 2999−3094.
(55) Frisch, M. J.; Trucks, G. W.; Schlegel, H. B.; Scuseria, G. E.; Robb, M. A.; Cheeseman, J. R.; Scalmani, G.; Barone, V.; Petersson, G. A.; Nakatsuji, H.; Li, X.; Caricato, M.; Marenich, A. V.; Bloino, J.; Janesko, B. G.; Gomperts, R.; Mennucci, B.; Hratch, J. B. *Gaussian 16*, Revision A.03; Gaussian Inc.: Wallingford, CT, 2016.
(56) Zheng, S.; Pfaendtner, J. Enhanced Sampling of Chemical and Biochemical Reactions with Metadynamics. *Mol. Simul.* **2015**, *41* (1−3), 55−72.
(57) VandeVondele, J.; Krack, M.; Mohamed, F.; Parrinello, M.; Chassaing, T.; Hutter, J. Quickstep: Fast and Accurate Density Functional Calculations Using a Mixed Gaussian and Plane Waves Approach. *Comput. Phys. Commun.* **2005**, *167* (2), 103−128.
(58) Grimme, S. Supramolecular Binding Thermodynamics by Dispersion-Corrected Density Functional Theory. *Chem. - Eur. J.* **2012**, *18* (32), 9955−9964.
(59) Hutter, J.; Iannuzzi, M.; Schiffmann, F.; VandeVondele, J. Cp2k: Atomistic Simulations of Condensed Matter Systems. *Wiley Interdiscip. Rev. Comput. Mol. Sci.* **2014**, *4* (1), 15−25.
(60) Goedecker, S.; Teter, M.; Hutter, J. Separable Dual-Space Gaussian Pseudopotentials. *Phys. Rev. B: Condens. Matter Mater. Phys.* **1996**, *54* (3), 1703−1710.
(61) Mardirossian, N.; Head-Gordon, M. Thirty Years of Density Functional Theory in Computational Chemistry: An Overview and Extensive Assessment of 200 Density Functionals. *Mol. Phys.* **2017**, *115*, 2315−2372.
(62) Lippert, G.; Hutter, J.; Parrinello, M. A Hybrid Gaussian and Plane Wave Density Functional Scheme. *Mol. Phys.* **1997**, *92* (3), 477−488.
(63) Lippert, G.; Hutter, J.; Parrinello, M. The Gaussian and Augmented-Plane-Wave Density Functional Method for Ab Initio Molecular Dynamics Simulations. *Theor. Chem. Acc.* **1999**, *103* (2), 124−140.
(64) Martyna, G. J.; Klein, M. L.; Tuckerman, M. Nosé-Hoover Chains: The Canonical Ensemble via Continuous Dynamics. *J. Chem. Phys.* **1992**, *97* (4), 2635−2643.

https://dx.doi.org/10.1021/acs.macromol.0c00865
Macromolecules 2020, 53, 3832−3846

(65) Nosé, S. A Molecular Dynamics Method for Simulations in the Canonical Ensemble. *Mol. Phys.* **1984**, *52* (2), 255−268.
(66) Emenike, B. U.; Bey, S. N.; Spinelle, R. A.; Jones, J. T.; Yoo, B.; Zeller, M. Cationic CH···π Interactions as a Function of Solvation. *Phys. Chem. Chem. Phys.* **2016**, *18* (45), 30940−30945.
(67) Emenike, B. U.; Bey, S. N.; Bigelow, B. C.; Chakravartula, S. V. S. Quantitative Model for Rationalizing Solvent Effect in Noncovalent CH-Aryl Interactions. *Chem. Sci.* **2016**, *7* (2), 1401−1407.
(68) Gallivan, J. P.; Dougherty, D. A. A Computational Study of Cation-π Interactions vs Salt Bridges in Aqueous Media: Implications for Protein Engineering. *J. Am. Chem. Soc.* **2000**, *122* (5), 870−874.
(69) Yamada, S.; Yamamoto, N.; Takamori, E. A Molecular Seesaw Balance: Evaluation of Solvent and Counteranion Effects on Pyridinium-π Interactions. *Org. Lett.* **2015**, *17* (19), 4862−4865.
(70) Nagy, E.; St. Germain, E.; Cosme, P.; Maity, P.; Terentis, A. C.; Lepore, S. D. Ammonium Catalyzed Cyclitive Additions: Evidence for a Cation-π Interaction with Alkynes. *Chem. Commun.* **2016**, *52* (11), 2311−2313.
(71) Li, P.; Vik, E. C.; Maier, J. M.; Karki, I.; Strickland, S. M. S.; Umana, J. M.; Smith, M. D.; Pellechia, P. J.; Shimizu, K. D. Electrostatically Driven CO-π Aromatic Interactions. *J. Am. Chem. Soc.* **2019**, *141* (32), 12513−12517.
(72) Zhechkov, L.; Heine, T.; Patchkovskii, S.; Seifert, G.; Duarte, H. A. An Efficient a Posteriori Treatment for Dispersion Interaction in Density-Functional-Based Tight Binding. *J. Chem. Theory Comput.* **2005**, *1* (5), 841−847.
(73) Seifert, G.; Porezag, D.; Frauenheim, T. Calculations of Molecules, Clusters, and Solids with a Simplified LCAO-DFT-LDA Scheme. *Int. J. Quantum Chem.* **1996**, *58* (2), 185−192.
(74) Porezag, D.; Frauenheim, T.; Köhler, T.; Seifert, G.; Kaschner, R. Construction of Tight-Binding-like Potentials on the Basis of Density-Functional Theory: Application to Carbon. *Phys. Rev. B: Condens. Matter Mater. Phys.* **1995**, *51* (19), 12947−12957.
(75) Elstner, M.; Porezag, D.; Jungnickel, G.; Elsner, J.; Haugk, M.; Frauenheim, T.; Suhai, S.; Seifert, G. Self-Consistent-Charge Density-Functional Tight-Binding Method for Simulations of Complex Materials Properties. *Phys. Rev. B: Condens. Matter Mater. Phys.* **1998**, *58* (11), 7260−7268.
(76) Elstner, M.; Seifert, G. Density Functional Tight Binding. *Philos. Trans. R. Soc., A* **2014**, *372*, 20120483.
(77) Davis, M. R.; Dougherty, D. A. Cation-π Interactions: Computational Analyses of the Aromatic Box Motif and the Fluorination Strategy for Experimental Evaluation. *Phys. Chem. Chem. Phys.* **2015**, *17* (43), 29262−29270.
(78) Marshall, M. S.; Steele, R. P.; Thanthiriwatte, K. S.; Sherrill, C. D. Potential Energy Curves for Cation-π Interactions: Off-Axis Configurations Are Also Attractive. *J. Phys. Chem. A* **2009**, *113* (48), 13628−13632.
(79) Giorgino, T. PLUMED-GUI: An Environment for the Interactive Development of Molecular Dynamics Analysis and Biasing Scripts. *Comput. Phys. Commun.* **2014**, *185* (3), 1109−1114.
(80) Humphrey, W.; Dalke, A.; Schulten, K. VMD: Visual Molecular Dynamics. *J. Mol. Graphics* **1996**, *14* (1), 33−38.
(81) Van Erp, T. S.; Moroni, D.; Bolhuis, P. G. A Novel Path Sampling Method for the Calculation of Rate Constants. *J. Chem. Phys.* **2003**, *118* (17), 7762−7774.
(82) Noble, B. B.; Coote, M. L. First Principles Modelling of Free-Radical Polymerisation Kinetics. *Int. Rev. Phys. Chem.* **2013**, *32*, 467−513.
(83) Torrie, G. M.; Valleau, J. P. Nonphysical Sampling Distributions in Monte Carlo Free-Energy Estimation: Umbrella Sampling. *J. Comput. Phys.* **1977**, *23* (2), 187−199.
(84) Torrie, G. M.; Valleau, J. P. Monte Carlo Free Energy Estimates Using Non-Boltzmann Sampling: Application to the Sub-Critical Lennard-Jones Fluid. *Chem. Phys. Lett.* **1974**, *28* (4), 578−581.
(85) Tribello, G. A.; Bonomi, M.; Branduardi, D.; Camilloni, C.; Bussi, G. PLUMED 2: New Feathers for an Old Bird. *Comput. Phys. Commun.* **2014**, *185* (2), 604−613.
(86) Grubmüller, H.; Heymann, B.; Tavan, P. Ligand Binding: Molecular Mechanics Calculation of the Streptavidin-Biotin Rupture Force. *Science (Washington, DC, U. S.)* **1996**, *271* (5251), 997−999.
(87) Souaille, M.; Roux, B. Extension to the Weighted Histogram Analysis Method: Combining Umbrella Sampling with Free Energy Calculations. *Comput. Phys. Commun.* **2001**, *135* (1), 40−57.
(88) Kumar, S.; Rosenberg, J. M.; Bouzida, D.; Swendsen, R. H.; Kollman, P. A. THE Weighted Histogram Analysis Method for Free-Energy Calculations on Biomolecules. I. The Method. *J. Comput. Chem.* **1992**, *13* (8), 1011−1021.
(89) Grossfield, A. WHAM: The Weighted Histogram Analysis Method, Version 2.09. http://membrane.urmc.rochester.edu/content/wham/, 2015.
(90) Bailleul, S.; Rogge, S. M. J.; Vanduyfhuys, L.; Van Speybroeck, V. Insight into the Role of Water on the Methylation of Hexamethylbenzene in H-SAPO-34 from First Principle Molecular Dynamics Simulations. *ChemCatChem* **2019**, *11*, 3993.
(91) Contreras-García, J.; Johnson, E. R.; Keinan, S.; Chaudret, R.; Piquemal, J.-P.; Beratan, D. N.; Yang, W. NCIPLOT: A Program for Plotting Noncovalent Interaction Regions. *J. Chem. Theory Comput.* **2011**, *7* (3), 625−632.
(92) Alonso, M.; Woller, T.; Martín-Martínez, F. J.; Contreras-García, J.; Geerlings, P.; De Proft, F. Understanding the Fundamental Role of π / π, σ / σ, and σ / π Dispersion Interactions in Shaping Carbon-Based Materials. *Chem. - Eur. J.* **2014**, *20* (17), 4931−4941.
(93) Değirmenci, I.; Eren, Ş.; Aviyente, V.; De Sterck, B.; Hemelsoet, K.; Van Speybroeck, V.; Waroquier, M. Modeling the Solvent Effect on the Tacticity in the Free Radical Polymerization of Methyl Methacrylate. *Macromolecules* **2010**, *43* (13), 5602−5610.
(94) De Sterck, B.; Vaneerdeweg, R.; Du Prez, F.; Waroquier, M.; Van Speybroeck, V. Solvent Effects on Free Radical Polymerization Reactions: The Influence of Water on the Propagation Rate of Acrylamide and Methacrylamide. *Macromolecules* **2010**, *43* (2), 827−836.
(95) Furuncuŏglu Özaltn, T.; Děgirmenci, I.; Aviyente, V.; Atlgan, C.; De Sterck, B.; Van Speybroeck, V.; Waroquier, M. Controlling the Tacticity in the Polymerization of N-Isopropylacrylamide: A Computational Study. *Polymer* **2011**, *52* (24), 5503−5512.
(96) Hermosilla, L.; Catak, S.; Van Speybroeck, V.; Waroquier, M.; Vandenbergh, J.; Motmans, F.; Adriaensens, P.; Lutsen, L.; Cleij, T.; Vanderzande, D. Kinetic and Mechanistic Study on P-Quinodimethane Formation in the Sulfinyl Precursor Route for the Polymerization of Poly(p-Phenylenevinylene)(PPV). *Macromolecules* **2010**, *43* (18), 7424−7433.
(97) Değirmenci, I.; Aviyente, V.; Van Speybroeck, V.; Waroquier, M. DFT Study on the Propagation Kinetics of Free-Radical Polymerization of Alpha-Substituted Acrylates. *Macromolecules* **2009**, *42* (8), 3033−3041.
(98) Lobachevsky, S.; Schiesser, C. H.; Lin, C. Y.; Coote, M. L. First-Principles Prediction of Rate Coefficients for Free-Radical Cyclization Reactions at Selenium. *J. Phys. Chem. A* **2008**, *112* (51), 13622−13627.
(99) Lin, C. Y.; Izgorodina, E. I.; Coote, M. L. First Principles Prediction of the Propagation Rate Coefficients of Acrylic and Vinyl Esters: Are We There Yet? *Macromolecules* **2010**, *43* (1), 553−560.
(100) Vergaelen, M.; Verbraeken, B.; Monnery, B. D.; Hoogenboom, R. Sulfolane as Common Rate Accelerating Solvent for the Cationic Ring-Opening Polymerization of 2-Oxazolines. *ACS Macro Lett.* **2015**, *4* (8), 825−828.
(101) Arraez, F. J.; Xu, X.; Van Steenberge, P. H. M.; Jerca, V. V.; Hoogenboom, R.; D'Hooge, D. R. Macropropagation Rate Coefficients and Branching Levels in Cationic Ring-Opening Polymerization of 2-Ethyl-2-Oxazoline through Prediction of Size Exclusion Chromatography Data. *Macromolecules* **2019**, *52* (11), 4067−4078.
(102) Izgorodina, E. I.; Coote, M. L. Accurate Ab Initio Prediction of Propagation Rate Coefficients in Free-Radical Polymerization: Acrylonitrile and Vinyl Chloride. *Chem. Phys.* **2006**, *324* (1), 96−110.

https://dx.doi.org/10.1021/acs.macromol.0c00865
Macromolecules 2020, 53, 3832−3846

VI

Therapeutic nanofibers: solvent electrospun poly(2-ethyl-2-oxazoline) based amorphous solid dispersions boost bioavailability of poorly soluble flubendazole

Jana Becelaere, Elias Van Den Broeck, Valérie Vanhoorne, Ella Schoolaert, Joachim F.R. Van Guyse, Maarten Vergaelen, Sander Borgmans, Karolien Creemers, Veronique Van Speybroeck, Chris Vervaet, Richard Hoogenboom, and Karen De Clerck.
Submitted to Advanced Functional Materials

Elias Van Den Broeck has performed the computational research and prepared the computational part of the manuscript with shared first authorship.

Stable Amorphous Solid Dispersions of Flubendazole with Ultrahigh Drug Loading through Solvent Electrospinning

Jana Becelaere[1,‡], Elias Van Den Broeck[2,‡], Ella Schoolaert[1], Valérie Vanhoorne[3], Joachim F.R. Van Guyse[4], Maarten Vergaelen[4], Sander Borgmans[2], Karolien Creemers[2], Veronique Van Speybroeck[2,], Chris Vervaet[3,*], Richard Hoogenboom[4,*], and Karen De Clerck[1,*]*

[1] Ghent University, Center for Textile Science and Engineering, Faculty of Engineering and Architecture, Tech Lane Science Park 70A, B-9052 Ghent, Belgium, Karen.DeClerck@UGent.be

[2] Ghent University, Center for Molecular Modeling, Faculty of Engineering and Architecture, Tech Lane Science Park 46, B-9052 Ghent, Belgium, Veronique.VanSpeybroeck@UGent.be

[3] Ghent University, Laboratory of Pharmaceutical Technology, Faculty of Pharmaceutical Sciences, Ottergemsesteenweg 460, B-9000 Ghent, Belgium, Chris.Vervaet@UGent.be

[4] Ghent University, Supramolecular Chemistry Group, Faculty of Sciences, Krijgslaan 281-S4, B-9000 Ghent, Belgium, Richard.Hoogenboom@UGent.be

Abstract

In this work, an important step is taken towards the bioavailability improvement of poorly water-soluble drugs, such as flubendazole (Flu), posing a challenge in the current development of many novel oral-administrable therapeutics. Solvent electrospinning of a solution of the drug and poly(2-ethyl-2-oxazoline) is demonstrated to be a viable strategy to produce stable nanofibrous amorphous solid dispersions (ASDs) with ultrahigh drug-loadings (up to 55 wt% Flu) and long-term stability (at least one year). Importantly, at such high drug loadings, the concentration of the polymer in the electrospinning solution has to be lowered below the concentration where it can be spun in absence of the drug as the interactions between the polymer and the drug result in increased solution viscosity. A combination of experimental analysis and molecular dynamics simulations revealed that this formulation strategy provides strong, dominant and highly stable hydrogen bonds between the polymer and the drug, which is crucial to obtain the high drug-loadings and to preserve the long-term amorphous character of the ASDs upon storage. *In vitro* drug release studies confirm the remarkable potential of this electrospinning formulation strategy by significantly increased drug solubility values and dissolution rates (respectively tripled and quadrupled compared to the crystalline drug), even after storing the formulation for one year.

Keywords: amorphous solid dispersions, solvent electrospinning, in vitro drug delivery, molecular dynamics, computational chemistry, poly(2-ethyl-2-oxazoline), flubendazole

Introduction

Approximately 40% of all marketed drugs and an estimated 90% of drugs in the pipeline can be classified as poorly water-soluble.[1] According to the Biopharmaceutical Classification System (BCS), these class II or IV active pharmaceutical ingredients (APIs) suffer from dissolution-related problems, which directly lowers their bioavailability.[2] Flubendazole (Flu) is a poorly water-soluble benzimidazole methylcarbamate anthelmintic, categorized as a BCS class IV compound. It is commonly used against gastrointestinal parasites in pigs and chickens.[3,4] Research has shown that Flu is highly effective as a microfilaricidal drug for *e.g.* lymphatic filariasis (river blindness) and onchocerciasis (elephantiasis), which are tropical diseases caused by filariae, *i.e.* parasitic roundworms. These human filarial infections affect over 150 million people in tropical areas.[3–10] Current oral formulations appear to be significantly less effective compared to parenterally administered doses due to the poor water-solubility of this highly crystalline drug. Unfortunately, severe reactions were reported around the injection site.[4,6,8,9,11] Therefore, a new formulation, preferably for oral administration, with enhanced Flu-bioavailability is required, which remains a major challenge. In fact, solubility-limited bioavailability is a significant general problem for poorly water-soluble drugs, since oral drug delivery is, and remains, the preferred route for drug administration.[12]

The formation of amorphous solid dispersions (ASDs) is one of the prominent routes to overcome poor water-solubility.[13] Chiou and Riegelman gave a broad definition of the term solid dispersion entailing all types of solid dispersions.[13,14] However, the focus nowadays lies mostly on the completely amorphous solid dispersion of a hydrophobic API dispersed into an amorphous hydrophilic polymeric matrix to form a glass solution.[13,15] Vialpando *et al.* successfully obtained stable Flu-containing ASDs using polyvinylpyrrolidone (PVP), spray drying and ordered mesoporous silica (OMS) with a maximum Flu-loading of 30 wt% with OMS.[3] Nonetheless, several processing and stability issues remained. Indeed, while the amorphous state ensures a higher solubility and a faster dissolution rate due to its higher internal energy, it also provides an increased molecular mobility. This mobility is the cause of a lower overall physical stability, often resulting in recrystallization of the API in the formulation over time.[2,12,16] This physical instability can, however, be overcome by a rational selection of both the processing technique used to form the ASD and the polymer support, thereby ensuring a molecularly dispersed system which

promotes API-polymer interactions and a high enough glass transition temperature to store the formulations in the glassy state.[12,16–19]

Solvent electrospinning is a polymer processing technique that produces membranes of nanofibers, with a diameter typically below 500 nm, upon application of electrostatic forces onto a viscous polymer solution.[20,21] It is hypothesized that the exceptionally fast solvent evaporation during solvent electrospinning compared to other solvent processing techniques, *e.g.* solvent casting,[22] results in the random and higly dispersed kinetic entrapment of the API molecules within the rapidly dried polymer matrix.[16,23–25] The consequently reduced API-mobility is key for lowering the driving force for recrystallization, thus enhancing the physical stability of the ASD.[23,25] Moreover, the high porosity and large specific surface area of the nanofibrous nonwovens are beneficial for enhancing the dissolution rate of ASDs.[25–29] Combined with its easy implementation and up-scalability, solvent electrospinning of API-polymer solutions is a promising ASD formulation technique.[24,26,30] Vigh *et al.* successfully applied solvent electrospinning of PVP as a formulation technique for Flu, and explored its upscaling. Although promising, the obtained stable ASDs had a maximal Flu-loading of only 20 wt%.[31] To enhance patient compliance and comfort, it is preferred to reach as high as possible drug loadings, as this allows to reduce tablet size and the amount of excipient that is introduced into the body.

By selecting a proper polymeric carrier that induces specific API-polymer interactions such as Van der Waals forces or hydrogen bonds, the API-mobility can be reduced, hindering nucleation and recrystallization, and consequently enhancing biopharmaceutical properties such as shelf life-stability and solubility, even at higher API-loadings.[17,18,25] Good API-polymer miscibility is necessary[16–18] and the polymer should ideally maintain a supersaturated state upon dissolution, allowing a higher amount of API to be absorbed by the body.[17,18,32] Recent research demonstrated a better physical stability of ASDs of glipizide with poly(2-ethyl-2-oxazoline) (PEtOx) compared to ASDs with PVP.[33,34] Indeed, thanks to its amorphous nature combined with the presence of good hydrogen bond accepting groups, PEtOx is a good alternative to the generally applied amorphous hydrophilic polymers such as polyethylene glycol, polyvinyl alcohol and PVP(-derivatives).[16,25,35–43] PEtOx is a biocompatible, hydrophilic polymer comprised of tertiary amide units as part of the main chain and does not readily interact with proteins and cells, *i.e.* stealth behavior.[37–39,42–44] Several studies on PEtOx have shown zero cytotoxicity, high stability in the human body and no mucosal irritation or tissue damage, indicating that the polymer is safe to be used inside the

body.[41,45,46] Based on limited research, it is already clear that PEtOx is a suitable and promising candidate as excipient for ASD formulations, enabling increased dissolution rates for the APIs it is being formulated with.[33,34,46]

In this work, the solubility enhancement (hence bioavailability, as soluble Flu can be taken up through the intestines) of Flu was investigated following formulation of highly drug-loaded PEtOx-based nanofibrous ASDs by solvent electrospinning of Flu-PEtOx blends. Based on the chemical structures of Flu and PEtOx, it was expected that hydrogen bonding would occur between the two compounds, which is crucial for the physical stability of the ASDs. The Flu-PEtOx interactions were indeed revealed by infrared spectroscopy (ATR-FTIR) and additionally supported by an innovative multi-scale modeling approach, combining static density functional theory (DFT) calculations and molecular dynamics simulations using a new in-house derived polymer force field. For the latter, the complete electrospun Flu-PEtOx ASD structure was computationally mimicked resulting in the construction of realistic Flu-PEtOx ASD configurations, which were subjected to an extensive equilibration protocol. These models not only provided a tool to fundamentally understand the API-polymer interactions, but also to predict their influence on the final ASD behavior. Interestingly, the strong Flu-PEtOx hydrogen bonds allowed for ultra-high Flu-loadings (up to 55 wt%) in combination with decreased PEtOx concentrations in the spinning solutions, without affecting electrospinnability. The amorphous character of the ASDs was experimentally observed by modulated temperature differential scanning calorimetry (MDSC) and X-ray analysis, even after storage of one year. Theoretical self-diffusivity coefficients were calculated to investigate the Flu dynamics and underpin the long-term kinetic stability of the produced ASDs. Finally, the solubility and *in vitro* release of Flu was evaluated under sink conditions for various drug loadings. A comparison with ASDs formulated by solvent casting demonstrated the superior potential of solvent electrospinning as a formulation technique that provides time-stable ASDs with high drug-loading and significanlty enhanced drug-solubility.

Mapping the electrospinnability of highly loaded Flu-PEtOx blends

Literature on electrospinning of PEtOx is limited, especially for well-defined ($Đ < 1.5$) PEtOx, and is mostly focused on waterborne electrospinning due to the water-solubility of the polymer.[29,47] On the other hand, to the best of our knowledge, the only available study on combined electrospinning

of Flu with a polymer described the use of an ethanol-formic acid (FA) solvent system combined with PVP K90 as the polymer carrier. However, only 20 wt% Flu-loadings could be achieved due to the low solubility of Flu in this solvent system.[31] The low solubility of Flu in both water and ethanol inspired the selection of pure FA as a solvent system for electrospinning in the present work, as Flu shows significant solubility in this solvent, *i.e.* 340 mg/mL,[3] which might allow for higher Flu-loadings and consequently a decrease in pill burden, being beneficial for futher downstream processing and patient compliance.

To the best of our knowledge, electrospinning of PEtOx from FA was not reported before, but is here shown to result in uniform nanofibers within a polymer concentration range of 30-35 wt% (**Figure 1**, 0 wt% Flu). In general, an increasing fiber diameter was obtained with increasing polymer concentration, which is explained by the increase in viscosity, hence inter-chain interactions and entanglements. Subsequently, solutions with different polymer and Flu concentrations were prepared and electrospun, resulting in uniform beadless nanofibers when specific Flu-PEtOx ratios were used (**Figure 1**). Within the PEtOx concentration range of 20-25 wt%, blends with a Flu-loading up to 30 wt% could be electrospun, but the available Flu-loading halved as the PEtOx concentration increased. At high polymer concentrations, *i.e.* 35 wt%, the Flu-loading was found to be limited to 15 wt%. If this limit was exceeded, inhomogeneous, phase-separated solutions were obtained, which could not be electrospun (**Figure 1**, b), indicating that important interactions between the two components occur, leading to phase separation of Flu-PEtOx aggregates as both individual components were well-soluble in FA at the utilized concentrations. It is hypothesized that these interactions reduce the solubility through the formation of hydrogen-bonded coacervates. As a verification of this hypothesis, both components were solubilized in FA seperately and subsequently added together. Although the separate components were fully solubilized, the combination produced a phase-separated solution, indeed indicating the formation of the coacervate. As can be seen from **Figure 1** (a), however, the formation of the coacervates can be delayed if more solvent is present, *i.e.* the PEtOx concentration is reduced. In this way, higher Flu-loadings can be achieved. Interestingly, the occurrence of the Flu-PEtOx interactions allows for the fabrication of uniform nanofibers at PEtOx-concentrations (15-25 wt%), which is out of the electrospinning range of pure PEtOx in FA, as this leads to electrospraying in the absence of Flu due to a too low solution viscosity. A minimum Flu-loading of 35 wt% is even required for electrospinning of nanofibers if only 15 wt% of PEtOx is present in the spinning

solution to ensure enough inter-chain interactions and entanglements, thus solution viscosity, for uniform nanofiber formation (**Table S1**). As such, ultra-high Flu-loadings up to 55 wt% could be achieved by lowering the PEtOx concentration without affecting electrospinnability. To the best of our knowledge, it is the first time that it is demonstrated that nanofibers with increased drug-loading can be achieved by reducing the polymer concentration below its individual electrospinnability window.

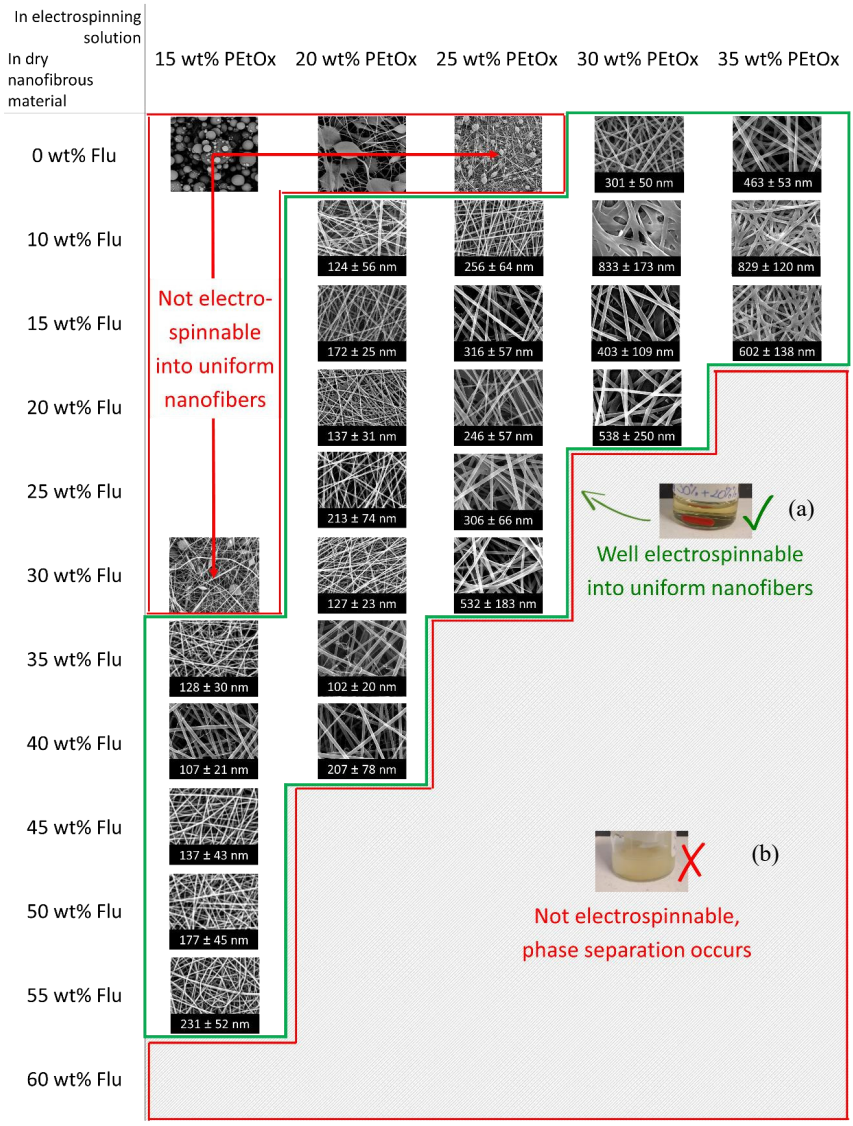

Figure 1. Overview of all electrospinnable Flu-PEtOx blend solutions. All electrospinnable solutions were spun from a clear single-phase solution (a). When the amount of Flu exceeded its maximum solubility, a phase-separated system was obtained which was not electrospinnable (b). Clear evidence for Flu-PEtOx interactions can be seen for the 15 wt% PEtOx solutions, as a minimal concentration of Flu was required to obtain a stable solvent electrospinning process. If the Flu concentration was below this limit (< 35 wt%), the viscosity of the solution was too low.

This result indicates that the strong Flu-PEtOx interactions determine the electrospinnability window of the blend and that this window is shifted towards higher Flu-loadings to provide sufficient interaction with lower PEtOx concentrations. In other words, the Flu-PEtOx interactions allow, within a specific range, to increase the drug-loading simply by reducing the polymer concentration. Thus, these strong API-polymer interactions are not only necessary to achieve physical stability of the ASD, but they are also key to achieve high drug-loadings through electrospinning, and it is, therefore, crucial to investigate and understand the possible interactions of the intended API-polymer system.

Experimental and computational analysis of Flu-PEtOx interactions

The PEtOx-Flu interactions observed during electrospinning are crucial for the success of the produced formulation. Indeed, certain API-polymer interactions are required to enhance the physical stability of the ASDs.[48,49] ATR-FTIR spectroscopy was first performed to investigate these interactions.[50] As shown in **Figure 2** (inset b) the spectrum of a Flu-PEtOx ASD significantly differs from both the spectra of the pure components, suggesting intermolecular interactions. PEtOx has two hydrogen bond acceptors (**Figure 2**, inset a, highlighted in red) and no hydrogen bond donors, while Flu has two hydrogen bond donors (**Figure 2**, inset a, highlighted in blue). Hydrogen bonding between both components is hence expected to occur and confirmed by the three spectral regions highlighted in **Figure 2**. The distinctive secondary amine N-H stretch of Flu at 3306 cm^{-1} has disappeared in the ASDs, which is consistent with the appearance of hydrogen bridges, shown in **Figure 2** (inset c).[51] Furthermore, the characteristic PEtOx peak representing the C=O stretch of the carbonyl group (**Figure 2**, inset d) is shifted to higher wavenumbers, confirming the presence of interactions with Flu. Additionally, this peak decreases in intensity with increasing Flu-loading, which is explained by a lower PEtOx fraction present in the ASDs. Lastly, **Figure 2** (inset e) shows the Flu peak shift for the characteristic C-N stretch of the secondary amine, further indicating the presence of hydrogen bridges. The most probable hydrogen bonding interactions between Flu and PEtOx are illustrated in **Figure 2** (inset a) and were theoretically supported by DFT calculations and radial distribution functions (rdfs) extracted from molecular dynamics simulations (see **section S2.1**).

DFT calculations were first performed to assess whether Flu-PEtOx interactions are occurring and if they are competitive with respect to Flu-Flu interactions (resembling the interactions present within a crystal). For this, the most stable configurations of the polymer, the Flu-Flu complex and the Flu-PEtOx complex were determined and the calculated negative complexation energies indicated that the formation of hydrogen bonds is of major importance for the stability of these complexes and that interactions between PEtOx and Flu are favorable (**Figure 2**, inset f, and **Figure S3**). However, based on the complexation energies, it is also expected that, with increasing concentration of Flu-molecules, Flu-Flu complexation will start dominating, eventually resulting in phase separation. Other Flu-Flu complexation energies were within the same range as Flu-PEtOx complexation energies, indicating that the hydrogen bond (NH-O) strength is similar, hence competition for the hydrogen bond donor sites is present.

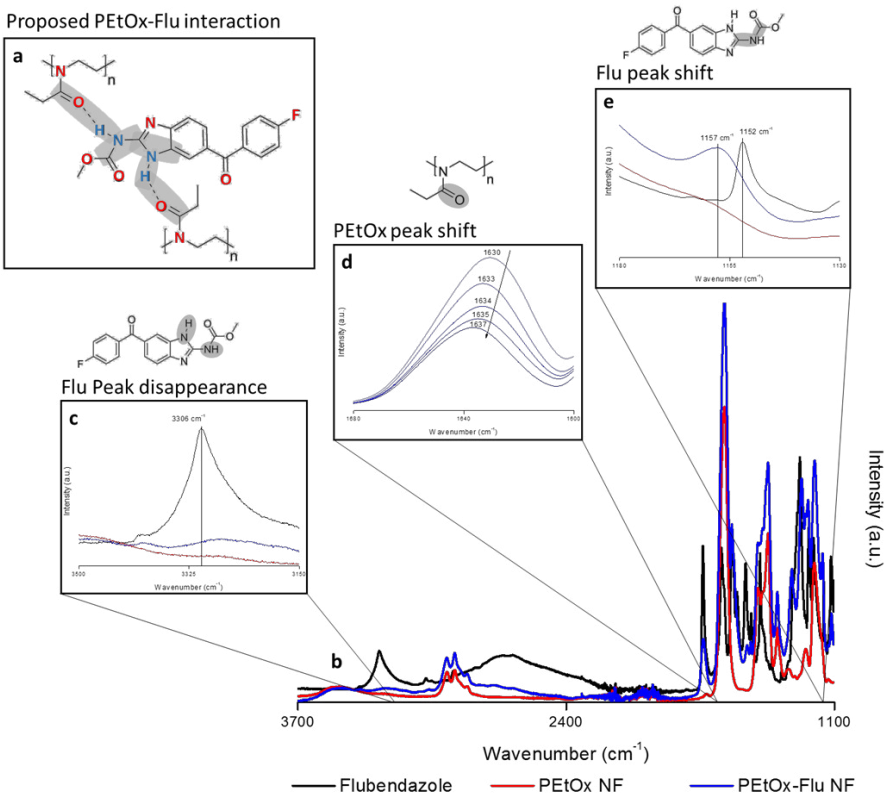
Proposed PEtOx-Flu interaction
a
Flu peak shift
e
1157 cm⁻¹
1152 cm⁻¹
PEtOx peak shift
d
1630
1633
1634
1635
1637
Flu Peak disappearance
c
3306 cm⁻¹
b
Intensity (a.u.)
3700
2400
1100
Wavenumber (cm-1)
Flubendazole
PEtOx NF
PEtOx-Flu NF

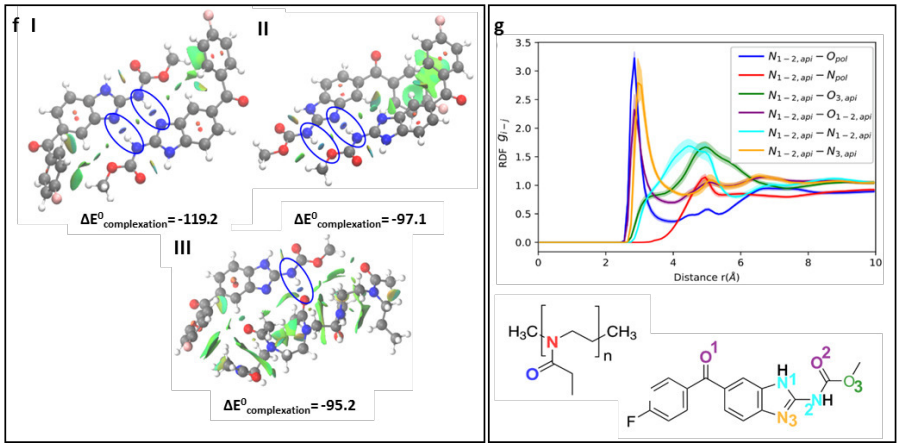
f I
II
III
ΔE⁰complexation= -119.2
ΔE⁰complexation= -97.1
ΔE⁰complexation= -95.2
g
RDF gi−j
Distance r(Å)
N1−2,api − Opol
N1−2,api − Npol
N1−2,api − O3,api
N1−2,api − O1−2,api
N1−2,api − N1−2,api
N1−2,api − N3,api

Figure 2. Results of ATR-FT-IR spectroscopy. (a) The proposed interaction between PEtOx and Flu. (b) ATR-FTIR spectrum of Flu (black), PEtOx nanofibers (red) and the prepared Flu-PEtOx ASDs (blue). Insets (c), (d) and (e) highlight areas in the ATR-FTIR spectrum where Flu-PEtOx interaction is noticeable. (c) The inherent Flu peak at 3306 cm^{-1}, N-H stretch of the secondary amine, has disappeared for all ASDs. (d) A peak shift of the distinctive C=O stretch of PEtOx is observed. This peak shift is related to the Flu-loading, the peak shifts further to the left when more Flu is present and due to a decrease in PEtOx present in the material the peak also decreases in intensity. (darker blue equals a higher Flu-loading). (e) Irrespective of the Flu-loading, a peak shift is noticed for the distinctive C-N stretch of the secondary amine of Flu when formulated as an ASD. (f) Overview of the most stable configurations based on DFT calculations: I) Most stable Flu-Flu complex with two hydrogen bonds (N-H-N); II) Flu-Flu complex with two hydrogen bonds (N-H-N and N-H-O(ether)) and π-π interactions; III) Flu-PEtOx complex with one hydrogen bond (N-H-O(carbonyl). ΔG and ΔE (complexation energies) are given in units of kJ·mol-1 and calculated at the ωB97XD-6-311+g(d,p) level of theory (1 atm, 297.15 K) with inclusion of BSSE-corrections when appropriate; green surfaces represent weak van der Waals interactions, red surfaces represent repulsive interactions and blue attractive/stabilizing interactions (displayed using the NCI-plot tool, see **section S2.2**). Hydrogen bonds are highlighted with blue ellipses. (g) Radial distribution functions (with 95% confidence intervals) for the different highlighted atom pairs in the ASDs.

Subsequently, to simulate interactions present in realistic systems allowing to study the PEtOx-Flu ASDs in detail, large-scale force field calculations were performed to mimic the electrospun Flu-PEtOx ASDs as completely as possible (**Figure 3** and **section S2.2**). For this, Flu and PEtOx force fields were derived and realistic electrospun ASDs were constructed as a whole and subjected to an extensive equilibration protocol (for a more elaborate overview of this protocol the reader is referred to **Figure S4**, **section S2.2.1-S2.2.4** and **section S2.2.8**), which were validated by density, glass transition (T_g) and X-ray diffractogram (XRD) calculations (used protocols are available in **section S2.2.6-S2.2.7**). **Table 1** shows that the calculated densities and T_gs were in good agreement to the experimental values (**section Evaluation of the amorphous structure and compound miscibility**). The uncertainty for the density is well below 1%, from which it can be concluded that the equilibration protocol has 'sufficiently relaxed' the structure and has eliminated the dependence of the starting configuration.[52] Hence, the relatively good agreement between computational and experimentally obtained results provides strong evidence that the developed computational procedure can consistently construct ASDs and that the simulated systems perform well to describe the real Flu-PEtOx ASDs, allowing to not only study and underpin in detail the present interactions in known systems, but also to predict the ASD characteristics and behavior under different experimental conditions.

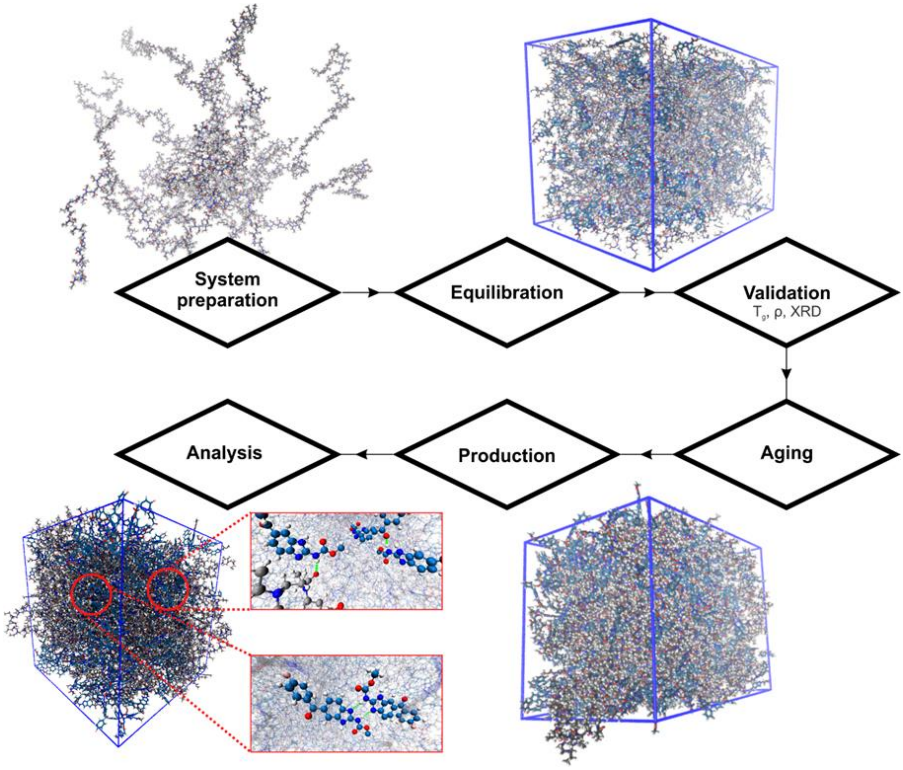

Figure 3. Workflow of the computational procedure to simulate and investigate realistic electrospun ASDs, highlighting each step of the computational protocol. Structures illustrate the change in packing during the equilibration protocol. Upon visual inspection of the generated structure, the present interactions can be clearly observed (as highlighted under 'Analysis'). A more elaborate representation of the applied workflow is shown in **section S2.2.4**.

Table 1. Density and T_g validation results obtained from the equilibrated and aged structures. ρequilibration represents the density of the equilibrated system (before aging), ρ_{aged} represents the density of the system after the physical aging step of the protocol. T_g are the glass transition temperatures of the equilibrated structures obtained through the protocol discussed in **section S.2.2.6**, Δ-values represent the difference between the T_g for the pure polymeric amorphous system and the ASD containing 50 wt% Flu. #Flu = 0 wt%, 50 wt%, 5 mg·mL^{-1} and 5x5x5 crystal represent the pure polymeric system, the ASD containing 50 wt% Flu, an aqueous solution of Flu at a concentration of 5 mg·mL^{-1} and a Flu 5x5x5 crystal configuration, respectively.

# Flu	$\rho_{equilibration}$ [g·mL^{-1}] [a]	ρ_{aged} [g·mL^{-1}]		T_g [K]			
		MD [b]	Exp.	MD [b]	Δ	Exp.[c]	Δ
0 (0 wt%)	1.1226 ± 0.0018	1.1326 ± 0.0058	1.14[53]	348 ± 10	22	335 ± 0.6	25
476 (50 wt%)	1.2095 ± 0.0009	1.2180 ± 0.0053	-	370 ± 11		360 ± 0.8	
10 (5 mg·mL^{-1})	1.01468 ± 0.00004	-	-	-			
250 (5x5x5 crystal)	1.462	-	1.444	-			

[a] 95%-Confidence intervals are constructed based on the results of ten different input structures which are subsequently bootstrapped with replacement.
[b] 95%-Confidence intervals are constructed based standard uncertainty value for the results of three different input structures for which a coverage factor of 4.30 (t-distribution) is used, assuming a gaussian-distributed observable.
[c] Standard deviation given after three measurements.

Taking into account the necessity of the aging step within the procedure (**Figure 3** and **section S2.2.8**), production runs were subsequently performed at the experimental conditions (**section S2.2.9**) which were used to analyze the various pairwise interactions present in the ASDs by means of rdfs (**Figure 2**, inset g) and visual inspection (**Figure 3** and **Figure S11**). Additionally, the total number of hydrogen bonds throughout the simulations and continuous hydrogen bond lifetimes were determined, to assess the amount and dynamics of the different hydrogen bonding pairs (**section S2.2.10**).[54]

Figure 2 (inset g) shows the rdfs of various possible hydrogen bonding pairs within the simulated 50 wt% Flu-PEtOx ASDs. Hydrogen bonds were, indeed, observed within the simulated ASDs and

the patterns observed throughout the different rdfs highlight that mainly N_3 (**Figure 2**, inset g, orange curves) and the carbonyl oxygen atoms **Figure 2**, inset g, blue and purple curves) were participating as hydrogen bond acceptors, both in PEtOx-Flu and Flu-Flu hydrogen bonding. Furthermore, from the confidence intervals, it is clear that these persisted within the different input structures used in the study. Visual inspection of the simulated PEtOx-Flu ASD configuration further confirms these results, as the various interactions in the ASD could be clearly observed upon zooming in (highlighted in **Figure 3** and **Figure S11**). Hence, it can be concluded that mainly the carbonyl oxygen groups of the PEtOx participate in the hydrogen bonding interactions between PEtOx and Flu, which supports the experimental ATR-FTIR analysis.

In order to study which hydrogen bonding pairs are dominating (*i.e*. Flu-Flu or Flu-PEtOx) in the simulated ASD with 50 wt% Flu, and whether a difference exists between the trends observed for the ASDs and the crystal structure, the total number of hydrogen bonds present within the production runs was determined (**Table 2**). Additionally, to assess the persistency (and hence the dynamics) of the various hydrogen bonds, continuous hydrogen bond lifetimes were determined (**Table 2** and **Figure S13**),[54] which represent the average time that a hydrogen bonding pair remains intact and, therefore, provides information on the average life time of a hydrogen bond (once a bond is broken it will be considered broken from that moment on).

Table 2. Fraction of occupied hydrogen bond donors and continuous hydrogen bond lifetimes within the crystal and the ASD for the different constituents within the materials. For comparability, the results were normalized by the total amount of available hydrogen donors within the system (*i.e.* two times the number of Flu-molecules present within the system). For a graphical overview of the occupied hydrogen bonds during the production runs and the correlation functions used to derive the lifetimes, the reader is referred to **Figure S12** and **Figure S13**

System	Hydrogen bond occupied by	Fraction occupied hydrogen bonds[a]	Continuous hydrogen bond lifetime τ_c [ns] [b]
50 wt% ASD	Total	0.271 ± 0.017	1.76 ± 0.420
	Flu	0.104 ± 0.018	1.25 ± 0.348
	PEtOx	0.167 ± 0.006	2.12 ± 0.464
Flu-crystal	Flu	0.145 ± 0.005	1.06 ± 0.169

[a] 95%-Confidence intervals are constructed based on the results of ten different input structures which are subsequently bootstrapped with replacement.
[b] 95%-Confidence intervals are constructed based standard uncertainty value for the results of three different input structures for which a coverage factor of 2.26 (t-distribution) is used, assuming a gaussian-distributed observable.

Simulated 50 wt% Flu-PEtOx ASDs show a significant increase in the total number of occupied hydrogen bond donor sites with respect to crystalline Flu. As was already indicated by DFT calculations, a competition occurs between PEtOx and Flu for donor sites. According to the simulations (**Table 2**), this competition is, at least for this weight percentage, dominated by PEtOx, *i.e.* 16.7% compared to 10.4% of the sites for Flu, which is favorable for the experimental electrospinability of the system as well as the physical stability of the ASD. Additionally, τ_c indicates that for Flu-PEtOx the bonds are much stronger and are preserved during relatively long periods of time within the material, *i.e.* once a hydrogen bond was formed it remained intact for 2.12 ns while for Flu-Flu this was 'only' 1.25 ns. Furthermore, a significant increase was observed for the lifetimes in the Flu-PEtOx ASD (1.8 ns) with respect to the Flu-crystal (1.0 ns) when accounting for all hydrogen bonds present **Table 2**, 'Total'). Both for the Flu-crystal and the Flu-PEtOx ASDs these lifetimes indicate that the formed hydrogen bonds are very stable within the material and far from dynamic (*e.g.* with respect to results reported by Gower et al.[54]), indicating that the formed material could be stabilized by these type of interactions. A result, which is, indeed, experimentally observed by the amorphous nature of the ASDs and its long term stability.

Amorphous nature of the Flu-PEtOx ASDs and its long term stability

Evaluation of the amorphous structure and compound miscibility

To study the amorphous nature of Flu in the ASDs, XRD and MDSC measurements were performed. Based on the XRD spectra of Flu-PEtOx physical mixtures with varying Flu-loadings, a distinctive Bragg peak at 6.5° could be distinguished when at least 3 wt% crystalline Flu was present (**Figure 4**, a). By further increasing the Flu-loading, other Flu-related Bragg peaks started to appear. In contrast, no Bragg peaks could be observed in the XRD spectra of any of the nanofibrous Flu-PEtOx ASDs, clearly displaying a fully amorphous nature,[55] even up to a Flu-loading of 55 wt% (**Figure 4**, b). It can thus be concluded that all electrospun ASDs contained less than 3 wt% detectable crystalline Flu, a result which is crucial for the solubility enhancement of Flu. Solvent electrospinning of Flu-PEtOx blends, therefore, allows to fabricate fully amorphous ASDs containing Flu-loadings as high as 55 wt%, which is unprecedented. The amorphous nature of the electrospun Flu-PEtOx ASDs was additionally predicted by XRD-patterns generated by the computational model (**Figure S8**).

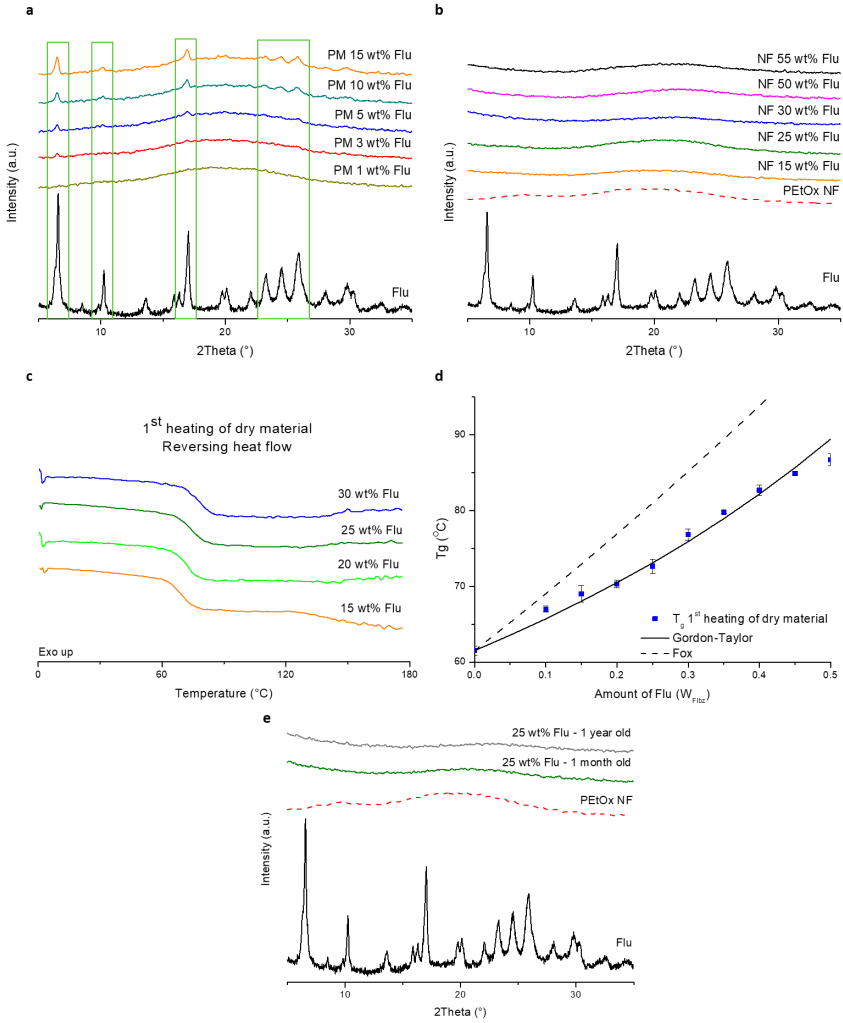

Figure 4. XRD spectra of physical Flu-PEtOx mixtures with an increasing amount of Flu show Bragg peaks from 3 wt% Flu-loading onwards (a, Flu-related Bragg peaks are highlighted in the green boxes), while Flu-PEtOx ASDs show no Bragg peaks up to Flu-loadings of 55 wt%, confirming the amorphous nature of the ASDs (b). (c) MDSC analysis of the prepared Flu-PEtOx ASDs shows a clear single T_g is observed in between the Tg of the pure components (156 °C for Flu[3] and 61.5 °C for PEtOx NF). (d) T_g analysis of Flu-PEtOx ASDs. Values were compared to the theoretical values predicted by Fox equation and fitted against the Gordon-Taylor equation with a k value of 0.42. (e) The XRD spectrum shows no sign of Bragg peaks related to crystalline Flu, indicating a fully amorphous ASD even after one year.

MDSC was additionally applied to assess the miscibility and single-phase character of the ASDs, which relates to the Flu-PEtOx interactions and, consequently, the ASDs physical stability.[3] Note that MDSC could not be used to assess crystallinity as the melting peak of Flu (238 °C)[3] is located above the degradation temperature of Flu (225 °C, **Figure S1**). The MDSC thermograms of the nanofibrous ASDs (**Figure 4**, c) revealed a homogeneous system, similar to what was expected from the force field calculations. Moreover, all T_gs were situated in between the T_g of pure Flu (156 °C)[3] and PEtOx (61.5 °C) (**Table S2**), suggesting a good miscibility between both components. The T_gs were analyzed using the Fox (Eq. (1)) and Gordon-Taylor (Eq. (2)) models.

$$\frac{1}{T_g} = \frac{w_1}{T_{g1}} + \frac{w_2}{T_{g2}} \tag{1}$$

$$T_g = \frac{w_1 T_{g1} + k w_2 T_{g2}}{w_1 + k w_2} \tag{2}$$

with T_g being the glass transition temperature of the ASD, wi and T_{gi} the respective weight fraction and T_g of the pure components. The subscript 2 refers to the component with the highest T_g, which is Flu in this case.[56] The Fox model assumes homogeneous mixing and no specific interactions between both components.[57] The Gordon-Taylor model, on the other hand, takes into account the specific coefficients of expansion in the rubbery and glassy state of the pure components based on the constant k (Eq. (3)).[58]

$$k = \frac{\Delta\alpha_2 \rho_1}{\Delta\alpha_1 \rho_2} \tag{3}$$

where $\Delta\alpha_i$ and ρ_i are the change in cubic expansion coefficient and the density of the components at the T_g, respectively.[59] The experimentally obtained T_gs correspond well with the theoretically predicted values using the Gordon-Taylor model with a fitting parameter k of 0.42 (**Figure 4**, d, and **Table S2**). The Gordon-Taylor model also assumes ideal mixing, hence complete miscibility, of both components.[56] Therefore, the obtained fit confirms the miscibility between Flu and PEtOx, a result that is crucial for the physical stability of the ASDs, as intimately mixed systems are more likely to resist crystallization.[49,60–62] Moreover, it experimentally confirms the results obtained by the performed simulations.

Flu mobility and long term ASD stability

For real-life applications, the long term stability of the ASDs is a crucial factor. Molecular dynamic simulations (see **section Experimental and computational analysis of Flu-PEtOx interactions**) indicated that the obtained ASDs could be significantly stabilized due to the presence of the strong and stable Flu-PEtOx hydrogen bonds. This statement was verified by evaluating the stability of an electrospun Flu-PEtOx ASD with a Flu-loading of 25 wt% that was stored at 23 °C and 25% relative humidity for one year. **Figure 4** (e) shows the XRD spectrum of this stored sample, still revealing a fully amorphous material, which indicated the long term physical stability of electrospun nanofibrous Flu-PEtOx ASDs. To further understand the experimentally observed stability of the solvent electrospun ASDs, the mobility of Flu within the ASDs was investigated by computation of self-diffusivity coefficients with respect to pure Flu (crystal) and Flu dissolved in water (5 mg/mL, **section S2.2.11**). As the self-diffusivity coefficients of a 50 wt% Flu-PEtOx ASD ($5.459 \pm 1.183 \cdot 10\text{-}8\ cm^2 \cdot s^{-1}$) and a Flu-crystal ($5.456 \pm 3.2 \cdot 10\text{-}8\ cm^2 \cdot s^{-1}$) were very similar, it could be concluded that the Flu-molecules are effectively trapped within the ASDs, as is the case for Flu-molecules within a Flu-crystal. To put this into perspective, the self-diffusivity of Flu-molecules in an aqueous environment was two orders of magnitude higher ($2.679 \pm 1.403 \cdot 10\text{-}6\ cm^2 \cdot s^{-1}$), highlighting the relatively fast dynamics of the molecules in biological environments. The observed trend nicely illustrates how the polymer matrix can serve as a kinetic trap for the Flu-molecules in case the ASD is prepared by solvent electrospinning, thereby inducing long-term stability, which is perfectly in line with the long-term stability experiments and hydrogen bond lifetimes presented above.

Solubility and release rate enhancement through in vitro sink drug delivery testing

APIs belonging to the BCS class II and IV, such as Flu, suffer from a low bioavailability due to their limited solubility and, therefore, low dissolution rate. The effect of solvent electrospinning Flu-PEtOx ASDs as a formulation strategy to increase aqueous solubility and dissolution rates was, therefore, analyzed by in vitro Flu release tests. To determine the sink conditions that were used for the in vitro release testing, the equilibrium solubility of Flu and several ASDs was determined in both pH 1 and pH 6.75 media (**Table S3**). The positive effect of the amorphous structure on the solubility is already evident, as the equilibrium solubility of Flu is 2.6 times higher (pH 1) when formulated as an ASD compared to its crystalline counterpart. Note that the equilibrium solubility of Flu is 32 times higher in acidic medium compared to neutral medium, which can be attributed

to the protonation of the benzimidazole group at low pH.[63,64] In vitro sink dissolution tests were subsequently performed to assess dissolution rates (**Table S4**). A substantial difference between Flu in its crystalline form and within the ASD formulations was observed. While after five hours only 37% of crystalline Flu was dissolved (**Figure S2**), all ASDs reached almost full Flu release during the first hour already (**Figure 5**, a).

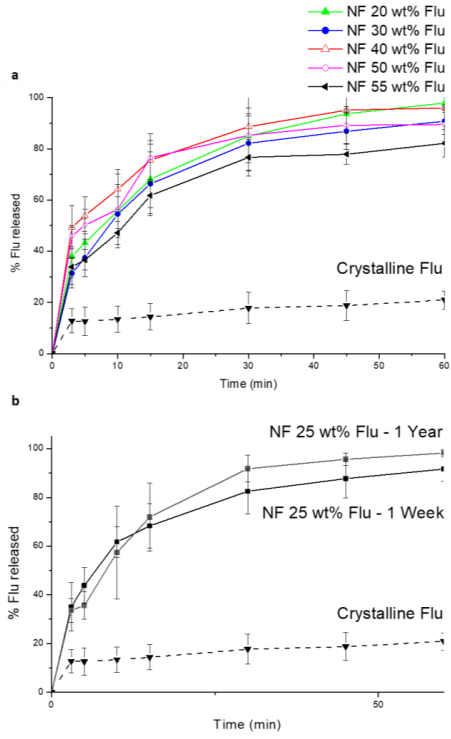

Figure 5. (a) Dissolution profile of Flu-PEtOx ASDs vs. crystalline Flu, representing the cumulative release of Flu after one hour in a pH 1 dissolution medium. (b) A comparison of sink dissolution testing of a 25 wt% Flu-PEtOx ASD after one week vs. one year shows that no significant difference is found between the sink dissolution profiles of both ASDs. In the first hour full dissolution is already obtained, while crystalline Flu only reaches a 20% dissolution during the first hour.

The initial dissolution rates (**Table S4**), clearly demonstrate that formulating Flu in a PEtOx-based ASD nanofibers via solvent electrospinning increased the dissolution rate by 4.3 times on average. No significant effect of the Flu-loading was noticed in the dissolution profiles of the ASDs. **Figure**

5 (b) additionally shows the sink dissolution profile of an ASD that was stored for one year compared to crystalline Flu and an ASD stored for one week. Remarkably, no significant differences were observed, revealing the same dissolution profile after one week and one year, with respective dissolution rates of 0.31 ± 0.03 $\mu g \cdot mL^{-1} \cdot min^{-1}$ and 0.30 ± 0.08 $\mu g \cdot mL^{-1} \cdot min^{-1}$ during the first ten minutes (**Table S5**). A similarity factor f_2, as described by Shah et al.,[65] of 60.5 was obtained, meaning that the average difference between the two dissolution profiles is only around 6%. These results indicate the potential of solvent electrospinning and the ability of PEtOx as an excipient to stabilize the amorphous form of Flu and inhibit recrystallization, both upon dissolution and over time.

Solvent electrospinning vs. solvent casting

The ability of solvent electrospinning to obtain fully amorphous ASDs is hypothesized to be a consequence of the extremely rapid solvent evaporation throughout the electrospinning process, which leaves very limited time for the system to reorganize and phase separate (due to Flu crystallization) before it is frozen into place.[25,66] As a validation of this hypothesis, another solvent method for the creation of Flu-PEtOx ASDs was evaluated, *i.e*. solvent casting (SC). Identical Flu-PEtOx solutions as those used for solvent electrospinning were prepared and the solution was left to evaporate at ambient temperature. This means that a considerable timespan was provided for full solvent evaporation, in which there was molecular mobility of Flu. Given that there is more time for rearrangement of Flu, it was expected that recrystallization was more likely to occur, which was indeed confirmed by XRD analysis. From 15 wt% Flu-loadings onwards, the SC ASDs were no longer fully amorphous, as the SC ASDs with 20 and 25 wt% Flu-loadings clearly showed a small Bragg peak at 6.5° (**Figure 6**). SC could, therefore, only guarantee a fully amorphous ASD material at low Flu-loadings, which is in strong contrast with the solvent electrospun nanofibrous ASDs enabling Flu-loadings up to 55 wt% without losing the amorphous nature. It can be hypothesized that, due to the added timespan with increased molecular mobility during SC, the Flu-molecules were able to rearrange themselves in such a manner that Flu-Flu hydrogen bonds became dominant over Flu-PEtOx hydrogen bonds, unlike the solvent electrospun ASDs where Flu-PEtOx hydrogen bonds remained dominant.

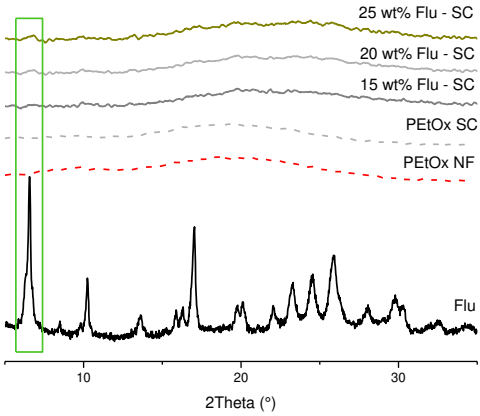

Figure 6. XRD spectra of SC ASDs compared to the spectra of the pure components. From 15 wt% Flu-loadings onwards, a small Bragg peak at 6.5° becomes distinguishable. As proven by Figure 4 (a), this peak is significant in indicating a higher ordening of the molecules leading up to a crystalline material. The SC technique can only guarantee complete amorphicity for low Flu-loadings.

Conclusion

Even though Flu is proven to be a highly effective API against tropical diseases that are still affecting millions of people, sufficient bioavailability upon oral administration remains challenging due to the low solubility of the API and the limited physical stability of the currently applied formulations. In this work, solvent electrospinning was proven to be a highly promising alternative formulation technique using PEtOx as the excipient, as the produced nanofibrous Flu-PEtOx ASDs containing up to 55 wt% Flu showed a significant increase in solubility, hence bioavailability, in (acidic) aqueous media. Two important phenomena were considered to improve the physical stability of the formulations and, thereby, the efficacy of the drug delivery: the API-polymer interactions within the ASDs and the (long-term) amorphous nature of the ASDs. Experimental ATR-FTIR analysis and computational molecular dynamics simulations supported the presence of strong, dominant and stable Flu-PEtOx hydrogen bond interactions, which enabled to significantly increase the Flu-loading in the ASDs up to 55 wt% by reducing the amount of PEtOx in the spinning solutions. It is hypothesized that, thanks to the rapid solvent evaporation during the

electrospinning process, crystallization is inhibited as the dispersed Flu-molecules are quickly frozen into place and kinetically trapped within the PEtOx-matrix. Indeed, calculated self-diffusivity coefficients confirmed that the Flu-mobility within the ASDs was limited, as the coefficients were of the same order of magnitude as within a Flu-crystal. Additionally, XRD and MDSC analysis demonstrated the amorphous and single-phase nature of the Flu-PEtOx ASDs up to the high Flu-loadings of 55 wt%. As a consequence, Flu dissolution rates were quadrupled compared to crystalline Flu, and complete Flu release was achieved within one hour opposed to only 30% after five hours for crystalline Flu. The kinetic entrapment of amorphous Flu-molecules together with the Flu-PEtOx miscibility and the presence of strong and stable Flu-PEtOx hydrogen bond interactions led to the promising result that, even after one year of storage, the nanofibrous Flu-PEtOx ASDs remained amorphous and a complete API-release within one hour could still be achieved. Based on these findings, it is clear that both the solvent electrospinning technique and the excipient PEtOx provide several vital features for the formulation of high-loaded, time-stable ASDs with significantly improved drug-solubility, which is promising for the oral administration of not only Flu, but possibly also other BCS class II and IV APIs. This work further indicates that the strategy of combining experimental and computational work can add true value to obtain breakthroughs in the bioavailability improvement of future API-polymer ASD formulations. A new protocol was here established to simulate multi-scale Flu-PEtOx ASDs realistically, thereby providing a tool to thoroughly investigate and clarify the experimental observations and predict the characteristics of the real ASD. Indeed, such computational procedure allows to simulate possible API-polymer formulations and investigate the influence on ASD behavior under different experimental conditions, enabling to select which API-polymer formulations are promising to test experimentally. The expansion of this strategy will, therefore, be the subject of our future work, with the ultimate goal of developing a guide for drug selection and loading optimization for PEtOx-based electrospun ASDs.

Experimental Section/Methods

Materials. Flu was purchased from UTAG (Almere, Netherlands). Defined PEtOx with an M_n of 50 kDa was synthesized as described below and according to previous literature.[67] 2-Phenyl-2-oxazoline (99%), tetrafluoroboric acid (48 wt% in H_2O) and methanol (>99.8%) were purchased

from Sigma-Aldrich (Overijse, Belgium). Ninhydrin, barium oxide and ethyl acetate (acroseal® grade) were bought from Acros Organics (Geel, Belgium) and used as received. 2-Ethyl-2-oxazoline (Polymer Chemistry Innovations, Tuscon, USA) was purified by distillation over ninhydrin and bariumoxide. Formic acid (FA) (>98%) and hydrochloric acid (HCl) (37% in H_2O) were purchased from Sigma Aldrich (Overijse, Belgium) and used as such. All tests requiring an aqueous solution (pure H_2O or 0.1 M HCl solution) were carried out with distilled water of type III as considered in ISO Standard 3696.

Synthesis of poly(2-ethyl-2-oxazoline) with an Mn of 50 kDa. PEtOx with a molar mass of 50 kDa was synthesized according to a recently reported method.[67,68] Prior to polymerization, the solvent, ethyl acetate, and the monomer, 2-ethyl-2-oxazoline, were dried and purified. The initiator was a proton-initiated 2-phenyl-2-oxazoline tetrafluoroborate (HPheBF4) salt that was recrystallized from methanol, which was melted under vacuum overnight. Using a VIGOR Sci-Lab SG 1200/750 Glovebox System, all reactants were added in the actual polymerization vessel containing the right amount of initiator needed for the polymerization. The reaction was aimed at a 70% conversion using a monomer-to-initiator ratio of 714:1 leading to an expected M_n of 50 kDa. Maintaining an inert, nucleophile free atmosphere, the reaction mixture was stirred at 60 °C in an oil bath for 5 days and 4 hours until the desired M_n of 50 kDa was reached. Subsequently, the polymer mixture was terminated using an excess of a 1 M methanolic KOH solution. The polymer solution was purified by four consecutive steps of dilution with distilled water followed by rotary evaporation of the solvent under reduced pressure.

Polymer characterization. Size- exclusion chromatography was performed on an Agilent 1260-series HPLC system equipped with a 1260 online degasser, a 1260 ISO-pump, a 1260 automatic liquid sampler, a thermostatted column compartment set at 50°C equipped with two PLgel 5 µm mixed-D columns (7.5 mm × 300 mm) and a precolumn in series, a 1260 diode array detector, and a 1260 refractive index (RI) detector. The used eluent was *N*,*N*-dimethyl acetamide containing 50 mM of LiCl at a flow rate of 0.5 mL/min. The spectra were analyzed using the Agilent Chemstation software with the GPC add on. Molar mass values and molar mass distribution, that is, dispersity (Đ), values were calculated against in-house synthesized PEtOx standards. A M_n of 47 kDa and a Đ of 1.28 was obtained.

Electrospinning of solid dispersions. Electrospinning solutions were prepared by dissolving different amounts of Flu in FA. After full dissolution of Flu, the polymer was added and the solution

was stirred until a homogeneous transparent solution was obtained. Mass concentrations are expressed by weight percentages defined for the polymer as the ratio of PEtOx mass and the sum of the PEtOx and solvent mass (Eq. (5)). For the amount of Flu in the system, the wt% is defined as the ratio of the mass of Flu to the sum of the Flu and PEtOx mass (Eq. (6)). The dynamic viscosity of the solutions was determined by an LVDV-II Brookfield viscometer (spindle S18, average error of 8%). All solvent electrospinning experiments were carried out using a mononozzle set-up with an 18 gauge Terumo mixing needle without bevel. A stable Taylor cone was typically achieved at a flow rate of 0.1 ml·h^{-1}, a tip-to-collector distance of 20 cm, a voltage between 20 and 27 kV and a negative voltage at the collector of -5 kV. All electrospinning experiments were carried out under climatized conditions at 25°C and 30% relative humidity in a Weisstechnik WEKK 10.50.1500 climate chamber. After electrospinning all samples were stored in a climatized lab at (23 ± 1)°C and a relative humidity of (25 ± 2)%.

$$wt\%_{PEtOx} = \frac{m_{PEtOx}}{m_{PEtOx} + m_{solvent}} \quad (5)$$

$$wt\%_{Flu} = \frac{m_{Flu}}{m_{Flu} + m_{PEtOx}} \quad (6)$$

Solvent casting. An entire range of ASDs with a Flu-loading ranging from 5 to 55 wt% was prepared *via* solvent casting (SC). In order to obtain homogeneous solutions a 15 wt% concentration of PEtOx was used. All solutions were prepared by dissolving different amounts of Flu in FA. After full dissolution of Flu the polymer was added and the solution was stirred. Once homogeneous solutions were obtained, the solutions were left overnight in a fumehood for FA evaporation. To ensure full solvent evaporation, the samples were stored in a desiccator and kept under vacuum for 1 week after which the samples were stored in a climatized lab at (23 ± 1)°C and a relative humidity of (25 ± 2)%.

Scanning electron microscopy. All produced nanofibrous membranes were analyzed on a Phenom XL Scanning Electron Microscope (SEM) at an accelerating voltage of 10 kV. Prior to analysis the samples were coated with gold using a sputter coater (LOT MSC1T). The nanofiber diameters were measured using FiberMetric software. The average diameters and their standard deviations were based on 500 measurements per sample.

Attenuated total reflectance Fourier transform infrared spectroscopy. Infrared (IR) spectra were recorded with a Nicolet^{TM} IS50 Fourier Transform Infrared (FTIR) spectrometer equipped

with an Attenuated Total Reflectance (ATR) accessory (diamond crystal) from Thermo Scientific. Samples were excited with light of wavenumbers ranging from 4000 up to 400 cm^{-1}. A resolution of 1 cm^{-1} and 32 scans for each sample was applied.

Thermogravimetric analysis. Thermogravimetric analysis (TGA) was performed on a Mettler-Toledo TGA/SDTA851e with Large Furnace and autosampler, using 70 µL alumina cubicles. Measurements were performed at 10°C/min from 25 to 400°C under nitrogen atmosphere. Evaluation was done *via* the STARe software, using blank corrections.

Temperature modulated differential scanning calorimetry. Temperature Modulated Differential Scanning Calorimetry (MDSC) was used to measure T_gs. A TA Instruments Q2000 equipped with a refrigerated cooling system (RCS90) was applied using nitrogen as purge gas (50 $mL \cdot min^{-1}$). The instrument was calibrated using Tzero technology for standard Tzero aluminum pans using indium at the heating rate applied during the measurements. The heating rate was set at 2 $°C \cdot min^{-1}$ and samples of 2 ± 0.5 mg were used. A temperature modulation of ± 0.3 °C every 60 s was selected. The samples were analyzed through an initial isothermal drying step at 100 °C for 30 min after which a heat-cool-heat cycle was set from 0 to 180 °C. The T_g was determined with TA TRIOS software. Experiments were performed in triplicate.

X-ray diffraction. All ASDs, both nanofibrous and solvent casted, were measured on an ARL™ X'TRA Powder Diffractometer of Thermo Scientific. The monochromatic X-rays are produced by a copper X-ray tube; Cu K-shell energy levels are equivalent to $\lambda = 0.154056$ nm. The diffraction patterns are recorded at an interval of 5 to 60° 2θ with a step size of 0.02° and a measuring time of 45 min. A Si (Li) solid state detector was used for data collection. To determine the sensitivity of the diffractometer towards the crystalline Flu, physical mixtures of PEtOx and Flu were prepared and measured accordingly. The nanofibrous ASDs were measured as such, while the SC samples were grinded to a powder.

UV-visible spectroscopy. UV-Vis spectra were recorded using a double beam Perkin-Elmer Lambda 900 UV-Vis spectrophotometer. Solutions were measured in transmission mode using quartz cells. The spectra were recorded from 250 nm to 400 nm with a data interval of 1 nm. Transmission was converted into absorbance (A) as these values provide a correlation with Flu concentration.

Determination of solubility. The solubility of Flu in its pure form and in the ASDs was determined in both H_2O and 0.1 M HCl using an ultrasonic bath. An excess amount of Flu, 50 ± 15 mg, or of

the produced ASDs, containing 1 ± 0.05 mg Flu, was added to 10 ml H_2O (pH 6.75) or 0.1 M HCl (pH 1) solution. Mixtures were left in an 1510E Bransonic ultrasonic bath (42 kHz ± 6%) for three hours after which they rested vertically overnight prior to measurement. Samples were taken and filtered through a 0.45 µm PTFE filter, diluted and consequently measured *via* UV-Vis spectroscopy. The Flu content was determined with respect to a calibration curve at 283 nm obtained prior to the measurements. Experiments were performed in triplicate.

***In vitro* dissolution tests under sink conditions**. For both pure Flu and the produced SDs, *in vitro* dissolution tests were performed in 0.1 M HCl. After determination of the respective solubility, all measurements were performed under sink conditions, an equivalent of 5 mg of Flu was added to 1000 ml 0.1 M HCl dissolution medium (pH 1). The medium was stirred at a constant speed of 100 rpm throughout the measurements and samples were taken at different time intervals, *i.e.* 3, 5, 10, 15, 30, 45, 60, 90, 120, 150, 180, 240 and 300 minutes. Samples were filtered through a 0.45 µm PTFE filter, diluted and consequently measured *via* UV-Vis spectroscopy. The concentration of Flu present was determined with respect to a calibration curve at 283 nm obtained prior to the measurements. Experiments were performed in triplicate.

Computational Methodology. As Flu-PEtOx interactions are crucial for the ASD stability, hence the solubility enhancement of Flu, the Flu-PEtOx interactions were also investigated by a multi-scale modelling approach to support and better understand the experimental observations. To this end, two types of simulations were performed. Firstly, a set of density functional theory (DFT) calculations was performed to assess whether Flu-PEtOx interactions are competitive with respect to Flu-Flu interactions (resembling the interactions present within a Flu-crystal). Secondly, large-scale atomistic force field-based simulations (>40000 atoms) were performed on 50 wt% Flu-PEtOx ASDs, which were then compared to their pure compound counterparts regarding the nature and dynamics of occurring hydrogen bonds. Prior to these simulations, force fields were constructed for both PEtOx and Flu with the necessary validation performed in terms of density, T_g and XRD-pattern determination. For a full elaboration on the computational methodology, the reader is referred to **section S2** of Supporting Information.

Corresponding Author

*K. De Clerck, Ghent University, Center for Textile Science and Engineering, Faculty of Engineering and Architecture, Tech Lane Science Park 70A, B-9052 Ghent, Belgium, E-mail: Karen.DeClerck@UGent.be

*V. Van Speybroeck, Ghent University, Center for Molecular Modeling, Faculty of Engineering and Architecture, Tech Lane Ghent Science Park Campus A 46, B-9052 Ghent, Belgium, E-mail: Veronique.VanSpeybroeck@UGent.be

*C. Vervaet, Ghent University, Laboratory of Pharmaceutical Technology, Faculty of Pharmaceutical Sciences, Ottergemsesteenweg 460, B-9000 Ghent, Belgium, E-mail: Chris.Vervaet@UGent.be

*R. Hoogenboom, Ghent University, Supramolecular Chemistry Group, Faculty of Sciences, Krijgslaan 281-S4, B-9000 Ghent, Belgium, E-mail: Richard.Hoogenboom@UGent.be

Author Contributions

The manuscript was written through contributions of all authors. All authors have given approval to the final version of the manuscript. JB‡ and EVDB‡ contributed equally.

Notes

The authors declare the following competing financial interest(s): JB, CV, RH and KDC are listed as inventors on a filed patent application covering high drug-loading ASD nanofibers as presented in this work. RH is one of the founders of Avroxa BV that commercializes poly(2-oxazoline)s as Ultroxa ®. The other authors declare no competing financial interest.

Acknowledgement

Financial support from the Research Foundation – Flanders (FWO) is gratefully acknowledged for funding the research through SB PhD grants 1S89118N of JB and 1S05517N of ES. Ghent University is also thanked by KDC, RH and CV for its continued support. The computational

resources and services used were provided by Ghent University (Stevin Supercomputer Infrastructure), the VSC (Flemish Supercomputer Centre), funded by Ghent University, the Research Foundation - Flanders (FWO) and the Flemish Government. EVDB, SB. and VVS acknowledge the Research Foundation - Flanders (FWO) and the Research Fund of Ghent University (BOF).

References

1. Xiong, X. *et al.* Solid dispersions of telaprevir with improved solubility prepared by co-milling: formulation, physicochemical characterization, and cytotoxicity evaluation. *Mater. Sci. Eng. C* **105**, 110012 (2019).

2. Brough, C. & Williams, R. O. Amorphous solid dispersions and nano-crystal technologies for poorly water-soluble drug delivery. *Int. J. Pharm.* **453**, 157–166 (2013).

3. Vialpando, M. *et al.* Evaluation of Three Amorphous Drug Delivery Technologies to Improve the Oral Absorption of Flubendazole. *J. Pharm. Sci.* **105**, 2782–2793 (2016).

4. O'Neill, M. *et al.* Profiling the macrofilaricidal effects of flubendazole on adult female Brugia malayi using RNAseq. *Int. J. Parasitol. Drugs Drug Resist.* **6**, 288–296 (2016).

5. O'Neill, M., Geary, J. F., Agnew, D. W., Mackenzie, C. D. & Geary, T. G. Invitro flubendazole-induced damage to vital tissues in adult females of the filarial nematode Brugia malayi. *Int. J. Parasitol. Drugs Drug Resist.* **5**, 135–140 (2015).

6. Sjoberg, H. T. *et al.* Short-course, oral flubendazole does not mediate significant efficacy against Onchocerca adult male worms or Brugia microfilariae in murine infection models. *PLoS Negl. Trop. Dis.* **13**, 1–19 (2019).

7. Hübner, M. P. *et al.* Macrofilaricidal efficacy of single and repeated oral and subcutaneous doses of flubendazole in Litomosoides sigmodontis infected jirds. *PLoS Negl. Trop. Dis.* **13**, 1–17 (2019).

8. de Araujo, G. L. B. *et al.* A New Thermodynamically Favored Flubendazole/Maleic Acid Binary Crystal Form: Structure, Energetics, and *in Silico* PBPK Model-Based Investigation. *Cryst. Growth Des.* acs.cgd.7b01807 (2018). doi:10.1021/acs.cgd.7b01807

9. Ceballos, L., Mackenzie, C., Geary, T., Alvarez, L. & Lanusse, C. Exploring the Potential of Flubendazole in Filariasis Control: Evaluation of the Systemic Exposure for Different Pharmaceutical Preparations. *PLoS Negl. Trop. Dis.* **8**, e2838 (2014).

10. Chami, G. F. *et al.* Diffusion of treatment in social networks and mass drug administration. *Nat. Commun.* **8**, 1929 (2017).

11. Dominguez-Vazquez, A. *et al.* Comparison of flubendazole and diethylcarbamazine in treatment of onchocerciasis. *Lancet* **321**, 139–143 (1983).

12. Knopp, M. M. *et al.* Effect of polymer type and drug dose on the in vitro and in vivo behavior of amorphous solid dispersions. *Eur. J. Pharm. Biopharm.* **105**, 106–114 (2016).

13. Van Den Mooter, G. The use of amorphous solid dispersions: A formulation strategy to overcome poor solubility and dissolution rate. *Drug Discov. Today Technol.* **9**, e79–e85 (2012).

14. Chiou, W. L. & Riegelman, S. Pharmaceutical Applications of Solid Dispersion Systems. *J. Pharm. Sci.* **60**, 1281–1302 (1971).

15. Smeets, A., Koekoekx, R., Clasen, C. & Van den Mooter, G. Amorphous solid dispersions of darunavir: Comparison between spray drying and electrospraying. *Eur. J. Pharm. Biopharm.* **130**, 96–107 (2018).

16. Dedroog, S., Huygens, C. & Van den Mooter, G. Chemically identical but physically different: A comparison of spray drying, hot melt extrusion and cryo-milling for the formulation of high drug loaded amorphous solid dispersions of naproxen. *Eur. J. Pharm. Biopharm.* **135**, 1–12 (2019).

17. Chakravarty, P., Lubach, J. W., Hau, J. & Nagapudi, K. A rational approach towards development of amorphous solid dispersions: Experimental and computational techniques. *Int. J. Pharm.* **519**, 44–57 (2017).

18. Pacułt, J., Rams-Baron, M., Chrząszcz, B., Jachowicz, R. & Paluch, M. Effect of Polymer Chain Length on the Physical Stability of Amorphous Drug-Polymer Blends at Ambient Pressure. *Mol. Pharm.* **15**, 2807–2815 (2018).

19. Persch, C. *et al.* The potential of chemical bonding to design crystallization and vitrification kinetics. *Nat. Commun.* **12**, 4978 (2021).

20. Shang, L. *et al.* Spinning and Applications of Bioinspired Fiber Systems. *ACS Nano* **13**, 2749–2772 (2019).

21. Ogueri, K. S. & Laurencin, C. T. Nanofiber Technology for Regenerative Engineering. *ACS Nano* **14**, 9347–9363 (2020).

22. Démuth, B. *et al.* Detailed stability investigation of amorphous solid dispersions prepared by single-needle and high speed electrospinning. *Int. J. Pharm.* **498**, 234–244 (2016).

23. Yu, D. G. *et al.* Third generation solid dispersions of ferulic acid in electrospun composite nanofibers. *Int. J. Pharm.* **400**, 158–164 (2010).

24. Ding, Y. *et al.* Electrospun Fibrous Architectures for Drug Delivery, Tissue Engineering and Cancer Therapy. *Adv. Funct. Mater.* **29**, 1802852 (2019).

25. Yu, D. G., Li, J. J., Williams, G. R. & Zhao, M. Electrospun amorphous solid dispersions of poorly water-soluble drugs: A review. *J. Control. Release* **292**, 91–110 (2018).

26. Bhardwaj, N. & Kundu, S. C. Electrospinning: A fascinating fiber fabrication technique. *Biotechnology Advances* **28**, 325–347 (2010).

27. Greiner, A. & Wendorff, J. H. Electrospinning: A fascinating method for the preparation of ultrathin fibers. *Angew. Chemie - Int. Ed.* **46**, 5670–5703 (2007).

28. Schoolaert, E. *et al.* Blend electrospinning of dye-functionalized chitosan and poly(ϵ-caprolactone): Towards biocompatible pH-sensors. *J. Mater. Chem. B* **4**, 4507–4516 (2016).

29. Stubbe, B. *et al.* Aqueous electrospinning of poly(2-ethyl-2-oxazoline): Mapping the parameter space. *European Polymer Journal* **88**, 1–9 (2016).

30. Persano, L., Camposeo, A., Tekmen, C. & Pisignano, D. Industrial upscaling of electrospinning and applications of polymer nanofibers: A review. *Macromolecular Materials and Engineering* **298**, 504–520 (2013).

31. Vigh, T. *et al.* Oral bioavailability enhancement of flubendazole by developing nanofibrous solid dosage forms. *Drug Dev. Ind. Pharm.* **9045**, 1–8 (2017).

32. Saboo, S., Mugheirbi, N. A., Zemlyanov, D. Y., Kestur, U. S. & Taylor, L. S. Congruent

release of drug and polymer: A “sweet spot” in the dissolution of amorphous solid dispersions. *J. Control. Release* **298**, 68–82 (2019).

33. Fael, H., Ràfols, C. & Demirel, A. L. Poly(2-Ethyl-2-Oxazoline) as an Alternative to Poly(Vinylpyrrolidone) in Solid Dispersions for Solubility and Dissolution Rate Enhancement of Drugs. *J. Pharm. Sci.* **107**, 2428–2438 (2018).

34. Boel, E. *et al.* Comparative study of the potential of poly(2-ethyl-2-oxazoline) as carrier in the formulation of amorphous solid dispersions of poorly soluble drugs. *Eur. J. Pharm. Biopharm.* **144**, 79–90 (2019).

35. Chen, B. M., Cheng, T. L. & Roffler, S. R. Polyethylene Glycol Immunogenicity: Theoretical, Clinical, and Practical Aspects of Anti-Polyethylene Glycol Antibodies. *ACS Nano* (2021). doi:10.1021/acsnano.1c05922

36. Bhardwaj, S. P. *et al.* Mechanism of amorphous itraconazole stabilization in polymer solid dispersions: Role of molecular mobility. *Mol. Pharm.* **11**, 4228–4237 (2014).

37. De La Rosa, V. R. Poly(2-oxazoline)s as materials for biomedical applications. *J. Mater. Sci. Mater. Med.* (2014). doi:10.1007/s10856-013-5034-y

38. Friedl, J. D., Nele, V., De Rosa, G. & Bernkop-Schnürch, A. Bioinert, Stealth or Interactive: How Surface Chemistry of Nanocarriers Determines Their Fate In Vivo. *Adv. Funct. Mater.* **31**, 2103347 (2021).

39. Konradi, R., Acikgoz, C. & Textor, M. Polyoxazolines for nonfouling surface coatings - A direct comparison to the gold standard PEG. *Macromol. Rapid Commun.* **33**, 1663–1676 (2012).

40. Lapuk, S. E. *et al.* Kinetic stability of amorphous solid dispersions with high content of the drug: A fast scanning calorimetry investigation. *Int. J. Pharm.* **562**, 113–123 (2019).

41. Lorson, T. *et al.* Poly(2-oxazoline)s based biomaterials: A comprehensive and critical update. *Biomaterials* **178**, 204–280 (2018).

42. Sedlacek, O., Monnery, B. D., Filippov, S. K., Hoogenboom, R. & Hruby, M. Poly(2-oxazoline)s - Are they more advantageous for biomedical applications than other polymers? *Macromol. Rapid Commun.* **33**, 1648–1662 (2012).

43. Muljajew, I. *et al.* Stealth Effect of Short Polyoxazolines in Graft Copolymers: Minor Changes of Backbone End Group Determine Liver Cell-Type Specificity. *ACS Nano* **15**, 12298–12313 (2021).

44. Hoogenboom, R. Poly(2-oxazoline)s: A polymer class with numerous potential applications. *Angew. Chemie - Int. Ed.* **48**, 7978–7994 (2009).

45. Luxenhofer, R. *et al.* Structure-property relationship in cytotoxicity and cell uptake of poly(2-oxazoline) amphiphiles. *J. Control. Release* **153**, 73–82 (2011).

46. Claeys, B. *et al.* Poly (2-ethyl-2-oxazoline) as Matrix Excipient for Drug Formulation by Hot Melt Extrusion and Injection Molding. *Macromol. Rapid Commun.* **33**, 1701–1707 (2012).

47. Buruaga, L., Gonzalez, A. & Iruin, J. J. Electrospinning of poly (2-ethyl-2-oxazoline). *J. Mater. Sci.* **44**, 3186–3191 (2009).

48. Pacułt, J., Rams-Baron, M., Chrząszcz, B., Jachowicz, R. & Paluch, M. Effect of Polymer

Chain Length on the Physical Stability of Amorphous Drug-Polymer Blends at Ambient Pressure. *Mol. Pharm.* **15**, 2807–2815 (2018).

49. Chakravarty, P., Lubach, J. W., Hau, J. & Nagapudi, K. A rational approach towards development of amorphous solid dispersions: Experimental and computational techniques. *Int. J. Pharm.* **519**, 44–57 (2017).

50. Punčochová, K., Heng, J. Y. Y., Beránek, J. & Štěpánek, F. Investigation of drug-polymer interaction in solid dispersions by vapour sorption methods. *Int. J. Pharm.* **469**, 159–167 (2014).

51. Li, N. & Taylor, L. S. Tailoring supersaturation from amorphous solid dispersions. *J. Control. Release* **279**, 114–125 (2018).

52. Li, D., Panchal, K., Mafi, R. & Xi, L. An Atomistic Evaluation of the Compatibility and Plasticization Efficacy of Phthalates in Poly(vinyl chloride). *Macromolecules* **51**, 6997–7012 (2018).

53. Sigma Aldrich. *Safety Data Sheet Ultroxa®: Poly(2-ethyl-2-oxazoline), average Mn 50,000, PDI ≤ 1.25*. **3**, (2018).

54. Gowers, R. J. & Carbone, P. A multiscale approach to model hydrogen bonding: The case of polyamide. *J. Chem. Phys.* **142**, (2015).

55. Chen, H. *et al.* Multistep nucleation and growth mechanisms of organic crystals from amorphous solid states. *Nat. Commun.* **10**, 3872 (2019).

56. Young, R. J. & Lovell, P. A. *Introduction to Polymers*. (CRC Press, 2011).

57. Qian, F. *et al.* Is a distinctive single Tg a reliable indicator for the homogeneity of amorphous solid dispersion? *Int. J. Pharm.* **395**, 232–235 (2010).

58. Gordon, M. & Taylor, J. S. Ideal Copolymers and the Second-Order Transitions of Synthetic Rubbers. I. Noncrystalline Copolymers. *Rubber Chem. Technol.* **26**, 323–335 (1953).

59. Jerca, V. V. *et al.* Synthesis and characterization of side-chain oxazoline–methyl methacrylate copolymers bearing azo-dye. *React. Funct. Polym.* **70**, 827–835 (2010).

60. Baird, J. A. & Taylor, L. S. Evaluation of amorphous solid dispersion properties using thermal analysis techniques. *Adv. Drug Deliv. Rev.* **64**, 396–421 (2012).

61. Davis, M. & Walker, G. Recent strategies in spray drying for the enhanced bioavailability of poorly water-soluble drugs. *J. Control. Release* **269**, 110–127 (2018).

62. Djuris, J., Nikolakakis, I., Ibric, S., Djuric, Z. & Kachrimanis, K. Preparation of carbamazepine-Soluplus® solid dispersions by hot-melt extrusion, and prediction of drug-polymer miscibility by thermodynamic model fitting. *Eur. J. Pharm. Biopharm.* **84**, 228–237 (2013).

63. Franco, L. F. M. & Pessôa Filho, P. de A. On the solubility of proteins as a function of pH: Mathematical development and application. *Fluid Phase Equilib.* **306**, 242–250 (2011).

64. George, M. & Abraham, T. E. Polyionic hydrocolloids for the intestinal delivery of protein drugs: Alginate and chitosan - a review. *J. Control. Release* **114**, 1–14 (2006).

65. Shah, V. P., Tsong, Y., Sathe, P. & Liu, J. P. In vitro dissolution profile comparison--statistics and analysis of the similarity factor, f2. *Pharm. Res.* **15**, 889–96 (1998).

66. Paaver, U. *et al.* Electrospun nano fi bers as a potential controlled-release solid dispersion system for poorly water-soluble drugs. *Int. J. Pharm.* **479**, 252–260 (2015).

67. Monnery, B. D. *et al.* Defined High Molar Mass Poly(2-Oxazoline)s. *Angew. Chemie - Int. Ed.* **57**, 15400–15404 (2018).

68. Vergaelen, M. *et al.* Ethyl acetate as solvent for the synthesis of poly(2-ethyl-2-oxazoline). *Green Chem.* **22**, 1747–1753 (2020).

TABLE OF CONTENTS

Solvent electrospinning is shown to be a promising alternative formulation technique for the poorly-soluble drug flubendazole, using poly(2-ethyl-2-oxazoline) as excipient. The nanofibrous amorphous solid dispersions demonstrate a superior physical stability and significant increase in flubendazole solubility and dissolution rates, thereby boosting flubendazole bioavailability, even after long term storage. The underlying mechanisms are investigated by experimental analysis and molecular dynamics simulations.

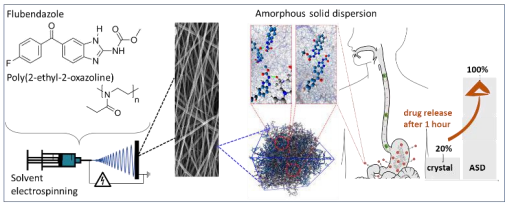

VII

List of Publications

Publications in international peer-reviewed journals

1. Elias Van Den Broeck, Massimo Bocus, Matthias Bal, Xian Wu, Jeroen Bomon, Louis Vanduyfhuys, Bert Maes, Bert Sels, Veronique Van Speybroeck, The concerted *O*-demethylation of guaiacol in hot-pressurized water catalyzed by Brønsted acids, to be submitted

2. Jana Becelaere, Elias Van Den Broeck, Valérie Vanhoorne, Ella Schoolaert, Joachim F.R. Van Guyse, Maarten Vergaelen, Sander Borgmans, Karolien Creemers, Veronique Van Speybroeck, Chris Vervaet, Richard Hoogenboom, and Karen De Clerck, Stable amorphous solid dispersions of flubendazole with ultrahigh drug loading through solvent electrospinning, to be submitted.

3. Kim Phan, Elias Van Den Broeck, Katleen Raes, Karen De Clerck, Veronique Van Speybroeck, and Steven De Meester. A comparative theoretical study on the solvent dependency of anthocyanin extraction profiles. *Journal of Molecular Liquids*, 351:118606, 2022. doi: $10.1016/\mathrm{j.molliq.2022.118606}$ IF:6.165

4. Sari Deketelaere, Elias Van Den Broeck, Lore Cools, Daan Deturck, Hannes Naeyaert, Kristof Van Hecke, Christian V. Stevens, Veronique Van Speybroeck, and Matthias D'hooghe. Unexpected Formation of 2,2-Dichloro-N-(chloromethyl)acetamides during Attempted Staudinger 2,2-Dichloro-β-

lactam Synthesis. *European Journal of Organic Chemistry*, 2021(42):5823–5830, 2021. doi: 10.1002/ejoc.202100975 IF: 3.021

5. K.N.R Dumoleijn, E. Van Den Broeck, J. Stavinoha, V. Van Speybroeck, K. Moonen, and C.V. Stevens. Reductive imino-pinacol coupling reaction of halogenated aromatic imines and iminium ions catalyzed by precious metal catalysts using hydrogen. *Journal of Catalysis*, 400:103–113, 2021. doi: 10.1016/j.jcat.2021.05.023 IF: 7.92

6. Fabiana Siragusa, Elias Van Den Broeck, Connie Ocando, Alejandro J. Müller, Gilles De Smet, Bert U W Maes, Julien De Winter, Veronique Van Speybroeck, Bruno Grignard, and Christophe Detrembleur. Access to biorenewable and CO2-based polycarbonates from exovinylene cyclic carbonates. *ACS Sustainable Chemistry & Engineering*, 9(4):1714–1728, 2021. doi: 10.1021/acssuschemeng.0c07683 IF: 8.198

7. Elias Van Den Broeck, Bart Verbraeken, Karen Dedecker, Pieter Cnudde, Louis Vanduyfhuys, Toon Verstraelen, Kristof Van Hecke, Valentin Victor Jerca, Saron Catak, Richard Hoogenboom, and Veronique Van Speybroeck. Cation-π interactions accelerate the living cationic ring-opening polymerization of unsaturated 2-alkyl-2-oxazolines. *Macromolecules*, 53(10):3832–3846, 2020. doi: 10.1021/acs.macromol.0c00865 IF: 5.985

8. Kim Phan, Elias Van Den Broeck, Veronique Van Speybroeck, Karen De Clerck, Katleen Raes, and Steven De Meester. The potential of anthocyanins from blueberries as a natural dye for cotton: A combined experimental and theoretical study. *Dyes and Pigments*, 176:108180, 2020. doi: 10.1016/j.dyepig.2019.108180 IF: 4.889

9. Jeroen Bomon, Elias Van Den Broeck, Mathias Bal, Yuhe Liao, Sergey Sergeyev, Veronique Van Speybroeck, Bert F. Sels, and Bert U. W. Maes. Brønsted acid catalyzed tandem defunctionalization of biorenewable ferulic acid and derivates into bio-catechol. *Angewandte Chemie International Edition*, 59(8):3063–3068, 2020. doi: 10.1002/anie.201913023 IF: 15.336

10. Farid Ouhib, Bruno Grignard, Elias Van Den Broeck, André Luxen, Koen Robeyns, Veronique Van Speybroeck, Christine Jerome, and Christophe Detrembleur. A switchable domino process for the construction of novel CO2 - sourced sulfur-containing building blocks and poolymers. *Angewandte Chemie International Edition*, 58(34):11768–11773, 2019. doi: 10.1002/anie.201905969 IF: 15.336

11. Nicola Piens, Hannelore Goossens, Dietmar Hertsen, Sari Deketelaere, Lieselotte Crul, Lotte Demeurisse, Jelle De Moor, Elias Van den Broeck, Karen Mollet, Kristof Van Hecke, Veronique Van Speybroeck, and Matthias D'hooghe.

Reactivity of 3-oxo-β-lactams with respect to primary amines-an experimental and computational approach. *Chemistry - A European Journal*, 23(71): 18002–18009, 2017. doi: 10.1002/chem.201703852 IF: 5.236

Master's thesis

Reactivity of 3-oxo-β-lactams with regard to primary amines: an experimental and computational approach. E. Van Den Broeck. Supervisors: prof. dr. ir. Veronique Van Speybroeck, prof. dr. ir. Matthias D'hooghe, **2017**.

Conference and workshop contributions

Oral presentations

1. Cation-π Interactions Accelerate the Living Cationic Ring-Opening Polymerization of Unsaturated 2-Alkyl-2-oxazolines. Elias Van Den Broeck, Bart Verbraeken, Richard HoogenBoom, Veronique Van Speybroeck.
   ChemCys, Blankenberge, Belgium, 19-21 February 2020 in Blankenberge (Belgium); Achievement: Second price for best oral presentation in the topic 'Physical and Theoretical Chemistry'

Poster presentations

1. Towards an understanding of the role of π-cation interactions in accelerating living cationic ring-opening polymerization of unsaturated 2-alkyl-2-oxazolines. Elias Van Den Broeck, Bart Verbraeken, Pieter Cnudde, Saron Catak, Richard HoogenBoom, Veronique Van Speybroeck.
   Frontiers and challenges of computing metals for biochemical, medical and technological applications, CECAM workshop, Paris, France, 11th – 13th July 2018.

2. Towards an understanding of the role of π-cation interactions in accelerating living cationic ring-opening polymerization of unsaturated 2-alkyl-2-oxazolines. Elias Van Den Broeck, Bart Verbraeken, Pieter Cnudde, Saron Catak, Richard HoogenBoom, Veronique Van Speybroeck.
   Hybrid Quantum Mechanics / Molecular Mechanics (QM/MM) Approaches to Biochemistry and Beyond, CECAM workshop, Lausanne, Switzerland, 8-12 April 2019.

3. A computational study on the tandem defunctionalization of biorenewable dihydroconiferyl alcohol into Biocatechol Catalyzed by Brønsted Acids in hot pressurized water. Elias Van Den Broeck, Jeroen Bomon, Bert Sels, Bert Maes, Veronique Van Speybroeck.
   NCCC conference, Noordwijkerhout, The Netherlands), 2-4 March 2020

A

Rate constants and thermodynamics from enhanced sampling simulations

A.1 Rate constants and Transition state Theory

As a starting point one can consider the Bennett-Chandler expression which is the conventional way to express the rate constant (see Eq. A.1).[22,52,53] This expression can be related to the transition-state theory of Eyring by taking the limit of the Bennet-Chandler expression (Eq. A.2) which implies that no recrossing is allowed of the free energy barrier which is one of the fundamental assumptions of the TST. In what follows only the latter will be considered. The approach requires that we can define a value $q^{\ddagger}$ as the value of the RC in the transition state region. Furthermore, given $q^{\ddagger}$, the reactant region is spanned by all values of $q < q^{\ddagger}$ and the product region by all values of $q > q^{\ddagger}$. Using the data obtained from the (enhanced sampling) MD simulations k_{TST} can be computed (approximately) by computing the ratios of the two ensemble averages shown in Equation A.2. For more detailed information on the derivation and theory of the equations presented

below the reader is referred to the following references:[22,50,51]

$$k(t) = \frac{\langle \dot{q}\theta\left(q(t) - q^{\ddagger}\right)\delta\left(q^{\ddagger} - q(0)\right)\rangle}{\langle \theta\left(q^{\ddagger} - q\right)\rangle} \tag{A.1}$$

$$k^{TST} = \lim_{t\to 0+} k(t) = \frac{\langle \dot{q}\theta\left(\dot{q}\right)\delta\left(q - q^{\ddagger}\right)\rangle}{\langle \theta\left(q^{\ddagger} - q\right)\rangle} \tag{A.2}$$

In Eq. A.2 $\dot{q}$ refers to the rate of variation of the reaction coordinate q, $\theta(\dot{q})$ only includes samples from phase space which are directed to the product state by natural time evolution, $\delta\left(q - q^{\ddagger}\right)$ only includes sample from within the transition state region (i.e. $q = q^{\ddagger}$) and $\theta\left(q^{\ddagger} - q\right)\rangle$ only includes the reactant state samples i.e. $(q < q^{\ddagger})$.

Finally, in resemblance to the work performed by Bučko et al., k_{TST} can be expressed as:[50]

$$k^{TST} = A \cdot \frac{e^{-\beta F(q^{\ddagger})}}{\int_{-\infty}^{q^{\ddagger}} e^{-\beta F(q)} dq} \tag{A.3}$$

$$A = \frac{1}{2}\langle|\dot{q}|\rangle_{TS} \tag{A.4}$$

In these equations A is expressed in terms of $\langle|\dot{q}|\rangle_{TS}$ which represents the ensemble average of (the absolute value) of the rate of change of q. The absolute value (and the proceeding factor $1/2$) can be traced back to the fact that a system starting at the transition state is assumed to transition symmetrically towards products and reactants. However, within transition state theory, we only count the forward transitions towards the product state and assume that once transitioning towards the product, the system never recrosses. It is hence a direct translation of the TST as no recrossings or movements towards the reactant region are accounted for.

Practically A is calculated by performing an analytical integration over momentum space under the assumption that the momenta are Gaussian distributed (*vide infra*). It can furthermore be shown that the data required is extracted either of a biased or unbiased simulation as long as it contains sufficient data to represent the ensemble average. $\int_{-\infty}^{q^{\ddagger}} e^{-\beta F(q)} dq$ represents the ensemble of states defining the reactant region, i.e. integration over all reactant states defined by $(q < q^{\ddagger})$.

A.1.1 Determining prefactor A

In order to calculate the prefactor A, under the assumption that the momenta are Gaussian distributed, the rate factor can be expressed as follows:

$$A = \frac{1}{2}\frac{\int d\vec{r}^N \int d\vec{p}^N \left|\dot{q}\left(\vec{r}^N, \vec{p}^N\right)\right| \delta\left(q\left(\vec{r}^N\right) - q^{\dagger}\right) e^{-\beta\left(\sum_{i=1}^{N} \frac{\vec{p}_i^2}{2m_i} + V(\vec{r}^N)\right)}}{\int d\vec{r}^N \int d\vec{p}^N \delta\left(q\left(\vec{r}^N\right) - q^{\dagger}\right) e^{-\beta\left(\sum_{i=1}^{N} \frac{\vec{p}_i^2}{2m_i} + V(\vec{r}^N)\right)}} \tag{A.5}$$

where the convention is used that vectors with a superscript N represents 3N-dimensional concatenated vectors of all atomic contributions (e.g. $\vec{p}^N = (\vec{p}_1, \vec{p}_2, \ldots, \vec{p}_N)$) and $\dot{q}\left(\vec{r}^N, \vec{p}^N\right)$ is:

$$\dot{q}\left(\vec{r}^N, \vec{p}^N\right) = \frac{dq}{dt}\left(\vec{r}^N, \vec{p}^N\right) = \sum_{i=1}^{N} \frac{\partial q}{\partial \vec{r}_i} \cdot \frac{d\vec{r}_i}{dt} = \sum_{i=1}^{N} \frac{\partial q}{\partial \vec{r}_i} \cdot \frac{\vec{p}_i}{m_i} \tag{A.6}$$

In Equation A.6 Hamilton's equation of motion $\dot{\vec{r}_i} = \frac{\vec{p}_i}{m_i}$ is applied.

In principle we can now proceed in two ways to perform the integral over momentum space, i.e. analytically or numerically, we will however limit ourselves to the analytical approach. Remark that this is allowed since the momentum distribution is Gaussian.[51]

Integrating over momentum space analytically

First we transform the phase space variables $(\vec{r}^N, \vec{p}^N)$ to their mass-weighted counterparts:

$$\vec{x}_i = \sqrt{m_i} \cdot \vec{r}_i$$
$$\vec{P}_i = \frac{1}{\sqrt{m_i}} \cdot \vec{p}_i$$

Resulting in:

$$\dot{q}\left(\vec{r}^N, \vec{p}^N\right) = \sum_{i=1}^{N} \frac{\partial q}{\partial \vec{r}_i} \cdot \frac{\vec{p}_i}{m_i} = \sum_{i=1}^{N} \frac{\partial q}{\partial \vec{x}_i} \cdot \vec{P}_i = \vec{\nabla}_x^N q \cdot \vec{P}^N$$

It can then be shown that[51]:

$$\begin{aligned} A &= \sqrt{\frac{1}{2\pi\beta}} \cdot \left\langle \left| \vec{\nabla}_x q \right| \right\rangle_{q^\dagger} \\ &= \sqrt{\frac{1}{2\pi\beta}} \cdot \frac{\int \left| \vec{\nabla}_x q \right| \delta(q(\vec{x}^N) - q^\dagger) e^{-\beta V(\vec{x}^N)} d\vec{x}^N}{\int \delta(q(\vec{x}^N) - q^\dagger) e^{-\beta V(\vec{x}^N)} d\vec{x}^N} \end{aligned}$$

Hence, the prefactor A represents a (to the transition state) constrained ensemble average of the (mass-weighted) gradient of the collective variable.

$$\begin{aligned} k^{TST} &= A \cdot \frac{e^{-\beta F(q^\dagger)}}{\int_{-\infty}^{q^\dagger} e^{-\beta F(q)} dq} \\ A &= \sqrt{\frac{1}{2\pi\beta}} \cdot \left\langle \left| \vec{\nabla}_x q \right| \right\rangle_{q^\dagger} \end{aligned} \tag{A.7}$$

A.1.2 Biased simulations

Practically, the transition state region (and the corresponding free energy surface) is often sampled by means of biased equilibrium simulations, such as umbrella sampling, instead of unbiased equilibrium simulations. In order to determine the rate factor A from these simulations it is important to show that Eq. A.7 remains valid for biased simulations, i.e. when a bias potential $U_b(q)$ is imposed on the collective variable q. To prove this, we need to revisit the expression of $\left\langle \left| \vec{\nabla}_x q \right| \right\rangle_{q^\dagger}$ in terms of the phase integrals:

$$
\begin{aligned}
\left\langle \left| \vec{\nabla}_x q \right| \right\rangle_{q^\dagger} &= \frac{\int \left| \vec{\nabla}_x q(\vec{x}^N) \right| \delta\left(q(\vec{x}^N) - q^\dagger\right) e^{-\beta V(\vec{x}^N)} d\vec{x}^N}{\int \delta\left(q(\vec{x}^N) - q^\dagger\right) e^{-\beta V(\vec{x}^N)} d\vec{x}^N} \\
&= \frac{\int \left| \vec{\nabla}_x q(\vec{x}^N) \right| \delta\left(q(\vec{x}^N) - q^\dagger\right) e^{-\beta V(\vec{x}^N)} e^{-\beta U_b(q^\dagger)} d\vec{x}^N}{\int \delta\left(q(\vec{x}^N) - q^\dagger\right) e^{-\beta V(\vec{x}^N)} e^{-\beta U_b(q^\dagger)} d\vec{x}^N} \\
&= \frac{\int \left| \vec{\nabla}_x q(\vec{x}^N) \right| \delta\left(q(\vec{x}^N) - q^\dagger\right) e^{-\beta V(\vec{x}^N)} e^{-\beta U_b(q(\vec{x}^N))} d\vec{x}^N}{\int \delta\left(q(\vec{x}^N) - q^\dagger\right) e^{-\beta V(\vec{x}^N)} e^{-\beta U_b(q(\vec{x}^N))} d\vec{x}^N} \\
&= \frac{\int \left| \vec{\nabla}_x q(\vec{x}^N) \right| \delta\left(q(\vec{x}^N) - q^\dagger\right) e^{-\beta \left[V(\vec{x}^N) + U_b(q(\vec{x}^N))\right]} d\vec{x}^N}{\int \delta\left(q(\vec{x}^N) - q^\dagger\right) e^{-\beta [V(\vec{x}^N) + U_b(q(\vec{x}^N))]} d\vec{x}^N} \\
&= \left\langle \left| \vec{\nabla}_x q \right| \right\rangle_{q^\dagger, biased}
\end{aligned}
$$

Hence, showing that we can indeed extract A from biased simulations.

B

Modeling workflow I

B.1 Preparation of a solvated system

First of all, it is worth mentioning that the workflow presented below is definitly not a unique one. Instead I will present the workflow which I find most convenient to generate solvated molecular systems (solvent boxes) or more complex simulation set-ups.

It is important to keep the goal of this section in mind, i.e. we are trying to prepare a solvent box (solvated solute) which is well equilibrated at the desired condition (p,T). The reason why we will focus on a force field approach below is because equilibrating a system can take a prohibitivly long time when using a DFT approach. Nonetheless, it is worth mentioning that semi-empirical methods can alternatively be used if time and resourses allow it. The final structures can directly be used in subsequent *ab initio* MD simulations to investigate intermediate stability or reactivity while accounting for the explicit solvent environment. Alternatively it can be used as a starting point for ONIOM calculations and/or QM/MM simulations. Furthermore the presented workflow highlights some general concepts when performing force field parameterization in combination with MD simulations using OpenMM as an MD engine (*vide infra*).

The presented workflow mainly relies on two software packages: 1. **openff-toolkit** (further refered to as openff) which is an open-source python-based package enabling facile parameterization of small-molecules.[105] To this end, one can use

the force fields developed by their consortium, i.e. the Open Force Field Initiative force fields, or other general force fields like GAFF and GAFF2(Generalized amber force field).[86–88] Recently the consortium published a first version of their second generation small molecule forcefield hence the code presented below will rely on this 'new' force field to illustrate the concepts, i.e. the sale force field. 2. **openmm**, which is an open-source MD engine with a user friendly python interface. The main advantages of openmm are the tremendous performance of the code on GPUs and the tunability/customizability of the force field terms. It will mainly be used to run NPT/NVT runs as efficiently as possible.[106]

Additionally two very usefull packages, which make life much easier when using the aformentioned tools, are openmmforcefields and openmoltools.[349] Below we will illustrate how these packages can be used in combination with openmm and openff. A package which is worth mentioning, though not used, is **parmed** which can be used for force field system creation, conversion and manipulation.[350]

The following molecule (4,4-Dimethyl-5-methylene-1,3-dioxolan-2-one) αCC is used to illustrate the concepts tackled in this workflow.

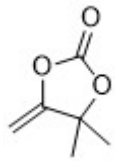

Scheme B.1. 4,4-Dimethyl-5-methylene-1,3-dioxolan-2-one ($\alpha CC1$).

The workflow itself is structured such as a jupyter notebook.

General imports

```
from sys import stdout
import time
import requests
import numpy as np
import ipywidgets
import matplotlib.pyplot as plt
import pandas as pd
```

Modeling related imports

```
from openff.toolkit.topology import Molecule, Topology
from openff.toolkit.utils.toolkits import OpenEyeToolkitWrapper
from openff.toolkit.typing.engines.smirnoff import ForceField
from openmmforcefields.generators import SystemGenerator
from openmmforcefields.generators import SMIRNOFFTemplateGenerator
from simtk import openmm
```

```
from openmoltools import packmol
import parmed as pmd
import mdtraj as md
import nglview
from openbabel import openbabel,pybel
```

B.1.1 Creating/Loading molecular input files

Loading Solute and Solvent molecules

Multiple approaches exist to load or create the files necessary for the generation of solvent boxes. Though I could tackle all of them, I will highlight a few interesting approaches:

- Build molecules via your molecular builder tool of choice: GaussView, Avogadro, IQmol, ...
- Load molecules using their Pubchem chemical ids, simultaneously the molecular coordinates can be saved and converted into the desired formats using openbabel. Circumventing the need of molecular building software.
- Define molecules based on their SMILES (Simplified Molecular Input Line Entry System) which is easily processed by many programs and packages.

Nonetheless, it is worth noting that it all boils down to generating a molecule object with attributes discribing the coordinates of the atoms and the topology of the molecule (i.e. how atoms are linked). Hence in many cases .xyz files will not do, though OpenEye (*vide infra*) is able to process (and convert) these as well.[351]

Prior to going in more detail, it is worthwhile to shortly explain some key features of the openff force fields and the specific structure files required in general force fields. The main difference is the way atom typing is performed, openff establishes typing by chemically perceiving each atom using SMARTS language and the atom-tagging extensions from SMIRKS. SMARTS are basically an extensions of the well-known SMILES string and allow you to specify substructures within a molecule, providing more flexibility.[352] SMIRKS on the other hand is a hybrid form of SMILES and SMARTS which is designed to describe generic reactions: i.e. expression of reaction graphs and indirect effects.[353] The combination of using SMARTS and the atom-tagging extensions of SMIRKS to encode molecular mechanics force fields is named SMIRNOFF (SMIRKs Native Open Force Field) specification by the Open Force Field Initiative.[88] Most importantly, their typing tools are very straightforward to use and can utilize many different input structures. Other (older) force fields perform typing by encoding force fields within a discrete set of atom types containing all information ever needed for force field simulations. Parameterization is then performed by assigning tabulated data to specific combinations of atom types.[88] The main disadvantages of this are that: 1. Often the atom-typing machinery

is inextensible 2. It is difficult to expand parmeters encoded by atom types 3. An unnecessarily proliferation of encoded parameters. These all result in poor tranferability and accuracy of these force fields.

Additionally it is -in my experience- often a tedious task to create unique topology files containing all required information to parameterize the system (bonding information, atom names, residue names, ...). For example GAFF require you to use -in my opinion- rather user-unfriendly software packages such as antechamber and tleap from the AmberTools suite (though nowadays many other (more user-friendly) packages can be used to this end).[354] Generally the construction of a unique topology file is an important step in the construction of custom force fields (which are not relying on SMARTS encoding). This method is employed in Appendix C

Loading molecules by means of Pubchem ids:

```
    #### Pubchem ids
    # 4,4-Dimethyl-5-methylene-1,3-dioxolan-2-one, Paper 1 and 2
    solutes = ["78175"]
    # Solvent DMSO, Paper 2
    solvents = ["679"]

#generate sdf files and transform them to pdb using openbabel.
obConversion = openbabel.OBConversion()
obConversion.SetInAndOutFormats("sdf", "pdb")
mol = openbabel.OBMol()
for cid in solutes+solvents:
    url = f"https://pubchem.ncbi.nlm.nih.gov/
    rest/pug/compound/CID/{cid}/record/SDF/
    ?record_type=3d&response_type=save"
    with open(f"CID_{cid}.sdf", "w") as f:
        f.write(requests.get(url).text)
    obConversion.ReadFile(mol, f"CID_{cid}.sdf")
    obConversion.WriteFile(mol, f"CID_{cid}.pdb")
```

It is important to note that the applied format should be compatible with the software used. Furthermore we will use specific toolkits such as RDKit or OpenEyeTools to recognize the topology of the molecule in an automate fashion. The prerequisite for this, depending on the kit and/or commands used, is that the input file contains sufficient information to ascribe the topology to the molecule. For example OpenEyeTools, which is a free software package for academia (on request) can handle much more formats because of its ability to 'better' recognize the topology. RDKit on the other hand which is open-source can also do the trick for a limited number of formats. Remark that especially for the latter toolkit special care should be taken with the .sdf or .pdb topology file to ensure that it indeed holds the correct information. Below, we will rely on OpenEyeTools.

```
view = nglview.show_file(f"CID_{solutes[0]}.pdb",ext='pdb')
view
# Remark that these input lines will be omited in future visualizations
# to limit the amount of repetition and keep the workflow as condensed
# as possible.
```

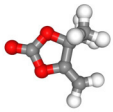

Figure B.1. Three dimensional representation of $\alpha CC1$.

An initial solvent box

Deciding the amount of solvent molecules Determining the number of solvent molecules will mainly depend on the following:

1. What properties do you want to observe/investigate. For example if one is interested in proton hopping events in water one would necessarily need to take two solvent layers into account; do you want to observe the influence of solvent rearrangements in the TS then maybe 1 is sufficient, or perhaps you want to investigate a system at a specific concentration?
2. Computational resources and the desired level of theory. If one has an unlimited number of resources once can take many solvent layers into account even in the case of DFT simulation. However more often this is not true and one is limited by both time and available resources forcing you to limit the number of atoms in the system and hence the computational cost of the simulations. When using a force field description to model the solvent or system, then the amount of solvent accounted can be increased drastically.

Assuming limited resources, I'll focus on the first point distinguishing three scenarios: 1. Simulating the molecule at a specific concentration. 2. Simulating solvation behavior of a molecule or molecules. 3. Simulating mechanisms in which the solvent plays an active role. Evidently combination of these options are possible.

In first instance one needs to know the conditions used in the experiments or in case of e.g. screenings, the desired conditions. Hence temperature, pressure and concentrations should be know. In the case of αCC, we are using a temperature of 298.15 K and a pressure of 1 bar. Here a concentration of 0.1 mol/L is used, however one can match the experimental conditions as well.

These conditions can then be used to extract the density of the solvent used from literature or online databases such as NIST (National institute for standards and technology, https://webbook.nist.gov/chemistry/fluid/).[355]

Concentration

```
from molmod.units import mol as mol_unit, liter,gram
## Known variables ###
C_solute = 0.1*mol_unit/liter #mol/L
n_solute_0 = 1 #number of molecules for solutes[0]
rho_dmso = 1100*gram/liter #g/mL
# https://pubchem.ncbi.nlm.nih.gov/compound/Dimethyl-sulfoxide#section=Density
M_dmso = 78.14*gram/mol_unit
# alternatively this can be extracted from molecule object later on based
# on atom masses.

# assuming a negligable density change  upon adding a solute molecule
Minv_solute = C_solute/rho_dmso # mol CC / gram DMSO
# mol CC/mol DMSO (no unit) = molecules CC/molecules DMSO
molsolute_per_molsolvent = Minv_solute*M_dmso
# n_solute molecules/n_solvent molecules = molsolute_per_molsolvent
n_solvent = n_solute_0/(molsolute_per_molsolvent)
print(round(n_solvent,0))
```

141

Meaning we will need 141 molecules of DMSO per molecule of αCC to have a concentration similar to the experimental one. It is obvious that the number of solute molecules can drastically increase or decrease depending on the solute concentration. Important however is that the molecular environment around a single solute is described completely. Another important aspect are the role of finite-size effects which one should consider carefully to avoid drawing wrong conclusions due to the artefacts arising. In essence this boils down to consider systems sizes which are sufficiently large and hence eliminate artifacts arising due to the finite size of the system. Numerous studies have been reported for different systems and properties which provide empirical and/or theoretical corrections for these effects (*vide supra*).[356,357]

Solvation behavior and solvent as active role. In both case 2 and 3, it is of importance to estimate the volume and/or length of the solute(s). As in this case we will want to estimate the size of the simulation box (*vide infra*) which will be filled with solvent molecules depending on the needs of the investigation. Multiple methods exist of which we will highlight to most simple ones but it is important to mention that a unique method to determine molecular volumes does not exist and it mostly depends on the flavor of the computational chemist what is used, below we will only discuss the most naive/easy appoaches.

1. Calculate the largest distance within the molecule, this can be done mathematically based on the coordinates though many visualization software provide ways to measure these interactively.

2. Calculate the volume based on DFT calculations, e.g. using the 'Density' keyword in Gaussian16: 'This keyword requests that the molecular volume be computed, defined as the volume inside a contour of 0.001 electrons/Bohr^3 density'.

3. Use the Van der Waals radii of the atoms to calculate a corresponding volume.

While all 3 approaches can be used, the most convenient/quickest one is 1. Furthermore it is worth noting that we are actually only interested in a lower limit needed for the system, if computational resources allow it, one can increase this number appropriately.

Depending on the process you are trying to describe, you'll want to account for a discrete number of solvent layer around each solute. The extent of these solvent layers, i.e. up to which distance in space the solvent is surrounding a certain solute, could be derived from RDFs available in literature. A well known example for this is the solvation layers of water which are well discribed within this formalism. If the RDFs are not known, one can use the volume or length of the solvent molecules themselves (which can be determined in similar fashion) in combination with the desired amount of solvent layer around each solute to estimate the size of the simulation boxes.

The resulting box size can then be used to estimate the amount of solvent molecules needed at the desired density.

```
from molmod.units import mol as mol_unit, liter,gram,nanometer

### Define the features
# from Gaussview
length_aCC = 0.55 *nanometer# nm
length_DMSO = 0.5*nanometer #nm
# solvent layers to account for (two), no rdfs are availble we will hence
# use the length of the solvent molecule.
# two could for example be used in case you need to be able to observe a
# Grotthus mechanism in the case of water - \acrshort{dft}
n_layer = 2
rho_dmso = 1100*gram/liter # g/mL
# https://pubchem.ncbi.nlm.nih.gov/compound/Dimethyl-sulfoxide#section=Density
M_dmso = 78.14*gram/mol_unit
# alternatively this can be extracted from molecule object later on based on
# atom masses.

### estimated box volume
# 2 here originates from the fact you want to solvate both left and right side
box_diagonal = n_layer*2*(length_DMSO) + length_aCC
box_volume = (box_diagonal)**3
# Remark this is an upper limit (box_diagonal > box_length)
```

```
### Determine the number of solvent molecules
n_solvent = int((rho_dmso * box_volume / M_dmso))
print(f'The number of solvent molecules:{n_solvent}')
```

```
The number of solvent molecules:140
```

packing the solvent around the solutes Using packmol we can then pack the solute inside a simulation box together with the desired number of solvent molecules. Packmol is however a command line program, hence here we use openmoltools which provides a python interface and some basic functionalities to produce **cubic** boxes.

```
### Define the solute and solvent topologies
pdb_filenames = [f"CID_{cid}.pdb" for cid in solutes+solvents]
n_molecules = [n_solute_0,n_solvent]

if OpenEyeToolkitWrapper.is_available():
    print('Succesfuly using OpenEye')
    # we need smiles codes (for the approximate volume by density function)
    # to estimate a more appropriate box size:
    smiles_codes = [Molecule.from_file(f"CID_{cid}.sdf").to_smiles() for cid
     in solutes+solvents]
    box_size = packmol.approximate_volume_by_density(smiles_codes,
                                                     n_molecules,
                                                     density=1.1)
    print('old box size:',box_diagonal, 'new box size:',box_size,)
else:
    box_size = box_diagonal

# create box-file with corresponding md_traj coordinates and topology
md_traj_trajectory = packmol.pack_box(pdb_filenames,
                                      n_molecules,
                                   box_size=box_size)
md_traj_trajectory.save_pdb(f'solvated_solute_{n_solvent}DMSO.pdb')
```

Alternatives Alternatively one can use: 1. Packmol on the command line 2. The solvation toolkit (https://github.com/MobleyLab/SolvationToolkit) 3. Or one can use the build in solvation tools implemented within many MD codes and visualization software. For openmm an example is provided below in case water is used as a solvent (which is often the case for protein chemistry, or other biological systems). It is even possible in this case to specify ionic strength. Remark that tip3p refers to the force field (and force field typing) which is used to define the water molecules (see section below).

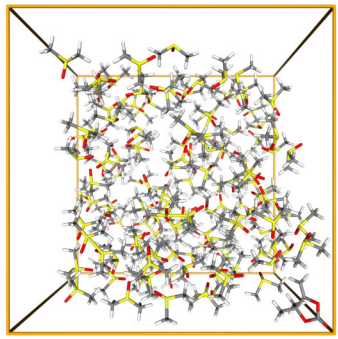

Figure B.2. Solvated system generated with packmol.

B.1.2 Preparing the OpenMM system to perform simulation with parameterization by openff-toolkit (under-the-hood)

In first instance we define the solvent which we would like to use for parameterization of the solvated system. In this case we illustrate how to use it to parameterize both DMSO and αCC simultaneously. Though we will also illustrate how the Generator class from openmmforcefields can be used to combine multiple force fields to parameterize a single pdb file e.g. describe the solute with the openff force field and the solvent with a older force field such as tip3p in the case of water.

Openff-toolkit

```
### Specifying the openff-sage force field.
off_forcefield = ForceField('openff-2.0.0.offxml')

# Define openmm pdb object using the solvated system from before.
pdb_box = openmm.app.PDBFile(f'solvated_solute_{n_solvent}DMSO.pdb')

#Define the unique molecules present in the pdb_box
unique_molecules = [Molecule.from_file(name) for name in pdb_filenames]
# Generate an Openff topology and openmm system object
off_box_topology = Topology.from_openmm(pdb_box.topology,
                                        unique_molecules=unique_molecules)
omm_box_system = off_forcefield.create_openmm_system(off_box_topology)
```

Generators

```
# Load force fields files available in openmm which will be used for,
# in this case, the water force field parameters
omm_forcefield = openmm.app.ForceField( "tip3p.xml")
# We will now 'Teach' openmm what molecules need to be parameterized
# using the Sale force field of openff.
solute_molecule = unique_molecules[0]
```

```
smirnoff = SMIRNOFFTemplateGenerator(
    forcefield="openff-2.0.0.offxml", molecules=solute_molecule
)
omm_forcefield.registerTemplateGenerator(smirnoff.generator)
```

Remark that this approach can also be used for GAFF(2) (Generalized Amber Force field). This is very interesting as it used to be a very tedious process involving many parts of the AmberTools suite. Nowadays I would strongly advice to use openff instead as it strongly collaborates with Amber, is very up-to-date, open-source and improving constantly.

```
pdb = openmm.app.PDBFile(pdb_filenames[0])
modeller = openmm.app.Modeller(pdb.topology, pdb.positions)
# Surround the solute with water using 5 angstrom to each side.
modeller.addSolvent(
    omm_forcefield,
    model="tip3p",
    padding=5.0 * openmm.unit.angstrom,
)
# Generate the system object, the omm_forcefield will automatically
# detect the part which needs to be parameterized with the sale force field.
system = omm_forcefield.createSystem(
    modeller.topology,
    nonbondedMethod=openmm.app.PME,
    nonbondedCutoff=8 * openmm.unit.angstrom,
)
```

A slightly different but equivalent approach is the use of SystemGenerators which helps in managing different forcefields for a single input file. Furthermore It allows us to combine customized force fields such as the ones created with **QuickFF** with existing ones such as openff or tip3p (boils down to extending forcefields=["tip3p.xml"] with the force fields you want to use). Evidently it is only possible if the pdb files and molecule files are compatible (which can in some cases be a tedious task requiring different packages or manual manipulations) and a conversion of the custom force field to a format compatible with openMM i.e. .xml format. Luckily OpenMM is very flexible in this regard. As mentioned in section 2.3.3. Concerning QuickFF, the newly developed OpenYaff package can be of help.[358]

```
system_generator = SystemGenerator(forcefields=["tip3p.xml"],
                            small_molecule_forcefield='openff-2.0.0.offxml',
                            molecules=unique_molecules)
system = system_generator.create_system(pdb_box.topology,
                                        molecules=unique_molecules)
# evidently tip3p.xml is not necessary here, it will hence be ignored
```

B.1.3 Parameterizing a 'new' solvent

In case one is using a 'new' solvent, i.e. a solvent which is not used to train the force fields which one uses for the parameterization, then it is worthwhile exploring a few of the properties for a simulation box which contains only the solvent molecules studied and hence no solute. Though many organic solvents are included in the training data of the force fields of the open force field consortium, it is worthwhile illustrating this concept for the system at hand. It can furthermore be used to show a typical simulation setup using OpenMM. Remark it is not the goal to give an elaborate introduction to OpenMM.

Pure solvent system

Box preparation

```
#settings for solvent box
solvent_box_name = 'pure_solvent_box'
number_of_solvent_molecules = 100
# number of molecules for each solute and solvent species
# in the order of the solutes and solvents provided before
n_molecules = [number_of_solvent_molecules]
smiles_codes = [Molecule.from_file(f"CID_{cid}.sdf").to_smiles()
                for cid in solvents]
box_size = packmol.approximate_volume_by_density(smiles_codes,
                                                 n_molecules,
                                                 density=1.1)
print('box_size for 100 solvent molecules',box_size)
pdb_filenames = [f"CID_{cid}.pdb" for cid in solvents]
# create box with corresponding md_traj trajectory and topology
md_traj_trajectory = packmol.pack_box(pdb_filenames,
                                      n_molecules,
                                      box_size=box_size)
md_traj_trajectory.save_pdb(
    f'{solvent_box_name}_{number_of_solvent_molecules}DMSO.pdb')
print(f'{solvent_box_name}_{number_of_solvent_molecules}DMSO.pdb written')
```

Parameterization

```
pdb_solvent_box =
    openmm.app.PDBFile(
        f'{solvent_box_name}_{number_of_solvent_molecules}DMSO.pdb')
unique_molecules = [Molecule.from_file(pdb_filenames[0])]
pure_solvent_box_positions = pdb_solvent_box.getPositions()
off_solvent_box_topology = Topology.from_openmm(pdb_solvent_box.topology,
                                        unique_molecules=unique_molecules)
omm_solvent_box_system =
    off_forcefield.create_openmm_system(off_solvent_box_topology)
```

The resulting system object can then be used to perform an MD simulation.

B.1.4 Equilibration simulation

Though multiple approaches are highlighted above on how to obtain an initial solvated structure and how to parameterize the created solvent box, an important step is still missing, i.e. the equailibration step. At the moment the solvent molecules are far from ideally oriented with respect to the solute molecule and the simulation box size might still be to big or to small hence representing a wrong density. To solve this one needs to perform a simulations resembling the experimental conditions as close as possible, i.e. in the isothermal-isobaric ensemble. This is a key step in order to use the solvent boxes as reliable input for DFT simulations. Alternatively one can also do this with DFT-based MD simulations but this can take a prohibitivly long time. Assessing when a simulation has equilibrated can be done by 'measuring' some macroscopic observable, e.g. the density, which should remain constant after equilibration has occured (i.e. the ensemble average doesn't vary anymore). Due to the expense of DFT, it is more straightforward to perform the equilibration with force field methods (or alternatively semi-empirical methods).

Simulations with Openmm

Below is illustrated how we can perform a simple equilibration simulation with openmm.

```
### Simulation settings
temperature = 298.15 #in K
pressure = 1 #in bar, for an isobaric simulation
timestep = 2 #in femtoseconds
total_simulation_steps = 100000 # i.e.~steps of 2 fs
# Depending on the property to equilibrate, the simulation time needed can
# vary
```

Pure solvent system The prepared pure solvent box (*vide suura*) is equilibrated using the code snippet presented below:

```
from simtk.unit import *

#Thermostat
integrator = openmm.LangevinIntegrator(temperature*kelvin,
                                       1/picosecond,
                                       timestep*femtoseconds)
#for isobaric simulation we define a barostat
omm_solvent_box_system.addForce(openmm.MonteCarloBarostat(pressure*bar,
                                                          temperature*kelvin))

#setting up the simulation
simulation = openmm.app.Simulation(pdb_solvent_box.topology,
                                   omm_solvent_box_system,
                                   integrator)
```

```
simulation.context.setPositions(pure_solvent_box_positions)

#minimize the system to avoid steric clashes and relax the molecules.
simulation.minimizeEnergy()

#Define what needs to be reported and how often
simulation.reporters = []
#report the trajectory in dcd format
simulation.reporters.append(
    openmm.app.DCDReporter(
        f'traj_{solvent_box_name}_N{number_of_solvent_molecules}.dcd',
        100))
# report some basic output at low frequency
simulation.reporters.append(
               openmm.app.StateDataReporter(stdout,
                                            500,
                                            step=True,
                                            temperature=True, elapsedTime=True))
# report all properties of interest at a higher frequency
# (remark that this frequency as really high, and one should
# pay atention for very large system)
simulation.reporters.append(
    openmm.app.StateDataReporter(
        f"scalars_{solvent_box_name}_N{number_of_solvent_molecules}.csv",
        100,
        time=True,
        potentialEnergy=True,
        totalEnergy=True,
        temperature=True,
        volume=True,
        density=True))
#Perform the simulation
print("Starting simulation")
start = time.process_time()

simulation.step(total_simulation_steps)

end = time.process_time()
print("Elapsed time %.2f seconds" % (end-start))
print("Done!")

#Save last frame:
positions = simulation.context.getState(getPositions=True).getPositions()
simulation.topology.setPeriodicBoxVectors(
    simulation.context.getState(getPositions=True).getPeriodicBoxVectors())
openmm.app.PDBFile.writeFile(simulation.topology,
                             positions,
                             open('final_frame_solvent_box_traj.pdb', 'w'))
```

Solvated system The prepared solvated αCC1 system (*vide supra*) is equilibrated here.

```
from simtk.unit import *
import time
#Thermostat
integrator = openmm.LangevinIntegrator(temperature*kelvin,
                                       1/picosecond,
                                       timestep*femtoseconds)
#for isobaric simulation we define a barostat
omm_box_system.addForce(openmm.MonteCarloBarostat(pressure*bar,
                                                  temperature*kelvin))

#setting up the simulation
simulation = openmm.app.Simulation(pdb_box.topology,
                                   omm_box_system,
                                   integrator)
simulation.context.setPositions(pdb_box.getPositions())

#minimize the system to avoid steric clashes and relax the molecules.
simulation.minimizeEnergy()

#Define what needs to be reported and how often
simulation.reporters = []
#report the trajectory in dcd format
simulation.reporters.append(
    openmm.app.DCDReporter(f'traj_solvated_solute_box.dcd', 100))
#report some basic output at low frequency
simulation.reporters.append(openmm.app.StateDataReporter(stdout, 500,
                                                         step=True,
                                                         temperature=True,
                                                         volume=True,
                                                         density=True,
                                                         elapsedTime=True))
# report all properties of interest at a higher frequency
# (remark that this frequency as really high,
# and one should pay atention for very large system)
simulation.reporters.append(
    openmm.app.StateDataReporter(f"scalars_solvated_solute_box.csv",
                                 500,
                                 time=True,
                                 potentialEnergy=True,
                                 totalEnergy=True,
                                 temperature=True,
                                 volume=True,
                                 density=True))

#Perform the simulation
print("Starting simulation")
start = time.process_time()
```

```
simulation.step(total_simulation_steps)

end = time.process_time()
print("Elapsed time %.2f seconds" % (end-start))
print("Done!")

#Save last frame:
positions = simulation.context.getState(getPositions=True).getPositions()
simulation.topology.setPeriodicBoxVectors(
    simulation.context.getState(getPositions=True).getPeriodicBoxVectors())
openmm.app.PDBFile.writeFile(simulation.topology,
                             positions,
                             open('final_frame_solvated_traj.pdb', 'w'))
```

Verifying that the desired property is equilibrated

As we are preparing a solvent box to perform *ab initio* molecular dynamics simulations in the NVT (or NVE) ensemble one wants to equilibrate the density and hence the volume of the system (or in the case of an NVE, 1st the volume then the temperature). The volume is required as input in the subsequent NVT runs. Hence below one can trace both the Volume and the density in terms of time. It's easy to decide, based on a visual inspection, when the observable is converged though automated ways also exist to detect the equilibration period and then extract the equilibrated volume and/or density, i.e. timeseries module from pymbar (which can furthermore account for the statistical inefficiency of the sampling).[359] For the subsequent *ab intio* MD runs, the volume and the initial structure can be extracted from the trajectory file (take care that the corresponding volume of this structure is lower than or equal to the final volume). Alternatively you can visualize the trajectory and extract the desired frame manually.

Pure solvent system

```
data = pd.read_csv(
    f'scalars_{solvent_box_name}_N{number_of_solvent_molecules}.csv')
time = data['#"Time (ps)"']
rho = data["Density (g/mL)"]
plt.plot(time,rho)
plt.xlabel('Time (ps)')
plt.ylabel('Density (g/mL)')
plt.show()
```

This density can be used to have a first indication for the validity of the solvent force field.

```
volume = data["Box Volume (nm^3)"]
plt.plot(time,volume)
plt.xlabel('Time (ps)')
```

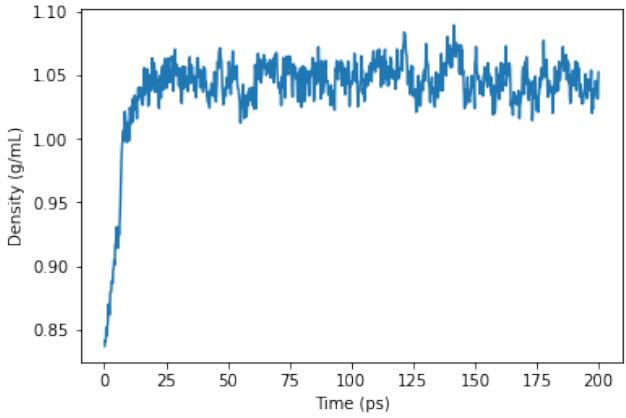

Figure B.3. Density variation during equilibration run of a pure solvent box.

```
plt.ylabel('Box Volume ($nm^3$)')
plt.show()
```

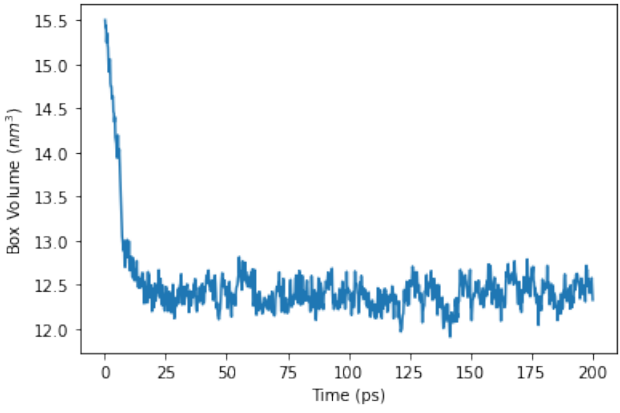

Figure B.4. Volume variation during equilibration run of a pure solvent box.

```
from pymbar import timeseries
V = volume.to_numpy()
t = time.to_numpy()
[t0, g, Neff_max] = timeseries.detectEquilibration(V)
print(' t0 :',t0,' g:',g,' Neff_max:',Neff_max)
V_t_equil = V[t0:]
# compute indices of uncorrelated timeseries
indices = timeseries.subsampleCorrelatedData(V_t_equil, g=g)
V_n = np.take(V_t_equil,indices)
t_equil= t[t0:]
```

```
t_n = t_equil[indices]
plt.plot(time,Volume)
plt.scatter(t_n,V_n,c='black')
plt.xlabel('Time (ps)')
plt.ylabel('Box Volume ($nm^3$)')
plt.show()
print('The equilibrated volume is:',round(np.mean(V_n),3),'$nm^3$')
```

```
t0 : 75  g: 11.7066765  Neff_max: 79.10016
```

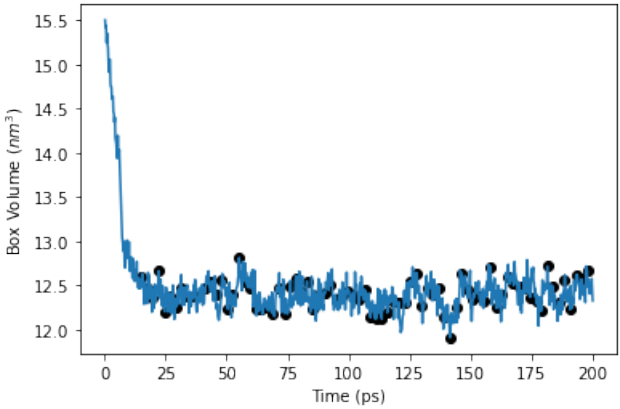

Figure B.5. Volume variation during equilibration run of a pure solvent box, accounting for the statistical inefficiency and equilibration time.

```
The equilibrated volume is: 12.404 $nm^3$
```

Solvated system

```
data = pd.read_csv(f'scalars_solvated_solute_box.csv')
time = data['#"Time (ps)"']
rho = data["Density (g/mL)"]
plt.plot(time,rho)
plt.xlabel('Time (ps)')
plt.ylabel('Density (g/mL)')
plt.show()
```

```
volume = data["Box Volume (nm^3)"]
plt.plot(time,volume)
plt.xlabel('Time (ps)')
plt.ylabel('Box Volume ($nm^3$)')
plt.show()
```

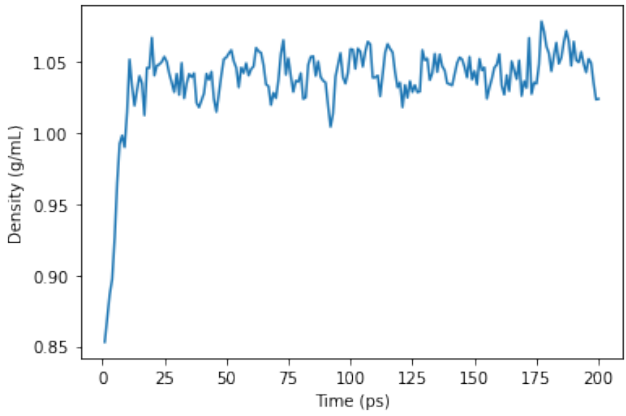

Figure B.6. Density variation during equilibration run of a solvated system.

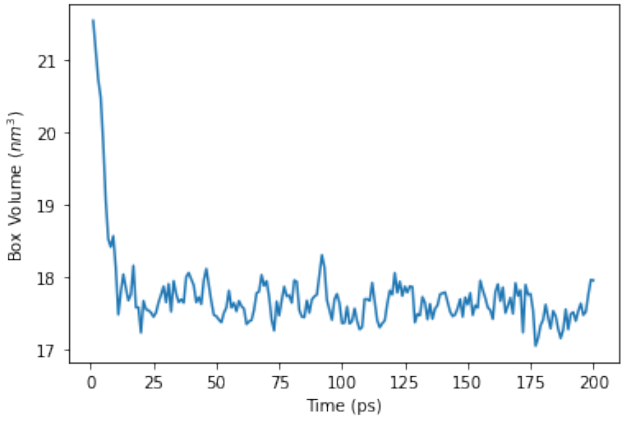

Figure B.7. Volume variation during equilibration run of a solvated system.

```
from pymbar import timeseries
V = volume.to_numpy()
t = time.to_numpy()
[t0, g, Neff_max] = timeseries.detectEquilibration(V)
print(' t0 :',t0,' g:',g,' Neff_max:',Neff_max)
V_t_equil = V[t0:]
# compute indices of uncorrelated timeseries
indices = timeseries.subsampleCorrelatedData(V_t_equil, g=g)
V_n = np.take(V_t_equil,indices)
t_equil= t[t0:]
t_n = np.take(t_equil,indices)
plt.plot(time,volume)
plt.scatter(t_n,V_n,c='black')
plt.xlabel('Time (ps)')
```

```
plt.ylabel('Box Volume ($nm^3$)')
plt.show()
print('The equilibrated volume is:',round(np.mean(V_n),3),r'$nm^3$')
```

```
t0 : 41  g: 3.3215666  Neff_max: 48.17004
```

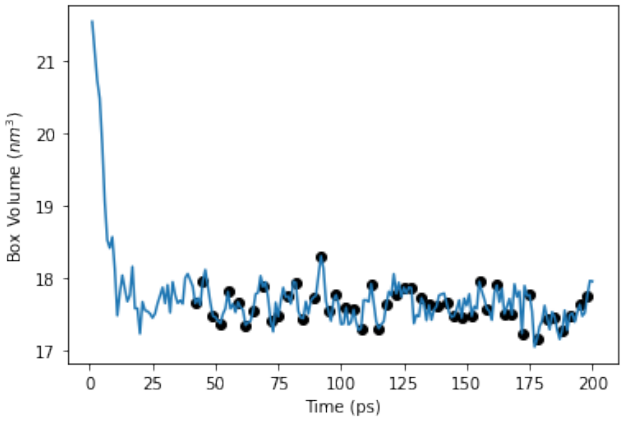

Figure B.8. Volume variation during equilibration run of a solvated system, accounting for the statistical inefficiency and equilibration time.

```
The equilibrated volume is: 17.611 $nm^3$
```

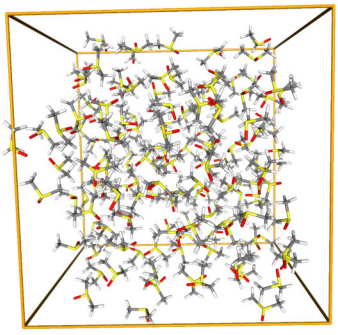

Figure B.9. Equilibrated solvated system.

B.1.5 Extra consideration

This workflow can also be used to prepare for example ONIOM or QM/MM solvated systems. To this end the resulting box can be used in combination with a distance cutoff to construct a solvation sphere around a solute.

C

Modeling workflow II

C.1 Polymer system generation and parameterization

The section below illustrates how to setup a large scale polymer simulation using two monomers which are discussed in Chapter 4, i.e. bis-(α-alkylidenecarbonate) (bisαCCs) and catechol. Remark that for the former one, the oxo-carbonate derivative is taken as this is the repeating unit within the resulting polymers (see **Paper IV**). We will show how to generate large polymeric structures tackling both homo- and copolymers, single - and multichain configurations and how one can alter polymer capping units or the copolymer type. In a second part the force fields used to model polymers are discussed in combination with some technical aspects concerning the use of the generated structure and force field files in polymer simulations. Remark that the code snippets are provided in the form of jupyter-notebook cell blocks which can be coppied manually providing the means for new researchers to start their own research concerning polymer science.

General imports

```
from IPython import display
import sys,os,time
import numpy as np
```

```
import nglview as nv
import openbabel as openbabel
```

Custom view function for pysimm

```
def display_system(sstm, fname=None, labels_on=False):
    is_temp = False
    if not fname:
        fname = 'tmp_file.pdb'
        is_temp = True

    sstm.write_pdb(fname)
    if 'nglview' in sys.modules.keys():
        view = nv.show_structure_file(fname)
        if labels_on:
            view.add_label(color='black', scale=1.3, labelType='text',
                           labelText = [str(pt.tag) for pt in sstm.particles],
                           zOffset=2.0, attachment='middle_center')
        view.add_unitcell()
    if is_temp:
        os.remove(fname)
    return view
```

C.1.1 Polymer construction: pysimm

In order to generate a realistic (co-)polymer or a system containing multiple (co-)polymers a limited number of programs exist. A few examples are the commercial Materials Studio package from BIOVIA[360], Xenoview[361](which is no longer maintained hence out-dated, though it is open-source and provides a user interface), nuSimm[362] (nanohub's polymer builder excellent for teaching purposes), polymatic[363] (probably the most popular one) and pysimm[104]. Remark that the latter three are all published by the Colina research group [colina.chem.ufl.edu] with the latter being a python package able to interface with polymatic and providing additional features for creating copolymers and linear chains. In general in case a well known polymer configuration is desired I would advise to use pysimm, while the polymatic suite can be used to generate more randomized structures with the possibility to have branching or linkages containing multiple atoms (though with sufficient expertise in using pysimm, some workarounds are possible to achieve similar structures). Instead of growing the chain polymatic starts from a simulation box filled with monomers which are allowed to 'react' with each other based on specific combinations. Because I have only worked with well-defined polymers, only pysimm is discussed. It is furthermore shown that this tool is excellent to create amorphous polymer systems (i.e. in combination with an appropriate equilibration protocol). In my opinion the disadvantage of pysimm is that it lack generality as special cases are not easy to tackle and (which is often the case for python packages) the rather limited documentation available.

```
# Import relevant pysimm modules
from pysimm import lmps
from pysimm import system
from pysimm import forcefield
from pysimm.apps.equilibrate import *
from pysimm.apps.random_walk import random_walk,copolymer

# Settings:
ff_general = forcefield.Dreiding()
proc =36
gpu = 0
sets = {'np':proc} #gpus are not supported by pysimm (yet)
path = '/data/gent/vo/000/gvo00003/vsc41963/PhD_workflows/figures_polymer/'
```

Remark that in case other force fields are used sometimes errors occur in case new 'unknown' force field terms arise, e.g. if the gaff2 force field is used some specific angle terms are not recognized for specific examples listed below. The Dreiding force field does not have this issue.

Defining the monomers

Here a monomer unit is defined in order to perform subsequent polymerization simulations. The following function is unique to every monomer, care should be taken with defining the linker atoms/groups in the system (*vide infra*)

```
def create_custom_monomer(index_head, index_tail,mol2=None,pubchem_smiles=None
                          ,pdb=None):
    # Index head: index of the atom (starting at 1),
    # which is to be the head of the monomer
    # Index tail: index of the atom (starting at 1),
    # which is to be the tail of the monomer
    # mol2: a mol2 file used to extract coordinates and topology information
    # pubchem_smiles: canonical smiles,
    # which can be used to retrieve the structure from pubchem.
    # pdb: a pdb file used to extract coordinates and topology information
    ### index head and tail are non-hydrogen atoms
    if pubchem_smiles:
        #This should be a registered pubchem smiles!
        s = system.read_pubchem_smiles(pubchem_smiles)
        print('Smiles read')
    elif pdb:
        s = system.read_pdb(pdb)
        #at the moment errors occur with bond-order perception,
        # I hence advice to use mol2
        print('Pdb read')
    elif mol2:
        s = system.read_mol2(mol2)
        print('mol2 read')
    else:
```

```
        print("No valid input file or string provided")
    f = ff_general
    s.add_particle_bonding()
    s.apply_forcefield(f,charges='gasteiger')
    c1 = s.particles[index_head] #index + 1
    c2 = s.particles[index_tail]
    c1.linker = 'head'
    c2.linker = 'tail'
    # Remove H-cap
    for b in c1.bonds:
         if b.a.elem == 'H' or b.b.elem == 'H':
            pb = b.a if b.b is c1 else b.b
            s.particles.remove(pb.tag, update=False)
            break
    for b in c2.bonds:
        if b.a.elem == 'H' or b.b.elem == 'H':
            pb = b.a if b.b is c2 else b.b
            s.particles.remove(pb.tag, update=False)
            break

    s.remove_spare_bonding()
    s.pair_style = 'lj/cut'
    try:
        lmps.quick_min(s,min_style='fire')
    except:
        #Checking interactive node
        print('trying different setup')
        lmps.quick_min(s,np=proc,min_style='fire')
    return s
```

Catechol First we generate a structure file based on the smiles code, remark that alternatively the smiles code is provided directly to the function defined above.

```
obConversion = openbabel.OBConversion()
obConversion.SetInAndOutFormats("smi", "mol2")
mol = openbabel.OBMol()
obConversion.ReadString(mol, 'C1=CC=C(C(=C1)O)O')
gen3d = openbabel.OBOp.FindType("gen3D")
gen3d.Do(mol, "--best")
obConversion.WriteFile(mol, "catechol.mol2")
```

Test the pysimm system generation and visualize the structure to extract the head and tail indices.

```
pysimm_system = system.read_mol2("catechol.mol2")
view=display_system(pysimm_system,fname='catechol.pdb', labels_on=True)
view
```

Create the catechol monomer used for the generation of the corresponding polymers.

```
catechol_system = create_custom_monomer(7,8,mol2='catechol.mol2')
```

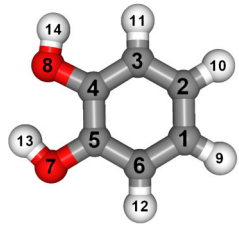

Figure C.1. Catechol with atom index labels.

bis(oxo-carbonate)

```
obConversion = openbabel.OBConversion()
obConversion.SetInAndOutFormats("smi", "mol2")
mol = openbabel.OBMol()
#C's at the end are added for polymerization purposes
obConversion.ReadString(mol, 'C(=O)OC(C)(C(=O)C)CCC(C)(C(=O)C)OC(=O)')
gen3d = openbabel.OBOp.FindType("gen3D")
gen3d.Do(mol, "--best")
obConversion.WriteFile(mol, "bisoxocarbonate.mol2")
```

Test the pysimm system generation and visualize the structure to extract the head and tail indices.

```
pysimm_system_b = system.read_mol2("bisoxocarbonate.mol2")
display_system(pysimm_system_b, fname='bisoxocarbonate.pdb',labels_on=True)
```

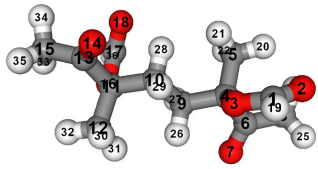

Figure C.2. Bis(oxo-carbonate) with atom index labels.

Create the bis(oxo-carbonate) monomer used for the generation of the corresponding polymers.

```
bisoc_system = create_custom_monomer(1,17,mol2='bisoxocarbonate.mol2')
```

Creating oligomers: two examples

Catechol decamer Here the random_walk function is called from the pysimm module to grow a polymer containing 10 monomeric units. At this point the oligomer is not capped and the generated structure thus contains dangling bonds which need to be saturated afterwards (manually or via the snippets provided below).

```
oligomer_chain_catechol = random_walk(catechol_system, 10,
                          forcefield=ff_general,
                          density=0.01,
                          print_to_screen='false',
                          traj=False,
                          wrap=False,
                          capped=False,
                          settings=sets)

display_system(oligomer_chain_catechol, fname='oligomer_catechol_H_wrapped.pdb')
```

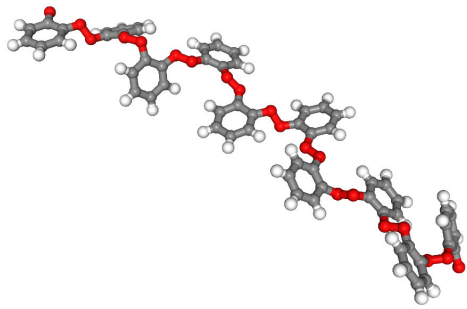

Figure C.3. Deca(catechol) with dangling bonds.

Bis(oxo-carbonate) decamer Grow a polymer containing 10 monomeric units.

```
oligomer_chain = random_walk(bisoc_system, 10,
                          forcefield=ff_general,
                          density=0.01,
                          print_to_screen='false',
                          traj=False,
                          wrap=False,
                          settings=sets)

display_system(oligomer_chain, fname='oligomer_bisoxo_dangling.pdb')
```

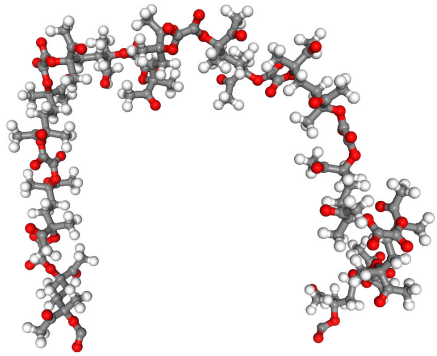

Figure C.4. Deca(bis(oxo-carbonate)) with dangling bonds.

Capping homopolymers with CH_3-units

Below, two approaches are discussed to cap the polymers with methyl-groups. Similar methodologies can in principle be designed for other custom capping units though more in-depth knowledge is required about pysimm to do so.

Approach one

```
def create_methyl_cap(cap='head'):
    # cap: can be either head or tail, in this case a CH3 cap is defined
    # Define methyl system
    s = system.read_pubchem_smiles('C')
    f = ff_general
    s.add_particle_bonding()
    s.apply_forcefield(f,charges='gasteiger')
    c1 = s.particles[1]
    c2 = s.particles[3]
    c1.linker = cap
    c2.linker = 'tail' if cap is 'head' else 'head'
    # Here we remove one hydrogen
    # this is needed for the copolymer script of pysimm
    for b in c1.bonds:
        if b.a.elem == 'H' or b.b.elem == 'H':
            pb = b.a if b.b is c1 else b.b
            s.particles.remove(pb.tag, update=False)
            break
    s.remove_spare_bonding()
    s.pair_style = 'lj/cut'
    lmps.quick_min(s,np=proc, min_style='fire')
    s.add_particle_bonding()
    return s
```

Creating capped monomers and a capped homopolymer using the copolymer function of the pysimm module.

```
capping_unit1 = create_methyl_cap('head')
capping_unit2 = create_methyl_cap('tail')
chainlength = 10
polym = copolymer([capping_unit1,bisoc_system,capping_unit2],
                  chainlength+2,
                  pattern=[1,chainlength,1],
                  forcefield=ff_general,
                  density=0.01,
                  settings=sets)

display_system(polym, fname='oligomer_bisoxo_C_capped.pdb',labels_on=True)
```

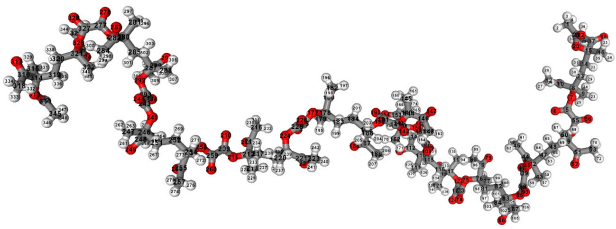

Figure C.5. Deca(bis(oxo-carbonate)).

approach two[364] This approach makes sure that any dangling (undercoordinated) bonds are saturated with a methyl group. In contrast to the previous approach it can be used in nearly any setup. Remark that depending on the applied force field and/or the atoms to be saturated some alterations may be required. We will illustrate this approach again for bis(oxo-carbonate).

```
# Check force field particle types
for index,type in enumerate(ff_general.particle_types):
    print(type.name)

# Check system particle types
for index,type in enumerate(bisoc_system.particle_types):
    print(type.name)

def cap_with_methyls(input_sst, ff):
    '''
        Capping of the free ends of polymer chains with methyl groups
```

```
    in all-atom forcefield representation
'''

# Define the number of bonds the polymer capping atom (head or tail) should
# have theoretically.
cap_bonds_O = 2
cap_bonds_C = 3
captypes = []
# Define atom types of the capping unit
# these should match the atom types of the force field used.
for cpn in ['C_3', 'H_']:
    tmp = input_sst.particle_types.get(cpn)
    if tmp:
        cpt = tmp[0]
    else:
        cpt = ff.particle_types.get(cpn)[0].copy()
        input_sst.particle_types.add(cpt)
    captypes.append(cpt)

for p in input_sst.particles:
    if p.linker is not None:
        if 'C' in p.type_name:
            cap_bonds =cap_bonds_C
        elif 'O' in p.type_name:
            cap_bonds = cap_bonds_O
        if len(p.bonded_to) < cap_bonds:
            # assuming that the linker atom is sp3 hybridized C,
            # let's define the last non-occupied direction
            # of the tetrahedron
            dir = np.zeros(3)
            for p_ in p.bonded_to:
                dir += np.array([p.x, p.y, p.z]) - np.array([p_.x, p_.y,
                ↪  p_.z])

            dir = dir / np.linalg.norm(dir)
            cap_c = system.Particle(x=p.x + 1.53 * dir[0],
                                    y=p.y + 1.53 * dir[1],
                                    z=p.z + 1.53 * dir[2],
                                    type=captypes[0])
            input_sst.add_particle_bonded_to(cap_c, p, f=ff)

            dir_h = np.array([1.0, 1.0, 1.0])
            dir_h[0] = -(dir_h[1] * dir[1] + dir_h[2] * dir[2]) / dir[0]
            dir_h = dir_h / np.linalg.norm(dir_h)

            dir_h2 = np.array([1.0, 1.0, -1.0])
            dir_h2[1] = (dir[2] / dir[0] - dir_h[2] / dir_h[0])
                        / (dir[1] / dir[0] - dir_h[1] / dir_h[0])
            dir_h2[0] = dir[2] / dir[0] - dir[1] * dir_h2[1] / dir[0]
            dir_h2 = dir_h2 / np.linalg.norm(dir_h2)
```

```
                stretch = 0.78
                input_sst.add_particle_bonded_to(
                    system.Particle(x=cap_c.x + stretch * dir[0] + stretch *
                    ↪  dir_h[0],
                                    y=cap_c.y + stretch * dir[1] + stretch *
                                    ↪  dir_h[1],
                                    z=cap_c.z + stretch * dir[2] + stretch *
                                    ↪  dir_h[2],
                                    type=captypes[1]), cap_c, f=ff)
                input_sst.add_particle_bonded_to(
                    system.Particle(x=cap_c.x + stretch * dir[0] + stretch *
                    ↪  dir_h2[0],
                                    y=cap_c.y + stretch * dir[1] + stretch *
                                    ↪  dir_h2[1],
                                    z=cap_c.z + stretch * dir[2] + stretch *
                                    ↪  dir_h2[2],
                                    type=captypes[1]), cap_c, f=ff)
                input_sst.add_particle_bonded_to(
                    system.Particle(x=cap_c.x + stretch * dir[0] - stretch *
                    ↪  dir_h2[0],
                                    y=cap_c.y + stretch * dir[1] - stretch *
                                    ↪  dir_h2[1],
                                    z=cap_c.z + stretch * dir[2] - stretch *
                                    ↪  dir_h2[2],
                                    type=captypes[1]), cap_c, f=ff)
    input_sst.objectify()
    input_sst.center(what='particles', at=[0.0, 0.0, 0.0], move_both=False)
    sim = lmps.Simulation(input_sst, log='capping_opt.log')
    sim.add_min(min_style='cg',
                name='min_cg',
                etol=1.0e-6,
                ftol=1.0e-6,
                maxiter=int(1e+6),
                maxeval=int(1e+7))
    sim.run(np=proc)
```

Generate bis(oxo-carbonate) oligomer with dangling bonds.

```
oligomer_chain = random_walk(bisoc_system, 2,
                         forcefield=ff_general,
                         density=0.01,
                         print_to_screen='false',
                         traj=False,
                         wrap=False,
                         capped=False,
                         settings=sets)
display_system(oligomer_chain, fname='oligomer_bisoxo_dangling.pdb')
```

Cap the polymer with CH_3 units:

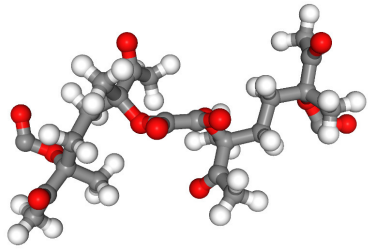

Figure C.6. Di(bis(oxo-carbonate)) with dangling bonds.

```
oligomer_CH3_capped = oligomer_chain.copy()
cap_with_methyls(oligomer_CH3_capped,ff_general)
display_system(oligomer_CH3_capped, fname='oligomer_bisoxo_post_process_capped.pdb')
```

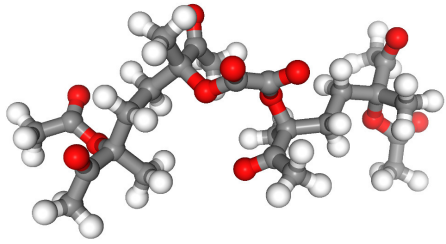

Figure C.7. Di(bis(oxo-carbonate)).

Creating Copolymers

Here we introduce the construction of copolymers, i.e. Alternating copolymers from catechol and bis(oxo-carbonate). Experimentally the resulting polymer is constructed via a step-polymerization this is however not of importance for its computational construction procedure. However, one does need to have prior knownledge about the size and copolymerization patterns to perform this step consistently (*vide infra*).

poly(catechol-co-bis(oxo-carbonate)) Generate a copolymer altering catechol and bis(oxo-carbonate) using a 1-1 pattern:

```
chainlength = 10
polym = copolymer([bisoc_system,catechol_system],
                  chainlength,
                  pattern=[1,1],
                  forcefield=ff_general,
                  density=0.01,
                  settings=sets)

display_system(polym, fname='copolymer_bisoxo_catechol_dangling.pdb')
```

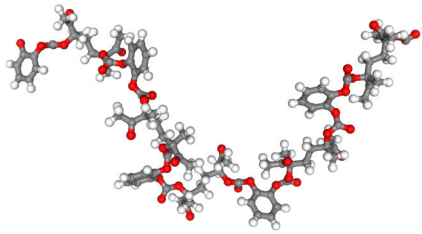

Figure C.8. Poly(catechol-co-bis(oxo-carbonate)) with dangling bonds.

Cap the copolymer:

```
polym_capped = polym.copy()
cap_with_methyls(polym_capped,ff_general)
display_system(polym_capped, fname='copolymer_bisoxo_catechol_process_capped.pdb')
```

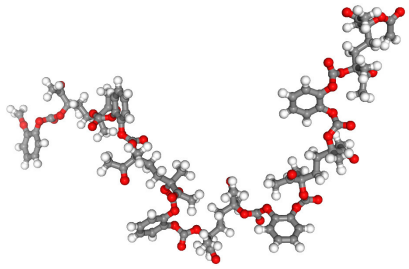

Figure C.9. Catechol-co-bis(oxo-carbonate)).

Create a Multiple-chain copolymer system

Increasing the amount of polymer chains present in the system is fairly trivial. Importantly is that one accounts for the number of chains in the density provided to the functions as this will decide how much space the chain can take within a specific unit cell.

Five chains of poly(catechol-co-bis(oxo-carbonate))

```
chainlength = 10
chains = 5
density= 0.1
polym = copolymer([bisoc_system,catechol_system],
                chainlength,
                pattern=[1,1],
                forcefield=ff_general,
                density=density/chains,
                settings=sets)
for chain in range(chains-1):
        polym = copolymer([bisoc_system,catechol_system],
                        chainlength,
                        pattern=[1,1],
                        forcefield=ff_general,
                        density=density/chains,
                        s_=polym,
                        settings=sets)
```

Cap all polymer chains:

```
polym_capped = polym.copy()
cap_with_methyls(polym_capped,ff_general)
polym_capped.unwrap()

display_system(polym_capped,
            fname='copolymer_bisoxo_catechol_5chains_CH3capped.pdb')
```

Remark that in principle one can use the copolymer functionality to produce branched polymers or polymers which have multiple linking atoms though a small workaround is required (The pysimm github page does have an example for the latter case[364]).

Print box information:

```
### Unit cell info
print('Volume =',polym.volume) # nm3
print('box dimensions =',polym.dim.dx,polym.dim.dy,polym.dim.dz) # nm
```

```
Volume = 212837.5311422526
box dimensions = 59.705738 59.705738 59.705738
```

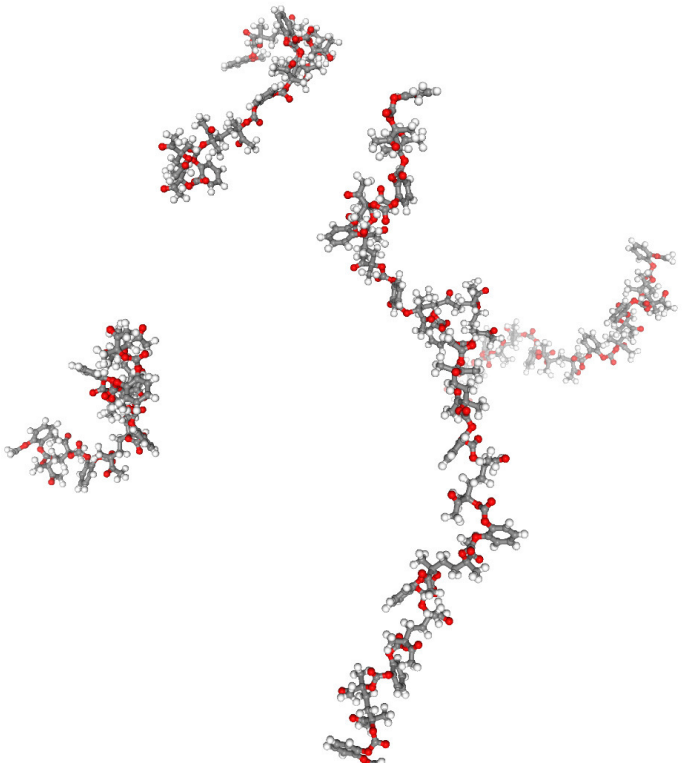

Figure C.10. Five chains of poly(catechol-co-bis(oxo-carbonate)).

Ultimately one can perform an equilibration protocol for polymer systems using pysimm which will perform the well-established 21-step MD protocol (*vide infra*).[365] In case one has experience with lammps, alterations can be made to the protocol to meet the needs of your system. Alternatively one can perform the protocol within openMM using the desired force field (*vide infra*).

Defining the system size

Here by system size I refer to the length of the polymer chains and the number of polymer chains included in a simulation cell. Choosing an appropriate system size is not a trivial thing to do and can depend on many factors, including but not limited to: experimental polydispersity, computational cost, property of interest, ... For instance one could try to mimic experiments as closely as possible and hence use a chain length equal to the experimental degree of polymerization. Then choosing an appropriate number of polymer chains could be chosen based on what is feasible computationally, or one could try to limit finite-size effects. In some cases one can opt to use a single long chain to reduce the effects of the chain ends.[365] Furthermore it has been shown multiple times already that the properties

of interest can be highly influenced by these choises and often correction need to be applied or the effect of the system size should be determined explicitly.[337,366]

C.1.2 Polymer force fields

Though omnipresent in everyday life, only a few dedicated general polymer force fields exist to date. By far the most used one is the COMPASS (condensed-phase optimized molecular potentials for atomistic simulation studies)[367] force field and the recently improved version of it: COMPASS II from BIOVIA Materials studios[368]. However due to the limited number of MD engines supporting the COMPASS force field (LAMMPS[369] (support but limited) and the developers' BIOVIA Materials studio suite but not OpenMM, Gromacs, CHARMM, ...) and due to the fact Materials studio is a commercial software package, often more general force fields are used for the parameterization of these molecules. Typical examples which are all open-source are CGenFF (the general all-atom forcefield by Charmm)[370], GAFF and GAFF2(Generalized amber force field)[86,87], OPLS (Optimized potential for liquid simulations)[371] or the Dreiding force field used in the above example[372]. These open-source force fields have the advantage of being compatible with many MD codes and provide reasonably accurate results in many cases. Noteworthy is that the strength of the COMPASS force fields originates from taking into account experimental data from polymer science to alter/finetune the *ab initio* based force field.

Remark that in principle also the force fields developed by the open force fields consortium (see Workflow B) (openff) can be used for the parameterization of polymers. However, at the moment the openff-toolkit package does not provide an automated way to fragmentate the molecule and hence perform an efficient charge calculation limiting the size of the polymers to be used.[105] However, a workflow to automatically fragment and charge polymers, define residue seprators (in the form of a SMARTS string), and a method to treat capping units will be included in a future version of the toolkit. For now a possible workaround is to define a set of Library charges circumventing the need to calculate charges for the full polymer, which is the limiting factor for the parameterization procedure with openff-toolkit.

Below I've illustrated the use of one of a general force field like the Sage force field used in Appendix B, combining it with openMM and the set of tools introduced in Appendix B. Furthermore some importants aspects are highlighted with some specific code examples for the set-up of your own polymer force field which can be run with openMM or other MD engines.

Literature forcefields: Sage force field[373]

```
# Import relevant packages
from openff.toolkit.topology import Molecule, Topology
```

```
from openff.toolkit.utils.toolkits import OpenEyeToolkitWrapper
from openff.toolkit.typing.engines.smirnoff import ForceField
from openmmforcefields.generators import SystemGenerator
from openmmforcefields.generators import SMIRNOFFTemplateGenerator
from simtk import openmm

# Define openMM pdb object using the solvated system from before.
pdb_box = openmm.app.PDBFile('copolymer_bisoxo_catechol_process_capped.pdb')
# Define the unique molecules present in the pdb_box,
# this is an isolated polymer chain!
unique_molecules
        = [Molecule.from_file('copolymer_bisoxo_catechol_process_capped.pdb')]
```

Advantageous in this approach is that naming in the pdb file is no longer really important in case the system needs to be parameterized by openff. However the molecule defined in unique molecules and hence its .pdb file should match the structure inside the pdb_box (i.e. an individual polymer chain and the combined polymer chains should all have the same ordering and connectivity data as defined in the .pdb file).

```
system_generator = SystemGenerator(forcefields=[],
                                   small_molecule_forcefield='openff-2.0.0.offxml',
                                   molecules=unique_molecules)
```

Remark that the force fields defined in the forcefields attribute will use the 'old' atom-typing methodology and hence require one to specify a topology file containing atom types which correspond to the force field one would like to use. For example in case one would like to use the TIP3P water force fields it is important that the hydrogens and oxygen atoms of the water molecules have a correct atom and residue name (i.e. H1, H2, O and residue name HOH).

```
system = system_generator.create_system(pdb_box.topology,
                                        molecules=unique_molecules)
```

The system object can now be used to perform simulation, or one can serialize the system to perform simulations later on or to transfer the parameterized system. This can be used to circumvent the need to redo the often 'lengthy' parameterization procedure for these systems.

```
serialized_system = openmm.openmm.XmlSerializer.serialize(system)
with open('copolymer_bisoxo_catechol_process_capped_system.xml','w') as oxml:
    oxml.write(serialized_system)
```

Constructing polymer force field from scratch based on *ab-initio* simulations

Here we highlight the key steps in deriving a force field for polymer simulations with the QuickFF 2.2.4 protocol (also see **Paper VI**).[84,85] An in-depth discussion on the QuickFF protocol is beyond the scope of this workflow, though some key features are highlighted which one should consider carefully.

Force field derivation: QuickFF It is worthwhile to first consider the polymer under investigation and think about which distinct chemical fragments are present in the chains. Typically we will distinguish atleast three fragments that is an initiator fragment (or chain end, I), a propagating fragment (A) and a terminating fragment (or chain end, T). Evidently each of these fragments can be subdived more depending on the desired features of the system or in some cases one can just use a single fragment to describe both chain ends and the propagating units (e.g. simple polymers like poly(ethylene)). For copolymers it might be usefull to subdivide the repeating unit into its original building blocks such as the case presented above, i.e. subdivide the repeating unit into the catechol-derived unit and the bis(αCC)-derived unit. However it often will suffice to distinguish the repeating unit and the chain ends.

Making this distinction is important to determine unique parameters for every chemically differing fragment, to ensure charge neutrality and finetune important torsion terms. Though not discussed below, evidently the level of theory used in the DFT calculation will influence the results. A good and reliable level of theory to use is ωB97X-D with a relatively large (Pople) basis set such as '6-311+g(d,p)'.[78]

System size The goal is to describe every fragment present within a polymer which is chemically different and hence possesses unique features such as atomic charges, dihedral angles, ... Based on the work performed by Coote et al. and the results presented in **Paper V** and **Paper VI** it is suggested to use a trimeric or pentameric system in the optimization step of the protocol.[122,283] I would advice to use pentameric structures (I-A-A-A-T) for the parameterization procedure because it covers both initiator-propagator interactions (I-A), propagator-propagator interactions (A-A both in the neighborhood of each capping unit) and the propagator-terminator interactions (A-T). This is specifically interesting if intramolecular interactions are present which is the case for PEtOx (see **Paper VI**).

If torsion terms need to be adjusted due to discrepancies between the *ab initio* data and force field data, it is usefull to limit the degrees of freedom and solely take into account the part directly influenced by the parameter, i.e. we want to perform a rigid torsional scan from a representative dimeric system. In some cases atomic overlap within the system during a rigid scan might force you to use a relaxed torsional scan. Fitting a custom torsion term to this will evidently result in a torsional term including more than just the contribution of the dihedral angle (it will for example also include some dicrepancy between the force field angle terms). Remark that one should use periodic functions in the fitting procedure.

Charges These can be derived using the in-house developed HORTON program.[374] A good scheme to use for basic organic chemistry is the MBIS (minimal

basis iterative stockholder) scheme.[375] However two important features need to be stressed:

1. For compatibility purposes one needs to know whether to describe charges as point charges or as gaussian distributions (default in horton). Specifically for OpenMM, point charges are required.
2. All molecules (unless ionic in nature) should be charge neutral. The danger with polymers however is that a small offset in the net charge of a repeating unit can result in a large net charge of the parameterized polymer (in a subsequent phase) which contains this small offset multiple times. Hence importantly one needs to insure charge neutrality within each defined propagating unit. This can be achieved by including bond-charge increments (bci) combined with a proper definition of the bonds to include in this analysis, i.e. one should exclude bonds between residues of interest in order to ensure the neutrality within a residue.[376] In this case it is assumed that no charge is shared across bonds connecting propagating units which thus ensures that the net charge within a unit is zero.

In some cases it is worthwhile to average over the different propagating units assuming the the net behavior is described correctly by the averaged charge. For example for the pentamer introduced above the three propagating units (A-A-A) all have three distinct molecular environments, i.e. A-A, I-A and A-T, while we only need one set of charges for the propagating unit A. Hence in this case it is usefull the average the charges obtained for A.

Van der Waals parameters Dispersion interactions can be described by different schemes as highlighted Chapter 2 Section 2.3.3. Importantly for the parameterization procedure is that compatability with openMM is ensured i.e. the functional form is supported (or can be implemented). When taking specific parameters from an existing force field such as CGenFF or GAFF2 one should carefully match the atom types ascribed by QuickFF and those ascribed by GAFF2 or CGenFF. Most importantly is that one is consistently using the same set of VdW interactions within a molecular system.

Whortwhile noting is that actually one needs to refit these VdW parameters for every different covalent force field and/or charge scheme used.[377] Evidently this is an unfeasible and tedious job in many cases and could be a reason to stick to well-established force fields in the future (which have performed this procedure for their atom-types).[377] The Sage force field is one of the force fields tackling this 'problem'.[373]

Parameterizing the polymer system

Once the parameters are derived for the small polymeric system, we would like to parameterize all chains in the polymeric system (constructed with e.g. pysimm or polymatic). To this end we distinguish a few key steps:

1. We convert the polymeric systems xyz file (or another file format containing cartesian coordinates) to a -.chk which has equal atom typing as used in the Quickff protocol. An example script is shown below -which can most certainly be improved-:

```
import numpy as np
import argparse
from molmod import *
from yaff import *
log.set_level(0)
parser = argparse.ArgumentParser()
parser.add_argument('-c', '--chk_output_name',type=str)
parser.add_argument('-d', '--dimension',type=float,default=None)
parser.add_argument('-x', '--xyz_input_name',type=str)
parser.add_argument('-o', '--original_chk',type=str,
                    help='provide the original, \
                    small system chk file constructed with QuickFF')
args = parser.parse_args()

def get_base_ffatypes(original_chk):

    s_base = System.from_file(original_chk)
    return s_base.ffatypes
atom_numbers = {'H':1,'C':6,'N':7,'O':8}

def prepare_ffatypes(ffatypes):

    atom_types = {}
    for ffatype in ffatypes:

        nr = atom_numbers[ffatype.split('_')[0][:-1]]
        nr_neighs = int(ffatype.split('_')[0][-1])
        neighbours = []
        for el in ffatype.split('_')[1:]:
            digit_present = el[-1].isdigit()
            nr_el = int(el[-1]) if digit_present else 1
            for i_el in range(nr_el):
                neighbours.append(el[:-1].upper())
                if digit_present else neighbours.append(el.upper())
        for i in range(nr_neighs-len(neighbours)):
            neighbours.append('H')

        neighbours = [atom_numbers[n] for n in neighbours]
        atom_types[ffatype] = CritAnd(HasAtomNumber(nr),\
                              HasNeighborNumbers(*neighbours))

    return atom_types

def detect_types(mol, atom_types):
    print('Detecting atom types of extended system')
```

```
    # loop to detect all atom types
    detected = {}
    for i in range(mol.size):
        # match label is going to be the label of the matching atom type.
        match_label = None
        for label, atom_type in atom_types.items():
            if atom_type(i, mol.graph):
                # We have a match.
                if match_label is None:
                    # This is how it should be.
                    match_label = label
                else:
                    # This should not happen after a previous match.
                    raise TypeError("Atom %i matches more than one type,\
                                at least %s and %s" % (i, label, match_label))
        if match_label is None:
            # No matching type detected, so raise an error.
            raise TypeError("Atom %i does not have any type." % i)
        # Get the list of atom indexes associated with match_label. If such a list
        # is not present in the detected dictionary yet, an empty list is assigned
        # to the match_label key and returned.
        l = detected.setdefault(match_label, [])
        # Add the current atom index to the list.
        l.append(i)

    ffas = []
    for i in range(len(mol.numbers)):
        for key, value in detected.items():
            if i in value:
                ffas.append(key)
    assert len(ffas) == len(mol.numbers)
    return np.array(ffas)

if __name__ == "__main__":

        ffatypes = get_base_ffatypes(args.original_chk)
        atom_type_dict = prepare_ffatypes(ffatypes)
        mol = Molecule.from_file(args.xyz_input_name)
        mol.set_default_graph()
        ffatypes_extended = detect_types(mol, atom_type_dict)
        s = System.from_file(args.xyz_input_name, ffatypes=ffatypes_extended)
        if args.dimension is None:
                print('No dimensions are provided, proceeding without')
        else:
                rvecs=np.array([[args.dimension, 0.0, 0.0],
                                [0.0,args.dimension, 0.0],
                                [0.0, 0.0,args.dimension]])*angstrom
                s.cell = pes.ext.Cell(rvecs)
        s.detect_bonds()
        s.to_file(args.chk_output_name)
```

An example of how to use the above mentioned script is shown below:

```
example_script.py   -o small_system.chk
                    -x large_system.xyz
                    -c large_system.chk
                    -d dimension
```

2. Convert the system -.chk file to a pdb compatible with openMM introducing residue names for each distinct unit within the polymer, i.e. repeating unit and the chain ends. Remark that this is just an example script to avoid one has to start from scratch. It is an essential step and one should carefully inspect the resulting -.pdb file (though many codes will complain in case the resulting pdb file does not satisfy the prerequisites). Remark that residue names should be unique.

```
from yaff import *
from molmod import *
from  simtk.openmm.app import *
import argparse,os
import mdtraj as md
import openbabel as openbabel


parser = argparse.ArgumentParser()
parser.add_argument('-c', '--chk_input_name',type=str,
                    help='provide system checkpoint file')
parser.add_argument('-p', '--pdb_output_name',type=str,
                    help='provide a pdb output filename')
parser.add_argument('-d', '--dimension',type=float,
                    help='provide the box dimension of \
                    a cubic periodic box in nanometer!',
                    default=None)
parser.add_argument('-x', '--xyz_input_name',type=str,
                    help='provide xyz input filename, \
                    IMPORTANT, indexing of the atoms is based \
                     on a correct ordering within the XYZ file')
parser.add_argument('-i', '--initiator_res_name',type=str,
                    help='3 letter residue name of the initiator')
parser.add_argument('-t', '--terminator_res_name',type=str,
                    help='3 letter residue name of the terminator')
parser.add_argument('-m', '--monomer_res_name',type=str,
                    help='3 letter residue name of the terminator')
parser.add_argument('--initiator_atoms',type=int,
                    help='number of atoms in the initiator')
parser.add_argument('--monomer_atoms',type=int,
                    help='number of atoms in the monomer')
parser.add_argument('--polymer_length',type=int,
                    help='number monomers = polymer length - \
                    initiator and terminator unit')
parser.add_argument('--terminator_atoms',type=int,
```

```
                    help='number of atoms in the terminator')
args = parser.parse_args()

def getStartingIndices(initiator_atoms,
                       monomer_atoms,
                       terminator_atoms,
                       polymerMonomerLength,
                       total_atoms):

    polymer_length = int(initiator_atoms + polymerMonomerLength*monomer_atoms
                    + terminator_atoms)
    polymer_units = int(total_atoms/polymer_length)
    print(total_atoms,polymer_units,polymer_length)
    assert total_atoms % polymer_length == 0
    monomer_starting_indices = []
    initiator_starting_indices = []
    terminator_starting_indices = []

    #add polymer starting indices
    print(polymer_units)
    for k in range(polymer_units):
        index = k+k*(polymer_length-1)
        initiator_starting_indices.append(index)
    for k in range(polymer_units):
        index = polymer_length+k*polymer_length - terminator_atoms
        terminator_starting_indices.append(index)
    count = initiator_atoms - monomer_atoms
    for k in range(polymer_units):
        for i in range(polymerMonomerLength):
            index = count + monomer_atoms
            count = index
            monomer_starting_indices.append(index)
        count = count + terminator_atoms + initiator_atoms
    return initiator_starting_indices,monomer_starting_indices,\
            terminator_starting_indices


# Generate pdb_topology from xyz
obConversion = openbabel.OBConversion()
mol = openbabel.OBMol()
obConversion.SetInAndOutFormats("xyz", "pdb")
obConversion.ReadFile(mol,args.xyz_input_name)
obConversion.WriteFile(mol, f"xyz_top.pdb")
s = System.from_file(args.chk_input_name)

# Indexed based pdb manipulation
print('Make sure to check the output pdb in vmd, \
    this should be the same as the xyz')
xyz_traj = md.load(args.xyz_input_name,top='xyz_top.pdb')
topology = xyz_traj.topology
```

```
#Change atom types (to fit in pdb file)

new_atom_types = []
old_atom_types = {}
changed_atom_types_dict = {}
atom_type_index = 0
with open('changed_atom_types.txt','w') as cat:
    for index,atom_type in enumerate(s.ffatypes[s.ffatype_ids]):
        if atom_type not in old_atom_types:
            new_atom_type = atom_type[0]+str(atom_type_index)
            atom_type_index=atom_type_index+1
            cat.write(f'old atom type is: {atom_type},\
                    corresponding new atom type is {new_atom_type}\n')
            changed_atom_types_dict[atom_type]=new_atom_type
            old_atom_types[atom_type] = new_atom_type
        else:
            new_atom_type = old_atom_types[atom_type]
        new_atom_types.append(new_atom_type)

new_atom_types = np.array(new_atom_types)
np.savetxt('all_atom_types_indexed.txt',new_atom_types,fmt='%s')

# Create residues and chains with these new atom types

init_indices,monomer_indices,term_indices
               = getStartingIndices(args.initiator_atoms,
                                    args.monomer_atoms,
                                    args.terminator_atoms,
                                    args.polymer_length,
                                    topology.n_atoms)
residue_name = ''
residue_id = 0
chain_id = 0
atom_counter = 0
# It is best practice to check the atom type and base
# the numbering on each atom type.
for atom in topology.atoms:
    if atom.index in init_indices:
        atom_counter = 0
        residue_name = args.initiator_res_name
        residue_id = residue_id + 1
        chain_id =chain_id + 1
        Chain = topology.add_chain()
        Residue = topology.add_residue(args.initiator_res_name,
                                    Chain,
                                    resSeq=residue_id)
    elif atom.index in monomer_indices:
        atom_counter = 0
        residue_id = residue_id + 1
        residue_name = args.monomer_res_name
```

```
        Residue = topology.add_residue(args.monomer_res_name,
                                       Chain,
                                       resSeq=residue_id)
    elif atom.index in term_indices:
        residue_id = residue_id + 1
        atom_counter = 0
        residue_name = args.terminator_res_name
        residue_id = residue_id + 1
        Residue = topology.add_residue(args.terminator_res_name,
                                       Chain,
                                       resSeq=residue_id)
    atom.resname = residue_name
    atom.resid = residue_id
    atom.resSeq = residue_id
    atom.residue = Residue
    atom.chainid = chain_id
    atom.name = new_atom_types[atom.index][0] +str(atom_counter)
    # needed to link atom names to atom classes via atom types
    # in the force field conversion script.
    atom_counter=atom_counter + 1

table,bonds = topology.to_dataframe()
new_topology = md.Topology.from_dataframe(table,bonds)
table,bonds = new_topology.to_dataframe()
assert(topology.bonds==new_topology.bonds)
print(f'number of residues = {topology.n_residues},\
     number of chains = {topology.n_chains},\
      number of bonds = {topology.n_bonds}')


cell_lengths = np.array([[args.dimension*angstrom/nanometer,
                         args.dimension*angstrom/nanometer,
                         args.dimension*angstrom/nanometer]])
cell_angles = np.array([[90,90,90]])

new_traj = md.Trajectory(xyz_traj.xyz,
                         new_topology,
                         unitcell_lengths=cell_lengths,
                         unitcell_angles=cell_angles)
# Remark that standard_names=False is a feature which
# is not included in the save_pdb function of MDTraj
# and should hence manually be included.
new_traj.save_pdb(args.pdb_output_name,
                  force_overwrite=True,
                  standard_names=False)
```

An example of how to use the above mentioned script is shown below:

```
example_script.py   -c large_system.chk
                    -p large_system.pdb
```

```
-x large_system.xyz
-i INI -m REP -t TET
--initiator_atoms XX
--monomer_atoms YY
--terminator_atoms ZZ
--polymer_length number_of_propagating_units
-d dimension
```

with INI the residue name for the initiator, REP for the repeating unit and TET for the terminator.

3. Convert the system -.chk file to a force field -.xml or system -.xml file which is compatible with openMM by means of OpenYaff.[358]

    a) Construct a system.xml file directly usable (by (de)serialization) in openMM. This is an option if no extra molecules are needed.

    b) Generate a force field -.xml file, this is a feature which is currently under development. This force field -.xml file is then straightforward to combine with other force fields using the system generator tool illustrated above and in Appendix B (cfr. SystemGenerator).

The constructed -.xml file and -.pdb file can be used to perform simulations with openMM (Appendix B).

C.1.3 Equilibration procedure

Depending on the system under investigation, different equilibration procedures have been proposed in literature.[337,365,378,379] These are typically required to converge the density of the system, remove anomalies and hence make the system as realistic as possible. The resulting systems can then be used in subsequent production runs, the aim of these simulations will be different depending on the goal of the project and hence the properties of interest, e.g. diffusive properties, interaction analysis, ... Important to keep in mind is that one should always consider ensemble averages of different structures. Hence it is good practice to repeat the protocol presented here (and preferably also the structure generation step) for multiple structures (I would advice a minimum of 10) to ensure that sufficient (ideally all) configurations are sampled, i.e. the phase space, and calculated properties are representative for the investigated material. Alternative to repeating the protocol and production runs for different input structures one could opt to perform a single (very) long simulations which covers the full phase space of interest. For efficiency reasons this is not adviced. Furthermore in the latter approach one needs to assume that all states can be visited without the need to apply an external bias to the system i.e. phase and/or configurational transitions etc. happen spontaneously.

Furthermore, depending on the desired properties it might be usefull to change the ensemble used to sample the phase space, e.g. diffusive properties can be best sampled in the microcanonical ensemble because thermostats and/or barostats would interfere with the dynamics of the system.[380] Important to this end is that intermediate equilibration runs should be performed when altering the ensemble, i.e. isothermal-isobaric $\rightarrow$ canonical $\rightarrow$ microcanonical. As an example, before running a simulation in the canonical ensemble, one would first like to equilibrate the pressure and hence converge the volume using the isothermal-isobaric ensemble. If this is not done the wrong volume and hence density is used within the production runs and properties might be determined incorrectly or differ significantly from experimental values.

Equilibrating polymeric systems: 21-step MD protocol

A well-known procedure to equilibrate polymeric systems in literature is the 21-step MD protocol used to compress and relax polymers towards their realistic (experimentally observed) densities. It is proposed by Larson et al. who have based their scheme on the work proposed by Karayannis et al. and Hofmann and coworkers.[365,378,379] It is also referred to as the 21-step compression/relaxation scheme or the 21-slow decrompression scheme and provides consistent final densities independent of the maximal pressure and temperature used within the scheme.

pysimm In case the systems are sufficiently small or in case one does not require the GPU-acceleration to model the systems at hand, one can use the pysimm implementation of the equilibration protocol (In principle, if you are familiar with LAMMPS, one can transfer the files and perform GPU-accelerated simulations directly with LAMMPS). The code snippet below illustrates the simplicity of using pysimm for this:

```
equil(polym_capped,**sets)
```

an equil.lmps and .xyz structure are written which can be used in subsequent production runs.

```
polym_capped.write_xyz('equilibrated_5chains_wrapped.xyz')
polym_capped.write_pdb('equilibrated_5chains_wrapped.pdb')
polym_capped.unwrap()
polym_capped.write_xyz('equilibrated_5chains_unwrapped.xyz')
polym_capped.write_pdb('equilibrated_5chains_unwrapped.pdb')

display_system(polym_capped, fname='equilibrated_5chains_unwrapped.pdb')
```

Remark the difference with the structure before equilibration:

In case computational cost of the simulations is the limiting factor (or in case one is not to familiar with LAMMPS simulations) it is worthwhile transfering the input files to OpenMM (*vide infra*)

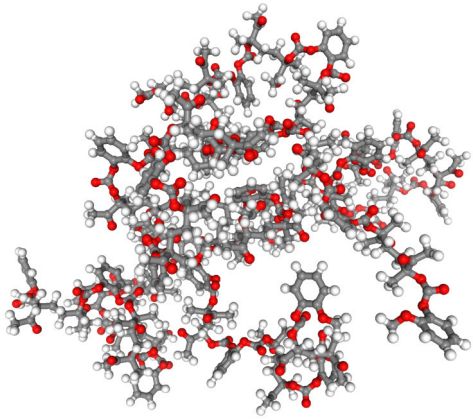

Figure C.11. Equilibrated system containing five copolymer chains.

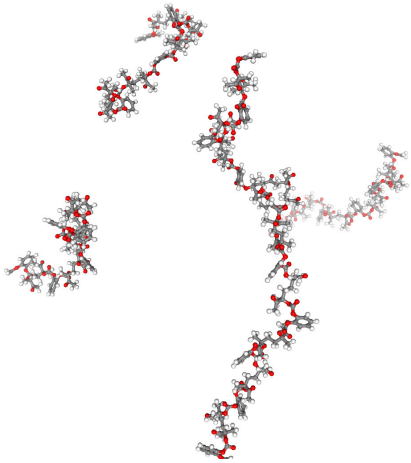

Figure C.12. System containing five copolymer chains generated with pysimm.

OpenMM Each of the steps in the 21-step MD protocol can be translated to OpenMM. Thusfar this is not done. It simply boils down to changing the ensemble, the temperature, the number of timesteps and in case of the isothermal-isobaric simulations changing the pressure. As each of the simulation steps takes less than a nanosecond, the process can easily be performed within one hour of simulation time by making use of the fast GPU-acceleration of OpenMM (ofcourse this depends on the system size).

Amorphous solid dispersions

Depending on the investigated polymer application it is worthwhile engineering different equilibration protocols with the same goal as before. Hence for ASDs

this counts too, and custom equilibration protocols are designed in literature - often inspired by the aforementioned 21-step MD protocol-. In the work presented **Paper VI**, we have proposed a customized equilibration protocol for the investigated systems based on the work of Li et al. to produce reliable amorphous solid dispersions.[337] The different steps (with some minor alterations with respect to the aforementioned paper) are highlighted in **Paper VI**. here some specific code examples are provided for the 'non-trivial' steps in the protocol which is used in the simulations with openMM.

Step: Active pharmaceutical ingredient (API) redistribution In this step one would like to keep the polymer fixed and make sure only the API molecules can move at an elevated temperature (to increase the kinetic energy of the molecules). This can be easily achieved by setting the polymer mass to 0. In OpenMM this can be done via the following piece of code:

```
for i in range(0,polymer_indices):
    omm_system.setParticleMass(i, 0*dalton)
```

Step: Relax all components at 600K Here we want to avoid steric clashes and hence increase the temperature gradually before running a 2ns relaxation run. The gradual increase in temperature can be achieved by altering the temperature of the thermostat (integrator) linked to the simulation:

```
# example simulation definition
simulation = Simulation(pdb_box.topology, system, integrator)
# Heating from 300L to 600K
integrator.setTemperature(300*kelvin)
for i in range(100):
    integrator.setTemperature(3*(100+i)*kelvin)
    simulation.step(5000) # timestep of 2 fs, hence 10 ps for each temperature
# Run relaxation run at elevated temperature
```

This is the general strategy to elevate or decrease the temperature.

Step: Gradually ramp up the density Now a barostat is added to the system which is allowed to interact with the system at a much lower frequency than in the 'normal' case. Instead of setting the frequency at which the barostat attempts to change the volume of the cell to 25*timestep (default in OpenMM) we set it to a frequency which is significantly lower, i.e. attempt to change the volume once every 15*25*timestep, meaning it will try to adjust the pressure less often. Alternativelly one could increase the pressure to speed things up (like in the 21-step MD protocol). Remark that in any case one should carefully monitor this step and decrease or increase the frequency (or the pressure) appropriately to obtain the desired behavior.

```
barostat = MonteCarloBarostat(pressure, temperature,frequency*25)
forceIndex = system.addForce(barostat)
```

Here defining the force index allows one to easily delete the barostat afterwards.

All subsequent steps boil down to using the aforementioned snippets, snippets presented in Appendix B or general (well-documented) simulation commands in OpenMM.

D

Acknowledgements

This research was supported by the Research Foundation Flanders (FWO) (BioFact Excellence of Science project Grant No. 30902231). Further funding was also received from the European Union's Horizon 2020 research and innovation program (consolidator ERC grant agreement no. 647755 - DYNPOR (2015-2020)), the Fund for Scientific Research Flanders and the Research Board of the Ghent University (BOF).

The computational resources and services used were provided by Ghent University (Stevin Supercomputer Infrastructure), the VSC (Flemish Supercomputer Center), funded by Ghent University, FWO and the Flemish Government - department EWI.

Bibliography

[1] M. Nic, J. Jirat, and B. Kosata. *The IUPAC Compendium of Chemical Terminology*. Blackwell Scientific Publications, Oxford, 2019. doi: 10.1351/goldbook.

[2] Lutz Bornmann, Robin Haunschild, and Rüdiger Mutz. Growth rates of modern science: a latent piecewise growth curve approach to model publication numbers from established and new literature databases. *Humanities and Social Sciences Communications*, 8(1):1–15, 2021. doi: 10.1057/s41599-021-00903-w.

[3] Computation sparks chemical discovery. *Nature Communications*, 11(1):4811, 2020. doi: 10.1038/s41467-020-18651-x.

[4] Tom Renders, Gil Van den Bossche, Thijs Vangeel, Korneel Van Aelst, and Bert Sels. Reductive catalytic fractionation: state of the art of the lignin-first biorefinery. *Current Opinion in Biotechnology*, 56:193–201, 2019. doi: 10.1016/j.copbio.2018.12.005.

[5] Francisco Zaera. In-situ and operando spectroscopies for the characterization of catalysts and of mechanisms of catalytic reactions, 2021.

[6] B H Bransden and C J Joachain. *Quantum Mechanics*. Prentice Hall, 2000.

[7] B.H. Bransden and C.J. Joachain. *Physics of Atoms and Molecules (2nd Edition)*. Addison-Wesley, 2003.

[8] J J Sakurai and J Napolitano. *Modern Quantum Mechanics*. Cambridge University Press, 2017.

[9] M. Born and R. Oppenheimer. Zur quantentheorie der molekeln. *Annalen der Physik*, 389(20):457–484, 1927. doi: 10.1002/andp.19273892002.

[10] M. Born, K Huang, and M. Lax. Dynamical theory of crystal lattices. *American Journal of Physics*, 23(7):474–474, 1955. doi: 10.1119/1.1934059.

[11] Baron Peters. *Reaction Rate Theory and Rare Events*. Elsevier, 2017.

[12] F Mandl. *Statistical physics*. Wiley, New York, 2nd edition, 1988.

[13] Donald A. McQuarrie and John D. Simon. *Molecular thermodynamics*. University Science Books, 1999.

[14] Luis G. Arnaut, Sebastiao J. Formosinho, and Hugh. Burrows. Chemical kinetics: From molecular structure to chemical reactivity. *Focus on Catalysts*, 2019(6):7, 2019. doi: 10.1016/j.focat.2019.05.048.

[15] Luís P. De Oliveira, Damien Hudebine, Denis Guillaume, and Jan J Verstraete. A review of kinetic modeling methodologies for complex processes. *Oil and Gas Science and Technology*, 71(3), 2016. doi: 10.2516/ogst/2016011.

[16] Henry Eyring. The activated complex in chemical reactions. *The Journal of Chemical Physics*, 3(2):63–71, 1935. doi: 10.1063/1.1749604.

[17] M. G. Evans and M. Polanyi. Inertia and driving force of chemical reactions. *Transactions of the Faraday Society*, 34(0):11–24, 1938. doi: 10.1039/TF9383400011.

[18] H. Bernhard Schlegel. Optimization of equilibrium geometries and transition structures. *Journal of Computational Chemistry*, 3(2):214–218, 1982. doi: 10.1002/jcc.540030212.

[19] J. B. Frisch, M. J.; Trucks, G. W.; Schlegel, H. B.; Scuseria, G. E.; Robb, M. A.; Cheeseman, J. R.; Scalmani, G.; Barone, V.; Petersson, G. A.; Nakatsuji, H.; Li, X.; Caricato, M.; Marenich, A. V.; Bloino, J.; Janesko, B. G.; Gomperts, R.; Mennucci, B.; Hratch. Gaussian 16, Revision A.03, 2016.

[20] Chunyang Peng and H. Bernhard Schlegel. Combining synchronous transit and quasi-Newton methods to find transition states. *Israel Journal of Chemistry*, 33(4): 449–454, 1993. doi: 10.1002/ijch.199300051.

[21] Chunyang Peng, Philippe Y Ayala, H Bernhard Schlegel, and Michael J Frisch. Using redundant internal coordinates to optimize equilibrium geometries and transition states. *Journal of Computational Chemistry*, 17(1):49–56, 1996. doi: 10.1002/(SICI)1096-987X(19960115)17:1⟨49::AID-JCC5⟩3.0.CO;2-0.

[22] Daan Frenkel and Berend Smit. *Understanding molecular simulation: from algorithms to applications*, volume 2. Elsevier, 2002.

[23] Erik Lindahl. Molecular dynamics simulations. *Methods in Molecular Biology*, 1215: 3–26, 2015. doi: 10.1007/978-1-4939-1465-4_1.

[24] Katherine A. Henzler-Wildman, Ming Lei, Vu Thai, S. Jordan Kerns, Martin Karplus, and Dorothee Kern. A hierarchy of timescales in protein dynamics is linked to enzyme catalysis. *Nature*, 450(7171):913–916, 2007. doi: 10.1038/nature06407.

[25] Benedict Leimkuhler and Charles Matthews. Rational construction of stochastic numerical methods for molecular sampling. *Applied Mathematics Research eXpress*, 2013(1):34–56, 2013. doi: 10.1093/amrx/abs010.

[26] H. Nyquist. Certain topics in telegraph transmission theory. *Transactions of the American Institute of Electrical Engineers*, 47(2):617–644, 1928. doi: 10.1109/T-AIEE.1928.5055024.

[27] Claude E. Shannon. Communication in the Presence of Noise. *Proceedings of the IRE*, 37(1):10–21, 1949. doi: 10.1109/JRPROC.1949.232969.

[28] Hans C. Andersen. Molecular dynamics simulations at constant pressure and/or temperature. *The Journal of Chemical Physics*, 72(4):2384–2393, 1980. doi: 10.1063/1.439486.

[29] Shūichi Nosé. An extension of the canonical ensemble molecular dynamics method. *Molecular Physics*, 57(1):187–191, 1986. doi: 10.1080/00268978600100141.

[30] William G. Hoover. Canonical dynamics: Equilibrium phase-space distributions. *Physical Review A*, 31(3):1695–1697, 1985. doi: 10.1103/PhysRevA.31.1695.

[31] William G. Hoover. Constant-pressure equations of motion. *Physical Review A*, 34 (3):2499–2500, 1986. doi: 10.1103/PhysRevA.34.2499.

[32] Glenn J. Martyna, Michael L. Klein, and Mark Tuckerman. Nosé–Hoover chains: The canonical ensemble via continuous dynamics. *The Journal of Chemical Physics*, 97(4):2635–2643, 1992. doi: 10.1063/1.463940.

[33] H. J.C. Berendsen, J. P.M. Postma, W. F. Van Gunsteren, A. Dinola, and J. R. Haak. Molecular dynamics with coupling to an external bath. *The Journal of Chemical Physics*, 81(8):3684–3690, 1984. doi: 10.1063/1.448118.

[34] Andreea Moga, Iuliana Marin, Nicolae Goga, Anton Hadar, Dragoi Geroge, and Kamoru Oluwatoyin. Improved OpenMM algorithms for CUDA and OpenCL using new stochastic dynamics and the Berendsen thermostat. In *6th International Conference on Computing, Communications and Networking Technologies, ICCCNT 2015*. Institute of Electrical and Electronics Engineers Inc., 2016. doi: 10.1109/ICCCNT.2015.7395220.

[35] Kim Hung Chow and David M. Ferguson. Isothermal-isobaric molecular dynamics simulations with Monte Carlo volume sampling. *Computer Physics Communications*, 91(1-3):283–289, 1995. doi: 10.1016/0010-4655(95)00059-O.

[36] Johan Åqvist, Petra Wennerström, Martin Nervall, Sinisa Bjelic, and Bjørn O. Brandsdal. Molecular dynamics simulations of water and biomolecules with a Monte Carlo constant pressure algorithm. *Chemical Physics Letters*, 384(4-6):288–294, 2004. doi: 10.1016/j.cplett.2003.12.039.

[37] S. Kirkpatrick, C. D. Gelatt, and M. P. Vecchi. Optimization by simulated annealing. *Science*, 220(4598):671–680, 1983. doi: 10.1126/science.220.4598.671.

[38] David J. Earl and Michael W. Deem. Parallel tempering: Theory, applications, and new perspectives. *Physical Chemistry Chemical Physics*, 7(23):3910, 2005. doi: 10.1039/b509983h.

[39] G. M. Torrie and J. P. Valleau. Nonphysical sampling distributions in Monte Carlo free-energy estimation: Umbrella sampling. *Journal of Computational Physics*, 23 (2):187–199, 1977. doi: 10.1016/0021-9991(77)90121-8.

[40] Alessandro Laio and Michele Parrinello. Escaping free-energy minima. *Proceedings of the National Academy of Sciences of the United States of America*, 99(20): 12562–12566, 2002. doi: 10.1073/PNAS.202427399.

[41] Christoph Dellago, Peter G. Bolhuis, Félix S. Csajka, and David Chandler. Transition path sampling and the calculation of rate constants. *Journal of Chemical Physics*, 108(5):1964–1977, 1998. doi: 10.1063/1.475562.

[42] Peter G. Bolhuis, David Chandler, Christoph Dellago, and Phillip L. Geissler. Transition path sampling: Throwing ropes over rough mountain passes, in the dark. *Annual Review of Physical Chemistry*, 53:291–318, 2002. doi: 10.1146/annurev.physchem.53.082301.113146.

[43] Alessandro Barducci, Giovanni Bussi, and Michele Parrinello. Well-tempered metadynamics: A smoothly converging and tunable free-energy method. *Physical Review Letters*, 100(2), 2008. doi: 10.1103/PhysRevLett.100.020603.

[44] Paolo Raiteri, Alessandro Laio, Francesco Luigi Gervasio, Cristian Micheletti, and Michele Parrinello. Efficient reconstruction of complex free energy landscapes by multiple walkers metadynamics. *Journal of Physical Chemistry B*, 110(8):3533–3539, 2006. doi: 10.1021/jp054359r.

[45] Cameron Abrams and Giovanni Bussi. Enhanced sampling in molecular dynamics using metadynamics, replica-exchange, and temperature-acceleration. *Entropy*, 16 (1):163–199, 2014. doi: 10.3390/e16010163.

[46] Fabio Pietrucci. Strategies for the exploration of free energy landscapes: Unity in diversity and challenges ahead. *Reviews in Physics*, 2:32–45, 2017. doi: 10.1016/j.revip.2017.05.001.

[47] Pratyush Tiwary and Axel van de Walle. A review of enhanced sampling approaches for accelerated molecular dynamics. In *Springer Series in Materials Science*, volume 245, pages 195–221. Springer, Cham, 2016. doi: 10.1007/978-3-319-33480-6_6.

[48] Yi Isaac Yang, Qiang Shao, Jun Zhang, Lijiang Yang, and Yi Qin Gao. Enhanced sampling in molecular dynamics. *The Journal of Chemical Physics*, 151(7):070902, 2019. doi: 10.1063/1.5109531.

[49] Shankar Kumar, John M. Rosenberg, Djamal Bouzida, Robert H. Swendsen, and Peter A. Kollman. The weighted histogram analysis method for free-energy calculations on biomolecules. I. The method. *Journal of Computational Chemistry*, 13(8):1011–1021, 1992. doi: 10.1002/jcc.540130812.

[50] Tomáš Bučko, Siwar Chibani, Jean François Paul, Laurent Cantrel, and Michael Badawi. Dissociative iodomethane adsorption on Ag-MOR and the formation of AgI clusters: An ab initio molecular dynamics study. *Physical Chemistry Chemical Physics*, 19(40):27530–27543, 2017. doi: 10.1039/c7cp05562e.

[51] Peter Hänggi, Peter Talkner, and Michal Borkovec. Reaction-rate theory: Fifty years after Kramers. *Reviews of Modern Physics*, 62(2):251–341, 1990. doi: 10.1103/RevModPhys.62.251.

[52] C H Bennett. Algorithms for chemical computations. In *ACS symposium Series*, volume 46, pages 63–97. Am. Chem. Soc Washington, 1977.

[53] David Chandler. Statistical mechanics of isomerization dynamics in liquids and the transition state approximation. *The Journal of Chemical Physics*, 68(6):2959–2970, 1978. doi: 10.1063/1.436049.

[54] Louis Vanduyfhuys. ThermoLIB, 2022.

[55] Simon Bailleul, Karen Dedecker, Pieter Cnudde, Louis Vanduyfhuys, Michel Waroquier, and Veronique Van Speybroeck. Ab initio enhanced sampling kinetic study on MTO ethene methylation reaction. *Journal of Catalysis*, 388:38–51, 2020. doi: 10.1016/j.jcat.2020.04.015.

[56] Riccardo Baron, Daniel Trzesniak, Alex H. De Vries, Andreas Elsener, Siewert J. Marrink, and Wilfred F. Van Gunsteren. Comparison of thermodynamic properties of coarse-grained and atomic-level simulation models. *ChemPhysChem*, 8(3):452–461, 2007. doi: 10.1002/cphc.200600658.

[57] Christopher J Cramer. *Essentials of computational chemistry: theories and models*. John Wiley & Sons, 2013.

[58] D. R. Hartree. The Wave Mechanics of an Atom with a Non-Coulomb Central Field Part I Theory and Methods. *Mathematical Proceedings of the Cambridge Philosophical Society*, 24(1):89–110, 1928. doi: 10.1017/S0305004100011919.

[59] V. Fock. Näherungsmethode zur Lösung des quantenmechanischen Mehrkörperproblems. *Zeitschrift für Physik*, 61(1-2):126–148, 1930. doi: 10.1007/BF01340294.

[60] J. C. Slater. Note on Hartree's Method. *Physical Review*, 35(2):210–211, 1930. doi: 10.1103/PhysRev.35.210.2.

[61] J. E. Lennard-Jones. The electronic structure of some diatomic molecules. *Transactions of the Faraday Society*, 25(0):668–686, 1929. doi: 10.1039/tf9292500668.

[62] S. F. Boys. Electronic wave functions - I. A general method of calculation for the stationary states of any molecular system. *Proceedings of the Royal Society of London. Series A. Mathematical and Physical Sciences*, 200(1063):542–554, 1950. doi: 10.1098/rspa.1950.0036.

[63] Chr. Møller and M. S. Plesset. Note on an approximation treatment for many-electron systems. *Physical Review*, 46(7):618–622, 1934. doi: 10.1103/PhysRev.46.618.

[64] Robert G. Parr and Yang Weitao. *Density-Functional Theory of Atoms and Molecules*. Oxford University Press, 1995. doi: 10.1093/oso/9780195092769.001.0001.

[65] Richard M. Martin. *Electronic Structure*. Cambridge University Press, 2004. doi: 10.1017/CBO9780511805769.

[66] P. Hohenberg and W. Kohn. Inhomogeneous Electron Gas. *Physical Review*, 136 (3B):B864–B871, 1964. doi: 10.1103/PhysRev.136.B864.

[67] W. Kohn and L. J. Sham. Self-consistent equations including exchange and correlation effects. *Physical Review*, 140(4A):A1133–A1138, 1965. doi: 10.1103/PhysRev.140.A1133.

[68] Lars Goerigk and Nisha Mehta. A trip to the density functional theory zoo: Warnings and recommendations for the user. *Australian Journal of Chemistry*, 72(8):563, 2019. doi: 10.1071/CH19023.

[69] A. D. Becke. Density-functional exchange-energy approximation with correct asymptotic behavior. *Physical Review A*, 38(6):3098–3100, 1988. doi: 10.1103/PhysRevA.38.3098.

[70] Chengteh Lee, Weitao Yang, and Robert G. Parr. Development of the Colle-Salvetti correlation-energy formula into a functional of the electron density. *Physical Review B*, 37(2):785–789, 1988. doi: 10.1103/PhysRevB.37.785.

[71] John P. Perdew. Jacob's ladder of density functional approximations for the exchange-correlation energy. In *AIP Conference Proceedings*, volume 577, pages 1–20. AIP, 2001. doi: 10.1063/1.1390175.

[72] P. J. Stephens, F. J. Devlin, C. F. Chabalowski, and M. J. Frisch. Ab Initio calculation of vibrational absorption and circular dichroism spectra using density functional force fields. *Journal of Physical Chemistry*, 98(45):11623–11627, 1994. doi: 10.1021/j100096a001.

[73] Axel D. Becke and Axel D. Density-functional thermochemistry. III. The role of exact exchange. *The Journal of Chemical Physics*, 98(7):5648–5652, 1993. doi: 10.1063/1.464913.

[74] Jeng Da Chai and Martin Head-Gordon. Systematic optimization of long-range corrected hybrid density functionals. *Journal of Chemical Physics*, 128(8):084106, 2008. doi: 10.1063/1.2834918.

[75] Amy Austin, George A. Petersson, Michael J. Frisch, Frank J. Dobek, Giovanni Scalmani, and Kyle Throssell. A density functional with spherical atom dispersion terms. In *Journal of Chemical Theory and Computation*, volume 8, pages 4989–5007. American Chemical Society, 2012. doi: 10.1021/ct300778e.

[76] Stefan Grimme, Jens Antony, Stephan Ehrlich, and Helge Krieg. A consistent and accurate ab initio parametrization of density functional dispersion correction (DFT-D) for the 94 elements H-Pu. *The Journal of Chemical Physics*, 132(15):154104, 2010. doi: 10.1063/1.3382344.

[77] Jeng-Da Chai and Martin Head-Gordon. Long-range corrected hybrid density functionals with damped atom–atom dispersion corrections. *Physical Chemistry Chemical Physics*, 10(44):6615, 2008. doi: 10.1039/b810189b.

[78] Narbe Mardirossian and Martin Head-Gordon. Thirty years of density functional theory in computational chemistry: An overview and extensive assessment of 200 density functionals, 2017.

[79] Michael J.S. Dewar, Eve G. Zoebisch, Eamonn F. Healy, and James J.P. Stewart. AM1: A new general purpose quantum mechanical molecular model 1. *Journal of the American Chemical Society*, 107(13):3902–3909, 1985. doi: 10.1021/ja00299a024.

[80] James J.P. Stewart. Optimization of parameters for semiempirical methods II. Applications. *Journal of Computational Chemistry*, 10(2):221–264, 1989. doi: 10.1002/jcc.540100209.

[81] James J.P. Stewart. Optimization of parameters for semiempirical methods I. Method. *Journal of Computational Chemistry*, 10(2):209–220, 1989. doi: 10.1002/jcc.540100208.

[82] James J.P. Stewart. Optimization of parameters for semiempirical methods V: Modification of NDDO approximations and application to 70 elements. *Journal of Molecular Modeling*, 13(12):1173–1213, 2007. doi: 10.1007/s00894-007-0233-4.

[83] James J.P. Stewart. Optimization of parameters for semiempirical methods VI: More modifications to the NDDO approximations and re-optimization of parameters. *Journal of Molecular Modeling*, 19(1):1–32, 2013. doi: 10.1007/s00894-012-1667-x.

[84] Louis Vanduyfhuys, Steven Vandenbrande, Toon Verstraelen, Rochus Schmid, Michel Waroquier, and Veronique Van Speybroeck. QuickFF: A program for a quick and easy derivation of force fields for metal-organic frameworks from ab initio input. *Journal of Computational Chemistry*, 36(13):1015–1027, 2015. doi: 10.1002/jcc.23877.

[85] Louis Vanduyfhuys, Steven Vandenbrande, Jelle Wieme, Michel Waroquier, Toon Verstraelen, and Veronique Van Speybroeck. Extension of the QuickFF force field protocol for an improved accuracy of structural, vibrational, mechanical and thermal properties of metal–organic frameworks. *Journal of Computational Chemistry*, 39 (16):999–1011, 2018. doi: 10.1002/jcc.25173.

[86] Junmei Wang, Romain M. Wolf, James W. Caldwell, Peter A. Kollman, and David A. Case. Development and testing of a general Amber force field. *Journal of Computational Chemistry*, 25(9):1157–1174, 2004. doi: 10.1002/jcc.20035.

[87] Xibing He, Viet H. Man, Wei Yang, Tai Sung Lee, and Junmei Wang. A fast and high-quality charge model for the next generation general AMBER force field. *Journal of Chemical Physics*, 153(11):114502, 2020. doi: 10.1063/5.0019056.

[88] David L. Mobley, Caitlin C. Bannan, Andrea Rizzi, Christopher I. Bayly, John D. Chodera, Victoria T. Lim, Nathan M. Lim, Kyle A. Beauchamp, David R. Slochower, Michael R. Shirts, Michael K. Gilson, and Peter K. Eastman. Escaping atom types in force fields using direct chemical perception. *Journal of Chemical Theory and Computation*, 14(11):6076–6092, 2018. doi: 10.1021/acs.jctc.8b00640.

[89] James A. Maier, Carmenza Martinez, Koushik Kasavajhala, Lauren Wickstrom, Kevin E. Hauser, and Carlos Simmerling. ff14SB: Improving the accuracy of protein side chain and backbone parameters from ff99SB. *Journal of Chemical Theory and Computation*, 11(8):3696–3713, 2015. doi: 10.1021/acs.jctc.5b00255.

[90] Robert B. Best, Xiao Zhu, Jihyun Shim, Pedro E.M. Lopes, Jeetain Mittal, Michael Feig, and Alexander D. MacKerell. Optimization of the additive CHARMM all-atom protein force field targeting improved sampling of the backbone ϕ, ψ and side-chain χ1 and χ2 Dihedral Angles. *Journal of Chemical Theory and Computation*, 8(9): 3257–3273, 2012. doi: 10.1021/ct300400x.

[91] Lee Ping Wang, Todd J Martinez, and Vijay S Pande. Building force fields: An automatic, systematic, and reproducible approach. *Journal of Physical Chemistry Letters*, 5(11):1885–1891, 2014. doi: 10.1021/jz500737m.

[92] Thomas P Senftle, Sungwook Hong, Md Mahbubul Islam, Sudhir B Kylasa, Yuanxia Zheng, Yun Kyung Shin, Chad Junkermeier, Roman Engel-Herbert, Michael J Janik, Hasan Metin Aktulga, Toon Verstraelen, Ananth Grama, and Adri C T van Duin. The ReaxFF reactive force-field: development, applications and future directions. *npj Computational Materials*, 2(1):15011, 2016. doi: 10.1038/npjcompumats.2015.11.

[93] Lung Wa Chung, W. M. C. Sameera, Romain Ramozzi, Alister J. Page, Miho Hatanaka, Galina P. Petrova, Travis V. Harris, Xin Li, Zhuofeng Ke, Fengyi Liu, Hai-Bei Li, Lina Ding, and Keiji Morokuma. The ONIOM method and its applications. *Chemical Reviews*, 115(12):5678–5796, 2015. doi: 10.1021/cr5004419.

[94] Dean J. Tantillo. *Applied theoretical organic chemistry*. World Scientific Publishing Co. Pte. Ltd., 2018. doi: 10.1142/q0119.

[95] Jacopo Tomasi, Benedetta Mennucci, and Roberto Cammi. Quantum mechanical continuum solvation models. *Chemical Reviews*, 105(8):2999–3094, 2005. doi: 10.1021/cr9904009.

[96] Jin Zhang, Haiyang Zhang, Tao Wu, Qi Wang, and David Van Der Spoel. Comparison of implicit and explicit solvent models for the calculation of solvation free energy in organic solvents. *Journal of Chemical Theory and Computation*, 13 (3):1034–1043, 2017. doi: 10.1021/acs.jctc.7b00169.

[97] Jithin John Varghese and Samir H. Mushrif. Origins of complex solvent effects on chemical reactivity and computational tools to investigate them: A review, 2019.

[98] Benedetta Mennucci and Roberto Cammi. *Continuum Solvation Models in Chemical Physics*. John Wiley & Sons, Ltd, Chichester, UK, 2007. doi: 10.1002/9780470515235.

[99] Josefredo R. Pliego and Jose M. Riveros. Hybrid discrete-continuum solvation methods. *Wiley Interdisciplinary Reviews: Computational Molecular Science*, 2019. doi: 10.1002/wcms.1440.

[100] Yasemin Basdogan, Alex M. Maldonado, and John A. Keith. Advances and challenges in modeling solvated reaction mechanisms for renewable fuels and chemicals. *Wiley Interdisciplinary Reviews: Computational Molecular Science*, 10 (2):e1446, 2020. doi: 10.1002/wcms.1446.

[101] Ramu Anandakrishnan, Aleksander Drozdetski, Ross C. Walker, and Alexey V. Onufriev. Speed of conformational change: Comparing explicit and implicit solvent molecular dynamics simulations. *Biophysical Journal*, 108(5):1153–1164, 2015. doi: 10.1016/j.bpj.2014.12.047.

[102] Sumit Sharma, Pramod Kumar, and Rakesh Chandra. Introduction to molecular dynamics. In *Molecular Dynamics Simulation of Nanocomposites using BIOVIA Materials Studio, Lammps and Gromacs*, pages 1–38. Elsevier, 2019. doi: 10.1016/B978-0-12-816954-4.00001-2.

[103] Roy Dennington, Todd A Keith, and John M Millam. GaussView Version 6, 2019.

[104] Michael E. Fortunato and Coray M. Colina. pysimm: A python package for simulation of molecular systems. *SoftwareX*, 6:7–12, 2017. doi: 10.1016/j.softx.2016.12.002.

[105] Jeff Wagner, David L. Mobley, Matt Thompson, John Chodera, Caitlin Bannan, Andrea Rizzi, Trevorgokey, David Dotson, Jaime Rodríguez-Guerra, Camila, Pavan Behara, Christopher Bayly, Josh A. Mitchell, JoshHorton, Nathan M. Lim, Victoria Lim, Sukanya Sasmal, Lily Wang, Andrew Dalke, SimonBoothroyd, Iván Pulido,

Daniel Smith, Lee-Ping Wang, and Yutong Zhao. openforcefield/openff-toolkit: 0.10.0 Improvements for force field fitting. 2021. doi: 10.5281/ZENODO.5153946.

[106] Peter Eastman, Jason Swails, John D Chodera, Robert T. McGibbon, Yutong Zhao, Kyle A Beauchamp, Lee Ping Wang, Andrew C Simmonett, Matthew P Harrigan, Chaya D Stern, Rafal P Wiewiora, Bernard R Brooks, and Vijay S Pande. OpenMM 7: Rapid development of high performance algorithms for molecular dynamics. *PLoS Computational Biology*, 13(7), 2017. doi: 10.1371/journal.pcbi.1005659.

[107] Thomas D. Kühne, Marcella Iannuzzi, Mauro Del Ben, Vladimir V. Rybkin, Patrick Seewald, Frederick Stein, Teodoro Laino, Rustam Z. Khaliullin, Ole Schütt, Florian Schiffmann, Dorothea Golze, Jan Wilhelm, Sergey Chulkov, Mohammad Hossein Bani-Hashemian, Valéry Weber, Urban Borštnik, Mathieu Taillefumier, Alice Shoshana Jakobovits, Alfio Lazzaro, Hans Pabst, Tiziano Müller, Robert Schade, Manuel Guidon, Samuel Andermatt, Nico Holmberg, Gregory K. Schenter, Anna Hehn, Augustin Bussy, Fabian Belleflamme, Gloria Tabacchi, Andreas Glöß, Michael Lass, Iain Bethune, Christopher J. Mundy, Christian Plessl, Matt Watkins, Joost VandeVondele, Matthias Krack, and Jürg Hutter. CP2K: An electronic structure and molecular dynamics software package -Quickstep: Efficient and accurate electronic structure calculations, 2020.

[108] Gareth A. Tribello, Massimiliano Bonomi, Davide Branduardi, Carlo Camilloni, and Giovanni Bussi. PLUMED 2: New feathers for an old bird. *Computer Physics Communications*, 185(2):604–613, 2014. doi: 10.1016/j.cpc.2013.09.018.

[109] Toon Verstraelen, Louis Vanduyfhuys, S. Vandenbrande, and S.M.J. Rogge. Yaff, yet another force field, http://molmod.ugent.be/software/, 2022.

[110] Robert T. McGibbon, Kyle A. Beauchamp, Matthew P. Harrigan, Christoph Klein, Jason M. Swails, Carlos X. Hernández, Christian R. Schwantes, Lee Ping Wang, Thomas J. Lane, and Vijay S. Pande. MDTraj: A modern open library for the analysis of molecular dynamics trajectories. *Biophysical Journal*, 109(8):1528–1532, 2015. doi: 10.1016/j.bpj.2015.08.015.

[111] Richard Gowers, Max Linke, Jonathan Barnoud, Tyler Reddy, Manuel Melo, Sean Seyler, Jan Domański, David Dotson, Sébastien Buchoux, Ian Kenney, and Oliver Beckstein. MDAnalysis: A python package for the rapid analysis of molecular dynamics simulations. In *Proceedings of the 15th Python in Science Conference*, pages 98–105. SciPy, 2016. doi: 10.25080/majora-629e541a-00e.

[112] Julia Contreras-García, Erin R. Johnson, Shahar Keinan, Robin Chaudret, Jean-Philip Piquemal, David N. Beratan, and Weitao Yang. NCIPLOT: A program for plotting noncovalent interaction regions. *Journal of Chemical Theory and Computation*, 7(3):625–632, 2011. doi: 10.1021/ct100641a.

[113] William Humphrey, Andrew Dalke, and Klaus Schulten. VMD: Visual molecular dynamics. *Journal of Molecular Graphics*, 14(1):33–38, 1996. doi: 10.1016/0263-7855(96)00018-5.

[114] C.Y. Legault. CYLview Visualization Software, 2020.

[115] Timothy P. Lodge and Paul C. Hiemenz. Polymer Chemistry. page 676, 2020. doi: 10.1201/9780429190810.

[116] Jr. Charles E. Carraher. *Introduction Polymer Chemistry*. 2017.

[117] Robert J. Young and Peter A. Lovell. *Introduction to Polymers*. CRC Press, 2011. doi: 10.1201/9781439894156.

[118] NobelPrize.org. The Nobel Prize in Chemistry 1953, 2022.

[119] NobelPrize.org. The Nobel Prize in Chemistry 1974, 2022.

[120] Frank L. McCrackin. Configuration of isolated polymer molecules adsorbed on solid surfaces studied by Monte-Carlo computer simulation. *The Journal of Chemical Physics*, 47(6):1980–1986, 1967. doi: 10.1063/1.1712225.

[121] Thomas E Gartner and Arthi Jayaraman. Modeling and simulations of polymers: A roadmap, 2019.

[122] Benjamin B. Noble and Michelle L. Coote. First principles modelling of free-radical polymerisation kinetics, 2013.

[123] Doros N. Theodorou. Hierarchical modelling of polymeric materials, 2007.

[124] Pragati Sharma, Sudip Roy, and Hossein Ali Karimi-Varzaneh. Validation of force fields of rubber through glass-transition temperature calculation by microsecond atomic-scale molecular dynamics simulation. *Journal of Physical Chemistry B*, 120 (7):1367–1379, 2016. doi: 10.1021/acs.jpcb.5b10789.

[125] George Odian and Francis Group. *Principles of Polymerization, 4th Edition*. 2004.

[126] Durairaj Baskaran and Axel H.E. Müller. Anionic vinyl polymerization-50 years after Michael Szwarc, 2007.

[127] Eric J. Goethals and Filip Du Prez. Carbocationic polymerizations, 2007.

[128] Matyjaszewski Krzysztof and Jianhui Xia. Atom transfer radical polymerization. *Chemical Reviews*, 101(9):2921–2990, 2001. doi: 10.1021/CR940534G.

[129] Craig J. Hawker, Anton W. Bosman, and Eva Harth. New polymer synthesis by nitroxide mediated living radical polymerizations. *Chemical Reviews*, 101(12):3661–3688, 2001. doi: 10.1021/CR990119U.

[130] Julien Nicolas, Yohann Guillaneuf, Catherine Lefay, Denis Bertin, Didier Gigmes, and Bernadette Charleux. Nitroxide-mediated polymerization. *Progress in Polymer Science*, 38(1):63–235, 2013. doi: 10.1016/j.progpolymsci.2012.06.002.

[131] Christopher. Barner-Kowollik. *Handbook of RAFT Polymerization*. 2008. doi: 10.1002/9783527622757.

[132] M. Szwarc. 'Living' polymers. *Nature*, 178(4543):1168–1169, 1956. doi: 10.1038/1781168a0.

[133] S PENCZEK, M CYPRYK, A DUDA, P KUBISA, and S SLOMKOWSKI. Living ring-opening polymerizations of heterocyclic monomers. *Progress in Polymer Science*, 32(2):247–282, 2007. doi: 10.1016/j.progpolymsci.2007.01.002.

[134] D. A. Tomalia and D. P. Sheetz. Homopolymerization of 2-alkyl- and 2-aryl-2-oxazolines. *Journal of Polymer Science Part A-1: Polymer Chemistry*, 4(9):2253–2265, 1966. doi: 10.1002/pol.1966.150040919.

[135] W. Seeliger, E. Aufderhaar, W. Diepers, R. Feinauer, R. Nehring, W. Thier, and H. Hellmann. Recent Syntheses and Reactions of Cyclic Imidic Esters. *Angewandte Chemie International Edition in English*, 5(10):875–888, 1966. doi: 10.1002/anie.196608751.

[136] T. G. Bassiri, A. Levy, and M. Litt. Polymerization of cyclic imino ethers. I. Oxazolines. *Journal of Polymer Science Part B: Polymer Letters*, 5(9):871–879, 1967. doi: 10.1002/pol.1967.110050927.

[137] Tsutomu Kagiya, Shizuo Narisawa, Taneo Maeda, and Kenichi Fukui. Ring-opening polymerization of 2-substituted 2-oxazolines. *Journal of Polymer Science Part B: Polymer Letters*, 4(7):441–445, 1966. doi: 10.1002/pol.1966.110040701.

[138] Tim A. Osswald, Erwin Baur, and Natalie Rudolph. *Plastics Handbook : The Resource for Plastics Engineers*. 2019.

[139] Lars Biermann, Esther Brepohl, Carsten Eichert, Mandy Paschetag, Marcus Watts, and Stephan Scholl. Development of a continuous PET depolymerization process as a basis for a back-to-monomer recycling method. *Green Processing and Synthesis*, 10(1):361–373, 2021. doi: 10.1515/gps-2021-0036.

[140] The Nature Conservancy. Plastic Pollution, 2022.

[141] Yu Miao, Annette von Jouanne, and Alexandre Yokochi. Current technologies in depolymerization process and the road ahead, 2021.

[142] Jonas Kühlborn, Jonathan Groß, and Till Opatz. Making natural products from renewable feedstocks: Back to the roots?, 2020.

[143] IPCC, V. Masson-Delmotte, P Zhai, A Pirani, S. L. Connors, C Péan, S Berger, N Caud, Y Chen, L Goldfarb, M. I. Gomis, M Huang, K Leitzell, E Lonnoy, J. B. R. Matthews, T. K. Maycock, T Waterfield, O Yelekçi, R Yu, and Zhou] B. Climate change 2021: The physical science basis. Contribution of working group I to the sixth assessment report of the intergovernmental panel on climate change. Technical report, International Panel for Climate Change, 2021.

[144] James H. Clark. From waste to wealth using green chemistry: The way to long term stability. *Current Opinion in Green and Sustainable Chemistry*, 8:10–13, 2017. doi: 10.1016/j.cogsc.2017.07.008.

[145] Jiří Vohlídal. Polymer degradation: a short review. *Chemistry Teacher International*, 3(2):213–220, 2021. doi: 10.1515/cti-2020-0015.

[146] K. Horie, Máximo Barón, R. B. Fox, J. He, M. Hess, J. Kahovec, T. Kitayama, P. Kubisa, E. Maréchal, W. Mormann, R. F. T. Stepto, D. Tabak, J. Vohlídal, E. S. Wilks, and W. J. Work. Definitions of terms relating to reactions of polymers and to functional polymeric materials (IUPAC Recommendations 2003). *Pure and Applied Chemistry*, 76(4):889–906, 2004. doi: 10.1351/pac200476040889.

[147] H. H. G. Jellinek. *Aspects of degradation and stabilization of polymers*. Elsevier, Amsterdam, 1978.

[148] Shahriar Shafiee and Erkan Topal. When will fossil fuel reserves be diminished? *Energy Policy*, 37(1):181–189, 2009. doi: 10.1016/j.enpol.2008.08.016.

[149] Nino Dimitrov, Ljerka Kratofil Krehula, Anita Ptiček Siročić, and Zlata Hrnjak-Murgić. Analysis of recycled PET bottles products by pyrolysis-gas chromatography. *Polymer Degradation and Stability*, 98(5):972–979, 2013. doi: 10.1016/j.polymdegradstab.2013.02.013.

[150] Jeannette M. García. Catalyst: Design Challenges for the Future of Plastics Recycling, 2016.

[151] The Ellen MacArthur Foundation. Circular Economy Introduction, 2022.

[152] Paul Anastas and Nicolas Eghbali. Green chemistry: Principles and practice. *Chemical Society Reviews*, 39(1):301–312, 2010. doi: 10.1039/b918763b.

[153] Paul T. Anastas and Julie B. Zimmerman. Peer reviewed: Design through the 12 principles of green engineering. *Environmental Science & Technology*, 37(5): 94A–101A, 2003. doi: 10.1021/es032373g.

[154] László T. Mika, Edit Cséfalvay, and Áron Németh. Catalytic conversion of carbohydrates to initial platform chemicals: Chemistry and sustainability. *Chemical Reviews*, 118(2):505–613, 2018. doi: 10.1021/acs.chemrev.7b00395.

[155] Zhuohua Sun, Bálint Fridrich, Alessandra de Santi, Saravanakumar Elangovan, and Katalin Barta. Bright side of lignin depolymerization: Toward new platform chemicals. *Chemical Reviews*, 118(2):614–678, 2018. doi: 10.1021/acs.chemrev.7b00588.

[156] W. Schutyser, T. Renders, S. Van Den Bosch, S. F. Koelewijn, G. T. Beckham, and B. F. Sels. Chemicals from lignin: An interplay of lignocellulose fractionation, depolymerisation, and upgrading, 2018.

[157] S. Van Den Bosch, W. Schutyser, S. F. Koelewijn, T. Renders, C. M. Courtin, and B. F. Sels. Tuning the lignin oil OH-content with Ru and Pd catalysts during lignin hydrogenolysis on birch wood. *Chemical Communications*, 51(67):13158–13161, 2015. doi: 10.1039/c5cc04025f.

[158] T. Renders, S. Van den Bosch, S.-F. Koelewijn, W. Schutyser, and B. F. Sels. Lignin-first biomass fractionation: the advent of active stabilisation strategies. *Energy & Environmental Science*, 10(7):1551–1557, 2017. doi: 10.1039/C7EE01298E.

[159] Yuhe Liao, Steven Friso Koelewijn, Gil van den Bossche, Joost van Aelst, Sander van den Bosch, Tom Renders, Kranti Navare, Thomas Nicolaï, Korneel van Aelst, Maarten Maesen, Hironori Matsushima, Johan M. Thevelein, Karel van Acker, Bert Lagrain, Danny Verboekend, and Bert F. Sels. A sustainable wood biorefinery for low-carbon footprint chemicals production. *Science*, 367(6484):1385–1390, 2020. doi: 10.1126/science.aau1567.

[160] Mahdi M. Abu-Omar, Katalin Barta, Gregg T. Beckham, Jeremy S. Luterbacher, John Ralph, Roberto Rinaldi, Yuriy Román-Leshkov, Joseph S. M. Samec, Bert F. Sels, and Feng Wang. Guidelines for performing lignin-first biorefining. *Energy & Environmental Science*, 14(1):262–292, 2021. doi: 10.1039/D0EE02870C.

[161] Andrew W. Bartling, Michael L. Stone, Rebecca J. Hanes, Arpit Bhatt, Yimin Zhang, Mary J. Biddy, Ryan Davis, Jacob S. Kruger, Nicholas E. Thornburg, Jeremy S. Luterbacher, Roberto Rinaldi, Joseph S.M. Samec, Bert F. Sels, Yuriy Román-Leshkov, and Gregg T. Beckham. Techno-economic analysis and life cycle assessment of a biorefinery utilizing reductive catalytic fractionation. *Energy and Environmental Science*, 14(8):4147–4168, 2021. doi: 10.1039/d1ee01642c.

[162] Roger A. Sheldon. Biocatalysis and biomass conversion: Enabling a circular economy: Biocatalysis and Biomass Conversion. In *Philosophical Transactions of the Royal Society A: Mathematical, Physical and Engineering Sciences*, volume 378. Royal Society Publishing, 2020. doi: 10.1098/rsta.2019.0274.

[163] Daniel A. Mazmanian, John Jurewitz, and Hal T. Nelson. A governing framework for climate change adaptation in the built environment. *Ecology and Society*, 18 (4), 2013. doi: 10.5751/ES-05976-180456.

[164] Maxim V. Galkin and Joseph S.M. Samec. Lignin Valorization through Catalytic Lignocellulose Fractionation: A Fundamental Platform for the Future Biorefinery, 2016.

[165] Roberto Rinaldi, Robin Jastrzebski, Matthew T. Clough, John Ralph, Marco Kennema, Pieter C. A. Bruijnincx, and Bert M. Weckhuysen. Paving the way for lignin valorisation: Recent advances in bioengineering, biorefining and catalysis. *Angewandte Chemie International Edition*, 55(29):8164–8215, 2016. doi: 10.1002/anie.201510351.

[166] Ruben Vanholme, Brecht Demedts, Kris Morreel, John Ralph, and Wout Boerjan. Lignin biosynthesis and structure. *Plant Physiology*, 153(3):895–905, 2010. doi: 10.1104/pp.110.155119.

[167] Murray W. Nabors. *Introduction to Botany*. Pearson Benjamin Cummings, 2004.

[168] Chonlong Chio, Mohini Sain, and Wensheng Qin. Lignin utilization: A review of lignin depolymerization from various aspects. *Renewable and Sustainable Energy Reviews*, 107:232–249, 2019. doi: 10.1016/j.rser.2019.03.008.

[169] Fumiko Yaku, Ryutaro Tanaka, and Tetsuo Koshijima. Lignin-Kohlenhydrat-Komplex. Teil IV. Lignin als Seitenkette der Kohlenhydrate im Björkman LCC. *Holzforschung*, 35(4):177–181, 1981. doi: 10.1515/hfsg.1981.35.4.177.

[170] S. Van den Bosch, S.-F. Koelewijn, T. Renders, G. Van den Bossche, T. Vangeel, W. Schutyser, and B. F. Sels. Catalytic strategies towards lignin-derived chemicals. *Topics in Current Chemistry*, 376(5):36, 2018. doi: 10.1007/s41061-018-0214-3.

[171] Jeong Myeong Ha, Kyung Ran Hwang, Young Min Kim, Jungho Jae, Kwang Ho Kim, Hyung Won Lee, Jae Young Kim, and Young Kwon Park. Recent progress in the thermal and catalytic conversion of lignin. *Renewable and Sustainable Energy Reviews*, 111:422–441, 2019. doi: 10.1016/j.rser.2019.05.034.

[172] Micaela Graglia, Narasimharao Kanna, and Davide Esposito. Lignin refinery: towards the preparation of renewable aromatic building blocks. *ChemBioEng Reviews*, 2(6):377–392, 2015. doi: 10.1002/cben.201500019.

[173] Xudong Liu, Florent P. Bouxin, Jiajun Fan, Vitaliy L. Budarin, Changwei Hu, and James H. Clark. Recent advances in the catalytic depolymerization of lignin towards phenolic chemicals: A review. *ChemSusChem*, 13(17):4296–4317, 2020. doi: 10.1002/cssc.202001213.

[174] Roger A. Sheldon. Green and sustainable manufacture of chemicals from biomass: State of the art, 2014.

[175] Ning Yan, Chen Zhao, Paul J. Dyson, Chen Wang, Ling Tao Liu, and Yuan Kou. Selective degradation of wood lignin over noble-metal catalysts in a two-step process. *ChemSusChem*, 1(7):626–629, 2008. doi: 10.1002/cssc.200800080.

[176] Qi Song, Feng Wang, Jiaying Cai, Yehong Wang, Junjie Zhang, Weiqiang Yu, and Jie Xu. Lignin depolymerization (LDP) in alcohol over nickel-based catalysts via a fragmentation-hydrogenolysis process. *Energy and Environmental Science*, 6(3): 994–1007, 2013. doi: 10.1039/c2ee23741e.

[177] Paola Ferrini and Roberto Rinaldi. Catalytic biorefining of plant biomass to non-pyrolytic lignin bio-oil and carbohydrates through hydrogen transfer reactions. *Angewandte Chemie - International Edition*, 53(33):8634–8639, 2014. doi: 10.1002/anie.201403747.

[178] Maxim V. Galkin and Joseph S. M. Samec. Selective Route to 2-Propenyl Aryls Directly from Wood by a Tandem Organosolv and Palladium-Catalysed Transfer Hydrogenolysis. *ChemSusChem*, 7(8):2154–2158, 2014. doi: 10.1002/cssc.201402017.

[179] Trenton Parsell, Sara Yohe, John Degenstein, Tiffany Jarrell, Ian Klein, Emre Gencer, Barron Hewetson, Matt Hurt, Jeong Im Kim, Harshavardhan Choudhari, Basudeb Saha, Richard Meilan, Nathan Mosier, Fabio Ribeiro, W. Nicholas Delgass, Clint Chapple, Hilkka I. Kenttämaa, Rakesh Agrawal, and Mahdi M. Abu-Omar. A synergistic biorefinery based on catalytic conversion of lignin prior to cellulose starting from lignocellulosic biomass. *Green Chemistry*, 17(3):1492–1499, 2015. doi: 10.1039/c4gc01911c.

[180] S. Van Den Bosch, W. Schutyser, R. Vanholme, T. Driessen, S. F. Koelewijn, T. Renders, B. De Meester, W. J.J. Huijgen, W. Dehaen, C. M. Courtin, B. Lagrain, W. Boerjan, and B. F. Sels. Reductive lignocellulose fractionation into soluble lignin-derived phenolic monomers and dimers and processable carbohydrate pulps. *Energy and Environmental Science*, 8(6):1748–1763, 2015. doi: 10.1039/c5ee00204d.

[181] Tom Renders, Sander Van den Bosch, Thijs Vangeel, Thijs Ennaert, Steven-Friso Koelewijn, Gil Van den Bossche, Christophe M. Courtin, Wouter Schutyser, and Bert F. Sels. Synergetic effects of alcohol/water mixing on the catalytic reductive fractionation of poplar wood. *ACS Sustainable Chemistry & Engineering*, 4(12): 6894–6904, 2016. doi: 10.1021/acssuschemeng.6b01844.

[182] Fabiana Siragusa, Elias Van Den Broeck, Connie Ocando, Alejandro J. Müller, Gilles De Smet, Bert U W Maes, Julien De Winter, Veronique Van Speybroeck, Bruno Grignard, and Christophe Detrembleur. Access to biorenewable and CO2-based polycarbonates from exovinylene cyclic carbonates. *ACS Sustainable Chemistry & Engineering*, 9(4):1714–1728, 2021. doi: 10.1021/acssuschemeng.0c07683.

[183] W. Schutyser, S. Van den Bosch, T. Renders, T. De Boe, S.-F. Koelewijn, A. Dewaele, T. Ennaert, O. Verkinderen, B. Goderis, C. M. Courtin, and B. F. Sels. Influence of bio-based solvents on the catalytic reductive fractionation of birch wood. *Green Chemistry*, 17(11):5035–5045, 2015. doi: 10.1039/C5GC01442E.

[184] J Dijkmans, W Schutyser, M Dusselier, and B F Sels. Snβ-zeolite catalyzed oxido-reduction cascade chemistry with biomass-derived molecules. *Chemical Communications*, 52(40):6712–6715, 2016. doi: 10.1039/c6cc00199h.

[185] Maxence Fache, Camille Montérémal, Bernard Boutevin, and Sylvain Caillol. Amine hardeners and epoxy cross-linker from aromatic renewable resources. *European Polymer Journal*, 73:344–362, 2015. doi: 10.1016/j.eurpolymj.2015.10.032.

[186] Maxence Fache, Emilie Darroman, Vincent Besse, Rémi Auvergne, Sylvain Caillol, and Bernard Boutevin. Vanillin, a promising biobased building-block for monomer synthesis. *Green Chemistry*, 16(4):1987–1998, 2014. doi: 10.1039/c3gc42613k.

[187] Joseph F. Stanzione, Joshua M. Sadler, John J. La Scala, Kaleigh H. Reno, and Richard P. Wool. Vanillin-based resin for use in composite applications. *Green Chemistry*, 14(8):2346–2352, 2012. doi: 10.1039/c2gc35672d.

[188] Hajime Nakajima, Peter Dijkstra, and Katja Loos. The recent developments in biobased polymers toward general and engineering applications: Polymers that are upgraded from biodegradable polymers, analogous to petroleum-derived polymers, and newly developed. *Polymers*, 9(12):523, 2017. doi: 10.3390/polym9100523.

[189] Song Song, Jiaguang Zhang, Gökalp Gözaydın, and Ning Yan. Production of terephthalic acid from corn stover lignin. *Angewandte Chemie International Edition*, 58(15):4934–4937, 2019. doi: 10.1002/anie.201814284.

[190] Shou Zhao and Mahdi M. Abu-Omar. Renewable thermoplastics based on lignin-derived polyphenols. *Macromolecules*, 50(9):3573–3581, 2017. doi: 10.1021/acs.macromol.7b00064.

[191] Roland Geyer, Jenna R. Jambeck, and Kara Lavender Law. Production, use, and fate of all plastics ever made. *Science Advances*, 3(7):e1700782, 2017. doi: 10.1126/sciadv.1700782.

[192] Jeroen Bomon, Elias Van Den Broeck, Mathias Bal, Yuhe Liao, Sergey Sergeyev, Veronique Van Speybroeck, Bert F. Sels, and Bert U. W. Maes. Brønsted acid catalyzed tandem defunctionalization of biorenewable ferulic acid and derivates into bio-catechol. *Angewandte Chemie International Edition*, 59(8):3063–3068, 2020. doi: 10.1002/anie.201913023.

[193] Helmut Fiege, Heinz-Werner Voges, Toshikazu Hamamoto, Sumio Umemura, Tadao Iwata, Hisaya Miki, Yasuhiro Fujita, Hans-Josef Buysch, Dorothea Garbe, and Wilfried Paulus. Phenol Derivatives. In *Ullmann's Encyclopedia of Industrial Chemistry*. Wiley-VCH Verlag GmbH & Co. KGaA, Weinheim, Germany, 2000. doi: 10.1002/14356007.a19_313.

[194] Jeroen Bomon, Mathias Bal, Tapas Kumar Achar, Sergey Sergeyev, Xian Wu, Ben Wambacq, Filip Lemière, Bert F. Sels, and Bert U. W. Maes. Efficient

demethylation of aromatic methyl ethers with HCl in water. *Green Chemistry*, 23(5):1995–2009, 2021. doi: 10.1039/d0gc04268d.

[195] Xiaoyu Wu, Jie Fu, and Xiuyang Lu. Kinetics and mechanism of hydrothermal decomposition of lignin model compounds, 2013.

[196] Le Yang, Wei Zhou, K. Seshan, and Yongdan Li. Green and efficient synthesis route of catechol from guaiacol. *Journal of Molecular Catalysis A: Chemical*, 368-369: 61–65, 2013. doi: 10.1016/j.molcata.2012.11.024.

[197] Zheng Li, Eka Sutandar, Thomas Goihl, Xiao Zhang, and Xuejun Pan. Cleavage of ethers and demethylation of lignin in acidic concentrated lithium bromide (ACLB) solution. *Green Chemistry*, 22(22):7989–8001, 2020. doi: 10.1039/d0gc02581j.

[198] A. Pérez de Alba Ortíz, A. Tiwari, R. C. Puthenkalathil, and B. Ensing. Advances in enhanced sampling along adaptive paths of collective variables. *The Journal of Chemical Physics*, 149(7):072320, 2018. doi: 10.1063/1.5027392.

[199] Lars Melander. Isotope effects in proton-transfer reactions. *ACTA CHEMICA SCANDINAVICA*, 25(10):3821–3826, 1971.

[200] J. Bigeleisen. Correlation of kinetic isotope effects with chemical bonding in three-centre reactions. *Pure and Applied Chemistry*, 8(3-4):217–224, 1964. doi: 10.1351/pac196408030217.

[201] A. J. Kresge and D. P. Onwood. The secondary isotope effect on proton transfer from the hydronium ion in aqueous solution. *Journal of the American Chemical Society*, 86(22):5014–5016, 1964. doi: 10.1021/ja01076a063.

[202] Arthur J Ragauskas, Gregg T Beckham, Mary J Biddy, Richard Chandra, Fang Chen, Mark F Davis, Brian H Davison, Richard A Dixon, Paul Gilna, Martin Keller, Paul Langan, Amit K Naskar, Jack N Saddler, Timothy J Tschaplinski, Gerald A Tuskan, and Charles E Wyman. Lignin valorization: Improving lignin processing in the biorefinery. *Science*, 344(6185), 2014. doi: 10.1126/science.1246843.

[203] Jessica J. Cash, Matthew C. Davis, Michael D. Ford, Thomas J. Groshens, Andrew J. Guenthner, Benjamin G. Harvey, Kevin R. Lamison, Joseph M. Mabry, Heather A. Meylemans, Josiah T. Reams, and Christopher M. Sahagun. High Tg thermosetting resins from resveratrol. *Polymer Chemistry*, 4(13):3859–3865, 2013. doi: 10.1039/c3py00438d.

[204] Benjamin G. Harvey, Andrew J. Guenthner, Heather A. Meylemans, Shannon R.L. Haines, Kevin R. Lamison, Thomas J. Groshens, Lee R. Cambrea, Matthew C. Davis, and William W. Lai. Renewable thermosetting resins and thermoplastics from vanillin. *Green Chemistry*, 17(2):1249–1258, 2015. doi: 10.1039/c4gc01825g.

[205] Mohamed Naceur Belgacem and Alessandro Gandini. *Monomers, Polymers and Composites from Renewable Resources*. Elsevier Ltd, 2008. doi: 10.1016/B978-0-08-045316-3.X0001-4.

[206] IfBB – Institute for Bioplastics and Biocomposites. Biopolymers facts and statistics 2020. Technical report, Institute for Bioplastics and Biocomposites, 2020.

[207] European Bioplastics. Market update 2020: Bioplastics continue to become mainstream as the global bioplastics market is set to grow by 36 percent over the next 5 years, 2020.

[208] Chao Rong Qi and Huan Feng Jiang. Efficient synthesis of β-oxopropylcarbamates in compressed co2 without any additional catalyst and solvent. *Green Chemistry*, 9(12):1284–1286, 2007. doi: 10.1039/b707893e.

[209] Neha Yadav, Farzad Seidi, Daniel Crespy, and Valerio D'Elia. Polymers based on cyclic carbonates as Trait d'Union between polymer chemistry and sustainable CO2 utilization. *ChemSusChem*, 12(4):724–754, 2019. doi: 10.1002/cssc.201802770.

[210] Farid Ouhib, Leire Meabe, Abdelfattah Mahmoud, Nicolas Eshraghi, Bruno Grignard, Jean Michel Thomassin, Abdelhafid Aqil, Frederic Boschini, Christine Jérôme, David Mecerreyes, and Christophe Detrembleur. CO2-sourced polycarbonates as solid electrolytes for room temperature operating lithium batteries. *Journal of Materials Chemistry A*, 7(16):9844–9853, 2019. doi: 10.1039/c9ta01564g.

[211] Saumya Dabral and Thomas Schaub. The use of carbon dioxide (CO2) as a building block in organic synthesis from an Industrial perspective. *Advanced Synthesis & Catalysis*, 361(2):223–246, 2019. doi: 10.1002/adsc.201801215.

[212] Farid Ouhib, Leire Meabe, Abdelfattah Mahmoud, Bruno Grignard, Jean-Michel Thomassin, Frederic Boschini, Haijin Zhu, Maria Forsyth, David Mecerreyes, and Christophe Detrembleur. Influence of the cyclic versus linear carbonate segments in the properties and performance of CO2-sourced polymer electrolytes for lithium batteries. *ACS Applied Polymer Materials*, 2(2):922–931, 2020. doi: 10.1021/acsapm.9b01130.

[213] Shinsuke Fukuoka, Masahiro Tojo, Hiroshi Hachiya, Muneaki Aminaka, and Kazumi Hasegawa. Green and sustainable chemistry in practice: Development and industrialization of a novel process for polycarbonate production from CO2 without using phosgene. *Polymer Journal*, 39(2):91–114, 2007. doi: 10.1295/polymj.PJ2006140.

[214] Deny Kyriacos. Polycarbonates. In *Brydson's Plastics Materials: Eighth Edition*, pages 457–485. Butterworth-Heinemann, 2017. doi: 10.1016/B978-0-323-35824-8.00017-7.

[215] Sandro Gennen, Bruno Grignard, Thierry Tassaing, Christine Jérôme, and Christophe Detrembleur. CO2-sourced α-alkylidene cyclic carbonates: A step forward in the quest for functional regioregular poly(urethane)s and poly(carbonate)s. *Angewandte Chemie*, 129(35):10530–10534, 2017. doi: 10.1002/ange.201704467.

[216] Zhi-Hua Zhou, Qing-Wen Song, and Liang-Nian He. Silver(I)-promoted cascade reaction of propargylic alcohols, carbon dioxide, and vicinal diols: thermodynamically favorable route to cyclic carbonates. *ACS Omega*, 2(1):337–345, 2017. doi: 10.1021/acsomega.6b00407.

[217] Qing Wen Song, Zhi Hua Zhou, Mei Yan Wang, Kan Zhang, Ping Liu, Jia Yao Xun, and Liang Nian He. Thermodynamically favorable synthesis of 2-oxazolidinones through silver-catalyzed reaction of propargylic alcohols, CO2, and 2-aminoethanols. *ChemSusChem*, 9(16):2054–2058, 2016. doi: 10.1002/cssc.201600470.

[218] Yanfei Zhao, Zhenzhen Yang, Bo Yu, Hongye Zhang, Huanjun Xu, Leiduan Hao, Buxing Han, and Zhimin Liu. Task-specific ionic liquid and CO2-cocatalysed efficient hydration of propargylic alcohols to α-hydroxy ketones. *Chemical Science*, 6(4):2297–2301, 2015. doi: 10.1039/c5sc00040h.

[219] Lise Maisonneuve, Océane Lamarzelle, Estelle Rix, Etienne Grau, and Henri Cramail. Isocyanate-free routes to polyurethanes and poly(hydroxy urethane)s. *Chemical Reviews*, 115(22):12407–12439, 2015. doi: 10.1021/acs.chemrev.5b00355.

[220] Adrien Cornille, Marine Blain, Rémi Auvergne, Bruno Andrioletti, Bernard Boutevin, and Sylvain Caillol. A study of cyclic carbonate aminolysis at room temperature: Effect of cyclic carbonate structures and solvents on polyhydroxyurethane synthesis. *Polymer Chemistry*, 8(3):592–604, 2017. doi: 10.1039/c6py01854h.

[221] Alvaro Gomez-Lopez, Satyannarayana Panchireddy, Bruno Grignard, Inigo Calvo, Christine Jerome, Christophe Detrembleur, and Haritz Sardon. Poly(hydroxyurethane) adhesives and coatings: state-of-the-art and future directions. *ACS Sustainable Chemistry & Engineering*, 9(29):9541–9562, 2021. doi: 10.1021/acssuschemeng.1c02558.

[222] Matthew M. Matlock, Kevin R. Henke, and David A. Atwood. Effectiveness of commercial reagents for heavy metal removal from water with new insights for future chelate designs. *Journal of Hazardous Materials*, 92(2):129–142, 2002. doi: 10.1016/S0304-3894(01)00389-2.

[223] Yang Li, Han-Yi Duan, Ming Luo, Ying-Ying Zhang, Xing-Hong Zhang, and Donald J. Darensbourg. Mechanistic study of regio-defects in the copolymerization of propylene oxide/carbonyl sulfide catalyzed by (Salen)CrX complexes. *Macromolecules*, 50(21):8426–8437, 2017. doi: 10.1021/acs.macromol.7b01867.

[224] Farid Ouhib, Bruno Grignard, Elias Van Den Broeck, André Luxen, Koen Robeyns, Veronique Van Speybroeck, Christine Jerome, and Christophe Detrembleur. A switchable domino process for the construction of novel CO2 -sourced sulfur-containing building blocks and poolymers. *Angewandte Chemie International Edition*, 58(34):11768–11773, 2019. doi: 10.1002/anie.201905969.

[225] Hui Zhou, Hui Zhang, Sen Mu, Wen-zhen Zhang, Wei-Min Ren, and Xiao-bing Lu. Highly regio- and stereoselective synthesis of cyclic carbonates from biomass-derived polyols via organocatalytic cascade reaction. *Green Chemistry*, 21(23): 6335–6341, 2019. doi: 10.1039/C9GC03013A.

[226] Meta M. Bloksma, Ulrich S. Schubert, and Richard Hoogenboom. Poly(cyclic imino ether)s beyond 2-substituted-2-oxazolines. *Macromolecular Rapid Communications*, 32(18):1419–1441, 2011. doi: 10.1002/marc.201100138.

[227] A. J. Hallett, T. M. O'Brien, E. Carter, B. M. Kariuki, D. M. Murphy, and B. D. Ward. Copper(II) complexes of pyridine-oxazoline (Pyox) ligands: Coordination chemistry, ligand stability, and catalysis. *INORGANICA CHIMICA ACTA*, 441: 86–94, 2016.

[228] Sung-Gon Kim, Kyung-Hyun Kim, Junyang Jung, Seung Koo Shin, and Kyo Han Ahn. Unprecedented chiral molecular recognition in a C3-symmetric environment. *Journal of the American Chemical Society*, 124(4):591–596, 2002. doi: 10.1021/ja0119696.

[229] Michael J. Frisch, John A. Pople, and J. Stephen Binkley. Self-consistent molecular orbital methods 25. Supplementary functions for Gaussian basis sets. *The Journal of Chemical Physics*, 80(7):3265–3269, 1984. doi: 10.1063/1.447079.

[230] Keigo Aoi, Hiroshi Suzuki, and Masahiko Okada. Architectural control of sugar-containing polymers by living polymerization: ring-opening polymerization of 2-oxazolines initiated with carbohydrate derivatives. *Macromolecules*, 25(25):7073–7075, 1992. doi: 10.1021/ma00051a056.

[231] Richard Hoogenboom and Helmut Schlaad. Bioinspired poly(2-oxazoline)s. *Polymers*, 3(1):467–488, 2011. doi: 10.3390/polym3010467.

[232] Robert Luxenhofer, Yingchao Han, Anita Schulz, Jing Tong, Zhijian He, Alexander V. Kabanov, and Rainer Jordan. Poly(2-oxazoline)s as polymer therapeutics. *Macromolecular Rapid Communications*, 33(19):1613–1631, 2012. doi: 10.1002/marc.201200354.

[233] Samuel Zalipsky, Christian B. Hansen, Jan M. Oaks, and Theresa M. Allen. Evaluation of blood clearance rates and biodistribution of poly(2-oxazoline)-grafted liposomes. *Journal of Pharmaceutical Sciences*, 85(2):133–137, 1996. doi: 10.1021/js9504043.

[234] Richard Hoogenboom. Poly(2-oxazoline)s: A polymer class with numerous potential applications. *Angewandte Chemie International Edition*, 48(43):7978–7994, 2009. doi: 10.1002/anie.200901607.

[235] Katrin Knop, Richard Hoogenboom, Dagmar Fischer, and Ulrich S. Schubert. Poly(ethylene glycol) in drug delivery: Pros and cons as well as potential alternatives. *Angewandte Chemie International Edition*, 49(36):6288–6308, 2010. doi: 10.1002/anie.200902672.

[236] Klaus P. Luef, Charlotte Petit, Bettina Ottersböck, Gernot Oreski, Francis Ehrenfeld, Bruno Grassl, Stéphanie Reynaud, and Frank Wiesbrock. UV-mediated thiol-ene click reactions for the synthesis of drug-loadable and degradable gels based on copoly(2-oxazoline)s. *European Polymer Journal*, 88:701–712, 2017. doi: 10.1016/j.eurpolymj.2016.08.012.

[237] Víctor R De Rosa, Bryn D Monnery, An Van Den Bulcke, and Richard Hoogenboom. The versatile polymer platform for biomedicine poly(2-oxazoline)s, 2014.

[238] Kathleen Lava, Bart Verbraeken, and Richard Hoogenboom. Poly(2-oxazoline)s and click chemistry: A versatile toolbox toward multi-functional polymers, 2015.

[239] Brieuc Guillerm, Sophie Monge, Vincent Lapinte, and Jean Jacques Robin. How to modulate the chemical structure of polyoxazolines by appropriate functionalization, 2012.

[240] Elisabeth Rossegger, Verena Schenk, and Frank Wiesbrock. Design strategies for functionalized poly(2-oxazoline)s and derived materials, 2013.

[241] A. Levy and M. Litt. Polymerization of cyclic imino ethers. II. Oxazines. *Journal of Polymer Science Part B: Polymer Letters*, 5(9):881–886, 1967. doi: 10.1002/pol.1967.110050928.

[242] Jeffrey S. Hrkach and Krzysztof Matyjaszewski. Reaction of 2-methyl-2-oxazoline with trimethylsilyl initiators: an unusual mode of ring opening. *Macromolecules*, 25(8):2070–2075, 1992. doi: 10.1021/ma00034a002.

[243] Shiro Kobayashi, Taro Tokuzawa, and Takeo Saegusa. Cationic ring-opening isomerization polymerization of 2-[p-(substituted)phenyl]-2-oxazolines. Effects of the substituent on the reactivities. *Macromolecules*, 15(3):707–710, 1982. doi: 10.1021/ma00231a005.

[244] Takeo Saegusa, Shiro Kobayashi, and Yoshitomi Nagura. Isomerization polymerization of 1,3-oxazine. III. kinetic studies on the ring-opening polymerization of 2-phenyl-5,6-dihydro-4H-1,3-oxazine by methyl tosylate and methyl iodide initiators. *Macromolecules*, 7(3):272–277, 1974. doi: 10.1021/ma60039a004.

[245] Takeo Saegusa and Hiroharu Ikeda. Isomerization Polymerization of 2-Oxazoline. VI. Kinetic Study on the Polymerization of 2-Methyl-2-oxazoline Initiated by Methyl Iodide. *Macromolecules*, 6(6):808–811, 1973. doi: 10.1021/ma60036a004.

[246] Takeo Saegusa, Hiroharu Ikeda, and Hiroyasu Fujii. Isomerization polymerization of 2-oxazoline. V. kinetic studies on the polymerization of 2-oxazoline. *Macromolecules*, 6(3):315–319, 1973. doi: 10.1021/ma60033a002.

[247] Martin W.M. Fijten, Richard Hoogenboom, and Ulrich S. Schubert. Initiator effect on the cationic ring-opening copolymerization of 2-ethyl-2-oxazoline and 2-phenyl-2-oxazoline. *Journal of Polymer Science, Part A: Polymer Chemistry*, 46(14):4804–4816, 2008. doi: 10.1002/pola.22814.

[248] Andrzej Dworak. The role of cationic and covalent active centers in the polymerization of 2-methyl-2-oxazoline initiated with benzyl bromide. *Macromolecular Chemistry and Physics*, 199(9):1843–1849, 1998. doi: 10.1002/(SICI)1521-3935(19980901)199:9⟨1843::AID-MACP1843⟩3.0.CO;2-I.

[249] Richard Hoogenboom, Renzo M. Paulus, Martin W.M. Fijten, and Ulrich S. Schubert. Concentration effects in the cationic ring-opening polymerization of 2-ethyl-2-oxazoline in N,N-dimethylacetamide. *Journal of Polymer Science, Part A: Polymer Chemistry*, 43(7):1487–1497, 2005. doi: 10.1002/pola.20603.

[250] Bart Verbraeken, Bryn D. Monnery, Kathleen Lava, and Richard Hoogenboom. The chemistry of poly(2-oxazoline)s. In *Encyclopedia of Polymer Science and Technology*, pages 1–59. American Cancer Society, 2018. doi: 10.1002/0471440264.pst626.pub2.

[251] Christian J. Waschinski, Vera Herdes, Fabian Schueler, and Joerg C. Tiller. Influence of satellite groups on telechelic antimicrobial functions of polyoxazolines. *Macromolecular Bioscience*, 5(2):149–156, 2005. doi: 10.1002/mabi.200400169.

[252] Yali Yang, Kazunori Kataoka, and Françoise M. Winnik. Synthesis of diblock copolymers consisting of hyaluronan and poly(2-ethyl-2-oxazoline). *Macromolecules*, 38(6):2043–2046, 2005. doi: 10.1021/ma047439m.

[253] Robert Luxenhofer, Manuela Bezen, and Rainer Jordan. Kinetic investigations on the polymerization of 2-oxazolines using pluritriflate initators. *Macromolecular Rapid Communications*, 29(18):1509–1513, 2008. doi: 10.1002/marc.200800293.

[254] Agnieszka Kowalczuk, Juraj Kronek, Kornelia Bosowska, Barbara Trzebicka, and Andrzej Dworak. Star poly(2-ethyl-2-oxazoline)s-synthesis and thermosensitivity. *Polymer International*, 60(7):1001–1009, 2011. doi: 10.1002/pi.3103.

[255] Ralf Weberskirch, Rainer Hettich, Oskar Nuyken, Dirk Schmaljohann, and Brigitte Voit. Synthesis of new amphiphilic star polymers derived from a hyperbranched macroinitiator by the cationic 'grafting from' method. *Macromolecular Chemistry*

and Physics, 200(4):863–873, 1999. doi: 10.1002/(sici)1521-3935(19990401)200:4⟨863::aid-macp863⟩3.3.co;2-e.

[256] Richard Hoogenboom, Martin W. M. Fijten, Hanneke M. L. Thijs, Bart M. van Lankvelt, and Ulrich S. Schubert. Microwave-assisted synthesis and properties of a series of poly(2-alkyl-2-oxazoline)s. *Designed Monomers & Polymers*, 8(6):659–671, 2005. doi: 10.1163/156855505774597704.

[257] Oskar Nuyken, Gerhard Maier, Aurelia Groß, and Herbert Fischer. Systematic investigations on the reactivity of oxazolinium salts. *Macromolecular Chemistry and Physics*, 197(1):83–95, 1996. doi: 10.1002/macp.1996.021970106.

[258] Hannelore Goossens, Saron Catak, Mathias Glassner, Victor R. de la Rosa, Bryn D. Monnery, Frank De Proft, Veronique Van Speybroeck, and Richard Hoogenboom. Cationic ring-opening polymerization of 2-propyl-2-oxazolines: understanding structural effects on polymerization behavior based on molecular modeling. *ACS Macro Letters*, 2(8):651–654, 2013. doi: 10.1021/mz400293y.

[259] Petra J.M. Bouten, Dietmar Hertsen, Maarten Vergaelen, Bryn D Monnery, Marcel A Boerman, Hannelore Goossens, Saron Catak, Jan C M Van Hest, Veronique Van Speybroeck, and Richard Hoogenboom. Accelerated living cationic ring-opening polymerization of a methyl ester functionalized 2-oxazoline monomer. *Polymer Chemistry*, 6:514–518, 2014. doi: 10.1039/c4py01373e.

[260] Petra J. M. Bouten, Dietmar Hertsen, Maarten Vergaelen, Bryn D. Monnery, Saron Catak, Jan C. M. van Hest, Veronique Van Speybroeck, and Richard Hoogenboom. Synthesis of poly(2-oxazoline)s with side chain methyl ester functionalities: Detailed understanding of living copolymerization behavior of methyl ester containing monomers with 2-alkyl-2-oxazolines. *Journal of Polymer Science Part A: Polymer Chemistry*, 53(22):2649–2661, 2015. doi: 10.1002/pola.27733.

[261] Klaus P Luef, Richard Hoogenboom, Ulrich S Schubert, and Frank Wiesbrock. Microwave-assisted cationic ring-opening polymerization of 2-oxazolines. *Advances in Polymer Science*, 274:183–208, 2015. doi: 10.1007/12_2015_340.

[262] Matthias Lobert, Uwe Köhn, Richard Hoogenboom, and Ulrich S. Schubert. Synthesis and microwave assisted polymerization of fluorinated 2-phenyl-2-oxazolines: the fastest 2-oxazoline monomer to date. *Chemical Communications*, 0(12):1458, 2008. doi: 10.1039/b717455a.

[263] Joon-Sik Park and Kazunori Kataoka. Comprehensive and accurate control of thermosensitivity of poly(2-alkyl-2-oxazoline)s via well-defined gradient or random copolymerization. *Macromolecules*, 40(10):3599–3609, 2007. doi: 10.1021/ma0701181.

[264] Anja Gress, Antje Völkel, and Helmut Schlaad. Thio-click modification of poly[2-(3-butenyl)-2-oxazoline]. *Macromolecules*, 40(22):7928–7933, 2007. doi: 10.1021/ma071357r.

[265] Andrew M. Kelly, Angela Hecke, Bianca Wirnsberger, and Frank Wiesbrock. Synthesis of poly(2-oxazoline)-based hydrogels with tailor-made swelling degrees capable of stimuli-triggered compound release. *Macromolecular Rapid Communications*, 32(22):1815–1819, 2011. doi: 10.1002/marc.201100409.

[266] Florian Manzenrieder, Robert Luxenhofer, Marco Retzlaff, Rainer Jordan, and M. G. Finn. Stabilization of virus-like particles with poly(2-oxazoline)s. *Angewandte Chemie - International Edition*, 50(11):2601–2605, 2011. doi: 10.1002/anie.201006134.

[267] Golnaz Bissadi and Ralf Weberskirch. Efficient synthesis of polyoxazoline-silica hybrid nanoparticles by using the "grafting-onto" approach. *Polymer Chemistry*, 7 (6):1271–1280, 2016. doi: 10.1039/C5PY01775K.

[268] Lutz Tauhardt, Kristian Kempe, W Ab, Michael Gottschaldt, and Ulrich S Schubert. Poly(2-oxazoline) functionalized surfaces: from modification to application. *Chem. Soc. Rev. Chem. Soc. Rev*, 42(42):7998–8011, 2013. doi: 10.1039/c3cs60161g.

[269] Nadine Engelhardt, Andrea Ernst, Anne-Larissa Kampmann, and Ralf Weberskirch. Synthesis and characterization of surface functional polymer nanoparticles by a bottom-up approach from tailor-made amphiphilic block copolymers. *Macromolecular Chemistry and Physics*, 214(24):2783–2791, 2013. doi: 10.1002/macp.201300573.

[270] David L. Trumbo. Epoxidized poly(decenyloxazoline) in thermoset coatings. *Journal of Coatings Technology and Research*, 3(1):87–88, 2006. doi: 10.1007/s11998-006-0009-2.

[271] Terunari Hayashi and Akinori Takasu. Design of Electrophoretic and Biocompatible Poly(2-oxazoline)s Initiated by Perfluoroalkanesulfoneimides and Electrophoretic Deposition with Bioactive Glass. *Biomacromolecules*, 16(4):1259–1266, 2015. doi: 10.1021/acs.biomac.5b00043.

[272] Martin Rother, Martin G. Nussbaumer, Kasper Renggli, and Nico Bruns. Protein cages and synthetic polymers: a fruitful symbiosis for drug delivery applications, bionanotechnology and materials science. *Chemical Society Reviews*, 45(22):6213–6249, 2016. doi: 10.1039/C6CS00177G.

[273] Wu Bin Ying, Sohee Kim, Min Woo Lee, Na Yeong Go, Hyunsook Jung, Sam Gon Ryu, Bumjae Lee, and Kyung Jin Lee. Toward a detoxification fabric against nerve gas agents: guanidine-functionalized poly[2-(3-butenyl)-2-oxazoline]/Nylon-6,6 nanofibers. *RSC Advances*, 7(25):15246–15254, 2017. doi: 10.1039/C7RA01278K.

[274] Niels ten Brummelhuis and Helmut Schlaad. Stimuli-responsive star polymers through thiol–yne core functionalization/crosslinking of block copolymer micelles. *Polymer Chemistry*, 2(5):1180, 2011. doi: 10.1039/c1py00002k.

[275] Christina Diehl and Helmut Schlaad. Thermo-responsive polyoxazolines with widely tuneable LCST. *Macromolecular Bioscience*, 9(2):157–161, 2009. doi: 10.1002/mabi.200800213.

[276] Matthias Hartlieb, Kristian Kempe, and Ulrich S. Schubert. Covalently cross-linked poly(2-oxazoline) materials for biomedical applications – from hydrogels to self-assembled and templated structures. *Journal of Materials Chemistry B*, 3(4): 526–538, 2015. doi: 10.1039/C4TB01660B.

[277] Martin Fimberger, Klaus Peter Luef, Claudia Payerl, Roland C. Fischer, Franz Stelzer, Mihály Kállay, and Frank Wiesbrock. The π-electron delocalization in 2-oxazolines revisited: Quantification and comparison with its analogue in esters. *Materials*, 8(8):5385–5397, 2015. doi: 10.3390/ma8085249.

[278] Michael Schmitz, Matthias Kuhlmann, Oliver Reimann, Christian P. R. Hackenberger, and Jürgen Groll. Side-chain cysteine-functionalized poly(2-oxazoline)s for multiple peptide conjugation by native chemical ligation. *Biomacromolecules*, 16 (4):1088–1094, 2015. doi: 10.1021/bm501697t.

[279] Tim R. Dargaville, Kathleen Lava, Bart Verbraeken, and Richard Hoogenboom. Unexpected switching of the photogelation chemistry when cross-linking poly(2-oxazoline) copolymers. *Macromolecules*, 49(13):4774–4783, 2016. doi: 10.1021/acs.macromol.6b00167.

[280] Jong-Ryul Park, Eleonore C. L. Bolle, Amanda Dos Santos Cavalcanti, Annelore Podevyn, Joachim F. R. Van Guyse, Aurelien Forget, Richard Hoogenboom, and Tim R. Dargaville. Injectable biocompatible poly(2-oxazoline) hydrogels by strain promoted alkyne–azide cycloaddition. *Biointerphases*, 16(1):011001, 2021. doi: 10.1116/6.0000630.

[281] Ondrej Sedlacek, Daniel Jirak, Martin Vit, Natalia Ziołkowska, Olga Janouskova, and Richard Hoogenboom. Fluorinated Water-Soluble Poly(2-oxazoline)s as Highly Sensitive 19F MRI Contrast Agents. *Macromolecules*, 53(15):6387–6395, 2020. doi: 10.1021/acs.macromol.0c01228.

[282] Michał Cegłowski, Grzegorz Schroeder, and Richard Hoogenboom. Porous poly(2-oxazoline)-based polymers for removal and quantification of phenolic compounds. *Chemistry of Materials*, 32(15):6425–6436, 2020. doi: 10.1021/acs.chemmater.0c01559.

[283] Elias Van Den Broeck, Bart Verbraeken, Karen Dedecker, Pieter Cnudde, Louis Vanduyfhuys, Toon Verstraelen, Kristof Van Hecke, Valentin Victor Jerca, Saron Catak, Richard Hoogenboom, and Veronique Van Speybroeck. Cation-π interactions accelerate the living cationic ring-opening polymerization of unsaturated 2-alkyl-2-oxazolines. *Macromolecules*, 53(10):3832–3846, 2020. doi: 10.1021/acs.macromol.0c00865.

[284] Ekaterina I. Izgorodina and Michelle L. Coote. Accurate ab initio prediction of propagation rate coefficients in free-radical polymerization: Acrylonitrile and vinyl chloride. *Chemical Physics*, 324(1 SPEC. ISS.):96–110, 2006. doi: 10.1016/j.chemphys.2005.09.042.

[285] I. Değirmenci, V. Aviyente, V. Van Speybroeck, and M. Waroquier. DFT study on the propagation kinetics of free-radical polymerization of alpha-substituted acrylates. *Macromolecules*, 42(8):3033–3041, 2009. doi: 10.1021/ma802875z.

[286] Iesa Değirmenci, Şükrü Eren, Viktorya Aviyente, Bart De Sterck, Karen Hemelsoet, Veronique Van Speybroeck, and Michel Waroquier. Modeling the solvent effect on the tacticity in the free radical polymerization of methyl methacrylate. *Macromolecules*, 43(13):5602–5610, 2010. doi: 10.1021/ma100608g.

[287] Lyuben Zhechkov, Thomas Heine, Serguei Patchkovskii, Gotthard Seifert, and Helio A. Duarte. An efficient a posteriori treatment for dispersion interaction in density-functional-based tight binding. *Journal of Chemical Theory and Computation*, 1(5):841–847, 2005. doi: 10.1021/ct050065y.

[288] M. Elstner, D. Porezag, G. Jungnickel, J. Elsner, M. Haugk, and Th. Frauenheim. Self-consistent-charge density-functional tight-binding method for simulations of complex materials properties. *Physical Review B - Condensed Matter and Materials Physics*, 58(11):7260–7268, 1998. doi: 10.1103/PhysRevB.58.7260.

[289] D. Porezag, Th. Frauenheim, Th. Köhler, G. Seifert, and R. Kaschner. Construction of tight-binding-like potentials on the basis of density-functional theory: Application to carbon. *Physical Review B*, 51(19):12947–12957, 1995. doi: 10.1103/PhysRevB.51.12947.

[290] G. Seifert, D. Porezag, and Th. Frauenheim. Calculations of molecules, clusters, and solids with a simplified LCAO-DFT-LDA scheme. *International Journal of Quantum Chemistry*, 58(2):185–192, 1996. doi: 10.1002/(SICI)1097-461X(1996)58:2⟨185::AID-QUA7⟩3.0.CO;2-U.

[291] Polymer chemistry innovations Inc. Aquazol, 2022.

[292] Richard Hoogenboom, Hanneke M.L. Thijs, Mark J.H.C. Jochems, Bart M. Van Lankvelt, Martin W.M. Fijten, and Ulrich S. Schubert. Tuning the LCST of poly(2-oxazoline)s by varying composition and molecular weight: Alternatives to poly(N-isopropylacrylamide)? *Chemical Communications*, (44):5758–5760, 2008. doi: 10.1039/b813140f.

[293] Pinyen Lin, C. Clash, Eli M. Pearce, T. K. Kwei, and M. A. Aponte. Solubility and miscibility of poly(ethyl oxazoline). *Journal of Polymer Science Part B: Polymer Physics*, 26(3):603–619, 1988. doi: 10.1002/polb.1988.090260312.

[294] Huub P.C. Van Kuringen, Joke Lenoir, Els Adriaens, Johan Bender, Bruno G. De Geest, and Richard Hoogenboom. Partial Hydrolysis of Poly(2-ethyl-2-oxazoline) and Potential Implications for Biomedical Applications? *Macromolecular Bioscience*, 12(8):1114–1123, 2012. doi: 10.1002/mabi.201200080.

[295] Thomas Lorson, Michael M. Lübtow, Erik Wegener, Malik S. Haider, Solomiia Borova, Daniel Nahm, Rainer Jordan, Marina Sokolski-Papkov, Alexander V. Kabanov, and Robert Luxenhofer. Poly(2-oxazoline)s based biomaterials: A comprehensive and critical update. *Biomaterials*, 178:204–280, 2018. doi: 10.1016/j.biomaterials.2018.05.022.

[296] Robert Luxenhofer, Gaurav Sahay, Anita Schulz, Daria Alakhova, Tatiana K. Bronich, Rainer Jordan, and Alexander V. Kabanov. Structure-property relationship in cytotoxicity and cell uptake of poly(2-oxazoline) amphiphiles. *Journal of Controlled Release*, 153(1):73–82, 2011. doi: 10.1016/j.jconrel.2011.04.010.

[297] Tacey X Viegas, Michael D Bentley, J Milton Harris, Zhihao Fang, Kunsang Yoon, Bekir Dizman, Rebecca Weimer, Anna Mero, Gianfranco Pasut, and Francesco M Veronese. Polyoxazoline: Chemistry, properties, and applications in drug delivery. *Bioconjugate Chemistry*, 22(5):976–986, 2011. doi: 10.1021/bc200049d.

[298] Bart Claeys, Anouk Vervaeck, Chris Vervaet, Jean Paul Remon, Richard Hoogenboom, and Bruno G. De Geest. Poly(2-ethyl-2-oxazoline) as matrix excipient for drug formulation by hot melt extrusion and injection molding. *Macromolecular Rapid Communications*, 33(19):1701–1707, 2012. doi: 10.1002/marc.201200332.

[299] Sandeep Kalepu and Vijaykumar Nekkanti. Insoluble drug delivery strategies: Review of recent advances and business prospects, 2015.

[300] Bethlehem. Biopharmaceutical Classification System and Formulation Development. *Particle Sciences*, 9:1–4, 2011.

[301] Guy Van Den Mooter. The use of amorphous solid dispersions: A formulation strategy to overcome poor solubility and dissolution rate, 2012.

[302] Christian Leuner and Jennifer Dressman. Improving drug solubility for oral delivery using solid dispersions, 2000.

[303] Navnit Shah, Sandhu Harpreet, Soon Choi Duk, Chokshi Hitesh, and Malick A. Waseem. *Amorphous Solid Dispersions*. Advances in Delivery Science and Technology. Springer New York, New York, NY, 2014. doi: 10.1007/978-1-4939-1598-9.

[304] Charles Kittel and Donald F. Holcomb. Introduction to solid state physics. *American Journal of Physics*, 35(6):547–548, 1967. doi: 10.1119/1.1974177.

[305] Chris Brough and R. O. Williams. Amorphous solid dispersions and nano-crystal technologies for poorly water-soluble drug delivery, 2013.

[306] Matthias Manne Knopp, Nabil Chourak, Fauzan Khan, Johan Wendelboe, Peter Langguth, Thomas Rades, and René Holm. Effect of polymer type and drug dose on the in vitro and in vivo behavior of amorphous solid dispersions. *European Journal of Pharmaceutics and Biopharmaceutics*, 105:106–114, 2016. doi: 10.1016/j.ejpb.2016.05.017.

[307] Sien Dedroog, Christophe Huygens, and Guy Van den Mooter. Chemically identical but physically different: A comparison of spray drying, hot melt extrusion and cryo-milling for the formulation of high drug loaded amorphous solid dispersions of naproxen. *European Journal of Pharmaceutics and Biopharmaceutics*, 135:1–12, 2019. doi: 10.1016/j.ejpb.2018.12.002.

[308] Annelies Smeets, Robin Koekoekx, Christian Clasen, and Guy Van den Mooter. Amorphous solid dispersions of darunavir: Comparison between spray drying and electrospraying. *European Journal of Pharmaceutics and Biopharmaceutics*, 130 (June):96–107, 2018. doi: 10.1016/j.ejpb.2018.06.021.

[309] Scott V. Jermain, Chris Brough, and Robert O. Williams. Amorphous solid dispersions and nanocrystal technologies for poorly water-soluble drug delivery – An update. *International Journal of Pharmaceutics*, 535(1-2):379–392, 2018. doi: 10.1016/j.ijpharm.2017.10.051.

[310] Sugandha Saboo, Naila A. Mugheirbi, Dmitry Y. Zemlyanov, Umesh S. Kestur, and Lynne S. Taylor. Congruent release of drug and polymer: A "sweet spot" in the dissolution of amorphous solid dispersions. *Journal of Controlled Release*, 298 (January):68–82, 2019. doi: 10.1016/j.jconrel.2019.01.039.

[311] Khadijah Edueng, Denny Mahlin, and Christel A. S. Bergström. The need for re-structuring the disordered science of amorphous drug formulations. *Pharmaceutical Research*, 34(9):1754–1772, 2017. doi: 10.1007/s11095-017-2174-7.

[312] Shimin Kang, Xianglan Li, Juan Fan, and Jie Chang. Hydrothermal conversion of lignin: A review, 2013.

[313] Deng Guang Yu, Jiao Jiao Li, Gareth R. Williams, and Min Zhao. Electrospun amorphous solid dispersions of poorly water-soluble drugs: A review, 2018.

[314] Sripal Bangalore, Gayathri Kamalakkannan, Sanobar Parkar, and Franz H. Messerli. Fixed-dose combinations improve medication compliance: A meta-analysis. *The American Journal of Medicine*, 120(8):713–719, 2007. doi: 10.1016/j.amjmed.2006.08.033.

[315] Nandana Bhardwaj and Subhas C Kundu. Electrospinning: A fascinating fiber fabrication technique, 2010.

[316] Luana Persano, Andrea Camposeo, Cagri Tekmen, and Dario Pisignano. Industrial upscaling of electrospinning and applications of polymer nanofibers: A review, 2013.

[317] Deng Guang Yu, Jian Mao Yang, Christopher Branford-White, Ping Lu, Li Zhang, and Li Min Zhu. Third generation solid dispersions of ferulic acid in electrospun composite nanofibers. *International Journal of Pharmaceutics*, 400(1-2):158–164, 2010. doi: 10.1016/j.ijpharm.2010.08.010.

[318] Justyna Pacułt, Marzena Rams-Baron, Beata Chrząszcz, Renata Jachowicz, and Marian Paluch. Effect of polymer chain length on the physical stability of amorphous drug–polymer blends at ambient pressure. *Molecular Pharmaceutics*, 15(7):2807–2815, 2018. doi: 10.1021/acs.molpharmaceut.8b00312.

[319] Paroma Chakravarty, Joseph W. Lubach, Jonathan Hau, and Karthik Nagapudi. A rational approach towards development of amorphous solid dispersions: Experimental and computational techniques. *International Journal of Pharmaceutics*, 519 (1-2):44–57, 2017. doi: 10.1016/j.ijpharm.2017.01.003.

[320] Hanan Fael, Clara Ràfols, and A. Levent Demirel. Poly(2-ethyl-2-oxazoline) as an alternative to poly(vinylpyrrolidone) in solid dispersions for solubility and dissolution rate enhancement of drugs. *Journal of Pharmaceutical Sciences*, 107(9):2428–2438, 2018. doi: 10.1016/j.xphs.2018.05.015.

[321] Eline Boel, Annelies Smeets, Maarten Vergaelen, Victor R. De la Rosa, Richard Hoogenboom, and Guy Van den Mooter. Comparative study of the potential of poly(2-ethyl-2-oxazoline) as carrier in the formulation of amorphous solid dispersions of poorly soluble drugs. *European Journal of Pharmaceutics and Biopharmaceutics*, 144(September):79–90, 2019. doi: 10.1016/j.ejpb.2019.09.005.

[322] Tian Xiang Xiang and Bradley D. Anderson. Molecular dynamics simulation of amorphous indomethacin-poly(Vinylpyrrolidone) glasses: Solubility and hydrogen bonding interactions. *Journal of Pharmaceutical Sciences*, 102(3):876–891, 2013. doi: 10.1002/jps.23353.

[323] Patrick J. Marsac, Sheri L. Shamblin, and Lynne S. Taylor. Theoretical and practical approaches for prediction of drug-polymer miscibility and solubility. *Pharmaceutical Research*, 23(10):2417–2426, 2006. doi: 10.1007/s11095-006-9063-9.

[324] Bradley D. Anderson. Predicting solubility/miscibility in amorphous dispersions: It is time to move beyond regular solution theories. *Journal of Pharmaceutical Sciences*, 107(1):24–33, 2018. doi: 10.1016/j.xphs.2017.09.030.

[325] Sunny P. Bhardwaj, Kapildev K. Arora, Elizabeth Kwong, Allen Templeton, Sophie Dorothee Clas, and Raj Suryanarayanan. Mechanism of amorphous itraconazole stabilization in polymer solid dispersions: Role of molecular mobility. *Molecular Pharmaceutics*, 11(11):4228–4237, 2014. doi: 10.1021/mp5004515.

[326] Ralm G. Ricarte, Nicholas J. Van Zee, Ziang Li, Lindsay M. Johnson, Timothy P. Lodge, and Marc A. Hillmyer. Recent advances in understanding the micro- and nanoscale phenomena of amorphous solid dispersions. *Molecular Pharmaceutics*, 16(10):4089–4103, 2019. doi: 10.1021/acs.molpharmaceut.9b00601.

[327] Afroditi Kapourani, Kalliopi Eleftheriadou, Konstantinos N. Kontogiannopoulos, and Panagiotis Barmpalexis. Evaluation of rivaroxaban amorphous solid dispersions physical stability via molecular mobility studies and molecular simulations. *European Journal of Pharmaceutical Sciences*, 157:105642, 2021. doi: 10.1016/j.ejps.2020.105642.

[328] Tian Xiang Xiang and Bradley D. Anderson. Effects of Molecular Interactions on Miscibility and Mobility of Ibuprofen in Amorphous Solid Dispersions With Various Polymers. *Journal of Pharmaceutical Sciences*, 108(1):178–186, 2019. doi: 10.1016/j.xphs.2018.10.052.

[329] Monica Vialpando, Stefanie Smulders, Scott Bone, Casey Jager, David Vodak, Michiel Van Speybroeck, Loes Verheyen, Katrien Backx, Peter Boeykens, Marcus E. Brewster, Jens Ceulemans, Hector Novoa de Armas, Katrien Van Geel, Emma Kesselaers, Vera Hillewaert, Sophie Lachau-Durand, Greet Meurs, Petros Psathas, Ben Van Hove, Geert Verreck, Marieke Voets, Ilse Weuts, and Claire Mackie. Evaluation of three amorphous drug delivery technologies to improve the oral absorption of flubendazole. *Journal of Pharmaceutical Sciences*, 105(9):2782–2793, 2016. doi: 10.1016/j.xphs.2016.03.003.

[330] Maeghan O'Neill, Cristina Ballesteros, Lucienne Tritten, Erica Burkman, Weam I. Zaky, Jianguo Xia, Andrew Moorhead, Steven A. Williams, and Timothy G. Geary. Profiling the macrofilaricidal effects of flubendazole on adult female Brugia malayi using RNAseq. *International Journal for Parasitology: Drugs and Drug Resistance*, 6(3):288–296, 2016. doi: 10.1016/j.ijpddr.2016.09.005.

[331] Laura Ceballos, Laura Moreno, Juan J. Torrado, Carlos Lanusse, and Luis Alvarez. Exploring flubendazole formulations for use in sheep. Pharmacokinetic evaluation of a cyclodextrin-based solution. *BMC Veterinary Research*, 8(1):71, 2012. doi: 10.1186/1746-6148-8-71.

[332] Maeghan O'Neill, James F. Geary, Dalen W. Agnew, Charles D. Mackenzie, and Timothy G. Geary. In vitro flubendazole-induced damage to vital tissues in adult females of the filarial nematode Brugia malayi. *International Journal for Parasitology: Drugs and Drug Resistance*, 5(3):135–140, 2015. doi: 10.1016/j.ijpddr.2015.06.002.

[333] Hanna T. Sjoberg, Nicolas Pionnier, Ghaith Aljayyoussi, Haelly M. Metuge, Abdel J. Njouendou, Valerine C. Chunda, Fanny F. Fombad, Dizzle B. Tayong, Narcisse V.T. Gandjui, Desmond N. Akumtoh, Patrick W.N. Chounna, Bertrand L. Ndzeshang, Sophie Lachaud, Fetene Tekle, Ludo Quirynen, Marc Engelen, Benny Baeten, Andrew Steven, Stephen A. Ward, Mark J. Taylor, Samuel Wanji, and Joseph D. Turner. Short-course, oral flubendazole does not mediate significant efficacy against Onchocerca adult male worms or Brugia microfilariae in murine infection models. *PLoS Neglected Tropical Diseases*, 13(1):1–19, 2019. doi: 10.1371/journal.pntd.0006356.

[334] Marc P. Hübner, Alexandra Ehrens, Marianne Koschel, Bettina Dubben, Franziska Lenz, Stefan J. Frohberger, Sabine Specht, Ludo Quirynen, Sophie Lachau-Durand, Fetene Tekle, Benny Baeten, Marc Engelen, Charles D. Mackenzie, and Achim Hoerauf. Macrofilaricidal efficacy of single and repeated oral and subcutaneous doses of flubendazole in Litomosoides sigmodontis infected jirds. *PLoS Neglected Tropical Diseases*, 13(1):1–17, 2019. doi: 10.1371/journal.pntd.0006320.

[335] Gabriel L.B. De Araujo, Fabio Furlan Ferreira, Carlos E.S. Bernardes, Juliana A.P. Sato, Otávio M. Gil, Dalva L.A. De Faria, Raimar Loebenberg, Stephen R. Byrn, Daniela D.M. Ghisleni, Nadia A. Bou-Chacra, Terezinha J.A. Pinto, Selma G. Antonio, Humberto G. Ferraz, Dmitry Zemlyanov, Débora S. Gonçalves, and Manuel E. Minas Da Piedade. A New Thermodynamically Favored Flubendazole/Maleic Acid Binary Crystal Form: Structure, Energetics, and in Silico PBPK Model-Based Investigation. *Crystal Growth and Design*, 18(4):2377–2386, 2018. doi: 10.1021/acs.cgd.7b01807.

[336] Laura Ceballos, Charles Mackenzie, Timothy Geary, Luis Alvarez, and Carlos Lanusse. Exploring the potential of flubendazole in Filariasis control: Evaluation of the systemic exposure for different pharmaceutical preparations. *PLoS Neglected Tropical Diseases*, 8(5):e2838, 2014. doi: 10.1371/journal.pntd.0002838.

[337] Dongyang Li, Kushal Panchal, Roozbeh Mafi, and Li Xi. An atomistic evaluation of the compatibility and plasticization efficacy of phthalates in poly(vinyl chloride). *Macromolecules*, 51(18):6997–7012, 2018. doi: 10.1021/acs.macromol.8b00756.

[338] J. M. Hutchinson and S. Montserrat. The application of modulated differential scanning calorimetry to the glass transition of polymers. I. A single-parameter theoretical model and its predictions. *Thermochimica Acta*, 286(2):263–296, 1996. doi: 10.1016/0040-6031(96)02967-X.

[339] John J. Tribone, J. M. O'Reilly, and Jehuda Greener. Analysis of enthalpy relaxation in poly(methyl methacrylate): effects of tacticity, deuteration, and thermal history. *Macromolecules*, 19(6):1732–1739, 1986. doi: 10.1021/ma00160a043.

[340] Sigma Aldrich. Safety Data Sheet Ultroxa®: Poly(2-ethyl-2-oxazoline), average Mn 50,000, PDI < 1.25. Technical report, Sigma Aldrich, 2018.

[341] Richard J. Gowers and Paola Carbone. A multiscale approach to model hydrogen bonding: The case of polyamide. *Journal of Chemical Physics*, 142(22), 2015. doi: 10.1063/1.4922445.

[342] Maurice L. Huggins. Theory of solutions of high polymers 1. *Journal of the American Chemical Society*, 64(7):1712–1719, 1942. doi: 10.1021/ja01259a068.

[343] Paul J. Flory. Themodynamics of high polymer solutions. *The Journal of Chemical Physics*, 10(1):51–61, 1942. doi: 10.1063/1.1723621.

[344] Kim Phan, Elias Van Den Broeck, Katleen Raes, Karen De Clerck, Veronique Van Speybroeck, and Steven De Meester. A comparative theoretical study on the solvent dependency of anthocyanin extraction profiles. *Journal of Molecular Liquids*, 351: 118606, 2022. doi: 10.1016/j.molliq.2022.118606.

[345] Sari Deketelaere, Elias Van Den Broeck, Lore Cools, Daan Deturck, Hannes Naeyaert, Kristof Van Hecke, Christian V. Stevens, Veronique Van Speybroeck, and Matthias D'hooghe. Unexpected Formation of 2,2-Dichloro-N-(chloromethyl)acetamides during Attempted Staudinger 2,2-Dichloro-β-lactam Synthesis. *European Journal of Organic Chemistry*, 2021(42):5823–5830, 2021. doi: 10.1002/ejoc.202100975.

[346] K.N.R Dumoleijn, E. Van Den Broeck, J. Stavinoha, V. Van Speybroeck, K. Moonen, and C.V. Stevens. Reductive imino-pinacol coupling reaction of halogenated aromatic imines and iminium ions catalyzed by precious metal catalysts using hydrogen. *Journal of Catalysis*, 400:103–113, 2021. doi: 10.1016/j.jcat.2021.05.023.

[347] Kim Phan, Elias Van Den Broeck, Veronique Van Speybroeck, Karen De Clerck, Katleen Raes, and Steven De Meester. The potential of anthocyanins from blueberries as a natural dye for cotton: A combined experimental and theoretical study. *Dyes and Pigments*, 176:108180, 2020. doi: 10.1016/j.dyepig.2019.108180.

[348] Nicola Piens, Hannelore Goossens, Dietmar Hertsen, Sari Deketelaere, Lieselotte Crul, Lotte Demeurisse, Jelle De Moor, Elias Van den Broeck, Karen Mollet, Kristof Van Hecke, Veronique Van Speybroeck, and Matthias D'hooghe. Reactivity of 3-oxo-β-lactams with respect to primary amines-an experimental and computational approach. *Chemistry - A European Journal*, 23(71):18002–18009, 2017. doi: 10.1002/chem.201703852.

[349] John Chodera, Rafal Wiewiora, Chaya Stern, and Peastman. openmm/openmm-forcefields: Fix GAFF AM1-BCC charging bug for some molecules, 2020.

[350] Michael R. Shirts, Christoph Klein, Jason M. Swails, Jian Yin, Michael K. Gilson, David L. Mobley, David A. Case, and Ellen D. Zhong. Lessons learned from comparing molecular dynamics engines on the SAMPL5 dataset. *Journal of Computer-Aided Molecular Design*, 31(1):147–161, 2017. doi: 10.1007/s10822-016-9977-1.

[351] OpenEye Scientific Software. OpenEye Toolkits 2020.2.2, 2020.

[352] Daylight Chemical Information Systems Inc. Daylight Theory: SMARTS - A Language for Describing Molecular Patterns, 2012.

[353] Daylight Chemical Information Systems Inc. Daylight Theory: SMIRKS - A Reaction Transform Language, 2019.

[354] D.A. Case, H.M. Aktulga, K. Belfon, I.Y. Ben-Shalom, S.R. Brozell, D.S. Cerutti, T.E. Cheatham, G.A. Cisneros, V.W.D. Cruzeiro, T.A. Darden, R.E. Duke, G. Giambasu, M.K. Gilson, H. Gohlke, A.W. Goetz, R. Harris, S. Izadi, S.A. Izmailov, C. Jin, K. Ka, and P.A. Kollman. Amber 2021, 2021.

[355] Eric W. Lemmon, Mark O. McLinden, and Daniel G. Friend. Thermophysical properties of fluid systems. In P.J. Linstrom and W.G. Mallard, editor, *NIST Chemistry WebBook, NIST Standard Reference Database Number 69*, chapter Thermophys. National Institute of Standards and Technology, Gaithersburg MD, 20899. doi: https://doi.org/10.18434/T4D303.

[356] In Chul Yeh and Gerhard Hummer. System-size dependence of diffusion coefficients and viscosities from molecular dynamics simulations with periodic boundary conditions. *Journal of Physical Chemistry B*, 108(40):15873–15879, 2004. doi: 10.1021/jp0477147.

[357] Maziar Heidari, Kurt Kremer, Raffaello Potestio, and Robinson Cortes-Huerto. Fluctuations, finite-size effects and the thermodynamic limit in computer simulations: Revisiting the spatial block analysis method, 2018.

[358] Sander Vandenhaute, Sven M. J. Rogge, and Veronique Van Speybroeck. Large-scale molecular dynamics simulations reveal new insights into the phase transition mechanisms in MIL-53(Al). *Frontiers in Chemistry*, 9:699, 2021. doi: 10.3389/fchem.2021.718920.

[359] John D Chodera. A simple method for automated equilibration detection in molecular simulations. *Journal of Chemical Theory and Computation*, 12(4):1799–1805, 2016. doi: 10.1021/acs.jctc.5b00784.

[360] BIOVIA; and Dassault Systèmes. Materials studio.

[361] S.; Shenogin and R.; Ozikin. Xenoview, 2007.

[362] Michael E. Fortunato, Lauren J. Abbott, Kyle E Hart, and Coray M. Colina. nuSIMM: nanoHUB user Simulation Interface for Molecular Modeling, 2015.

[363] Lauren J. Abbott, Kyle E. Hart, and Coray M. Colina. Polymatic: A generalized simulated polymerization algorithm for amorphous polymers. *Theoretical Chemistry Accounts*, 132(3):1–19, 2013. doi: 10.1007/s00214-013-1334-z.

[364] Michael E. Fortunato and Coray M. Colina. polysimtools/pysimm: python simulation interface for molecular modeling.

[365] Gregory S Larsen, Ping Lin, Kyle E Hart, and Coray M Colina. Molecular simulations of pim-1-like polymers of intrinsic microporosity. *Macromolecules*, 44(17):6944–6951, 2011. doi: 10.1021/ma200345v.

[366] Martin Vögele and Gerhard Hummer. Divergent diffusion coefficients in simulations of fluids and lipid membranes. *The Journal of Physical Chemistry B*, 120(33):8722–8732, 2016. doi: 10.1021/acs.jpcb.6b05102.

[367] H. Sun. Compass: An ab initio force-field optimized for condensed-phase applications - Overview with details on alkane and benzene compounds. *Journal of Physical Chemistry B*, 102(38):7338–7364, 1998. doi: 10.1021/jp980939v.

[368] Huai Sun, Zhao Jin, Chunwei Yang, Reinier L.C. Akkermans, Struan H. Robertson, Neil A. Spenley, Simon Miller, and Stephen M. Todd. COMPASS II: extended coverage for polymer and drug-like molecule databases. *Journal of Molecular Modeling*, 22(2):1–10, 2016. doi: 10.1007/s00894-016-2909-0.

[369] Aidan P. Thompson, H. Metin Aktulga, Richard Berger, Dan S. Bolintineanu, W. Michael Brown, Paul S. Crozier, Pieter J. in 't Veld, Axel Kohlmeyer, Stan G. Moore, Trung Dac Nguyen, Ray Shan, Mark J. Stevens, Julien Tranchida, Christian Trott, and Steven J. Plimpton. LAMMPS - a flexible simulation tool for particle-based materials modeling at the atomic, meso, and continuum scales. *Computer Physics Communications*, 271:108171, 2022. doi: 10.1016/j.cpc.2021.108171.

[370] K. Vanommeslaeghe, E. Hatcher, C. Acharya, S. Kundu, S. Zhong, J. Shim, E. Darian, O. Guvench, P. Lopes, I. Vorobyov, and A. D. Mackerell. CHARMM general force field: A force field for drug-like molecules compatible with the CHARMM all-atom additive biological force fields. *Journal of Computational Chemistry*, 31(4):671–690, 2010. doi: 10.1002/jcc.21367.

[371] William L. Jorgensen, David S. Maxwell, and Julian Tirado-Rives. Development and testing of the OPLS all-atom force field on conformational energetics and properties of organic liquids. *Journal of the American Chemical Society*, 118(45): 11225–11236, 1996. doi: 10.1021/ja9621760.

[372] Stephen L. Mayo, Barry D. Olafson, and William A. Goddard. DREIDING: A generic force field for molecular simulations. *Journal of Physical Chemistry*, 94 (26):8897–8909, 1990. doi: 10.1021/j100389a010.

[373] Jeff Wagner, Matt Thompson, David Dotson, Hyejang, SimonBoothroyd, and Jaime Rodríguez-Guerra. openforcefield/openff-forcefields: Version 2.0.0 "Sage". *zenodo.org*, 2021. doi: 10.5281/ZENODO.5214478.

[374] T. D.; Verstraelen, T.; Tecmer, P.; Heidar-Zadeh, F.; Boguslawski, K.; Chan, M.; Zhao, Y.; Kim, D.; Vandenbrande, S.; Yang, D.; González-Espinoza, C. E.; Fias, S.; Limacher, P. A.; Berrocal, and P. W. Malek, A.; Ayers. Horton 2.0.0, 2015.

[375] Toon Verstraelen, Steven Vandenbrande, Farnaz Heidar-Zadeh, Louis Vanduyfhuys, Veronique Van Speybroeck, Michel Waroquier, and Paul W. Ayers. Minimal basis iterative Stockholder: Atoms in molecules for force-field development. *Journal of Chemical Theory and Computation*, 12(8):3894–3912, 2016. doi: 10.1021/acs.jctc.6b00456.

[376] Bruce L. Bush, Christopher I. Bayly, and Thomas A. Halgren. Consensus bond-charge increments fitted to electrostatic potential or field of many compounds: Application to MMFF94 training set. *Journal of Computational Chemistry*, 20(14): 1495–1516, 1999. doi: 10.1002/(sici)1096-987x(19991115)20:14⟨1495::aid-jcc3⟩3.0.co;2-3.

[377] Michael Schauperl, Paul S. Nerenberg, Hyesu Jang, Lee Ping Wang, Christopher I. Bayly, David L. Mobley, and Michael K. Gilson. Non-bonded force field model with advanced restrained electrostatic potential charges (RESP2). *Communications Chemistry*, 3(1):1–11, 2020. doi: 10.1038/s42004-020-0291-4.

[378] Nikos Ch Karayiannis, Vlasis G. Mavrantzas, and Doros N. Theodorou. Detailed atomistic simulation of the segmental dynamics and barrier properties of amorphous poly(ethylene terephthalate) and poly(ethylene isophthalate). *Macromolecules*, 37 (8):2978–2995, 2004. doi: 10.1021/ma0352577.

[379] Dieter Hofmann, Lydia Fritz, Jens Ulbrich, Claudia Schepers, and Martin Bhning. Detailed-atomistic molecular modeling of small molecule diffusion and solution processes in polymeric membrane materials. *Macromolecular Theory and Simulations*, 9(6):293–327, 2000. doi: 10.1002/1521-3919(20000701)9:6⟨293::AID-MATS293⟩3.0.CO;2-1.

[380] Edward J. Maginn, Richard A. Messerly, Daniel J. Carlson, Daniel R. Roe, and J. Richard Elliot. Best practices for computing transport properties 1. self-diffusivity and viscosity from equilibrium molecular dynamics [Article v1.0]. *Living Journal of Computational Molecular Science*, 2(1):6324, 2020. doi: 10.33011/livecoms.1.1.6324.

Large-scale molecular systems of guaiacol in hot pressurized water (front) and poly(2-ethyl-2-oxazoline)-based therapeutic nanofibers (back).